Physics of the Solid State, Vol. 44, No. 6, 2002, pp. 1003–1007. Translated from Fizika Tverdogo Tela, Vol. 44, No. 6, 2002, pp. 961–965.

METALS AND SUPERCONDUCTORS

The Fine Structure of FCC Nanocrystals in Al- and Ni-Based Alloys

G. E. Abrosimova and A. S. Aronin

Institute of Solid State Physics, Russian Academy of Sciences, Chernogolovka, Moscow oblast, 142432 Russia

e-mail: gabros@issp.ac.ru

Received July 30, 2001

Abstract—The structural perfection of nanocrystals in alloys of different chemical composition is studied by x-ray diffraction and high-resolution electron microscopy. In all the alloys studied, crystallization of the amorphous phase produces a nanocrystalline structure. The nanocrystal size depends on the chemical composition of the alloy and varies in aluminum-based alloys from 5 nm in $Al_{89}Ni_5Y_6$ to 12 nm in $Al_{82}Ni_{11}Ce_3Si_4$. Nanocrystals in nickel-based alloys vary in size from 15 to 25 nm. Al nanocrystals are predominantly defect-free, with microtwins observed only in some nanocrystals. The halfwidth of the diffraction lines is proportional to $\sec\theta$, which implies the small grain size provides the major contribution to the broadening. Nanocrystals in nickel alloys contain numerous twins, stacking faults, and dislocations. © *2002 MAIK "Nauka/Interperiodica".*

1. INTRODUCTION

A nanocrystalline structure that forms during crystallization of an amorphous phase attracts considerable interest both from the viewpoint of the possibility of developing novel materials with promising physical chemical properties and as an unusual material in which the structural constituents do not exceed a few tens of nanometers in size [1, 2]. In most cases, the nanocrystalline structure is two-phase and consists of nanoparticles of a crystalline phase embedded in an amorphous host [3]. In some cases, however, the nanocrystalline structure may also be made up of nanoparticles of different crystalline phases [4]. The degree of structural perfection of nanocrystals is one of the most important characteristics of nanocrystalline materials. It is known, for instance, that light nanocrystalline alloys have a high strength [5, 6]. Aluminum-based alloys containing 6–15% of a transition metal (Fe or Ni) and a few percent of a rare-earth metal may feature a yield strength as high as 1.6 GPa [7] while having, at the same time, a good plasticity. To properly understand the processes involved in the plastic deformation of such materials, one has to know the specific features of their structure (the fraction of nanocrystals, their mutual arrangement) and the possibility of deformation, i.e., the degree of perfection of the nanocrystals. It is important to compare this characteristic of perfection in alloys of different mechanical properties and establish the relation connecting the structure with the properties of the material. This paper reports on a study of the perfection of nanocrystals in aluminum- and nickel-based alloys.

2. EXPERIMENTAL

Al–Ni–*Re* (*Re* = Y, Ce, Yb) and Ni–Mo–B amorphous alloys were prepared in the form of ribbons by melt quenching on a rapidly rotating wheel. The cooling rate was ~10^6 K/s, and the ribbons thus obtained were 3 mm wide and ~30 μm thick. X-ray measurements were performed on a Siemens D-500 diffractometer with CuK_α radiation. The microstructure was studied with a high-resolution JEM-4000EX electron microscope at an accelerating voltage 400 kV. A direct image of the nanocrystal lattice was obtained by recording a series of images made with different defocusing, followed by computer processing. In this paper, we present photomicrographs obtained at an optimum defocusing $\delta = -46$ nm corresponding to the Scherzer focus ($\delta \cong -1.2 C_s^{1/2} \lambda^{1/2}$, where C_s is the spherical-aberration constant equal to 1 mm and λ is the electron wavelength). The foils for the electron microscopy studies were prepared by ion milling. The alloy composition was determined by x-ray spectral analysis.

3. RESULTS AND DISCUSSION

The as-prepared samples were amorphous. The corresponding x-ray and electron diffraction patterns exhibit only broad maxima, with no peaks due to crystalline phases present. The high-resolution images of the structure of the as-prepared alloy feature only the mazy contrast typical of an amorphous structure. Following controlled crystallization, a nanocrystalline structure formed in all the alloys.

When heated, all the samples crystallized by the primary mechanism. In aluminum-based alloys, fcc Al crystals precipitate. At the end of the first crystallization stage, the structure of the Al–Ni–*Re* alloys consists

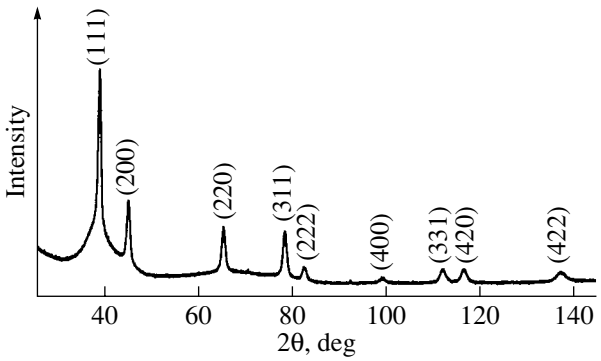

Fig. 1. Diffraction pattern of the $Al_{88}Ni_6Y_6$ nanocrystalline alloy.

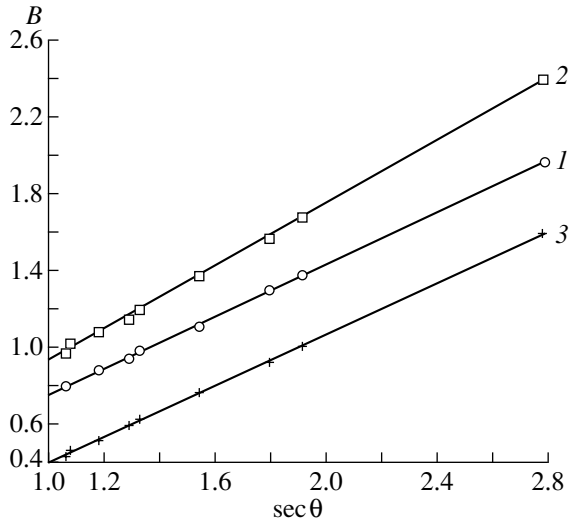

Fig. 2. Halfwidth of the reflections of (*1*) the $Al_{88}Ni_6Y_6$, (*2*) $Al_{88}Ni_{10}Y_2$, and (*3*) $Al_{82}Ni_{11}Ce_3Si_4$ nanocrystalline alloys plotted vs. $\sec\theta$.

of fcc Al nanocrystals dispersed randomly throughout the amorphous host, whose size depends on the chemical alloy composition and varies from 5 nm in $Al_{89}Ni_5Y_6$ to 12 nm in $Al_{82}Ni_{11}Ce_3Si_4$.

Figure 1 presents a typical x-ray diffraction pattern of an aluminum-based nanocrystalline alloy. The pattern is seen to contain both broad lines due to fcc Al nanocrystals and a diffuse halo originating from the amorphous phase.

The width of the diffraction line may depend on a number of factors. Among them are the small size of the crystals, the presence of various defects, and inhomogeneities in the chemical composition.

The broadening due to the small grain size is described by the Selyakov–Scherrer expression [8]

$$L = \lambda(1/\cos\theta)/\Delta(2\theta),$$

where L is the grain size, λ is the wavelength of the radiation used, θ is the reflection angle, and $\Delta(2\theta)$ is the halfwidth of the corresponding reflection. The halfwidth of the diffraction lines is usually denoted by B; this notation will be employed in the graphs below. As the halfwidth of diffraction reflections in nanocrystalline materials is large, one can neglect the instrumental broadening.

The broadening proportional to $1/\cos\theta$ (i.e., to $\sec\theta$) can also be caused by stacking faults in the material. For instance, a stacking fault in an fcc structure changes the ...*ABCABC*... sequence of the {111} planes to ...*ABCACABC*... . The broadening caused by stacking faults is similar to that originating from small particle size, but its magnitude depends on the defect concentration and interference indices; i.e., stacking faults can produce crystallographic anisotropy in the calculated grain size, even if the true particle dimensions are independent of crystallographic direction.

If crystals contain randomly distributed dislocations, the displacement of atoms from lattice sites is determined by the superposition of displacements due to each dislocation and, therefore, the action of dislocation fields can be treated phenomenologically as a local change in the interplanar distance [9]. The diffraction line broadening $2\Delta(2\theta)$ (or B) can be written in this case as

$$2\Delta(2\theta) = 4(\Delta d_m/d_0)\tan\theta,$$

where Δd_m is the average maximum change in the distance between the *hkl* planes and d_0 is the interplanar distance in a perfect crystal. Thus, the broadening originating from a random dislocation distribution is proportional to $\tan\theta$.

By analyzing the angular dependence of the broadening, one can reveal the factor responsible for the major contribution to it; indeed, if the broadening is proportional to $\sec\theta$, it is caused by the small crystallite size, but if it is proportional to $\tan\theta$, the broadening originates from dislocations and their clusters, which generate long-range distortion fields.

Part of the reflections presented in Fig. 1 is due to the superposition of reflections from the crystalline phase and from nanocrystals; therefore, one should first separate them. For this purpose, special computer codes were used which permit background correction, smoothening, and deconvolution of overlapping maxima, as well as determination of the halfwidth of the maxima. The shape of a diffuse maximum was fitted by a Gaussian $h\exp(-ax^2)$, the fitting of the calculations to experimental data being preformed in both parameters h and a.

Figure 2 plots the dependence of the halfwidth B of diffraction reflections on $\sec\theta$ for a sample of the $Al_{88}Ni_6Y_6$ alloy (curve *1*) whose diffraction pattern is shown in Fig. 1. Similar curves for other aluminum-based alloys are also presented in Fig. 2.

All three dependences can be fitted with good accuracy by straight lines, with the variance $\Sigma(y - y_i)^2$ (y_i are the experimental values, and y are obtained in calculations) not exceeding 0.005; the variance is 0.0008 for $Al_{88}Ni_6Y_6$, 0.0035 for $Al_{88}Ni_{10}Y_2$, and 0.001 for $Al_{82}Ni_{11}Ce_3Si_4$. At the same time, the similar dependence of the halfwidth of diffraction peaks on $\tan\theta$ is obviously not linear (Fig. 3). An attempt to fit it with a linear function yields a substantially larger variance (0.045).

Thus, analysis of the angular dependences of diffraction reflections allows one to conclude that the broadening of diffraction lines in aluminum-based nanocrystalline alloys is dominated by the small grain size. This conclusion also correlates with the data obtained by high-resolution electron microscopy. The corresponding studies show the nanocrystals in aluminum-based alloys to be predominantly defect-free. Microtwins are observed only in rare cases. A typical image of nanocrystals in such a structure is displayed in Fig. 4.

The nanocrystalline structure was also studied in nickel-based alloys. The studies were performed on three alloys of the following compositions: $(Ni_{70}Mo_{30})_{90}B_{10}$, $(Ni_{70}Mo_{30})_{95}B_5$, and $(Ni_{65}Mo_{35})_{90}B_{10}$. The as-prepared alloys were amorphous; indeed, diffraction studies did not reveal any indication of crystalline phases and only diffuse maxima typical of an amorphous structure were observed. Heating amorphous alloys gives rise to their crystallization. The crystallization proceeds by the primary mechanism. By this mechanism, the amorphous matrix produces crystals (in our case, of a nickel-based solid solution) whose composition differs from that of the original alloy. The composition of the matrix changes after the precipitation of the primary crystals. The lattice parameters of the fcc solid-solution grains of the alloys under study were changed depending on the time the alloys were maintained isothermally at 600°C. After a 6 h annealing at 600°C, the average size of the nanocrystals was 13 nm for $(Ni_{70}Mo_{30})_{90}B_{10}$ and $(Ni_{65}Mo_{35})_{90}B_{10}$ and 17 nm for $(Ni_{70}Mo_{30})_{95}B_5$. A typical x-ray diffraction pattern for a nickel-based nanocrystalline alloy is displayed in Fig. 5. It closely resembles the pattern shown in Fig. 1, which gives one grounds to assume that the angular dependences of the diffraction peak halfwidth would also be the same. Figure 6 presents the dependence of the diffraction maximum halfwidth on $\sec\theta$ for the $(Ni_{65}Mo_{35})_{90}B_{10}$ alloy obtained for two anneal times, 5 and 144 h. The average nanocrystal size after annealing for 144 h is 17 nm for $(Ni_{70}Mo_{30})_{90}B_{10}$, 19 nm for $(Ni_{70}Mo_{30})_{95}B_5$, and 27 nm for $(Ni_{65}Mo_{35})_{90}B_{10}$. A high-resolution image of such a microstructure is presented in Fig. 7. The particle on the right reveals numerous stacking faults.

It appears natural that as the thermal treatment duration increases, the size of the nanocrystals should also slightly increase and the halfwidth of the diffraction

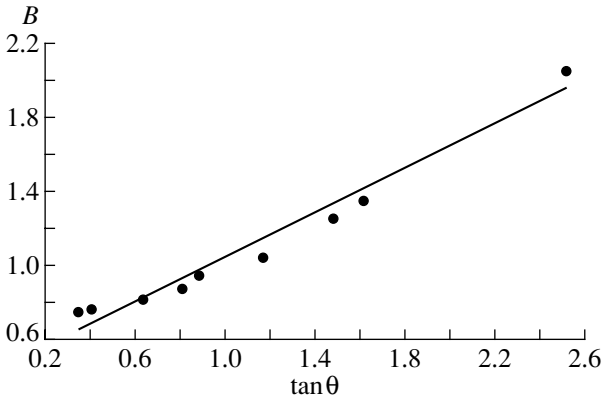

Fig. 3. Halfwidth of the reflections of the $Al_{86}Ni_{11}Yb_3$ nanocrystalline alloy plotted vs. $\tan\theta$.

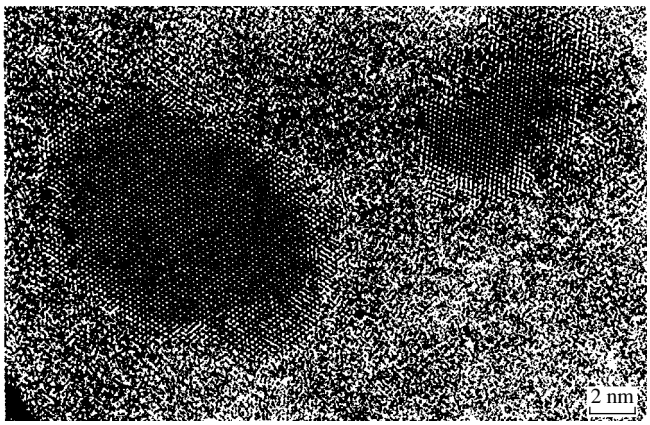

Fig. 4. Microstructure of the $Al_{88}Ni_6Y_6$ alloy.

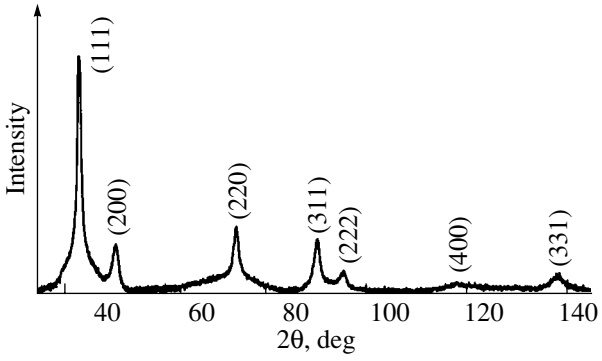

Fig. 5. Diffraction pattern of the $(Ni_{65}Mo_{35})_{90}B_{10}$ alloy after annealing at 600°C for 5 h.

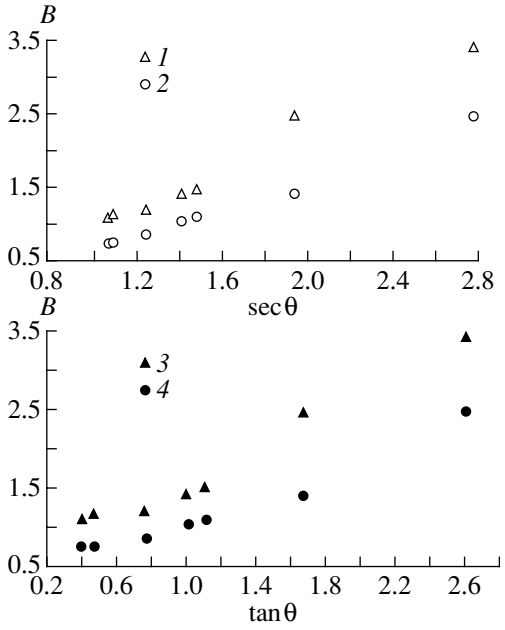

Fig. 6. Angular dependences of the halfwidth of diffraction maxima of the $(Ni_{65}Mo_{35})_{90}B_{10}$ alloy annealed at 600°C for (*1*, *3*) 5 and (*2*, *4*) 144 h.

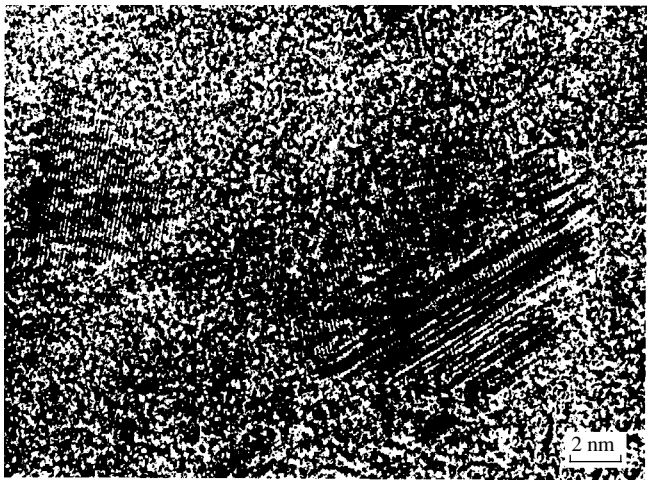

Fig. 7. High-resolution image of the microstructure of the $(Ni_{65}Mo_{35})_{90}B_{10}$ alloy.

maxima should decrease. It is seen, however, that none of the relations presented is linear; in other words, both the small size of the nanocrystals and the dislocations contribute to the line broadening. The high-resolution electron microscope image also exhibits numerous defects. Hence, both x-ray diffraction and electron microscopy indicate the presence of numerous twins, stacking faults, and dislocations in nanocrystals in the Ni–Mo–B alloys.

A question naturally arises as to the reason for such differences in the nanocrystal structure. We consider two main factors which can account for these differences.

(1) Size factor. As already mentioned, aluminum nanocrystals do not exceed 10 nm in size, whereas the size of the Ni(Mo) particles is about 20 nm. When dislocations form (by the Frank–Read or another mechanism), the dislocation loop size is about $10^2 b$ (**b** is the Burgers vector) [10]. The magnitude of the Burgers vector is $b = a/2[110] = 0.349$ nm for Al and 0.2501 nm for Ni. We thus see that while in Ni(Mo) nanocrystals a loop can still exist (because the nanocrystals are 70–110*b* in size), the presence of loops ≈30*b* in size in aluminum nanocrystals is not likely.

(2) The formation of stacking faults depends on their energy. The stacking fault energy for aluminum is 135 erg cm^{-2}; for nickel, 240 erg cm^{-2} [11]. One should, however, bear in mind that nanocrystals in Al–Ni–*Re* alloys are actually Al precipitates [12], but in Ni–Mo–B alloys, they contain about 17 at. % Mo [3]. As follows from [13], when fcc materials are alloyed, the stacking fault energy decreases with increasing electron concentration. For instance, in copper and silver alloys, the stacking fault energy decreases by about ten times, with an increase in the electron concentration of 20% [13, 14]. Adding 17 at. % Mo to nickel alloys also increases the electron concentration by about 20%. Therefore, if we assume that the dependence of stacking fault energy in nickel alloys on electron concentration is similar to that for other fcc alloys, we can expect a substantial decrease (by a few times) in this energy in the above alloys. In these conditions, the energy of the Ni(Mo) stacking faults will be lower than that of the Al stacking faults and, hence, the probability of stacking fault formation in these alloys will be higher.

Both these factors can account for the differences in the structure of nanocrystals observed experimentally in our work, namely, the perfect structure of the Al nanocrystals and defects in the Ni(Mo) nanocrystals.

Thus, our study shows that nanocrystals in alloys of the Al–Ni–*Re* systems (*Re* = Y, Ce, Yb) have a substantially better structural perfection than those in the nickel-based alloy.

ACKNOWLEDGMENTS

The study was supported by the Russian Foundation for Basic Research (project nos. 99-02-17459 and 99-02-17477).

REFERENCES

1. A. Inoue, Mater. Sci. Eng. A **179/180**, 57 (1994).
2. K. Nakazato, Y. Kawamura, A. P. Tsai, and A. Inoue, Appl. Phys. Lett. **63**, 2644 (1993).
3. G. Abrosimova, A. Aronin, Yu. V. Kir'janov, *et al.*, J. Mater. Sci. **34** (7), 1611 (1999).

4. V. Cremaschi, B. Arcondo, H. Sirkin, *et al.*, J. Mater. Res. **15** (9), 1936 (2000).
5. Y. He, J. F. Poon, and G. Y. Shiflet, Science **241**, 1640 (1988).
6. A. Inoue, T. Ochiai, Y. Horio, and T. Masumoto, Mater. Sci. Eng. A **179/180**, 649 (1994).
7. Y. H. Kim, A. Inoue, and T. Masumoto, Mater. Trans., JIM **32**, 331 (1991).
8. A. A. Rusakov, *X-ray Diffraction of Metals* (Atomizdat, Moscow, 1977).
9. Ya. S. Umanskiĭ, Yu. A. Skakov, A. N. Ivanov, and L. N. Rastorguev, *Crystallography, x-ray Diffraction, and Electron Microscopy* (Metallurgiya, Moscow, 1982).
10. J. P. Hirth and J. Lothe, *Theory of Dislocations* (McGraw-Hill, New York, 1967; Atomizdat, Moscow, 1972).
11. P. S. Dabson and L. M. Clarebrough, Philos. Mag. **9**, 865 (1964).
12. G. E. Abrosimova, A. S. Aronin, Yu. V. Kir'janov, *et al.*, Nanostruct. Mater. **12**, 617 (1999).
13. P. C. J. Gallagher, Trans. AIME **1**, 2429 (1970).
14. A. Howie and P. R. Swann, Philos. Mag. **6**, 1215 (1961).

Translated by G. Skrebtsov

Physics of the Solid State, Vol. 44, No. 6, 2002, pp. 1008–1015. Translated from Fizika Tverdogo Tela, Vol. 44, No. 6, 2002, pp. 966–972.

METALS AND SUPERCONDUCTORS

Hyperfine Interactions of Tin Atoms in Samarium

I. N. Rozantsev and V. P. Gor'kov

Skobeltsyn Research Institute of Nuclear Physics, Moscow State University, Vorob'evy gory, Moscow, 119899 Russia

e-mail: roz@srd.msu.ru

Received August 6, 2001

Abstract—The hyperfine interactions of ^{119}Sn impurity atoms in samarium at temperatures from 5 to 70 K are investigated by Mössbauer spectroscopy. The distributions P of magnetic hyperfine fields B_{hf} for tin atoms at sites of the hexagonal $[P_h(B_{hf})]$ and cubic $[P_c(B_{hf})]$ samarium sublattices are determined from the experimental absorption spectra. Ion ordering in pairs of magnetic centers located in layers of the cubic sublattice is observed by Mössbauer spectroscopy for the first time. Each magnetic center involves ordered ions at the nearest neighbor sites of the tin atom replacing the samarium ion at the hexagonal lattice site. The quadrupole coupling constant $e^2q_hQ = 0.59 \pm 0.12$ mm/s is determined for tin atoms at the hexagonal sublattice sites of samarium. The quadrupole interaction of tin atoms in heavy rare-earth metals (from Tb to Er) with a hexagonal close-packed structure is discussed. *© 2002 MAIK "Nauka/Interperiodica".*

1. INTRODUCTION

Hyperfine interactions of nonmagnetic impurity atoms in rare-earth metals have long since attracted the particular attention of physicists. In heavy rare-earth metals (from Gd to Er), the hyperfine interactions have been investigated by Mössbauer spectroscopy for tin atoms [1–8] and by perturbed-angular-correlation spectroscopy for cadmium atoms [9, 10]. However, similar studies of hyperfine interactions in light rare-earth metals have been hampered by the fact that these metals exhibit a complex local magnetic structure. Some insight into these difficulties can be gained, for example, from the results of Mössbauer measurements for tin in neodymium [11]. Samarium has a relatively simple magnetic structure [12]. The first investigations into hyperfine interactions of tin and cadmium atoms in samarium revealed a few magnetic hyperfine fields B_{hf}(Sn) at Sn nuclei in the hexagonal sublattice at low temperatures [13] and only one field B_{hf} at Cd nuclei in the same sublattice over the entire range of magnetic ordering [14]. With the aim of resolving this contradiction, we undertook the present investigation. Earlier, Reĭman and Rozantsev [15] determined the magnetic hyperfine field B_{hf}(Sn) in samarium and used the result obtained to analyze the dependence of the field B_{hf}(Sn) in rare-earth metals on the projections of the spin and the orbital angular momentum of rare-earth ions and the radial dependence of the partial contributions of these ions to the field B_{hf}(Sn).

Samarium has a rhomobohedral crystal lattice that consists of nine layers with cubic (*c*) and hexagonal (*h*) symmetries of the environment (*chhchh*…). For brevity, hereafter, the sites located in the *c* and *h* layers will be referred to as the *c* and *h* sites, respectively. Samarium is an antiferromagnet with two Néel temperatures: T_{N1} = 106 K and T_{N2} = 13.8 K. At temperatures below T_{N1}, the magnetic moments of samarium ions in the hexagonal sublattice are collinearly ordered with respect to the hexagonal axis *c*. These moments of samarium ions are ferromagnetically ordered in pairs of adjacent *h* layers and antiferromagnetically alternate in pairs of *h* layers separated by the *c* layer. At temperatures below T_{N2}, samarium ions in the *c* layers are ordered to form an *A*1-type antiferromagnetic structure composed of pairs of adjacent ferromagnetic rows aligned parallel to the a_2 axis. Pairs of these rows with oppositely aligned moments of the samarium ions alternate along the a_1 axis (+ + – – …). The magnetic moments of samarium ions at the *c* and *h* sites are collinear to the *c* axis. The magnetic structure of the *h* layers is retained at temperatures below 14 K.

In rare-earth metals and their compounds, the locality of the magnetic hyperfine field B_{hf} at nonmagnetic atoms and the additivity of the contributions from individual rare-earth ions (at the nearest neighbor sites of these nonmagnetic atoms) to the field B_{hf} [16, 17] make it possible to predict changes in the field B_{hf} at a tin atom with variations in the local magnetic structure in the neighborhood of this atom. The contributions of the ferromagnetically ordered ions of a particular rare-earth element to the hyperfine field B_{hf} have the same sign, and their total contribution is proportional to the number of these ions, because the sign of the contribution of a rare-earth ion correlates with the direction of its spin [15, 17]. The contributions of the antiferromagnetically ordered ions to the field B_{hf} are of opposite sign. In this case, the total contribution is equal to the difference between the contributions of the ions with oppositely aligned moments and depends on the effective number of the ions inducing this field. The contribution of an individual rare-earth ion to the field B_{hf} consists of the spin and orbital contributions, which are

1063-7834/02/4406-1008$22.00

proportional to the projections of the spin and the orbital momentum of this ion [15, 17]. The contributions of samarium ions located at sites with different symmetries of the environment to the hyperfine field B_{hf} are proportional to the projections of the sums of the spins and the orbital momenta of the ions at the relevant sites. Each of the sites in the samarium lattice has 12 nearest neighbor sites, of which six sites are located in the same layer as the site under consideration, three sites occupy one of the two adjacent layers, and three sites occupy the other adjacent layer.

Let us analyze how the ordering of samarium ions affects the magnetic hyperfine field B_{hf} at tin atoms whose environment retains the local magnetic structure of pure samarium. In what follows, the magnetic hyperfine field B_{hf} for tin atoms at the *h* sites will be designated as $B_{hf}(9)$. In the temperature range from T_{N1} to T_{N2}, the field $B_{hf}(9)$ for tin atoms at the *h* sites is determined by samarium ions with parallel magnetic moments at the nine nearest neighbor *h* sites of each tin atom, because the samarium ions of two adjacent *h* layers are ordered ferromagnetically. The Mössbauer spectrum should exhibit a magnetic sextet attributed to these tin atoms and a paramagnetic line of tin atoms at the *c* sites. This line transforms into a sextet as the samarium ions in the *c* layers are ordered. Note that the field B_{hf} at tin atoms in the aforementioned layers is effectively determined by two samarium ions with parallel magnetic moments at the nearest neighbor *c* sites which are occupied by four samarium ions with the same direction of the magnetic moments and two samarium ions with opposite moments. The contributions of the samarium ions of two adjacent *h* layers (on opposite sides of the *c* layer) to the field B_{hf} at these tin atoms cancel each other due to antiferromagnetic ordering of the ions.

In the case when the samarium ions are ordered at the *c* sites, the magnetic hyperfine field $B_{hf}(9)$ should split into four components. Each of these components is induced either by nine ferromagnetically ordered ions at the nearest neighbor *h* sites of the tin atom and three ions with parallel moments or, effectively, by one ion at the nearest neighbor *c* site. In the *h* layers, tin atoms occupy equally probable positions in which the net moments of the ions at the nearest neighbor *c* and *h* sites are parallel and antiparallel to each other, respectively, whereas the moments of three ions at the nearest neighbor *c* sites are parallel to each other or the moment of one of these three ions is antiparallel to the moments of the two other ions. The Mössbauer spectra should exhibit four sextets with identical intensities rather than one sextet.

If the samarium ion at the *h* site is replaced by a tin atom, the interactions between each of the three ions at the nearest neighbor *c* sites of this atom and the antiferromagnetically ordered ions of the two adjacent *h* layers do not cancel each other. The resultant interaction with ions of these layers is equivalent to the interaction with one ordered ion at the *h* site free of a tin atom. This interaction, together with the interaction of ions in the *c* layer, should bring about their ordering at temperatures above T_{N2}.

The aim of the present work was to determine the magnetic-hyperfine-field distributions for tin atoms at sites of the cubic $[P_c(B_{hf})]$ and hexagonal $[P_h(B_{hf})]$ samarium sublattices and the hyperfine parameters of tin atoms in samarium.

2. EXPERIMENTAL TECHNIQUE AND RESULTS

The samples were prepared by melting samarium (purity, 99.7%) with a calculated content of 1.5 at. % ^{119}Sn in an induction furnace in an argon atmosphere.

The absorption Mössbauer spectra of ^{119}Sn in samarium were measured in the temperature range 5–70 K on a spectrometer operating in a constant-acceleration mode. The spectrometer was equipped with a $CaSnO_3$ resonance detector. The samples under investigation were cooled in a helium-flow cryostat. A radioactive source in the form of $CaSnO_3$ was used at room temperature.

Figure 1 shows typical experimental Mössbauer spectra. All the spectra were processed with the aim to determine the distributions $P(B_{hf})$ in the form of histograms. The distribution function $P(B_{hf})$ was determined by minimizing the χ^2 functional according to the FUMILI program. The calculated Mössbauer spectrum was represented as a convolution of the distribution $P(B_{hf}) = P_c(B_{hf}) + P_h(B_{hf})$ and an elementary magnetic sextet with a Lorentzian linewidth of 1 mm/s. Apart from the components of the distribution, we varied the quadrupole shifts Δ_c and Δ_h and the isomer shift. Selected histograms are displayed in Fig. 2. In these histograms, one interval corresponds to two scale divisions in the spectrum. The distributions P_c and P_h are shifted with respect to each other, because their edges overlap at 5 K. For each of the histograms P_c and P_h, the relative intensity is taken equal to unity. The widths of discrete components (including those falling in two adjacent intervals), as a rule, do not exceed the width of one interval of the histogram. The distribution P_c contains up to nine components P_i, which are numbered in order of increasing magnetic hyperfine field $B_{hf}(i)$. The component P_0 corresponds to hyperfine fields $B_{hf} <$ 0.35 T.

The most intense component of the distribution P_h at 70 K (Fig. 2) is assigned to the expected field $B_{hf}(9)$, which is induced by nine ferromagnetically ordered ions at the nearest neighbor *h* sites of the tin atom. This component is designated as P_9. The components $P_i^<$ are numbered in order of increasing hyperfine fields $B_{hf}^<(i) < B_{hf}(9)$, and the components $P_i^>$ are numbered

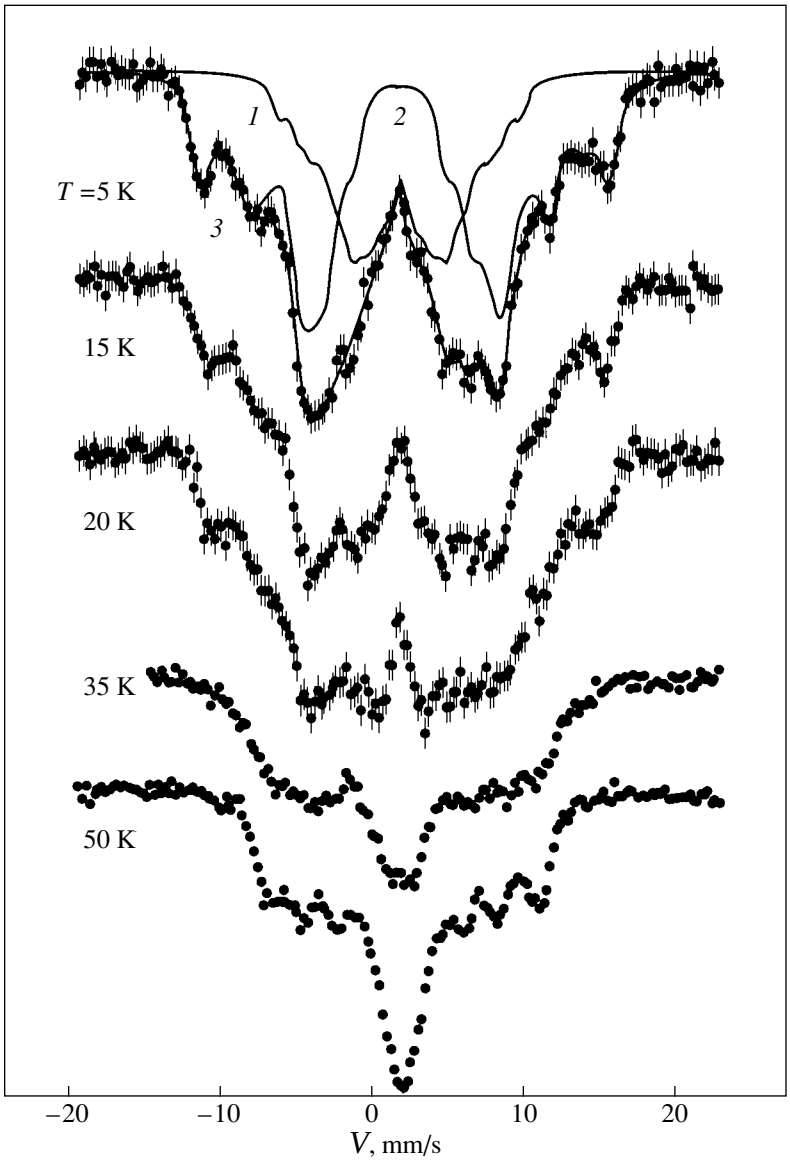

Fig. 1. The absorption Mössbauer spectra of ^{119}Sn impurity atoms in samarium at temperatures from 50 to 5 K. For the Mössbauer spectrum measured at 5 K, solid lines represent (*1*) the spectrum corresponding to the distribution $P_c(B_{hf})$ for Sn atoms at sites of the cubic samarium sublattice, (*2*) the spectrum corresponding to the distribution $P_h(B_{hf})$ for Sn atoms at sites of the hexagonal samarium sublattice, and (*3*) the overall spectrum.

in order of decreasing hyperfine field $B_{hf}^{>}(i) \geq B_{hf}(9)$. The components of the distribution P_h at temperatures from 15 to 50 K are divided into two types reasoning from the constancy of the sum of the intensities of all the components $P_i^{>}$ (0.35 ± 0.01), including the P_9 component. At 50 K, the separation of the P_i components from the P_9 component is reflected in its shape.

For both sublattices of samarium, the ^{119}Sn isomer shifts coincide and are equal to 1.95 ± 0.05 mm/s at 5 K. The quadrupole shifts are as follows: $\Delta_c <$ 0.08 mm/s and $\Delta_h = 0.15 \pm 0.03$ mm/s. These quantities correspond to both the quadrupole coupling constant for tin atoms at the *h* sites of samarium ($e^2q_hQ = 0.59 \pm$ 0.12 mm/s, where *q* is the electric-field gradient at the ^{119}Sn nucleus and *Q* is the quadrupole moment of the ^{119}Sn nucleus) and the upper limit of its magnitude for tin atoms at the *c* sites ($|e^2qQ| < 0.3$ mm/s) in the case when the hyperfine field B_{hf}(Sn) is aligned parallel to the hexagonal axis *c*.

The distribution P_h even at 70 K includes at least four components. The number of components increases to 12 with a decrease in the temperature to 35 K. A fur-

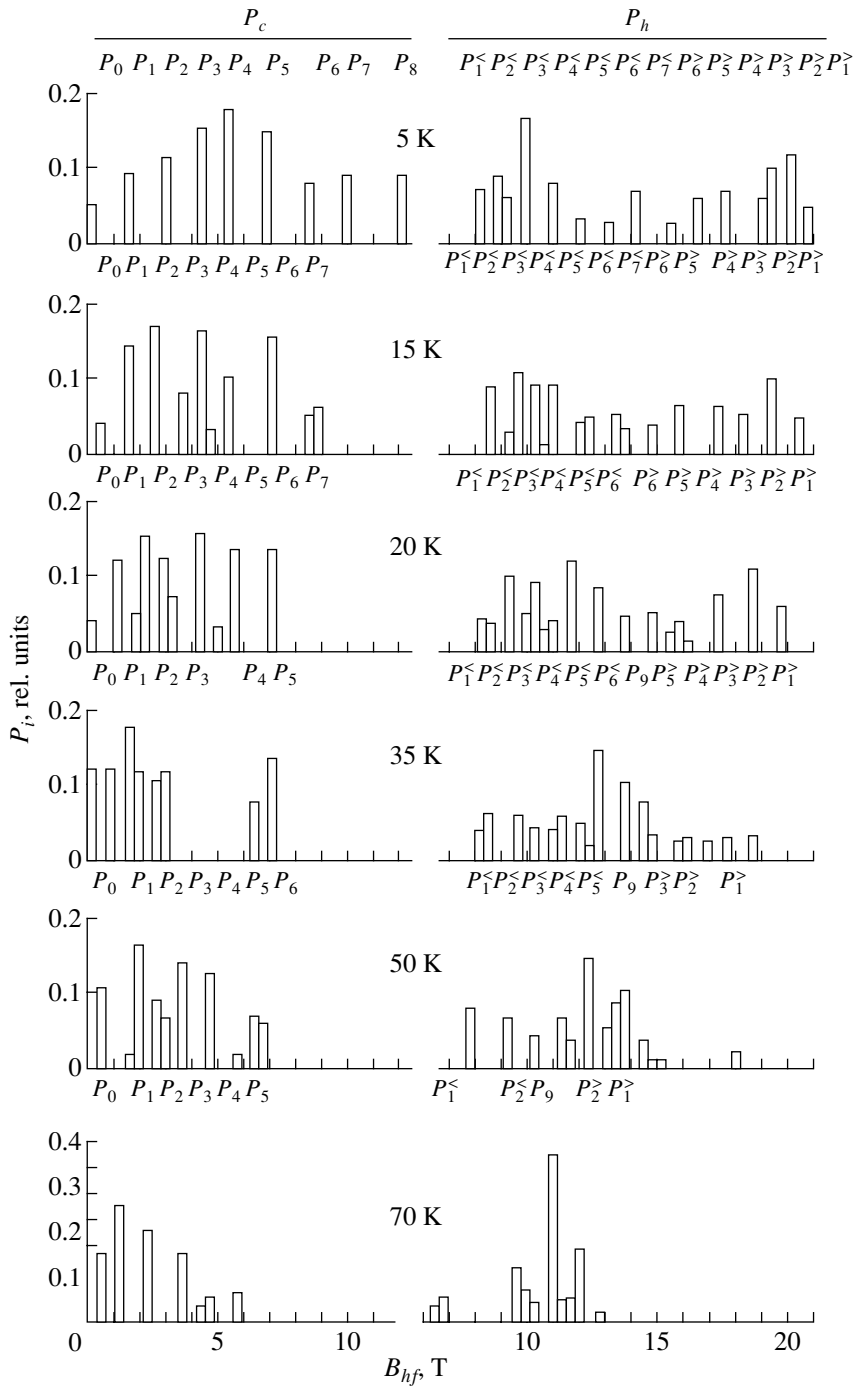

Fig. 2. Histograms of the magnetic-hyperfine-field distributions $P_c(B_{hf})$ and $P_h(B_{hf})$ for Sn atoms at sites of the cubic and hexagonal samarium sublattices at temperatures from 70 to 5 K.

ther decrease in the temperature is accompanied by redistribution of the intensities among the components.

3. DISCUSSION

The replacement of samarium by tin (up to 1.5 at. %) leaves the T_{N1} temperature unchanged and, most likely, does not affect the ordering of ions in the *h* layers. This assumption underlies the subsequent discussion. However, the above replacement contributes to ion ordering at the *c* sites. At temperatures above T_{N2}, this ordering manifests itself in the form of components at $B_{hf}(i) \neq 0$ in the P_c histograms and as additional components (apart from the expected component P_9) in the P_h histograms (Fig. 2).

Parameters for pairs of Sn impurity atoms in the same and adjacent *h* layers

i	R_i, a	n_i	i	r_i, a	n_i
1	1	6	1	$1/\sqrt{3}$	3
			2	$2/\sqrt{3}$	3
2	$\sqrt{3}$	6	3	$\sqrt{7}/3$	6
			4	$\sqrt{13}/3$	6
3	2	6	5	$4/\sqrt{3}$	3
			6	$\sqrt{19}/3$	6
4	$\sqrt{7}$	12	7	$5/\sqrt{3}$	3
			8	$2/\sqrt{7}/3$	6
5	3	6			

Note: R_i stands for the distances between the sites occupied by Sn atoms, r_i is the distance between the centers of the nearest neighbor *c* sites of the Sn atoms (for pairs of Sn atoms in the same *h* layer, $r_i = R_i$), n_i is the number of sites located in a layer at the distance R_i from any site in the same or adjacent *h* layer, and *i* is the number of the atomic pair in order of increasing distances R_i and r_i (R_i and r_i are given in terms of the lattice parameter *a*).

An increase in the number of components of the P_h distribution with a decrease in the temperature to 35 K and the constancy of the intensities of the extreme components in the temperature range from 50 to 35 K (Fig. 2) suggest that the change in both the number and the hyperfine field B_{hf} of the components in this distribution accounts for the ordering of samarium ions in the vicinity of the pairs of tin atoms whose nearest neighbor *c* sites are located in the same *c* layer. The interaction of samarium ions at the *c* sites near the tin atoms of these pairs is responsible for ion ordering at higher temperatures compared to those of ion ordering in the vicinity of widely spaced atoms.

Since the *c* layer contains the nearest neighbor sites of tin atoms of the two *h* layers adjacent to this *c* layer, it is necessary to consider the pairs of tin atoms located not only in the same layer but also in the neighboring *h* layers on opposite sides of the *c* layer adjacent to these *h* layers. Let us assume that R_i is the distance between the sites occupied by tin atoms of a pair. The pairs of the nearest neighbor tin atoms in the same and adjacent *h* layers are characterized by the distances between the centers of the nearest neighbor *c* sites of these atoms, i.e., by the distances R_i and r_i, respectively. These centers coincide with the projections of the *h* sites (occupied by the tin atoms) onto the *c* layer. Hence, the distance between the centers of the nearest neighbor *c* sites of the tin atoms located in the same layer is equal to the distance between the *h* sites occupied by these atoms. For these distances, we used the same designation (for pairs in the adjacent *h* layers, r_i is the projection of the distance R_i between the sites occupied by the atoms of a particular pair onto the *c* layer).

The probability that two atoms located at sites of the same *h* layer or at sites of the adjacent *h* layers (on opposite sides of the *c* layer) are separated by a distance R_i is proportional to the number n_i of sites located at this distance from an arbitrary site in the same or adjacent *h* layer. This probability increases with an increase in the concentration of atoms in the *h* layer and decreases with an increase in the distance R_i at a fixed number n_i. The shortest distances R_i and r_i and the corresponding numbers n_i are listed in the table.

Reasoning from the concentration of tin atoms (1.5 at. %) introduced into the sample and their binomial distribution in the *h* layers, we calculated the probabilities of finding these atoms at a distance R_i from each other, i.e., in the pairs characterized by the interatomic distances R_i (in the same *h* layers) and r_i (in the adjacent *h* layers). We took into account the atomic pairs in which the distances between the centers of the nearest neighbor *c* sites of tin atoms were less than the distance from each of these centers to a similar center of any other tin atom in the same *c* layer. The probability of finding tin atoms in the pairs characterized by the distance R_1 is equal to 0.080. The probabilities of finding tin atoms in the pairs characterized by the distances R_i satisfy the following ratio:

$$W(R_1) : W(R_2) : W(R_3) : W(R_4) : W(R_5) = 1 : 0.86 : 0.76 : 1.15 : 0.50.$$

The probability of finding tin atoms in the pairs characterized by the distance r_3 is equal to 0.033. The ratio of the probabilities of finding tin atoms in the pairs characterized by the distances r_i has the form

$$W(r_1) : W(r_2) : W(r_3) : W(r_4) : W(r_5) : W(r_6) : W(r_7) : W(r_8) = 0.61 : 0.53 : 1 : 0.70 : 0.33 : 0.60 : 0.22 : 0.38.$$

A comparison of the probabilities of finding tin atoms in pairs and the intensities of the components of the P_h distribution at 35 K (and 50 K) enables us to assign the components $P_1^<$–$P_5^<$ to the tin atoms in the pairs with R_1–R_5 and the components $P_1^>$, $P_2^>$, and $P_3^>$ to the tin atoms in the pairs with r_3, r_4, and r_6, respectively. We failed to reveal discrete components that could be attributed to the tin atoms in the pairs with r_1, r_2, and r_5 at 50 and 35 K, even though the probabilities of finding tin atoms in these pairs correspond to component intensities that are sufficiently high for observation. At 35 K, the uncertainties in the component intensities are equal to 20% for the $P_1^<$ and $P_4^<$ components; 30% for the $P_2^<$ and $P_1^>$ components; and 50, 60, and 75% for the $P_3^<$, $P_2^>$, and $P_3^>$ components, respectively.

The ordering of samarium ions in the *c* layer near a pair of tin atoms depends not only on the distance between these atoms but also on the mutual arrangement of their nearest neighbor *c* sites (located at vertices of equilateral triangles). In particular, the nearest neighbor *c* sites of the tin atoms in the pairs with r_1, r_2, r_5, and r_7 form figures with two mutually perpendicular axes of symmetry in their plane. One axis passes through the centers of the nearest neighbor *c* sites of the atoms linked by the r_i segment in the pair. The other axis passes through the midpoint of the r_i segment. The latter axis is the boundary between the *c* sites that are located at a shorter distance from one or the other atom in the pair. The magnetic moments of samarium ions at the sites of this boundary can be ordered only along the normal to the *c* axis owing to the mutual compensation for their interaction with ions lying in the *c* layer on opposite sides of the boundary due to antiferromagnetic ordering of the magnetic moments of the ions in the *h* layers adjacent to the atoms of the pair. Since the magnetic moments of samarium ions at the other *c* sites, as in pure samarium, are collinearly ordered with respect to the *c* axis, it is clear that the occurrence of this boundary brings about a weakening of the interaction between the ions located on opposite sides of the boundary and, hence, affects the ion ordering.

Among the tin atoms in the adjacent *h* layers, only the atoms in the pairs with r_1 and r_2 have common nearest neighbor *c* sites. For an ion at this site, the interactions with antiferromagnetically ordered ions of these layers cancel each other. Each tin atom in the pair with r_1 (or r_2) has two (or one) common nearest neighbor *c* sites. The line passing through these sites forms a boundary between the atoms of each pair such that the magnetic moments of the ions at the sites of this boundary can be ordered only along the normal to the *c* axis. Consequently, at three nearest neighbor *c* sites of each tin atom in the pairs with r_1 (or r_2), the magnetic moments of only one (or two) samarium ion can be collinearly ordered with respect to the *c* axis. The temperature of ion ordering and the hyperfine field B_{hf} at the tin atoms should substantially depend on the number of these ions, because their contribution to the field dominates over the contribution from the ions with magnetic moments perpendicular to the *c* axis. The separation of the components associated with tin atoms in the pairs with r_1 and r_2 can be complicated, because the hyperfine fields B_{hf} at these atoms, in at least a certain temperature range, can be close to the fields B_{hf} of the other components of the distribution P_h.

Among the tin atoms in the same *h* layer, only the atoms forming the pairs with R_1 have a common nearest neighbor *c* site. For a samarium ion at this site, the interaction with antiferromagnetically ordered ions of two adjacent *h* layers is equivalent to the interaction with two ions at its nearest neighbor *h* sites in the layer without atoms of the pair. This interaction and the minimum distances between the nearest neighbor *c* sites of the tin atoms in the pairs with R_1 suggest that samarium ions at these sites can be ordered at a higher temperature compared to that of ion ordering near the atoms in other pairs.

For the P_h distribution at 70 K (Fig. 2), only the $P_1^<$ component is characterized by the relatively low intensity expected for tin atoms in the pairs with R_1. Only for this component does the intensity remain constant in the temperature range from 70 to 5 K and is the hyperfine field $B_{hf}^<(1)$ minimum among the fields B_{hf} of the components in the distribution P_h. It is this hyperfine field B_{hf} at the tin atoms in the pairs with r_1 that can be less than the fields B_{hf} at other atoms at the *h* sites, i.e., can correspond to the field $B_{hf}^<(1)$. To accomplish this, the maximum contribution of three ions at the nearest neighbor *c* sites of the tin atom and the contribution of only eight ions at its nine nearest neighbor *h* sites (with the other atom of the pair) to the hyperfine field B_{hf} should have opposite signs; i.e., the magnetic moments of three ions at the nearest neighbor *c* sites of the tin atom should be antiparallel to the moments of the ions at the nearest neighbor *h* sites of the atom. The minimum field B_{hf} automatically provides a constant intensity of the component corresponding to this field with variations in the temperature. Therefore, the constant intensity of the $P_1^<$ component with a minimum field $B_{hf}^<(1)$ can be considered a consequence of antiparallel ordering of the magnetic moments of samarium ions at the nearest neighbor sites of the tin atoms in the pairs with R_1.

The hyperfine fields B_{hf} of the components in the P_c and P_h distributions at 5 K allow us to judge the contributions of ions at the nearest neighbor sites of the relevant tin atoms. It can be assumed that the hyperfine fields $B_{hf}(7)$ and $B_{hf}(8)$ are induced by five and six ions with parallel magnetic moments at the nearest neighbor *c* sites of the tin atoms in the *c* layer. The hyperfine fields $B_{hf}^>(1)$ and $B_{hf}^<(2)$ represent the sum and the difference of the contributions from nine ions at the nearest neighbor *h* sites and three ions with parallel moments at the nearest neighbor *c* sites of the same tin atoms. These inferences follow from the fact that the hyperfine fields $B_{hf}^>(1) = 20.8 \pm 0.2$ T, $B_{hf}^<(2) = 9.1 \pm 0.2$ T, and $B_{hf}(8) = 12.0 \pm 0.2$ T satisfy the relationship $B_{hf}(8) = B_{hf}^>(1) - B_{hf}^<(2)$ and $B_{hf}(7)/B_{hf}(8) = 5/6$. Note that $B_{hf}(9) = [B_{hf}^>(1) + B_{hf}^<(2)]/2 = 15.0 \pm 0.2$ T can be regarded as an estimate of the magnetic hyperfine field induced by nine samarium ions at the nearest neighbor *h* sites of the tin atoms at 5 K. At this temperature, the hyperfine fields $B_{hf}^<(6)$ and $B_{hf}^>(5)$ correspond to the

difference and the sum of the contributions from nine samarium ions at the nearest neighbor *h* sites and one ion at three nearest neighbor *c* sites of the same tin atoms.

The total contributions of samarium ions at the nearest neighbor *c* and *h* sites of the tin atoms to the hyperfine fields $B_{hf}^{<}(i)$ and $B_{hf}^{>}(i)$ have opposite and identical signs, respectively. The correspondence between the extreme components of the P_h distribution ($P_1^{<}$, $P_5^{<}$ and $P_1^{>}$, $P_3^{>}$) and the atoms of pairs in the same and adjacent *h* layers indicates that there is a correlation between the location of the pair of atoms in the same layer (or in two adjacent layers) and the relative signs of the total contributions from samarium ions at the nearest neighbor *c* and *h* sites of the tin atoms to the hyperfine fields $B_{hf}(i)$. For at least the shortest interatomic distances in the pairs, the total contributions of samarium ions at the nearest neighbor *c* and *h* sites of the tin atoms in the pairs in the same and adjacent *h* layers to the fields $B_{hf}(i)$ have opposite and identical signs, respectively. For collinear moments of all the samarium ions at the nearest neighbor sites of the tin atoms, this implies that the net moments of the samarium ions at the nearest neighbor *c* and *h* sites of the tin atoms are antiparallel and parallel, respectively. The distribution P_h at temperatures from 15 to 50 K is asymmetric with respect to the sums of the intensities of all the components $P_i^{<}$ and $P_i^{>}$ (0.35 ± 0.01). This suggests that, at temperatures above 35 K, the aforementioned assignment of the P_h components to the pairs of the tin atoms in the same and adjacent *h* layers can hold for larger values of R_i and r_i, because the number of tin atoms in the pairs located in the same *h* layers is twice as large as that in the adjacent *h* layers.

Thus, ion ordering in pairs of magnetic centers located in the *c* layers of samarium was observed for the first time. Each magnetic center involves ions at three nearest neighbor *c* sites of the tin atom located at the *h* site. These ions are ordered at temperatures above T_{N2} due to the disturbance of their interaction with antiferromagnetically ordered (below T_{N1}) ions of two adjacent *h* layers on opposite sides of the *c* layer with a pair of magnetic centers. For tin atoms involved in pairs of the same *h* layers, the hyperfine field B_{hf} is determined by the difference between the total contributions of samarium ions at the nearest neighbor *c* and *h* sites of the tin atoms (for at least the shortest interatomic distances).

Precision measurements of the Mössbauer spectra of tin in samarium in the temperature range of magnetic ordering make it possible to determine the temperature dependences of the hyperfine fields B_{hf} at the tin atoms located at different distances from each other in the same and adjacent *h* layers. These dependences can give a more accurate account of the ordering of samarium ions at the nearest neighbor *c* sites of the tin atoms.

The above interpretation of the distribution $P_h(B_{hf})$ allows for the difference in the number of hyperfine fields B_{hf} observed by the different methods at Sn and Cd atoms in samarium. This difference is explained by different concentrations of nonmagnetic probing atoms used in the measurements. In the case when the hyperfine interactions are investigated by perturbed-angular-correlation spectroscopy, the concentration of these atoms is at least one order of magnitude (or, more frequently, several orders of magnitude) less than that used in Mössbauer measurements. Consequently, the number of pairs with short interatomic distances is also smaller in the former case. Forker and Fraise [14] did not reveal cadmium atoms in pairs with short distances between nonmagnetic impurity atoms. These authors determined the temperature dependence of the hyperfine field B_{hf} for cadmium atoms located at large distances from the other nonmagnetic impurity atoms.

All heavy rare-earth metals (from gadolinium to erbium) have a hexagonal close-packed structure. The lattice parameter *a* decreases from 0.3636 nm for gadolinium to 0.3560 nm for erbium. The lattice parameter ratio *c*/*a* varies from 1.590 to 1.570, respectively. For samarium, these parameters are as follows: $a = 0.3663$ nm and $2c/9a = 1.595$ [18]. Since the changes in the lattice parameters and their ratios are insignificant, it can be expected that, in heavy rare-earth metals and the hexagonal samarium sublattice, the electric-field gradients q_h at nonmagnetic impurity atoms will be close to each other. This assumption is confirmed by the experimental data for cadmium atoms in these rare-earth metals, according to which the electric-field gradient q_h changes only by a factor of 1.4 [10, 14].

The shifts observed in the sextet components of the Mössbauer spectra for tin in terbium [4], dysprosium [3, 4], holmium [5, 6], and erbium [6–8] indicate that Sn nuclei are involved not only in the magnetodipole interaction but also in the electric quadrupole interaction. The signs of the quadrupole shifts in these spectra are in agreement with those expected from both the determined sign of the electric-field gradient q_h at tin atoms in samarium and the available data on magnetic structures of rare-earth metals at low temperatures [18]. The quadrupole shifts of the sextet components, which were roughly estimated from the known Mössbauer spectra, proved to be of the same order of magnitude as those expected in the case of identical electric-field gradients q_h at tin atoms in the rare-earth metals under consideration and samarium.

The Mössbauer spectra of tin in dysprosium [3, 4], holmium [5], and erbium [6–8] have been interpreted in terms of two fields whose strengths are related through the expression $B_{hf}(x) \cong 0.75B_{hf}$. It should be noted that, in either case, a lower field corresponds to a weaker sextet with an intensity of several times less than the

intensity of the principal sextet. These lower fields result from misinterpretation. When processing Mössbauer spectra whose components could not be unresolved even at low temperatures, the quadrupole shifts of the sextet lines and their broadening due to the widths of the distributions $P(B_{hf})$ were disregarded. These spectra were fitted using two sextets in which all the lines had the same width. As a result, the sextet with quadrupole shifts of the components was decomposed into two sextets without quadrupole shifts but with different isomer shifts. The location and intensity of the principal sextet were determined from the extreme lines of the measured sextet. The parameters of the weak sextet were derived using the second and fifth lines remaining after the separation of the intense sextet. Certainly, this procedure led to the aforementioned ratio between the two fields. The isomer shifts of the two resultant sextets for tin in holmium and erbium at low temperatures differed by 0.5–1 mm/s [5–8].

ACKNOWLEDGMENTS

We are grateful to N.N. Delyagin for supplying the program used in processing the Mössbauer spectra and helpful discussions of the results and S.I. Reĭman for his participation in the initial stage of this work.

REFERENCES

1. V. Gotthardt, H. S. Moller, and R. L. Mössbauer, Phys. Lett. A **28** (7), 480 (1969).
2. A. S. Kuchma, V. P. Parfenova, and V. S. Shpinel, Pis'ma Zh. Éksp. Teor. Fiz. **13** (2), 192 (1971) [JETP Lett. **13**, 135 (1971)].
3. S. K. Godovikov, M. G. Kozin, V. V. Turovtsev, and V. S. Shpinel, Phys. Status Solidi B **78** (1), 103 (1976).
4. P. V. Bogdanov, S. K. Godovikov, M. G. Kozin, *et al.*, Zh. Éksp. Teor. Fiz. **72** (6), 2120 (1977) [Sov. Phys. JETP **45**, 1113 (1977)].
5. P. V. Bogdanov, S. K. Godovikov, M. G. Kozin, and V. S. Shpinel, Hyperfine Interact. **5** (2), 333 (1978).
6. S. K. Godovikov, Fiz. Tverd. Tela (Leningrad) **27** (5), 1291 (1985) [Sov. Phys. Solid State **27**, 782 (1985)].
7. S. K. Godovikov, N. I. Moreva, A. A. Sadovskiĭ, and A. I. Firsov, Izv. Akad. Nauk SSSR, Ser. Fiz. **54** (9), 1674 (1990).
8. S. A. Nikitin, S. K. Godovikov, V. Yu. Bodryakov, and I. A. Avenarius, Izv. Akad. Nauk, Ser. Fiz. **58** (4), 15 (1994).
9. M. Forker and A. Hammesfahr, Z. Phys. **263** (1), 33 (1973).
10. W. Witthuhn and W. Engel, in *Hyperfine Interactions of Radioactive Nuclei*, Ed. by J. Christiansen (Springer-Verlag, Berlin, 1983), Topics in Current Physics, Vol. 31, p. 205.
11. S. I. Reĭman and N. I. Rokhlov, Fiz. Tverd. Tela (Leningrad) **27** (5), 1587 (1985) [Sov. Phys. Solid State **27**, 960 (1985)].
12. W. C. Koehler and R. M. Moon, Phys. Rev. Lett. **29** (21), 1468 (1972).
13. S. I. Reĭman, N. I. Rokhlov, I. N. Rozantsev, and F. D. Khamdamov, Izv. Akad. Nauk SSSR, Ser. Fiz. **50** (12), 2392 (1986).
14. M. Forker and L. Fraise, Hyperfine Interact. **34** (2), 329 (1987).
15. S. I. Reĭman and I. N. Rozantsev, Zh. Éksp. Teor. Fiz. **102** (2), 704 (1992) [Sov. Phys. JETP **75**, 378 (1992)].
16. K. Eckrich, E. Dorman, A. Oppelt, and K. H. J. Buschow, Z. Phys. B **23** (1), 157 (1976).
17. N. I. Delyagin, V. I. Krylov, N. I. Moreva, *et al.*, Zh. Éksp. Teor. Fiz. **88** (1), 300 (1985) [Sov. Phys. JETP **61**, 176 (1985)].
18. S. A. Nikitin, *Magnetic Properties of Rare-Earth Metals and Alloys* (Mosk. Gos. Univ., Moscow, 1989), p. 21.

Translated by O. Borovik-Romanova

Physics of the Solid State, Vol. 44, No. 6, 2002, pp. 1016–1021. Translated from Fizika Tverdogo Tela, Vol. 44, No. 6, 2002, pp. 973–978.

METALS AND SUPERCONDUCTORS

Behavior of the Lorenz Number in the Light Heavy-Fermion System $YbInCu_4$

A. V. Golubkov*, L. S. Parfen'eva*, I. A. Smirnov*, H. Misiorek, J. Mucha**, A. Jezowski**, F. Ritter***, and W. Assmus*****

**Ioffe Physicotechnical Institute, Russian Academy of Sciences, ul. Politekhnicheskaya 26, St. Petersburg, 194021 Russia*
e-mail: Igor.Smirnov@pop.ioffe.rssi.ru

***Institute of Low-Temperature and Structural Research, Polish Academy of Sciences, Wroclaw, 50-950 Poland*

****Goethe University, Frankfurt-am-Main, 60054 Germany*

Received August 21, 2001

Abstract—The electrical resistivity and thermal conductivity of two polycrystalline $YbInCu_4$ samples prepared by different techniques at the Ioffe Physicotechnical Institute, RAS (St. Petersburg, Russia), and the Goethe University (Frankfurt-am-Main, Germany) are studied within the temperature range 4.2–300 K. At $T_v \sim 75$–78 K, these samples exhibited an isostructural phase transition from a state with an integer valence (at $T > T_v$) to a state with an intermediate valence (at $T < T_v$) of the Yb ions. It is shown that at $T < T_v$; i.e., in the temperature range where $YbInCu_4$ is assumed to be a light heavy-fermion compound, the Lorenz number behaves as it should in a classical heavy-fermion system. At $T > T_v$, where $YbInCu_4$ is a semimetal, the Lorenz number has a value characteristic of standard metals. © *2002 MAIK "Nauka/Interperiodica".*

In the last decade, the physical properties of $YbInCu_4$ have received increasing interest from researchers in the leading laboratories of the USA, Germany, and Japan.[1]

At $T_v \sim 40$–80 K and atmospheric pressure, $YbInCu_4$ undergoes an isostructural phase transition from a Curie–Weiss paramagnet with localized magnetic moments (at $T > T_v$) to a Pauli paramagnet with a nonmagnetic Fermi-liquid state and intermediate valence of the Yb ions (at $T < T_v$).

At the phase transition, the Yb valence changes from 3 ($T > T_v$) to 2.9 ($T < T_v$).

The high- and low-temperature phases are a semimetal and metal, with the Yb 4*f* electrons weakly and strongly hybridized with the conduction electrons, respectively. At $T < T_v$, $YbInCu_4$ possesses a high density of states at the Fermi level, a feature characteristic of heavy-fermion systems and compounds with intermediate rare-earth ion valence. The parameter γ (the coefficient of the linear-in-temperature term in the electronic specific heat) for the low-temperature phase is ~50 mJ/mol K^2 [4–6], which indicates a large carrier effective mass. The $YbInCu_4$ system is classed among light heavy-fermion systems [2, 7].

$YbInCu_4$ crystallizes in an $AuBe_5$ cubic lattice (*C*15*b* structure, space group $F\bar{4}3m(T_d^2)$ [8]).

We measured the total thermal conductivity κ_{tot} and the electrical resistivity ρ of two polycrystalline samples of $YbInCu_4$ within the temperature range 4.2–300 K on a setup similar to the one employed in [9].

The samples were prepared at the Ioffe Physicotechnical Institute (St. Petersburg, Russia) and at the Goethe University (Frankfurt-am-Main, Germany) by different techniques [10–14]. $YbInCu_4$ was rf melted in sealed tantalum crucibles. However, the starting materials used in the synthesis in the two laboratories differed in purity. In what follows, we shall label the sample prepared in St. Petersburg by 1P and the one made in Frankfurt-an-Main by 2F.[2]

The samples were subjected to x-ray diffraction characterization on a DRON-2 setup (CuK_α radiation) and found to be single-phase with an $AuBe_5$-type structure and the lattice constant *a* equal to 7.133(4) Å (sample 1P) and 7.139(5) Å (sample 2F).

The Yb–In–Cu system is homogeneous within a fairly broad range of compositions. It can be presented as $YbIn_{1-x}Cu_{4+x}$ [11, 12, 15]. The composition of a sample depends substantially on the method by which it was prepared. Within the homogeneity region, the phase transition temperature *T* varies from 40 to 70–80 K. $T_v = 40$ K corresponds to the $YbInCu_4$ stoichiometry. The $YbIn_{0.8}Cu_{4.2}$ composition with the highest melting temperature has $T_v \sim 70$–80 K. For the $YbIn_{1-x}Cu_{4+x}$ samples prepared by the techniques

[1] References to numerous publications dealing with $YbInCu_4$ can be found in [1–3].

[2] The experimental data on κ_{tot} and ρ of sample 2F were used earlier in [3].

employed in St. Petersburg and Frankfurt-am-Main, the melt starts to solidify with the formation of crystals corresponding to the transition at $T_v \sim 70$ K [11, 12]. According to [16],[3] our samples with $a = 7.133$–7.139 Å were close in composition to $YbIn_{0.83}Cu_{4.17}$. The thermal conductivity of $YbInCu_4$ was studied in [3, 17]; however, no detailed analysis of the data was made.

The main purpose of this work was to study the behavior of the Lorenz number (L) of the light heavy-fermion system $YbInCu_4$ for $T < T_v$. We were interested in whether this behavior would exhibit features characteristic of classical heavy-fermion systems [18, 19]. Earlier, we found L to behave in a manner typical of such systems in the light heavy-fermion system $YbIn_{0.7}Ag_{0.3}Cu_4$ [20].

Figures 1 and 2 display our experimental results on $\kappa_{tot}(T)$ and $\rho(T)$ obtained on $YbIn_{0.83}Cu_{4.17}$ samples 1P and 2F at temperatures extending from 300 to 4 K. Measurements performed in the reverse run (4 to 300 K) revealed a highly hysteretic behavior of $\rho(T)$ [23] and $\kappa_{tot}(T)$ at $T > T_v$, which is due to defects associated with the lattice stresses forming as the temperature passes through T_v.[4]

Despite the difference in the starting material purity and in the techniques employed in the preparation of samples 1P and 2F, their $\kappa_{tot}(T)$ and $\rho(T)$ dependences were found to be sufficiently similar. The average value of T_v estimated from these dependences is ~75–78 K for both samples. We made an attempt to estimate the composition of samples 1P and 2F using the data on $T_v(x)$ obtained in [22] for the $YbIn_{1-x}Cu_{4+x}$ system (Fig. 2b). It was again found that samples 1P and 2F are close in composition to $YbIn_{0.83}Cu_{4.17}$. To simplify exposition of the experimental material, we shall assume that, on the average, the samples studied by us have the same composition, although, as seen from Figs. 1 and 2 (as well as from Figs. 3, 4), these samples differ slightly in the magnitude of κ_{tot}, κ_{ph} (the lattice component of thermal conductivity), and ρ. This difference can be apparently assigned to the fact that the samples do differ in composition (though very slightly) and probably contain different amounts of residual impurities.

According to Hall effect measurements [2, 24], both phases (at $T > T_v$ and $T < T_v$) have a fairly high carrier concentration, such that κ_{tot} should have both lattice and electronic (κ_e) components:[5]

$$\kappa_{tot} = \kappa_e + \kappa_{ph}. \quad (1)$$

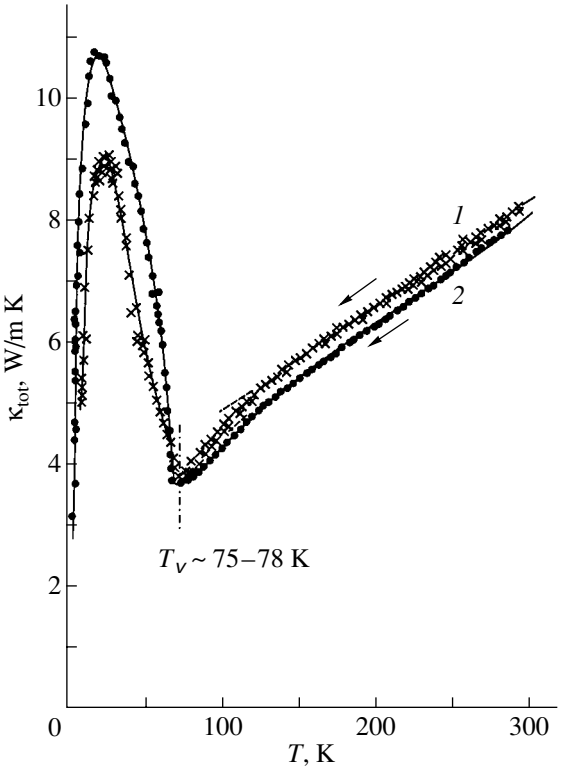

Fig. 1. Temperature dependence of κ_{tot} for samples (*1*) 1P and (*2*) 2F.

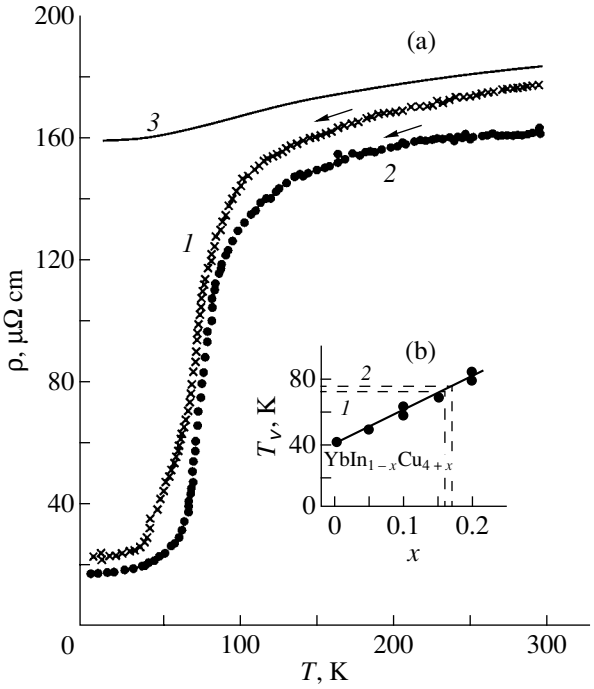

Fig. 2. (a) Temperature dependence of ρ for $YbIn_{0.83}Cu_{4.17}$ samples (*1*) 1P and (*2*) 2F and (*3*) for $LuInCu_4$, a compound with no phase transition [21]. (b) Dependence of T_v on x in the $YbIn_{1-x}Cu_{4+x}$ system [22]. The dashed lines are drawn to determine the values of x for samples (*1*) 1P and (*2*) 2F.

[3] He *et al.* [16] presented the dependence of a on x measured for $YbIn_{1-x}Cu_{4+x}$.

[4] We will devote a separate paper to the study and discussion of the behavior of $\kappa_{tot}(T)$ in the direct and reverse measurement runs.

[5] Because $YbInCu_4$ is a semimetal at $T > T_v$, one could also expect the bipolar thermal conductivity κ_{bip} to contribute to κ_{tot} at certain band parameters of this material [21, 25], but, as follows from [3], the component κ_{bip} in κ_{tot} of $YbInCu_4$ at $T < 300$ K is negligible.

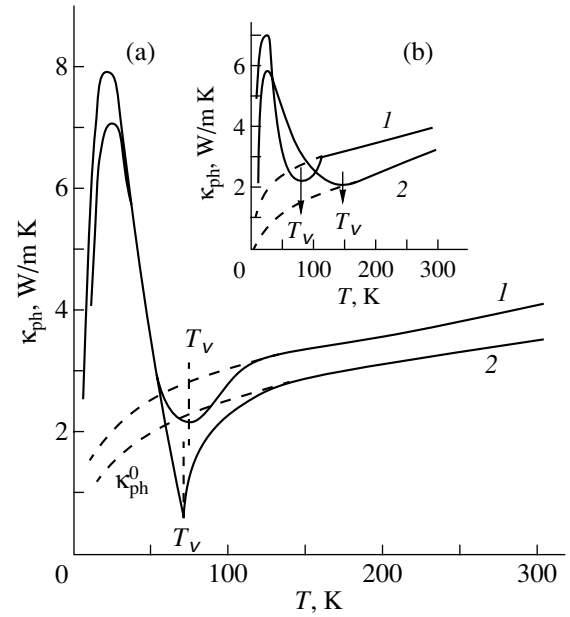

Fig. 3. (a) Temperature dependence of κ_{ph} for $YbIn_{0.83}Cu_{4.17}$ samples (*1*) 1P and (*2*) 2F (see Fig. 4 for the explanation of κ_{ph}^0). (b) Temperature dependence of κ_{ph} of (*1*) sample 1P and (*2*) the $YbIn_{0.7}Ag_{0.3}Cu_4$ sample [20].

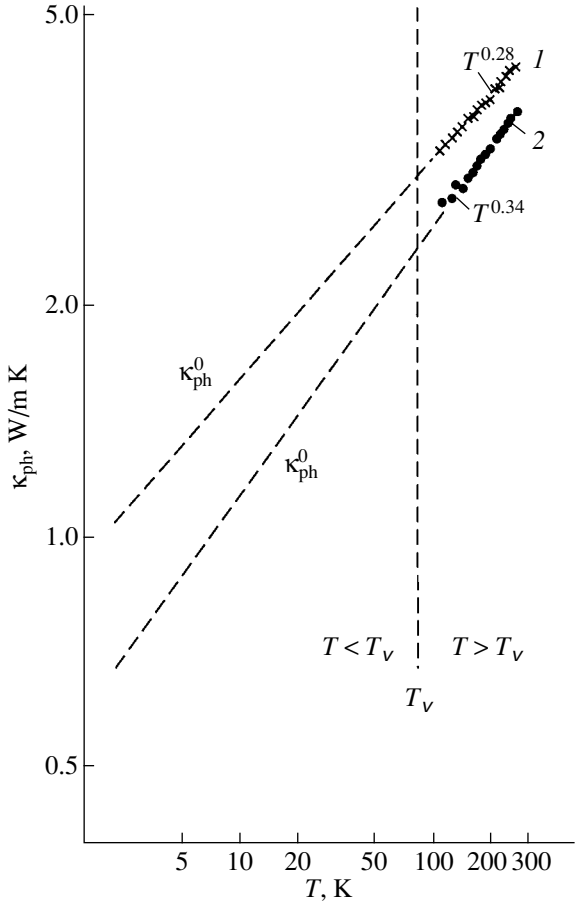

Fig. 4. Temperature dependence of κ_{ph} for $YbIn_{0.83}Cu_{4.17}$ samples (*1*) 1P and (*2*) 2F.

According to the classical theory of the thermal conductivity of solids, κ_e should obey the Wiedemann–Franz law

$$\kappa_e = LT/\rho. \quad (2)$$

At $T \gtrsim \Theta/3$ (Θ is the Debye temperature) and very low temperatures in pure metals, as well as at low and high temperatures in dirty metals, we have $L = L_0$ [26], where L_0 is the Sommerfeld value of the Lorenz number ($L_0 = 2.45 \times 10^{-8}$ W Ω/K^2). The $YbIn_{0.83}Cu_{4.17}$ samples belong neither to very pure metals nor to semimetals, and, thus, one may accept, as the first approximation, $L = L_0$ throughout the temperature range (4–300 K) studied by us.

Figure 3a plots the $\kappa_{ph}(T)$ relation calculated from Eqs. (1) and (2) under the assumption of $L = L_0$. As is evident from this figure, as well as from Fig. 4, within the temperature interval ~120–300 K, κ_{ph} follows a power law: $\kappa_{ph} \sim T^{0.28}$ for sample 1P and $\kappa_{ph} \sim T^{0.34}$ for sample 2F. As the temperature is lowered, κ_{ph} passes through a minimum, then reaches a maximum, and finally falls off to zero.

What could be the explanation for this behavior of κ_{ph}? First, we consider the data obtained for $T > T_v$. At these temperatures, our compound is not a heavy-fermion system but rather a semimetal; therefore, using the value $L = L_0$ in calculations of κ_e is fully valid. However, the reasons for the growth of κ_{ph} with increasing temperature remain unclear. This behavior of $\kappa_{ph}(T)$ is characteristic of amorphous or heavily defected materials. In our case, defects can form in $YbIn_{0.83}Cu_{4.17}$ through copper substituting for indium [11] (we stressed this point when analyzing data on $\kappa_{ph}(T)$ for $YbIn_{0.7}Ag_{0.3}Cu_4$ [20]). Such defects should affect the behavior of $\kappa_{ph}(T)$ noticeably for both $T > T_v$ and $T < T_v$.

A growth of κ_{ph} with temperature was also observed to occur in a number of other compounds which can be classed among heavy-fermion systems (light $YbIn_{0.7}Ag_{0.3}Cu_4$ [20], moderate $YbAgCu_4$ [27] and $UInCu_5$ [28], and classical $CeAl_3$ [29]) (Fig. 5). It appears highly unlikely that in all the above compounds, the increase in $\kappa_{ph}(T)$ is associated only with a high defect concentration.[6] It is possible that this behavior of $\kappa_{ph}(T)$ is characteristic of a certain class of heavy-fermion systems.

Now, we consider the behavior of $\kappa_{ph}(T)$ for $T < T_v$. It is important to understand the reason for such a

[6] In [28, 29], the growth of κ_{ph} as $\sim T^n$ is explained in terms of the theoretical model developed in [30]. We believe, however, that this interpretation is unsatisfactory, because, as shown in [30], $\kappa_{ph} \sim T$ (in our case, $\kappa_{ph} \sim T^{0.3}$) and the relation proposed in [30] is valid only at very low temperatures ($T < \Theta/20$), whereas in our experiment, the effect is observed at substantially higher temperatures (up to 300 K).

strong increase in κ_{ph}, more specifically, whether it stems from a real growth of κ_{ph} inherent in this compound or originates from our having wrongly taken into account the quantity L when calculating κ_e from Eq. (2). One cannot exclude the possibility that L, rather than being equal to L_0, varies in a complicated way with temperature. The soundness of the latter conjecture is argued for by the following observations.

(1) To explain the sharp growth of κ_{ph} at $T > T_v$, one has to assume that a mechanism causing strong phonon scattering becomes operative at this temperature. We have not found thus far a reasonable explanation for the nature of such a mechanism. At $T < T_v$, the valence of the Yb ion changes from 3 to 2.9, the Yb ionic radius increases, and the lattice becomes looser and, hence, more defected, which should entail a decrease in $\kappa_{ph}(T)$ rather than its growth.

(2) According to the elementary theory of thermal conductivity, we have

$$\kappa_{ph} \sim C v l, \quad (3)$$

where C, v, and l are the specific heat, sound velocity, and phonon mean free path, respectively. In $YbInCu_4$, C [5] and v [10] vary abruptly within a narrow temperature interval around T_v. The quantities C and v decrease smoothly at $T < T_v$ and increase as smoothly at $T > T_v$; i.e., if one excludes the narrow interval near the phase transition (around T_v), one observes a smooth variation of $C(T)$ and $v(T)$ throughout the temperature range studied by us.[7] This is naturally only an indirect indication of the absence of a bell-shaped behavior of $\kappa_{ph}(T)$ plotted in Fig. 3 for samples 1P and 2F in the $T < T_v$ range.

(3) $YbIn_{0.7}Ag_{0.3}Cu_4$ undergoes a gradual phase transition (without an abrupt change in ρ, a, and other parameters at T_v) which is similar in nature to the one observed in $YbInCu_4$. Assuming $L = L_0$ throughout the temperature range studied, we isolated $\kappa_{ph}(T)$ from $\kappa_{tot}(T)$ using Eqs. (1) and (2) and found that, at $T < T_v$, $\kappa_{ph}(T)$ of this compound follows a bell-shaped pattern similar to the one obtained for $\kappa_{ph}(T)$ of $YbIn_{0.83}Cu_{4.17}$ (Fig. 3). In [20], we explained this behavior of $\kappa_{ph}(T)$ as being due to our having incorrectly taken the Lorenz number into account in κ_e; it was found that the Lorenz number varies in a complex way with temperature and is substantially larger than L_0. It is possible that we also have a similar situation in $YbIn_{0.83}Cu_{4.17}$.

Thus, the above arguments suggest that κ_e, rather than κ_{ph}, is most likely responsible in our case for the strong increase in thermal conductivity at $T < T_v$.

Now, we consider the behavior of L in $YbIn_{0.83}Cu_{4.17}$ at $T < T_v$.

[7] Unfortunately, we have not been able to directly estimate the character of l variation within the temperature range covered.

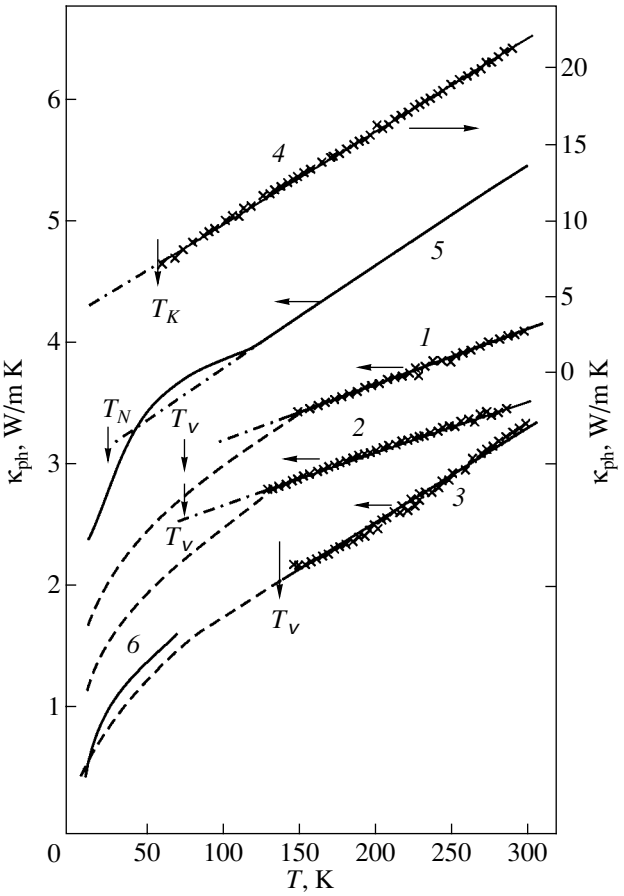

Fig. 5. Temperature dependence of κ_{ph} for $YbIn_{0.83}Cu_{4.17}$ samples (*1*) 1P and (*2*) 2F, (*3*) $YbIn_{0.7}Ag_{0.3}Cu_4$ [20], (*4*) $YbAgCu_4$ [27], (*5*) $UInCu_5$ [28], and (*6*) $CeAl_3$ [29]. For all curves, the dashed lines plot κ_{ph}^0, which was derived by extrapolating the high-temperature data by the power laws found for each compound. T_K and T_N are, respectively, the Kondo and Néel temperatures.

As already mentioned more than once, $YbIn_{0.83}Cu_{4.17}$ transfers to the state corresponding to a light heavy-fermion system at $T < T_v$. The behavior of the Lorenz number in a classical heavy-fermion system differs substantially both in magnitude and in the temperature dependence from that in both pure and dirty metals. According to [18, 19], L_x/L_0 for this system increases from unity (at $T \sim 0$), then passes through a maximum and falls off down to 0.648, and then grows again to reach unity at $T \sim T_K$ (T_K is the Kondo temperature).

To find $L_x/L_0(T)$ for $T < T_v$, we shall assume that $\kappa_{ph} \sim T^n$ (where n, as pointed out earlier, is 0.28 and 0.34 for samples 1P and 2F, respectively) throughout the temperature range covered by us (4–300 K). To do this, we extrapolate $\kappa_{ph}(T)$ using this relation from the

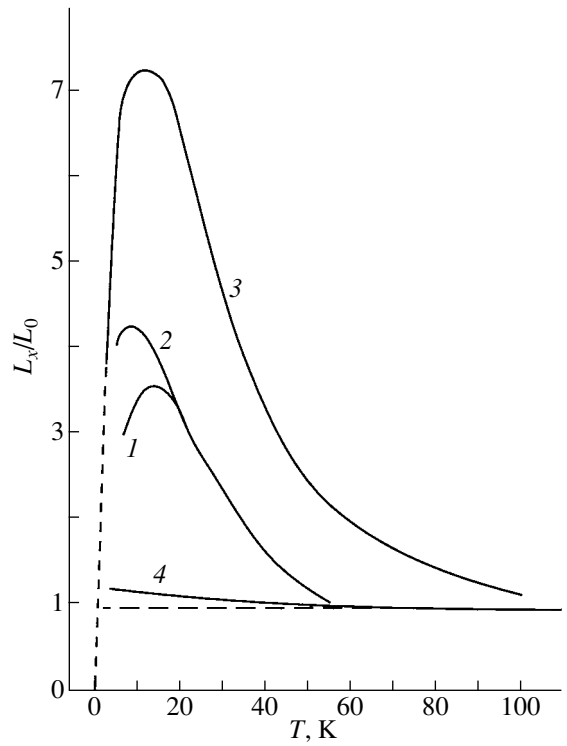

Fig. 6. Temperature dependences of L_x/L_0 for the $YbIn_{0.83}Cu_{4.17}$ samples (*1*) 1P and (*2*) 2F, (*3*) $YbIn_{0.7}Ag_{0.3}Cu_4$ [20], and (*4*) $YbAgCu_4$ [27].

region $T > T_v$ to $T < T_v$ (Fig. 4; κ_{ph}^0 in Figs. 3 and 4 and dashed lines in Fig. 5)[8] and apply the relation

$$\kappa_e = \kappa_{tot} - \kappa_{ph}^0 \quad (4)$$

for the range 4–50 K to determine $L_x/L_0(T)$ (we excluded the temperature interval around T_v) from consideration. The results of this calculation are plotted in Fig. 6.

We readily see from Fig. 6 that the behavior of $L_x/L_0(T)$ in samples 1P and 2F fits the above theoretical pattern of the behavior of the Lorenz number in a heavy-fermion system [18].

We may thus conclude that the Lorenz number behaves similarly in a classical and a light heavy-fermion system.

For comparison, Fig. 6 presents data for $L_x/L_0(T)$ of $YbIn_{0.7}Ag_{0.3}Cu_4$ [20] and our refined data for $YbAgCu_4$ from [27]. In [27], we determined the ratio $L_x/L_0(T)$ using a slightly different technique. By contrast, here we have applied to $YbAgCu_4$ the method of $\kappa_{ph}^0(T)$ and $L_x/L_0(T)$ determination (Fig. 5) proposed in this work and, as it seems, have obtained more accurate information on the behavior of the Lorenz number in this compound. Note, however, the specific features in the behavior of $L_x/L_0(T)$ in $YbAgCu_4$ which still remain unclear. We come up against a paradox. Indeed, in light heavy-fermion systems, such as $YbInCu_4$ and $YbIn_{0.7}Ag_{0.3}Cu_4$, whose parameter $\gamma \simeq 50$ mJ/mol K^2, $L_x/L_0(T)$ behaves as it should in classical heavy-fermion systems (with $\gamma \geq 400$ mJ/mol K^2). At the same time, in moderately heavy-fermion systems with $\gamma \sim$ 200–250 mJ/mol K^2, to which $YbAgCu_4$ belongs, the $L_x/L_0(T)$ ratio (determined in the temperature range 4–300 K) exhibits only a slight deviation from unity (in the region $T < T_K$).

[8] That κ_{ph}^0 of the $YbIn_{0.83}Cu_{4.17}$ samples can behave in this way at low temperatures follows indirectly from the data published in [28, 29], which testify that $\kappa_{ph}(T)$ for $YbIn_{0.83}Cu_{4.17}$ behaves exactly as it does in $CeAl_3$ and $UInCu_5$ (Fig. 5).

ACKNOWLEDGMENTS

The authors express gratitude to N.F. Kartenko and N.V. Sharenkova for x-ray structural measurements.

This work was conducted within bilateral agreements between the Russian Academy of Sciences, Deutsche Forschungsgesellschaft, and the Polish Academy of Sciences and was supported by the Russian Foundation for Basic Research (project no. 99-02-18078) and the Polish Committee for Scientific Research (grant no. 2PO3B 129-19).

REFERENCES

1. J. L. Sarrao, C. D. Immer, Z. Fisk, *et al.*, Phys. Rev. B **59** (10), 6855 (1999).
2. A. V. Goltsev and G. Bruls, Phys. Rev. B **63** (15), 155109 (2001).
3. I. A. Smirnov, L. S. Parfen'eva, A. Jezowski, *et al.*, Fiz. Tverd. Tela (St. Petersburg) **41** (9), 1548 (1999) [Phys. Solid State **41**, 1418 (1999)].
4. A. L. Cornelius, J. M. Lawrence, J. L. Sarrao, *et al.*, Phys. Rev. B **56** (13), 7993 (1997).
5. J. L. Sarrao, A. P. Ramírez, T. W. Darling, *et al.*, Phys. Rev. B **58** (1), 409 (1998).
6. N. Pillmayer, E. Bauer, and K. Yoshimura, J. Magn. Magn. Mater. **104–107**, 639 (1992).
7. I. Felner, I. Nowik, D. Vakin, *et al.*, Phys. Rev. B **35** (13), 6956 (1987).
8. R. Kojima, Y. Nakai, T. Susuki, *et al.*, J. Phys. Soc. Jpn. **59** (3), 792 (1990).
9. A. Jezowski, J. Mucha, and G. Pompe, J. Phys. D **20**, 1500 (1987).
10. B. Kindler, D. Finsterbusch, R. Graf, *et al.*, Phys. Rev. B **50** (2), 704 (1994).
11. A. Löffert, M. L. Aigner, F. Ritter, and W. Assmus, Cryst. Res. Technol. **34** (2), 267 (1999).
12. A. Löffert, S. Hautsch, F. Ritter, and W. Assmus, Physica B (Amsterdam) **259–261**, 134 (1999).
13. E. Feschbach, A. Löffert, F. Ritter, and W. Assmus, Cryst. Res. Technol. **33**, 267 (1998).

14. A. V. Golubkov, T. B. Zhukova, and V. M. Sergeeva, Izv. Akad. Nauk SSSR, Neorg. Mater. **2**, 77 (1966).
15. A. V. Golubkov, L. S. Parfen'eva, I. A. Smirnov, *et al.*, Fiz. Tverd. Tela (St. Petersburg) **44** (6), 973 (2002) [Phys. Solid State **44** (2002)].
16. J. He, N. Tsujii, K. Yoshimura, *et al.*, J. Phys. Soc. Jpn. **66** (8), 2481 (1997).
17. E. Bauer, E. Gratz, G. Hutflesz, *et al.*, Physica B (Amsterdam) **186/188**, 494 (1993).
18. V. I. Belitsky and A. V. Goltsev, Physica B (Amsterdam) **172**, 459 (1991).
19. I. A. Smirnov and V. S. Oskotskii, in *Handbook on the Physics and Chemistry of Rare Earth*, Ed. by K. A. Gschneidner, Jr. and L. Eyring (Elsevier, Amsterdam, 1993), Vol. 16, p. 107.
20. A. V. Golubkov, L. S. Parfen'eva, I. A. Smirnov, *et al.*, Fiz. Tverd. Tela (St. Petersburg) **43** (10), 1739 (2001) [Phys. Solid State **43**, 1811 (2001)].
21. A. V. Golubkov, L. S. Parfen'eva, I. A. Smirnov, *et al.*, Fiz. Tverd. Tela (St. Petersburg) **42** (8), 1357 (2000) [Phys. Solid State **42**, 1394 (2000)].
22. K. Yoshimura, N. Tsujii, K. Sorada, *et al.*, Physica B (Amsterdam) **281/282**, 141 (2000).
23. J. L. Sarrao, C. D. Immer, C. L. Benton, *et al.*, Phys. Rev. B **54** (17), 12207 (1996).
24. Y. Itoh, H. Kadomatsu, J. Sakurai, and H. Fujiwara, Phys. Status Solidi A **118**, 513 (1990).
25. A. V. Golubkov, L. S. Parfen'eva, I. A. Smirnov, *et al.*, Fiz. Tverd. Tela (St. Petersburg) **42** (11), 1938 (2000) [Phys. Solid State **42**, 1990 (2000)].
26. I. A. Smirnov and V. I. Tamarchenko, *Electron Heat Conductivity in Metals and Semiconductors* (Nauka, Leningrad, 1977).
27. A. V. Golubkov, L. S. Parfen'eva, I. A. Smirnov, *et al.*, Fiz. Tverd. Tela (St. Petersburg) **43** (2), 210 (2001) [Phys. Solid State **43**, 218 (2001)].
28. D. Kaczorowski, R. Troc, A. Czopnik, *et al.*, Phys. Rev. B **63**, 144401 (2001).
29. H. R. Ott, O. Marti, and F. Hulliger, Solid State Commun. **49** (12), 1129 (1984).
30. I. E. Zimmerman, J. Phys. Chem. Solids **11**, 299 (1959).

Translated by G. Skrebtsov

Physics of the Solid State, Vol. 44, No. 6, 2002, pp. 1022–1027. Translated from Fizika Tverdogo Tela, Vol. 44, No. 6, 2002, pp. 979–984.

METALS AND SUPERCONDUCTORS

Evolution of the Pd–Ta–H Alloy Structure in the Edwards Thermodynamic Representation

V. M. Avdyukhina, A. A. Katsnel'son, A. I. Olemskoĭ, D. A. Olemskoĭ, and G. P. Revkevich

Moscow State University, Vorob'evy gory, Moscow, 119899 Russia

e-mail: albert@solst.phys.msu.su

Received August 24, 2001

Abstract—It is shown that the time evolution of x-ray diffraction patterns of a deformed Pd–Ta alloy after its saturation with hydrogen can be determined by the multiwell energy profile of the states of the system. Within the Lorenz synergetic approach, a phenomenological model is proposed in which the evolution of the alloy structure is represented as a random walk of the nonergodic system from one internal-energy minimum to another. In this case, the order parameter is the fraction of states with minimum energy occupied by the system, the conjugate field is associated with the Edwards entropy, and the control parameter is the internal energy. The evolution of the Pd–Ta–H alloy structure is interpreted as that of a complex nonergodic system in terms of thermodynamics. © *2002 MAIK "Nauka/Interperiodica"*.

1. INTRODUCTION

Considerable recent attention has been focused on complex nonergodic systems, such as spin and structural glasses, disordered heteropolymers, granular media, and transport flows (see review [1]). The main feature of such systems is that their phase space is separated into isolated domains, each of which corresponds to a metastable thermodynamic state, and the number of these domains N_0 is much larger than the total number of (quasi)particles N and exponentially increases as the latter tends to infinity: $N_0 = \exp(sN)$, where s is the so-called Edwards entropy per particle (complexity) [2, 3]. In contrast to the Boltzmann measure, which characterizes the disorder in a given statistical ensemble, the Edwards entropy characterizes the disorder in the distribution of states of a nonergodic system over internal-energy minima, each of which corresponds to a statistical ensemble. In complex systems, statistical ensembles play the role of particles and the distribution over these ensembles is characterized by the effective temperature T and entropy s (introduced by Edwards [3]). For example, at $T = 0$, the complex system corresponds to a granular medium characterized by a flat distribution over all energy minima.

The Edwards systems have an exponentially large number of energy minima $N_0 \gg 1$, in contrast to ergodic systems, for which $N_0 = 1$. It is of interest to consider an intermediate case where the number of energy minima N_0 is not exponentially large but exceeds unity.

In this paper, it will be shown that this is the case with deformed Pd–Ta alloys saturated electrolytically with hydrogen. When heavily deformed, a solid can be so far from its equilibrium state that self-organization effects become significant and dissipative structures arise [4, 5]. In a metal saturated with hydrogen, strong internal stresses are produced by hydrogen atoms and the state of the system can become nonequilibrium as in the case under an external load. Investigations of annealed Pd–W–H [6] and deformed Pd–Sm–H, Pd–Er–H, Pd–Mo–H, and Pd–Ta–H alloys [7–13] revealed that these alloys can undergo nonmonotonic nonregular transformations. The main features of the behavior of such systems have been explained in terms of synergetic models [6, 10]. However, these models cannot adequately describe the evolution of the Pd–Ta–H alloy structure (see also [12]). We deal with this problem in the present paper.

2. EXPERIMENTAL DATA

The experimental technique is described in detail in [9–12]; here, we only point out that a deformed Pd–Ta (7 at. % Ta) alloy was first saturated with hydrogen electrolytically (current density 40 mA/cm^2) for 15 min. After relaxation for 176 h, the sample was saturated once again for the same time at 80 mA/cm^2. An x-ray diffraction study was carried out using a computerized diffractometer (Cu$K_{\alpha 1}$ doublet component); the (220) and (311) diffraction maxima were analyzed and their deconvolution was performed using the Origin computer code and assuming that the components are Lorentzian-shaped [14, 15].

The x-ray diffraction study revealed that, after the deformed Pd–Ta alloy was saturated with hydrogen, a regular shift in the position of diffraction maxima occurred, which indicated that the crystal lattice expanded and then anisotropically contracted. During the relaxation, stochastic changes were observed in the positions, widths, and symmetry of diffraction maxima; their shape also varied in a random fashion, with several peaks appearing and disappearing. Figure 1 shows

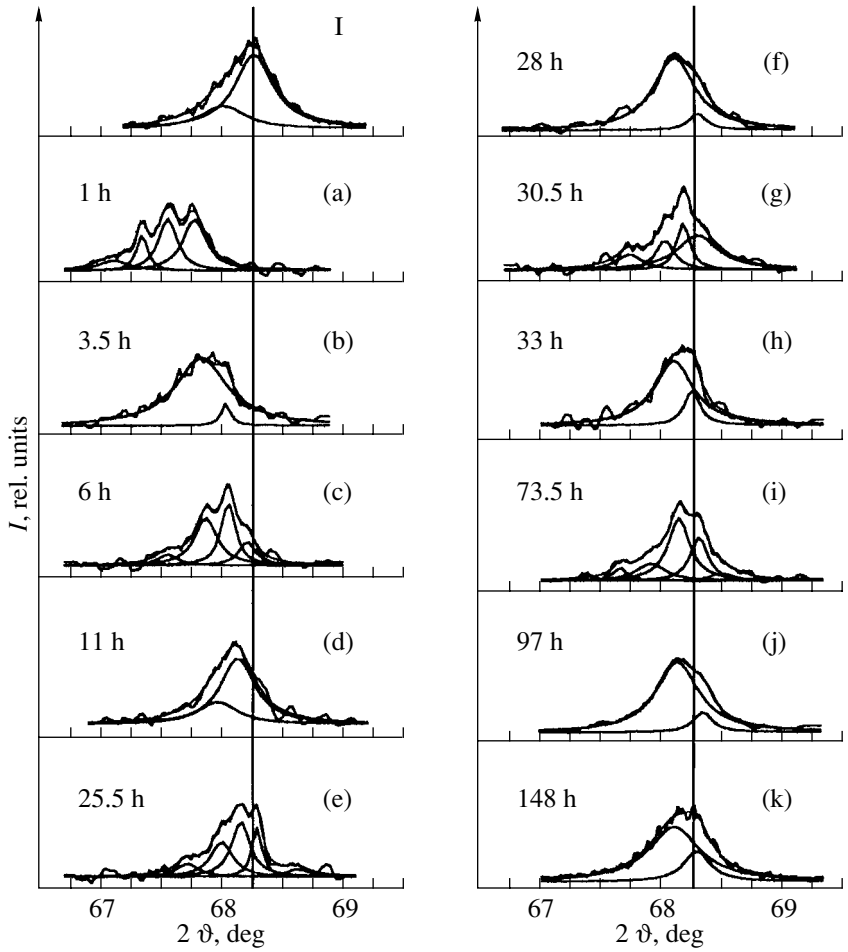

Fig. 1. Time variations in position and shape of the (220) diffraction line after the second saturation. I is the initial state. Vertical lines indicate the position corresponding to the initial state (after the first saturation and subsequent relaxation for 173 h).

diffraction curves and their deconvolutions for the (220) maximum at different instants of time after the second sample saturation. It is clearly seen that there is a complex structure of diffraction peaks which vary nonmonotonically in time. The parameters of the diffraction curves are listed in the table.

Since a homogeneous phase is represented by a bell-shaped diffraction peak, one can conclude that this type of diffraction pattern variation is a consequence of interconversions of several phases associated with redistribution of Pd, Ta, and H atoms among different regions of the system. A characteristic feature of these structural changes is that they can be repeated but are not periodic. On the other hand, different widths of the deconvoluted components and their nonmonotonic variations with time imply that these processes are accompanied by a nonmonotonic evolution of the defect structure and of the elastic fields produced by this structure. The presence of long-range fields, as well as the marked difference in the binding energy of hydrogen to the perfect and defect lattices of palladium [16], causes the state of the system under study to be highly nonequilibrium [5]. According to the theory of the glasslike state [1], the phase space of a nonequilibrium system is characterized by a complex energy profile in this case. This energy profile is dictated by the initial defect structure and the atom distribution in the alloy, which are a result of a prior mechanical treatment, saturation with hydrogen, and subsequent relaxation. The difference in time variation between the regions producing the (220) and (311) coherent-scattering maxima and differing in orientation relative to the sample surface is indicative of energy transfer from some degrees of freedom to others, which can give rise to diffusion-flow turbulence [12].

3. THEORETICAL MODEL

The nonmonotonic structural transformations described above can be explained if one assumes that the saturation of a deformed Pd–Ta alloy with hydrogen produces a set of metastable states corresponding to different phases and defect structures. In this case, the migration of the system from one internal-energy minimum to another, corresponding to the states mentioned

Time dependence of the number of peaks of the (220) diffraction maximum

Elapsed time from saturation, h	Number of peaks N	Relative number of peaks n	Panel of Fig. 1
1.0	4	0.8	a
3.5	2	0.4	b
6.0	4	0.8	c
11.0	2	0.4	d
25.5	5	1	e
28.0	1	0.2	f
30.5	4	0.8	g
33.0	2	0.4	h
73.5	4	0.8	i
97.0	2	0.4	j
148	2	0.4	k

above, will lead to the stochastic structural transformations observed experimentally.

The essential point is that the structural evolution is nonmonotonic but is not periodic. The variations in structure bear a resemblance to the behavior of a strange attractor, which can be described in terms of the Lorenz model [17]. Using this model, we have explained [6] the nonmonotonic behavior of a two-phase Pd–Er–H alloy. The parameters of the system were taken to be the volume fraction of the Er-rich phase, concentration of Er atoms in this phase, and concentration of erbium-atom traps in the matrix.

Such parametrization cannot be realized in a multiphase Pd–Ta–H alloy, where the situation is much more complex. At first glance, it would be reasonable not to describe the behavior of many phases but, instead, to introduce parameters averaged over these phases or to consider only the dominant phase separately. In this case, however, one does not take into account an essential feature of the evolution of a multiphase Pd–Ta–H alloy, namely, the fact that not only the relationship among the volumes of the coexisting phases and their composition but also their number vary in the alloy with time. Therefore, selection of the proper parameters is of importance in order for a synergetic model to describe the stochastic behavior of the Pd–Ta–H system.

According to the Ruelle–Takens theorem [18], such a system exhibits a nontrivial behavior when the number of the degrees of freedom characterized by the parameters of the system is not less than three. The behavior of a system in phase transitions is controlled by a hydrodynamic mode, with its amplitude being an order parameter whose magnitude is determined by the thermostat. The characteristic feature of a self-organizing (synergetic) system is that both the influence of the thermostat on the selected subsystem and the backward action of the subsystem on the thermostat are of fundamental importance. The backward action can be both direct and indirect. The former action is determined by the conjugate field, while the latter depends on the control parameter. For example, in a synergetic model for alloy ordering, the order parameter is the usual long-order parameter, the conjugate field corresponds to the difference in the chemical potential of the alloy components, and the control parameter is the difference in the unit-cell site occupation number of atoms of different species [19]. The usual dissipative regime of a phase transition is realized when the relaxation times of the order parameter and of the conjugate field are much longer than that of the control parameter. In the opposite extreme, the transition to the strange-attractor regime, rather than to an ordered state, occurs in the system when the steady-state value of the control parameter becomes larger than a certain critical value [20].

We will explain the nonmonotonic variation in the phase composition of a Pd–Ta–H alloy under the assumption that its saturation with hydrogen leads to the formation of a complex internal-energy profile of the states of the system with a great number of minima separated by energy barriers (multivalley structure). This allows us to explain the critical slowing-down of the structural transformation in systems of the Pd–H type [21]. This slowing-down is due to the hierarchic structure of the energy profile: the deep minima are serrated, having profiles with a set of shallower minima, which, in turn, have profiles with still shallower minima, and so on. In its time evolution, the system has to occupy the shallowest minima first, then deeper ones, then still deeper ones, and so on, down to the deepest minimum, which determines the behavior of the system as a whole.

In our case, it will suffice to consider only one class of minima which differ in depth only slightly. The minima are numbered by index α, running the values 1, 2, …, N_0, and the evolution of the system is described by the time-dependent probability distribution p_α over these minima. The dependence of p_α on time t can be found by solving the Fokker–Planck equation, which is a very complicated problem [22]. However, as a preliminary, it will suffice to find integral quantities which characterize the distribution p_α and the thermodynamic behavior of the system as a whole. Such quantities are (a) the number N of internal-energy minima occupied by the system at a given instant of time (this number characterizes the halfwidth of the spread of probabilities p_α); (b) the entropy, characterizing the spread of the system over the minima,

$$S = -\sum_\alpha p_\alpha \ln p_\alpha; \tag{1}$$

and (c) the specific internal energy e_α at a minimum α, from which the total specific energy can be found as

$$e = \sum_\alpha p_\alpha e_\alpha. \tag{2}$$

The order parameter is defined as the ratio $n = N/N_0$ of the number N of internal-energy minima occupied by the system to the total number of minima N_0. Then, the specific Edwards entropy $s = S/N_0$, which characterizes the disorder in the distribution over the minima α, is the conjugate field and the internal-energy density e is a control parameter.

In order to describe the evolution of the system phenomenologically, one should relate the rates dn/dt, ds/dt, and de/dt of changes in the basic parameters to the parameters n, s, and e themselves. The Lorenz model has the advantage that it corresponds to the simplest Hamiltonian in the corresponding microscopic representation [5]. The linear Lorenz equation has the form

$$\frac{dn}{dt} = -\frac{n}{\tau_n} + g_n s, \tag{3}$$

where the first term on the right-hand side describes the Debye relaxation of $n(t)$ to the value $n = 0$ with characteristic time τ_n and the second term (with positive coefficient g_n) is an increase in the number of internal-energy minima occupied by the system, which is accompanied by an increase in the entropy s that characterizes the spread over these minima.

The equations for the rates ds/dt and de/dt, in contrast to Eq. (3), contain nonlinear terms which describe the backward action of the selected subsystem on the thermostat mentioned above (i.e., the feedback). The change in the entropy is described by the equation

$$\frac{ds}{dt} = -\frac{s}{\tau_s} + g_s n e, \tag{4}$$

where the first term on the right-hand side describes the Debye relaxation to the value $s = 0$ characterized by the relaxation time τ_s. In accordance with the second law of thermodynamics, the nonlinear term with positive coefficient g_s is the increase in entropy s due to the system spreading over less deep minima of the internal energy.

Finally, the equation for the rate of change in the internal energy is

$$\frac{de}{dt} = -\frac{e - e_0}{\tau_e} - g_e s n. \tag{5}$$

Here, we have taken into account that the Debye relaxation with characteristic time τ_e leads not to a zero value of the internal energy e but rather to a finite value e_0 determined by the position of the system in the phase diagram and by the prior treatment of the alloy. The nonlinear term with positive coefficient g_e describes negative feedback, which means that a redistribution over the internal-energy minima must lead to a decreased total energy e because the system goes over to deeper minima. It should be noted that the nonlinear terms are of fundamental importance; the behavior of the self-organizing system is a compromise between their competing effects: the positive feedback in Eq. (4) is due to coupling between the relative number of minima n and internal energy e and causes the entropy s to increase, whereas the negative feedback in Eq. (5) is due to correlation between the number of minima n and entropy s and tends to decrease the internal energy e.

In general, the set of differential equations (3)–(5) cannot be solved analytically. These equations can be conveniently expressed in terms of dimensionless variables n, s, e, and t, which are normalized to the respective quantities

$$n_m = (\tau_s g_s)^{1/2}(\tau_e g_e)^{1/2}, \quad s_m \frac{n_m}{\tau_n g_n},$$
$$e_m = (\tau_n g_n)^{-1}(\tau_s g_s)^{-1}, \quad \tau_n. \tag{6}$$

As a result, Eqs. (3)–(5) take the simple form

$$\frac{dn}{dt} = -n + s, \tag{7}$$

$$\tau\frac{ds}{dt} = -s + ne, \tag{8}$$

$$\theta\frac{de}{dt} = (E - e) - sn, \tag{9}$$

where we have also introduced the dimensionless parameters

$$\tau = \frac{\tau_s}{\tau_n}, \quad \theta = \frac{\tau_e}{\tau_n}, \quad E = \frac{e_0}{e_m}. \tag{10}$$

In the adiabatic regime $\tau, \theta \ll 1$, one can employ the slaving principle, which asserts that the conjugate field $s(t)$ and control parameter $e(t)$ follow the order parameter $n(t)$ in their variations [18]. In this case, the left-hand sides of Eqs. (8) and (9) can be taken equal to zero, which gives

$$s = \frac{En}{1 + n^2}, \quad e = \frac{E}{1 + n^2}. \tag{11}$$

These equations imply that, in accordance with the second law of thermodynamics, the Edwards entropy monotonically increases and the internal energy decreases with increasing number of phases. Eliminating the variable n between Eqs. (11), we obtain a simple relation between the entropy and internal energy,

$$s = \sqrt{e(E - e)}. \tag{12}$$

Using the relation defining the temperature

$$T \equiv \frac{\partial e}{\partial s}, \tag{13}$$

we arrive at the expression

$$T = -\left(1 - \frac{E}{2e}\right)^{-1}\sqrt{\frac{E}{e} - 1}. \tag{14}$$

It follows from Eq. (14) that in the internal-energy range $E/2 < e < E$, the Edwards temperature T is nega-

tive and the system becomes self-organizing. Indeed, according to the definition of Eq. (13), if $T < 0$, any increase in the internal energy $\delta e > 0$ leads to a decrease in entropy $\delta s < 0$, i.e., to ordering.

By substituting the first of Eqs. (11) into Eq. (7), the Lorenz equations are reduced to the Landau–Khalatnikov equation

$$\frac{\partial n}{\partial t} = -\frac{\partial W}{\partial n}, \tag{15}$$

where the role of the free energy is played by the synergetic potential

$$W = \frac{1}{2}n^2 - \frac{E}{2}\ln(1 + n^2). \tag{16}$$

If the internal energy E acquired by the system during its prior treatment is small, then the function $W(n)$ has a minimum at $n = 0$ and increases monotonically; that is, a multiphase state is synergetically unfavorable. As the energy increases and exceeds the critical value $E = 1$, the minimum of the synergetic potential $W(n)$ is shifted to the point

$$n_0 = \sqrt{E - 1}. \tag{17}$$

In this case, a dissipative relaxation process in which the number of phases in the system varies and becomes equal to $n_0 \neq 0$ is favorable; the Edwards temperature given by Eq. (14) has a steady-state value

$$T_0 = -\frac{\sqrt{E-1}}{1 - E/2}, \tag{18}$$

which is negative for supercritical energy values $E > 1$ and decreases monotonically with increasing internal energy acquired by the system during its prior treatment.

In the above-described adiabatic regime $\tau, \theta \ll 1$, the dissipative system monotonically goes over to a nonergodic steady state. In this paper, however, our interest is in describing the nonmonotonic behavior; therefore, we should assume that the characteristic-time ratios τ and θ are not small. In this case, the Lorenz equations cannot be solved analytically. However, an analysis performed in [20] revealed that the regime of a strange attractor of a self-organizing system (characteristic of the experimental situation in question) is realized in the case of $\theta > \tau > 1$. Therefore, the internal-energy relaxation time must be longer than the relaxation times of the entropy and of the number of minima occupied by the system. This condition is likely to be satisfied in the experiment discussed above [12].

In addition to the inequality for the relaxation times indicated above, the condition $E > 1$ must be satisfied for a strange attractor to occur [20]. Therefore, stochastic changes in structure caused by redistribution of the states of the system over the energy minima corresponding to different phases will occur only under the condition that the internal energy e_0 acquired by the system during its prior treatment exceeds the critical value e_m given by the next to last expression in Eq. (6). From this expression, it follows that the systems characterized by large positive linear (g_n) and nonlinear (g_s) coupling constants and by long relaxation times τ_n and τ_s are prone to stochastic behavior.

The analysis performed above revealed that a stochastic structural transformation is a compromise between the competing effects of the order parameter on the conjugate field and on the control parameter of the self-organizing system. In the case of the multiphase Pd–Ta–H alloy considered above, the last two parameters are the specific entropy s and internal energy e and the competition between them is due to the thermodynamic identity

$$f = e - Ts, \tag{19}$$

where T is the effective Edwards temperature. This identity is derived from the definition of the Edwards temperature given by Eq. (13) and from the definition of its conjugate (entropy)

$$s = -\frac{\partial f}{\partial T}. \tag{20}$$

Recently, one of the present authors (A.I.O.) showed [23] that these definitions [and, therefore, Eq. (19)] follow from a simple field model in which the behavior of a self-organizing system is described by three two-component fields: the order parameter, conjugate field, and control parameter. The first components of these fields are reduced to the quantities considered above, namely, to the relative number of occupied minima n, the entropy s, and the internal energy e of the nonergodic system. The second components are generalized fluxes conjugate to the quantities indicated above: the probability density flux $\mathbf{q}$ characterizing the redistribution over the internal-energy minima; the thermodynamic force $-\nabla f$, which is the negative of the free-energy gradient; and the negative of the temperature gradient $-\nabla T$. Changes in these components become essential when the system is in a nonsteady state (such as the state of a multiphase Pd–Ta–H alloy exhibiting nonmonotonic behavior). There is reason to believe that the synergetic model proposed in this paper is a variant of the thermodynamic theory of highly nonequilibrium systems, which is far from being complete [24, 25].

As shown above, the kinematic condition for the system to exhibit nonmonotonic behavior is that the relaxation times of the internal energy and temperature gradient exceed those of the entropy and free-energy gradient, as well as the relaxation times for the number of minima occupied by the system and for the conjugate probability flux. This condition explains the anomalously long periods of time over which the system exhibits stochastic behavior. The dynamic condition is that an increase in entropy produce a noticeable increase in the growth rate of the number of minima occupied by the system and, on the other hand, that the

decrease in the internal energy due to the redistribution of the system over these minima give rise to a significant increase in the entropy itself. This condition can be satisfied in the case of large values of the parameters g_n and g_s, that is, in the case where the barriers separating the energy minima are low and the internal-energy profile is not "hard." Finally, the thermodynamic condition is that the system be far from the equilibrium state, which can be realized by subjecting the system to prior treatment, such as quenching, irradiation, or heavy deformation. In the case of the Pd–Ta–H alloy under study, the treatment employed was prior deformation and saturation with hydrogen, which produced elastic stresses as high as roughly 10% of the characteristic elastic modulus. Therefore, one can assume that the internal energy e_m acquired by the system during this treatment is also high.

In closing, we note that the critical slowing-down of the structural transformation observed in the Pd–H system [21] may also be expected to occur in a Pd–Ta–H alloy. Our preliminary data obtained after repeated hydrogenation lend support to this conjecture. This means that when the number of repeated hydrogenations is large, the multivalley structure of the energy profile (with minima of equal depth) is transformed into a multilevel hierarchical structure, which leads to the slowing-down of the alloy evolution reported in [21].

Another remark should be made with reference to the deformed multiphase Pd–Mo–H alloy, which also undergoes nonmonotonic structural transformations similar to those considered above [26]. Here, as in the Pd–Ta–H alloy, a regular shift in the position of diffraction maxima occurred immediately after saturation with hydrogen, which is indicative of expansion and subsequent anisotropic contraction of the crystal lattice. Thereafter, stochastic changes in the number, position, width, and intensity of the components of diffraction maxima were observed. Therefore, it can be concluded that the nonregular behavior of a highly nonequilibrium multiphase system is inherent in structural transformations of alloys saturated with hydrogen.

ACKNOWLEDGMENTS

This study was supported by the Russian Foundation for Basic Research, project no. 99-02-16135.

REFERENCES

1. J. P. Bouchaud, L. F. Gugliandolo, and J. Kurchan, in *Spin Glasses and Random Fields*, Ed. by A. P. Young (World Scientific, Singapore, 1998).
2. S. F. Edwards and A. Metha, J. Phys. (Paris) **50**, 2489 (1989).
3. S. F. Edwards, in *Granular Matter: An Interdisciplinary Approach*, Ed. by A. Metha (Springer, New York, 1994).
4. A. I. Olemskoĭ and I. A. Sklyar, Usp. Fiz. Nauk **162** (6), 29 (1992) [Sov. Phys. Usp. **35**, 455 (1992)].
5. A. I. Olemskoi, *Theory of Structure Transformations in Non-Equilibrium Condensed Matter* (Nova Science, New York, 1999).
6. A. A. Katsnel'son, A. I. Olemskoĭ, I. V. Sukhorukova, and G. P. Revkevich, Usp. Fiz. Nauk **165** (3), 331 (1995) [Phys. Usp. **38**, 317 (1995)]; Vestn. Mosk. Univ., Ser. 3: Fiz., Astron. **35** (3), 94 (1994).
7. V. M. Avdyukhina, A. A. Katsnel'son, and G. P. Revkevich, Poverkhnost, No. 2, 30 (1999).
8. V. M. Avdyukhina, A. A. Katsnel'son, and G. P. Revkevich, Vestn. Mosk. Univ., Ser. 3: Fiz., Astron. **38** (3), 44 (1997).
9. V. M. Avdyukhina, A. A. Katsnel'son, and G. P. Revkevich, Kristallografiya **44** (1), 49 (1999) [Crystallogr. Rep. **44**, 44 (1999)]; Vestn. Mosk. Univ., Ser. 3: Fiz., Astron. **40** (5), 44 (1999).
10. V. M. Avdyukhina, A. A. Katsnel'son, A. I. Olemskoĭ, *et al.*, Fiz. Met. Metalloved. **88** (6), 63 (1999).
11. A. V. Knyaginichev, Khan Kha Sok, V. M. Avdyukhina, *et al.*, Fiz. Tverd. Tela (St. Petersburg) **43** (2), 200 (2001) [Phys. Solid State **43**, 207 (2001)].
12. V. M. Avdyukhina, A. A. Katsnel'son, G. P. Revkevich, *et al.*, Al'tern. Énerg. Ékol., No. 1, 11 (2000).
13. V. M. Avdyukhina, A. A. Katsnel'son, N. A. Prokof'ev, and G. P. Revkevich, Vestn. Mosk. Univ., Ser. 3: Fiz., Astron. **39** (2), 94 (1998).
14. D. M. Vasil'ev, *Diffraction Methods for Study of Structures* (Metallurgiya, Moscow, 1957).
15. M. A. Krivoglaz, *Diffraction of X-rays and Neutrons in Nonideal Crystals* (Naukova Dumka, Kiev, 1983).
16. S. M. Myers, M. I. Baskers, and H. K. Birbaum, Rev. Mod. Phys. **64** (2), 559 (1992).
17. E. Lorenz, J. Atmos. Sci. **20**, 130 (1963).
18. H. Haken, *Synergetics: An Introduction* (Springer, Berlin, 1977; Mir, Moscow, 1980).
19. A. A. Katsnel'son and A. I. Olemskoĭ, *The Microscopic Theory of Inhomogeneous Structures* (Mosk. Gos. Univ., Moscow, 1987).
20. A. I. Olemskoĭ and A. V. Khomenko, Zh. Éksp. Teor. Fiz. **110**, 2144 (1996) [JETP **83**, 1180 (1996)].
21. A. A. Katsnel'son, M. A. Knyazeva, and A. I. Olemskoĭ, Fiz. Tverd. Tela (St. Petersburg) **41** (9), 1621 (1999) [Phys. Solid State **41**, 1486 (1999)]; Fiz. Met. Metalloved. **89** (6), 5 (2000).
22. H. Risken, *The Fokker-Planck Equation* (Springer, Berlin, 1989).
23. A. I. Olemskoi, cond-mat/0106270.
24. J. Marro and R. Dickmann, *Nonequilibrium Phase Transitions in Lattice Models* (Cambridge Univ. Press, Cambridge, 1999).
25. D. Helbing, cond-mat/0012229.
26. V. M. Avdyukhina, A. A. Anishchenko, A. A. Katsnel'son, and G. P. Revkevich, in *Abstracts of RSNÉ-2001 Conference, Moscow, 2001*, p. 133; Perspekt. Mater. **6**, 52 (2001).

Translated by Yu. Epifanov

Physics of the Solid State, Vol. 44, No. 6, 2002, pp. 1028–1030. Translated from Fizika Tverdogo Tela, Vol. 44, No. 6, 2002, pp. 985–987.

SEMICONDUCTORS AND DIELECTRICS

Hole Trapping on the Twofold-Coordinated Silicon Atom in SiO_2

A. V. Shaposhnikov*, V. A. Gritsenko*, G. M. Zhidomirov, and M. Roger*****

** Institute of Semiconductor Physics, Siberian Division, Russian Academy of Sciences, pr. Akademika Lavrent'eva 13, Novosibirsk, 630090 Russia*

*** Boreskov Institute of Catalysis, Siberian Division, Russian Academy of Sciences, pr. Akademika Lavrent'eva 5, Novosibirsk, 630090 Russia*

**** DRECAM, SPEC, Orme des Merisiers CEA Saclay, Gif sur Yvette Cedex, 91191 France*

Received August 1, 2001

Abstract—The ability of a neutral diamagnetic twofold-coordinated silicon atom with two paired electrons (=Si: silylene center) in SiO_2 to capture charge carriers is investigated by the *ab initio* density-functional method. It is found that this defect is a hole trap in SiO_2. Hole trapping brings about the formation of paramagnetic twofold-coordinated silicon atoms with an unpaired electron =Si·. According to this prediction, the silylene center and the silicon–silicon bond can be responsible for the accumulation of the positive charge in metal–oxide–semiconductor structures under ionizing radiation. © *2002 MAIK "Nauka/Interperiodica"*.

The understanding of the trap nature in amorphous SiO_2 is a key factor in the development of reliable radiation-resistant metal–oxide–semiconductor devices. Considerable theoretical and experimental efforts have been made to investigate the atomic structure of intrinsic defects in SiO_2 [1–3]. Four of the most important neutral intrinsic defects in SiO_2 have been studied to date. These are the ≡Si–Si≡ bond or the oxygen vacancy [2–4], the nonbridging oxygen ≡SiO· [1, 4–6], the superoxide radical ≡SiOO· [6], and the twofold-coordinated silicon atom with two unpaired electrons (silylene center) =Si: [7, 8].

Here, symbols (–) and (·) denote the chemical bond and an unpaired electron, respectively. At present, the optical (absorption and luminescence) and magnetic (electron paramagnetic resonance) properties of these defects have been investigated in sufficient detail. However, the ability to localize (or to capture) electrons and holes has been analyzed only for the Si–Si bond. It was shown that the Si–Si bond can capture a hole through the reaction ≡Si–Si≡ + hole $\longrightarrow$ ≡Si^+·Si≡ with the formation of a positively charged paramagnetic *E'* center [3, 9, 10]. In the present work, we investigate the ability of the twofold-coordinated silicon atom in SiO_2 to capture electrons and holes.

Skuja [7] experimentally observed the absorption band at an energy of 5.0 eV (B_2 absorption band) for SiO_2. Excitation into this band leads to the excitation of luminescence with energies of 2.7 eV (blue band) and 4.4 eV (ultraviolet band). According to [7, 8], the B_2 absorption band of SiO_2 can be assigned to the silylene center. However, some authors also attributed the B_2 absorption band to the Si–Si bond [7, 11].

A blue band at 2.7 eV was observed for a SiO_2 thermal layer on Si [12], B^+-, P^+-, and Ar^+-implanted SiO_2 thermal layers [13, 14], chemically deposited SiO_2 [15], and an oxide prepared by oxygen implantation into Si [16]. The 2.7-eV blue band was also observed in the luminescence spectrum of the SiO_xN_y silicon oxynitride [17]. The origin of this band in all the above cases can be associated with the silylene center.

We carried out *ab initio* calculations in the framework of the density-functional theory (DFT) according to the Amsterdam Density Functional (ADF) program [18]. All the calculations were performed in the cluster approximation. The structure of SiO_2 was simulated using fragments of crystalline α-quartz. Dangling bonds at the cluster boundary were saturated with hydrogen. In order to simulate the bulk of SiO_2 and the =Si: defect, we used the $Si_5O_{16}H_{12}$ and $Si_3O_8H_6$ clusters, respectively.

The Kohn–Sham molecular orbitals were constructed using Slater atomic orbitals. The basis set involved the double-zeta basis set with 3*d* polarization functions for all the silicon atoms, which corresponds to the basis set III in the ADF terminology [18]. The location of all the Si and O atoms was optimized using a gradient-corrected DFT potential that included the form for the exchange term [19] and the form for electron correlation [20]. The positions of hydrogen atoms were fixed. The energy gain due to charge carrier trap-

ping on a defect was determined from the following formulas:

$$\Delta E^{e} = (E^{0}_{bulk} + E^{-}_{def}) - (E^{-}_{bulk} + E^{0}_{def}), \quad (1)$$

$$\Delta E^{h} = (E^{0}_{bulk} + E^{+}_{def}) - (E^{+}_{bulk} + E^{0}_{def}). \quad (2)$$

Here, E^{0}_{bulk}, E^{-}_{bulk}, and E^{+}_{bulk} are the energies of neutral, negatively charged, and positively charged clusters which simulate the bulk and E^{0}_{def}, E^{-}_{def}, and E^{+}_{def} are the energies of neutral, negatively charged, and positively charged clusters which simulate the defect. In the case of negative ΔE^{h} (ΔE^{e}), the capture of a hole (electron) is energetically favorable.

With the aim of verifying the reliability of the cluster model used for the simulation of the electronic structure of the SiO_2 bulk, theoretical x-ray emission spectra, namely, the Si *K*, Si $L_{2,3}$, and O *K* spectra, were calculated and compared with the experimental data. The calculated discrete spectrum was broadened using a Lorentzian curve (0.5 eV in width) in order to obtain a continuous spectrum.

As follows from the results of calculations, better agreement with the experiment can be achieved with the inclusion of Si 3*d* polarization functions in the basis set. The calculations also demonstrated that the contribution of cross transitions must be taken into account in the case of the Si $L_{2,3}$ spectrum, even though these transitions can be ignored for the Si *K* and O *K* emission spectra. The figure shows the results of the calculations in comparison with experimental data for the Si *K*, Si $L_{2,3}$, and O *K* spectra of thermally grown SiO_2 on silicon [21]. By and large, the calculated and experimental spectra are in good agreement.

In order to answer the question as to whether the silylene center in SiO_2 can capture an electron and (or) a hole, we calculated the binding energy for negatively and positively charged clusters. The results obtained indicate that electron trapping on the =Si: defect is energetically unfavorable. For hole trapping, the energy gain is equal to –3.2 eV. Moreover, the calculations predict that the silylene center can capture a hole in SiO_2 through the reaction =Si: + h ⟶ =Si·. According to our prediction, the capture of a hole by a neutral diamagnetic silylene center leads to the formation of the positively charged paramagnetic atom of twofold-coordinated silicon with an unpaired electron =Si·.

However, our model ignores the long-range Coulomb polarization induced in the lattice by a positively charged defect. The correction to the energy gain ΔE^{h} for lattice polarization can be estimated in the framework of the classical Born model in the following way. Under the assumption that the charge of a trapped carrier is distributed within a sphere of radius *R*, the total

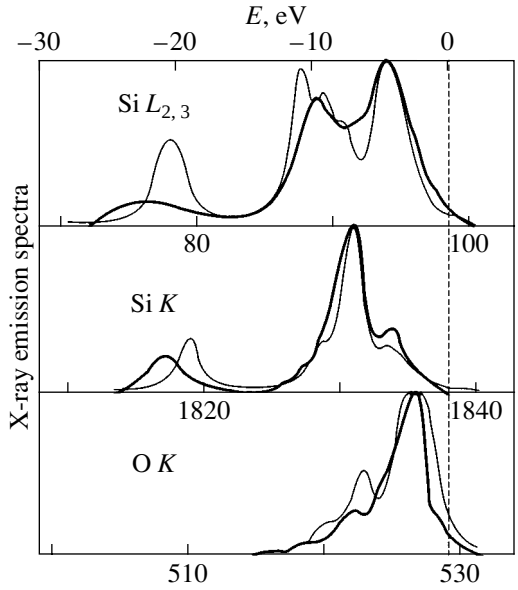

Experimental (thick line) and theoretically calculated (thin line) x-ray emission Si *K*, Si $L_{2,3}$, and O *K* spectra of SiO_2.

energy of electron polarization of the lattice can be estimated from the relationship

$$E_p = -[q^2/(8\pi R)][\varepsilon_0^{-1} - \varepsilon_\infty^{-1}], \quad (3)$$

where ε_0 is the permittivity of free space and ε_∞ is the permittivity of the medium. From relationships (1) and (2), we obtain the following expression for the correction to the energy gain ΔE^{h}:

$$E_p = -(q^2/8\pi)[R_{def}^{-1} - R_{bulk}^{-1}][\varepsilon_0^{-1} - \varepsilon_\infty^{-1}]. \quad (4)$$

Here, $2R_{def} \sim 5.5$ Å and $2R_{bulk} \sim 8$ Å correspond to the sizes of the defect and bulk clusters used in our calculations. For SiO_2, we accept $\varepsilon_\infty \sim 2.25\varepsilon_0$ and obtain $\Delta E_p = -0.45$ eV. This estimate shows that the correction to the energy gain for lattice polarization is relatively small compared with the energy gain due to local electronic and atomic relaxation.

It is generally believed that the accumulation of the positive charge in metal–oxide–semiconductor devices is associated with hole trapping on a neutral Si–Si bond with the formation of the positively charged *E*' center [3, 9, 10]. However, the experiments have revealed a continuous distribution of hole traps in SiO_2 in the energy range from 1.1 to 2.2 eV with two well-resolved peaks at $E_1 \sim 1.2$ eV and $E_1 \sim 1.9$ eV [22]. This two-peak structure can be due to the presence of traps of two types. Our calculated values (~1 and ~3.2 eV) were obtained for the trapping energies of the Si–Si bond and the silylene center, respectively. Taking into account the error in our theoretical calculations, we assume that these values correspond qualitatively to these two

experimental peaks. The verification of this hypothesis calls for further experimental investigation.

We assume that the silylene center in SiO_2 and the Si–Si bond can be responsible for the accumulation of the positive charge in metal–oxide–semiconductor structures under ionizing radiation and injection of hot holes. According to the data obtained, hole trapping on the silylene center leads to the formation of the paramagnetic $=Si^{\cdot}$ center. This effect can be revealed in experiments on electron paramagnetic resonance.

ACKNOWLEDGMENTS

This work was supported by the International Association of Assistance for the promotion of cooperation with scientists from the New Independent States of the former Soviet Union, project INTAS no. 97-0347.

REFERENCES

1. T. E. Tsai and D. L. Griscom, Phys. Rev. Lett. **67** (8), 2517 (1991).
2. V. A. Gritsenko, J. B. Xu, R. W. M. Kwok, *et al.*, Phys. Rev. Lett. **81** (5), 1054 (1998).
3. G. Pacchioni and G. Ierano, Phys. Rev. Lett. **79** (4), 753 (1997).
4. G. Pacchioni and G. Ierano, Phys. Rev. B **57** (2), 818 (1998).
5. L. N. Skuja, J. Non-Cryst. Solids **179** (3), 51 (1994).
6. E. J. Friebele, D. L. Griscom, M. Stapelbroek, and R. A. Weeks, Phys. Rev. Lett. **42** (20), 1346 (1979).
7. L. N. Skuja, J. Non-Cryst. Solids **239** (6), 16 (1998).
8. G. Pacchioni and R. Ferrario, Phys. Rev. B **58** (10), 6090 (1998).
9. J. K. Rudra and W. B. Fowler, Phys. Rev. B **35** (15), 8223 (1987).
10. T. E. Tsai, D. L. Griscom, and E. J. Frieble, Phys. Rev. Lett. **61** (4), 444 (1988).
11. R. Tohmon, Y. Shimogaichi, H. Mizuno, *et al.*, Phys. Rev. Lett. **62** (12), 1388 (1989).
12. W. C. Choi, M. S. Lee, E. K. Kim, *et al.*, Appl. Phys. Lett. **69** (22), 3402 (1996).
13. H. Nishikawa, E. Watanabe, D. Ito, *et al.*, J. Appl. Phys. **78** (2), 842 (1995).
14. B. Carrido, J. Samitier, S. Bota, *et al.*, J. Appl. Phys. **81** (1), 126 (1997).
15. T. Kanashima, R. Nagayoshi, M. Okuyama, and Y. Hamakawa, J. Appl. Phys. **74** (9), 5742 (1993).
16. M. Martini, F. Meinardi, E. Rosetta, *et al.*, IEEE Trans. Nucl. Sci. **45** (7), 1396 (1998).
17. V. A. Gritsenko, Yu. G. Shavalgin, P. A. Pundur, *et al.*, Philos. Mag. B **80** (10), 1857 (2000).
18. C. Fonseca Guerra, J. G. Snijders, G. Te Velde, and E. J. Baerends, Theor. Chem. Acc. **99** (2), 391 (1998).
19. A. D. Becke, Phys. Rev. A **38** (6), 3098 (1988).
20. C. Lee, W. Yang, and R. G. Parr, Phys. Rev. B **37** (2), 785 (1988).
21. V. A. Gritsenko, R. M. Ivanov, and Yu. N. Morokov, Zh. Éksp. Teor. Fiz. **108** (12), 2216 (1995) [JETP **81**, 1208 (1995)].
22. S. L. Miller, D. M. Fleetwood, and P. J. McWhorter, Phys. Rev. Lett. **69** (5), 820 (1992).

Translated by N. Korovin

Physics of the Solid State, Vol. 44, No. 6, 2002, pp. 1031–1034. Translated from Fizika Tverdogo Tela, Vol. 44, No. 6, 2002, pp. 988–991.

SEMICONDUCTORS AND DIELECTRICS

Lattice Thermal Conductivity of Compounds with Inhomogeneous Intermediate Rare-Earth Ion Valence

A. V. Golubkov*, L. S. Parfen'eva*, I. A. Smirnov*, H. Misiorek, J. Mucha**, and A. Jezowski****

** Ioffe Physicotechnical Institute, Russian Academy of Sciences, ul. Politekhnicheskaya 26, St. Petersburg, 194021 Russia*

e-mail: Igor.Smirnov@pop.ioffe.rssi.ru

*** Institute of Low-Temperature and Structural Research, Polish Academy of Sciences, Wroclaw, 50-950 Poland*

Received August 21, 2001

Abstract—The thermal conductivity κ (within the range 4–300 K) and electrical conductivity σ (from 80 to 300 K) of polycrystalline Sm_3S_4 with the lattice parameter $a = 8.505$ Å (with a slight off-stoichiometry toward Sm_2S_3) are measured. For $T > 95$ K, charge transfer is shown to occur, as in stoichiometric Sm_3S_4 samples, by the hopping mechanism ($\sigma \sim \exp(-\Delta E/kT)$ with $\Delta E \sim 0.13$ eV). At low temperatures [up to the maximum in the lattice thermal conductivity $\kappa_{ph}(T)$], $\kappa_{ph} \sim T^{2.6}$; in the range 20–50 K, $\kappa_{ph} \sim T^{-1.2}$; and for $T > 95$ K, where the hopping charge-transfer mechanism sets in, $\kappa_{ph} \sim T^{-0.3}$ and a noticeable residual thermal resistivity is observed. It is concluded that in compounds with inhomogeneous intermediate rare-earthion valence, to which Sm_3S_4 belongs, electron hopping from Sm^{2+} (ion with a larger radius) to Sm^{3+} (ion with a smaller radius) and back generates local stresses in the crystal lattice which bring about a change in the thermal conductivity scaling of κ_{ph} from $T^{-1.2}$ to $T^{-0.3}$ and the formation of an appreciable residual thermal resistivity. © *2002 MAIK "Nauka/Interperiodica".*

Researchers in many laboratories of the world have still not lost interest in the behavior of thermal conductivity in systems with mixed (intermediate) valence (MV) [1–3]. The MV phenomenon is accounted for by the rare-earth (RE) ions in these compounds.

All intermediate-valence materials can be divided into three groups according to the crystallographic positions the RE ions occupy, as well as to the nature of their electronic relations [2].

The first two of these groups (1a and 1b) combine compounds whose RE ions sit at crystallographically equivalent sites in the lattice. In materials of group 1a, the $4f$ electrons transfer between RE-ion configurations with different average numbers of f electrons at the center, i.e., with different valence [transition between the $4f^n$ and $4f^{n-1} + (sd)$]. The frequency of these transitions does not depend on temperature and is ~10^{15} Hz. These materials are called compounds with homogeneous MV.

Materials of group 1b exhibit electron hopping between cations in different valence states with a temperature-dependent frequency from zero to ~10^{11} Hz (at 300 K). Such systems are referred to as materials with inhomogeneous MV.

Finally, the third group comprises compounds in which cations in different valence states occupy inequivalent crystallographic lattice sites, with no electron hopping between them. Such systems bear the name of materials with static MV.

Materials with homogeneous MV are exemplified by SmB_6, SmS (under hydrostatic pressure), and $Sm_{1-x}Ln_xS$ (*Ln* = Gd, Y, etc.); those with inhomogeneous MV, by Sm_3X_4 (*X* = S, Se, Te), etc., and static MV compounds, by Eu_3O_4, etc.

Let us see how the homogeneous, inhomogeneous, and static MVs become manifest in the total thermal conductivity $\kappa_{tot}(T) = \kappa_{ph} + \kappa_e$ of a compound (where κ_{ph} and κ_e are the lattice and electronic components of the thermal conductivity, respectively).

The literature does not mention anything unusual in the behavior of κ_{ph} in materials with homogeneous MV; they exhibit only some features in κ_e(a nontypical temperature dependence and magnitude of the Lorenz number) [1]. Systems with static MV behave as usual classic crystalline materials and do not reveal any features in κ_e and κ_{ph} associated with the MV of their RE ions.

There are practically no publications on the thermal conductivity of materials with inhomogeneous MV. The purpose of this work was to study whether or not electron hopping between ions with different valence affects κ_{ph}.

1063-7834/02/4406-1031$22.00 © 2002 MAIK "Nauka/Interperiodica"

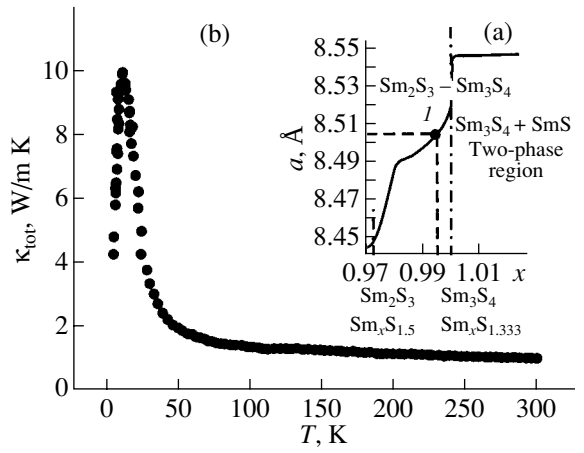

Fig. 1. (a) Dependence of the lattice constant of Sm_3S_4 ($Sm_xS_{1.333}$) on x [5]. (*1*) The a = 8.505 Å value corresponds to the sample studied. (b) Temperature dependence of $\kappa_{tot} = \kappa_{ph}$ of $Sm_{0.995}S_{1.333}$.

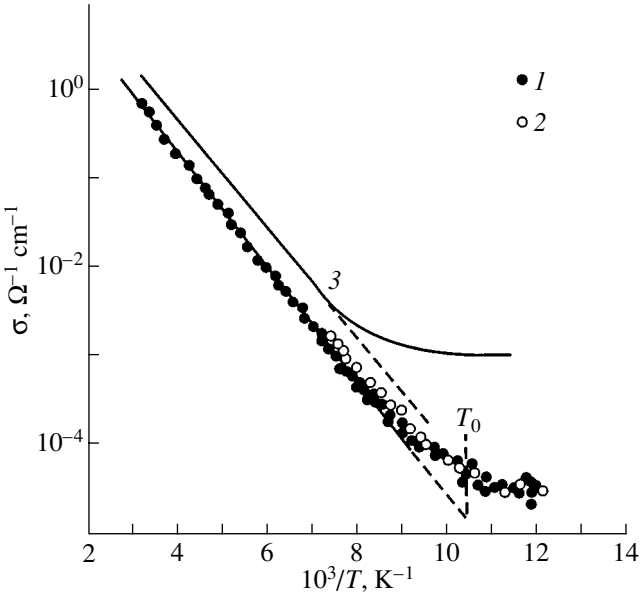

Fig. 2. logσ vs. $10^3/T$ plot for the $Sm_{0.995}S_{1.333}$ sample studied. (*1*, *2*) Direct (300–80 K) and reverse temperature runs, respectively, and (*3*) data for Sm_3S_4 (a = 8.5396 Å) from [3].

For the subject of our study, we chose Sm_3S_4, a compound that crystallizes in the Th_3P_4 cubic structure. The divalent (Sm^{2+}) and trivalent (Sm^{3+}) samarium ions are statistically distributed over the equivalent lattice sites in a 1 : 2 ratio ($Sm^{2+}Sm_2^{3+}S_4^{2-}$). Sm_3S_4 is an *n*-type semiconductor with a fairly high carrier concentration and low electrical conductivity, which grows exponentially with temperature (with an activation energy ~0.13 eV) due to the hopping mechanism of charge transfer.

Because of σ being small, the magnitude of κ_e of Sm_3S_4 is negligible; thus, what we measure in an experiment is $\kappa_{tot} = \kappa_{ph}$.

The polycrystalline Sm_3S_4 sample was prepared (as in [4]) by rf melting in a tantalum crucible which was placed in a sealed molybdenum container. X-ray diffraction analysis showed the sample to be single-phase with a well-defined crystal structure and a lattice constant a = 8.505 Å. According to [5], this value of a corresponds not to the stoichiometric formula Sm_3S_4 ($SmS_{1.333}$) but rather to a composition shifted slightly toward Sm_2S_3; as a result, our sample turned out to have the composition $Sm_{0.995}S_{1.333}$ (Fig. 1a).

The measurements of $\kappa_{tot} = \kappa_{ph}$ (within the range 4–300 K) and of σ (from 80 to 300 K) were carried out on a setup similar to that used in [6].

Figures 1b and 2 present experimental temperature dependences of κ_{tot} and σ for $Sm_{0.995}S_{1.333}$. The data for κ_{tot} obtained in the range 80–3000 K agree fairly well with our earlier measurements of κ in Sm_3S_4 [7]. The electrical conductivity σ of $Sm_{0.995}S_{1.333}$ grows exponentially in the range from 110 to 300 K: $\sigma \sim \exp(-\Delta E/kT)$, with $\Delta E \sim 0.13$ eV (Fig. 2). The temperature interval within which σ shows activated behavior and the magnitude of the activation energy coincide fairly well with those obtained on stoichiometric samples of Sm_3S_4 [2, 3] (see the $\sigma(T)$ curve in Fig. 2 relating to one of the Sm_3S_4 samples studied in [3]). This shows that charge transfer in $Sm_{0.995}S_{1.333}$, as in stoichiometric Sm_3S_4, occurs by the hopping mechanism.

Figure 3 presents a log–log plot of $\kappa_{ph}(T)$, and Fig. 4a shows the temperature dependences of the thermal resistivity $W_{ph} = 1/\kappa_{ph}$ for $Sm_{0.995}S_{1.333}$.

Consider again Fig. 1b. It would seem that the dependence of thermal conductivity on temperature should not have any anomalies, because $\kappa_{ph}(T)$ is a smooth curve. It was found, however, that the $\kappa_{ph}(T)$ relation plotted in the coordinates of Figs. 3 and 4a does exhibit a number of interesting features.

As is evident from Fig. 3, in the low-temperature domain [up to the maximum in $\kappa_{ph}(T)$], $\kappa_{ph} \sim T^{2.6}$, as is the case with most of the crystalline materials, and for temperatures from 20 to 50 K, $\kappa_{ph} \sim T^{-1.2}$, which is a behavior likewise characteristic of sufficiently perfect solids, for which theory suggests $\kappa_{ph} \sim T^{-1}$. As the temperature is raised still further ($T > T_0$), $\kappa_{ph} \sim T^{-0.3}$, which is a feature characteristic of heavily defected materials. It thus appears that for $T \geq T_0$, a new, fairly efficient phonon scattering mechanism becomes operative. This conclusion is also borne out by the data in Fig. 4. It is well known that the residual thermal resistivity of perfect solids $W_{ph}^0 = 0$ and, conversely, defected materials exhibit a fairly high residual thermal resistivity (Fig. 4b).

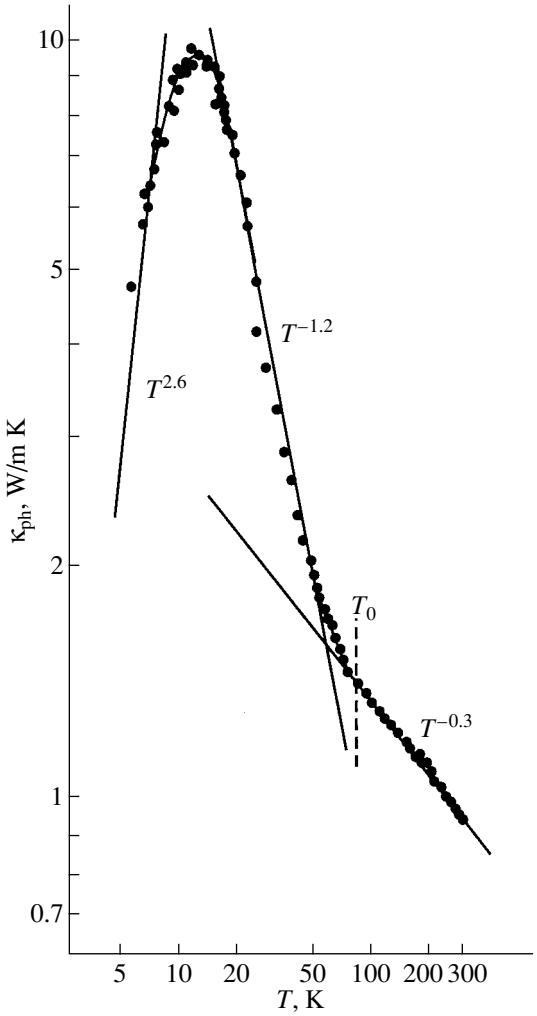

Fig. 3. Temperature dependence of κ_{ph} for the $Sm_{0.995}S_{1.333}$ sample studied.

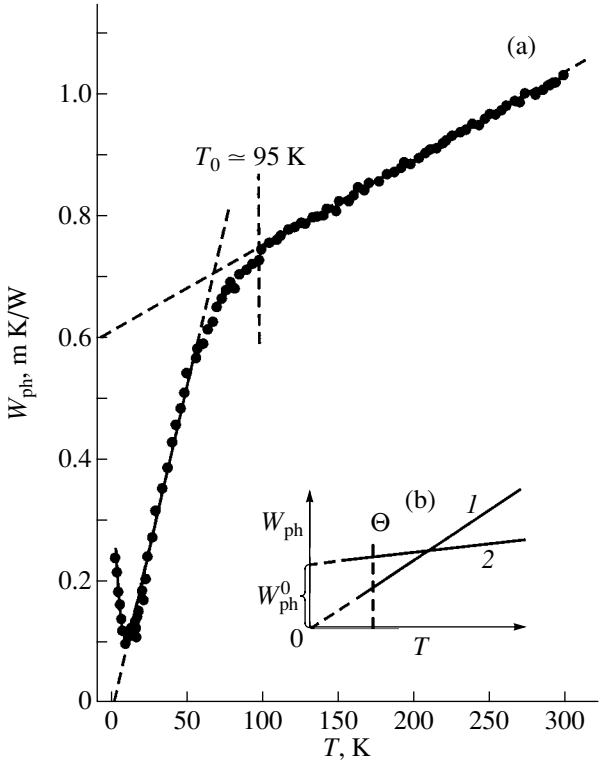

Fig. 4. (a) Temperature dependence of the lattice thermal resistivity ($W_{ph} = 1/\kappa_{ph}$) of the $Sm_{0.995}S_{1.333}$ sample studied, and (b) schematic of the temperature dependence of thermal resistivity of (*1*) a defect-free sample and (*2*) a sample with defects. W^0_{ph} is the residual thermal resistivity for a defected sample, and Θ is the Debye temperature.

The above is illustrated by the experimental $W_{ph}(T)$ relation for an $Sm_{0.995}S_{1.333}$ sample. The behavior of W_{ph} in the range 22–55 K remains, however, puzzling. It is unclear why W_{ph} tends to zero, i.e., $W^0_{ph} = 0$ (as though the crystal becomes perfect at low temperatures), although one could expect a finite residual thermal resistivity due to the presence of Sm vacancies in the sample, because $Sm_{0.995}S_{1.333}$ is not a stoichiometric composition but is shifted toward Sm_2S_3.

At $T = T_0$ (Fig. 4b), as already mentioned, some new mechanism of phonon scattering starts to operate. What could its nature be?

The results displayed in Fig. 2 for $Sm_{0.995}S_{1.333}$ and an analysis of published data permit one to conclude that the new phonon scattering mechanism becomes active after the charge transfer by hopping has become a dominant process.

The ionic radius of Sm^{2+} is considerably larger than that of Sm^{3+}. Electron hopping from Sm^{2+} to Sm^{3+} changes their ionic radii, and this results in a local lattice rearrangement generating stresses (compressive and tensile) around these ions. The lattice breathes, as it were, and cannot apparently relax completely in one electron hopping cycle. The local stresses thus created possibly act as additional phonon scatterers; this accounts for the formation of the noticeable thermal resistivity.

One may thus conclude that electron hopping from Sm^{2+} to Sm^{3+} in compounds with inhomogeneous MV, to which Sm_3S_4 belongs, generates local stresses in the lattice, resulting in a change of the temperature dependence from $\kappa_{ph} \sim T^{-1.2}$ to $\kappa_{ph} \sim T^{-0.3}$ and in an appreciable thermal resistivity.

ACKNOWLEDGMENTS

The authors express gratitude to N.F. Kartenko and N.V. Sharenkova for x-ray structural measurements.

This work was conducted within a bilateral agreement between the Russian and Polish Academies of

Sciences and was supported by the Russian Foundation for Basic Research (project no. 99-02-18078) and the Polish Committee for Scientific Research (grant no. 2PO3B 129-19).

REFERENCES

1. I. A. Smirnov and V. S. Oskotski, in *Handbook on Physics and Chemistry of Rare Earth*, Ed. by K. A. Gshneidner, Jr. and L. Eyring (Elsevier, Amsterdam, 1993), Vol. 16, p. 107.
2. B. Battlog, E. Kaldis, A. Schlegel, *et al.*, Solid State Commun. **19**, 673 (1976).
3. L. N. Vasil'ev, V. V. Kaminskiĭ, and M. V. Romanova, Fiz. Tverd. Tela (St. Petersburg) **38** (7), 2034 (1996) [Phys. Solid State **38**, 1122 (1996)].
4. A. V. Golubkov, T. B. Zhukova, and V. M. Sergeeva, Izv. Akad. Nauk SSSR, Neorg. Mater. **2**, 77 (1966).
5. E. Kaldis, J. Less-Common Met. **76**, 163 (1980).
6. A. Jezowski, J. Mucha, and G. Pompe, J. Phys. D **20**, 1500 (1987).
7. I. A. Smirnov, L. S. Parfen'eva, V. Ya. Khusnutdinova, and V. M. Sergeeva, Fiz. Tverd. Tela (Leningrad) **14** (9), 2783 (1972) [Sov. Phys. Solid State **14**, 2412 (1972)].

Translated by G. Skrebtsov

Physics of the Solid State, Vol. 44, No. 6, 2002, pp. 1035–1043. Translated from Fizika Tverdogo Tela, Vol. 44, No. 6, 2002, pp. 992–1000.

SEMICONDUCTORS AND DIELECTRICS

Effect of the Isotope Composition on the Energy Bands in a Semiconductor: Universal Relation for Monatomic Crystals

A. P. Zhernov

Kurchatov Institute Russian Research Center, pl. Kurchatova 1, Moscow, 123182 Russia

Received April 13, 2001; in final form, September 27, 2001

Abstract—The effect of the isotopic composition of a semiconductor compound on its energy band structure is considered. The role of the changes in the lattice unit-cell volume and of the renormalization of the electron–phonon interaction that are caused by isotopic-composition variations is discussed. A universal relation describing the dependence of the energy bands on isotopic composition and temperature is derived for monatomic crystals in the virtual-crystal approximation. *© 2002 MAIK "Nauka/Interperiodica".*

1. INTRODUCTION

Considerable recent attention has been given to the study of the properties of chemically pure and structurally perfect semiconductor single crystals of different isotopic content. There has been a great deal of work devoted to the study of classical, commercially important monatomic semiconductors such as diamond, silicon, and germanium. That work was favored by the availability of fabricated, virtually defect-free bulk isotope-rich single crystals of ^{12}C, ^{13}C, ^{28}Si, and ^{70}Ge and ^{76}Ge, as well as of crystals with an isotopic composition different from the natural abundance ratio (see, e.g., [1–5]). We note that diamond crystals of different isotope composition have been grown in a laboratory of the General Electric Company (USA) and that germanium crystals are the result of joint efforts of research groups at the Molecular-Physics Institute of the Russian Research Center Kurchatov Institute (Russia) and at the Lawrence National Laboratory (Berkeley, USA). Silicon crystals of high isotopic content are the result of collaborations of Russian, German, and Japanese researchers.

The effects of a variation in the isotopic composition of a compound can be linear in the isotopic-mass difference (first-order effects) or proportional to the mean square fluctuation in the atomic mass (second-order effects). The first-order effects can reveal themselves in static and thermodynamic properties. Strong first- and second-order effects should be observed in the behavior of the kinetic parameters and optical spectra (see, e.g., [6–8]).

As a first approximation, one can describe harmonic phonon modes in terms of the virtual-crystal model. In this case, a real lattice with randomly distributed isotopes is replaced by a lattice without isotopic disorder, but with the atomic masses of the compound constituents replaced by their mean values $\langle M\rangle = M_c^k = \sum_i c^k M_i^k$, where k specifies atoms in the unit cell and c_i^k is the concentration of the ith isotope of the given element. It is also assumed that the relative mean square fluctuation in the atomic mass $G_2 = (\langle M^2\rangle - \langle M\rangle^2)/\langle M\rangle^2$ is small. In the virtual-crystal model, the isotopic effect can take place directly or through anharmonic phonon–phonon and electron–phonon interactions.

In this paper, we consider the effect of the isotopic composition on the structure and position of energy bands in a semiconductor within the virtual-crystal model in the quasi-harmonic approximation.

It is well known that the temperature dependence of the energy bands and of the optical characteristics of a crystal is due to two basic effects. First, the $E_{n,\mathbf{f}}$ bands depend on the unit-cell volume of the crystal, which varies because of thermal expansion of the lattice, and, second, the energy $E_{n,\mathbf{f}}$ varies with increasing temperature T because of electron–phonon interaction (EPI). Due to EPI, the contribution from the elastic channel is renormalized, because the true amplitude of electron–ion interaction contains the dynamic Debye–Waller (DW) factor in addition to the static component. The contributions from inelastic intraband and interband EPI processes are also renormalized [9, 10].

Therefore, when the isotopic composition is varied and the phonon spectrum is distorted, the energy bands should also be markedly affected. The effect of the isotopic composition on the energy bands (isotope shift in energy) is due to a change in the unit-cell volume and to the EPI renormalization (the corresponding contribu-

1063-7834/02/4406-1035$22.00

tions will be designated by indices $D\Omega$ and EP, respectively). At some temperature T, we can write

$$\left(\frac{\partial E}{\partial M}\right)_M = \left(\frac{\partial E}{\partial M}\right)_{\text{tot}} = \left(\frac{\partial E}{\partial M}\right)_{D\Omega} + \left(\frac{\partial E}{\partial M}\right)_{EP}.$$

It should be noted that in recent years, the effect of the isotopic composition on the electronic band structure has been studied experimentally in considerable detail by Cardona and coworkers (the relevant references are cited in Section 4). As for theoretical papers on the subject under discussion, the present author knows of only three such publications. In [11], calculations were carried out for carbon and germanium using the NLPP method for electrons and the bond charge model for phonons; the changes in the renormalized interband transition energies produced by a change in the isotopic composition and associated with the term $(\partial E/\partial M)_{EP}$ were found. In [12, 13], the contributions from both terms $(\partial E/\partial M)_{D\Omega}$ and $(\partial E/\partial M)_{EP}$ were calculated for Ge, GaAs, and ZnSe using the NLPP and LCAO methods; the phonon modes were described in terms of the bond charge model, as well as in the shell model and the rigid-ion model.

In this paper, we show that there are universal relations that relate interband transition parameters for monatomic crystals of different isotope composition at any temperature. These relations allow one to find the parameters of isotope-enriched crystals when data for crystals of natural isotope composition is given.

In Section 2, we summarize the published results of studies of the influence of the temperature and isotopic composition on the energy band structure. The effects of both volume changes and EPI are considered. A universal relation describing the dependence of the energy bands of monatomic crystals on isotopic composition and temperature is derived in Section 3. This relation has a simple form, because in such crystals, the polarization vectors of phonon modes are independent of the atomic mass and the mass dependence of the phonon frequencies is $\omega(l) \sim M^{-1/2}$. In the case of polyatomic crystals, the situation is much more complicated, because the isotope shifts in frequency are proportional to the square of the magnitude of the corresponding polarization vector (see Appendix), which, in turn, depends on the atomic masses. This case will be analyzed separately. In Section 4, we discuss the data (obtained by linear and nonlinear spectroscopy methods) on the effect of the composition on the isotopic energy shifts of direct and indirect interband electron transitions and on the position of critical points in the optical spectra.

2. THE DEPENDENCE OF THE ENERGY BANDS ON THE ISOTOPE COMPOSITION AND TEMPERATURE

2.1. Volume Changes

Let us find the renormalization of the energy band E due to the change in the lattice unit-cell volume associated with phonon spectrum distortions that are produced by variations in the isotope composition. For this purpose, we calculate the derivative of the energy with respect to the atomic mass of a compound constituent for a fixed value of temperature. We have (see also [14])

$$\left(\frac{\partial E}{\partial M_c^k}\right)_{D\Omega} = -B\left(\frac{\partial E}{\partial P}\right)_V \left(\frac{\partial \ln\Omega}{\partial M_c^k}\right)_P, \quad (1)$$

where Ω is the unit-cell volume of the crystal, $B = -V/(\partial P/\partial V)_T$ is the bulk modulus, and $(\partial E/\partial P)_V$ characterizes the pressure dependence of the energy band. We note that the bulk modulus B and the coefficient $(\partial E/\partial P)_V$ usually depend on T only slightly.

In the quasi-harmonic approximation,

$$\Omega(T) = \Omega_0 + \frac{1}{B}\sum_l \gamma(l)\epsilon(l), \quad (2)$$

where Ω_0 is the unit-cell volume of the "frozen" (static) lattice; the index $l = \{\mathbf{q}, j\}$ specifies vibrational modes, with $\mathbf{q}$ and j being the quasi-momentum and polarization index of a phonon mode, respectively; $\gamma(l)$ is the partial Grüneisen constant for the lth vibrational mode (these constants account for the fact that the dependences of mode frequencies $\omega_c(l)$ on the unit-cell volume are different); and $\epsilon(l)$ is the contribution from this mode to the thermal energy. We have

$$\gamma(l) = -\frac{\partial\omega_c(l)/\partial\Omega}{\omega_c(l)/\Omega}, \quad \epsilon(l) = \hbar\omega_c(l)\left[n(l) + \frac{1}{2}\right], \quad (3)$$

where $n(l)$ is the Bose–Einstein factor. We note that the frequencies $\omega_c(l)$ are functions of the volume, temperature, and atomic masses.

The derivative $(\partial E/\partial M^k)_{D\Omega}$ given by Eq. (1) is positive definite as a rule, because the unit-cell volume Ω usually decreases with increasing isotope mass.

Given the quantity $(\partial E/\partial M_c^k)_{D\Omega}$, one can directly calculate the difference in the energy band of crystals with atomic masses M_c^k and $M_c^k + \Delta M^k$ from the formula

$$(\partial\tilde{E}^{D\Omega})(\Delta M^k) = \Delta E^{D\Omega}(M_c^k + \Delta M^k) - \Delta E^{D\Omega}(M_c^k) = \left(\frac{\partial E}{\partial M_c^k}\right)_{D\Omega}\Delta M^k. \quad (4)$$

From Eqs. (1) and (4), it follows that the energy in the band increases with increasing isotope mass because the crystal volume decreases.

It should be noted that for monatomic semiconductors C, Si, and Ge, the quantities involved in Eq. (4) have been investigated in detail. The values of coefficients such as $(\partial E/\partial P)_T$ can be found in [10]. As for the quantity $(\partial \ln\Omega/\partial M^k)_V$, its behavior in a wide range of parameter values was investigated theoretically within microscopical models, e.g., in [15–18].

From the above discussion, it follows that the energy renormalization due to the change in the unit-cell volume is given by

$$\Delta E_{\mathbf{f},n}^{D\Omega} \propto -B\left(\frac{\partial E_{\mathbf{f},n}}{\partial P}\right)_V \frac{\Omega(T)-\Omega_0}{\Omega_0} = -\left(\frac{\partial E_{\mathbf{f},n}}{\partial P}\right)_V \sum_l \gamma(l)\epsilon(l). \tag{5}$$

This formula for $\Delta E_{\mathbf{f},n}^{D\Omega}$ is used in Section 3 when deriving a universal relation for the electronic energy bands.

2.2. The Debye–Waller Factor and Inelastic Electron–Phonon Scattering

In this subsection, we summarize the published results of investigations of the influence of the temperature and isotope composition on EPI and on the energy band renormalization caused by this interaction. In the virtual-crystal approximation, this energy renormalization was calculated in [9]. In fact, Allen and Heine [9] laid the foundation for the theory of the temperature dependence of the electronic band structure. They calculated the energy bands $E_{\mathbf{f},n}(T)$ in the adiabatic approximation using second-order perturbation theory in the atomic displacements.

We assume the crystalline potential $V(\mathbf{r}, \mathbf{u})$ to be the sum of the potentials V_k of individual ions. The position of an ion in the lattice is determined by the equilibrium position vector of the unit cell $\mathbf{R}_\mathbf{m}^{(0)}$ and, within this cell, by index k. We write $\tilde{V}_k = V_k(\mathbf{r} - \mathbf{R}_\mathbf{m}^{(0)} - \mathbf{u}_{\mathbf{m}k})$, where vectors $\mathbf{u}_{\mathbf{m}k}$ are dynamic atomic displacements. The potentials $\tilde{V}_k$ can be expanded in a power series in displacements $\mathbf{u}_{\mathbf{m}k}$. Then, we find the states of electrons moving in the potential $V(\mathbf{r}, \mathbf{u} = 0)$ of the frozen lattice. The corresponding one-electron energy eigenvalues $\varepsilon_n(\mathbf{f})$ and eigenfunctions $|\mathbf{f}, n\rangle$ of the Kohn–Sham type are specified by the quasi-momentum $\mathbf{f}$ and band index n. The spin index will be dropped for the sake of simplicity.

It is generally agreed that such one-electron states describe long-lived excitations. Although the concept of quasiparticles is substantiated only when their energy is close to the Fermi energy, experiment suggests that the limits of applicability of this concept are wider.

Let us consider how the electronic structure is affected by the linear and quadratic terms (in dynamic atomic displacements) H_1 and H_2, respectively, that are present in the electron–ion interaction Hamiltonian. By definition, we have

$$H_{\text{int}} = H_1 + H_2 = \sum_{\mathbf{m},k} \frac{\partial V_k}{\partial \mathbf{R}_\mathbf{m}^{(0)\alpha}} u_{\mathbf{m},k}^\alpha + \frac{1}{2}\sum_{\mathbf{m},k;\,\mathbf{m}'} \frac{\partial^2 V_k}{\partial R_\mathbf{m}^{(0)\alpha}\partial R_{\mathbf{m}'}^{(0)\beta}} u_{\mathbf{m},k}^\alpha u_{\mathbf{m}',k'}^\beta + \ldots, \tag{6}$$

where $V_k = V_k(\mathbf{r} - \mathbf{R}_\mathbf{m}^0)$ and α and β are Cartesian coordinates.

In the adiabatic approximation [to the order of $\sim(m_e/M)^{1/2}$], one can consider the atomic displacements to be classical quantities when calculating the renormalized spectrum. In this case, using the time-independent perturbation theory, the energy renormalization of a particle in the state $|\mathbf{f}, n\rangle$ can be written as

$$\Delta E_{\mathbf{f},n}^{EP}(\{\mathbf{u}_{\mathbf{m},k}\}) = \langle \mathbf{f}, n|H_1 + H_2|\mathbf{f}, n\rangle + \sum_{\mathbf{f},\,n\neq\mathbf{f}',\,n'} \frac{|\langle \mathbf{f}', n'|H_1|\mathbf{f}, n\rangle|^2}{\varepsilon_n(\mathbf{f}) - \varepsilon_{n'}(\mathbf{f}') + i\eta}. \tag{7}$$

Next, we perform thermal ensemble averaging $\langle\ldots\rangle$ of Eq. (7) over small dynamic thermal atomic displacements, which allows one to directly find the temperature dependence of the energy bands, i.e., to go over from $E_{\mathbf{f},n}(\{\mathbf{u}_{\mathbf{m},k}\})$ to $E_{\mathbf{f},n}(T)$. In the harmonic approximation to atomic oscillations [9], we obtain

$$E_{\mathbf{f},n}(T) = \varepsilon_n(\mathbf{f}) + \Delta E_{\mathbf{f},n}^{EP}(T), \qquad E_{\mathbf{f},n}^{EP}(T) = \Delta E_{\mathbf{f},n}^{DW}(T) + \Delta E_{\mathbf{f},n}^{SE}(T), \tag{8}$$

where

$$\Delta E_{\mathbf{f},n}^{EP}(T) = \frac{1}{2}\sum_\mathbf{m} \left\langle \mathbf{f}, n\left|\frac{\partial^2 V_k}{\partial R_\mathbf{m}^{(0)\alpha}\partial R_\mathbf{m}^{(0)\beta}}\right|\mathbf{f}, n\right\rangle \langle u_{\mathbf{m},k}^\alpha u_{\mathbf{m},k}^\beta\rangle + \sum_{\mathbf{m},k;\,\mathbf{m}',k'} \sum_{\mathbf{f},\,n\neq\mathbf{f}',\,n'} \frac{\left\langle \mathbf{f}, n\left|\frac{\partial V_k}{\partial R_\mathbf{m}^{(0)\alpha}}\right|\mathbf{f}', n'\right\rangle \left\langle \mathbf{f}', n'\left|\frac{\partial V_{k'}}{\partial R_{\mathbf{m}'}^{(0)\beta}}\right|\mathbf{f}, n\right\rangle}{\varepsilon_n(\mathbf{f}) - \varepsilon_{n'}(\mathbf{f}') + i\eta} \times \langle u_{\mathbf{m},k}^\alpha u_{\mathbf{m}',k'}^\beta\rangle. \tag{9}$$

It will be recalled that the dynamic atomic displacement operator is defined as

$$\mathbf{u}_{\mathbf{m},k} = \sum_{\mathbf{q}i} \sqrt{\frac{\hbar}{2NM_c^k\omega_c(l)}} \times [\mathbf{e}^c(k|l)e^{i\mathbf{q}\mathbf{R}_m^{(0)}} b_l + \mathbf{e}^{c*}(k|l)e^{-i\mathbf{q}\mathbf{R}_m^{(0)}} b_l^*], \tag{10}$$

where $\omega_c(l)$ and $\mathbf{e}(k|l)$ are the frequency and polarization vector of phonon mode $l = \{\mathbf{q}j\}$, respectively, and b_l and b_l^* are the annihilation and creation operators of a quasiparticle, respectively.

There are two terms on the right-hand side of Eq. (9). The first of them describes the renormalization through the Debye–Waller factor, i.e., due to elastic scattering in which an electron in the state $|\mathbf{f}, n\rangle$ creates and destroys a phonon of wave vector $\mathbf{q}$ and polarization j. We denote the corresponding correction to the electronic energy spectrum of the crystal with frozen atomic displacements as $\Delta E_{\mathbf{f},n}^{DW}$. The second term describes the second-order contribution to electron–phonon interaction from inelastic processes (including interband and intraband transitions). The corresponding correction $\Delta E_{\mathbf{f},n}^{SE}$ to the electronic energy spectrum is a complex quantity; its real part gives the change in the effective electron mass, and the imaginary part determines the electron lifetime.

Thus, Eq. (9) can be represented in the form

$$E_{\mathbf{f},n}^{EP}(T) = \Delta E_{\mathbf{f},n}^{DW} + \Delta E_{\mathbf{f},n}^{SE} + i\Gamma_{\mathbf{f},n}. \tag{11}$$

Pick *et al.* [19] have derived the so-called acoustic sum rule for metals and insulators in the long-wavelength limit; this sum rule is a consequence of the electrical neutrality condition of the system. Based on this sum rule, one can redefine the first term in Eq. (9), which represents the renormalization through the DW factor [9–11]. Using Eq. (10) for the dynamic atomic displacements, one can thus obtain the following expression instead of Eq. (9) [12, 20]:

$$\Delta E_{\mathbf{f},n}^{EP}(T) = \sum_{\mathbf{q},j}\left(\left[\frac{\partial E_{\mathbf{f},n}}{\partial n(\mathbf{q},j)}\right]_{DW} + \left[\frac{\partial E_{\mathbf{f},n}}{\partial n(\mathbf{q},j)}\right]_{SE}\right) \times\left(n(\mathbf{q},j)+\frac{1}{2}\right), \tag{12}$$

$$\left[\frac{\partial E_{\mathbf{f},n}^{EP}}{\partial n(\mathbf{q},j)}\right]_{DW} = -\frac{1}{2N}\sum_{n';\,k,k'}\frac{Q_\alpha^*(\mathbf{f},n,n',0j,k)Q_\beta(\mathbf{f},n',n;0j,k')}{\varepsilon_n(\mathbf{f})-\varepsilon_{n'}(\mathbf{f})+i\eta} \tag{13}$$

$$\times\left[\frac{1}{M_c^k}e_\alpha^c(k|-\mathbf{q}j)e_\beta^c(k|\mathbf{q}j)+\frac{1}{M_c^{k'}}e_\alpha^c(k'|-\mathbf{q}j)e_\beta^c(k'|\mathbf{q}j)\right],$$

$$\left[\frac{\partial E_{\mathbf{f},n}}{\partial n(\mathbf{q},j)}\right]_{SE} = \frac{1}{N}\sum_{n';\,k,k'}\frac{Q_\alpha(\mathbf{f},n,n',\mathbf{q}j,k)Q_\beta(\mathbf{f},n,n';\mathbf{q}j,k')}{\varepsilon_n(\mathbf{f})-\varepsilon_{n'}(\mathbf{f}+\mathbf{q})} \tag{14}$$

$$\times\frac{1}{\sqrt{2M_c^kM_c^{k'}}}e_\alpha^c(k|-\mathbf{q}j)e_\beta^c(k'|\mathbf{q}j).$$

Here, the quantity $\mathbf{Q}$ is

$$\mathbf{Q}(\mathbf{f},\mathbf{n},\mathbf{n}';\mathbf{q}\mathbf{j},\mathbf{k}) = \left\{\frac{\hbar}{\omega_c(\mathbf{q},j)}\right\}^{1/2}\langle\mathbf{f}',n'|\nabla V_k|f,n\rangle, \tag{15}$$

where $\mathbf{f}' = \mathbf{f} + \mathbf{q} + \mathbf{G}$, with $\mathbf{G}$ being a reciprocal lattice vector.

The difference in the energy bands of crystals with atomic masses M_c^k and $M_c^k + \Delta M^k$ that is associated with EPI can be written as

$$\Delta\tilde{E}^{EP}(\Delta M^k) = \Delta E^{EP}(M_c^k+\Delta M^k)-\Delta E^{EP}(M_c^k) = \left(\frac{\partial E^{EP}}{\partial M_c^k}\right)_{T,V}\Delta M^k. \tag{16}$$

We note that the derivative $(\partial E^{EP}/\partial M_c^k)_{T,V}$ is positive. The energy renormalization due to EPI decreases with increasing atomic mass. In fact, crystal vibrations become frozen out as the atomic mass increases. The interband transition energies are increased in this case.

Thus, we have investigated the renormalization of the electronic energy spectrum due to EPI at a fixed crystal volume. Based on Eqs. (8), (9), and (12)–(14), one can analyze the influence of the isotope composition on the energy bands through EPI over a wide temperature range.

3. A UNIVERSAL RELATION DESCRIBING THE EFFECT OF THE ISOTOPE COMPOSITION ON THE ENERGY BANDS: MONATOMIC CRYSTALS

We consider the isotope-composition dependence of the energy bands $E_{\mathbf{f},n}$ of a crystal composed of atoms of the same element. It will be shown that in the virtual-crystal approximation, this dependence is described by a simple relation.

The basic equation determining the eigenfrequencies and polarization vectors of the vibrational modes $l = \{\mathbf{q}j\}$ of a monatomic crystal of an arbitrary isotopic composition (specified by index c) has the form

$$\omega_c^2(l)e_\alpha^c(k|l) = \sum_{k',\alpha'}\Phi_{\alpha\alpha'}^c(kk'|\mathbf{q})e_{\alpha'}^c(k'|l). \tag{17}$$

Here, $\Phi_{\alpha\alpha'}^c(kk'|\mathbf{q})$ is the dynamic matrix of the crystal and α and α' specify the Cartesian coordinate axes. The

matrix Φ has the form

$$\Phi^c_{\alpha\alpha'}(kk'|\mathbf{q}) = \frac{1}{M_c}\tilde{\Phi}_{\alpha\alpha'}(kk'|\mathbf{q}) = \frac{1}{NM_c}\sum_{\mathbf{mm}'}\varphi_{\alpha\alpha'}(\mathbf{m}k, \mathbf{m}'k')\exp(i\mathbf{q}(\mathbf{R}^{(0)}_{\mathbf{m}} - \mathbf{R}^{(0)}_{\mathbf{m}'})). \quad (18)$$

Here, $\varphi_{\alpha\alpha'}(\mathbf{m}k, \mathbf{m}'k')$ is the matrix of second-order force constants and N is the number of unit cells. We note that the matrix $\tilde{\Phi}$ is independent of the mean atomic mass M_c.

In the case of a monatomic crystal, as shown in the appendix, the frequencies of vibrational modes are subject to the relation

$$\frac{d\ln\omega_c^2(l)}{d\ln M_c} = -1 + O\left(\left(\frac{|\Delta M|}{M_c}\right)^2, \frac{\Delta M}{M_c}, \frac{\langle u^2\rangle}{a^2}\right), \quad (19)$$

from which it follows that

$$\omega_c(l) = w(l)M_c^{-1/2}. \quad (20)$$

By definition, $w(l)$ is independent of M_c.

Substituting Eqs. (20) and (18) into Eq. (17) yields

$$w^2(l)e^c_\alpha(k|l) = \sum_{k',\alpha'}\tilde{\Phi}^c_{\alpha\alpha'}(kk'|\mathbf{q})e^c_{\alpha'}(k'|l). \quad (21)$$

It is immediately obvious from Eq. (21) that, in contrast to the frequencies, the polarization vectors $e^c_\alpha(k|l)$ are independent of the atomic mass for a specified isotope composition of the crystal.

We will designate the parameters of the crystal of a certain isotope composition by index c_0 and in the case of an arbitrary isotope composition, by index c, as before. Let us consider the changes in the energy bands caused by isotope composition variations and associated with the altered volume and EPI.

First, we consider the energy band renormalization associated with the change in the unit-cell volume and described by Eq. (5). Differentiating $\gamma(l)$ with respect to M_c and using Eq. (19), one can verify that $\gamma(l)$ is independent of M_c. Therefore, in the sum over l in Eq. (5), only the following quantity depends on the mean atomic mass of the crystal at $T < T_D$ [through the frequency $\omega_c(l)$]:

$$X^{(1)}_c(l, T) = \omega_c(l)\left[n\left(\frac{\hbar\omega_c(l)}{k_BT}\right) + \frac{1}{2}\right]. \quad (22)$$

Next, we consider the contribution associated with EPI and described by Eqs. (12)–(14). In this case, the quantity dependent on the mean atomic mass M_c is

$$X^{(2)}_c(l, T) = \frac{1}{M_c\omega_c(l)}\left[n\left(\frac{\hbar\omega_c(l)}{k_BT}\right) + \frac{1}{2}\right] \sim \omega_c(l)\left[n\left(\frac{\hbar\omega_c(l)}{k_BT}\right) + \frac{1}{2}\right]. \quad (23)$$

Thus, for an arbitrary phonon spectrum, the energy band renormalizations associated with the unit-cell volume and EPI have the same dependence on the mean atomic mass. Using Eq. (20), we find

$$X^{(i)}_c(l, T) = \sqrt{M_{c0}/M_c}X^{(i)}_{c_0}(l, T'), \quad T' = T\sqrt{M_c/M_{c_0}}. \quad (24)$$

Therefore, the changes in the energy bands caused by isotope composition variations are described by the universal relation

$$\Delta E^{(c)}_{\mathbf{f}n}(T) = \sqrt{M_{c_0}/M_c}\Delta E^{(c_0)}_{\mathbf{f}n}(T'). \quad (25)$$

The quantity $\Gamma_{\mathbf{f},n}$ (inversely proportional to the electron lifetime) involved in Eq. (11) is also described by a universal relation similar to Eq. (25).

In the practically important case of very low temperatures, as follows from Eqs. (22) and (23), the atomic-mass dependences of the energy and decay constant of an electron in the state ($\mathbf{f}$, n) are given by

$$E^{(c)}_{\mathbf{f}n}(T = 0) = \varepsilon_n(\mathbf{f}) + \frac{C_1}{\sqrt{M_c}}, \quad \Gamma^{(c)}_{\mathbf{f},n} = \frac{C_2}{\sqrt{M_c}}. \quad (26)$$

We recall that $\varepsilon_n(\mathbf{f})$ is the energy of an electron in the frozen lattice. This energy and the constants C_1 and C_2 are independent of the atomic mass.

It should be noted that in the classical limit of high temperatures, the electronic energy spectrum does not depend on the isotope composition, as follows immediately from Eqs. (22)–(25).

Universal relations are useful in analyzing the experimental dependences of crystal parameters on the isotope composition. Given data for crystals of the natural isotope composition $c_0 = c_{\text{nat}}$, one can predict the values of the parameters for isotope-enriched crystals and compare them with the respective experimental values.

The universal relations derived above are simple in structure and take place in monatomic crystals, because the polarization vectors are independent of the atomic mass and the frequencies vary as $\omega(l) \sim M^{-1/2}$. In polyatomic crystals, the situation is more complicated, because the isotopic frequency shifts are proportional to the square of the magnitudes of the corresponding polarization vectors (see Appendix) and the polarization vectors themselves also depend on the atomic

mass. The case of polyatomic crystals calls for special investigation.

In some papers (see, e.g., [10, 21, 22]), the temperature and atomic-mass dependences of the energy bands E_i were described introducing a mean phonon frequency ϑ_c and a mean Bose–Einstein factor n_c and the following formula was used:

$$E_i = E_i^0 - B_i\left(\frac{M_{\text{nat}}}{M_c}\right)^{1/2}(2n_c + 1), \qquad (27)$$

where $n_c = 1/[\exp(\vartheta_c/T) - 1]$, E_i^0 is the nonrenormalized energy gap, and B_i is a constant. By definition, $\vartheta_c = \vartheta_{\text{nat}}(M_{\text{nat}}/M_c)^{1/2}$. The electron damping constant due to EPI was determined in much the same way. At $T > T_D$, we have

$$E_i(T > T_D) = E_i^0 - 2B_i\frac{T}{T_D}, \qquad (28)$$

where E_i is independent of the atomic mass. Therefore, the constant B_i can be determined from the dependence of E_i on T at high temperatures. We note that Eq. (27) is an analog of the empirical Varshni formula.

In connection with Eq. (27), we will make a few remarks with reference to the results of the studies presented in [12, 13], where the energy gap E_g in germanium was calculated as a function of isotope composition using the NLPP and LCAO methods. (The calculations made in [13] using the LCAO method seem to be more accurate. In particular, the derivative $(\partial E_g/\partial T)_{\text{tot}}$, which determines the temperature dependence of the energy gap, was calculated to an appropriate degree of accuracy.) The isotopic energy gap shifts due to the change in the DW factor (elastic processes) and to EPI (inelastic processes) were calculated, and the role of optical and acoustic phonon modes was analyzed. It was shown that the isotopic energy shifts due to elastic processes and to EPI are of the same order of magnitude. The influence of the acoustic and optical phonon modes on EPI was also found to be almost the same; acoustic phonons affect the energy spectrum through elastic scattering; optical phonons, through inelastic processes. We note that, according to [18], the value of the derivative $(\partial \ln\Omega/\partial M_c^k)_P$ and, therefore, the energy shift due to the change in volume are determined in large measure by optical phonon modes.

A comparison was also made between the isotopic energy shifts due to the change in volume and to EPI; they are of the same order of magnitude for E_0 and E_g bands. In the case of critical points of the E_1 type, the EPI mechanism is dominant.

Thus, it can be concluded that Eq. (27) is a very rough and, in general, inadequate approximation of the dependence of energy bands on isotope composition and temperature.

4. DISCUSSION OF THE EXPERIMENTAL DATA

To date, precise measurements have been made which provide reliable data on the energies of the interband transitions and critical points of optical spectra of monatomic semiconductors.

The effect of the isotope composition on the optical properties of semiconducting germanium was first investigated in [23]. Only two sets of samples were investigated: isotope-enriched, $^{75.7}$Ge crystals (84% ^{76}Ge, 15% ^{74}Ge, and less than 0.2% of each of the other isotopes) and a crystal of natural isotope composition. The near-gap photoluminescence spectra were measured in their short-wavelength region, and the transmission spectra were recorded in the region of direct exciton transitions at $T = 1.7$ K. Excitonic absorption spectra were also measured in the region of direct near-gap optical transitions. From these experimental data, the isotopic shifts of the band gap ΔE_g were found at the Γ and L points of the Brillouin zone.

The luminescence spectra of diamond crystals in the frequency region of indirect interband transitions of the E_g type were measured in [24] (see also [25]). In [24], measurements at liquid-nitrogen temperatures were also made only on two sets of samples, namely, on those enriched with ^{13}C and those of the natural isotope composition (98.9% ^{12}C, 1.1% ^{13}C). The shifts in position of the peaks corresponding to free excitons of all three types (*A*, *B*, *C*) were determined in the luminescence spectra. A shift was also observed in the position of the peaks that correspond to excitons localized on neutral boron impurities.

The role of the change in volume and of EPI was considered qualitatively in [23, 24], and it was found that the isotopic energy shifts are basically due to EPI.

Further, in [14], the energies of direct transitions $E_0(\Gamma_8^+ - \Gamma_7^-)$ and of indirect transitions $E_g(\Gamma_8^+ - L_6^+)$ and their isotope-composition dependences were determined for Ge at liquid-helium temperatures using the modulation spectroscopy method. The measurements were made on four isotope-enriched samples of germanium (^{70}Ge, $^{72.9}$Ge, $^{73.9}$Ge, $^{75.6}$Ge) and on a sample of the natural isotope composition. The energy E_0 was determined from measured spectra of photomodulated reflectance. The energy of indirect transitions E_g was found from data on photoluminescence spectra and measurements of the electric-field-modulated transmission coefficient. According to the results presented in [14], the isotope-composition dependences of the electronic-spectrum parameters corresponding to the transition energies E_0 and E_g can be closely approximated by the relation $E = E_\infty + B/\sqrt{M}$ with $B < 0$.

In [26], the behavior of the critical points of the E_1 type was investigated for samples of ^{70}Ge, $^{75.6}$Ge, and of the natural isotope composition. The dielectric function

ε_2 was measured using an ellipsometric technique. We note that, according to energy band calculations for germanium, the critical E_1 points (of the type of a 2D minimum and a saddle point) on the curve of the imaginary part of the dielectric constant are located in the range 1.8–22.6 meV. The structure and magnitude of ε_2 in this energy range are mainly determined by the doublet Λ_3–Λ_1 transitions. The energy ranges of other transitions overlap, and their contributions cannot be separated.

As in the case considered above, the isotope-composition dependence of E_1 can be described by the relation $E_1 = E_1^\infty + B/\sqrt{M}$ with $B < 0$. A similar relation also takes place for the line widths $\Gamma(M)$.

In [14, 26], the contributions due to the change in volume and EPI to the empirical parameter B were evaluated. The former contribution was determined from the experimental data on $(1/V)(dV/dM)$ and hydrostatic deformation potential V_g using the relation $\Delta E \propto V_g(1/V)(\Delta V/\Delta M)$. The contribution from EPI was estimated as the difference between the experimental value of B and the contribution due to the volume change. It was found that the isotopic shifts in the energies E_0 and E_g of optical transitions associated with the volume change and EPI are of the same order of magnitude, while the isotopic shifts of the critical points E_1 are mainly due to EPI.

Thus, the theory is in reasonable agreement with the experimental data for diamond and germanium and, therefore, there are situations in which the universal relations are valid. The influence of spin–orbit coupling and the possible specific role of the d band are discussed briefly in the following section.

5. CONCLUSION

In this paper, we investigated the effect of the isotope composition of a crystal on the energy bands $E_{\mathbf{f},n}$ within the virtual-crystal model in the quasi-harmonic approximation. The role of the change in the unit-cell volume of the lattice and of the EPI renormalization produced by a change in the isotope composition (i.e., the role of the elastic and inelastic channels, respectively) was discussed. For monatomic crystals, a universal relation describing the dependence of $E_{\mathbf{f},n}$ on the isotope composition and temperature was derived. A comparison was made with the experimental data on the interband transition energies and the critical points in optical spectra.

The actual electronic energy spectra are significantly affected by spin–orbit coupling (except in the case of crystals such as diamond composed of atoms of light elements). Spin–orbit coupling leads to doublet splitting of p and d states at certain points of the Brillouin zone. Since this coupling takes place in the region of the atom core, the spin–orbit coupling constant Δ should be determined, in principle, by core electron states, which, generally speaking, are affected by the crystal potential only slightly. It is agreed that the values of Δ in a free atom and in an atom in a crystal differ by roughly ten percent. The character of changes in the coupling constant Δ in an atom due to the isotopic energy shift is well known [27]. However, according to the experimental data presented in [26], the isotope effect for Δ in a crystal is much more profound than in a free atom. Furthermore, the coupling constant Δ has been found to be strongly temperature-dependent in GaSb and α-Sn crystals (see references in [26]). Therefore, the question concerning the role of spin–orbit coupling calls for special investigation.

It should be noted that in monatomic semiconductor crystals, the structure and magnitude of the density of states of the upper valence bands and lower conduction bands are mainly determined by s and p states slightly hybridized with d states (in germanium, the typical difference in energy between the p and d states of the valence bands is roughly 20 eV). Therefore, the d orbitals are certain to be of minor importance in optical transitions in these crystals. However, in some compounds, such as CuCl(Br) and CdS, the difference in energy between the atomic p and d states is of the order of 1 eV [28, 29]. In this case, the hybridization between the p and d orbitals is of considerable importance and the upper valence bands are significantly affected by the d states. In such compounds, the influence of a change in the isotope composition can be described as follows [28]. In the matrix element V_{pd} responsible for the hybridization between the p and d states, the cation (copper) pseudopotential is dominant, while the contribution from the anion pseudopotential is negligible [28]. An increase in the cation atomic mass causes the DW factor $\exp(-W)$ to decrease because $\exp(-W) \propto [1 - (1/2)\langle u^2\rangle G^2]$. At the same time, the magnitudes of the effective cation pseudopotential and of the matrix element V_{pd} are increased. In this case, the interband transition energy E_0 decreases; i.e., we have $\partial E/\partial M_c < 0$. As a consequence, the contribution to the energy band renormalization from EPI (which is of opposite sign, $\partial E/\partial M_c > 0$) is partly or even completely canceled. A change in the anion atomic mass affects the matrix element V_{pd} only slightly; the isotope shift in energy is mainly determined, as before, by EPI and, hence, $\partial E/\partial M_c > 0$. The question concerning the role of hybridization between p and d states also calls for detailed investigation in this case.

The dependences of the electronic energy spectrum on temperature and isotope composition are of the same origin. Knowledge of the behavior of the isotope shifts in energy is of importance, because it provides additional insight into the origin of the electronic structure.

ACKNOWLEDGMENTS

The author is grateful to L.A. Maksimov for his interest in this work and helpful suggestions, to Yu.M. Kagan for his encouragement, and to A.V. Inyu-

shkin and D.A. Zhernov for their assistance throughout this work.

APPENDIX

We consider the isotope shift in frequency of a vibrational mode in a crystal whose unit cell contains atoms of different elements. The elements are assigned variable mean atomic masses, and the atomic masses of the isotopes of the same element are assumed to differ little in value. We consider the effects linear in the isotope mass difference. In this approximation, the point symmetry group of the crystal lattice remains unchanged and so does its vibration spectrum; therefore, the degeneracy is not lifted. In actuality, in a crystal lattice with isotopic disorder, there are fields of static atomic displacements due to zero-point oscillations which vary with atomic mass. In the presence of these fields, the local symmetry is reduced. However, in conventional (not quantum) crystals, these displacements are proportional to an additional small parameter, $\langle u^2\rangle/a^2$, and can be neglected.

We consider polyatomic crystals composed of isotopes of different elements and assume that the isotopic content of one element (specified by index k_1) is varied.

Let two crystals differ in the isotopic content of element k_1. We will specify these crystals by indices c and $c1$. The mean atomic mass of element k_1 is equal to

$$M_c^{k_1} = \sum_i c_i^{k_1} M_i^{k_1} \tag{A1}$$

($c_i^{k_1}$ is the concentration of the ith isotope of the given element) and is assumed to differ little from the mean atomic mass of this element in the crystal with isotopic content $c1$; that is,

$$\left|M_c^{k_1} - M_{c1}^{k_1}\right|/M_c^{k_1} = \left|\Delta M^{k_1}\right|/M_c^{k_1} \ll 1. \tag{A2}$$

The dynamic matrix of a polyatomic crystal $\Phi_{\alpha\alpha'}(kk'|\mathbf{q})$ can be written as

$$\Phi_{\alpha\alpha'}(kk'|\mathbf{q}) = \frac{1}{N}\frac{1}{\sqrt{M_c^k M_c^{k'}}} \times \sum_{\mathbf{mm}'} \varphi_{\alpha\alpha'}(\mathbf{m}k, \mathbf{m}'k')\exp\left(i\mathbf{q}\left(\mathbf{R}_{\mathbf{m}}^{(0)} - \mathbf{R}_{\mathbf{m}'}^{(0)}\right)\right), \tag{A3}$$

where $\varphi_{\alpha\alpha'}(\mathbf{m}k, \mathbf{m}'k')$ is the matrix of the second-order force constants. The dynamic matrix is a Hermitian $3s \times 3s$ matrix (s is the number of atoms in the unit cell) and, therefore, satisfies the condition

$$\Phi_{\alpha\alpha'}(kk'|\mathbf{q}) = \Phi^*_{\alpha'\alpha}(k'k|\mathbf{q}). \tag{A4}$$

The eigenfrequencies $\omega_c(l)$ and orthonormal polarization vectors $\mathbf{e}^c(k|l)$ of the dynamic matrix Φ of Eq. (A3) for the virtual crystal are assumed to be known. Let us find the isotopic shift in frequency as one goes over to the crystal with isotopic content $c1$.

It is well known that, in order to calculate an eigenvalue to a certain order in a perturbation, one needs the eigenfunctions to be calculated through the unity lower order. The isotopic shift in an eigenvalue (square of a frequency) calculated to the first order is equal to the corresponding diagonal matrix element of the perturbation energy between the unperturbed eigenfunctions. Therefore, we can write

$$\left(\frac{\Delta\omega^2(l)}{\Delta M^{k_1}}\right)_c = \sum_{k,\alpha\,k',\alpha'} e_\alpha^{c*}(k|l)\left(\frac{\Delta\Phi_{\alpha\alpha'}(kk'|\mathbf{q})}{\Delta M^{k_1}}\right)_c e_{\alpha'}^c(k'|l). \tag{A5}$$

From Eq. (A3), it follows that

$$\left(\frac{\Delta\Phi_{\alpha\alpha'}(kk'|\mathbf{q})}{\Delta M^{k_1}}\right)_c = -\frac{1}{2}\Phi^c_{\alpha\alpha'}(kk'|\mathbf{q})\left[\frac{\delta_{kk_1}}{M_c^k}\frac{\delta_{k_1k'}}{M_c^{k'}}\right]. \tag{A6}$$

We substitute Eq. (A6) into Eq. (A5) and take into account that

$$\omega_c^2(l)e_\alpha^c(k|l) = \sum_{k',\alpha'}\Phi^c_{\alpha\alpha'}(kk'|\mathbf{q})e^c_{\alpha'}(k'|l). \tag{A7}$$

In addition, since the matrix $\Phi(\mathbf{q})$ is Hermitian, the polarization vectors satisfy the orthonormality and completeness conditions

$$\sum_{k,\alpha} e_\alpha^{c*}(k|\mathbf{q}j)e_\alpha^c(k|\mathbf{q}j') = \delta_{jj'},$$
$$\sum_j e_\alpha^{c*}(k|\mathbf{q}j)e_{\alpha'}^c(k'|\mathbf{q}j) = \delta_{kk'}\delta_{\alpha\alpha'}. \tag{A8}$$

We can also replace Δ by the differential sign, because the mean atomic mass varies continuously. The final result is

$$\frac{d\ln\omega_c^2(l)}{d\ln M_c^k} = -\sum_\alpha\left|e_\alpha^c(k|l)\right|^2. \tag{A9}$$

As seen from Eq. (A9), the shift in the frequency of a vibrational mode caused by a variation of the mean atomic mass of one of the components of the polyatomic crystal is proportional to the square of the magnitude of the corresponding polarization vector.

Relations of such type were first derived in [30], where the effect of the isotope composition on the properties of fullerenes was studied.

In the case of a monatomic crystal, the unit cell consists of atoms of the same element and Eq. (A9) takes the form

$$\frac{d\ln\omega_c^2(l)}{d\ln M_c} = -1 + O\left(\left(\frac{\Delta M}{M_c}\right)^2, \frac{\Delta M}{M_c}\frac{\langle u^2\rangle}{a^2}\right). \qquad \text{(A10)}$$

REFERENCES

1. H. Holloway, K. C. Hass, M. A. Tamor, *et al.*, Phys. Rev. B **44** (13), 7123 (1991).
2. W. S. Capinski, H. J. Maris, E. Bauser, *et al.*, Appl. Phys. Lett. **71** (15), 2109 (1997).
3. T. Ruf, R. W. Henn, M. Asen-Palmer, *et al.*, Solid State Commun. **115** (5), 243 (2000).
4. H. D. Fuchs, C. H. Grein, R. I. Devlen, *et al.*, Phys. Rev. B **44** (16), 8633 (1991).
5. V. I. Ozhogin, A. V. Inyushkin, A. N. Taldenkov, *et al.*, Pis'ma Zh. Éksp. Teor. Fiz. **63** (6), 463 (1996) [JETP Lett. **63**, 490 (1996)].
6. H. Bettger, *Principles of the Theory of Lattice Dynamics* (Akademie, Berlin, 1983).
7. G. Leibfried, in *Handbuch der Physik*, Ed. by S. Flugge (Springer, Berlin, 1955; Fizmatgiz, Moscow, 1963), Vol. 7, Part 1.
8. V. Cardona, Physica B (Amsterdam) **263–264**, 376 (1999).
9. P. B. Allen and V. Heine, J. Phys. C **9**, 2305 (1976).
10. V. V. Sobolev and V. V. Nemoshkalenko, *The Methods of Computational Physics in the Theory of Solid State. Electronic Structure of Semiconductors* (Naukova Dumka, Kiev, 1988).
11. S. Zollner, V. Cardona, and S. Gopalan, Phys. Rev. B **45** (7), 3376 (1992).
12. N. Garro, A. Cantarero, M. Cardona, *et al.*, Phys. Rev. B **54** (7), 4732 (1996).
13. D. Olguín, A. Cantarero, and M. Cardona, Phys. Status Solidi B **220** (1), 33 (2000).
14. C. Parks, A. K. Ramdas, S. Rodríguez, *et al.*, Phys. Rev. B **49** (20), 14244 (1994).
15. P. Pavone and S. Baroni, Solid State Commun. **90** (5), 295 (1994).
16. G.-M. Rignanese, J.-P. Michenaud, and X. Gonze, Phys. Rev. B **53** (8), 4488 (1996).
17. A. P. Zhernov, Zh. Éksp. Teor. Fiz. **114** (2), 654 (1998) [JETP **87**, 357 (1998)].
18. A. P. Zhernov, Fiz. Nizk. Temp. **26** (12), 1226 (2000) [Low Temp. Phys. **26**, 908 (2000)].
19. R. M. Pick, M. H. Cohen, and R. M. Martin, Phys. Rev. B **1** (2), 910 (1970).
20. P. Lautenschlager, P. B. Allen, and M. Cardona, Phys. Rev. B **31** (4), 2163 (1985).
21. L.F. Lastras-Martínez, T. Ruf, M. Konuma, *et al.*, Phys. Rev. B **61** (19), 12946 (2000).
22. S. D. Yoo, D. E. Aspnes, L. F. Lastras-Martínez, *et al.*, Phys. Status Solidi B **220** (1), 117 (2000).
23. V. F. Agekyan, V. M. Asnin, A. M. Kryukov, *et al.*, Fiz. Tverd. Tela (Leningrad) **31** (12), 101 (1989) [Sov. Phys. Solid State **31**, 2-82 (1989)].
24. A. T. Collins, S. C. Lawson, G. Davies, and H. Kanda, Phys. Rev. Lett. **65** (7), 891 (1990).
25. T. Ruf, M. Cardona, H. Sternshlute, *et al.*, Solid State Commun. **105** (5), 311 (1998).
26. D. Rönnow, L. F. Lastras-Martínez, and M. Cardona, Eur. Phys. J. B **5** (1), 29 (1998).
27. I. I. Sobelman, *Atomic Spectra and Radiative Transitions* (Fizmatgiz, Moscow, 1963; Springer, Berlin, 1979).
28. A. Göbel, T. Ruf, M. Cardona, *et al.*, Phys. Rev. B **57** (24), 15183 (1998).
29. J. M. Zhang, T. Ruf, R. Lauck, and M. Cardona, Phys. Rev. B **57** (16), 9716 (1998).
30. J. Menéndez, J. B. Page, and S. Guha, Philos. Mag. B **70** (3), 651 (1994).

Translated by Yu. Epifanov

Physics of the Solid State, Vol. 44, No. 6, 2002, pp. 1044–1049. Translated from Fizika Tverdogo Tela, Vol. 44, No. 6, 2002, pp. 1001–1005.

SEMICONDUCTORS AND DIELECTRICS

Temperature Dependence of the Spin–Lattice Relaxation Time for Quadrupole Nuclei under Conditions of NMR Line Saturation

V. M. Mikushev*, A. M. Ulyashev*, E. V. Charnaya*, and A. Chandoul**

** Research Institute of Physics, St. Petersburg State University, Ul'yanovskaya ul. 1, Petrodvorets, St. Petersburg, 198904 Russia*

*** Laboratoire de Physique de la Matière Condensée, Faculté des Sciences de Tunis, Tunis, 1080 Tunisie*

e-mail: mikushev@paloma.spbu.ru

Received September 13, 2001

Abstract—The contributions of different mechanisms of nuclear spin–lattice relaxation are experimentally separated for ^{69}Ga and ^{71}Ga nuclei in GaAs crystals (nominally pure and doped with copper and chromium), ^{23}Na nuclei in a nominally pure NaCl crystal, and ^{27}Al nuclei in nominally pure and lightly chromium-doped Al_2O_3 crystals in the temperature range 80–300 K. The contribution of impurities to spin–lattice relaxation is separated under the condition of additional stationary saturation of the nuclear magnetic resonance (NMR) line in magnetic and electric resonance fields. It is demonstrated that, upon suppression of the impurity mechanism of spin–lattice relaxation, the temperature dependence of the spin–lattice relaxation time T_1 for GaAs and NaCl crystals is described within the model of two-phonon Raman processes in the Debye approximation, whereas the temperature dependence of T_1 for corundum crystals deviates from the theoretical curve for relaxation due to the spin–phonon interaction. © *2002 MAIK "Nauka/Interperiodica".*

1. INTRODUCTION

Spin–lattice relaxation of quadrupole nuclei (with $I > 1/2$) in solid dielectrics is governed by two mechanisms, namely, the lattice mechanism responsible for relaxation in perfect samples and the impurity mechanism associated with the presence of impurity paramagnetic ions, radiation-induced centers, and other structural point defects in real crystals [1]. The overall process of spin–lattice relaxation is characterized by the time

$$T_1^{\Sigma} = ((T_1^{\text{lat}})^{-1} + (T_1^{\text{imp}})^{-1})^{-1}, \quad (1)$$

where T_1^{lat} and T_1^{imp} are the lattice and impurity components, respectively. The former mechanism of spin–lattice relaxation in perfect crystals predominantly occurs through the modulation of the internuclear separation in the crystal lattice by thermal vibrations and, consequently, through changes in the electric-field gradient at a nucleus. Since the density of phonon states at frequencies close to the Larmor frequency is relatively low, Raman processes involving all phonons of the spectrum more efficiently manifest themselves in spin–lattice relaxation. The ratio between the efficiencies of different Raman processes, which, in the general case, should lead to different temperature dependences of the lattice component T_1^{lat}, has been discussed, for example, in [2, 3]. Despite a large amount of available experimental data on the temperature dependence of the spin–lattice relaxation rate, their comparison with theoretical models is not entirely correct because of an uncertainty introduced by the impurity contribution T_1^{imp}, which, even for nominally pure crystals, remains significant due to spin diffusion. Unlike the lattice component, the impurity component T_1^{imp} characterizes the degree of perfection of a particular sample rather than the structure of the material. A theoretical evaluation of the impurity contribution is substantially complicated by the presence of undetectable paramagnetic centers, the dependence of T_1^{imp} on the external quantizing field [2], the complex dependence of the spin relaxation rate of paramagnetic centers on the temperature and concentration, etc.

Direct experimental measurements of the lattice component T_1^{lat} became possible with the advent of the new technique proposed in our earlier works [4, 5]. This technique consists in suppressing the impurity contribution to nuclear spin–lattice relaxation for samples with a low relative concentration of paramagnetic centers ($<10^{-5}$) through additional stationary saturation of the nuclear magnetic resonance (NMR) line. The thermodynamic idea underlying the proposed method is as follows. The impurity mechanism of relaxation proceeding through spin diffusion is efficient provided the reciprocal of the local spin temperature α_{loc} in the vicinity of defects is closer to the reciprocal of the lattice

temperature α_l as compared to the reciprocal of the mean spin temperature $\langle\alpha\rangle$ in other regions of the sample [1]. If the spin–lattice relaxation time T_1^{Σ} is measured in the course of the nuclear magnetization recovery after complete saturation of the NMR line by a sequence of rf pulses [6], the impurity relaxation makes a contribution to spin–lattice relaxation under the following condition:

$$\alpha_{loc} > \langle\alpha\rangle. \quad (2)$$

Strong additional stationary acoustical, magnetic, or electric saturation of the NMR line can result in local overheating of the nuclear spin system in the vicinity of defects to $\alpha_{loc} = 0$, whereas $\langle\alpha\rangle$ becomes equal to a certain steady-state value $\langle\alpha\rangle_{st} > 0$ [7, 8]. The effect of strong local heating was experimentally established in our earlier works [9, 10]. The phenomenological theory of this effect was developed in [11]. In the case when the regions near defects are overheated, inequality (2) becomes invalid and the impurity contribution to spin–lattice relaxation is suppressed. Under these conditions, the recovery of nuclear magnetization in the sample is governed by the lattice mechanism and the experimentally measured spin–lattice relaxation time T_1^{Σ} corresponds to spin–lattice relaxation in a perfect sample. The degree of local heating of the nuclear spin system depends on the nature of the paramagnetic centers in the sample. However, as was shown in [4, 8, 12, 13], an increase in the saturation in a stationary resonance field (i.e., a decrease in $\langle\alpha\rangle_{st}$) can bring about suppression of the impurity contribution T_1^{imp} of all the paramagnetic centers involved in impurity relaxation. Thus, the proposed technique made it possible for the first time to investigate separately the temperature dependence of the lattice contribution to spin–lattice relaxation in real crystals.

In the present work, we measured temperature dependences of the spin–lattice relaxation time T_1^{lat} in the temperature range 78–300 K for ^{71}Ga and ^{69}Ga nuclei in nominally pure and doped GaAs crystals, ^{23}Na nuclei in a nominally pure NaCl crystal, and ^{27}Al nuclei in nominally pure and chromium-doped Al_2O_3 crystals under the conditions of stationary saturation of the NMR lines.

2. SAMPLE PREPARATION AND EXPERIMENTAL TECHNIQUE

The experiments were performed on an ISP-1 pulsed NMR spectrometer operating at a frequency of 5.5 MHz. Under the conditions of stationary saturation of the NMR line in extra magnetic or electric resonance fields, the recovery time τ of nuclear magnetization was measured immediately after saturation of the spin system by a sequence of rf nonselective pulses (Fig. 1).

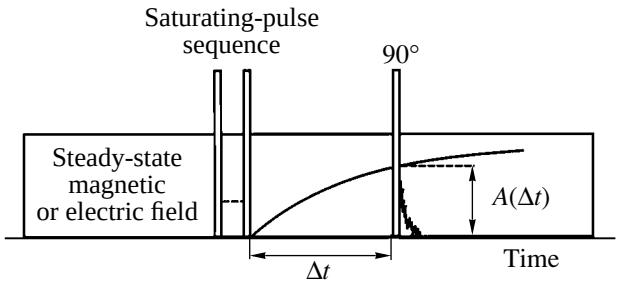

Fig. 1. A scheme of measuring the recovery time τ of nuclear magnetization to a steady-state value. $A(\Delta t)$ is the free-induction signal measured in the time interval Δt after rf-pulse saturation of the nuclear spin system.

Then, the spin–lattice relaxation time T_1 was calculated from the relationship [4, 14]

$$T_1 = \tau/Z^{st}, \quad (3)$$

where Z^{st} is the stationary-saturation factor defined as $Z^{st} = \langle\alpha\rangle_{st}/\alpha_l$ [14]. The factor Z^{st} was measured as the ratio of the free-nuclear-induction signal after a 90° pulse in an extra saturating field to the signal in the absence of an extra field. The thermal stabilization was accurate to better than 0.2 K.

High-resistance crystals of gallium arsenide (including a nominally pure GaAs sample and copper- and chromium-doped GaAs samples with an impurity ion concentration of 10^{18} cm^{-3}) were grown by the Czochralski method from the melt. The electrical resistivity of GaAs samples was approximately equal to 10^8 Ω cm. Crystals of gallium arsenide have a cubic symmetry without an inversion center. As a consequence, the NMR spectra of ^{69}Ga and ^{71}Ga isotopes with spin I = 3/2 exhibit a Zeeman structure; however, the transitions between spin levels can be excited in an external electric field at twice the Larmor frequency [9]. All three samples were cut out normally to the [001] crystallographic axis in the form of 1-mm-thick plates. Electrodes applied to the samples induced a stationary ac electric field with an amplitude up to 10^3 V cm^{-1} in the sample bulk. The [001] cubic axis was oriented along the magnetic field of the spectrometer.

A nominally pure crystal of sodium chloride was grown by zone melting from the melt with the use of high-purity materials. The sample was prepared in the form of a parallelepiped with edges aligned parallel to the crystallographic cubic axes. In measurements, the cubic axis of the crystal was directed along the dc field of the spectrometer. Stationary saturation of the ^{23}Na NMR lines (I = 3/2) was achieved in an extra magnetic field at the Larmor frequency with the use of an additional coil wound on the sample. The field amplitude was controlled in the range from 0 to 0.1 Oe.

A nominally pure single crystal of aluminum oxide was grown in a molybdenum crucible according to the

special procedure devised at the State Optical Institute (St. Petersburg, Russia). A chromium-doped Al_2O_3 sample was grown by the Verneuil method. The chromium concentration in the melt was approximately equal to 5×10^{16} cm^{-3}. The samples were prepared in the form of cylinders (~2 cm^3 in volume) whose axes were oriented perpendicular to the C_3 crystallographic axis. In a hexagonal Al_2O_3 crystal, the ^{27}Al levels (I = 5/2) are shifted as a result of quadrupole interaction. It should be noted that the relaxation of the difference in the populations of a particular pair of spin levels is generally a superposition of several exponential processes and cannot be described by a sole spin–lattice relaxation time [7, 15], which makes the quantitative interpretation of the experimental results considerably more difficult. For this reason, the measurements of Al_2O_3 crystals were performed at a magic angle between the C_3 crystallographic axis of the sample and the direction of the dc magnetic field such that the spin levels were equidistant and the recovery of nuclear magnetization occurred in an exponential manner [2]. As for NaCl crystals, the contributions of the mechanisms of ^{27}Al spin–lattice relaxation were separated under the conditions of magnetic saturation of the NMR line.

3. RESULTS AND DISCUSSION

Figure 2 depicts the experimental curves of the spin–lattice relaxation time for ^{71}Ga nuclei in nominally pure and doped GaAs crystals at different degrees of stationary electric saturation of the NMR signal at a temperature of 78 K. In the absence of an extra saturating field (Z^{st} = 1), the spin–lattice relaxation times T_1^{Σ} measured by the conventional technique are equal to 27.0 ± 0.4 s for the copper-doped crystal, 27.8 ± 0.4 s for the chromium-doped crystal, and 31.4 ± 0.5 s for the nominally pure sample.

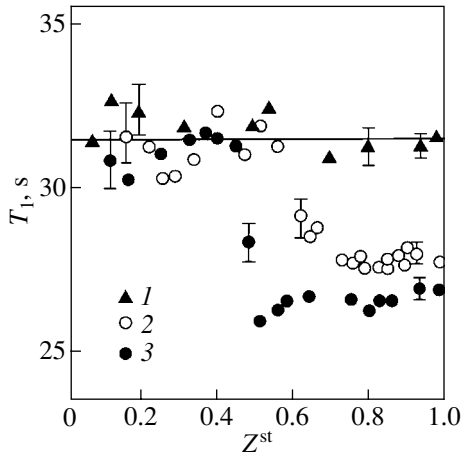

Fig. 2. Dependences of the spin–lattice relaxation time T_1 for ^{71}Ga nuclei on the electric-stationary-saturation factor Z^{st} for (*1*) nominally pure, (*2*) chromium-doped, and (*3*) copper-doped gallium arsenide samples at a temperature of 78 K. The straight line corresponds to the lattice component T_1^{lat}. The error bars are shown selectively.

It can be seen from Fig. 2 that, as the strength of the saturating electric field increases, the spin–lattice relaxation times for doped crystals increase to the relaxation time of ^{71}Ga nuclei in the nominally pure crystal. As a result, under the conditions of strong saturation of the NMR signals (Z^{st} < 0.4), the spin–lattice relaxation times for the nominally pure crystal and both doped samples become equal to each other. Therefore, this time can be treated as a relaxation time associated only with the lattice mechanism of spin–lattice relaxation, i.e., as the lattice component T_1^{lat}. By using relationship (1), it is possible to estimate the impurity contributions for chromium-doped (T_1^{imp} = 240 ± 40 s) and copper-doped (T_1^{imp} = 190 ± 40 s) crystals at the same concentration of impurity ions in the samples. Within the limits of experimental error, the T_1 time for the nominally pure sample remains constant with a change in the Z^{st} factor. This implies that undetectable paramagnetic centers contained in the pure sample do not contribute significantly to the relaxation rate; hence, $T_1^{\Sigma} = T_1^{lat}$. Similar results are obtained for ^{69}Ga isotopes at T = 78 K. Reasoning from a comparison of the spin–lattice relaxation time T_1^{Σ} and the lattice component T_1^{lat} = 12.4 ± 0.5 s, the impurity relaxation times T_1^{imp} for ^{69}Ga nuclei in chromium-doped (T_1^{Σ} = 11.5 ± 0.2 s) and copper-doped (T_1^{Σ} = 11.4 ± 0.2 s) samples are estimated at 160 ± 50 and 140 ± 50 s, respectively.

As the temperature of the crystal increases, the lattice relaxation time T_1^{lat} for both Ga isotopes decreases more rapidly than the impurity relaxation time T_1^{imp}. At temperatures $T \geq 100$ K, the total relaxation time T_1^{Σ} becomes equal to the lattice relaxation time T_1^{lat}; as a result, the spin–lattice relaxation times for all three samples are identical and do not change at any value of Z^{st}. The experimental temperature dependences of the spin–lattice relaxation time T_1^{Σ} for ^{71}Ga nuclei in nominally pure and doped crystals are displayed in Fig. 3. Similar dependences for ^{69}Ga nuclei in nominally pure and chromium-doped samples are plotted in Fig. 4. The theoretical curves $T_1^{lat}(T)$ depicted by solid lines in

Figs. 3 and 4 are calculated according to the standard relationship [2]

$$(T_1^{\text{lat}})^{-1} = C\int_0^{\Omega}\omega^6\exp\left(\frac{\hbar\omega}{kT}\right)\left[\exp\left(\frac{\hbar\omega}{kT}-1\right)\right]^{-2}d\omega, \quad (4)$$

where k is the Boltzmann constant, Ω is the Debye frequency, and C is the temperature-independent numerical coefficient. Relationship (4) is derived for relaxation within the model of two-phonon Raman processes. In this case, the thermal-phonon spectrum is described in the framework of the Debye approximation. Since the numerical coefficient C has defied exact calculation, the C value used in our case is chosen from the condition of equality between the theoretical and experimental times T_1^{lat} at a temperature of 78 K. The Debye frequency for gallium arsenide is calculated from the Debye temperature Θ = 345 K taken from [16]. As can be seen from Figs. 3 and 4, the temperature dependences of the lattice component of the spin–lattice relaxation time for Ga nuclei are adequately described within the chosen model.

As was shown above, the nominally pure GaAs crystal exhibits an ideal behavior from the standpoint of nuclear spin–lattice relaxation. In the nominally pure NaCl sample, unlike the GaAs crystal, the impurity mechanism of spin–lattice relaxation of ^{23}Na nuclei is comparable in efficiency to the lattice mechanism due to the presence of undetectable paramagnetic centers at a relative concentration of the order of 10^{-5}. This explains the wide scatter of the available data on the spin–lattice relaxation rate of Na nuclei [17]. Although the contributions of different relaxation mechanisms for different paramagnetic centers at certain temperatures have been experimentally separated under the conditions of acoustical [8] and magnetic [12] saturation of the ^{23}Na NMR line, the temperature dependence of the lattice component T_1^{lat} has not been conclusively established. In particular, Bakhramov *et al.* [18] obtained the experimental dependences $T_1^{\Sigma}(T)$ for nominally pure and copper-doped NaCl crystals and analyzed the impurity mechanism within the microscopic approach. The results obtained in [18] are in close agreement with the dependence represented by relationship (4), even though these authors accepted a substantial impurity contribution to the spin–lattice relaxation time T_1^{Σ}. On the other hand, considerable deviations from the dependence described by relationship (4) were revealed experimentally in a number of works and assigned to the contribution of optical branches of the phonon spectrum [19], covalence, [20], antiscreening effects [21], etc.

Figure 5 shows the temperature dependences of the spin–lattice relaxation time T_1^{Σ} and the lattice component T_1^{lat} for ^{23}Na nuclei in a nominally pure NaCl sample, which were measured under the conditions of magnetic saturation of the NMR signal. The theoretical curve was calculated from relationship (4) for the Raman process of quadrupole spin–lattice relaxation at the Debye temperature Θ = 275 K [16] and T_1^{lat} = 540 s at a sample temperature of 78 K. The calculated time

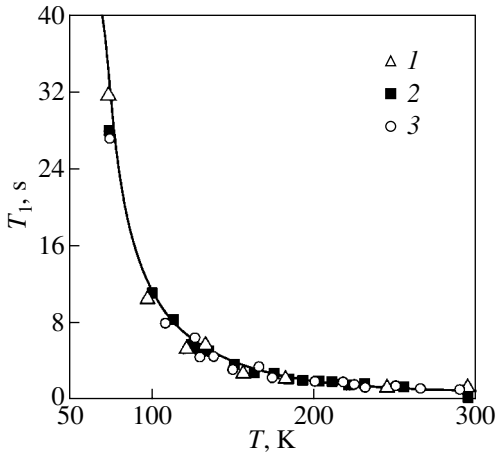

Fig. 3. Temperature dependences of the spin–lattice relaxation time T_1 for ^{71}Ga nuclei in (*1*) nominally pure, (*2*) chromium-doped, and (*3*) copper-doped gallium arsenide crystals. The solid line represents the theoretical temperature dependence of the lattice component T_1^{lat}.

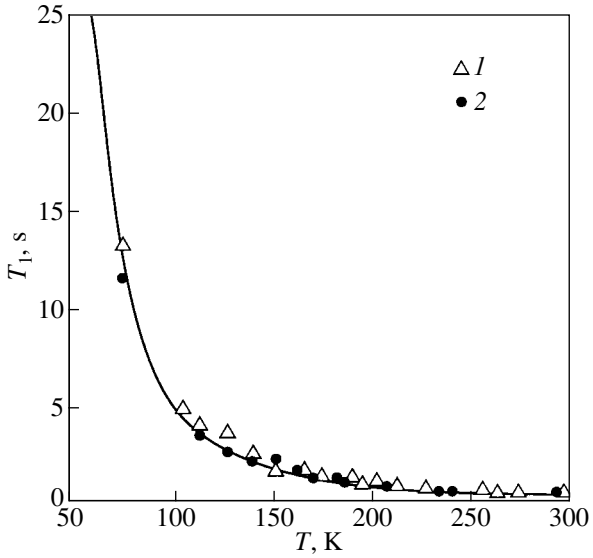

Fig. 4. Temperature dependences of the spin–lattice relaxation time T_1 for ^{69}Ga nuclei in (*1*) nominally pure and (*2*) chromium-doped gallium arsenide crystals. The solid line represents the theoretical temperature dependence of the lattice component T_1^{lat}.

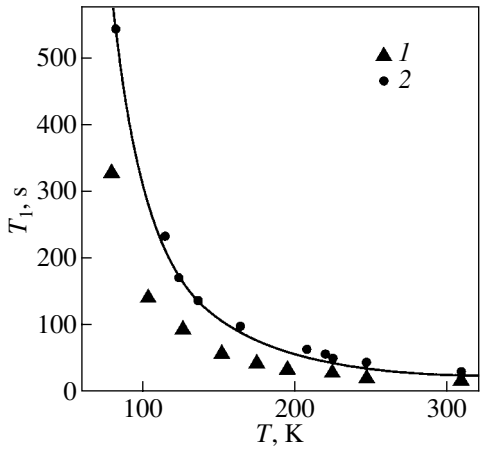

Fig. 5. Temperature dependences of (*1*) the spin–lattice relaxation time T_1^{Σ} measured by a conventional technique and (*2*) the lattice component T_1^{lat} for ^{23}Na nuclei in nominally pure NaCl crystals. The solid line represents the theoretical temperature dependence of the lattice component T_1^{lat}.

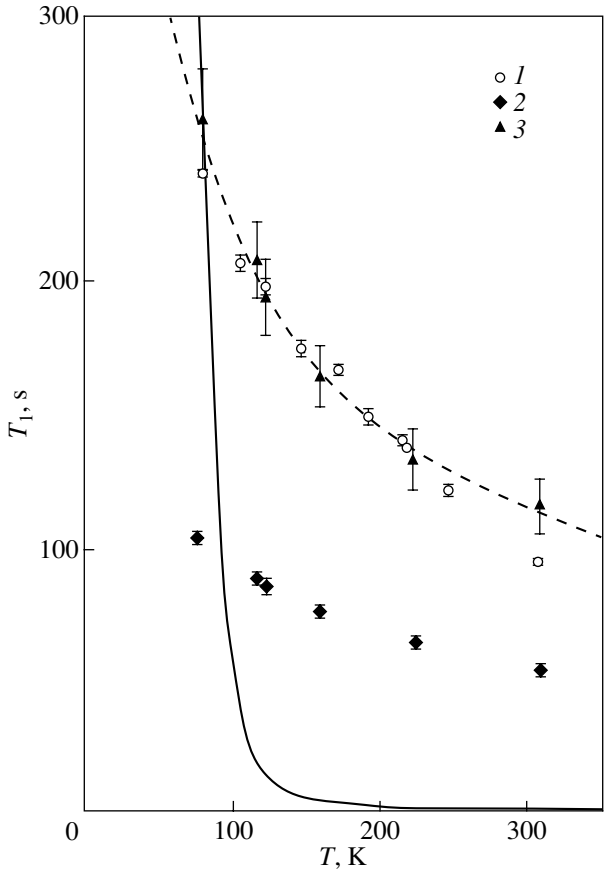

Fig. 6. Temperature dependences of the spin–lattice relaxation time T_1^{Σ} measured by a conventional technique for ^{27}Al nuclei in (*1*) nominally pure and (*2*) chromium-doped Al_2O_3 crystals. (*3*) Temperature dependence of the lattice component T_1^{lat} for ^{27}Al nuclei in a chromium-doped Al_2O_3 crystal (measurements under the conditions of magnetic suppression of the impurity contribution). The solid line represents the theoretical temperature dependence of the lattice component T_1^{lat} for Raman processes within the Debye approximation of the phonon spectrum. The dashed line corresponds to the dependence $T_1^{\text{lat}} \propto T^{-0.6}$.

T_1^{lat} coincides with the lattice relaxation times obtained under the conditions of suppression of the impurity relaxation mechanism in different NaCl crystals [8], including those exposed to gamma-ray irradiation [12]. As is clearly seen, the experimental dependence is consistent with the chosen model of spin–lattice relaxation. It should be noted that, within the limits of experimental error and with allowance made for the sample orientation in the spectrometer, the dependence $T_1^{\text{lat}}(T)$ is characteristic of the material and can be used to estimate the impurity component T_1^{imp} for other samples from the spin–lattice relaxation time T_1^{Σ} determined by the conventional technique.

The actual phonon spectrum in noncubic corundum crystals corresponds to the Debye approximation to a smaller extent [16]. Although the temperature dependence of the heat capacity of Al_2O_3, as a whole, is well described in the framework of this approximation, it is of interest to clarify whether the Debye approximation can be applied to the description of the nuclear spin–lattice relaxation rate. Note that doped Al_2O_3 crystals have been extensively studied as an example of materials with impurity relaxation proceeding through spin diffusion. Since the contribution of the lattice mechanism is relatively small, conventional techniques have failed to estimate T_1^{lat} even for specially synthesized pure Al_2O_3 samples. In our recent work [13], we studied a leucosapphire crystal grown using a special procedure devised at the State Optical Institute and found that the measured time $T_1^{\Sigma} = 240 \pm 5$ s for ^{27}Al nuclei in this crystal at $T = 78$ K exceeds any of the T_1^{Σ} times available in the literature for Al_2O_3. Under the conditions of magnetic suppression, we separated the contributions of the mechanisms of ^{27}Al spin–lattice relaxation in this crystal and demonstrated that the role played by the impurity mechanism is insignificant at temperatures higher than 78 K and that the lattice component T_1^{lat} is equal to the spin–lattice relaxation time T_1^{Σ} at temperatures above the liquid-nitrogen temperature. In the present work, we measured the temperature depen-

dence of the spin–lattice relaxation time T_1^{Σ} for the same corundum crystal with the use of the conventional technique without additional stationary saturation of the spin system. The experimental results obtained are represented in Fig. 6. The temperature dependence of the spin–lattice relaxation time T_1^{Σ} for ^{27}Al nuclei in a lightly doped sample indicates that the impurity component T_1^{imp} makes a considerable contribution over the entire temperature range under investigation. The temperature dependence of the lattice component T_1^{lat} for the doped Al_2O_3 sample, which was obtained under the conditions of magnetic suppression of the impurity relaxation, virtually coincides, to within the experimental error, with the dependence $T_1^{\Sigma}(T)$ for the leucosapphire sample. The time $T_1^{lat} = 260 \pm 20$ s for Al_2O_3 at 78 K agrees well with the results obtained in [7, 13]. However, the temperature dependence of the spin–lattice relaxation time is very weak and can be represented as $T_1^{lat} \propto T^{-0.6}$ (dashed line in Fig. 6). At the same time, according to [2], the lattice relaxation time T_1^{lat} should change inversely with temperature even in the case of direct one-phonon transitions whose contribution to relaxation is insignificant [2]. For comparison, the dependence calculated from relationship (4) at the Debye characteristic temperature $\Theta = 1042$ K [16] is shown by the solid line in Fig. 6. Thus, our results demonstrated that the model of Raman processes in the Debye approximation for the phonon spectrum is inapplicable to the description of spin–lattice relaxation of Al nuclei in corundum.

REFERENCES

1. G. R. Khutsishvili, Usp. Fiz. Nauk **87** (2), 211 (1965) [Sov. Phys. Usp. **8**, 743 (1966)].
2. A. Abragam, *The Principles of Nuclear Magnetism* (Clarendon, Oxford, 1961; Inostrannaya Literatura, Moscow, 1963).
3. A. R. Kessel', *Nuclear Acoustic Resonance* (Nauka, Moscow, 1969).
4. P. Yu. Efitsenko, V. M. Mikushev, and E. V. Charnaya, Pis'ma Zh. Éksp. Teor. Fiz. **54** (10), 583 (1991) [JETP Lett. **54**, 587 (1991)].
5. I. Mavlonazarov, V. M. Mikushev, and E. V. Charnaya, Pis'ma Zh. Éksp. Teor. Fiz. **56** (1), 15 (1992) [JETP Lett. **56**, 13 (1992)].
6. R. Ernst, G. Bodenhausen, and A. Wokaun, *Principles of NMR in One and Two Dimensions* (Clarendon, Oxford, 1987; Mir, Moscow, 1990).
7. E. V. Charnaya, V. M. Mikushev, and E. S. Shabanova, J. Phys.: Condens. Matter **6**, 7581 (1994).
8. E. V. Charnaya, I. Mavlonazarov, and V. M. Mikushev, J. Magn. Reson., Ser. A **112**, 96 (1995).
9. A. A. Kuleshov, V. M. Mikushev, A. L. Stolypko, *et al.*, Fiz. Tverd. Tela (Leningrad) **28** (11), 3262 (1986) [Sov. Phys. Solid State **28**, 1837 (1986)].
10. A. A. Kuleshov, A. L. Stolypko, E. V. Charnaya, and V. A. Shutilov, Dokl. Akad. Nauk SSSR **293** (6), 1361 (1987) [Sov. Phys. Dokl. **32**, 308 (1987)].
11. G. L. Antokol'skiĭ and E. V. Charnaya, Fiz. Tverd. Tela (Leningrad) **17** (6), 1552 (1975) [Sov. Phys. Solid State **17**, 1019 (1975)].
12. E. V. Charnaya, V. M. Mikushev, A. M. Ulyashev, and D. A. Yas'kov, Physica B (Amsterdam) **292**, 109 (2000).
13. A. Chandoul, E. V. Charnaya, A. A. Kuleshov, *et al.*, J. Magn. Reson. **135**, 113 (1998).
14. E. R. Andrew, *Nuclear Magnetic Resonance* (Cambridge Univ. Press, London, 1955; Inostrannaya Literatura, Moscow, 1957).
15. W. W. Simmons, W. J. O'Sullivan, and W. A. Robinson, Phys. Rev. **127** (4), 1168 (1962).
16. *Handbook of Physical Quantities*, Ed. by I. S. Grigoriev and E. Z. Meilikhov (Énergoatomizdat, Moscow, 1991; CRC Press, Boca Raton, 1997).
17. V. M. Mikushev and E. V. Charnaya, *Nuclear Magnetic Resonance in Solids* (Sankt.-Peterb. Gos. Univ., St. Petersburg, 1995).
18. A. Bakhramov, A. L. Stolypko, E. V. Charnaya, and V. A. Shutilov, Fiz. Tverd. Tela (Leningrad) **28** (3), 844 (1986) [Sov. Phys. Solid State **28**, 470 (1986)].
19. B. I. Kochelaev, Zh. Éksp. Teor. Fiz. **37** (1), 242 (1959) [Sov. Phys. JETP **10**, 171 (1960)].
20. E. G. Wikner and E. L. Hahn, Bull. Am. Phys. Soc. **3** (5), 325 (1958).
21. J. van Kranandonk, Physica (Amsterdam) **29** (10), 781 (1954).

Translated by O. Borovik-Romanova

Physics of the Solid State, Vol. 44, No. 6, 2002, pp. 1050–1054. Translated from Fizika Tverdogo Tela, Vol. 44, No. 6, 2002, pp. 1006–1010.

SEMICONDUCTORS AND DIELECTRICS

Interaction of Light Waves on a Reflecting Holographic Grating in Cubic Photorefractive Crystals

A. G. Mart'yanov, S. M. Shandarov, and R. V. Litvinov

Tomsk State University of Control Systems and Radio Electronics, Tomsk, 634050 Russia

e-mail: shand@stack.ru

Received July 2, 2001

Abstract—The interaction of two antiparallel light waves on a reflecting grating is analyzed theoretically in arbitrarily oriented optically active cubic crystals of point group 23. The effect of nonunidirectional energy transfer on the interaction efficiency is investigated in the undepleted-pump-power approximation in (100)-, (111)-, and $(11\bar{2})$-cut $Bi_{12}TiO_{20}$ crystals. © *2002 MAIK "Nauka/Interperiodica".*

1. INTRODUCTION

The interaction of light waves on reflecting photorefractive gratings is of interest for the development of holographic-interferometry devices [1] and narrow-band optical filters [2]. In sillenites, reflecting gratings have been investigated only for (111) cuts [1] and (100) cuts [3] of $Bi_{12}TiO_{20}$ and $Bi_{12}SiO_{20}$ crystals. In this paper, the interaction of two light beams on reflecting gratings is investigated in arbitrarily oriented optically active cubic crystals of point group 23.

2. RESULTS AND DISCUSSION

We consider two antiparallel (signal and pump) waves of intensities I_S and I_P, respectively, propagating along the x axis in a photorefractive crystal of point group 23 (Fig. 1). The crystal end faces ($x = 0$, $x = -d$) are assumed to be antireflection-coated; therefore, there are no reflected waves in the crystal. The signal and pump light fields in the crystal are represented as sums of two circularly polarized eigenwaves (with allowance for their attenuation):

$$\mathbf{E}_P(x) = [C_{P1}(x)\mathbf{e}_1\exp(-ik_0n_1x) + C_{P2}(x)\mathbf{e}_2\exp(-ik_0n_2x)]\exp\left(-\frac{\alpha}{2}x\right), \quad (1)$$

$$\mathbf{E}_S(x) = [C_{S1}(x)\mathbf{e}_1^*\exp(ik_0n_1x) + C_{S2}(x)\mathbf{e}_2^*\exp(ik_0n_2x)]\exp\left(\frac{\alpha}{2}x\right), \quad (2)$$

where $\mathbf{e}_{1,2} = (\mathbf{y}_0 \pm i\mathbf{z}_0)/\sqrt{2}$ are the polarization vectors of the eigenwaves; $n_{1,2} = n_0 \pm \rho/k_0$ are the refractive indices for these waves; $k_0 = 2\pi/\lambda$ is the wavenumber in vacuum; n_0 and α are the refractive index and the absorption coefficient of the crystal, respectively; and ρ is its rotatory power. The interference pattern formed in the crystal is characterized by the grating vector $\mathbf{K} = 2k_0n_0\mathbf{x}_0$ and by the contrast

$$m(x) = 2\frac{C_{S1}C_{P2}^* + C_{S2}C_{P1}^*}{(|C_{P1}|^2 + |C_{P2}|^2)\exp(-\alpha x) + (|C_{S1}|^2 + |C_{S2}|^2)\exp(\alpha x)} \quad (3)$$

and gives rise to a charge redistribution over defect centers. In the case of a low contrast $m \ll 1$, the space charge field (which forms through diffusion) contains only the first spatial harmonic with vector $\mathbf{K}$. Within the single-level band model of the photorefractive crystal, the first-harmonic amplitude is given by [4]

$$E_1 = -imE_{SC} = -im\frac{E_D}{1 + E_D/E_q}, \quad (4)$$

where $E_D = (k_BT/e)K$ is the diffusion field and $E_q = eN_A/\varepsilon K$ is the trap saturation field, with $K = |\mathbf{K}| = 2\pi/\Lambda$ and Λ being the spatial period of the photorefractive grating. For an arbitrary crystal orientation relative to the grating vector $\mathbf{K}$ (Fig. 1), the change in the optical properties of the medium is due to both the linear electrooptic effect and an additional photoelastic contribution associated with elastic strains of the crystal that are produced through the piezoelectric effect [5]. Using well-known formulas from [6, 7] and Eq. (4), the total

1063-7834/02/4406-1050$22.00

amplitude of the change in the permittivity tensor in the electrooptic crystal can be found to be

$$\Delta\varepsilon_{mn} = -n_0^4 r_{41}^S \Delta b_{mn} E_1 = imn_0^4 E_{SC} \Delta b_{mn},$$
$$\Delta b_{mn} = \left[|\delta_{mnp}| m_p + \frac{1}{r_{41}^S} (P_{mnkl}^E m_l \gamma_{ki} e_{pir} m_p m_r) \right], \quad (5)$$

where r_{mnp}^S and p_{mnkl}^E are the electrooptic tensor of the clamped crystal and the photoelastic tensor measured in a static electric field, respectively; γ_{ki} is the tensor inverse of $\Gamma_{ik} = (C_{ijkl}^E m_j m_l)$; C_{ijkl}^E and e_{pir} are the elastic moduli tensor and the piezoelectric constants, respectively; δ_{mnp} is the unit antisymmetric tensor of third rank; and m_p are the direction cosines of the grating vector **K**, which in our case is taken to be parallel to the unit vector $\mathbf{x}_0$ of the crystallographic coordinate frame. Within the slowly varying amplitude approximation, the wave equation for gyrotropic media can be reduced to the following equations for coupled waves describing two-wave interaction on the reflecting grating:

$$\frac{dC_{S1}}{dx} = -\frac{\gamma}{4} m [g_I^* C_{P1} \exp(-i2\rho x) + g_E C_{P2}] \exp(-\alpha x),$$
$$\frac{dC_{S2}}{dx} = -\frac{\gamma}{4} m [g_E C_{P1} + g_I C_{P2} \exp(i2\rho x)] \exp(-\alpha x),$$
$$\frac{dC_{P1}}{dx} = -\frac{\gamma}{4} m^* [g_I C_{S1} \exp(i2\rho x) + g_E C_{S2}] \exp(\alpha x),$$
$$\frac{dC_{P2}}{dx} = -\frac{\gamma}{4} m^* [g_E C_{S1} + g_I^* C_{S2} \exp(-i2\rho x)] \exp(\alpha x), \quad (6)$$

where $\gamma = k_0 n_0^3 r_{41}^S E_{SC}$ is the coupling constant and $g_I = (\mathbf{e}_1^* \Delta b \mathbf{e}_2)$ and $g_E = (\mathbf{e}_1^* \Delta b \mathbf{e}_1) = (\mathbf{e}_2^* \Delta b \mathbf{e}_2)$ are the tensor contractions describing the contributions from intramode (without a change in the refractive-index eigenvalues) and intermode processes, respectively, to the interaction between waves propagating in opposite directions.

In the undepleted pumping wave approximation, the eigenwave amplitudes C_{P1} and C_{P2} are independent of the coordinate x and a solution for the components of the signal light wave field can be found to be

$$C_{S1}(x) = C_{S1}(0) + \frac{m(0)}{2} \{ C_{P2} [\exp G(x) - 1] + C_{P1}^* \Phi(x) \},$$
$$C_{S2}(x) = C_{S2}(0) + \frac{m(0)}{2} \{ C_{P1} [\exp G(x) - 1] - C_{P2}^* \Phi(x) \}, \quad (7)$$

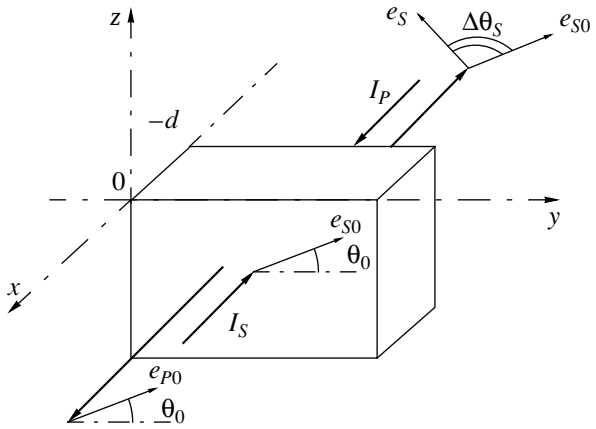

Fig. 1. Schematic diagram of two-wave interaction.

where

$$G(x) = -\frac{\gamma x}{2} \left\{ g_E + 2\mathrm{Im} \left[g_I \frac{C_{P1}^* C_{P2}}{I_{P0}} \frac{\exp(i2\rho x) - 1}{2\rho x} \right] \right\}, \quad (8)$$

$$\Phi(x) = -\frac{\gamma}{2I_{P0}} \int_0^x \exp[G(\xi)] \times [g_I^* C_{P1}^2 \exp(-i2\rho\xi) - g_I C_{P2}^2 \exp(i2\rho\xi)] d\xi, \quad (9)$$

and $I_{P0} = |C_{P1}|^2 + |C_{P2}|^2$ is the pumping wave intensity at $x = 0$. The signal-wave gain due to the reflecting grating and the polarization of this wave are determined by the contractions g_E and g_I, as seen from Eqs. (2), (3), and (7)–(9). Using Eq. (5), it can be easily verified that when the grating vector points along a ⟨110⟩ direction we have $g_E = g_I = 0$ and there is no interaction between the waves.

In (111)-cut crystals with **K** ∥ [111], we have

$$g_I = 0, \quad g_E = \Delta b_{11} - \Delta b_{12} = -\frac{1}{\sqrt{3}} \left[1 - \frac{2e_{14}(p_{11} + p_{12} + p_{13} - 2p_{44}^E)}{r_{41}^S (C_{11} + 2C_{12} + 4C_{44}^E)} \right]. \quad (10)$$

With the values of the electrooptic constant for a clamped crystal r_{41}^S, piezoelectric and photoelastic constants e_{14} and p_{mn}^E, respectively, and elastic moduli C_{mn}^E of bismuth titanate, which can be found in [8], we obtain $g_E = -0.266$. In this case, efficient energy transfer occurs between the left-circularly polarized signal wave ($C_{S1}(0) \neq 0$, $C_{S2}(0) = 0$) and the right-circularly polarized pumping wave ($C_{P2} \neq 0$, $C_{P1} = 0$):

$$\mathbf{E}_S^c(x) = \mathbf{e}_1^* C_{S1}(0) \exp\left[-\frac{g_E \gamma - \alpha}{2} x \right] \exp(ik_0 n_1 x). \quad (11)$$

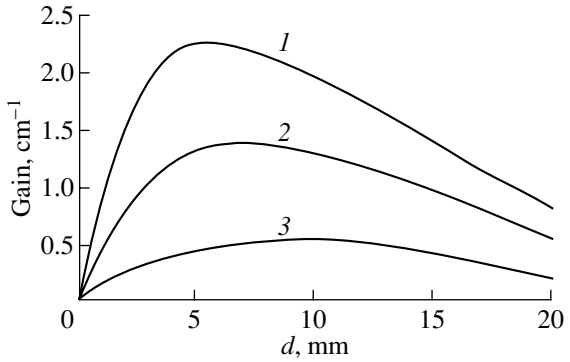

Fig. 2. Dependence of the signal-wave gain due to two-wave interaction in a $Bi_{12}TiO_{20}$ crystal on its thickness for the grating vector **K** pointing along the [100] axis and for the coupling constant γ equal to (*1*) 2, (*2*) 4, and (*3*) 6 cm^{-1}.

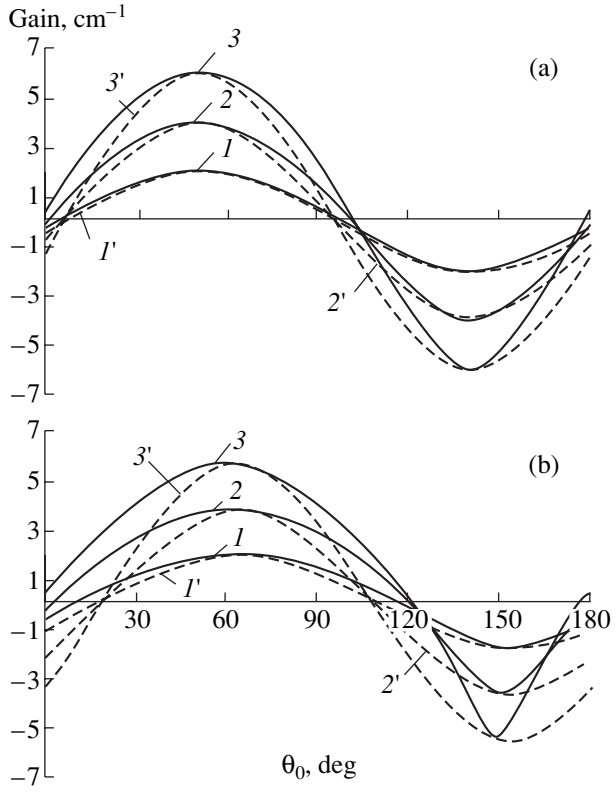

Fig. 3. Signal-wave gain due to two-wave interaction calculated without (dashed curves) and with allowance for nonunidirectional energy transfer (solid curves) as a function of the angle θ_0 for $Bi_{12}TiO_{20}$ crystals of thickness *d* equal to (a) 2 and (b) 6 mm with the grating vector **K** pointing along the [100] axis. The coupling constant γ is equal to (*1*, *1*') 2, (*2*, *2*') 4, and (*3*, *3*') 6 cm^{-1}.

The polarization of the signal wave remains unchanged. The signal-wave gain due to the two-wave interaction is defined in terms of the signal-wave intensities ($I_S^P(-d)$) and ($I_S^0(-d)$) in the presence and absence of the pumping wave, respectively, as

$$\Gamma = \frac{1}{d}\ln\left[\frac{I_S^P(-d)}{I_S^0(-d)}\right]; \tag{12}$$

in the case at hand, it is found to be

$$\Gamma^c_{[111]} = g_E\gamma = \frac{2\pi}{\lambda}n_0^3 r_{41}^S \frac{g_E E_D}{1 + E_D/E_q}. \tag{13}$$

The same signal-wave gain characterizes the interaction between the signal and pump waves linearly polarized in the same direction

$$\Gamma^l_{[111]} = g_E\gamma; \tag{14}$$

the polarization structure of the signal wave also remains unchanged.

In (100)-cut crystals, for $\mathbf{y}_0 \parallel [010]$ and $\mathbf{z}_0 \parallel [001]$, we have

$$g_E = 0, \quad g_I = -i\Delta b_{23} = -i. \tag{15}$$

It should be noted that when the pumping wave is circularly polarized ($C_{P1} = 0$ or $C_{P2} = 0$), there is no signal-wave gain in (100)-cut crystals since $G(x) = 0$. If the signal and pump waves are of the same circular polarization (say, right-handed, i.e., $C_{P1} = 0$, $C_{S1} = 0$), they do not interact, because there is no interference between them, $m(0) = 0$. In the case where the pumping wave is left-circularly polarized and the signal wave at the entrance of the crystal is of the right-hand polarization ($C_{S2}(0) = 0$), the amplitudes of the eigenwaves in the crystal can be found from Eqs. (7) to be

$$\begin{aligned} C_{S1}(x) &= C_{S1}(0), \\ C_{S2}(x) &= C_{S1}(0)\frac{\gamma}{4\rho}[\exp(i2\rho x) - 1]. \end{aligned} \tag{16}$$

Thus, the left-circularly polarized signal wave, in combination with the pumping wave, produces a photorefractive grating in this case but is not involved directly in the energy transfer. The energy of the pumping wave is transferred, through its diffraction by grating, to the right-circularly polarized component of the signal wave. The corresponding gain due to two-wave interaction

$$\Gamma^c_{[100]} = \frac{1}{d}\ln\left[1 + \left(\frac{\gamma}{2\rho}\right)^2 \sin^2(\rho d)\right] \tag{17}$$

is independent of the sign of the electrooptical constant and characterizes the nonunidirectional energy transfer effect, which was considered earlier only in the transmission geometry of wave interaction [9]. For crystals with low rotatory power, the gain $\Gamma^c_{[100]}$ can reach high values. Figure 2 shows the dependence of $\Gamma^c_{[100]}$ on the $Bi_{12}TiO_{20}$ sample thickness ($\rho = 6.5°$/mm for the wavelength $\lambda = 633$ nm) for different values of the coupling constant γ. We note that the maximum efficiency of the nonunidirectional energy transfer is reached at certain

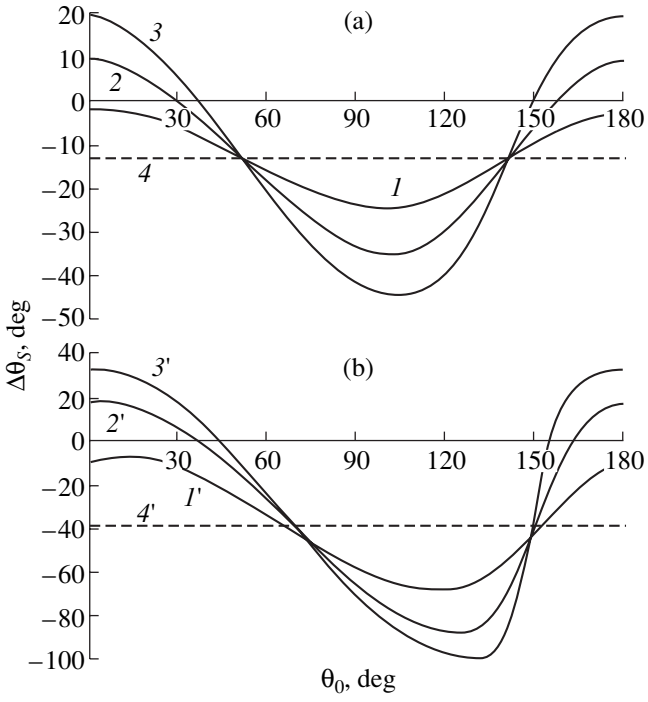

Fig. 4. Polarization rotation angle of the signal wave as a function of the angle θ_0 in $Bi_{12}TiO_{20}$ crystals of thickness d equal to (a) 2 and (b) 6 mm with grating vector **K** pointing along the [100] axis. The coupling constant γ is equal to (*4*) 0, (*1*, *1*') 2, (*2*, *2*') 4, and (*3*, *3*') 6 cm^{-1}.

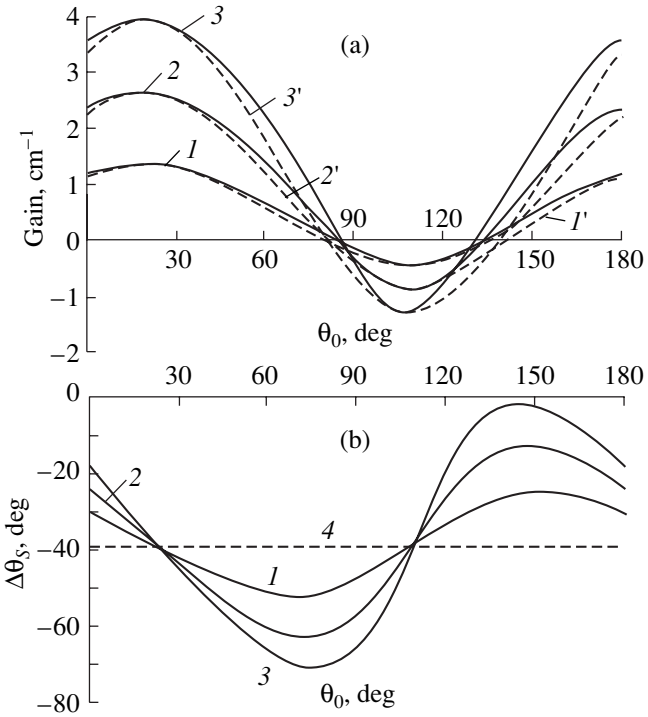

Fig. 5. (a) Signal-wave gain due to two-wave interaction calculated without (dashed curves) and with allowance for nonunidirectional energy transfer (solid curves) and (b) polarization rotation angle of the signal wave as functions of the angle θ_0 in a $Bi_{12}TiO_{20}$ crystal of thickness d = 6 mm with grating vector **K** pointing along the $[11\bar{2}]$ axis. The coupling constant γ is equal to (*4*) 0, (*1*, *1*') 2, (*2*, *2*') 4, and (*3*, *3*') 6 cm^{-1}.

optimal values of the interaction length, which decrease with increasing coupling constant.

In the case of linearly polarized waves interacting in (100)-cut crystals, the signal-wave amplification is due to both unidirectional and nonunidirectional energy transfer. The polarization dependences of the gain $\Gamma^l_{[100]}$ due to two-wave interaction as calculated from Eqs. (7)–(9) are shown in Fig. 3. The signal and pump waves at $x = 0$ are assumed to have identical polarization vectors $\mathbf{e}_{S0} = \mathbf{e}_{P0}$, making an angle θ_0 with the $\mathbf{y}_0$ axis. It should be noted that in a thin sample (d = 2 mm, Fig. 3a), the positions of the extrema in the polarization dependences calculated without (dashed curves) and with allowance for nonunidirectional energy transfer (solid curves) are almost the same and correspond to the polarization vector orientations $\mathbf{e}_P \parallel \langle 011 \rangle$ in the middle of the crystal. In a thicker crystal (d = 6 mm, Fig. 3b), the polarization vector orientation $\mathbf{e}_P \parallel [011]$ in the middle of the crystal (for $\theta_0 = 45° + \rho d/2$) differs from its optimal orientation, the difference increasing with the coupling constant γ. We note that the nonunidirectional energy transfer (always proceeding from a strong wave to a weak one) broadens the range of θ_0 values in which the gain $\Gamma^l_{[100]}(\theta_0)$ is positive.

In the case under discussion [a (100)-cut crystal and linearly polarized waves with their polarization vectors pointing along the same direction at the $x = 0$ crystal face, $\mathbf{e}_{S0} = \mathbf{e}_{P0}$], the polarization of the signal wave remains linear everywhere over the crystal. However, as the signal wave propagates through the crystal, its polarization vector $\mathbf{e}_S$ rotates, which is due to both the optical activity of the crystal and the interaction with the pumping wave. The dependence of the angle $\Delta\theta_S$ through which the vector $\mathbf{e}_S$ rotates as the signal wave propagates from the $x = 0$ to the $x = -d$ crystal face at an angle θ_0 (defining the direction of this vector at $x = 0$) is shown in Fig. 4. Dashed lines in this figure correspond to the absence of wave interaction ($\gamma = 0$) and, therefore, represent the angle of the polarization vector rotation due to optical activity of the crystal. In the presence of the pumping wave, the polarization rotation angle of the signal wave increases with the coupling constant and with the crystal thickness. When γ = 6 cm^{-1} and d = 6 mm (Fig. 4b), the maximum rotation angle is roughly 70°. We note that the maximum effect of the reflecting grating on the signal-wave polarization takes place in the case where the signal-wave gain is minimal in magnitude. This agrees with the results presented in [10] for the case of wave interaction on a transmission

grating characterized by vector $\mathbf{K} \parallel [\bar{1}10]$ in optically active (110)-cut crystals.

In general, both intramode and intermode interactions between waves take place. In the case of the reflecting-grating vector orientation $\mathbf{K} \parallel [11\bar{2}]$ in bismuth titanate, we have $g_I = 0.467$ and $g_E = 0.216$ for $\mathbf{y}_0 \parallel [1\bar{1}0]$ and $\mathbf{z}_0 \parallel [\bar{1}\bar{1}\bar{1}]$. Figure 5 shows numerically calculated polarization dependences of the gain $\Gamma^I_{[11\bar{2}]}$ due to two-wave interaction and of the polarization rotation angle $\Delta\theta_S$ for a linearly polarized signal and pump waves with their polarization vectors pointing along the same direction at $x = 0$ ($\mathbf{e}_{S0} = \mathbf{e}_{P0}$). We note that in this case, the positions of the extrema of the polarization rotation angle of the signal wave (Fig. 5b) coincide with those of the rate of change in the gain $\Gamma'(\theta_0)$ (Fig. 5a).

3. CONCLUSION

Thus, within the undepleted-pumping-wave approximation, we have derived relations that describe the interaction of two light waves on a reflecting photorefractive grating in cubic gyrotropic crystals. It was shown that the nonunidirectional energy transfer can significantly affect the wave interaction efficiency. The changes in the polarization of the signal wave in the presence of the pumping wave depend on the differently cut crystals and their thicknesses.

REFERENCES

1. N. V. Kukhtatev, B. S. Chen, P. Venkateswarlu, *et al.*, Opt. Commun. **104**, 23 (1993).
2. I. F. Kanaev, V. K. Malinovskiĭ, and N. V. Surovtsev, Fiz. Tverd. Tela (St. Petersburg) **42** (11), 2079 (2000) [Phys. Solid State **42**, 2142 (2000)].
3. S. Mallick, M. Miteva, and L. Nikolova, J. Opt. Soc. Am. B **14** (5), 1179 (1997).
4. N. V. Kukhtarev, V. B. Markov, S. G. Odulov, *et al.*, Ferroelectrics **22**, 949 (1979).
5. A. A. Izvanov, A. E. Mandel', N. D. Khat'kov, and S. M. Shandarov, Avtometriya, No. 2, 79 (1986).
6. S. I. Stepanov, S. M. Shandarov, and N. D. Khat'kov, Fiz. Tverd. Tela (Leningrad) **29** (10), 3054 (1987) [Sov. Phys. Solid State **29**, 1754 (1987)].
7. B. I. Sturman, E. V. Podivilov, K. H. Ringhofer, *et al.*, Phys. Rev. E **60**, 3332 (1999).
8. O. V. Kobozev, S. M. Shandarov, R. V. Litvinov, *et al.*, Neorg. Mater. **34** (12), 1486 (1998).
9. V. Yu. Krasnoperov, R. V. Litvinov, and S. M. Shandarov, Fiz. Tverd. Tela (St. Petersburg) **41** (4), 632 (1999) [Phys. Solid State **41**, 568 (1999)].
10. R. V. Litvinov, S. M. Shandarov, and S. G. Chistyakov, Fiz. Tverd. Tela (St. Petersburg) **42** (8), 1397 (2000) [Phys. Solid State **42**, 1435 (2000)].

Translated by Yu. Epifanov

Physics of the Solid State, Vol. 44, No. 6, 2002, pp. 1055–1060. Translated from Fizika Tverdogo Tela, Vol. 44, No. 6, 2002, pp. 1011–1016.

SEMICONDUCTORS AND DIELECTRICS

Manifestation of Liquid-State and Solid-State Properties in Electron Relaxation of Paramagnetic Ions in Solutions: Non-Markovian Processes

G. P. Vishnevskaya*, E. N. Frolova*, and R. M. Yulmetyev**

** Zavoĭskiĭ Physicotechnical Institute, Russian Academy of Sciences, Sibirskiĭ trakt 10/7, Kazan 29, 420029 Tatarstan, Russia*

*** Kazan State Pedagogical University, Kazan, Tatarstan, Russia*

e-mail: frolov@sci.kcn.ru

Received July 3, 2001

Abstract—The linewidth δH and the spin–spin relaxation time T_2 for Gd^{3+}, Mn^{2+}, and Cr^{3+} ions in aqueous, water–glycerol, and water–poly(ethylene glycol) solutions at paramagnetic ion concentrations providing the dipole–dipole mechanism of spin relaxation are measured using two independent methods, namely, electron paramagnetic resonance (EPR) and nonresonance paramagnetic absorption in parallel fields. Analysis of the experimental results indicates a gradual crossover from pure liquid-state (diffusion) to quasi-solid-state (rigid lattice) spin relaxation. It is demonstrated that the limiting cases are adequately described by standard, universally accepted formulas for dipole–dipole interactions in the liquid-state (the correlation time of translational motion satisfies the condition $\tau_c \ll T_2$) and solid-state ($\tau_c \gg T_2$) approximations. A complete theoretical treatment of the experimental dependences (including the observed gradual crossover of spin relaxation) is performed in the framework of the non-Markovian theory of spin relaxation in disordered media, which is proposed by one of the authors. Within this approach, the collective memory effects for spin and molecular (lattice) variables are taken into account using the first-order and second-order memory functions for spin–spin and spin–lattice interactions. A correlation between the spin magnitude and the temperature–viscosity conditions corresponding to the crossover to non-Markovian relaxation is revealed, and the situations in which structural transformations occurring in the solutions favor the crossover to solid-state spin relaxation are analyzed.

1. INTRODUCTION

It is well known that electron relaxation of paramagnetic ions in a condensed medium substantially depends on the spin–spin interactions and the properties of the medium. Intermolecular (dipole–dipole and exchange) interactions are governed by the distance between paramagnetic centers and the velocity of translational motion of particles in the solution. Radiospectroscopic investigations of the intermolecular interactions can provide valuable information on the spatial distribution of paramagnetic particles in the liquid-state lattice and, consequently, on the structure of the studied solutions and changes in the molecular mobility of the paramagnetic complexes in these solutions at different viscosities and concentrations.

The main objective of this work was to analyze the conditions corresponding to a change in the ratio between the spin–spin relaxation time T_2 and the correlation time of molecular motion τ_c in the following situations: $T_2 \gg \tau_c$, $T_2 \sim \tau_c$, and $T_2 \ll \tau_c$. According to the concept of non-Markovian random processes, this change is associated with a gradual crossover of a spin system from Markovian to quasi-Markovian and then to non-Markovian spin relaxation. Physically, this implies a gradual crossover from the liquid-state to the solid-state mechanism of spin relaxation.

2. EXPERIMENTAL TECHNIQUE

The solutions used in the experiments were prepared from chromium, manganese, and gadolinium nitrate salts (analytical grade). The concentrations of Cr^{3+} and Gd^{3+} ions in the solutions prepared varied in the range from 0.01 *M* to concentrations close to the solubility limits of these salts in aqueous solutions (2.7 and 3.6 *M*, respectively). It should be noted that intermolecular interactions occurring in these solutions are governed only by dipole–dipole interactions. However, the solutions with a high concentration of Mn^{2+} are characterized by exchange interactions in addition to dipole–dipole interactions. For this reason, the concentration of Mn^{2+} ions was chosen so as to exclude the occurrence of exchange interactions (0.5 *M*). The required changes in the viscosity of the solution were accomplished by varying either the salt concentration or the content of glycerol and poly(ethylene glycol) in the solvents. The viscosity was measured using an Ostwald viscometer or a viscometer designed by Goncharov [1].

1063-7834/02/4406-1055$22.00

The time and rate of the spin–spin relaxation were measured using two independent methods at room temperature: (i) nonresonance paramagnetic absorption in parallel fields [2, 3] and (ii) electron paramagnetic resonance (EPR) in the *X* band. Note that, even at an insignificant water content, the absorption signals observed in water–glycerol and water–poly(ethylene glycol) solutions are attributed to aqua ions [3, 4].

In order to determine the linewidth assigned to the dipole–dipole interaction δH_{dd}, the concentration-independent contribution δH_0, which is associated with intramolecular mechanisms of spin relaxation and, possibly, with an incompletely averaged fine structure, was subtracted from the measured total linewidth δH. The linewidth δH_{dd} was calculated from the following formulas: $\delta H_{dd} = \delta H - \delta H_0$ for a Lorentzian line shape and $\delta H_{dd} = (\delta H^2 - \delta H_0^2)^{1/2}$ for a Gaussian line shape. According to our estimates, the resonance line has a Lorentzian shape for aqueous and water–glycerol solutions in which the concentration of Gd^{3+} or Cr^{3+} ions does not exceed 2.5–2.7 *M*. At higher concentrations of Gd^{3+} ions, the resonance line has a Gaussian shape. In the case of nonresonance paramagnetic absorption measurements, there is no need to determine the concentration-independent contribution, because nonresonance absorption due to spin–lattice (T_1) and spin–spin (T_2) relaxations is measured separately; furthermore, the dipole–dipole interactions make a dominant contribution to the spin–spin relaxation time T_2 and do not affect the spin–lattice relaxation time T_1 [3].

3. RESULTS AND DISCUSSION

The experimental dependences of the total EPR linewidth on the concentration of paramagnetic centers are depicted in Fig. 1. The dependences of the linewidth and the relaxation time T_2 on the viscosity are shown in Figs. 2–6. As can be seen from Fig. 1, the concentration-independent contribution δH_0 is equal to 204 G for $Gd(NO_3)_3$ aqueous solutions and 150 G for $Cr(NO_3)_3$ aqueous solutions. In the case when the measurements were performed at a constant concentration of paramagnetic ions and the required viscosities were achieved by varying the content of glycerol or poly(ethylene glycol) in the solutions (Figs. 3, 5), the concentration-independent contribution δH_0 was determined from the EPR spectra of diluted solutions (~0.01 *M*) with a similar composition of the solvent and virtually the same viscosity.

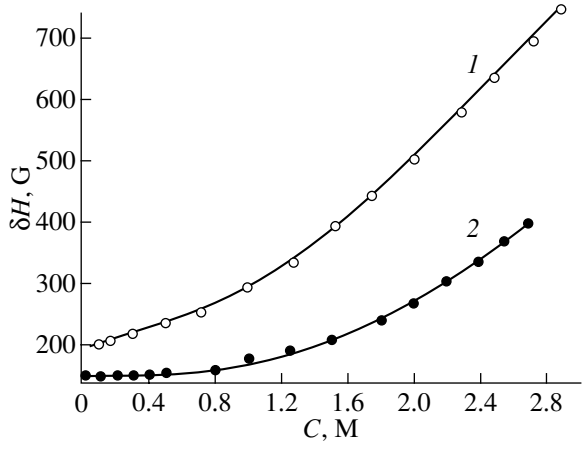

Fig. 1. Dependences of the total EPR linewidth on the concentration of (*1*) $Gd(NO_3)_3$ and (*2*) $Cr(NO_3)_3$ in aqueous solutions at 298 K.

It is seen from Figs. 2–6 that the experimental dependences of T_{2dd}, δH_{dd}, and $\delta H_{dd}/C$ on the viscosity for solutions of ions with different spins exhibit a similar behavior. As the viscosity increases in the low-viscosity solutions, the linewidth δH_{dd} increases, whereas the spin–spin relaxation time T_2 correspondingly decreases and gradually reaches a steady-state value independent of further change in the viscosity. Except in the range of the observed gradual crossover, the experimental dependences can be adequately described by standard, universally accepted formulas [5–7]:

$$\frac{1}{T_2} = 1.78 \times 10^{23} \frac{g^4 \beta^4}{h^2 k} \frac{\eta}{T} CS(S+1) \qquad (1)$$

in the liquid-state approximation (the correlation time of translational Brownian motion satisfies the condition $\tau_c < T_2$) and

$$\frac{1}{T_2} = 26.29 \times 10^{20} \frac{g^2 \beta^2}{\hbar} C\sqrt{S(S+1)} \qquad (2)$$

in the solid-state approximation when the dipole–dipole interactions are not averaged through molecular motion (the correlation time of translational Brownian motion satisfies the condition $\tau_c > T_2$). Here, η is the macroscopic viscosity of the solution and *C* is the concentration of paramagnetic ions in terms of *M*. The correlation time is defined as $\tau_c = \lambda^2/(12D)$, where λ is the root-mean-square length of hopping in an elementary diffusion event, $D = kT/(6\pi\eta a)$ is the diffusion coefficient described by the Stokes relationship, and *a* is the radius of the complex. The correlation time can be calculated from the formula

$$\tau_c = \frac{2\pi a^3 \eta}{kT}. \qquad (3)$$

This formula gives the most reliable estimate of τ_c in the framework of the diffusion and hopping models of particle motion in the course of spin-exchange interaction due to collisions [7].

At high concentrations of paramagnetic ions, the relaxation rate in the solid-state approximation for a

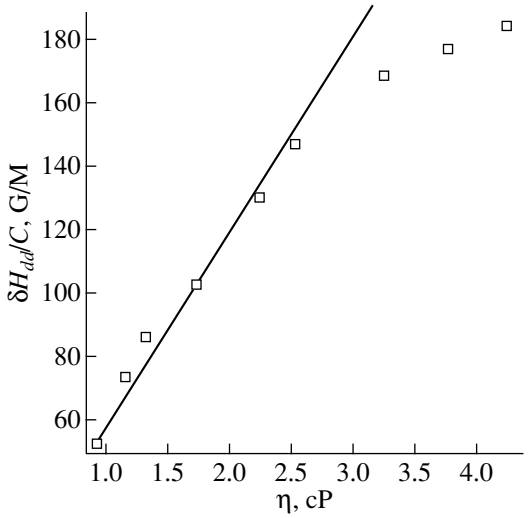

Fig. 2. Dependence of $\delta H_{dd}/C$ on the viscosity of $Gd(NO_3)_3$ in aqueous solutions at 298 K. Points are the experimental data. The solid line represents the theoretical results obtained in the liquid-state approximation.

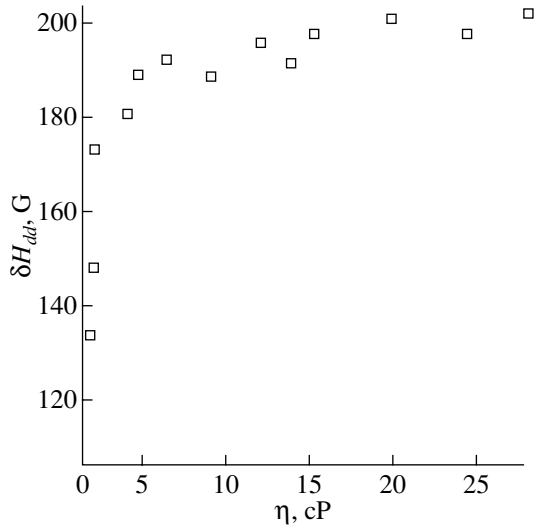

Fig. 3. Dependence of δH_{dd} on the viscosity of $Gd(NO_3)_3$ in 1.2 *M* water–glycerol solutions at 298 K. The viscosities η correspond to the specified concentrations of glycerol in the solutions.

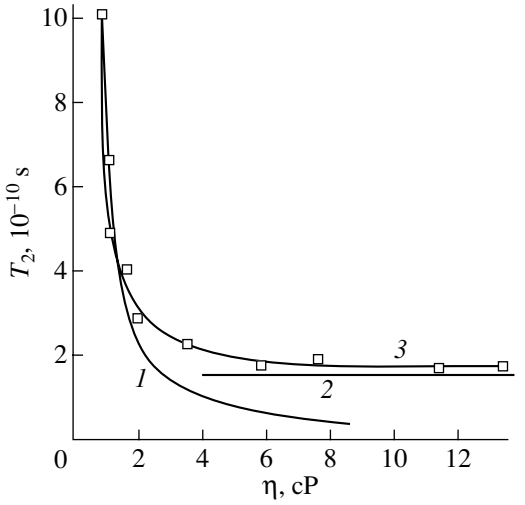

Fig. 4. Dependences of the spin–spin relaxation time on the viscosity of $Gd(NO_3)_3$ in aqueous solutions at 298 K. The viscosities η correspond to the specified concentrations of $Gd(NO_3)_3$ in the solutions. Points are the experimental data. Solid lines represent the theoretical results obtained in the framework of (*1*) liquid-state and (*2*) solid-state approximations and (*3*) our theory.

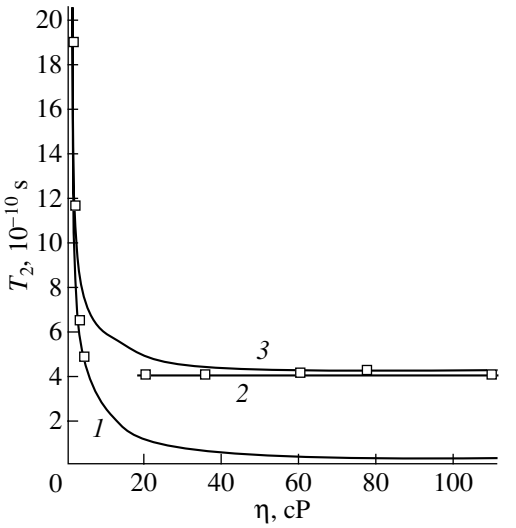

Fig. 5. Dependences of the spin–spin relaxation time on the viscosity of $Mn(NO_3)_2$ in 0.5 *M* water–poly(ethylene glycol) solutions at 298 K. The viscosities η correspond to the specified concentrations of poly(ethylene glycol) in the solutions. Points are the experimental data. Designations of the curves are the same as in Fig. 4.

Gaussian line shape can be expressed through the second moment; that is,

$$\frac{1}{T_2} = 2\left[\frac{3}{5}\frac{g^4\beta^4}{\hbar^2}S(S+1)\sum_k r_{jk}^{-6}\right]^{1/2}, \qquad (4)$$

where r_{jk} is the distance between the *j*th and *k*th paramagnetic centers ($r \sim C^{-1/3}$). For a simple cubic lattice with parameter *d*, we have $\sum_k r_{jk}^{-6} = 8.5d^{-6}$ [6].

If required, the linewidths and the spin–spin relaxation times can be recalculated from the following relationships:

$$\delta H = \frac{1}{\alpha\gamma T_2}, \quad T_2 \ll T_1,$$
$$\delta H = \frac{2}{\alpha\gamma T_2}, \quad T_2 \leq T_1, \qquad (5)$$

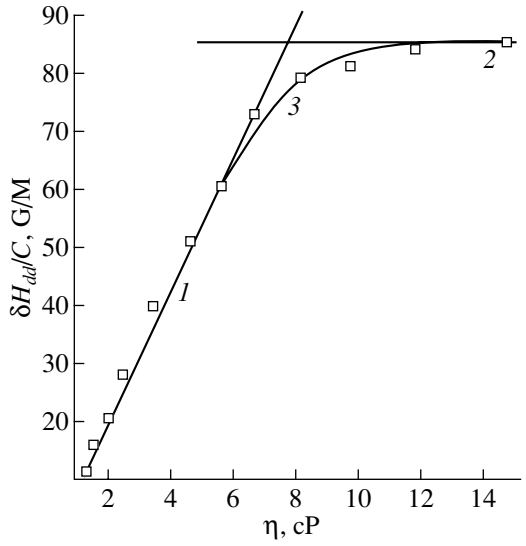

Fig. 6. Dependences of $\delta H_{dd}/C$ on the viscosity of $Cr(NO_3)_3$ in aqueous solutions of at 298 K. The viscosities η correspond to the specified concentrations of $Cr(NO_3)_3$ in the solutions. Points are the experimental data. Designations of the curves are the same as in Fig. 4.

where $\alpha = \sqrt{3}$ for a Lorentzian line shape and 1.18 for a Gaussian line shape, γ is the gyromagnetic ratio, and T_1 is the spin–lattice relaxation time.

By using the measured macroscopic viscosities and the radii $a = 4.15$ Å for Cr^{3+} aqua complexes, $a = 3$ Å for Mn^{2+} aqua complexes, and $a = 3.8$ Å for Gd^{3+} aqua complexes, we calculated the correlation times τ_c according to formula (3) and compared the obtained values with the experimental relaxation times T_2 (see table). It is seen from the table that, at the viscosities $\eta \geq 5$ cP for Cr^{3+} aqua complexes, $\eta \geq 10$ cP for Mn^{2+} aqua complexes, and $\eta \geq 3$ cP for Gd^{3+} aqua complexes, the ratio between the correlation time τ_c and the spin–spin relaxation time T_2 changes from $\tau_c < T_2$ to $\tau_c \sim T_2$ and $\tau_c > T_2$. These results are in agreement with the experimental dependences depicted in Figs. 2–5. Therefore, we can make the inference that the dipole–dipole interactions in systems with a low viscosity are averaged through diffusion motion. In the case when the viscosity is higher than the aforementioned values, the inequality $\tau_c < T_2$ becomes invalid and the molecular motion does not lead to the averaging of the dipole–dipole interactions, even though the lattice system remains in the liquid state. Note that the greater the spin and the larger the radius of the complex, the lower the viscosity at which the system exhibits solid-state behavior (in particular, at $\eta \geq 20$ cP in solutions of Mn^{2+} ions with $S = 5/2$ and at $\eta \geq 4$–6 cP in solutions of Gd^{3+} ions with $S = 7/2$).

It is quite possible that, in some cases, the crossover to the solid-state behavior can be caused by different structural transformations in solutions. For example, it is this situation that occurs in $Cr(NO_3)_3$ aqueous solutions in which stable multilayer hydrate shells are formed around Cr^{3+} ions [3, 8]. As a consequence, complete hydration—all water molecules are in the bound state—is attained in $Cr(NO_3)_3$ aqueous solutions even at concentrations in the range 2.2–2.3 *M* and viscosities $\eta = 10$–12 cP. For the concentrations and viscosities corresponding to complete hydration and above, the structure of solutions should be treated as a disordered pseudocrystalline structure. In these solutions, the dipole–dipole interactions are well described within the solid-state approximation (Fig. 6).

At intermediate concentrations, many aqueous solutions of salts undergo phase separation into microregions with a structure of the free solvent and microregions whose structure is similar to that of the crystal hydrate [9, 10]. Inside microregions of the latter type, ions are closely spaced and their translational motion is hindered. In this case, the dipole–dipole interactions can be described within the static approximation. This model was applied earlier to the description of the specific features of the dipole–dipole interaction in Mn^{2+} aqueous solutions at concentrations above 2 *M* [3]. A similar situation arises in aqueous solutions of gadolinium nitrate (Fig. 5). The solid-state approximation for dipole–dipole interactions is also valid at lower concentrations of paramagnetic ions in water–glycerol and water–poly(ethylene glycol) viscous solutions (Figs. 2, 4). However, the experimentally observed gradual crossover from liquid-state (diffusion) to solid-state behavior of the system has defied description with the use of relationships (1), (2), and (4).

In general, the experimental dependences (including the observed gradual crossover) can be interpreted within the statistical non-Markovian spin relaxation theory developed by one of the authors of the present work. This theory is based on the Zwanzig–Mori kinetic equations [11, 12] for normalized spin time correlation functions. It should be noted that statistical memory effects manifest themselves in many random processes of different physical nature. For example, the non-Markovian processes have been revealed in nuclear magnetic resonance, infrared spectroscopy, and dielectric relaxation [13–15]. The non-Markovian spin relaxation theory makes allowance for collective memory effects of the molecular (lattice) and spin variables with the use of the memory function for the description of the averaged dynamics of spin–spin and spin–lattice interactions. By using the results obtained in [16, 17], the kinetic equations for spin time correlation functions can be written in the following form:

$$\frac{d\mu_\alpha(t)}{dt} = -i\alpha\omega_0\mu_\alpha(t) - \int_0^t d\tau[k_a(t-\tau) + N_\alpha(t-\tau)]\mu_\alpha(\tau), \quad (6)$$

Correlation times τ_c calculated according to formula (3) and experimental relaxation times T_2 for aqua complexes of Cr^{3+} (T_2 are determined from the EPR linewidths), Mn^{2+}, and Gd^{3+} (T_2 are measured using nonresonance paramagnetic absorption)

η, cP	Cr^{3+}		Mn^{2+}		Gd^{3+}	
	τ_c, 10^{-10} s	T_2, 10^{-10} s	τ_c, 10^{-10} s	T_2, 10^{-10} s	τ_c, 10^{-10} s	T_2, 10^{-10} s
1.2	1.38		0.50	18.0	1.00	10.00
1.5	1.63		0.62	13.5	1.26	4.75
2.2	2.40	26.0	0.90	9.5	1.84	3.60
2.5	2.72	20.8	1.03	8.3	2.09	3.30
3.5	3.81	14.0	1.44	6.4	2.93	2.40
4.0	4.36	11.5	1.65	6.0	3.35	2.10
6.0	6.54	5.0	2.47	5.0	5.03	1.80
8.8	9.60	3.8	3.62	4.5	7.90	1.70
10.0	10.90	3.5	4.12	4.2	8.38	1.60
12.0	13.10	3.0	4.94	4.0	10.80	1.60
15.0	16.35	2.9	6.18	3.9	12.55	1.60
20.0			8.24	3.9	16.76	1.64
30.0			12.36	3.6		
40.0			16.50	4.0		
60.0			24.70	4.0		

where $\alpha = 0$ and ± 1 are the components of the total spin (the indices $\alpha = 0$ and ± 1 refer to the longitudinal and transverse components, respectively), ω_0 is the Larmor frequency, and $k_\alpha(t)$ is the nonsymmetric part of the spin memory function [$N_\alpha(t) \longrightarrow 0$]. For the transverse spin components and the transverse component of the memory function, we have

$$k_+(t) = \sum \sigma_{1\beta}^2 h_\beta(t), \tag{7}$$

where

$$\sigma_{1\beta}^2 = \frac{\langle [\hat{S}_-, \hat{H}_\beta^*], [\hat{H}_\beta, \hat{S}_+] \rangle}{\hbar^2 \langle |\hat{S}_+(0)|^2 \rangle},$$
$$h_\beta(t) = \frac{\langle [\hat{S}_-, \hat{H}_\beta^*] \exp\{i\hat{L}t\} [\hat{H}_\beta, \hat{S}_+] \rangle}{\langle [\hat{S}_-, \hat{H}_\beta^*], [\hat{H}_\beta, \hat{S}_+] \rangle}. \tag{8}$$

Here, $h_\beta(t)$ is the βth component of the first-order normalized memory function, $\sigma_{\alpha\beta}^2$ stands for the components of the second moment in magnetic resonance, $\hat{L}$ is the total Liouvillian of the whole system (including spins and motion), and ω_β is the frequency related to the Zeeman part $\hat{L}_0$ of the operator $\hat{L}$ through the expression

$$\hat{L}_0[\hat{H}_\beta, \hat{S}_+] = -\omega_\beta [\hat{H}_\beta, \hat{S}_+]. \tag{9}$$

After a number of simplifications, for the first-order memory function, we obtain the kinetic equation

$$\frac{dh_\beta(t)}{dt} = -i\omega_\beta h_\beta(t) - \int_0^t d\tau [\gamma_\beta^2 h_\beta(t) + \Omega_\beta^2 \pi(\tau)] h_\beta(t-\tau). \tag{10}$$

In this equation, we introduced two relaxation frequencies, γ_β and Ω_β. The former frequency squared γ_β^2 corresponds in dimension to the ratio of the components of the fourth moment to the components of the second moments of the EPR lines ($\gamma_\beta^2 \approx M_4/M_2$) for the quasi-solid-state lattice. The latter frequency Ω_β is related to the characteristic diffusion time τ_c. The function $\pi(\tau)$ is the normalized time correlation function for the velocity (momentum) of particles in the liquid. Therefore, owing to the hierarchical structure of the spin memory functions, the spin relaxation is described by two contributions, namely, the molecular diffusion (liquid-state) and static spin (solid-state) contributions.

The calculation of the relaxation rate gives the following formula:

$$\frac{1}{T_2} = \sum \sigma_{1\beta}^2 \tau_c^*. \tag{11}$$

Here, τ_c^* is the effective correlation time, which characterizes the coexistence of two spin memory channels associated with molecular diffusion motion and spin–spin interactions in the quasi-solid-state lattice; that is,

$$\tau_c^* = \frac{1}{2\gamma_\beta^2\tau_c}[\sqrt{1+4\gamma_\beta^2\tau_c^2}-1]. \quad (12)$$

In the two limiting cases, we obtain

$$\tau_c^* = \begin{cases} \tau_c \text{ at } \tau_c \longrightarrow 0 \text{ or } \tau_c\gamma_\beta \longrightarrow 0 \\ \tau_\gamma = \gamma_\beta^{-1} \text{ at } \tau_c \longrightarrow \infty \text{ or } \tau_c\gamma_\beta \longrightarrow \infty. \end{cases} \quad (13)$$

Here, the effective correlation time τ_c^* corresponds to either the liquid-state relaxation or the solid-state relaxation behavior. For the limiting Markovian or non-Markovian behavior of the system, the proposed theory is reduced to the standard relationships [1–3]. In actual fact, within the liquid-state (Markovian) approximation, the correlation time τ_c^* is determined by the formulas $\sum\sigma_{1\beta}^2 = M_2$ and $T_2^{-1} = \tau_c M_2$ [3]. Within the solid-state (non-Markovian) approximation, for a Lorentzian line shape, we have $\tau_\gamma = \sqrt{M_2}/\sqrt{M_4}$ and $T_2^{-1} = M_2\sqrt{M_2}/\sqrt{M_4}$.

Figures 4–6 (curves *3*) represent the results of theoretical calculations with the use of formulas (11) and (12) at $\tau_\gamma = 4.54 \times 10^{-10}$ s for Gd^{3+} solutions, $\tau_\gamma = 2.2 \times 10^{-10}$ s for Mn^{2+} solutions, and $\tau_\gamma = 17.8 \times 10^{-10}$ s for Cr^{3+} solutions and the correlation times τ_c calculated from formula (3).

4. CONCLUSION

Thus, the proposed theory provides the most adequate qualitative and quantitative description of the experimental results obtained for all the studied ions, including the range of the observed gradual crossover from Markovian to quasi-Markovian and non-Markovian behavior. It is in this range that both the liquid-state and solid-state properties manifest themselves in electron relaxation of paramagnetic ions in the studied solutions.

ACKNOWLEDGMENTS

This work was supported by the Russian Foundation for Basic Research (project no. 00-03-32915a) and the Tatar Foundation for Research and Development [project no. 14-78/2000 (F)].

REFERENCES

1. V. A. Goncharov, RF Patent No. 1749776.
2. B. A. Volkov, G. P. Vishnevskaya, V. A. Gorozhanin, and R. T. Ramazanov, Prib. Tekh. Éksp., No. 4, 167 (1973).
3. G. P. Vishnevskaya, *Radiospectroscopy of Condensed Matter* (Nauka, Moscow, 1990), p. 13.
4. G. P. Vishnevskaya, F. M. Gumerov, E. N. Frolova, and A. R. Fakhrutdinov, *Structure and Dynamics of Molecular Systems* (Inst. Fiz. Khim. Ross. Akad. Nauk, Moscow, 2000), Vol. VII, p. 329.
5. A. Abragam, *The Principles of Nuclear Magnetism* (Clarendon, Oxford, 1961; Inostrannaya Literatura, Moscow, 1963).
6. S. A. Altshuler and B. M. Kozyrev, *Electron Paramagnetic Resonance in Compounds of Transition Elements* (Nauka, Moscow, 1972; Halsted, New York, 1975).
7. K. I. Zamaraev, Yu. N. Molin, and K. M. Salikhov, *Spin Exchange* (Nauka, Novosibirsk, 1977).
8. R. Caminiti, G. Licheri, G. Piccaluga, and G. Pinna, J. Chem. Phys. **69** (1), 1 (1978).
9. O. Ya. Samoĭlov, *Structure of Aqueous Electrolytic Solutions and Ion Hydration* (Akad. Nauk SSSR, Moscow, 1957).
10. T. Erdey-Grüz, *Transport Phenomena in Aqueous Solutions* (Akadémiai Kiadö, Budapest, 1974; Mir, Moscow, 1976).
11. R. Zwanzig, Phys. Rev. **124**, 983 (1961).
12. H. Mori, Prog. Theor. Phys. **34**, 765 (1965).
13. B. B. Laird, J. Budimir, and J. L. Skinner, J. Chem. Phys. **94**, 4391 (1991).
14. A. G. Hernández, S. Velasco, and F. Mauricio, J. Chem. Phys. **86**, 4597 (1987); **86**, 4607 (1987).
15. R. G. Abbot and D. W. Oxtoby, J. Chem. Phys. **72**, 3972 (1980).
16. R. M. Yulmetyev, Theor. Math. Phys. **30**, 264 (1977).
17. V. Yu. Shurygin and R. M. Yulmetyev, Phys. Lett. A **174**, 433 (1990).

Translated by O. Borovik-Romanova

Physics of the Solid State, Vol. 44, No. 6, 2002, pp. 1061–1066. Translated from Fizika Tverdogo Tela, Vol. 44, No. 6, 2002, pp. 1017–1022.

SEMICONDUCTORS AND DIELECTRICS

Structural and Thermal Properties of the Opal–Epoxy Resin Nanocomposite

V. N. Bogomolov*, L. S. Parfen'eva*, L. M. Sorokin*, I. A. Smirnov*, H. Misiorek, A. Jezowski**, and J. Hutchison*****

** Ioffe Physicotechnical Institute, Russian Academy of Sciences, ul. Politekhnicheskaya 26, St. Petersburg, 194021 Russia*
e-mail: lev.sorokin@pop.ioffe.rssi.ru

*** W. Trzebiatowski Institute of Low-Temperature and Structural Research, Polish Academy of Sciences, Wroclaw, 50-950 Poland*

**** Department of Materials, University of Oxford, Oxford OX1 3PH, UK*

Received August 21, 2001

Abstract—Thermal conductivity of the opal–epoxy resin nanocomposite is measured in the range 4.2–250 K, and the material is studied by electron microscopy at 300 K. An analysis of the electron microscope images permits a conclusion on the character of opal void filling by the epoxy resin. It is shown that the thermal conductivity of the nanocomposite within the range 40–160 K can be fitted fairly well by the corresponding standard expressions for composites. For $T < 40$ K and $T > 160$ K, the experimental values of the nanocomposite thermal conductivity deviate strongly from the calculated figures. © *2002 MAIK "Nauka/Interperiodica".*

1. INTRODUCTION

Synthetic opals are extremely interesting subjects to physicists. They possess a unique fractal crystalline structure [1–3]. Opals consist of closely packed amorphous SiO_2 spheres, most frequently, 200–250 nm in diameter (first-order spheres). These spheres contain an array of closely packed amorphous spheres of a smaller diameter, 30–40 nm (second-order spheres), which are again made up of closely packed particles of amorphous SiO_2, now ~10 nm in diameter (third-order spheres).

The array of closely packed spheres has octahedral and tetrahedral voids which are interconnected by "channels." The first-order voids (and spheres of amorphous SiO_2) make up a regular cubic array with a giant period a = 300–400 nm. The diameters of the first-order octahedral and tetrahedral voids and channels are 80, 40, and 30 nm, respectively. The total theoretical opal porosity is 59% (the first-order voids add up to 26%). However, in actual fact, the total porosity of the opal single crystals grown by us is ~46–50% [4, 5]. The lower real porosity compared to the theoretical value is primarily due to the sintering of the second- and third-order spheres, as a result of which they are no longer in point contact. However, the first-order voids remain, as a rule, close in volume to the theoretical figure (26%).

There are methods (chemical techniques under pressure, melt injection, impregnation of the sample by a filler material) by which one can fill the first-order voids by metals, semiconductors, and dielectrics to design an opal-based regular three-dimensional composite with a cubic filler cluster array with the parameter a = 300–400 nm. Depending on the actual method used to fill the opal voids by various fillers and on the quality of the opal single crystals, one may conceive at least three versions of preparation of an opal-based nanocomposite: (a) the opal voids are completely filled (to 100%); (b) the voids are filled in an island pattern (to less than 100%), with the regularly filled voids in the opal crystal separated by the filler-free opal host; and (c) the filler can be randomly distributed over the opal voids, likewise filled to less than 100%.

Therefore, to ensure correct interpretation of the experimental data on the thermal conductivity of opal-based nanocomposites, one needs to know the real pattern of void filling. Electron microscopy is capable of providing an answer to this problem.

The thermal conductivity of opal and opal-based nanocomposites with PbSe and NaCl crystalline fillers is dealt with in [3, 5–7], and electron microscopic studies of nanocomposites of this type, with Te, GaAs, and InSb crystalline fillers, are discussed in [8, 9].

It was of interest to carry out simultaneous electron microscopy and thermal-physical measurements on the same samples of the opal-based nanocomposite with voids filled by an amorphous substance, epoxy resin, whose thermal conductivity is substantially lower (particularly, for $T > 40$ K) than that of amorphous quartz.

2. PREPARATION OF SAMPLES AND EXPERIMENTAL TECHNIQUE

The opal used in the work was perfect in terms of the ordering of its structural elements, i.e., silicate spheres. Epoxy resin was introduced into the opal host voids in

the following way. A parallelepiped-shaped opal sample (this shape was chosen to facilitate determination of the sample volume in subsequent density measurements and thermal conductivity studies) was placed in a quartz ampoule evacuated to 10^{-2} mm Hg. Next, epoxy resin of a liquid consistency was poured into the ampoule, which enveloped the sample over all of its surface. After this, air at atmospheric pressure was admitted into the ampoule. The time during which the sample was maintained in the epoxy resin determined the extent to which the opal first-order voids became filled. Next, the sample was removed from the epoxy resin which had not yet set, and after it became hard, a layer of epoxy resin was cut off down to the opal surface. Measurements of the sample density showed that the free host volume was filled to about 60%. The accuracy with which the percentage opal filling by the epoxy resin was inferred from the change in the sample density was not sufficiently high because the densities of the epoxy resin and of the opal were nearly equal.

We also measured the thermal conductivity of the epoxy resin used in the work. The corresponding sample was also parallelepiped-shaped.

The samples intended for electron microscopy studies were prepared by the standard technique [10], which included grinding to a thickness of 150 μm, cutting out a square-shaped sample with an ~3-mm diagonal, dimpling it to a thickness of ~50–60 μm, and subsequent thinning by ion milling until a pinhole formed.

EM 4000EXII and JEM 2010FX electron microscopes were employed with an attachment providing for elemental analysis of the clusters.

The temperature dependences of the thermal conductivity of the opal–epoxy resin and epoxy resin samples were obtained within the range 4.2–250 K by the technique described in [11].

Locating the epoxy clusters proved a hard task. The structural elements of the opal host, namely, the silicate spheres, are amorphous. Viewed from the structural standpoint, the epoxy clusters are likewise amorphous. Therefore, revealing the presence of epoxy resin in opal voids from microdiffraction patterns was found to be impossible, because both the resin and the silicate spheres produce a diffuse halo near the trace of the primary beam. Energy-dispersive x-ray (EDX) spectra contain, in addition to the lines of silicon and oxygen present in the silicate spheres, the lines of C, N, K, S, Ca, and Cl, with the first three elements dominant. The spectrum of epoxy resin also exhibits Zn, Fe, and Cu in trace amounts. It should be pointed out that all EDX spectra of samples with fillers have Cu lines. Control experiments (with the sample holder having a copper receptacle replaced by a beryllium base holder) established unambiguously that the Cu peak is produced by the holder, which had copper components in the immediate vicinity of the sample base. The good reproducibility of EDX spectra obtained from different points of the same sample, whose elemental peaks varied only slightly in intensity, permits one to conclude that all the observed excess elements, with the exception of copper, originate from the epoxy resin introduced into the opal pores. We readily see that most of the resin components are light elements which are close in scattering capacity and absorption to silicon. For this reason, electron microscopic images of this composite cannot reveal the presence of epoxy resin in the opal pores because of the zero diffraction contrast inherent to crystalline objects only; indeed, the difference in absorption between the silicate spheres and epoxy clusters is small. The EDX spectra of the original opal contain lines of oxygen and silicon only.

An attempt was made to reveal the presence of epoxy clusters by the Fresnel phase contrast technique, which has been recently employed to advantage in determining the oxygen depth profile in the oxide layer in the initial stage of silicon oxidation [12].

The Fresnel method is based on an analysis of both the shape and contrast of Fresnel fringes, which are seen at the interface lying perpendicular to the projection plane, from a series of electron microscope images made with different defocusing on both sides of the exact focus. These are analogs of the fringes formed in optical systems in studies on end-on opaque objects under Fresnel diffraction conditions.

In electron microscopy, any interface separating materials in a sample which differ in scattering capacity acts as a source of Fresnel contrast. The fringes are most visible if the interface is planar and nearly parallel to the electron beam; however, even if the surface is inclined and wavy, such interfaces will produce a noticeable contrast. Because Fresnel fringes are formed in interference between electrons that have suffered phase changes in elastic scattering from sample regions having different scattering potentials, it appears only natural to expect that the fringes will contain information on the nature of the material on both sides of the interface. Obtaining quantitative information with this technique would require, however, its refinement and taking account of the specific features of each object. In this work, we made use of the qualitative aspects of the Fresnel method only.

3. EXPERIMENTAL RESULTS

The presence of any other material besides silicate spheres could be revealed only in very thick samples with a large wedge near the edge. No other information could be extracted from these images because of the weak and uniform contrast. Defocusing smeared out the images even more.

The images obtained on thin samples (1–2 silicate sphere layers) studied with off-focussing at a few hundred nanometers were the most informative.

Remarkably, the pores (both octahedral and tetrahedral) between the silicate spheres, which are projected as squares and triangles with concave sides, seem, in

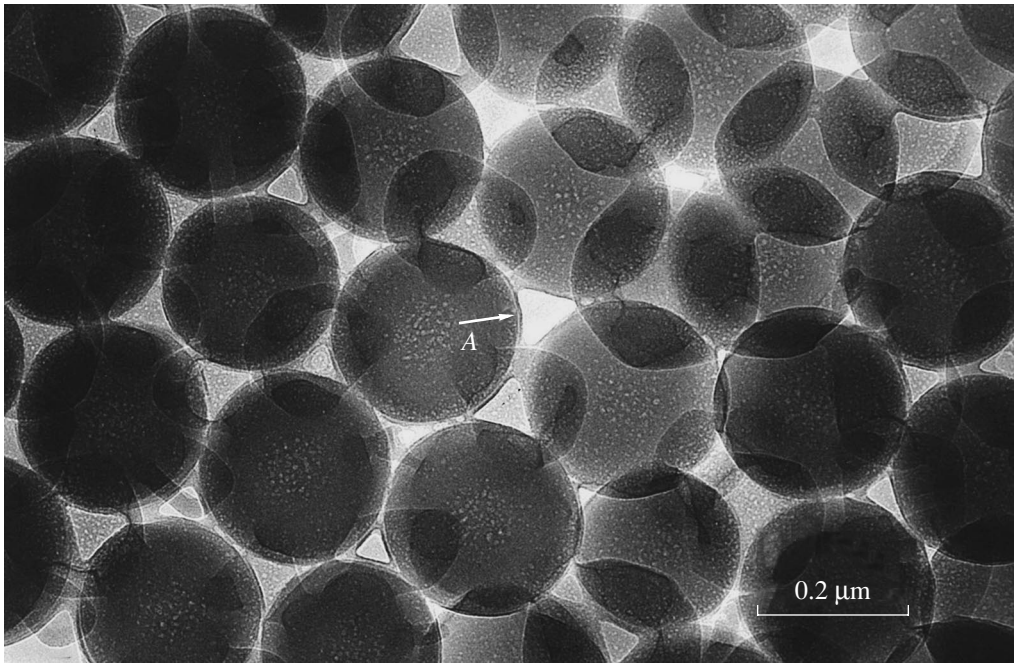

Fig. 1. Electron microscope image of the opal filled to 60% by epoxy resin. The sample thickness is of the order of the diameter of the silicate sphere. The central parts of the pores (*A*) do not contain the filler. Fresnel contrast is observed at the silicate-sphere–void interface.

most cases, to be filled only partially, with no filler in the middle of the pores. This is reliably established from the absence of Fresnel fringes at the filler–void interface (Fig. 1).

The contrast in the silicate spheres is very complex, and it differs substantially from that of these spheres in pure opal. In most cases, three regions of irregular shape are found to be projected onto the image of a silicate sphere. They are seen against the background of the lobes of the rosette formed by the superposition of the spheres. In the region of the lobes, the total sample thickness is larger than the thickness of a sphere because of the sphere superposition; therefore, the contrast of a rosette lobe is darker as a result of larger absorption than that of a region one sphere thick. The irregularly shaped regions that attracted our attention seem to be still darker in contrast. This indicates the presence of an additional mass of material in these regions, which increases absorption and, hence, produces a darker contrast (Fig. 2). The irregular regions are bounded by a very thin and dark, sharply contrasted line, which is apparently a Fresnel fringe. In about 50% of the observations, these regions are interconnected by channels that are 2–20 nm wide in the narrowest part. The narrowest channels are seen as one sharp and dark Fresnel fringe. The edges of broad channels are bounded by Fresnel fringes, the space within the channels having the same contrast as the main regions under study. These regions are, on the average, 0.2–0.25 of the silicate sphere diameter, i.e., 40–50 nm in size. The above regions cannot be identified with the sphere contact area becoming extended rather than pointed due to the opal having undergone deformation during the sintering (which is required to impart strength to the material). As the spheres have a nearly perfect surface, the extended sphere contact region should be circular. These regions are centered at approximately one half the sphere radius. To understand their origin, we consider three spheres lying in the (111) plane and a fourth placed on top (Fig. 3). The points of contact of the top sphere with the three bottom ones are denoted by *A*, *B*, and *C*. They are located on the triangle corners at the middle of the sphere radius. If we bound some regions a fraction of the sphere diameter in size by an irregular contour, the pattern thus obtained will resemble the electron microscope image of the composite near the sphere contact points. Thus, one can conjecture that these regions formed in the following way. The epoxy resin entering the opal leaks into the pores through the channels they are interconnected by, then flows over the sphere surface, and stops near the sphere contact points; in other words, the resin clusters form primarily in the vicinity of the sphere contacts. The central part of the pores may remain unfilled if there is not enough resin. It should be pointed out that the voids in the opal can be approximated by octahedra and tetrahedra only in the first approximation. The facets of these voids are the sphere surfaces, which converge at very small angles at the points of contact. These parts of the voids will exhibit capillary properties near the points of contact. It

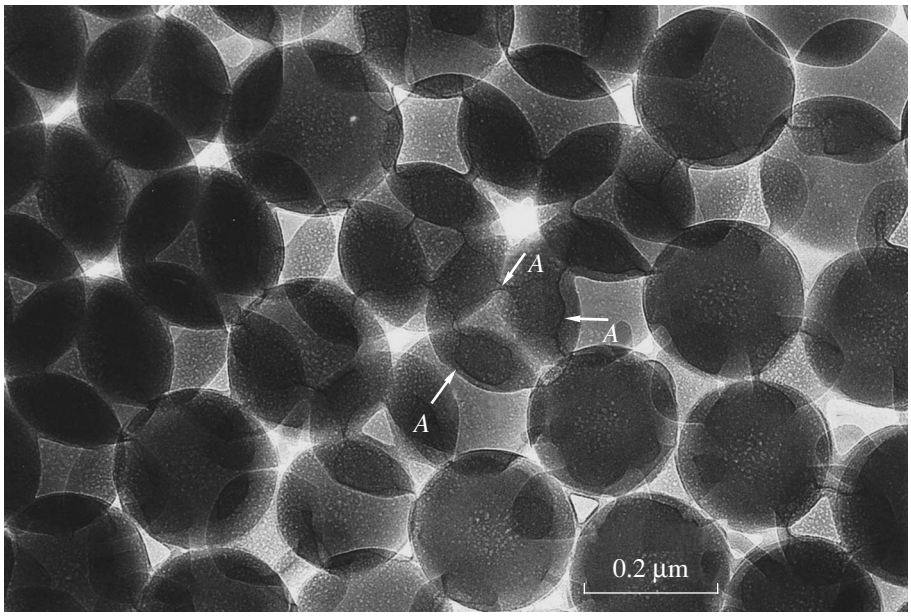

Fig. 2. Electron microscope image of the opal filled to 60% by epoxy resin (the region of superposition of two silicate-sphere layers). *A* is the interface between the filler material and the region (void) not occupied by it within the tetrahedral (octahedral) structural void. The interface appears due to the Fresnel contrast under defocusing.

is these points that the filler will be drawn to above all. At the same time, we may recall that this pattern of the pore filling by epoxy resin was revealed in a one- or two-layer opal prepared by ion milling.

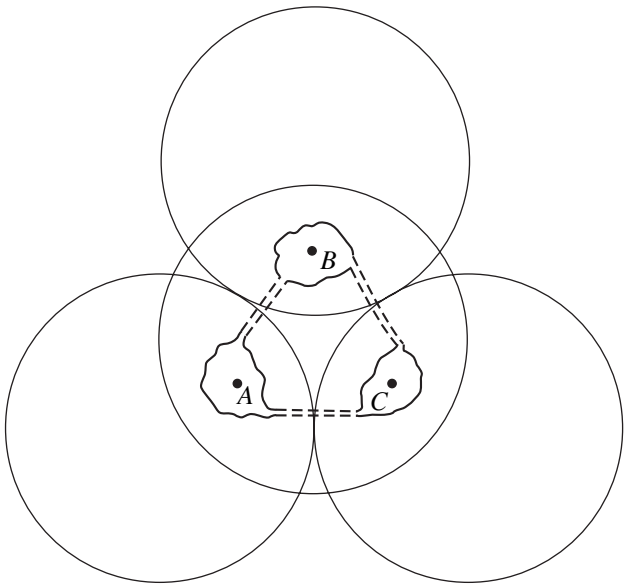

Fig. 3. Projection of closely packed silicate spheres in the opal array onto the (111) plane. Diagram explaining the epoxy cluster formation. *A*, *B*, and *C* are the points of contact of the silicate spheres near which the epoxy clusters form.

These regions with epoxy resin observed to exist in opal samples one or two silicate-sphere layers thick are located between the surfaces of the spheres, near the points they meet at; therefore, they are inaccessible for EDX analysis. As already mentioned, very thick samples exhibit a uniform fringe along all of the perforation perimeter. This is apparently the part of the compound by which the original opal was impregnated. In thicker regions, superposition of several silicate-sphere layers and the weak difference in electron absorption by these layers and by the epoxy resin precluded distinct discrimination of individual spheres and of the filler clusters. An analysis of the electron microscope image contrast in thick and thin samples of opal with the filler suggests the conclusion that the absence of the filler in the middle of the voids in thin samples is apparently due both to the opal pores being not filled to 100% of their volume and to the action of the ion beam used in the milling. It is possible that epoxy resin is sputtered by the ion beam at a higher rate than the silicate spheres.

Figure 4 shows the experimental data obtained for the opal–epoxy resin nanocomposite, epoxy resin,[1] and the data [5] for opal into which epoxy resin was introduced.

[1] The values obtained by us for κ of epoxy resin are in good agreement with the numerous figures available in the literature (see, e.g., [13]).

The opal–epoxy resin composite and epoxy resin are insulators. Therefore, the thermal conductivity measured in an experiment is that of the crystal lattice. The dashed lines in Fig. 4 relate to the thermal conductivity κ_{eff} of the opal–epoxy resin composite calculated for the case of the first-order opal voids filled by epoxy resin to 60% (curve *5*), 50% (*6*), and 90% (*4*). κ_{eff} was calculated from the well-known simple expression derived by Odelevskiĭ [14] for a standard composite:

$$\kappa_{eff}/\kappa_{mat} = 1 - \{m/[1/1 - \nu - (1 - m)/3]\}, \quad (1)$$

where $\nu = \kappa_{fill}/\kappa_{mat}$, m is the volume occupied by the filler material, and κ_{mat} and κ_{fill} are the thermal conductivities of the host matrix and the filler (epoxy resin), respectively. As already mentioned, the volume of the first-order voids is 26%, and 60% of these pores is occupied by the epoxy resin. Thus, in our case, m = 15.6%. κ_{mat} was calculated from the equation [15]

$$\kappa_{mat} = \kappa_{SiO_2(amorph)}[(1 - P)\sqrt{1 - P}], \quad (2)$$

where P is the porosity of the opal matrix with the epoxy resin. For the opal–60% epoxy resin composite, P = 0.324. When using Eq. (2), the data for $\kappa_{SiO_2(amorph)}$ were taken from [16, 17].[2]

As seen from Fig. 4, the $\kappa_{eff}(T)$ relation calculated for the opal–60% epoxy resin composite fits the experimental $\kappa_{exp}(T)$ curve within the range 40–160 K approximately well. For T < 40 K and T > 160 K, the experimental data deviate noticeably from the calculations. The reasons for these deviations remain unclear, but we intend to look more closely into the matter. The $\kappa_{exp}(T)$ curve for the opal–epoxy resin composite resembles the temperature dependence of thermal conductivity in amorphous materials. No features associated with the onset of coherent effects, which could have been expected because of the regular arrangement of the amorphous filler in the opal pores, were observed.

We note in conclusion that the above pattern of the epoxy resin in the opal concentrating at the interfaces between the amorphous SiO_2 spheres will permit us to carry out a more comprehensive analysis of the behavior of $\kappa(T)$ of our nanocomposite; in that work, we will not use the simple relations for the thermal conductivity of composite materials [14, 15] that were employed here but more sophisticated concepts and methods of calculation of the thermal conductivity of opals and opal-based nanocomposites which are being developed at the Ioffe Institute [18]. These points will be dealt with in a separate publication.

[2] The calculations of κ_{eff} shown in Fig. 4 for the cases of 50 and 90% opal filling by the epoxy resin were performed as in the case of 60% filling, but with due account of the values of m and P corresponding to these compositions.

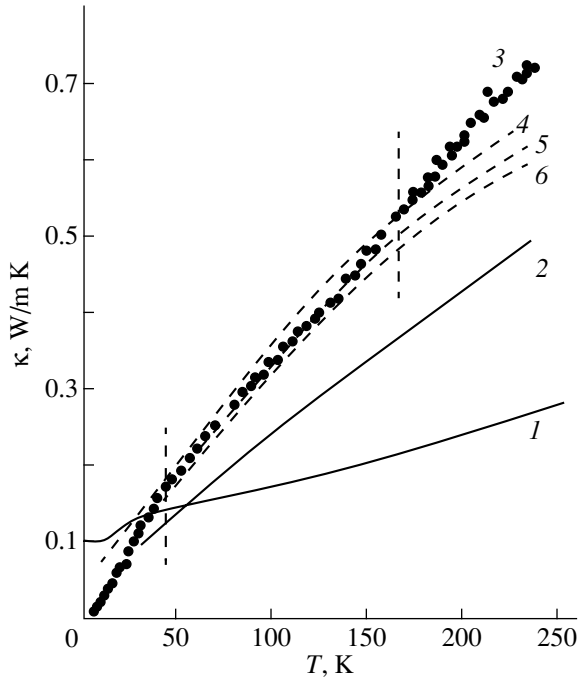

Fig. 4. Temperature dependences of the thermal conductivity of (*1*) epoxy resin, (*2*) synthetic opal [5], (*3*) opal–60% epoxy resin composite, and calculated κ_{eff} for the cases of the opal first-order voids filled by epoxy resin to (*4*) 90, (*5*) 60, and (*6*) 50%.

ACKNOWLEDGMENTS

The authors are indebted to L.I. Arutyunyan and A.V. Prokof'ev for preparation of the opal–epoxy resin nanocomposite.

This study was supported by the Russian Foundation for Basic Research (project no. 00-02-16883), the Polish Committee for Scientific Research (grant no. 2 P03B 127-19 KBN), and the Royal London Society.

REFERENCES

1. V. N. Bogomolov and T. M. Pavlova, Fiz. Tekh. Poluprovodn. (St. Petersburg) **29** (5–6), 826 (1995) [Semiconductors **29**, 428 (1995)].
2. V. G. Balakirev, V. N. Bogomolov, V. V. Zhuravlev, *et al.*, Kristallografiya **38** (3), 111 (1993) [Crystallogr. Rep. **38**, 348 (1993)].
3. V. N. Bogomolov, L. S. Parfen'eva, A. V. Prokof'ev, *et al.*, Fiz. Tverd. Tela (St. Petersburg) **37** (11), 3411 (1995) [Phys. Solid State **37**, 1874 (1995)].
4. V. V. Ratnikov, Fiz. Tverd. Tela (St. Petersburg) **39** (5), 956 (1997) [Phys. Solid State **39**, 856 (1997)].
5. V. N. Bogomolov, D. A. Kurdyukov, L. S. Parfen'eva, *et al.*, Fiz. Tverd. Tela (St. Petersburg) **39** (2), 392 (1997) [Phys. Solid State **39**, 341 (1997)].

6. L. I. Arutyunyan, V. N. Bogomolov, N. F. Kartenko, *et al.*, Fiz. Tverd. Tela (St. Petersburg) **39** (3), 586 (1997) [Phys. Solid State **39**, 510 (1997)].
7. V. N. Bogomolov, N. F. Kartenko, D. A. Kurdyukov, *et al.*, Fiz. Tverd. Tela (St. Petersburg) **41** (2), 348 (1999) [Phys. Solid State **41**, 313 (1999)].
8. V. N. Bogomolov, D. A. Kurdyukov, L. M. Sorokin, *et al.*, Inst. Phys. Conf. Ser. **160**, 95 (1997).
9. V. N. Bogomolov, J. L. Hutchison, S. M. Samoilovich, *et al.*, Inst. Phys. Conf. Ser. **157**, 35 (1997).
10. V. N. Bogomolov, L. M. Sorokin, V. A. Kurdyukov, *et al.*, Fiz. Tverd. Tela (St. Petersburg) **39** (11), 2090 (1997) [Phys. Solid State **39**, 1869 (1997)].
11. A. Jezowski, J. Mucha, and G. Pompe, J. Phys. D **20**, 1500 (1987).
12. F. M. Ross and W. M. Stobbs, Philos. Mag. A **63**, 1 (1991).
13. K. W. Garrett and H. M. Rosenberg, J. Phys. D **7**, 1247 (1974).
14. G. N. Dul'nev and Yu. P. Zarichnyak, *Heat Conductivity of Blends and Composite Materials* (Énergiya, Leningrad, 1974).
15. E. Ya. Litovskiĭ, Izv. Akad. Nauk SSSR, Neorg. Mater. **16** (3), 559 (1980).
16. R. C. Zeller and R. O. Pohl, Phys. Rev. B **4** (6), 2029 (1971).
17. R. B. Stephens, Phys. Rev. B **8** (6), 2896 (1973).
18. V. N. Bogomolov, L. S. Parfen'eva, I. A. Smirnov, *et al.*, Fiz. Tverd. Tela (St. Petersburg) **44** (1), 175 (2002) [Phys. Solid State **44**, 181 (2002)].

Translated by G. Skrebtsov

Physics of the Solid State, Vol. 44, No. 6, 2002, pp. 1067–1070. Translated from Fizika Tverdogo Tela, Vol. 44, No. 6, 2002, pp. 1023–1025.

SEMICONDUCTORS AND DIELECTRICS

The Debye Temperature and Grüneisen Parameter of the $CaLa_2S_4$–La_2S_3 System

S. M. Luguev, N. V. Lugueva, and Sh. M. Ismailov

Institute of Physics, Dagestan Scientific Center, Russian Academy of Sciences, ul. 26 Bakinskikh Komissarov 94, Makhachkala, 367003 Dagestan, Russia

e-mail: kamilov@datacom.ru

Received August 30, 2001

Abstract—The thermal expansion coefficient of solid solutions in the $CaLa_2S_4$–La_2S_3 system at a temperature of 300 K is investigated experimentally. The Debye temperature, the Grüneisen parameter, and the isothermal compressibility coefficient of solid solutions in the system under investigation are determined from the experimental thermal expansion coefficient. It is demonstrated that, upon substitution of calcium ions for cation vacancies in La_2S_3, the Debye temperature decreases, the isothermal compressibility coefficient increases, and the Grüneisen parameter remains constant for all compositions in the $CaLa_2S_4$–La_2S_3 system. A correlation between the ionic radii of Ca^{2+} and La^{3+}, the concentration of cation vacancies, and the rigidity of the lattice, on the one hand, and the Debye temperature, the Grüneisen parameter, and the isothermal compressibility coefficient, on the other, is revealed for the studied samples. *© 2002 MAIK "Nauka/Interperiodica".*

1. INTRODUCTION

Investigation into the thermal expansion coefficient α can provide valuable information on the Debye temperature Θ and the Grüneisen parameter γ. As is known, the Debye temperature is determined by the highest frequency of crystal lattice vibrations. Since the Debye temperature obeys the relationship $\Theta \sim \sqrt{\beta/\overline{M}}$ (where β is the quasi-elastic force coefficient and $\overline{M}$ is the average atomic weight), the value of Θ can be used to judge the strength of chemical bonding in the crystal structure [1]. The Grüneisen parameter characterizes the anharmonicity of atomic vibrations in the crystal lattice (in the harmonic approximation, $\gamma = 0$). From the aforesaid, it is clear that an analysis of the Debye temperature Θ and the Grüneisen parameter γ enables one to reveal the specific features of interatomic bonds and to gain a deeper insight into the dynamic properties of crystals.

Crystalline materials based on solid solutions in the $CaLa_2S_4$–La_2S_3 system show considerable promise for use in infrared technology [2]; however, their properties are not clearly understood. To our knowledge, reliable data on the Debye temperature and the Grüneisen parameter for solid solutions in this system are not available in the literature, except for the Debye temperature of the boundary composition La_2S_3 [3, 4].

Lanthanum trisulfide La_2S_3 crystallizes in a Th_3P_4-type structure with a large number of vacancies in the cation sublattice in such a way that each ninth cation site is vacant. Electrically, the La_2S_3 trisulfide is a dielectric. The cation vacancies can be filled either with trivalent and divalent rare-earth metal ions or with divalent alkaline-earth metal ions. In the case when the cation vacancies are filled with trivalent rare-earth metal ions, specifically with La^{3+} ions, two valence electrons are involved in chemical bonding and the third electron passes into the conduction band. As a consequence, the La_3S_4 tetrasulfide in which all the cation vacancies are completely filled exhibits metallic conduction. If the cation vacancies are filled with divalent alkaline-earth metal ions, for example, with Ca^{2+} ions, the compound contains no free electrons and remains dielectric. All compositions in the $CaLa_2S_4$–La_2S_3 system have a Th_3P_4-type structure [5]. Compounds with a Th_3P_4-type structure are characterized by ion-covalent interatomic bonds [3]. In these compounds, metal–sulfur ion-covalent bonds are combined with sulfur–sulfur covalent bonds. When the cation vacancies are filled with divalent calcium ions, the newly formed calcium–sulfur ion-covalent bonds accept electrons from sulfur–sulfur covalent bonds. This leads to a weakening of chemical bonds in the compounds.

In the present work, we measured the thermal expansion coefficient α of solid solutions in the $CaLa_2S_4$–La_2S_3 system in order to obtain reliable data on the Debye temperature Θ and the Grüneisen parameter γ, to elucidate the nature of interatomic bonds, and to reveal the dependence of these characteristics on the composition of compounds in the $CaLa_2S_4$–La_2S_3 system.

2. SAMPLES AND EXPERIMENTAL TECHNIQUE

The samples used in the measurements were prepared according to the procedure described earlier in

[6]. X-ray diffraction analysis revealed that all the studied samples have a Th_3P_4-type structure. The thermal expansion coefficient α was measured using a quartz dilatometer with a capacitive sensor [7].

3. RESULTS AND DISCUSSION

Figure 1 presents the results of our measurements of the thermal expansion coefficient α for samples in the $CaLa_2S_4$–La_2S_3 system and the data available in the literature on the thermal expansion coefficient for La_2S_3 [8] and $CaLa_2S_4$ [2]. It is seen that our results are in close agreement with the available data. This figure also shows the dependence of the lattice parameter *a* on the composition of solid solutions in the $CaLa_2S_4$–La_2S_3 system [6]. As can be seen from Fig. 1, a decrease in the lattice parameter for the $CaLa_2S_4$–La_2S_3 system is accompanied by an increase in the thermal expansion coefficient. In general, a decrease in the lattice parameter *a* corresponds to an increase in the interatomic interaction, which, in turn, results in a decrease in the thermal expansion coefficient α. Upon addition of CaS to La_2S_3 in the system under investigation, Ca^{2+} ions occupy cation vacancies and partially substitute for La^{3+} ions. Since the ionic radius of Ca^{2+} is considerably smaller that the ionic radius of La^{3+}, the interatomic distance decreases. At the same time, the difference between the electronegativities of calcium and sulfur is larger than that of lanthanum and sulfur. Consequently, the calcium–sulfur bond exhibits a more pronounced ionic character as compared to the lanthanum–sulfur bond. Therefore, in the case when the calcium ions occupy cation vacancies in the $CaLa_2S_4$–La_2S_3 system,

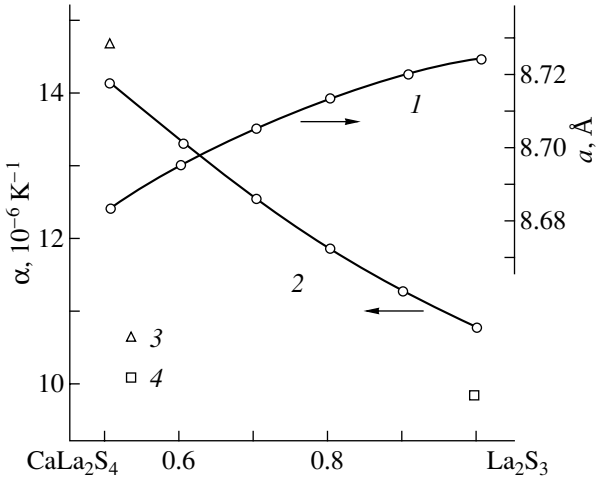

Fig. 1. (*1*) Composition dependence of the lattice parameter [6] and composition dependences of the thermal expansion coefficient for (*2*) solid solutions in the $CaLa_2S_4$–La_2S_3 system (our data), (*3*) $CaLa_2S_4$ [2], and (*4*) La_2S_3 [8].

the lattice parameter decreases and interatomic bonds become weaker. This explains the lack of any correlation in the composition dependences of the thermal expansion coefficient α and the lattice parameter *a* for compounds in the studied system.

The Debye temperature of $CaLa_2S_4$ was determined from the experimental data on the thermal expansion coefficient α and the data available in the literature [9] on the elastic constants for this compound. The thermal expansion coefficient and the Debye temperature are related by the following expression [10, 11]:

$$\Theta = \frac{C}{V_a^{1/3}\sqrt{\bar{A}}\alpha}, \quad (1)$$

where *C* is the constant for isostructural compounds, $\bar{A}$ is the mean-square atomic weight, and V_a is the volume per atom. The coefficient *C* was determined from both the empirical dependence of the thermal expansion coefficient on the melting temperature [12], which was derived for rare-earth sesquichalcogenides with a Th_3P_4-type structure, and the Lindemann formula [13]. We calculated the Debye temperature from formula (1) using experimental data on the thermal expansion coefficient for $CaLa_2S_4$ and obtained Θ = 273 K. On the other hand, the Debye temperature can be expressed through the elastic constants according to the formula [14]

$$\Theta = B\chi^{-1/2}\bar{M}^{-1/3}\rho^{-1/6}. \quad (2)$$

Here, *B* is the constant, χ is the isothermal compressibility coefficient, $\bar{M}$ is the average atomic weight, and ρ is the density. In our case, the density used in the calculation was taken from [9]. The isothermal compressibility coefficient χ was calculated from the Poisson ratio ν and Young's modulus *E* according to the formula [15]

$$\chi = -\frac{3(1-2\nu)}{E}. \quad (3)$$

The Poisson ratio ν and Young's modulus *E* for $CaLa_2S_4$ were taken from [2]. By substituting these data into formulas (2) and (3), we calculated the Debye temperature of the $CaLa_2S_4$ compound: Θ = 284 K. It is seen that this result agrees satisfactorily with the Θ temperature found from the experimental data on α. On this basis, we used relationship (1) to determine the Debye temperature of other compounds in the $CaLa_2S_4$–La_2S_3 system for which data on the elastic constants are unavailable.

The calculated dependence of the Debye temperature Θ on the number of cation vacancies per unit cell for the studied samples in the $CaLa_2S_4$–La_2S_3 system is shown in Fig. 2. It can be seen from Fig. 2 that, upon substitution of calcium ions for cation vacancies, the Debye temperature decreases. A similar decrease in the Debye temperature Θ is observed upon filling of cation

vacancies in the La_3S_4–La_2S_3 [4] and La_3Te_4–La_2Te_3 [16] systems, which are isostructural to the $CaLa_2S_4$–La_2S_3 system. At first glance, the fact that the Debye temperature Θ decreases with a decrease in the degree of structural imperfection seems to be unexpected. However, as was noted above, this behavior of the Debye temperature can be associated with a decrease in the number of covalent bonds upon filling of cation vacancies.

Figure 2 also depicts the dependence of the Debye temperature Θ on the number of cation vacancies per unit cell for samples in the La_3S_4–La_2S_3 system [4]. In this case, the Debye temperature was determined from the heat capacity measurements [4]. It was found that, upon filling of cation vacancies with La^{3+} ions in the La_3S_4–La_2S_3 system, the Debye temperature decreases drastically with a decrease in the number of vacancies beginning from the composition $LaS_{1.42}$. According to Ikeda *et al.* [4], the decrease observed in Θ upon changing over from La_2S_3 with a high content of defects to defect-free La_3S_4 is associated with a weakening of chemical bonds due to the screening of interatomic interactions by free electrons whose concentration increases upon filling of cation vacancies with La^{3+} ions. In the range where the number of vacancies per unit cell is larger than 0.8, the Debye temperatures for both systems are close in magnitude and change in a similar manner with a change in the number of vacancies. In this range of compositions, the concentration of free electrons in the La_2S_4–La_2S_3 system is still not very high and the electron screening of chemical bonds is of little importance. The observed decrease in the Debye temperature in the aforementioned composition range is due primarily to an increase in the average atomic weight upon filling of the cation vacancies with La^{3+} ions. In the $CaLa_2S_4$–La_2S_3 system, no screening of interatomic bonds by free electrons occurs and the average atomic weight decreases upon filling of the cation vacancies. A decrease in the average atomic weight should lead to an increase in the Debye temperature Θ. It seems likely that the weakening of chemical bonds upon filling of the cation vacancies with Ca^{2+} ions would be more pronounced than that in the case of La^{3+} ions without regard for the screening of chemical bonds by free electrons.

The Grüneisen parameter was determined from the relationship

$$\gamma = \frac{3\alpha V_a}{C_v \chi}, \tag{4}$$

where C_v is the atomic heat capacity at a constant volume. As far as we know, experimental data on the heat capacity of the compounds under investigation are unavailable, except for the composition La_2S_3. For this reason, the heat capacity C_v was calculated from the Debye interpolation formula [17]:

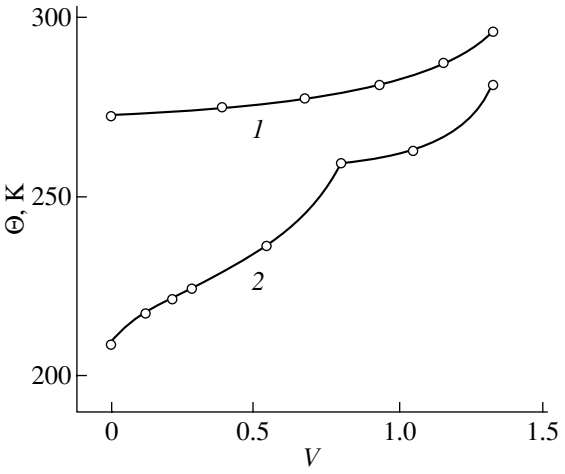

Fig. 2. Dependences of the Debye temperature on the number of cation vacancies per unit cell for solid solutions in (*1*) $CaLa_2S_4$–La_2S_3 (our data) and (*2*) La_3S_4–La_2S_3 [4] systems.

$$C_v = 3k\left\{D\left(\frac{\Theta}{T}\right) - \frac{\Theta}{T}D'\left(\frac{\Theta}{T}\right)\right\}, \tag{5}$$

where k is the Boltzmann constant and D is the Debye function. The satisfactory agreement between the results of our calculations of the heat capacity C_v according to formula (5) and the experimental data on the heat capacity of La_2S_3 [18] lends support to the validity of the use of formula (5) in our case. The calculation of the Grüneisen parameter from relationship (4) using the elastic constants taken from [2], experimental data on the thermal expansion coefficient α, and the heat capacity C_v calculated from formula (5) demonstrated that, for $CaLa_2S_4$, the Grüneisen parameter γ is equal to 1.60. For other compounds in the $CaLa_2S_4$–La_2S_3 system whose elastic constants are unknown, the isothermal compressibility coefficient χ was determined from the following relationship [10]:

$$\alpha V_a = K\chi, \tag{6}$$

where K is the constant for the given class of materials. The numerical value of K was obtained from the thermal expansion coefficient α and the isothermal compressibility coefficient χ for $CaLa_2S_4$. The Grüneisen parameter γ for the other compounds studied in the $CaLa_2S_4$–La_2S_3 system was determined using the isothermal compressibility coefficient χ calculated from relationship (6). The calculated data on χ and γ for solid solutions in the $CaLa_2S_4$–La_2S_3 system are given in the table. Our calculations proved that the Grüneisen parameter for compounds in the $CaLa_2S_4$–La_2S_3 system

Debye temperatures Θ, Grüneisen parameters γ, and isothermal compressibility coefficients χ for solid solutions in the $CaLa_2S_4$–La_2S_3 system at 300 K

Composition	Θ, K	γ	χ, 10^{-11} Pa^{-1}
La_2S_3	297	1.60	1.17
$0.9La_2S_3$–0.1CaS	288	1.60	1.23
$0.8La_2S_3$–0.2CaS	281	1.59	1.28
$0.7La_2S_3$–0.3CaS	277	1.60	1.34
$0.6La_2S_3$–0.4CaS	275	1.59	1.42
$CaLa_2S_4$	273	1.60	1.50

remains virtually constant. The constancy of γ can be explained by the fact that the decrease in the number of vacancies in the crystal leads to a decrease in the average atomic weight (the factor responsible for the decrease in the degree of anharmonicity of interatomic interactions) and an increase in the degree of ionicity of the chemical bonds (the factor responsible for the increase in the degree of anharmonicity).

4. CONCLUSIONS

Thus, we performed the experimental investigation of the thermal expansion coefficient. The results obtained were used to determine the Debye characteristic temperature, the Grüneisen parameter, and the isothermal compressibility coefficient for compounds in the $CaLa_2S_4$–La_2S_3 system. The decrease observed in the Debye temperature for the studied system indicates that, upon transition from La_2S_3 to $CaLa_2S_4$, the substitution of Ca^{2+} ions for cation vacancies brings about an increase in the ionicity and a weakening of interatomic bonds. The isothermal compressibility coefficient increases as the cation vacancies are filled with Ca^{2+} ions, and the Grüneisen parameter remains virtually insensitive to changes in the composition.

ACKNOWLEDGMENTS

We would like to thank G.N. Dronova for supplying the samples used in our investigations.

This work was supported by the Russian Foundation for Basic Research, project no. 01-02-16283.

REFERENCES

1. A. I. Anselm, *Introduction to Semiconductor Theory* (Nauka, Moscow, 1978; Prentice-Hall, Englewood Cliffs, 1981).
2. J. A. Savage and K. L. Lewis, Proc. SPIE **683**, 79 (1986).
3. *Physical Properties of Rare-Earth Chalcogenides* (Nauka, Leningrad, 1973).
4. K. Ikeda, K. A. Gschneidner, B. J. Beaudry, and U. Atzmony, Phys. Rev. B **25** (7), 4604 (1982).
5. J. Flahaut, *Progress in the Science and Technology of the Rare Earths* (Pergamon, Oxford, 1968), Vol. 3, p. 209.
6. O. V. Andreev, A. V. Kertman, and G. N. Dronova, in *Physics and Chemistry of Rare-Earth Semiconductors* (Nauka, Novosibirsk, 1990), p. 143.
7. M.-R. M. Magomedov, I. K. Kamilov, Sh. M. Ismailov, M. M. Rasulov, and M. M. Khamidov, in *Thermoelectrics and Their Applications* (St. Petersburg, 2000), p. 241.
8. V. I. Marchenko and G. V. Samsonov, Fiz. Met. Metalloved. **15** (4), 631 (1963).
9. K. J. Saunders, T. V. Wong, T. M. Hartnett, *et al.*, Proc. SPIE **683**, 72 (1986).
10. S. I. Novikova, *Thermal Expansion of Solids* (Nauka, Moscow, 1974).
11. M. N. Abdusalyamova, Zh. Vses. Khim. O-va. **26** (6), 673 (1981).
12. E. M. Dudnik, G. V. Lashkarev, Yu. B. Paderno, and V. A. Obolonchik, Izv. Akad. Nauk SSSR, Neorg. Mater. **2** (6), 980 (1966).
13. J. M. Ziman, *Electrons and Phonons* (Clarendon, Oxford, 1960; Inostrannaya Literatura, Moscow, 1962).
14. D J. R. Drabble and H. J. Goldsmid, *Thermal Conduction in Semiconductors* (Pergamon, Oxford, 1961; Inostrannaya Literatura, Moscow, 1963).
15. L. D. Landau and E. M. Lifshitz, *Course of Theoretical Physics: Theory of Elasticity* (Nauka, Moscow, 1965; Pergamon, New York, 1986), Vol. 7.
16. V. V. Tikhonov, V. N. Bystrova, R. G. Mitarov, and I. A. Smirnov, Fiz. Tverd. Tela (Leningrad) **17** (4), 1225 (1975) [Sov. Phys. Solid State **17**, 795 (1975)].
17. L. D. Landau and E. M. Lifshitz, *Course of Theoretical Physics: Statistical Physics* (Nauka, Moscow, 1964; Pergamon, Oxford, 1980), Vol. 5.
18. I. E. Paukov, V. V. Nogteva, and E. M. Yarembash, Zh. Fiz. Khim. **43** (9), 2351 (1969).

Translated by O. Borovik-Romanova

Physics of the Solid State, Vol. 44, No. 6, 2002, pp. 1071–1076. Translated from Fizika Tverdogo Tela, Vol. 44, No. 6, 2002, pp. 1026–1031.

SEMICONDUCTORS AND DIELECTRICS

Optical Properties of Thin Films of Closely Packed SiO_2 Spheres

A. V. Bazhenov, A. V. Gorbunov, K. A. Aldushin, V. M. Masalov, and G. A. Emel'chenko

Institute of Solid-State Physics, Russian Academy of Sciences, Chernogolovka, Moscow oblast, 142432 Russia

e-mail: gorbunov@issp.ac.ru

Received September 4, 2001

Abstract—Ordered, closely packed, defect-free one-, two-, and three-layer thick films of SiO_2 spheres of diameter D varying from 0.6 to 1.4 μm were obtained. Their optical transmittance and reflectance spectra were measured in the range 0.3–2.5 eV. The one-layer structures reveal a transmittance minimum whose spectral position is described by the Bragg law with the plane separation equal to the sphere radius $D/2$. As the number of the layers increases, a spectral feature appears which signals the formation of a photonic gap in the ⟨111⟩ direction of the fcc crystal lattice and is determined by the distance between the {111} planes equal to $0.816D$. The spectra of two- and three-layer structures measured with a diverging light beam contain additional lines originating from the formation of photonic gaps by the {211} and {221} planes. © *2002 MAIK "Nauka/Interperiodica".*

1. INTRODUCTION

Materials with a photonic gap, called photonic crystals, have been recently attracting increasing interest, which stems from their application potential in optoelectronics [1]. The numerous studies of natural and synthetic opals, which represent three-dimensional arrays of closely packed amorphous SiO_2 spheres varying in diameter from 0.2 to 0.5 μm, have shown that in the visible region, they exhibit properties characteristic of photonic crystals [2–6]. An intense search is presently under way for photonic structures with gaps near 1.5 μm [7, 8].

To develop such opal-based photonic crystals, SiO_2 spheres about 1 μm in diameter are required. The processes of sedimentation and ordering of large SiO_2 particles are poorly studied. Moreover, some authors maintain that particles 0.4 μm in size and larger do not order in the course of sedimentation [9, 10]. Structural studies of bulk opal samples showed them to be polycrystalline materials with single-crystal domains typically tens of microns in size [3]. The largest ordered regions in the best bulk samples do not exceed 200 μm in size [3]. The mechanism by which structural defects form in bulk opal samples remains unclear.

Preparation of thin, large-area, close-packed films of SiO_2 spheres is, in our opinion, a more controllable, bottom technological process than sedimentation of bulk samples and would broaden their application potential in the near future. Considerable progress has been demonstrated in recent years in this area [11]. Moreover, investigation of thin films of SiO_2 spheres could make it possible to follow the formation of structural defects in the transition to bulk opal samples and shed light on the mechanism of their formation.

In a recent publication [12], we reported on the preparation of uniform monolayers of ordered SiO_2 spheres on glass substrates a few square centimeters in area. The maximum dimensions of ordered regions (domains) in a film reach 600 μm. At the substrate periphery, one observes the formation of multilayer structures (two or more particle layers).

Here, we report an a study of the optical transmittance and reflectance spectra in the spectral range 0.3–2.5 eV from one-layer defect-free films as a function of the size of SiO_2 spheres, which was varied from 0.5 to 1.4 μm. We also studied the variation of optical spectra observed to occur as one crosses over from a one- to two- and three-layer defect-free structure of SiO_2 spheres 1.05 μm in diameter.

2. EXPERIMENTAL TECHNIQUES

Closeness in size of the nano- and microspheres of silicon oxide is a crucial condition of preparation of ordered opal structures. In this work, we prepared uniform silicate spheres through the hydrolysis of tetraethyl orthosilicate (TEOS) in a solution of ethyl alcohol in the presence of ammonium hydroxide, a process known as Stober's method [13].

Using this method, we prepared spheres over a broad range of diameters (0.1 to 1.6 μm), with a deviation of no more than 5% from the average size. Spheres with diameters above 0.5 μm were obtained in two stages. In the first stage, spheres ranging in diameter from 0.1 to 0.5 μm were obtained, which were subsequently used as seeds to produce particles up to 1.6 μm in size.

Uniform films of SiO_2 spheres were prepared by a combination of natural sedimentation with capillary extraction. The experiments were carried out at 20 ± 2°C. Glass plates measuring $70 \times 25 \times 2$ mm served as the substrates.

The structure of the films thus prepared was studied with a scanning electron microscope (SEM); in the case

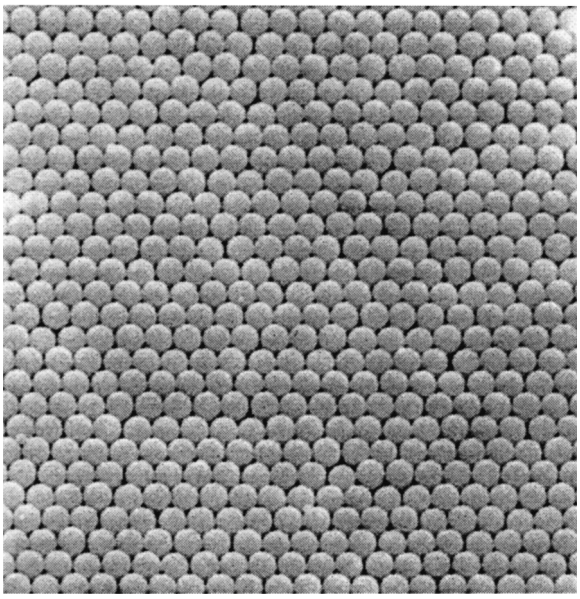

Fig. 1. A region of a one-layer film of close-packed SiO_2 spheres measuring 1.05 μm. The image was obtained with a scanning electron microscope.

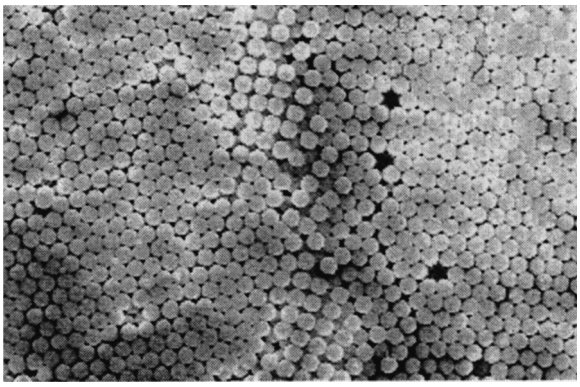

Fig. 2. Part of the boundary between a one- and a two-layer film of SiO_2 spheres measuring 1.05 μm, with square structures forming along the whole boundary. The image was obtained with a scanning electron microscope.

of SiO_2 spheres about 1 μm in diameter or greater, with a conventional optical microscope as well.

Spectral measurements were performed at room temperature by two methods. In the first method, optical transmittance spectra of monolayers of SiO_2 spheres in a parallel light beam were recorded in the spectral region from 0.6 μm (2.07 eV) to 2.3 μm (0.54 eV). The analyzed region of the film was about 1 mm in size.

Most of the measurements reported in this work were carried out by the second, microscopic–spectral method. It makes use of an optical microscope, and the spectra were obtained from a region 80 μm in size. Within the spectral range from 4 to 1.1 μm (0.3 to 1.1 eV), the spectra were measured with an IR microscope of a Fourier spectrometer. In the region from 1.1 to 0.5 μm (1.1 to 2.5 eV), another spectral setup provided with an optical microscope was employed. In this case, in contrast to the first method, optical transmittance and reflectance spectra were measured in a converging light beam. The light cone angle was ±16°.

3. EXPERIMENTAL RESULTS AND DISCUSSION

Figure 1 presents an SEM image of a one-layer film of SiO_2 spheres 1.05 μm in diameter. Numerous examinations of one-layer films have shown that they always feature the closest packed structure (triangular arrangement of spheres). In an fcc lattice, these layers correspond to the {111} face. The domains in a film typically vary in size from 10 to 50 μm. The largest domains may be as large as a few hundred microns.

The microstructure of a two-layer film is the closest hexagonal packing of spheres, with the packing in the first and second layers being correlated. However, along the whole boundary separating regions with one- and two-layer films, one observes sparsely packed square structures (Fig. 2). Such structures are also seen at transitions between two- and three-layer films, etc. In the case of thin films, a close-packed perfect crystalline structure is seen to form. We obtained perfect monolayers about 0.5×0.5 mm in size. The dimensions of single-domain regions in three-layer structures were of the order of 0.1 mm.

Figure 3 shows optical transmittance spectra of monolayers of SiO_2 spheres, with diameter D from 0.6 to 1.4 μm, measured by the microscopic–spectral method. The decrease in sample transparency with increasing photon energy is associated with the Rayleigh (elastic) light scattering from the spheres. In the limit of large wavelengths λ, the cross section of light scattering from a particle of size D is small and proportional to $(D/\lambda)^4$. Scattering losses become noticeable when the particle size is comparable to the wavelength. Therefore, as the sphere diameter decreases, the transmission edge associated with scattering shifts naturally toward the violet region.

All spectra in Fig. 3 have an absorption line at 0.42 eV ($\cong$3400 cm^{-1}), which does not vary in spectral position with variation of the sphere diameter. This line is of an extrinsic nature and will be discussed below.

Against the background of slowly varying transmittance, a broader line is observed whose spectral position depends on the diameter of the SiO_2 spheres. When measured in a parallel light beam, its halfwidth is 50 nm. If, however, the spectra are obtained with a microscope, the halfwidth increases to 90 nm, which is accounted for by the position of this transmittance minimum being angle-dependent.

Figure 4 plots the dependence of the wavelength λ_c corresponding to this minimum on the sphere diameter D. The experimental values fit, with high accuracy, to a straight line described by Bragg's diffraction law $N\lambda_c = 2n_{\text{eff}}d\sin\theta^B$, where N is the diffraction order, n_{eff} is the effective refractive index of the SiO_2 spheres/air composite, d is the interplanar distance, and θ^B is the Bragg angle (at normal incidence, $\theta^B = 90°$). Thus, the line changing its spectral position with variation of the SiO_2 sphere diameter results from interference of the light wave striking the sample and the wave that has undergone Bragg scattering from a monolayer of SiO_2 spheres. Assuming $N = 1$, as is usually observed in opal-type photonic crystals, we come to $n_{\text{eff}} = 1.316$ and $d = D/2 = r$, where r is the sphere radius.

This value of n_{eff} is noticeably less than the effective refractive index 1.348 of a bulk fcc crystal made up of SiO_2 spheres, whose material has a refractive index $n_{sph} \cong 1.45$. This discrepancy can be readily assigned to the smaller volume filling factor f of a monolayer compared with that for a bulk crystal, in which the spheres of each subsequent layer fit into the depressions between the spheres of the preceding layer. Calculation of f for a closely packed monolayer yields $f = \pi/(3 \times 3^{1/2})$, which differs from $f = \pi/(3 \times 2^{1/2})$ for a closely packed three-dimensional structure. The value of n_{eff} for a monolayer can be calculated roughly by averaging the dielectric function $\varepsilon = n_{\text{eff}}^2 = n_{sph}^2 f + n_a^2(1 - f)$. Here, n_a is the refractive index of the medium filling the space between the spheres (for air, $n_a = 1$). Then, we obtain $n_{\text{eff}} = 1.29$, which is not very far from the experimental value of 1.316.

That the relation displayed in Fig. 4 is determined by the interplanar distance d equal to the radius r rather than to the diameter of the spheres D might, at first glance, appear strange. It would seem that it is the thickness D of a film of SiO_2 spheres and its effective refractive index n_{eff} that should determine the path difference for the two interfering waves. Assuming that in actual fact $d = D$, the observed transmittance minima should be due to second-order diffraction ($N = 2$). In this case, one should expect the presence of deeper transmittance minima originating from first-order diffraction and lying at wavelengths equal to twice the experimental values for λ_c in Fig. 4. Therefore, optical transmittance spectra of the samples under study were also measured in the IR range up to 4 μm (the absorption edge of the glass substrate). In Fig. 3, the crosses identify the assumed positions of the transmittance minima corresponding to the first diffraction order for an interplanar distance $d = D$. As is evident from the experimental spectra, if such minima do exist, their depth is substantially less and width is much larger than those of the minima associated with second-order diffraction. Further, the dependence of the spectral position of the weak transmittance minima on the sphere diameter does not obey Bragg's law. Thus, the diffraction features seen in Figs. 3 and 4 are due to first-order diffraction at an interplanar distance d in Bragg's relation, which is equal to the sphere radius r.

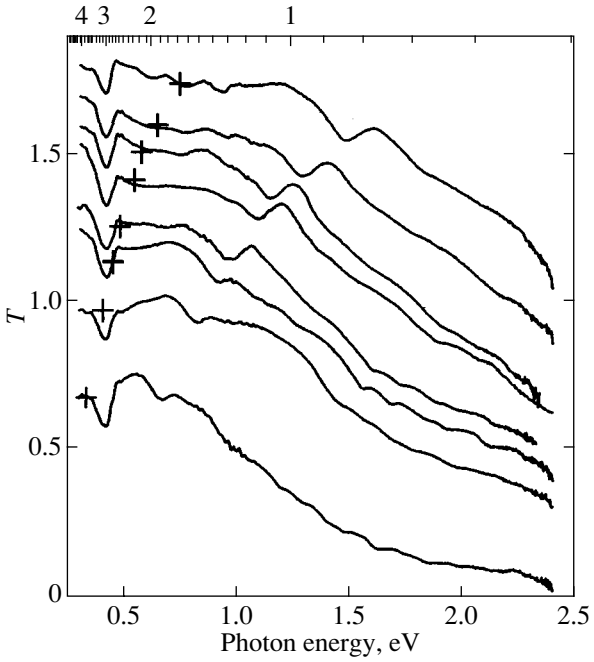

Fig. 3. Optical transmittance spectra T of a monolayer of SiO_2 spheres on a glass substrate. The spectra were translated vertically for convenience and were obtained with sphere diameters of 1.40, 1.12, 1.05, 0.96, 0.86, 0.80, 0.70, and 0.60 μm, bottom to top, respectively.

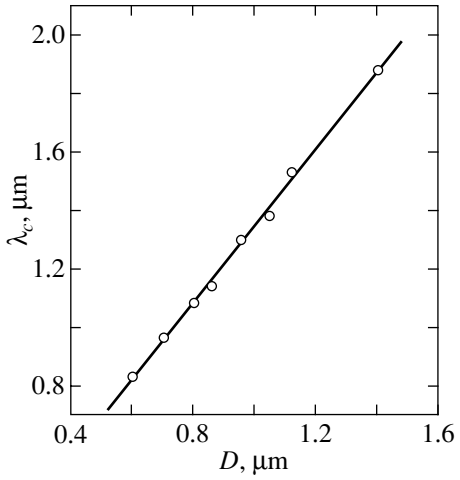

Fig. 4. Wavelength λ_c of the minima in the optical transmittance spectra of a monolayer of SiO_2 spheres plotted vs. their diameter D. The straight line is a linear fit to the experimental data.

This result can be explained in terms of the theory of diffraction of a plane electromagnetic wave from a

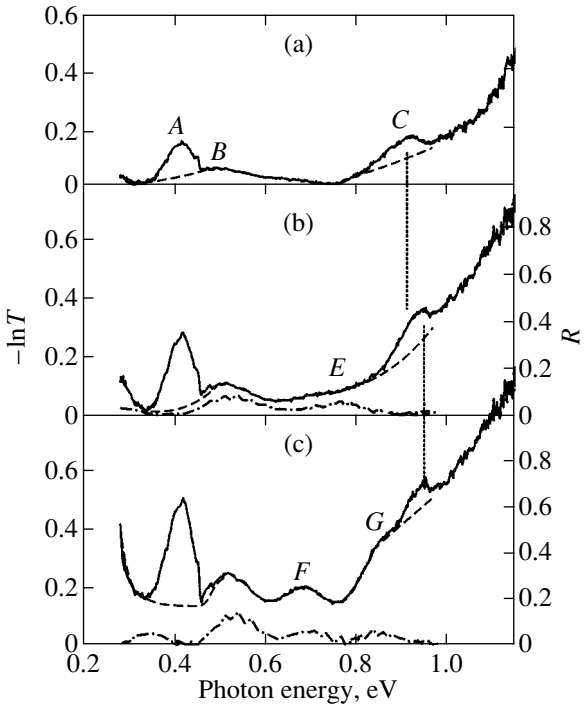

Fig. 5. Spectra of the optical density –ln*T* (solid lines) and of reflectance *R* (dot-and-dash curves) for a structure of (a) one, (b) two, and (c) three perfect, closely packed layers of SiO_2 spheres 1.05 μm in diameter. Dashed lines show a decomposition of the spectra into constituents in the region of impurity line *A* and line *C*.

homogeneous sphere. The fundamentals of this theory were published by G. Mie in 1908. The specific features of diffraction from a homogeneous sphere are described, for instance, in [14]. It was established that the light scattered by a sphere represents a set of spherical waves emanating from its center. Thus, in our case, the planes featured in Bragg's law are the plane passing through the centers of the SiO_2 spheres and the surface of the glass substrate on which these spheres are located.

To study the intensities of the lines observed in the transmittance spectra and their variation with increasing number of SiO_2 sphere layers, we measured transmittance and reflectance spectra of perfect structures consisting of one, two, and three layers of SiO_2 spheres 1050 nm in diameter. Films with larger spheres are here preferable, because, in contrast to spheres of a smaller diameter, one can readily check here the number of layers and the degree of their perfection with an optical microscope. The results of these studies are presented in Fig. 5 in the form of optical density spectra –ln*T*, where *T* is the transmittance, as well as of reflectance spectra *R*.

The monolayer optical density spectrum (Fig. 5a) exhibits a broad line *B* ($h\nu$ = 0.49 eV) in addition to the impurity line *A* (photon energy $h\nu$ = 0.42 eV) and a feature *C* ($h\nu$ = 0.91 eV) which changes its spectral position with variation of the sphere diameter. As already mentioned, attempts to interpret line *B* as being due to first-order diffraction with an interplanar distance equal to the sphere diameter fail, because its spectral position does not vary regularly with the sphere diameter. Moreover, estimation of the effective refractive index for this line yields a very low value of $n_{eff} \cong 1.20$. It should be pointed out that light reflectance spectra of a monolayer of SiO_2 spheres exhibit no maxima in the region of line *B* and even of line *C*, which is certainly of diffraction nature. This is apparently associated with extremely weak light reflection from this structure.

A line with $h\nu$ = 0.52–0.53 eV, to which a maximum in the reflectance spectrum corresponds, appears in the optical density spectrum of the closely packed perfect structure of two SiO_2 sphere layers (Fig. 5b) in the region of the *B* line. The fact that the maxima in the optical density and reflectance spectra coincide argues for the diffraction nature of this line. Its spectral position fits, with good accuracy, Bragg's law with n_{eff} = 1.34, which is close to the effective refractive index of a bulk fcc crystal constructed of SiO_2 spheres (n_{eff} = 1.348). In this case, the interplanar distance $d = (2/3)^{1/2}D \cong 0.8165D$ corresponds to the distance between the adjacent {111} planes in the close-packed fcc structure of SiO_2 spheres with diameter *D*.

When the second layer is deposited, line *C* shifts toward higher energies by about 0.03 eV ($h\nu \cong$ 0.94 eV). Thus, deposition of the second layer of spheres results in a decrease in the effective refractive index (by about 3%) for the diffraction feature determined by the substrate plane and the plane passing through the centers of the first-layer spheres. This effect may be interpreted as a result of the first-layer spheres being pushed apart by those of the second layer.

A broad feature *E* appears in the optical density spectrum of the two-layer structure and is accompanied by the corresponding broad line in the reflectance spectrum.

As the third layer of SiO_2 spheres is deposited (Fig. 5c), the intensity of the $h\nu$ = 0.52-eV line increases in both the optical-density and reflectance spectra. It is this behavior that should be expected in the formation of a photonic gap with increasing the number of SiO_2 sphere layers. Line *C* slightly narrows compared with the spectra of the mono- and bilayer structures, but the position of its maximum ($h\nu$ = 0.94 eV) remains the same as in the two-layer structure. Significantly, the intensity of this line in the optical-density and reflectance spectra does not grow with increasing the number of layers in the structure, in contrast to the line with $h\nu$ = 0.52 eV, which is produced by diffraction from the {111} planes. This is an additional argument for line *C* not being a result of second-order diffraction in a structure with the interplanar distance corresponding to the {111} planes. This feature forms only within the first layer of SiO_2 spheres and is determined by the interplanar distance being equal to the sphere radius *r*.

After a third layer of SiO_2 spheres has been deposited, the *E* feature, which formed in the two-layer structure, splits into two lines, *F* ($h\nu$ = 0.69 eV) and *G* ($h\nu$ = 0.84 eV), in both the optical-density and reflectance spectra. The most probable origin of these lines is diffraction caused by the formation of additional planes inclined to the {111} plane.

To check this assumption, we studied the changes in the transmittance spectra of the three-layer structure produced by variation of the cone angle γ of the light beam passing through the sample. The angle γ was varied by means of an iris diaphragm built into the measuring system. As seen from Fig. 6, in reducing γ from $\pm 16°$ to $\pm 7°$, the limit, determined in our case by the design of the microscope mirror objective, virtually does not affect the 0.52 and 0.94-eV lines. At the same time, line *G* disappears and line *F* shifts toward shorter wavelengths, with its intensity also decreasing with decreasing γ. This behavior of the *F* and *G* lines suggests that they are related to light diffraction from other planes of the structure which are inclined relative to {111}.

A rough calculation shows that such planes can be {211} and {221} for lines *F* and *G*, respectively. Because the {211} and {221} planes are inclined to {111} by 19.5° and 15.8°, respectively, the light beams striking these planes at a close to normal angle ($\theta^B \cong 90°$) should provide a substantial contribution to the transmittance spectrum for large γ. As γ decreases to $\pm 7°$, the light beam diffraction angle decreases to about $\theta^B \cong 70°$. In accordance with Bragg's relation, this should entail a decrease in λ_c, which is seen clearly to occur with line *F*. Moreover, it is well known that a decrease in θ^B also reduces the intensity of the diffraction minimum in the transmittance spectrum of opal [2, 6]. This is why the intensities of the *F* and *G* lines fall off with decreasing γ. In the first diffraction order (N = 1), the maxima in the optical-density spectrum (Fig. 6) that are determined by the {211} and {221} planes should be observed at $h\nu$ = 0.75 and 0.93 eV, respectively. These values compare satisfactorily with the experimental values $h\nu$ = 0.69 eV (line *F*) and $h\nu$ = 0.84 eV (line *G*). The slight disagreement can be associated with the fact that the estimation was based on the linear Bragg approximation. This discrepancy will be smaller if the dynamic approximation is employed.

In closing, we consider line *A* with $h\nu$ = 0.42 eV ($\cong$3400 cm^{-1}), whose spectral position does not change with variation of the SiO_2 sphere diameter (Fig. 3). Obviously enough, this line originates from an impurity containing O–H groups. The feature with $h\nu$ = 0.45 eV seen on its high-energy wing is apparently associated with the manifestation of N–H bonds. The presence of these impurities in the SiO_2 spheres is a consequence of the use of alcohol and NH_3 in the preparation of the structures. It was found that while the halfwidth of this line does not change under variation of the SiO_2 spheres in size, its intensity in the optical-density spectrum is proportional to their diameter. On the other hand, the intensity of this line in the optical-density spectra is proportional, for a given sphere diameter, to the number of SiO_2 sphere layers, with the line shape remaining the same with variation of the number of layers (Fig. 5). Thus, this line can be used in estimating the number of layers of SiO_2 spheres in structures with both large and small spheres.

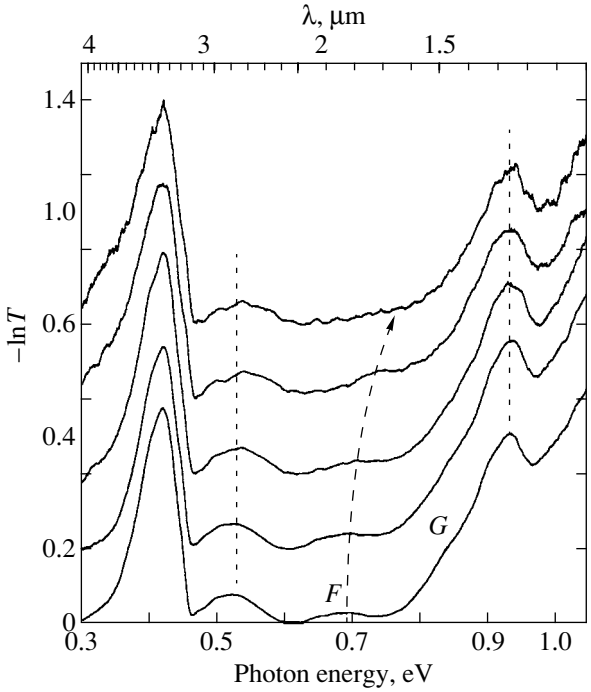

Fig. 6. Optical-density spectra (–ln*T*) of a perfect three-layer film of SiO_2 spheres 1.05 μm in diameter measured with the light cone angle γ reduced from $\pm 16°$ (bottom) to $\pm 7°$ (top). The spectra were translated vertically by 0.2 for the sake of convenience.

4. CONCLUSION

In summary, we have prepared ordered, closely packed one-, two-, and three-layer structures of SiO_2 spheres 0.6 to 1.4 μm in diameter on glass substrates and measured their optical transmittance and reflectance spectra in the range extending from 0.3 to 2.5 eV. In one-layer structures, a reflectance minimum has been revealed whose position fits to Bragg's law with the interplanar distance equal to the sphere radius. It was established that this diffraction feature forms in the interference of light waves diffracted from SiO_2 spheres with waves reflected from the substrate surface. As the number of layers in a structure increases, a feature appears in its optical spectra, which indicates the formation of a photonic gap in the ⟨111⟩ direction of the fcc crystal lattice and is determined by the separation between the {111} planes. The spectra of two- and three-layer structures measured with a diverging light

beam exhibit additional lines caused by the formation of photonic gaps due to the {211} and {221} planes. These additional lines disappear when a close-to-parallel light beam is used.

An absorption line originating from impurities which contain O–H and N–H bonds was observed in the spectra of the structures studied. It was shown that this line can be used to estimate the number of layers in ordered structures of SiO_2 spheres.

ACKNOWLEDGMENTS

This study was partially supported by the Russian Foundation for Basic Research (project no. 01-02-97024).

REFERENCES

1. T. E. Krauss and R. M. De La Rue, Prog. Quantum Electron. **23**, 51 (1999).
2. V. N. Bogomolov, D. A. Kurdyukov, A. V. Prokof'ev, and S. M. Samoĭlovich, Pis'ma Zh. Éksp. Teor. Fiz. **63**, 496 (1996) [JETP Lett. **63**, 520 (1996)].
3. Ju. A. Vlasov, V. N. Astratov, A. V. Baryshev, *et al.*, Phys. Rev. E **61**, 5784 (2000).
4. H. Migue, C. Lopez, F. Meseguer, *et al.*, Appl. Phys. Lett. **71**, 1148 (1997).
5. H. Migue, F. Meseguer, C. Lopez, *et al.*, Langmuir **13**, 6009 (1997).
6. V. N. Astratov, Ju. A. Vlasov, O. Z. Karimov, *et al.*, Phys. Lett. A **222**, 349 (1996).
7. J. K. Hwang, H. Y. Ryu, D. S. Song, *et al.*, Appl. Phys. Lett. **76**, 2982 (2000).
8. A. Blanco, E. Chromski, S. Grabtchak, *et al.*, Nature **405**, 437 (2000).
9. S. Emmett, S. C. Lubetkin, and B. Vincent, Colloids Surf. **42**, 139 (1989).
10. K. Davis, W. B. Russel, and W. J. Glantschnig, J. Chem. Soc., Faraday Trans. **87**, 411 (1991).
11. P. Jiang, J. F. Bertone, K. S. Hwang, and V. L. Colvin, Chem. Mater. **11**, 2132 (1999).
12. V. M. Masalov, K. A. Aldushin, P. V. Dolganov, and G. A. Emelchenko, Phys. Low-Dimens. Struct. **5–6**, 93 (2001).
13. W. Stober, A. Fink, and E. Bohn, J. Colloid Interface Sci. **26**, 62 (1968).
14. M. Born and E. Wolf, *Principles of Optics* (Pergamon, Oxford, 1969; Nauka, Moscow 1970).

Translated by G. Skrebtsov

Physics of the Solid State, Vol. 44, No. 6, 2002, pp. 1077–1084. Translated from Fizika Tverdogo Tela, Vol. 44, No. 6, 2002, pp. 1032–1038.

SEMICONDUCTORS AND DIELECTRICS

Mechanism of Protonic Conductivity in an NH_4HSeO_4 Crystal

Yu. N. Ivanov*, A. A. Sukhovsky*, I. P. Aleksandrova*, J. Totz, and D. Michel****

** Kirensky Institute of Physics, Siberian Division, Russian Academy of Sciences, Akademgorodok, Krasnoyarsk, 660036 Russia*

*** Leipzig University, D04103 Leipzig, Germany*

e-mail: rsa@iph.krasn.ru

Received July 20, 2001; in final form, October 25, 2001

Abstract—The chemical exchange of deuterons in a partly deuterated ammonium hydrogen selenate crystal is investigated by deuteron magnetic resonance (^{2}H NMR) spectroscopy over a wide range of temperatures. The changes observed in the line shape of the NMR spectra at temperatures above 350 K are characteristic of chemical exchange processes. The exchange processes are thoroughly examined by two-dimensional ^{2}H NMR spectroscopy. It is established that, over the entire temperature range, only deuterons of hydrogen bonds are involved in the exchange and the rates of exchange between deuterons of all types are nearly identical. No deuteron exchange between the ND_4 groups and hydrogen bonds is found. A new model of proton transport in ammonium hydrogen selenate is proposed on the basis of the experimental data. This model makes it possible, within a unified context, to explain all the available experimental data, including macroscopic measurements of the electrical conductivity. © *2002 MAIK "Nauka/Interperiodica".*

1. INTRODUCTION

Considerable recent interest expressed by researchers in crystals with a high ionic conductivity stems from both important practical applications of these compounds and the basic problems concerning electrical conductivity in superionic crystals [1–4]. In this respect, crystals whose structure involves quasi-one-dimensional chains of hydrogen bonds are of particular importance. These crystals are good model objects for use in verifying different assumptions on microscopic mechanisms of ionic conductivity. Ammonium hydrogen selenate (AHS) NH_4HSeO_4 belongs to these crystals. In the structure of AHS crystals, infinite quasi-one-dimensional chains are formed by SeO_4 tetrahedra joined through protons of hydrogen bonds. The deuteration of AHS makes it possible to apply the powerful method of nuclear magnetic resonance (NMR) at quadrupole nuclei to perform research into proton (deuteron) transport. In addition to conventional Fourier-transform NMR spectroscopy, elementary processes of deuteron chemical exchange have been investigated by two-dimensional (2*D*) NMR spectroscopy. As a rule, the 2*D* NMR data are compared with the results of dielectric measurements performed over a wide range of frequencies (10^{-2}–10^6 Hz). Dielectric measurements at very low frequencies permit one to increase appreciably the accuracy in determination of the dc conductivity σ_{dc} and to compare quantitatively the results of dielectric and NMR measurements for AHS crystals. The structure and properties of AHS single crystals have been described thoroughly in our earlier works [4–7]. In the present work, we analyzed our results with the aim of elucidating the microscopic mechanism of proton transport in AHS crystals.

2. SAMPLE PREPARATION AND EXPERIMENTAL TECHNIQUE

Partly deuterated (25%) AHS crystals were grown from an aqueous solution containing an excess of H_2SeO_4 and the appropriate amount of heavy water. Protons involved both in ammonium groups and in hydrogen bonds were partly replaced by deuterons. The degree of deuteration was chosen reasoning from the specific features of the phase diagram of the NH_4HSeO_4 compound, which, at a growth temperature of 30°C and a degree of deuteration higher than 45%, crystallizes in another phase [8]. The nuclear magnetic resonance and dielectric measurements were performed with the same samples. The ^{2}H NMR investigations were carried out on a BRUKER MSL 300 NMR spectrometer operating at a Larmor frequency of 46.073 MHz. The width of a 90° pulse was equal to approximately 4 μs. A spin echo sequence with a time interval of 25 μs between pulses was used in order to exclude the effect of the dead time of the NMR spectrometer receiver. Moreover, proton decoupling was applied to suppress the broadening of ^{2}H NMR lines due to the dipole–dipole interaction with the remaining protons. The two-dimensional NMR measurements were performed using the following spin echo sequence: $(\pi/2)_x$–t_1–$(\pi/2)_{-x}$–τ_m–$(\pi/2)_x$–τ–$(\pi/2)_y$–τ–t_2, where t_1 is the evolution time, t_2 is the measurement

time, τ is the time interval between pulses, and τ_m is the mixing time. The dielectric susceptibility was measured on a Schlumberger Solartron 1255 HF Frequency Response Analyzer in the frequency range from 10^{-2} to 10^6 Hz. Samples approximately 0.8 mm thick were cut from the AHS single crystal. For dielectric measurements, electrodes were prepared in the form of thin gold films applied to the sample surface under vacuum.

3. RESULTS AND DISCUSSION

The most interesting features inherent in the AHS crystal are as follows: the ferroelectric state associated with ordering of protons involved in hydrogen bonds, the incommensurate phase [6, 7], and the protonic conductivity [1–3]. In the paraelectric phase, the AHS crystal is characterized by a monoclinic unit cell with space group $B2$ and the lattice parameters a = 19.745 Å, b = 4.611 Å, c = 7.552 Å, and γ = 102.56° [9]. The crystal structure is built up of SeO_4^{2-} tetrahedral ions joined by hydrogen bonds into infinite chains aligned along the ferroelectric axis **b** (Fig. 1). The SeO_4 groups are linked by ammonium ions along the two other axes **a** and **c**. Hydrogen bonds between the different structural groups SeO_4 considerably differ from each other. The length of the hydrogen bonds between the $Se(1)O_4$ groups (α bonds) is equal to 2.56 Å, and the length of the hydrogen bonds between the $Se(2)O_4$ groups (β bonds) is 2.59 Å (Fig. 1). In the paraelectric phase, protons of the α bonds are disordered dynamically [6, 7]. Reasoning from the analysis of the ^{1}H NMR spectra and measurements of the ^{1}H spin–lattice relaxation time, Moskvich *et al.* [1] assumed that the isotropic diffusive motion of ammonium groups and protons of hydrogen bonds occurs in the paraelectric phase. These authors proposed a microscopic mechanism of proton transport through a correlated reorientation of SeO_4 groups with a sequential exchange of protons between SeO_4 groups along an infinite chain of hydrogen bonds. In this case, the activation energy for reorientational motion of SeO_4 groups is a controlling factor of the proton hopping rate. It should be noted that the activation energy for reorientational motion of SeO_4 groups is approximately equal to the activation energy for isotropic diffusion of ammonium groups which contribute significantly to the electrical conductivity of the crystal [1, 2]. However, for the most part, all these assumptions are based on analyzing the temperature dependence of the second moment (linewidth) of the ^{1}H NMR spectra. It is known that, over the entire temperature range, the ^{1}H NMR spectrum consists of a single line whose second moment is predominantly determined by the dipole–dipole interactions between protons of ammonium groups [1]. In our opinion, these investigations cannot provide detailed information on the microscopic mechanism of proton transport in the AHS crystal.

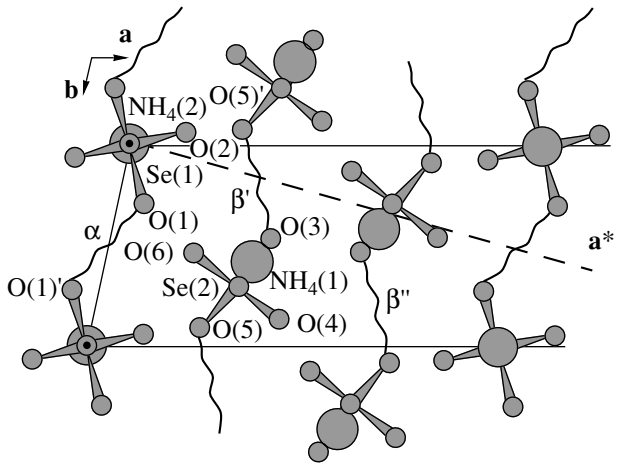

Fig. 1. Structure of NH_4HSeO_4 in the paraelectric phase. A half of the unit cell is shown. Wavy lines indicate hydrogen bonds between the oxygen atoms of the SeO_4 groups.

In this work, the microscopic characteristics of ammonium hydrogen selenate are determined from the ^{2}H NMR spectra of a partly deuterated AHS crystal. Unlike protons, deuterium nuclei possess a quadrupole moment. Nuclear magnetic resonance at quadrupole nuclei provides valuable information on the magnitude and symmetry of crystal-electric-field gradients at the studied nucleus. For a strong external magnetic field $\mathbf{B}_0$, when the Zeeman interaction energy substantially exceeds the energy of interaction between the nuclear quadrupole moment and the crystal field, the crystal field brings about a perturbation of equidistant Zeeman levels and a splitting of the NMR line into $2I$ components (I is the nuclear spin), which are symmetrically located with respect to the Larmor precession frequency ν_0 in the magnetic field $\mathbf{B}_0$ [10]. Consequently, the NMR spectrum of deuterons (I_D = 1) consists of doublets whose number for a single-crystal sample in the general case is equal to the number of magnetically nonequivalent deuterium nuclei. According to Pound [10], the quadrupole splitting ($\nu_2 - \nu_1$) can be represented by the relationship

$$\nu_2 - \nu_1 = \frac{6eQ}{4h} V_{zz}^{LAB} = \Phi_{zz}, \qquad (1)$$

where Q is the nuclear quadrupole moment, e is the elementary charge, h is the Planck constant, and V_{zz} is the zth component (the magnetic field $\mathbf{B}_0$ is aligned along the **z** axis) of the electric-field gradient at the nucleus. All the components V_{ij} of the electric-field gradient tensors for each structurally nonequivalent position of deuterium in the crystal in the laboratory coordinate system can be determined from the orientation dependences of the quadrupole splitting within the framework of the well-known Volkoff method [11]. The elec-

tric-field gradient tensor (for simplicity, the values of Φ_{ij} in frequency units will be used instead of V_{ij})—a symmetric second-rank tensor with zero spur—accounts for the point symmetry at the position of the nucleus under investigation. Specifically, for the α- and β-type hydrogen bonds in the AHS crystal, the principal axis Φ_{33} of the electric-field gradient tensor approximately coincides with the direction of the O–H···O hydrogen bond and the principal axis Φ_{22} is perpendicular to the plane of the Se–O···O bond. On this basis, each electric-field gradient tensor can be assigned to a particular hydrogen bond in the crystal. Thus, the magnetic resonance at ^{2}H nuclei in a partly deuterated AHS crystal appreciably extends the capabilities of the NMR technique and makes it possible to determine the individual dynamic characteristics of protons involved in hydrogen bonds and ammonium groups.

Figure 2 displays typical temperature dependences of the ^{2}H NMR spectra for an AHS crystal in the range 300–400 K. These spectra were measured for a crystal orientation at which the **b** axis is perpendicular to the external magnetic field $\mathbf{B}_0$ and the angle between the **a*** axis and the field $\mathbf{B}_0$ is equal to 15°. For this orientation, the ^{2}H NMR spectra contain two groups of lines. The central doublets (Fig. 2a) are assigned to the deuterons of the ammonium groups, and three doublets with splittings larger than 20 kHz (Fig. 2b) are attributed to the deuterons of the hydrogen bonds. As is clearly seen from Fig. 2a, no significant changes occur in the central portion of the spectrum over the entire temperature range of the existence of the paraelectric phase. Two electric-field gradient tensors for the deuterons of the ammonium groups (Table 1) were determined from the angular dependences of the ^{2}H NMR spectra at temperatures T = 300 and 390 K. One tensor is similar to an axially symmetrical tensor and corresponds to the deuterons of the ammonium groups in special positions. The other tensor is assigned to the deuterons of the ammonium groups in general positions. The small quadrupole coupling constant for these deuterons indicates a fast reorientation of the ammonium groups in the paraelectric phase. Therefore, in this case, the parameters of the electric-field gradient tensor account for an effective distortion of the ammonium group due to its environment. As follows from Table 1, an increase in the temperature leads to an insignificant change in the parameters of both electric-field gradient tensors in the paraelectric phase of the AHS crystal. These findings unambiguously demonstrate the absence of chemical exchange between two structurally nonequivalent ammonium groups over the entire range of the existence of the paraelectric phase. Consequently, the hypothesis proposed in [1] regarding isotropic diffusion of ammonium groups at 390 K should be revised. Analysis of the second moments of the ^{2}H NMR lines broadened at the expense of dipole–dipole interactions (hereafter, these lines will be referred to as the dipole-broadened lines) gives results that are in agreement with the

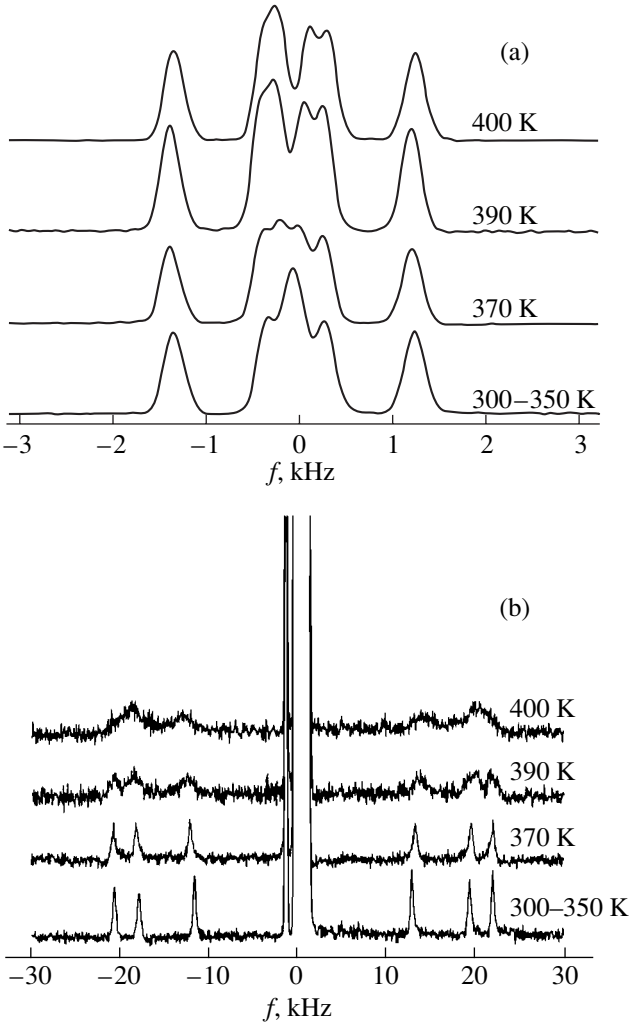

Fig. 2. Temperature dependences of the ^{2}H NMR spectra of an AHS crystal in the paraelectric phase: (a) the central quadrupole doublets assigned to the deuterons of the ammonium groups and (b) the side peaks attributed to the deuterons of the hydrogen bonds. The spectra are measured for a crystal orientation with the **b** axis perpendicular to the external magnetic field $\mathbf{B}_0$. The angle between the **a*** axis and the field $\mathbf{B}_0$ is equal to 15°.

aforementioned data and provides additional information on the deuteron motion. The dominant contribution to the width of the ^{2}H NMR lines assigned to the ammonium groups is made by the intermolecular dipole–dipole interaction of the ammonium deuterons with each other and the dipole–dipole interaction of the ammonium deuterons with deuterons of the hydrogen bonds. The dipole broadening of the ^{2}H NMR lines due to the dipole interaction of the deuterons with the remaining protons is suppressed by proton decoupling, whereas the intramolecular dipole interactions of the deuterons involved in the ammonium groups are averaged through fast reorientation of these groups. Taking into account the deuterons (with due regard for the

Table 1. Parameters of the electric-field gradient tensors for two structurally nonequivalent ammonium groups in the AHS crystal

Temperature, K	$NH_4(1)$				$NH_4(2)$			
	principal values of electric-field gradient tensors Φ_{ii}, Hz	direction cosines (magnitudes) with respect to crystallographic axes			principal values of electric-field gradient tensors Φ_{ii}, Hz	direction cosines (magnitudes) with respect to crystallographic axes		
		a*	**b**	**c**		**a***	**b**	**c**
300	$\Phi_{11} = -1196$	0.51	0.77	0.39	$\Phi_{11} = -1350$	0	0	1
	$\Phi_{22} = -402$	0.4	0.61	0.68	$\Phi_{22} = -1329$	0.73	0.68	0
	$\Phi_{33} = 1598$	0.76	0.19	0.62	$\Phi_{33} = 2679$	0.68	0.73	0
390	$\Phi_{11} = -920$	0.26	0.93	0.26	$\Phi_{11} = -850$	0	0	1
	$\Phi_{22} = -519$	0.47	0.35	0.81	$\Phi_{22} = -1306$	0.72	0.69	0
	$\Phi_{33} = 1439$	0.84	0.09	0.53	$\Phi_{33} = 2156$	0.69	0.72	0

Table 2. Theoretical (calculated with inclusion of all the magnetic nuclei, except for protons, and a random distribution of deuterons) and experimental (at 300 K) second moments of the ^2H NMR lines attributed to the ammonium groups in the AHS crystal

Orientation of field $\mathbf{B}_0$	Group $NH_4(1)$		Group $NH_4(2)$	
	M_2, Hz^2		M_2, Hz^2	
	Calculation	Experiment	Calculation	Experiment
$\|\|\mathbf{a}^*$	1.95×10^4	$(2 \pm 0.2) \times 10^4$	1.58×10^4	$(1.7 \pm 0.2) \times 10^4$
$\|\|\mathbf{b}$	1.96×10^4	$(2 \pm 0.2) \times 10^4$	1.81×10^4	$(2 \pm 0.2) \times 10^4$
$\|\|\mathbf{c}$	1.5×10^4	$(1.7 \pm 0.2) \times 10^4$	1.1×10^4	$(1.2 \pm 0.2) \times 10^4$

Table 3. Theoretical (calculated as described in Table 2, except for the contribution of the dipole–dipole interaction between the deuterons of ammonium groups and the deuterons of hydrogen bonds) and experimental (at 390 K) second moments of the ^2H NMR lines attributed to the ammonium groups in the AHS crystal

Orientation of field $\mathbf{B}_0$	Group $NH_4(1)$		Group $NH_4(2)$	
	M_2, Hz^2		M_2, Hz^2	
	calculation	experiment	calculation	experiment
$\|\|\mathbf{a}^*$	6.89×10^3	$(1.0 \pm 0.2) \times 10^4$	6.72×10^3	$(0.9 \pm 0.2) \times 10^4$
$\|\|\mathbf{b}$	1.5×10^4	$(1.6 \pm 0.2) \times 10^4$	1.48×10^4	$(1.6 \pm 0.2) \times 10^4$
$\|\|\mathbf{c}$	7.61×10^3	$(1.0 \pm 0.2) \times 10^4$	7.63×10^3	$(0.9 \pm 0.2) \times 10^4$

degree of deuteration) and other magnetic nuclei, except for protons, we calculated the second moments of the ^2H NMR lines. The lattice sums were calculated in a sphere of radius 40 Å. The calculated second moments are in agreement with the experimental data at 300 K (Table 2). An increase in the temperature leads to a decrease in the experimental second moments of the ^2H NMR lines associated with the ammonium groups (Table 3). It is interesting to note that the experimental second moments at 390 K agree well with the theoretical moments calculated without regard for the dipole interaction with the deuterons of the hydrogen bonds. This suggests a fast diffusive motion of these protons (deuterons). More detailed information can be obtained from analyzing the relevant lines of the NMR spectra.

It can be seen from Fig. 2b that the side components of the NMR spectra do not exhibit noticeable changes in the temperature range from 300 to 350 K. The parameters of two electric-field gradient tensors for two structurally nonequivalent positions of the protons involved in the α- and β-type hydrogen bonds were cal-

culated from the orientation dependences of the quadrupole splittings at 300 K. The results of calculations coincide with the data obtained in our earlier work [12]. At temperatures above 350 K, the side components of the NMR spectrum become broadened (Fig. 2b). This indicates that chemical exchange occurs in a system of hydrogen bonds in the crystal. However, the contribution of this exchange is substantially less than the quadrupole splitting up to the temperature of phase transition to the superionic phase (417 K). Hence, the mechanism of proton motion cannot be judged from these spectra. It is only possible to estimate the rate of chemical exchange from the NMR linewidth in the framework of the well-known Anderson theory (see, for example, [13]). The calculated rates of chemical exchange are as follows: 0.5×10^3 s^{-1} at 370 K, 2×10^3 s^{-1} at 390 K, and 4×10^3 s^{-1} at 400 K. In order to obtain information on the microscopic mechanism of the deuteron mobility, the exchange rate, and the activation energy of this process, we used two-dimensional ^{2}H NMR spectroscopy. The mathematical formalism of the chemical exchange processes and numerical calculations of the exchange rates from two-dimensional NMR spectra have been described in a number of well-known works [14, 15]. Here, we outline this method only briefly. The exchange kinetics, as a rule, is characterized by the probability (rate) p_{ij} of transferring an atom from the position i to the position j in a unit time. The chemical exchange can be represented by the basic equation (see, for example, [13])

$$\frac{\partial n_i}{\partial t} = \sum_j^n p_{ij} n_j \qquad (2)$$

or, in the matrix form, as $\dot{\mathbf{n}} = \mathbf{pn}$ with the solution

$$\mathbf{n}(t) = \exp(\mathbf{p} \cdot t)\mathbf{n}_0 = A(t)\mathbf{n}_0. \qquad (3)$$

Here, the components n_{0i} of the vector $\mathbf{n}_0\{n_{01}, \ldots, n_{0i}\}$ are equal to the number of deuterons at the ith position at the instant of time $t = 0$ and the components n_i of the vector $\mathbf{n}(t) = \{n_1, \ldots, n_i\}$ are equal to the number of deuterons at the same position at the instant $t = \tau_m$. The components $A_{ij}(t)$ of the exchange matrix $A(t)$ in relationship (3) completely determine the kinetics of deuteron (proton) exchange in the crystal and can be obtained from the intensities of the corresponding peaks in the two-dimensional ^{2}H NMR spectra [14, 15]. In our recent work [4], the AHS crystal was thoroughly investigated by two-dimensional ^{2}H NMR spectroscopy. Here, we present only the results that are essential to the understanding of the microscopic mechanism of protonic conductivity. The two-dimensional ^{2}H NMR experiments with the AHS crystal were performed in the temperature range 300–350 K. Figure 3 shows the left upper quadrant of the typical total two-dimensional ^{2}H NMR spectrum of the AHS crystal (at a temperature of 350 K and a mixing time of 3 ms). These spectra

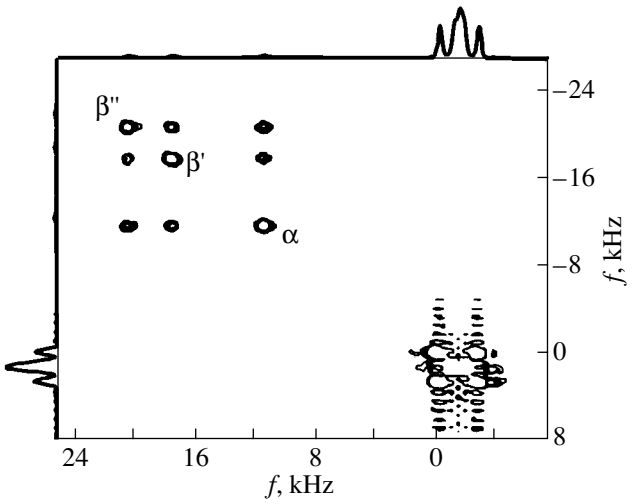

Fig. 3. Two-dimensional ^{2}H NMR exchange spectrum of the AHS crystal at a temperature of 350 K and a mixing time of 3 ms (only the upper left quadrant is shown). The crystal orientation is the same as in Fig. 2. The exchange is characterized by the off-diagonal peaks and occurs between deuterons at the positions α, β', and β".

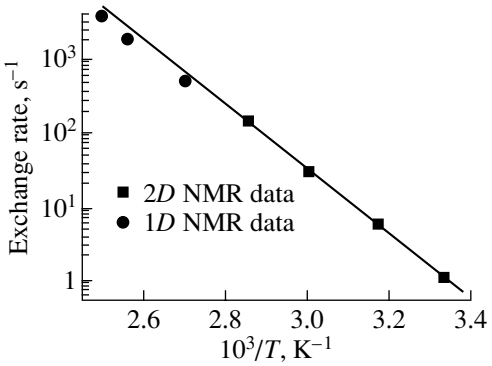

Fig. 4. Temperature dependence of the deuteron exchange rate for an AHS crystal according to 1*D* and 2*D* NMR data. $E_a = 81.1$ kJ mol^{-1} and $p_0 = 1.9 \times 10^{14}$ s^{-1}.

were measured at the same orientation as for the one-dimensional (1*D*) ^{2}H NMR spectra displayed in Fig. 2. The typical off-diagonal peaks (see, for example, [14, 15]) in Fig. 3 indicate deuteron exchange between hydrogen bonds of two types (the α and β bonds) and between magnetically nonequivalent positions of the adjacent bonds. Note that the rates of these processes are approximately equal to each other. The two-dimensional NMR spectra unambiguously demonstrate that no chemical exchange between the deuterons of the ammonium groups and the deuterons of the hydrogen bonds occurs over the entire temperature range of the existence of the paraelectric phase. Figure 4 depicts the temperature dependence of the exchange rate according

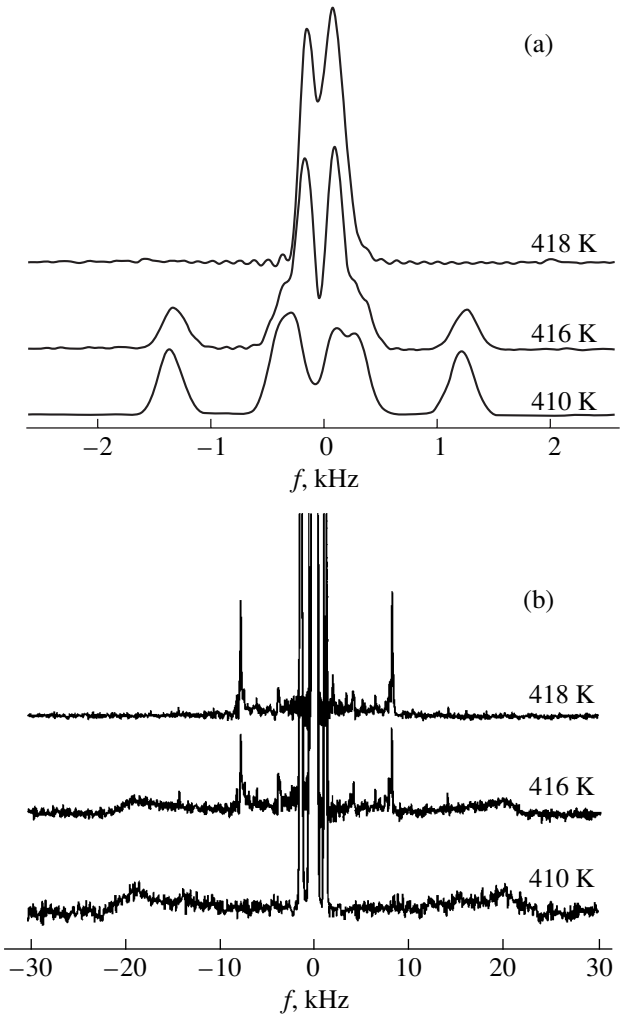

Fig. 5. Temperature dependences of the ^{2}H NMR spectra of an AHS crystal in the vicinity of the phase transition to the superionic state: (a) the central quadrupole doublets assigned to the deuterons of the ammonium groups and (b) the side peaks attributed to the deuterons of the hydrogen bonds. The crystal orientation is the same as in Fig. 2.

to the data of one-dimensional and two-dimensional NMR spectroscopy. The solid line in Fig. 4 represents the approximation of this dependence by the Arrhenius equation with the activation energy E_a:

$$p(T) = p_0 \exp(E_a/RT). \quad (4)$$

It should be noted that the $2D$ ^{2}H NMR data and the estimates made from the $1D$ ^{2}H NMR spectra at high temperatures are in good agreement and lead to the following parameters of the exchange process: the activation energy is approximately equal to 80 kJ mol^{-1} and the preexponential factor is estimated as $p_0 = 1.9 \times 10^{14}$ s^{-1}. This suggests that the proton mobility in the paraelectric phase occurs through a sole mechanism, namely, through sequential hoppings of protons from one chain of hydrogen bonds to the adjacent chain. Therefore, the conductivity anisotropy in the AHS crystal should be insignificant. From the results of dielectric measurements [5], we determined the conductivity parallel and perpendicular to the crystallographic axis **b** (the direction of hydrogen bond chains). Within the limits of experimental error, no conductivity anisotropy is revealed in the temperature range from 300 to 350 K. For proton exchange, the activation energies determined from our NMR data and the temperature dependence of the conductivity coincide to within good accuracy [5]. At temperatures above 360 K, the conductivity for both directions deviates from the Arrhenius behavior toward larger values. It should be noted that these deviations vary from sample to sample for the same orientation. This can be explained by the high hygroscopicity of the AHS crystal. All the samples are characterized by a sharp increase in the conductivity upon transition to the superionic phase.

At 417 K, the AHS crystal undergoes a transition to the high-temperature superionic phase. Unfortunately, the crystal in this phase rapidly loses protons and is destroyed. For this reason, the superionic phase cannot be investigated thoroughly by nuclear magnetic resonance and diffraction methods. There exist only the assumptions that the superionic phase has the $P2/n$ [16] or $P2_1/b$ [17] symmetry. We analyzed the ^{2}H NMR spectra for several orientations of the AHS crystal in the temperature range 410–420 K. For each new orientation, we used a particular sample. Figure 5 displays the temperature dependences of the ^{2}H NMR spectra for the AHS crystal oriented in such a manner that the **b** axis is perpendicular to the external magnetic field $\mathbf{B}_0$ and the angle between the **a*** axis and the field $\mathbf{B}_0$ is equal to 15°. The changes in the ^{2}H NMR spectra are observed at temperatures close to 417 K. A single doublet with extremely narrow components appears instead of the dipole-broadened NMR lines assigned to the deuterons of the hydrogen bonds. As the temperature increases, the intensity of the narrow lines increases, whereas the intensity of the dipole-broadened lines decreases to zero (the phase coexistence typical of first-order phase transitions). The results obtained indicate that deuterons (protons) in the superionic phase exhibit a high diffusive mobility. This leads to complete averaging of the dipole–dipole interactions of the deuterons involved in the hydrogen bonds. The central NMR lines attributed to the deuterons of the ammonium groups also change at a temperature of 417 K. The NMR quartet observed in the paraelectric phase for the given orientation transforms into a doublet with a splitting of approximately 200 Hz and a linewidth of 100 Hz for each component. Therefore, the transition to the superionic phase is accompanied by the change in the structural positions of the ammonium groups (one position instead of two structurally nonequivalent positions) and, possibly, their diffusive motion. However, the rate of this diffusion is relatively

low and cannot exceed the rate corresponding to the linewidth (~100 Hz). Consequently, the contribution of the ammonium groups to the conductivity of the AHS crystal in the superionic phase is negligible and the conductivity in this phase, as in the paraelectric phase, is completely governed by the mobility of protons involved in the hydrogen bonds.

Let us now consider structural characteristics that are important for proton transport in the AHS crystal. In the paraelectric phase, the shortest distance between the protons in equivalent positions is equal to the unit cell parameter *b* (4.61 Å). This distance exceeds the shortest distance (3.91 Å) between the positions of protons in the adjacent chains of the hydrogen bonds (Fig. 1). In the adjacent tetrahedra SeO_4, the shortest distance between the oxygen atoms, which are not involved in the formation of hydrogen bonds, is approximately equal to 3.3 Å. Moreover, protons can occupy positions, for example, between the O(3) and O(4) atoms separated by a distance of 3.18 Å. Owing to thermal vibrations (librations) of the SeO_4 groups, these distances can be even shorter. As a result, hydrogen bonds with a short lifetime can be formed between the relevant O atoms. The aforementioned structural features, the results of 2*D* ^{2}H NMR investigations, and the absence of conductivity anisotropy allow us to conclude that the main mechanism of proton transport in the paraelectric phase of the AHS crystal is associated with proton hoppings between the adjacent chains of hydrogen bonds.

A drastic increase in the conductivity of the AHS crystal at temperatures above 417 K can be caused by a jumpwise decrease in the height of potential barriers to proton diffusion and also by a disordering of the oxygen atoms of the SeO_4 groups in the superionic phase, as has been observed in $(NH_4)_3H(SeO_4)_2$ crystals [18, 19]. This assumption is confirmed by the data obtained by Dvorak *et al.* [16], who explained the overall sequence of phase transitions in the AHS crystal and its deuterated analog as the result of small distortions of the praphase with the space group of symmetry *Immm* and one formula unit per unit cell. In this phase, the Se and N atoms (the centers of the SeO_4 and NH_4 groups) occupy the special positions (0 0 0) and (1/2 1/2 0), respectively. According to [16], the space groups *Immm* and *P*2/*n* describe only an averaged symmetry of the AHS crystal. In particular, the positions of the tetrahedral groups in the praphase can have an inversion center only due to disordering of the oxygen atoms through reorientation of the SeO_4 groups. In any case, the number of possible relative positions of the oxygen atoms in the SeO_4 groups and the number of possible positions of the protons in the hydrogen bonds considerably increase compared to those in the paraelectric phase. As a consequence, the conductivity of the high-temperature phase increases jumpwise. According to the ^{2}H NMR data, all protons of the hydrogen bonds in the superionic phase are described by a sole averaged electric-field gradient tensor. This suggests a high diffusive mobility of these protons.

4. CONCLUSIONS

Thus, proton exchange between hydrogen bond chains extended along the **b** axis is the main mechanism of proton transport in the paraelectric phase of the AHS crystal. Unlike the model proposed in [1, 2], the mechanism considered above is not limited by the potential barrier to reorientation of the SeO_4 groups and does not require the simultaneous breaking of two hydrogen bonds. This mechanism makes it possible, within a unified context, to explain all the available experimental data, including macroscopic measurements of electrical conductivity. The superionic conductivity in the high-temperature phase of the AHS crystal is most likely associated with orientation disordering of the SeO_4 groups, which results in an increase in the number of sites providing proton diffusion.

It can be assumed that proton chemical exchange similar to that observed in the paraelectric phase of the AHS crystal occurs in other crystals with chains of hydrogen bonds. In this respect, it would be very interesting to carry out similar investigations with crystals characterized by another configuration of the hydrogen-bond system, especially with a $KHSeO_4$ crystal in which layers of hydrogen-bond chains alternate with layers of closed dimers consisting of SeO_4 groups [20]. At present, we are involved in such investigations.

ACKNOWLEDGMENTS

This work was supported by the Russian Foundation for Basic Research, project no. 00-15-96790.

REFERENCES

1. Yu. N. Moskvich, A. A. Sukhovsky, and O. V. Rozanov, Fiz. Tverd. Tela (Leningrad) **26**, 38 (1984) [Sov. Phys. Solid State **26**, 21 (1984)].
2. R. Blinc, J. Dolinsek, G. Lahajnar, *et al.*, Phys. Status Solidi B **123**, K83 (1984).
3. A. I. Baranov, R. M. Fedosyuk, N. M. Schagina, and L. A. Shuvalov, Ferroelectr. Lett. Sect. **2**, 25 (1984).
4. Yu. N. Ivanov, J. Totz, D. Michel, *et al.*, J. Phys.: Condens. Matter **11**, 3151 (1999).
5. J. Totz, D. Michel, Yu. N. Ivanov, *et al.*, Appl. Magn. Reson. **17**, 243 (1999).
6. I. P. Aleksandrova, O. V. Rozanov, A. A. Sukhovskii, and Yu. N. Moskvich, Phys. Lett. A **95**, 339 (1983).
7. I. P. Aleksandrova, Ph. Colomban, F. Denoyer, *et al.*, Phys. Status Solidi A **114**, 531 (1989).
8. A. A. Sukhovsky, Yu. N. Moskvich, O. V. Rozanov, and I. P. Aleksandrova, Ferroelectr. Lett. Sect. **3**, 45 (1984).
9. K. S. Aleksandrov, A. I. Kruglik, S. V. Misyul', and M. A. Simonov, Kristallografiya **25**, 1142 (1980) [Sov. Phys. Crystallogr. **25**, 654 (1980)].
10. R. V. Pound, Phys. Rev. **79** (4), 685 (1950).

11. G. V. Volkoff, H. E. Petch, and D. W. Smellie, Phys. Rev. **84**, 602 (1951).
12. Yu. N. Moskvich, O. V. Rozanov, A. A. Sukhovsky, and I. P. Aleksandrova, Ferroelectrics **63**, 83 (1985).
13. A. Abragam, *The Principles of Nuclear Magnetism* (Clarendon, Oxford, 1961; Inostrannaya Literatura, Moscow, 1963).
14. C. Schmidt, B. Blümich, and H. W. Spiess, J. Magn. Reson. **79**, 269 (1988).
15. S. Kaufmann, S. Wefing, D. Schaefer, and H. W. Spiess, J. Chem. Phys. **93**, 197 (1990).
16. V. Dvorak, M. Quilichini, N. Le Calvé, *et al.*, J. Phys. I **1**, 1481 (1991).
17. A. Onodera, A. Rozycki, and F. Denoyer, Ferroelectr. Lett. Sect. **9**, 77 (1988).
18. B. V. Merinov, M. Yu. Antipin, A. I. Baranov, *et al.*, Kristallografiya **36**, 872 (1991) [Sov. Phys. Crystallogr. **36**, 488 (1991)].
19. A. Piertaszko, B. Hilczer, and A. Pawlowski, Solid State Ionics **119**, 281 (1999).
20. J. Baran and T. Lis, Acta Crystallogr., Sect. C **C42**, 270 (1986).

Translated by O. Borovik-Romanova

Physics of the Solid State, Vol. 44, No. 6, 2002, pp. 1085–1092. Translated from Fizika Tverdogo Tela, Vol. 44, No. 6, 2002, pp. 1039–1047.

SEMICONDUCTORS AND DIELECTRICS

Transient Optical Absorption and Luminescence in $Li_2B_4O_7$ Lithium Tetraborate

I. N. Ogorodnikov*, V. Yu. Yakovlev, A. V. Kruzhalov*, and L. I. Isaenko*****

**Ural State Technical University, ul. Mira 19, Yekaterinburg, 620002 Russia*

e-mail: ogo@dpt.ustu.ru

***Tomsk Polytechnical University, Tomsk, 634021 Russia*

****Technological Institute of Single Crystals, Siberian Division, Russian Academy of Sciences, Novosibirsk, 630058 Russia*

Received June 1, 2001

Abstract—This paper reports on a study of the transient optical absorption exhibited by $Li_2B_4O_7$ (LTB) in the visible and UV spectral regions. Using absorption optical spectroscopy with nanosecond time resolution, it is established that the transient optical absorption (TOA) in these crystals originates from optical transitions in hole centers and that the kinetics of the optical-density relaxation is controlled by interdefect tunneling recombination, which involves these hole centers and electronic Li^0 centers representing neutral lithium atoms. At 290 K, the Li^0 centers migrate in a thermally stimulated, one-dimensional manner, without carrier ejection into the conduction or valence band. The kinetics of the pulsed LTB cathodoluminescence is shown to be controlled by a relaxation process connected with tunneling electron transfer from a deep center to a small hole polaron migrating nearby, a process followed by the formation of a self-trapped exciton (STE) in an excited state. Radiative annihilation of the STE accounts for the characteristic σ-polarized LTB luminescence at 3.6 eV, whose kinetics is rate-limited by the tunneling electron transfer. © *2002 MAIK "Nauka/Interperiodica".*

1. INTRODUCTION

Progress in solid-state laser technology has resulted in the development of compact and reliable optical radiation sources that can operate at a wavelength of about 1 μm, and high-power UV light sources for use in various areas of science and industry are in ever increasing demand. The most important components in solid-state UV radiation sources are frequency converters based on nonlinear crystals, in particular, on the borates of alkali and alkaline-earth metals, namely, β-BaB_2O_4 (BBO), LiB_3O_5 (LBO), and $CsLiB_6O_{10}$ (CLBO). $Li_2B_4O_7$ lithium tetraborate (LTB) has not been recognized as a possible candidate for such applications for a long time. LTB is traditionally employed in acousto- and optoelectronics and solid-state thermoluminescent dosimetry. Only very recently have its nonlinear properties been discovered and studied in the UV region and has the possibility of its use been demonstrated for second and fifth YAG:Nd laser harmonic generation [1]. While the efficiency of the nonlinear conversion in the LTB crystal was found to be slightly lower than that in BBO, LBO, and CLBO, the LTB has an obvious advantage in its higher radiation strength. The optical-damage threshold for LTB irradiated by high-power pulsed YAG:Nd laser radiation (1.5 J) (τ = 10 ns, λ = 1064 nm) is as high as 40 GW cm^{-2} [1], which exceeds the threshold for the other borates by a few times. A not less important aspect is the availability of well-developed technologies for growing large bulk LTB crystals of a high optical quality [2–5], including the methods of Czochralski [6] and Bridgman [7] and the low-temperature hydrothermal method [8]. At room temperature, the LTB crystal possesses tetragonal symmetry (point group 4*mm*) and its lattice parameters are $a = b$ = 0.9477 nm and c = 1.0286 nm [9, 10]. Its structural motif consists essentially of two equivalent tetrahedra and two equivalent trigonal structures, with the polar c axis parallel to the (001) crystallographic direction. LTB single crystals are good ionic conductors due to the lithium cations they contain; indeed, at 300 K, the one-dimensional ionic conductivity of LTB along the polar axis is 3.5×10^{-6} (Ω cm)$^{-1}$ [11, 12].

A large number of publications on LTB deal with its optical properties under irradiation. It is well known, for instance, that LTB crystals remain transparent in the spectral region 1.2–6.7 eV under irradiation by gamma rays or electrons (E = 1.25–1.3 MeV) up to an absorbed dose of 10^6 Gy [13]. At higher doses, weak bands ($\Delta k <$ 1.0 cm^{-1}) of stable optical absorption peaking at 4.1 and 5.2 eV appear [14]. At the same time, data on the transient optical absorption and the attendant relaxation of electronic excitations are lacking. The discovery of the nonlinear properties of LTB has stimulated studies in this direction.

The present study was aimed at investigating the LTB crystal by luminescence and optical spectroscopy with nanosecond time resolution under electron-beam excitation.

1063-7834/02/4406-1085$22.00

2. EXPERIMENTAL TECHNIQUE

In this work, we used $Li_2B_4O_7$ single crystals of high optical quality Czochralski-grown from a stoichiometry melt in platinum crucibles up to 200 cm^3 in volume. After the Grade Ch $Li_2B_4O_7$ reagent was recrystallized and maintained in this condition for the required time, the temperature was lowered to the melting point, 917°C. The crystals were grown on differently oriented seeds at pull rates of up to 3 mm/day and rotation speeds of about 20 rpm. $Li_2B_4O_7$ crystals grown for 15 days typically measured 40 mm in length and 35 mm in diameter and weighed up to 70 g. The results of preliminary studies of the grown crystals are described in detail in our publications [15, 16]. The samples were $7 \times 7 \times 1$-mm plane-parallel plates with polished faces perpendicular or parallel to the *c* crystallographic axis.

A detailed description of the experimental setup and of the luminescence and absorption spectroscopy with nanosecond time resolution employed is given in [17]. The transient optical absorption (TOA) and pulsed cathodoluminescence (PCL) were measured photoelectrically in the spectral region 1.2–5.5 eV with an MDR3 monochromator equipped with 1200- and 600-mm^{-1} interchangeable gratings, an FÉU-97 or FÉU-83 PM tube, and an S8-12 storage oscillograph. When measuring the dependence of the PCL and TOA on electron-beam power, the excitation pulse length was kept constant. The TOA was studied by the total internal reflection technique. Optical densities greater than unity were measured in the transmission geometry characterized by a shorter optical path with subsequent reduction.

A nanosecond-range electron accelerator was used as a source of excitation. The beam parameters were as follows: an average electron energy of 250 keV, an exciting-pulse duration of about 20 ns, a pulse current density variable from 10 to 1000 A cm^{-2}, and a maximum pulse energy of 0.16 J cm^{-2}. The excitation was envoked with pulse energies of 12 or 23% of the maximum level. For decay times up to 20 μs, the probing light was provided by an INP-5.50 pulsed lamp; for longer processes, by KGM12-100 and DDS-30 lamps.

Polarization measurements were performed with Rochon (TOA) and Frank–Richter (PCL) prisms. The degree of polarization was estimated from the relation $P = (I_\parallel - I_\perp)/(I_\parallel + I_\perp)$, where the indices ∥ and ⊥ refer to the probing-light electric vector oriented parallel or perpendicular to the crystal optical axis, respectively, and I is the luminescence intensity (PCL) or optical density (TOA).

3. EXPERIMENTAL RESULTS

Figure 1 presents polarized TOA spectra of an LTB crystal measured at 290 K 1.25 μs after an excitation pulse for two different orientations of the probing-light electric vector relative to the crystal optical axis, namely, for **E** ∥ **C** (σ polarization) and **E** ⊥ **C** (π polarization). The spectra of σ- and π-polarized TOA extend over a broad region from 2.0 eV to above 5.0 eV and represent a superposition of several constituent Gaussian-shaped bands (Table 1). As follows from an analysis of Table 1, the major part of the optical density is concentrated in a broad, weakly polarized band G_4 peaking at 4.52 eV. The observed spectral dependence of the polarization ratio (Fig. 1) is due to the contribution of differently polarized $G_1 \ldots G_3$ bands; more specifically, the G_2 and G_3 π bands are responsible for the negative value of P_D in the region 2.3–4.5 eV, while the contribution from the weak G_1 σ band results in the sign

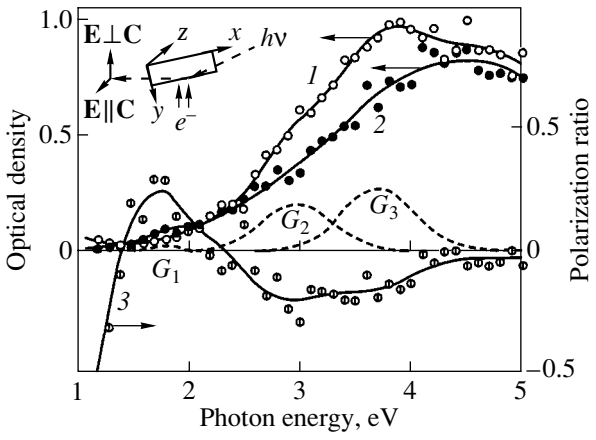

Fig. 1. (*1*, *2*) Polarized TOA spectra of LTB at 290 K, measured in (*1*) the **E** ⊥ **C** and (*2*) **E** ∥ **C** configurations, and (*3*) the polarization ratio. Points are experimental data, and solid lines are data fits. G_1, G_2, and G_3 are unfolded constituent bands.

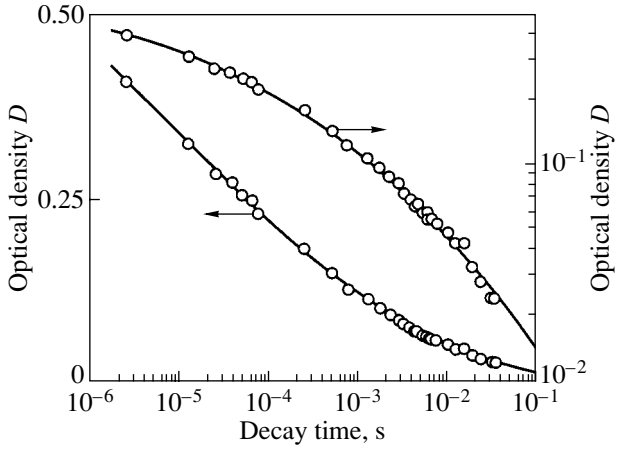

Fig. 2. TOA kinetics of LTB in the 3.8-eV band measured at 290 K. Points are experimental data, and solid lines are data fits.

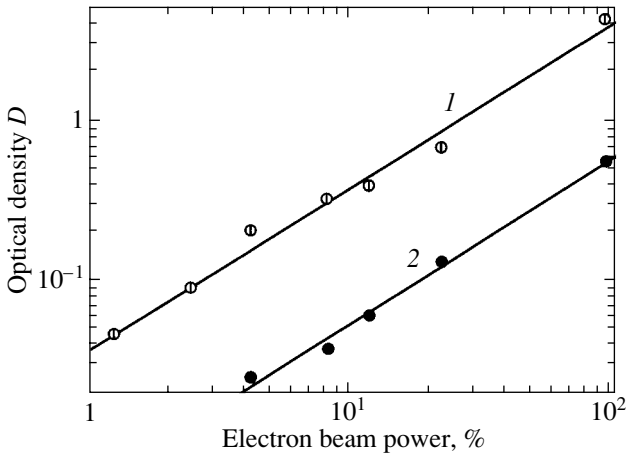

Fig. 3. Plots of optical density in the bands at (*1*) 3.8 and (*2*) 2.1 eV measured with a 1-μs delay vs. electron beam power obtained on an LTB crystal at 290 K.

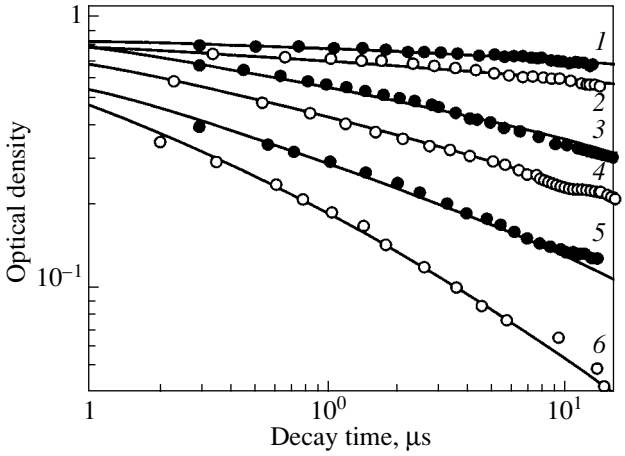

Fig. 4. TOA kinetics of LTB measured in the 3.8-eV band at different temperatures (K): (*1*) 325, (*2*) 334, (*3*) 425, (*4*) 461, (*5*) 538, and (*6*) 623.

reversal of P_D in the region 1.5–2.3 eV. Below 1.5 eV, the π-polarized TOA dominates (Fig. 1), which implies the existence of a TOA π band in LTB at longer wavelengths.

At 290 K, the TOA decays uniformly over the entire spectrum and the sample recovers to the original optical transmission level in a time of less than 1 s. No increase in optical density with increasing number of excitation pulses was observed. Figure 2 shows the TOA decay kinetics of LTB measured at 290 K in the 3.8-eV band. A characteristic feature of the kinetics is a comparatively slow, monotonic relaxation of optical density, which is observed over a decay time range covering about five decades. As follows from an analysis of Fig. 2, the decay kinetics is satisfactorily described by straight lines within a limited decay time interval of 2.5–3 decades when plotted both on the D–log(t) and log–log scale. In the latter case, the decay kinetics can be fitted by a linear relation,

$$-\log D(t) = A + p\log t. \quad (1)$$

This implies a power-law dependence of optical density on time, $D(t) \propto t^{-p}$. In the region of short decay times, the exponent p (the index of asymptotic behavior) is about 0.04, and it increases slightly for longer decay times. Such characteristics are usually typical of the kinetics of tunneling recharging (TR); in the case of a random distribution of fixed defects characterized by a concentration $n(t)$ and kinetics parameter N [$n(t) \ll N$], the TP kinetics is described by the relation [18]

$$n(t) = n_0\exp\left(-\frac{4\pi}{3}a^3N\ln^3(\sigma_0 t)\right), \quad (2)$$

where $n_0 = n(0)$, a is one half the Bohr radius of the defect wave function, and σ_0 is the prefactor of the tunneling probability $\sigma(r)$, which depends on the distance r between defects as

$$\sigma(r) = \sigma_0\exp(-r/a). \quad (3)$$

Figure 2 illustrates the fit of experimental data on $D(t)$ to Eq. (2) made within a decay time region extending over about five decades.

Increasing the power of the exciting electron beam brings about a proportional growth in the optical density uniformly over the whole spectrum. Figure 3 shows the dependences of TOA optical density in LTB on excitation power measured in the 2.1- and 3.8-eV bands. As seen from Fig. 3, these relations, when plotted on a log–log scale, can be fitted within two decades with straight lines with a slope of unity. The linear law of growth in the optical density and the absence of saturation within a broad range of exciting power variation may suggest that the corresponding color centers are associated with intrinsic lattice defects. Note that the TOA decay kinetics remains virtually unchanged. Only at a very low excitation power can weak components be distinguished at decay times of about 100 μs; these

Table 1. Polarized TOA band parameters of LTB measured at 290 K immediately after the pump pulse

Band	E_m, eV	ΔE, eV	P_D
G_1	1.80	0.30	>+0.5
G_2'	2.25	1.20	−0.418
G_2	2.97	0.64	−0.684
G_3	3.70	0.64	−0.692
G_4	4.52	2.20	−0.034

Note: E_m, ΔE, and P_D are the position of the maximum, FWHM, and the degree of polarization, respectively.

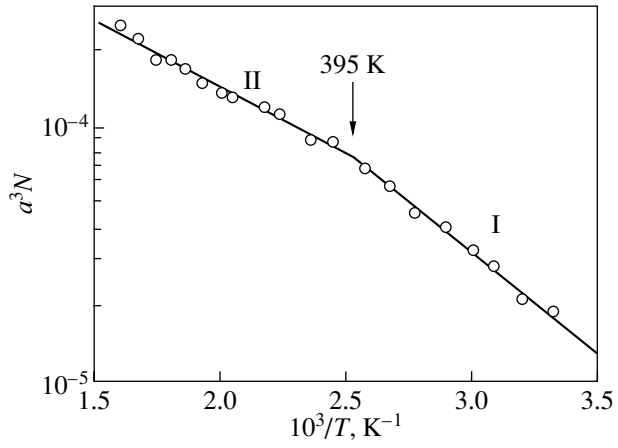

Fig. 5. Temperature dependence of the parameter a^3N of TOA kinetics in LTB measured in the 3.8-eV band.

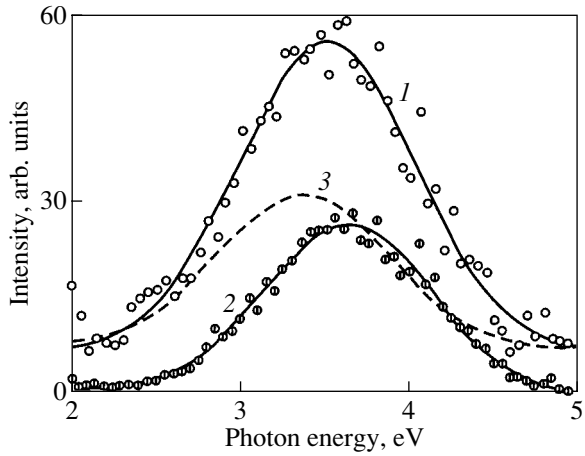

Fig. 6. PCL spectra of LTB measured (*1*) immediately after the pump pulse, (*2*) with a 100-ns delay, and (*3*) their difference.

components obey a first-order hyperbolic law and apparently originate from competing relaxation processes.

Figure 4 plots TOA kinetics in LTB measured at various temperatures. Throughout the temperature range covered (300–623 K), the TOA decay curves drawn on a log–log scale can be formally fitted with a linear relationship. For the microsecond-scale decay time region, the exponent p varies monotonically from 0.038 (300 K) to 0.480 (623 K); however, the initial intensity $D(t \longrightarrow 0)$ remains constant within the whole temperature interval studied. Figure 4 illustrates an approximation of the experimental data by Eq. (2) for a fixed value of the prefactor, $\sigma_0 = 270$ GHz.

The temperature dependence of the kinetics parameter a^3N is linearized in the Arrhenius coordinates (Fig. 5) and can be fitted by a linear relation,

$$\log(a^3N) = B_0 + B_1\frac{10^3}{T}, \qquad (4)$$

where B_0 and B_1 are the fitting parameters. In Fig. 5, one can separate two temperature intervals, 290–395 K (I) and 395–650 K (II), which differ in the slope of their straight lines; $B_1 = -0.78$ (I) and -0.52 (II), which correspond formally to activation energies of 0.16 eV (I) and 0.10 eV (II).

Table 2. Parameters of the time-resolved PCL spectra in LTB at 290 K

Band	E_m, eV	ΔE, eV	I_m, arb. units
G_F	3.36	1.00	24
G_S	3.62	0.99	25
G_T	3.50	1.05	49

Note: E_m, ΔE, and I_m are the position of the maximum, its FWHM, and the intensity at the maximum for the constituent PCL spectral bands, respectively.

Figure 6 and Table 2 present PCL spectra of LTB measured at 290 K immediately after an excitation pulse (G_T) and with a 100-ns delay (G_S) and their difference (G_F). The difference spectrum G_F, which is primarily due to the contribution of fast components with time constants shorter than 100 ns, is characterized by a long-wavelength shift of 0.26 eV relative to the slow-component spectrum. The fast-component spectrum has a wide-band pedestal whose height grows with excitation power; indeed, for an electron-beam power level of 23%, the pedestal height is about 14% of the G_T intensity.

The PCL decay kinetics of LTB in the nano- and microsecond ranges measured at 23%-excitation power can be approximated by the sum of two components with an initial intensity ratio of 1 : 1.1. The first of them is an exponential with $\tau = 30$ ns (in some cases, 110 ns), and the second is a hyperbola with an exponent of 1.6 and a characteristic decay time of about 340 ns (Fig. 7).

Figure 8 shows the PCL polarization in LTB in the 3.2-eV band measured with the polarizer rotated in the (100) plane. The angle θ is reckoned from the **E** || **C** orientation. The angular dependence of the PCL polarization is approximated by the relation

$$I = A_0 + A\cos^2(\theta). \qquad (5)$$

The degree of polarization $P_L = A/A_0$, estimated from the fitting parameters of this relation for the nanosecond range, increases from 35 to 50%.

Figure 9 plots the decay kinetics of the polarized luminescence of LTB measured for **E** || **C** and **E** ⊥ **C**, as well as the time evolution of the polarization ratio. The luminescence polarization of the centers usually decreases slightly with increasing decay time, whereas our measurements reveal an opposite tendency. As seen

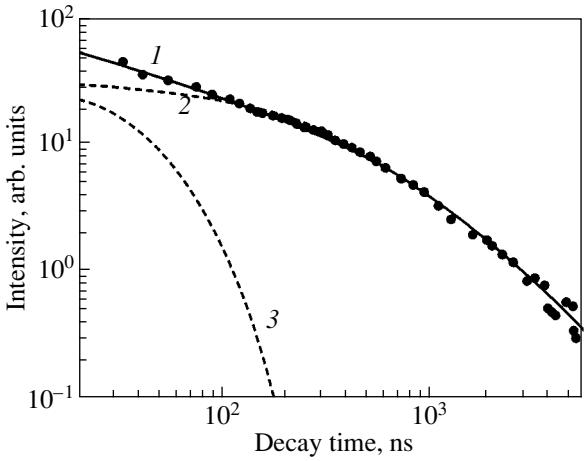

Fig. 7. PCL decay kinetics in LTB measured in the 3.5-eV band. Points are experimental data, solid line (*1*) is a fit using (*2*) a hyperbolic and (*3*) an exponential component.

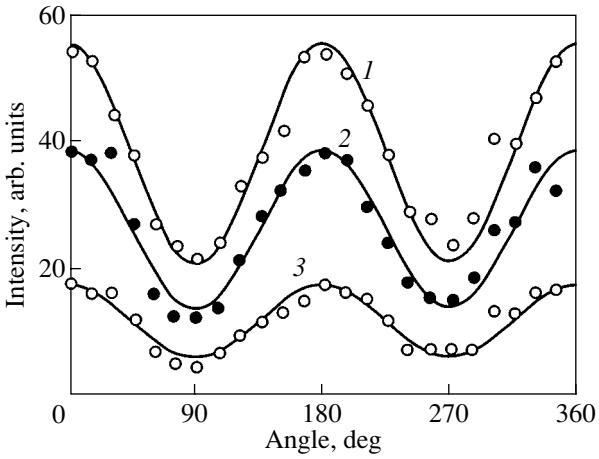

Fig. 8. LTB PCL polarization in the 3.2-eV band measured with the analyzer rotated in the (100) plane (*1*) immediately after the excitation pulse and with a delay of (*2*) 62 and (*3*) 300 ns. The angle is reckoned from the **E** ∥ **C** orientation.

from Fig. 9, the characteristic time of growth of the polarization ratio is about 30–40 ns. This may be a consequence of the PCL kinetics following a complex course in LTB. A quantitative analysis of the polarized PCL kinetics shows that the polarization ratio increases in opposite phase with the decay of the component with $\tau = 30$ ns. Unfolding of the curve into its constituents showed that the PCL decay components have a degree of polarization P_L of about –60% (the exponential component) and of +0.47% (the hyperbolic component). The variation of their contributions with time accounts for the observed evolution of the polarization ratio (Fig. 9).

4. DISCUSSION OF RESULTS

The first thing that draws one's attention when analyzing the results is the linear growth (on a log–log scale) of the color-center concentration, which occurs within two decades of pump power variation, and the absence of saturation. This gives one sound grounds to assume that the color centers responsible for the transient optical absorption in LTB are native lattice defects which are formed by the electron beam pulse and then decay in a time shorter than 1 s.

There are many publications on the optical and EPR spectroscopy of radiation defects in LTB (see, e.g., [13, 14, 19]). However, all known radiation defects involving boron and oxygen atoms (vacancies, interstitials, etc.) are stable at room temperature. At the same time, at 290 K, no stable color centers involving defects on the lithium sublattice have been observed in LTB. Moreover, at comparatively low temperatures, crystalline LTB is a quasi-one-dimensional Li^+ superionic conductor. The onset of efficient ion transport is preceded by an increase in the lithium sublattice anharmonicity along the polar axis, which becomes manifest at considerably lower temperatures [20]. Experimental data on LTB lattice dynamics show the lithium atoms to reveal a strong anharmonicity relative to the boron–oxygen framework already at temperatures above 230 K [21]. Viewed from this standpoint, defects involving an interstitial lithium ion and a lithium vacancy appear to be the most probable candidates. In

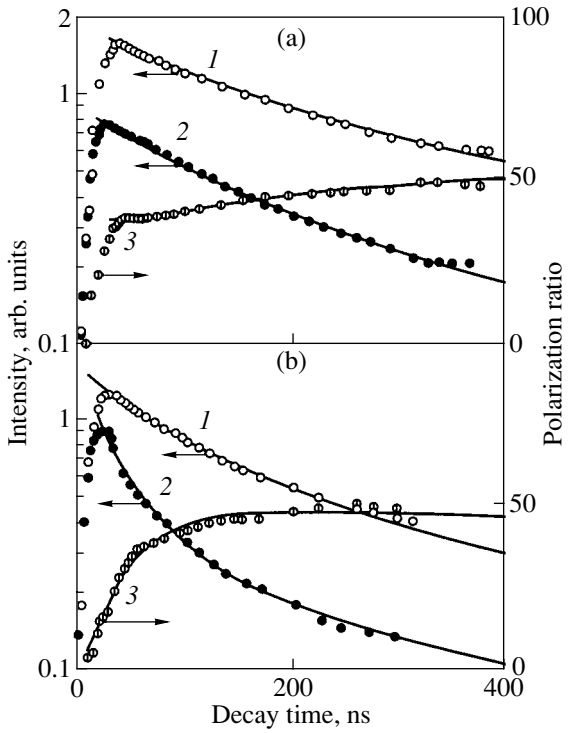

Fig. 9. Decay kinetics of polarized PCL in LTB in the bands at (a) 3.7 eV and (b) 2.9 eV for the orientations (*1*) **E** ∥ **C** and (*2*) **E** ⊥ **C**, and (*3*) the polarization ratio.

the first case, trapping of an itinerant electron by a lithium ion may bring about the formation of an Li^0 electronic center. In the second case, a hole center forms when one of the oxygen ions surrounding a lithium vacancy traps an itinerant hole. As shown earlier, it is such a color center (a hole O^- center) that is responsible for TOA in the region 2–5 eV in LiB_3O_5 [22]. The optical transitions in LBO are assigned to hole transfer from a local level of the O^- center, which is split off the valence-band top into the band gap, to states in the upper part of the valence band, which are derived from the O 2*p* orbitals. This actually reduces to hole transfer among the oxygen ions surrounding the defect and is treated within the small-polaron theory as interpolaron absorption. In this connection, it appears reasonable to relate the transient optical absorption in LTB in the region 2–5 eV to the color centers representing small polarons, which become optically absorbing when the hole is transferred in a photoinduced process from the localized ground state to one of the more or less equivalent oxygen ions surrounding the lithium vacancy.

A second point worth noting is that the TOA decay kinetics obeys the law of tunneling recombination between randomly distributed fixed defects over a time interval covering not less than five decades. As follows from the above analysis, the most probable partners in tunneling recombination may be native lattice defects, more specifically, the electronic Li^0 and the hole O^- center. At room temperature, the lithium cations are mobile, thus suggesting the existence of a diffusion-controlled reaction (DCR) of annihilation between the lithium vacancies and interstitials which is described by the relation

$$n(t) = \frac{n_0}{1 + t/t_h}, \tag{6}$$

where n_0 is the initial defect concentration and t_h is their half-life. As known from the theory of DCR [23], $t_h = 1/(Kn_0)$, where K is the DCR rate constant:

$$K = 4\pi R_0 D_R\left(1 + \frac{R}{\sqrt{\pi D_R t}}\right), \tag{7}$$

where R_0 is the radius of the recombination sphere and D_R is the diffusion coefficient. We use now the known data on the ionic electrical conductivity $\sigma(T)$ of LTB [24–26] and Einstein's relation to estimate t_h:

$$t_h \approx \frac{e^2}{4\pi R_0 k_b}(\sigma T)^{-1}, \tag{8}$$

where k_b is the Boltzmann constant. Assuming $R_0 = 5$ Å, we obtain $t_h \approx 0.03$ s for $\sigma \approx 3.5 \times 10^{-6}$ $(\Omega\ \mathrm{cm})^{-1}$ at 300 K. As follows from an analysis of Fig. 2, this time corresponds to the extreme points of the time interval of our measurements, where the optical density decreases by a factor of roughly 20. It can be maintained that the assumed diffusion-controlled annihilation of defects occurs at room temperature already after their TR. Because it is the tunneling recharging of defects that accounts for the TOA in LTB, it appears reasonable to use the theory of TR of randomly distributed fixed defects and to describe the TOA kinetics by Eq. (2).

At low temperatures, tunneling recombination of radiation defects is the major channel of their recharging. Indeed, TR has been detected and studied in a large number of crystalline nonmetallic solids, as well as in glasses and biological objects. The TR kinetics is usually assumed to be temperature-independent. In some cases, however, the TR kinetics is influenced by other, temperature-dependent processes. These processes are capable of affecting either the concentration of the defects taking part in the TR or the electron tunneling transfer probability. The first case relates to the conditions where, in addition to the two partners involved in tunneling recombination, there are defects of a third kind, whose diffusion brings about destruction of one of the pair components. A typical illustration of this process is provided by tunneling recombination of the $\{F, V_k\}$ pair in KCl occurring simultaneously with the thermally stimulated migration of the $H_{A(\mathrm{Na})}$ centers, which destroy one of the pair components [27]. The second case is realized in wide band-gap dielectrics with strong electron–vibration coupling. It is known [28] that the probability of the electron tunneling transfer can be affected in these conditions by interaction with local and collective vibrational modes, reorientation of low-symmetry centers taking part in the TR, slow diffusion of one of the tunneling recombination partners, and breakdown of the adiabatic electron–vibration coupling with increasing separation between the TR partners. In both cases, the defect distribution function changes in distance and angle (for low-symmetry centers), which affects the exponent p of the defect concentration decay kinetics in the asymptotic limit.

The temperature dependence of the TR kinetics parameter a^3N observed by us (Fig. 5) unambiguously implies the existence of a thermally stimulated process, which affects the tunneling recombination of defects and accounts for the TR kinetics being temperature-dependent. The kinetics parameter a^3N contains a component that influences the electron tunneling transfer probability (one half the Bohr radius a) and the initial concentration N of dominant defects. The initial concentration of the color centers produced by an electron beam is known to be usually temperature-independent [29]. Indeed, from an examination of Fig. 4, one may conclude that the TOA decay curves measured in LTB at various temperatures should converge to the same value of the optical density as $t \longrightarrow 0$.

Let us estimate the possible decrease in the concentration of one of the tunneling pair components due to the diffusion-controlled annihilation with mobile defects of the third type. Among them are primarily defects on the lithium sublattice. It is known [20] that

in LTB at room temperature, the lithium ions can migrate along the spontaneous-polarization direction (*c* axis). The ionic electrical conductivity of the LTB crystal was studied in [25, 26], and the activation energies of lithium ion migration along the polar axis were found to be 0.54 eV at 350–390 K and 0.39 eV at 390–530 K. These energies exceed, by a few times, the activation energies of the TOA kinetics parameter, 0.16 and 0.10 eV, determined by us. Furthermore, the above estimates of t_h show that diffusion-controlled defect annihilation involving lithium ions can become manifest at room temperature only for comparatively long decay times. This is at odds with the results presented in Fig. 4. Therefore, we believe that the observed temperature dependence of the product a^3N (Fig. 5) is due to its first component (a^3), which governs the probability of the electron tunneling transfer.

Let us discuss possible mechanisms which could account for the temperature dependence of the electron tunneling transport probability in LTB. The totality of the experimental data amassed in this study gives us grounds to suggest that one of the partners in the tunneling recombination could be a lithium sublattice defect (for instance, the lithium vacancy). In this case, diffusive transport of lithium cations along the polar axis should affect the defect distribution function in distance even for $t \ll t_h$. This should result, in particular, in an increase in the number of closely separated pairs and, hence, in an increase in the tunneling transport probability with increasing temperature. It is evident, however, that because of the intricate chain of causal relations, the slope of the asymptotic exponent *p* plotted in the Arrhenius coordinates can no longer be identified with the activation energy of the original diffusion process. At the same time, a qualitative relation should hold. Indeed, an analysis of the temperature dependence of exponent *p* in Fig. 4 revealed two temperature intervals differing in slope and a break at 395 K. The same temperature intervals (I, II) and a trend of decreasing slope in the crossover from the low-temperature linear part I for $T < 390$ K to the high-temperature part II are characteristic of the ionic (Li^+) electrical conductivity of LTB along the polar axis [24–26]. A difference is observed only in the slope of the linear portions plotted in the Arrhenius coordinates; namely, the slope of the linear portions I and II in the temperature dependence of the electrical conductivity exceeds by about fourfold that for the asymptotic exponent *p*. We note that the nature of this inflection in the temperature dependence of electric transport in LTB is of a fundamental character; indeed, above 390 K, the correlation effects acting between mobile lithium ions result in their cooperative migration along the polar axis of the crystal, thus reducing the activation energy [25, 26].

On the other hand, one cannot disregard the possibility that the observed temperature dependence of the tunneling probability originates from the interaction of a tunneling electron with local or collective vibrational modes. Assuming $a \propto \exp(-\hbar\omega/k_bT)$, we obtain from Eq. (4) an estimate $\hbar\omega = 0.16/3$ and $0.10/3$ eV. IR optical and Raman scattering spectroscopy measurements of LTB show [30–32] that the vibrational modes of lithium ions surrounded by four oxygen ions lie at 35–75 meV. Our estimate of $\hbar\omega$ is in agreement with this interval.

A comprehensive comparison of the TOA and PCL decay laws shows that the PCL decay kinetics cannot be described by a derivative of the optical-density decay with respect to time, which, in turn, is proportional to the color-center concentration. This means that the tunneling transport of electrons among the main defects governing the TOA is nonradiative and that it does not produce resonance (or close to resonance) conditions for tunneling electron transport from a defect to the excited state of a self-trapped exciton (STE) located nearby. In this connection, we believe the PCL and TOA in LTB to be governed by different relaxation processes.

The main PCL band of LTB at 3.6 eV is close in its characteristics to the fast intrinsic luminescence band of LTB [15], which originates from radiative annihilation of the STE. The decay kinetics under photoexcitation of this band is described by a component with $\tau \approx 1$ ns [15]; however, pumping by unfiltered synchrotron radiation in the x-ray range at 290 K revealed exponential components with time constants of 10 and 150 ns [33]. This compares favorably with the PCL exponential decay components with $\tau = 30$ and 110 ns observed in this study (Figs. 7, 9).

The slow hyperbolic PCL decay component with a characteristic time of 340 ns and an asymptotic exponent of 1.6 is apparently of another nature. This is suggested, in particular, by its degree of polarization (Fig. 8). We believe that the major part of the LTB PCL is due to interdefect tunneling recombination. It is known [34] that one-site small polarons can act as short-lived nuclei in the self-trapping of holes, excitons, or electron–hole pairs. Tunneling transport of an electron from a deep electronic level to an excited level of a hole polaron migrating near this trapping center may create an STE in the σ state. Radiative annihilation of such an STE accounts for the characteristic σ-polarized luminescence of LTB. Indeed, the observed PCL of LTB is σ polarized to about 50%. The kinetics of this luminescence is rate-limited by the tunneling recharging in the deep-electronic-center and hole polaron pair. We note for comparison that a similar hole–electron mechanism of tunneling electron transport from an Ag^0 deep trapping center to the excited state of a V_k center migrating in its vicinity has been recently detected experimentally in the RbCl : Ag alkali halide crystal [35]. One of the possible candidates for a deep electronic center in LTB can be an F center. An indirect indication of this is the presence of a rapidly decaying band at 3.36 eV in the PCL spectrum. Earlier, we observed luminescence bands of F-like centers in a

similar crystal, LBO, at 3.3 and 2.7 eV [36]. It is known [37, 38], that recombination luminescence, including one that is thermally stimulated at 400–500 K, in irradiated LTB crystals with impurities which do not produce activated luminescence bands is represented by the same dominant band at 3.38 eV. A conclusion was drawn that this luminescence center is of intrinsic nature and that it is related to F-type centers created in an LTB lattice irradiated by neutrons or electrons with energies E = 1.25–1.3 MeV [37]. These defects are stable at room temperature, and their annealing or carrier delocalization are assumed to be responsible for the thermally stimulated luminescence peaking at 418 K (0.94 eV) and 479 K (1.80 eV) [38].

REFERENCES

1. R. Komatsu, T. Sugawara, K. Sassa, *et al.*, Appl. Phys. Lett. **70** (26), 3492 (1997).
2. J. D. Garret, M. Natarajan, and J. E. Greedan, J. Cryst. Growth **41**, 225 (1977).
3. M. Adachi, T. Shiosaki, and A. Kawabata, Jpn. J. Appl. Phys., Part 1 **24** (S3), 72 (1985).
4. M. Adachi, S. Yamamichi, M. Ohira, *et al.*, Jpn. J. Appl. Phys., Part 1 **28** (S28-2), 111 (1989).
5. T. Kitagawa, K. Higuchi, and K. Kodaira, J. Ceram. Soc. Jpn. **105**, 616 (1997).
6. T. P. Balakireva, V. V. Lebold, V. A. Nefedov, *et al.*, Inorg. Mater. **25** (3), 462 (1989).
7. S. J. Fan, G. S. Shen, W. Wang, *et al.*, J. Cryst. Growth **99** (1–4), 811 (1990).
8. K. Byrappa, V. Rajeev, V. J. Hanumesh, *et al.*, J. Mater. Res. **11** (10), 2616 (1996).
9. J. Krogh-Moe, Acta Crystallogr. **15** (3), 190 (1962).
10. J. Krogh-Moe, Acta Crystallogr. B **24** (2), 179 (1968).
11. A. É. Aliev, Ya. V. Burak, and I. T. Lyseĭko, Izv. Akad. Nauk SSSR, Neorg. Mater. **26** (9), 1991 (1990).
12. S. F. Radaev, N. I. Sorokin, and V. I. Simonov, Fiz. Tverd. Tela (Leningrad) **33** (12), 3597 (1991) [Sov. Phys. Solid State **33**, 2024 (1991)].
13. A. O. Matkovskiĭ, D. Yu. Sugak, S. B. Ubizskiĭ, O. I. Shpotyuk, E. A. Chernyĭ, N. M. Vakiv, and V. A. Mokritskiĭ, *Influence of Ionizing Radiations on Electronics Materials* (Svit, L'vov, 1994).
14. Ya. V. Burak, B. N. Kopko, I. T. Lyseĭko, *et al.*, Izv. Akad. Nauk SSSR, Neorg. Mater. **25** (7), 1226 (1989).
15. I. N. Ogorodnikov, V. A. Pustovarov, A. V. Kruzhalov, *et al.*, Fiz. Tverd. Tela (St. Petersburg) **42** (3), 454 (2000) [Phys. Solid State **42**, 464 (2000)].
16. A. Yu. Kuznetsov, L. I. Isaenko, A. V. Kruzhalov, *et al.*, Fiz. Tverd. Tela (St. Petersburg) **41** (1), 57 (1999) [Phys. Solid State **41**, 48 (1999)].
17. B. P. Gritsenko, V. Yu. Yakovlev, and Yu. N. Safonov, in *Proceedings of All-Union Conference on Modern State and Advanced Aspects of High-Speed Photography, Cinematography, and Metrology of Fast Processes, Moscow, 1978*, p. 61.
18. V. N. Parmon, R. F. Khaĭrutdinov, and K. I. Zamaraev, Fiz. Tverd. Tela (Leningrad) **16** (9), 2572 (1974) [Sov. Phys. Solid State **16**, 1672 (1974)].
19. E. F. Dolzhenkova, M. F. Dubovik, A. V. Tolmachev, *et al.*, Pis'ma Zh. Tekh. Fiz. **25** (17), 78 (1999) [Tech. Phys. Lett. **25**, 709 (1999)].
20. S. Matyyasik and Yu. V. Shaldin, Fiz. Tverd. Tela (St. Petersburg) **43** (8), 1405 (2001) [Phys. Solid State **43**, 1464 (2001)].
21. A. É. Aliev, V. F. Krivorotov, and P. K. Khabibulaev, Fiz. Tverd. Tela (St. Petersburg) **39** (9), 1548 (1997) [Phys. Solid State **39**, 1378 (1997)].
22. I. N. Ogorodnikov, A. V. Porotnikov, S. V. Kudyakov, *et al.*, Fiz. Tverd. Tela (St. Petersburg) **39** (9), 1535 (1997) [Phys. Solid State **39**, 1366 (1997)].
23. Yu. R. Zakis, L. N. Kantorovich, E. A. Kotomin, V. N. Kuzovkov, I. A. Tale, and A. L. Shlyuger, *Models of Processes in Wide-Gap Solids with Defects* (Zinatne, Riga, 1991).
24. A. É. Aliev and R. R. Valetov, Kristallografiya **36** (6), 1507 (1991) [Sov. Phys. Crystallogr. **36**, 855 (1991)].
25. A. É. Aliev, I. N. Kholmanov, and P. K. Khabibullaev, Solid State Ionics **118** (1–2), 111 (1999).
26. A. É. Aliev, I. N. Kholmanov, and P. K. Khabibullaev, Dokl. Akad. Nauk **365** (2), 178 (1999) [Dokl. Phys. **44**, 147 (1999)].
27. Ch. B. Lushchik and A. Ch. Lushchik, *Decay of Electron Excitations with Defect Formation in Solids* (Nauka, Moscow, 1989).
28. U. T. Rogulis and I. K. Vitol, in *Electron Processes and Defects in Ionic Crystals* (Latv. Univ. im. P. Stuchki, Riga, 1985), pp. 22–23.
29. A. K. Pikaev, *Modern Radiation Chemistry. Solid and Polymers. Applied Aspects* (Nauka, Moscow, 1987).
30. Ya. V. Burak, Ya. O. Dovgiĭ, and I. V. Kityk, Zh. Prikl. Spektrosk. **52** (1), 126 (1989).
31. V. N. Moiseenko, A. V. Vdovin, and Ya. V. Burak, Opt. Spektrosk. **81** (4), 620 (1996) [Opt. Spectrosc. **81**, 565 (1996)].
32. A. V. Vdovin, V. N. Moiseenko, and Ya. V. Burak, Opt. Spektrosk. **90** (4), 625 (2001) [Opt. Spectrosc. **90**, 555 (2001)].
33. I. N. Ogorodnikov, V. A. Pustovarov, L. I. Isaenko, *et al.*, Nucl. Instrum. Methods Phys. Res. A **448** (1–2), 467 (2000).
34. S. Iwai, T. Tokizaki, A. Nakamura, *et al.*, Phys. Rev. Lett. **76** (10), 1691 (1996).
35. E. A. Vasil'chenko, I. A. Kudryavtseva, A. Ch. Lushchik, *et al.*, Fiz. Tverd. Tela (St. Petersburg) **40** (7), 1238 (1998) [Phys. Solid State **40**, 1128 (1998)].
36. I. N. Ogorodnikov, V. A. Pustovarov, M. Kirm, *et al.*, Fiz. Tverd. Tela (St. Petersburg) **43** (8), 1396 (2001) [Phys. Solid State **43**, 1454 (2001)].
37. M. Martini, C. Furetta, C. Sanipoli, *et al.*, Radiat. Eff. Defects Solids **135** (1–4), 133 (1995).
38. M. Martini, F. Meinardi, L. Kovács, and K. Polgar, Radiat. Prot. Dosim. **65** (1–4), 343 (1996).

Translated by G. Skrebtsov

Physics of the Solid State, Vol. 44, No. 6, 2002, pp. 1093–1097. Translated from Fizika Tverdogo Tela, Vol. 44, No. 6, 2002, pp. 1048–1052.

DEFECTS, DISLOCATIONS, AND PHYSICS OF STRENGTH

Effect of γ-Radiation-Induced Defects in Glass on Laser Destruction

M. R. Bedilov, Kh. B. Beisembaeva, and I. Yu. Davletov

Research Institute of Applied Physics, National University of Uzbekistan, Tashkent, 700174 Uzbekistan

e-mail: ravshan@vega.tashkent.su

Received June 7, 2001

Abstract—Processes of degradation and plasma ejection upon exposure of optical materials to a single laser pulse and γ-radiation in the subthreshold, threshold, and far-above-threshold regions are studied using a complex method. © *2002 MAIK "Nauka/Interperiodica".*

The progress in the development of high-power solid-state lasers, nonlinear optical media, and elements and devices in thermonuclear fusion reactors operating in extreme conditions is determined to a considerable extent by the development of radiation-resistant optical materials. It has been established that the production of such materials depends mainly on knowledge of the mechanisms of their degradation under the action of a high-power laser beam and nuclear radiation. It is well known that the surface of solids (including transparent insulators) is destroyed under the action of laser radiation after the attainment of a certain density of the incident luminous energy. Despite the large number of publications devoted to the analysis of laser-induced degradation of the surface of optical materials [1–14], its relation to the imperfection of the structure of the solid remains unclear [15]. It has been established that the presence of various dynamic (molecular vibrations, density and concentration fluctuations, etc.) and static (foreign impurities and inclusions) optical inhomogeneities in transparent dielectrics facilitates the occurrence of various nonlinear effects (including self-focusing), which lowers the radiation resistance of the optical material.

In the present work, we study the effect of γ-ray-induced defects in glass on laser degradation under the action of a laser beam with a power density q = 0.1–1000 GW/cm^2. Experiments were made in a wide range of laser power densities embracing the subthreshold (10^8–10^9 W/cm^2), threshold (10^9–4×10^9 W/cm^2, depending on γ-ray-irradiance), and far-above-threshold (4×10^9–10^{12} W/cm^2) regions of optical-material degradation. It should be noted that the experiments were carried out with single laser pulse irradiation of the objects under investigation and, hence, the accumulation effect was not manifested in the subthreshold region. In this case, the process of laser-induced degradation is connected with the formation of a dense high-temperature plasma. For this reason, the experiments were made using the mass-spectroscopic and optical microscopic methods [15]. This allowed us to analyze not only the morphology of laser-induced degradation in the threshold and far-above-threshold regions of laser power density but also the ion component of the plasma formed as a result of degradation of glass, as well as to determine the composition of the target and to find out which elements facilitate the destruction. In addition, the analysis of the results obtained by using the above methods revealed a correlation between the surface degradation of the solid and the characteristics of multiply charged ions emitted from the solid under the action of a high-power luminous flux.

The targets (silicate glasses of the GLS type) were prepared in the form of pellets ~2 mm thick and 10 mm in diameter. Radiation-induced defects were created by holding samples in the channel of a γ-radiation source with a power of 1500 R/s until the samples received a dose of 10^9 R. A laser pulse of duration 50 ns and power 60 MW was focused on the surface of a target in the form of a spot ~250 μm in diameter. In order to determine the radiation-damage threshold accompanied in the given case by degradation of the optical material, luminescence, and ejection of ionized mass, laser flares with a successive increase in the incident radiation intensity were used. The instant of the beginning of degradation was fixed microscopically from the emergence of ion peaks. These peaks were registered by a VEU-1A detector, whose signal was fed to a storage oscilloscope. Mass-, charge-, and energy separation of ion components was carried out by using a mass spectrometer. The relative error of measurements of the amplitude of ion signals did not exceed ~8%.

As a result of the experiments, we obtained information on the degradation of silicate glass in the subthreshold, threshold, and far-above-threshold regions in the case of a single interaction of laser radiation pulse with optical materials and on the formation of multiply charged ions of plasma in wide ranges of laser power densities and γ-radiation doses. The microscopic investigations revealed that the destruction of an unexposed

1063-7834/02/4406-1093$22.00

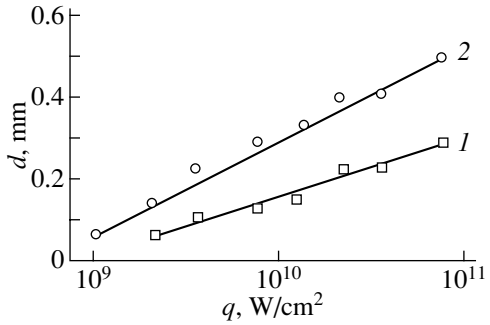

Fig. 1. Dependence of the diameter d of a crater formed on the surface of (*1*) the initial and (*2*) γ-ray-irradiated glass to a dose of 10^9 R on the laser radiation power density.

target produced in the threshold region has the form of a crater with fused brims containing small-sized defects in the form of indentations having a depth of the order of a tenth of a micrometer or less. The reason for the emergence of such microcraters in the threshold region is apparently associated with individual impurity inclusions and optical inhomogeneities in the sample, leading to the absorption of laser radiation at local centers [4]. The magnitude of the laser-induced degradation threshold of the surface of a glass of the GLS type, which was determined by using the above technique, amounted to ~4 GW/cm^2 under the given experimental conditions. The crater diameter d in this case was ~50 μm. As the laser power density q increases, the crater diameter becomes larger and attains the value ~300 μm in the far-above-threshold region for q = 1000 GW/cm^2 (Fig. 1). There exists the following dependence between the power density q and the crater diameter: $d \sim q^{0.4}$. The defects induced in the glasses under investigation by γ radiation lower the damage threshold. For example, the degradation threshold for a GLS-type glass receiving a radiation dose of 10^9 R amounts to ~1 GW/cm^2 under the given experimental conditions; i.e., it was equal to 1/4 of the threshold prior to irradiation. The diameter of the crater emerging on such an irradiated surface for q = 1 GW/cm^2 amounts to ~100 μm. With increasing radiation dose, the diameter of the degradation crater increases significantly and for $q \geq 1$ GW/cm^2, the glass surface experiences catastrophic breakdown. In this case, the size of the crater on the exposed surface is connected with the power density q through the relation $d \sim q^{0.55}$ (Fig. 1). Morphological analysis of the breakdown pattern proved that, after the action of γ radiation, shallow caverns existing in the initial crater coalesce into large damaged regions whose size may attain several tens of micrometers. It was found that the destruction begins in small isolated regions containing pile-ups of absorbing defects. In our opinion, the role of such defects may be played by foreign impurities and inclusions present in the glass before irradiation and the regions of accumulation of γ-ray-induced defects. In order to verify this assumption, we investigated the absorption spectra of the given samples in the UV, visible, and IR regions. It was established experimentally that as the γ-radiation dose increases, absorption in the regions under investigation becomes stronger. For example, for a dose of 10^9 R, the absorption of the given glass increases by 16% in the visible spectral region and by 7% in the region of incident laser radiation. It follows, hence, that the amount of luminous energy absorbed in the sample exposed to γ radiation is larger than that in the sample not subjected to irradiation, which increases the thickness of the material being evaporated. On the other hand, the emergence of a huge number of defects in γ-ray-irradiated samples absorbing in the UV and visible regions causes an increase in the diameter of the appearing crater due to additional heating by radiation emitted by the multiply charged laser-produced plasma.

A comparison of the experimental results obtained during investigation of various multiply charged ions emitted by the plasma proved that the number N, charge multiplicity Z, and energy E of the ions increase with the diameter of the crater formed on the unexposed surface. For example, in the far-above-threshold region, where q = 20 GW/cm^2, the crater diameter attains values of ~150 μm. It was found that the formed plasma contains, in its composition, all the elements constituting glass (Li, O, Na, Si, K, and Nd), as well as uncontrollable impurities (H, Be, B, C, etc.). The maximum charge multiplicities for ions forming the glass matrix obtained in this case are as follows: Z_{max} = 4 for the Si ions, Z_{max} = 3 for the Nd and O ions, and Z_{max} = 2 for the Li, Na, and K ions. All ion components were characterized by a broad energy spectrum with a single distribution peak. The maximum energy for the Li^{+1}, O^{+1}, Na^{+1}, Si^{+1}, K^{+1}, and Nd^{+1} ions was 300, 400, 800, 900, 950, and 2500 eV, respectively (Fig. 2). As the power density q in the far-above-threshold region increased to 90 GW/cm^2 (the corresponding crater diameter was 280 μm), Li and K ions with Z_{max} = 3, Si and Nd ions with Z_{max} = 4, and O and Na ions with Z_{max} = 5 were detected in the plasma formed (see Fig. 3 for 20 GW/cm^2 and Table 2 for 90 GW/cm^2). The maximal energy E_{max} increases in this case by a factor of 3.0–3.5 for Li^{+1}, O^{+1}, and K^{1+} ions and by a factor of 2.9–2.5 for Na^{+1}, Si^{+1}, and Nd^{+1} ions. The intensity of the ion beams also increases considerably. For example, an increase in the power density q of the laser from 20 to 90 GW/cm^2 leads to a 1.5–2.0 fold increase in the numbers of Li, O, Na, and Si ions of all charge multiplicities, while the intensity of multiply charged ions of K and Nd increases by a factor of 4–5. The increase in the values of parameters of multiply charged ions of the plasma upon an increase in the value of q can be explained by the fact that, as the diameter of the crater increases, the plasma attains its critical density more rapidly and, hence, a larger part of laser radiation power is spent for heating and ionization of the plasma cluster.

At the same time, it was established experimentally that γ-ray-irradiation of the samples under investigation considerably changes the parameters of multiply charged ions constituting the plasma in the threshold and far-above-threshold regions. It should be noted that as the γ-radiation dose becomes larger, the ion intensity increases with the crater diameter, while the values of Z_{max} and E_{max} of the multiply charged ions thereby decrease (Figs. 2–4 and Tables 1, 2). It should be emphasized that the extent of variation of the characteristics (N, Z, E) of multiply charged ions under investigation are determined to a considerable extent by the power density q of the laser. It can be seen from Tables 1 and 2 that a less significant change in the values of N and E of ions is observed when $q \geq 10$ GW/cm^2 (which is an order of magnitude higher than the damage threshold). This may be due to partial annealing of γ-ray-induced defects (for large values of q). The strong change in the characteristics of multiply charged ions of the plasma formed as a result of degradation of a γ-ray-irradiated target can be explained by the violation of the relation between the initial size d of the plasma and the characteristic recombination length $l(Z)$. This is clearly manifested in an analysis of the dependence between the diameter of the crater formed on the surface of the γ-ray-irradiated target and the parameters of multiply charged ions emitted by the plasma. It is found that an increase in the size of the crater (the value of d) on the given surface upon a transition from the threshold to the far-above-threshold region of degradation of the optical material leads to a considerable change in the characteristics of the ejected plasma. In this case, the values of Z and E of the plasma ions decrease sharply, while the number of low-charge ions increases. An increase in γ-radiation dose intensifies the degradation of the optical material and leads to the ejection of a low-charge high-density laser plasma.

The degradation of the surface of optical materials was analyzed by three independent (microscopic, spectroscopic, and mass-spectrometric) methods for the laser power density $q = 10^8$–10^{12} W/cm^2. We experimentally established the subthreshold, threshold, and far-above-threshold regions of optical material degradation induced by laser and nuclear radiation. Also established were the form of destruction and the defects and elements responsible for the beginning of degradation in the vicinity of the damage threshold for optical materials and, especially, for the formation of a high-density multi-elemental low-charge ion plasma in the far-above-threshold region of degradation of a γ-ray-irradiated material. The breakdown threshold in experiments with the unexposed object under investigation was $\sim 4 \times 10^9$ W/cm^2; after γ-ray-irradiation, this value decreased by a factor of four. It should be noted that experiments with multiple irradiation of optical materials in the subthreshold laser power region, in which the accumulation effect is manifested, are of certain interest. We specifically carried out experiments for detecting the degradation of the material under investigation depending on the number of laser pulses "fired" at the same spot (the laser power density q was 5×10^8 W/cm^2, which corresponds to the subthreshold region). It was

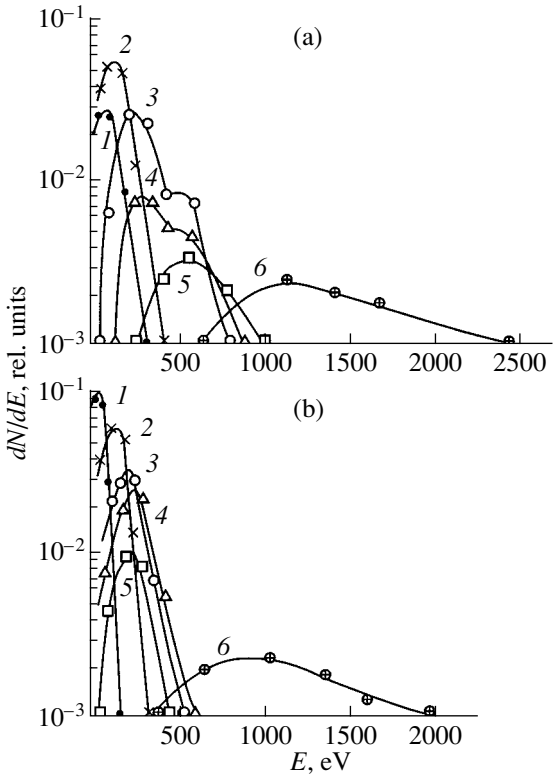

Fig. 2. Typical energy spectra of singly charged ions (*1*) Li^{+1}, (*2*) O^{+1}, (*3*) Si^{+1}, (*4*) Na^{+1}, (*5*) K^{+1}, and (*6*) Nd^{+1} in the plasma of (a) the initial and (b) γ-ray-irradiated GLS-1 glass with a radiation dose of 10^9 R for $q = 20$ GW/cm^2.

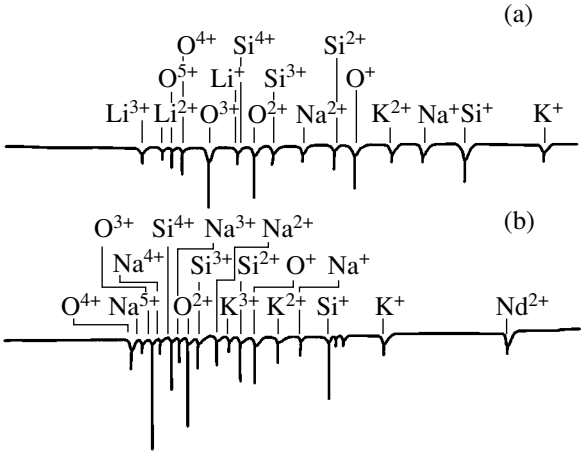

Fig. 3. Typical mass–charge spectra of ions in the plasma of GLS-1 glass formed as a result of action of laser radiation with $q = 20$ GW/cm^2. The ion energy E/Z is equal to (a) 200 and (b) 400 eV.

Table 1. Effect of γ radiation on the characteristics of multiply charged ions detected for $q = 20$ GW/cm^2

Characteristic	Dose, R	Elements					
		Li	O	Na	Si	K	Nd
Z_{max}	0	2	3	2	4	2	3
	10^9	1	2	1	2	2	2
E_{max}, eV	0	300	400	800	900	950	2500
($Z = 1$)	10^9	150	300	500	550	600	2000
$\left(\frac{dN}{dE}\right)_{max}$, rel. units	0	2.6	6.0	0.8	2.8	0.4	0.2
($Z = 1$)	10^9	10.0	6.5	2.0	3.0	1.0	0.1

Table 2. Effect of γ radiation on the characteristics of multiply charged ions detected for $q = 90$ GW/cm^2

Characteristic	Dose, R	Elements					
		Li	O	Na	Si	K	Nd
Z_{max}	0	3	5	5	4	3	4
	10^9	3	4	3	4	3	4
E_{max}, eV	0	800	1400	2000	2200	3000	3900
($Z = 1$)	10^9	600	1200	2000	2100	3000	3900
$\left(\frac{dN}{dE}\right)_{max}$, rel. units	0	3.7	9.0	2.5	10.0	2.0	1.0
($Z = 1$)	10^9	3.9	10.0	4.2	10.0	4.0	1.0

found that the destruction of the surface takes place after 12 laser shots owing to the accumulation effect. The form and size of the defects observed in the subthreshold region are close to the results obtained in the threshold range of q values. It should be noted that the methods used (especially the microscopic and mass-spectrometric methods) are sensitive to the accumulation effect and provide information on the absorption spectra, the pattern of material degradation, and the damage threshold, as well as information on the mass, charge, and energy composition of products after each action of laser and nuclear radiation on the optical-material surface. The methods of investigation used by us supplemented one another and allowed us to study the degradation of the surface of materials not only in the threshold and far-above-threshold regions but also in the subthreshold range of q values.

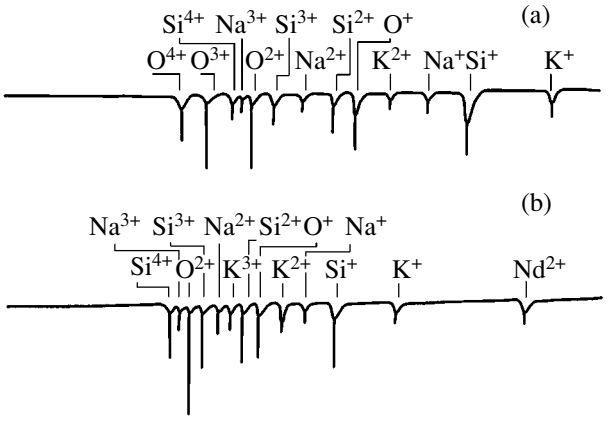

Fig. 4. Typical mass–charge spectra of ions in the plasma of GLS-1 glass subjected to the action of γ radiation with a dose of 10^9 R formed by laser radiation with q = 20 GW/cm^2. The ion energy E/Z is equal to (a) 200 and (b) 400 eV.

A comparison of the degradation of optical materials and the ejected charged particles in the threshold and far-above-threshold regions of q values proved that these regions differ in the type and extent of surface degradation of the material and in the character of the charged-particle ejection from the damaged region of the target. Indeed, the character of degradation of optical materials in the subthreshold, the threshold, and far-above-threshold regions is different; the information concerning this difference is essential for establishing the mechanism of material degradation in a wide range of power densities during a single act of exposure to the luminous flux. All these processes are interrelated; consequently, the optical-material degradation mechanism becomes more complicated as the power density of the

laser increases from 10^8 to 10^{12} W/cm^2. The dominating process in the subthreshold region is associated with the accumulation effect, which ultimately leads to the degradation of the optical material. In the threshold region, the processes determining the material degradation are thermal heating, melting, evaporation, and emission of particles. In the far-above-threshold region, the leading role is played by laser-induced thermal explosion, resulting in the formation of craters and multielemental plasma containing various ions in a wide range of charge multiplicity and energy. The results of mass-spectroscopic measurements showed that different defects and elements of the matrix of the material are responsible for the degradation of the optical material, depending on the laser power density. In the subthreshold region, radiation defects and uncontrollable impurities play the major role when the accumulation effect occurs; in the threshold region, radiation defects and some elements of the matrix are of importance, while in the far-above-threshold region, the degradation is associated with all defects and elements constituting the optical material. In our opinion, the three stages of degradation (subthreshold, threshold, and far-above-threshold) are manifested consecutively in the breakdown of a laser system as a result of interaction of a bell-shaped laser pulse with optical materials. In the far-above-threshold region of material degradation, various processes occur during a single laser pulse: from the accumulation effect to a laser-induced thermal explosion with the formation of a crater and the ejection of multielemental low-charge ion plasma. It should be noted in conclusion that the results obtained in this work on the type and extent of damage depending on the γ-radiation dose, on the form of degradation in the three regions of the q values, and on the formation of a plasma with known mass, charge, and energy parameters (especially in the threshold and far-above-threshold stages of degradation of the optical material) are useful in developing high-power solid-state lasers and in establishing the reasons for the failure of optical laser systems under the action of high-power laser and nuclear radiation.

REFERENCES

1. R. Abdupataev, M. R. Bedilov, Kh. B. Beĭsembaeva, and P. K. Khabibullaev, Dokl. Akad. Nauk SSSR **286** (4), 857 (1986) [Sov. Phys. Dokl. **31**, 130 (1986)].
2. N. G. Basov, Yu. A. Zakharenkov, A. A. Rupasov, G. V. Sklizkov, and A. S. Shikanov, *Diagnostics of Dense Plasma* (Nauka, Moscow, 1989).
3. M. R. Bedilov, P. K. Khabibullaev, and Kh. B. Beĭsembaeva, *Radiation-enhanced Processes in Solid-State Lasers* (Fan, Tashkent, 1988).
4. Z. T. Azamatov, P. A. Arsen'ev, M. R. Bedilov, Kh. S. Bogdasarov, A. A. Evdokimov, and V. M. Tsikhanovich, *Defects in Materials for Quantum Electronics* (Fan, Tashkent, 1991).
5. N. G. Basov, Yu. A. Zakharenkov, N. N. Zorev, A. A. Rupasov, G. V. Sklizkov, and A. S. Shikanov, *Advances in Science and Technology* (VINITI, Moscow, 1982), Vol. 26, Parts 1, 2, p. 304.
6. M. R. Bedilov and A. N. Ishmuratov, Fiz. Tverd. Tela (St. Petersburg) **38** (6), 1649 (1996) [Phys. Solid State **38**, 911 (1996)].
7. V. V. Artem'ev, A. M. Bonch-Bruevich, I. E. Morigev, *et al.*, Zh. Tekh. Fiz. **47** (1), 183 (1977) [Sov. Phys. Tech. Phys. **22**, 106 (1977)].
8. B. M. Ashkinadze, V. I. Vladimirov, V. A. Likhachev, and I. A. Ivanov, Zh. Éksp. Teor. Fiz. **50** (5), 1187 (1966) [Sov. Phys. JETP **23**, 788 (1966)].
9. P. I. Bal'kyavichyus, E. K. Kostenko, I. P. Lukoshyus, and É. K. Maldutis, Kvantovaya Élektron. (Moscow) **5** (9), 2032 (1978).
10. A. M. Bonch-Bruevich, I. V. Aleshin, Ya. A. Imas, and A.V. Pavshukov, Zh. Tekh. Fiz. **41** (3), 617 (1971) [Sov. Phys. Tech. Phys. **16**, 479 (1971)].
11. I. M. Buzhinskiĭ and A. E. Pozdnyakov, Kvantovaya Élektron. (Moscow) **2** (7), 1550 (1975).
12. Yu. K. Donileĭko, A. A. Manenkov, and V. S. Nechitaĭlo, Kvantovaya Élektron. (Moscow) **5** (7), 194 (1978).
13. Yu. I. Kyzylasov, V. S. Starunov, and I. A. Fabelinskiĭ, Fiz. Tverd. Tela (Leningrad) **12** (1), 233 (1970) [Sov. Phys. Solid State **12**, 186 (1970)].
14. A. G. Molchanov, Fiz. Tverd. Tela (Leningrad) **12** (3), 954 (1970) [Sov. Phys. Solid State **12**, 749 (1970)].
15. M. R. Bedilov, Kh. B. Beĭsembaeva, and M. S. Sabitov, Kvantovaya Élektron. (Moscow) **30** (2), 201 (2000).

Translated by N. Wadhwa

Physics of the Solid State, Vol. 44, No. 6, 2002, pp. 1098–1101. Translated from Fizika Tverdogo Tela, Vol. 44, No. 6, 2002, pp. 1053–1056.

DEFECTS, DISLOCATIONS, AND PHYSICS OF STRENGTH

The Influence of the Degree of Instability of a System on the Oscillating Behavior of Time Dependences of the Internal Friction

A. V. Oleĭnich-Lysyuk

Chernovtsy National University, Chernovtsy, 58012 Ukraine

Received November 13, 2001

Abstract—The specific features of the oscillations observed in the time dependences of the internal friction of polycrystalline beryllium irradiated with high-energy electrons and aged at T = 300 K within different time intervals are investigated. It is demonstrated that the ageing leads to a gradual decrease in the amplitude and the period of oscillations. The assumption is made that the observed phenomenon has a synergetic nature. *© 2002 MAIK "Nauka/Interperiodica".*

1. INTRODUCTION

In recent years, considerable research attention has been focused on systems in which a disordered chaotic motion of the elements involved transforms into an ordered motion under the action of external excitations. This crossover occurs through self-organization processes of nonequilibrium structures, such as the Belousov–Zhabotinsky reactions in chemistry, the Benard cells in hydrodynamics, the ordering of magnetic domains in the physics of magnetic phenomena, the formation of slip lines and bands and the formation of cellular and block dislocation structures in the physics of strength and plasticity, etc. [1]. Among similar phenomena are oscillating time variations in the internal friction observed in a number of systems after cyclic deformations [2, 3]. However, the nature of oscillations of the internal friction and the causes of their occurrence still remain unclear. The goal of the present work was to investigate how the degree of instability of the studied system affects the manifestation of the internal friction oscillations.

2. SAMPLE PREPARATION AND EXPERIMENTAL TECHNIQUE

The MTBK-1.5 Be samples irradiated with high-energy (~18 MeV) electrons and aged within different time intervals at room temperature in air were chosen as the object of investigation, because, as was established experimentally in [4], irradiation with high-energy electrons leads to the appearance of clearly defined oscillations in the time dependences of the internal friction. The samples to be studied were prepared from plates produced through the condensation of beryllium from the vapor phase onto substrates at temperatures in the range 500–600°C. Samples in the form of parallelepipeds $1 \times 1 \times 80$ mm in size were cut from these plates by the electroerosion method with subsequent elimination of the deformed layer.

According to the chemical analysis, the content of impurities in the condensate was as follows: 0.009–0.05 wt % Fe, 0.003–0.14 wt % Al, 0.0037–0.04 wt % C, 0.06–0.15 wt % O, 0.003–0.042 wt % Ga, and 0.01–0.017 wt % N. The electrical resistivity ratio $\rho_{295\,K}/\rho_{4.2\,K}$ for different samples was in the range 190–220, which corresponds to an estimated integral purity of better than 99.95 wt % Be.

The condensate had a columnar structure with a 40- to 70-μm mean cross section of grains. The length of the grains was equal to (0.2–1)d, where d = 1.5–3 mm is the thickness of the condensate plate.

The internal friction was measured on a low-frequency relaxometer of the inverse torsion pendulum type at frequencies ~1 s^{-1} according to standard techniques [2–4]. This made it possible to carry out the experiment with an accuracy of better than 1% and to record reliably the oscillating time dependences of the internal friction. The time dependences of the internal friction were measured at strains $\gamma = 9 \times 10^{-6} \pm 1 \times 10^{-7}$ both after the cyclic deformation of the sample at a constant strain amplitude γ_0 for 5 min followed by a sharp decrease in the strain to the aforementioned values and without cyclic deformation after the measurement of the amplitude dependence of the internal friction.

3. RESULTS AND DISCUSSION

Figure 1 shows the time dependences of the internal friction of the beryllium samples which were irradiated and then aged within six months at room temperature both after cyclic deformation for 5 min at stain amplitudes $\gamma_0 = 1.4 \times 10^{-5}$, 2.5×10^{-5}, and 6.6×10^{-5} and without cyclic deformation after measurement of the amplitude dependence of the internal friction to $\gamma_{max} = 6.6 \times$

1063-7834/02/4406-1098$22.00 © 2002 MAIK "Nauka/Interperiodica"

10^{-5}. A comparison of the data presented in Fig. 1 and the results obtained immediately after irradiation of the sample revealed the following features: (1) natural ageing of the sample leads to the appearance of clearly defined oscillations with a 10- to 11-min period at strains which did not induce oscillations in the as-irradiated material (cf. Fig. 1a of this work and Fig. 2a given in [4]), and (2) the time dependences of the internal friction at large strain amplitudes γ_0 exhibit quite a different behavior.

An increase in the ageing time to ten months leads to a specific localization of oscillations at $\gamma_0 = 2.2 \times 10^{-5}$. However, their amplitude and period are less than those observed after ageing within six months. At large strain amplitudes γ_0, the oscillations lose their periodicity. For example, after cyclic deformation for 5 min at $\gamma_0 = 3.5 \times 10^{-5}$, a shadow-type burst appears against the background of weak variations in the internal friction at the 17th minute of the measurements, whereas after the cyclic deformation for 5 min at $\gamma_0 = 6.6 \times 10^{-5}$, the oscillations arises only after a lapse of some time, more precisely, at the 15th–30th minutes of observation.

In this case, a pronounced temperature hysteresis is observed in the temperature dependences of the internal friction and the square of the frequency of free torsional vibrations f^2 (which is proportional to the effective shear modulus G_{eff}) of the samples aged within both six and ten months: the curves of heating and cooling do not coincide over a rather wide range of temperatures (Fig. 2). This suggests that a weakly pinned dislocation-impurity structure of beryllium undergoes a transformation in the course of heating (cooling) due to appreciable internal stresses [3, 4].

Ageing of the samples within 12 months leads to a decrease in the amplitude and the period of oscillations over virtually the entire range of the studied strains (Fig. 3). In this case, the defect structure of the samples is characterized by a higher stability (Fig. 4), as judged from the absence of specific anomalies in the temperature dependences of the internal friction and f^2 [3]: the absorption of the elastic energy weakly varies with temperature and corresponds to the background absorption over the entire temperature range covered; moreover, the curves $f^2(T)$ do not exhibit a temperature hysteresis. Analysis of the internal friction background and the temperature behavior of the amplitude dependence of the internal friction indicates a substantial stabilization of the beryllium defect structure.

Therefore, in the course of natural ageing, the stabilization of the dislocation-impurity structure, whose equilibrium was disturbed under irradiation, brings about a gradual decrease and appreciable suppression of the oscillating behavior of the time dependence of the internal friction. This corroborates our assumption that the oscillations of the internal friction actually occur only in a nonequilibrium system under the action of external factors. On this basis, some considerations

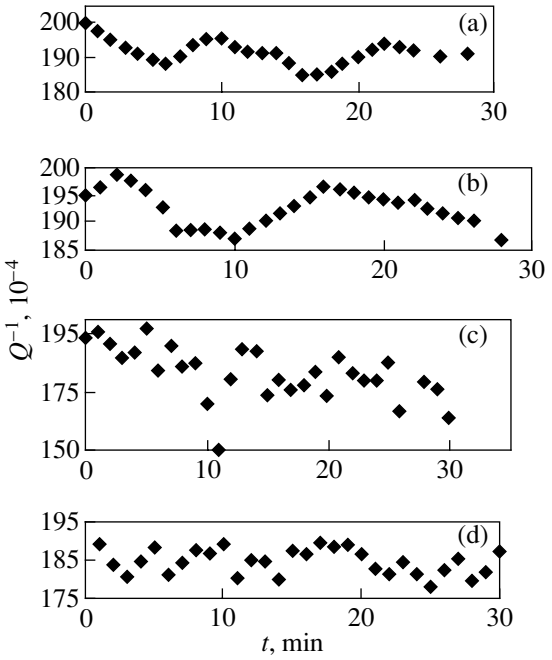

Fig. 1. Time dependences of the internal friction of the MTBK Be samples aged within six months after cyclic deformation for 5 min at γ_0 = (a) 1.4×10^{-5}, (b) 2.5×10^{-5}, and (c) 6.6×10^{-5} and (d) after measurement of the amplitude dependence of the internal friction up to $\gamma_{\max} = 6.6 \times 10^{-5}$.

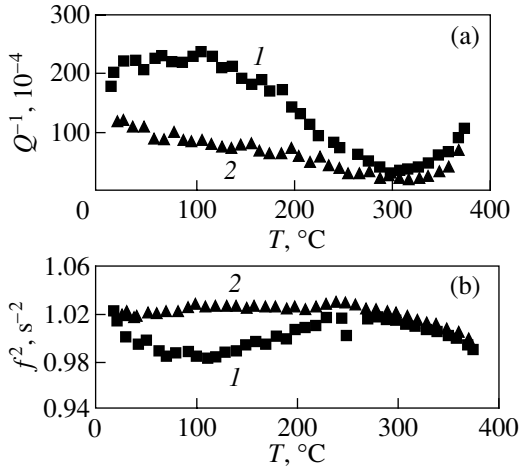

Fig. 2. Temperature dependences of (a) the internal friction and (b) f^2 for the MTBK Be samples after ageing within six months: (*1*) heating and (*2*) cooling.

can be applied to the possible mechanism of this phenomenon. To the best of my knowledge, the periodic increase and decrease in the absorption of the elastic energy have defied description in the framework of currently available models of time dependences of the internal friction that are based on simple notions of

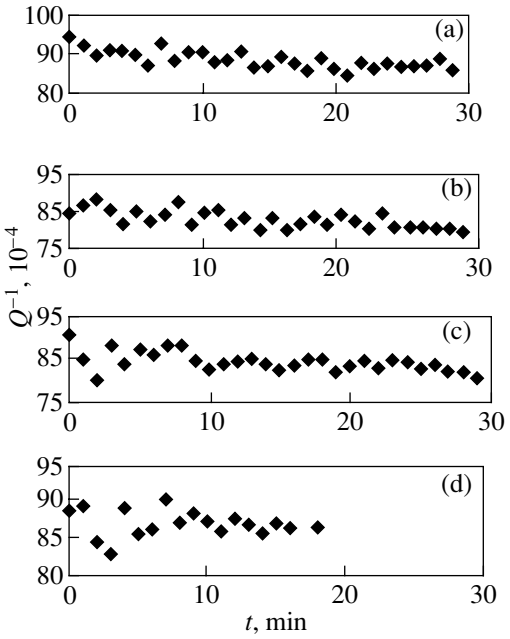

Fig. 3. Time dependences of the internal friction of the MTBK Be samples aged within 12 months at room temperature after cyclic deformation for 5 min at γ_0 = (a) 2.2×10^{-5}, (b) 3.5×10^{-5}, and (c) 6.6×10^{-5} and (d) after measurement of the amplitude dependence of the internal friction up to $\gamma_{max} = 12 \times 10^{-5}$.

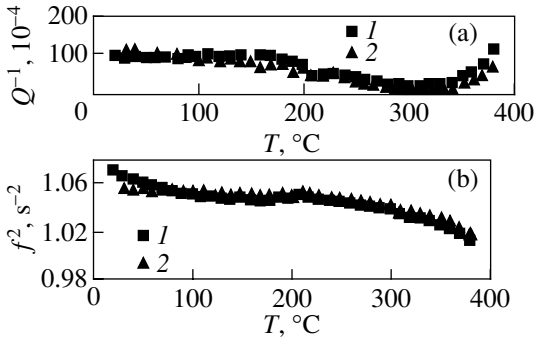

Fig. 4. Temperature dependences of (a) the internal friction and (b) f^2 for the MTBK Be samples aged within 12 months: (*1*) heating and (*2*) cooling.

interaction between dislocations and the dislocation environment. In my opinion, the phenomenon under consideration can be adequately described only in the framework of the concepts regarding the evolution of a dislocation-impurity ensemble and the development of collective and cooperative phenomena in this ensemble [1, 5]. Indeed, consideration of the kinetic nature of the interaction between dislocations and the dislocation environment destabilized under irradiation can provide an explanation for both the loss of spatial stability by a dislocation-impurity ensemble and the formation of inhomogeneities in dislocation-impurity structures [1]. Under external stresses, the evolution of these structures can occur through the generation of inhomogeneous density fluctuations pinning the dislocation of defects. In this case, proper allowance must be made for the fact that the probability of forming the aforementioned fluctuations along the dislocations is substantially larger than the probability of generating similar fluctuations in perpendicular directions, because the mobility of pinning defects along the dislocation pipes considerably exceeds the bulk mobility. This is confirmed by our estimates of the dislocation pipe diffusion coefficients D_d for the basic types of impurities in the MTBK Be material, the comparison of the estimated values with the volume diffusion coefficient D_V, and the binding energy of the dislocation with pinning defects E_b (for example, D_d for Fe in MTBK Be at the experimental temperatures was estimated at 5.29×10^{-13} m^2/s, $D_V = 1.25 \times 10^{-31}$ m^2/s, and $E_b = 0.056$ eV). Moreover, the density fluctuations pinning the dislocation of defects, according to [1, 5], become possible upon the attainment of a critical density. Reasoning from the above considerations, we can explain the absence of oscillations at $\gamma_0 = 1.4 \times 10^{-5}$ immediately after irradiation and their presence in the time dependences of the internal friction after ageing within six months. In actual fact, ageing is attended by the return of some part of the impurities to the dislocations. This is supported by the analysis of the amplitude dependences of the internal friction and the calculation of the binding energy of the dislocation with pinning defects. As a consequence, clearly defined oscillations appear in the time dependences of the internal friction of the aged samples after cyclic deformation for 5 min at $\gamma_0 = 1.4 \times 10^{-5}$ (Fig. 1a). Further ageing brings about an increase in the number of impurities at dislocations and stabilization of the dislocation-impurity system. As a result, the most distinct oscillations manifest themselves only after cyclic deformation for 5 min at $\gamma_0 = 2.2 \times 10^{-5}$, i.e., after the formation of an optimum amount of impurities involved in the dislocations. However, their amplitude and period are substantially less than those observed after ageing within six months. Hence, the stabilization of the system, as a whole, can lead to the fact that the optimum conditions for the generation of oscillations will not be achieved at any strain. This assumption is confirmed to some extent by the first publications concerning the oscillations revealed in the time dependences of the internal friction [2]. Strongin and Yakovishin [2] observed the oscillations in the Al–Ag system at a content of 0.01 wt % Ag after quenching and did not reveal oscillations at any other content of impurities and in the annealed samples. In my opinion, all the foregoing counts in favor of the assumption that the basic conditions of the occurrence of internal friction oscillations are as follows: (i) an optimum amount of impurities in the region of dislocations and (ii) a certain instability of the system due to either the formation of

a substructure or quenching, irradiation, or some other factor. Therefore, under certain conditions, oscillations of the internal friction can be considered to be an indication of the instability of the system.

4. CONCLUSION

Thus, it was demonstrated that the oscillations in time dependences of the internal friction can appear only under at least two conditions: (1) an optimum amount of impurities in the region of dislocations and (2) an instability of the dislocation-impurity system, as a whole, which allows one to assign this phenomenon to the synergetic type.

REFERENCES

1. G. A. Malygin, Usp. Fiz. Nauk **169** (9), 979 (1999).
2. B. G. Strongin and P. A. Yakovishin, Fiz. Khim. Obrab. Mater., No. 4, 123 (1982).
3. A. V. Oleĭnich, N. D. Raranskiĭ, and B. G. Strongin, Metallofiz. Noveĭshie Tekhnol. **16** (4), 47 (1994).
4. A. V. Oleĭnich, B. G. Strongin, N. D. Raranskiĭ, *et al.*, Metallofiz. Noveĭshie Tekhnol. **19** (1), 62 (1997).
5. G. A. Malygin, Fiz. Tverd. Tela (Leningrad) **33** (11), 3267 (1991) [Sov. Phys. Solid State **33**, 1844 (1991)].

Translated by O. Moskalev

Physics of the Solid State, Vol. 44, No. 6, 2002, pp. 1102–1105. Translated from Fizika Tverdogo Tela, Vol. 44, No. 6, 2002, pp. 1057–1059.

DEFECTS, DISLOCATIONS, AND PHYSICS OF STRENGTH

Effect of Dislocation Distribution in Twin Boundaries on the Nucleation of Microcracks at the Twin Tip

V. A. Fedorov, V. A. Kuranova, Yu. I. Tyalin, and S. N. Pluzhnikov

Derzhavin State University, Tambov, 392622 Russia

e-mail: feodorov@tsu.tmb.ru

Received September 4, 2001

Abstract—The effect of dislocation distribution in the boundaries of an arrested twin on the nucleation of microcracks at its tip is investigated. The twin is simulated by a double step pileup (cluster) of twinning dislocations located in adjacent slip planes. The equilibrium equations for dislocations are solved numerically. Clusters with different total numbers of dislocations and with different ratios of the numbers of dislocations at the upper and lower twin boundaries are considered. The formation of microcracks as a result of coalescence of head dislocations according to the force and thermally activated mechanisms is analyzed. The equilibrium configurations of a single twin boundary and of the twin are calculated. It is found that the condition for microcrack formation at the twin tip considerably depends on the ratio of the numbers of dislocations in twin boundaries. In the limit, this condition coincides with the condition of crack formation at the tip of a single twin boundary with the same total number of dislocations. It is shown that thermally activated formation of a microrack corresponds to lower values of the critical stress. © *2002 MAIK "Nauka/Interperiodica".*

It was shown in [1, 2] that the actual structure of dislocation pileups may considerably change the conditions for the formation of microcracks in them. From this point of view, twins and twin boundaries wherein each twinning dislocation moves in its own slip plane are of special interest. Such defects are usually simulated by step dislocation clusters [3, 4], the dislocations being distributed in pairs symmetrically relative to the twinning plane passing through the twin tip. Obviously, in the general case, twin boundaries may contain different numbers of dislocations. In the present work, we consider the conditions for the initiation of microcracks at the tip of an arrested twin with different ratios of twinning dislocations in its boundaries in calcite.

The boundary of a twin is simulated by a solitary step pileup of twinning dislocations, each of which is displaced relative to a neighboring dislocation by a distance equal to the separation h between the planes (3.82×10^{-10} m). The twin is represented by a double step pileup of twinning dislocations. We assume that the head dislocation is fixed at a point with coordinates $x = y = 0$ and belongs simultaneously to the upper and lower boundaries. The dislocation pileup is pressed against the head dislocation by an external stress τ.

Let us consider twin boundaries containing different numbers (n_1, n_2) of dislocations. Formally, this means that each boundary must be analyzed separately and the equilibrium equations for dislocations must be written for each boundary. The equilibrium equations for the upper boundary with n_1 dislocations have the form

$$\sum_{\substack{j=1,\\ j\neq i}}^{n_1}(x_i-x_j)\frac{(x_i-x_j)^2-(y_i-y_j)^2}{[(x_i-x_j)^2+(y_i-y_j)^2]^2}$$

$$+\sum_{j=2}^{n_2}(x_i-x_j)\frac{(x_i-x_j)^2-(y_i+y_j)^2}{[(x_i-x_j)^2+(y_i+y_j)^2]^2} \qquad (1)$$

$$-\frac{\tau}{Db}=0,\quad i=2,3,\ldots,n,$$

where x_i and y_i are the coordinates of the ith dislocation, $D = G/[2\pi(1-\nu)]$, G is the shear modulus (3.2×10^{10} N/m^2), ν is the Poisson ratio ($\nu = 0.3$), and b is the Burgers vector for twinning dislocations (1.269×10^{-10} m). The first and second terms describe the interaction of the ith dislocation with dislocations from the upper and lower boundary, respectively.

The equations for dislocations in the lower boundary have a similar form,

$$\sum_{\substack{j=1,\\ j\neq i}}^{n_2}(x_i-x_j)\frac{(x_i-x_j)^2-(y_i-y_j)^2}{[(x_i-x_j)^2+(y_i-y_j)^2]^2}$$

1063-7834/02/4406-1102$22.00 © 2002 MAIK "Nauka/Interperiodica"

$$+\sum_{j=2}^{n_1}(x_i-x_j)\frac{(x_i-x_j)^2-(y_i+y_j)^2}{[(x_i-x_j)^2+(y_i+y_j)^2]^2} \qquad (2)$$

$$-\frac{\tau}{Db}=0,\quad i=2,3,\ldots,n.$$

Thus, we obtain a system of nonlinear equations (1) and (2) with the number of unknowns $n_1 + n_2 - 1$. The numerical solution of Eqs. (1) and (2) by the method of successive approximations [5] gives the equilibrium coordinates x_i of dislocations, which are functions of the elastic constants G and b, of the numbers of dislocations n_1 and n_2, and of the external stress τ. From the standpoint of microcrack initiation, the distance d between the head dislocations whose coalescence leads to the formation of a crack nucleus is of interest to us. The mechanisms of coalescence of head dislocations can be divided into force mechanisms and thermally activated mechanisms.

In a planar pileup, the coalescence of head dislocations occurs when they approach each other to a distance $d = b$ [6]. In a step pileup, head dislocations experience coalescence after approaching each other to the critical distance $d_{c1} = 2.41h$. The force with which the first dislocation repels the second one attains its maximum value in this case. The subsequent approaching of dislocations until they merge into one occurs without an increase in the external stress. Consequently, we can assume that the critical stresses τ_{cr} required for the nucleation of cracks are equal to the stresses required for head dislocations approaching each other to a distance d_{cr}. This criterion will be referred to as the force criterion.

In the case of thermally activated nucleation of microcracks, we assume that head dislocations experience coalescence not simultaneously over their entire length, but initially only over a short segment as a result of ejection of a double kink by the second dislocation of the cluster due to thermal fluctuations. A microcrack nucleus of length l that is formed upon the coalescence of this kink and the first dislocation subsequently expands over the entire dislocation length. It was shown in [7] that the energy barrier for the crack nucleation is completely determined by the first stage of the process, viz., the formation of a double kink. An expression for the energy W of the double-kink formation is given in [3].

In order to determine the critical external stress τ_{cr}, we calculated the dependence of W on τ and determined the value of τ for which the value of W coincides with a preset value. In the case under investigation, this energy was chosen equal to 1 eV, which is comparable to the minimum height of the potential barrier for the formation of a double kink and amounts to a value of the order of Gb^3 [8].

In our calculations, we analyzed a symmetric twin (ST) with equal numbers of dislocations in the boundaries, an asymmetric twin (AT) with different numbers of dislocations in the boundaries, and a single twin boundary (TB). We considered pileups with different total numbers n of dislocations and with different ratios of the numbers n_1 and n_2 of dislocations in the upper and lower boundaries of the AT. It should be noted that dislocations in the ST boundaries are arranged in pairs (Fig. 1). In other words, the values of coordinates x_i for the ith dislocations of the upper and lower twin boundaries coincide, while the coordinates y_i are equal in magnitude but have opposite signs. This result is obvious and is a consequence of the interaction of dislocations moving in parallel slip planes. If we assume that one of the dislocations is stationary, the equilibrium state of the other dislocation corresponds to two positions, namely, $x = h$ and $x = 0$, in which the force of interaction is equal to zero, the stable position being the one with $x = 0$. In the case of deviation from this position, a moving dislocation will experience the action of a force returning it to the equilibrium position.

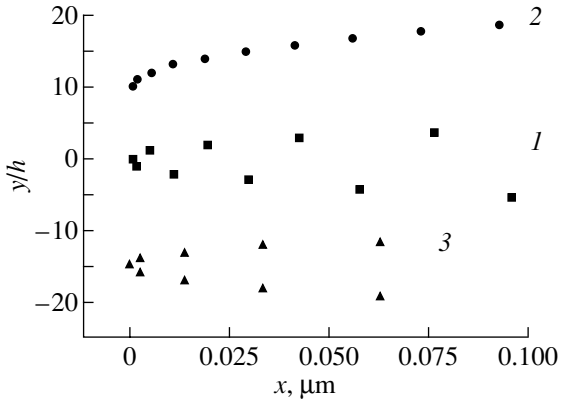

Fig. 1. Distribution of dislocations at the tip of defects: (*1*) AT; (*2*) TB, and (*3*) ST.

If the equality of the numbers of dislocations in the ST boundaries is violated, i.e., the ST is converted into an AT, the arrangement of dislocations changes considerably (Fig. 1). However, pairwise arrangement of dislocations in the AT boundaries is also encountered, but the total number of such pairs does not exceed a few percent. We denote by d the distance between the head and second dislocations in the twin boundary. The values of d for the upper and lower AT boundaries are the smaller, the larger the number of dislocations in the boundary, and the values of d for both AD boundaries may differ by a factor of several units for an insignificant difference between n_1 and n_2. For example, for $n_1 = 10$ and $n_2 = 12$, the ratio $d_1/d_2 \approx 4$. Moreover, the smaller of d_1 and d_2 turns out to be much smaller than the value of d for an ST. This can be clearly seen from Fig. 1, which shows the distribution of dislocations directly at the cluster tips. If we take into account the fact that it is the value of d that determines the crack nucleation stresses, we can expect the crack formation conditions to change at the AT tip.

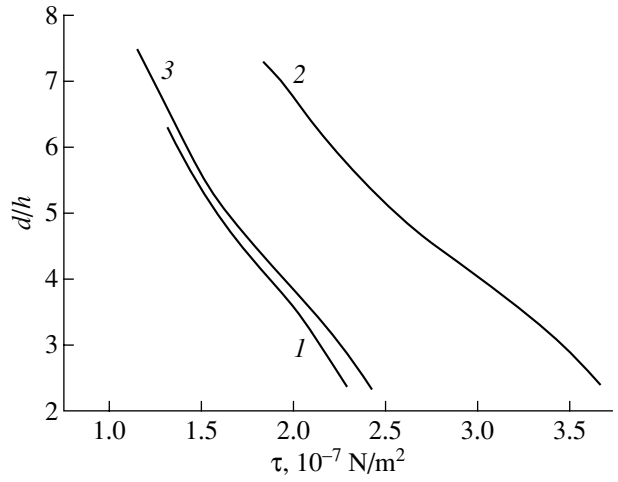

Fig. 2. Dependence of the distance between head dislocations on the applied stress for various dislocation clusters: (*1*) TB, $n = 50$; (*2*) ST, $n_1 = n_2 = 25$; and (*3*) AT, $n_1 = 20$, $n_2 = 30$.

It is worth noting that in the distribution of dislocations at the tip of a twin, the values of coordinates of dislocations at the AT boundaries are close to the values of the dislocation coordinates in a single boundary with the total number of dislocations $n = n_1 + n_2$. This result will become clear if we consider the expression for the stresses exerted by the jth dislocation on the ith dislocation,

$$\tau_{ij} = \frac{Gb}{2\pi(1-\nu)}\frac{(x_i - x_j)[(x_i^2 - x_j^2) - (y_i^2 - y_j^2)]}{[(x_i - x_j)^2 + (y_i - y_j)^2]^2}. \quad (3)$$

For adjacent dislocations, we have $y_i - y_j = h$ and $x_i - x_j$ is comparable with h only for dislocations adjoining the head of the pileup ($x_2 - x_1 = 2.41h$ in the case of coalescence). For the remaining dislocations, with larger numbers, we have $x_i - x_j \gg h$. For example, $(x_i - x_j)/h > 10$ for $n > 10$; i.e., in this case, adjacent dislocations and, even more so, dislocations with a larger difference in the indices interact as if they are located in the same plane. Indeed, we can disregard, to a high degree of accuracy, the terms $(y_i - y_j)^2$ in Eq. (3). In other words, the tail part in step clusters can be replaced by a planar configuration of dislocations and the shape of the defect tip, as well as the coalescence conditions for head dislocations, is determined by the interaction of a small number of head dislocations for which $\Delta y = |y_i - y_j|$ is comparable to $\Delta x = |x_i - x_j|$.

Figure 2 shows the calculated dependences of d on the external stress τ for three types of clusters: TB, ST, and AT. It can be seen that the dependences for TB and AT are quite similar. This is a consequence of the above-mentioned coincidence of equilibrium positions of dislocations in TB and in AT boundaries; i.e., TB can be regarded as a limiting case of AT for which $n_1 \gg n_2$ (or $n_2 \gg n_1$).

By comparing the values of τ for AT and ST (with equal total numbers of dislocations in the boundaries), we find that, for $d = 2.41h$, the crack nucleation according to the force mechanism in AT takes place at much lower stresses (by a factor of approximately 1.7).

We tried to find out whether the obtained result depends on the number of dislocations in the clusters under investigation. If we plot the dependence $d = f(\tau)$ (or of W on τ) in relative units $d = f(\tau n/D)$, the obtained points corresponding to different values of n for the same cluster fit into the same curve to a high degree of accuracy. By way of example, Fig. 3 shows a curve describing such a dependence for an AT. Thus, the results presented in Fig. 2 can be generalized to the case of other values of n by simple renormalization of the critical stress.

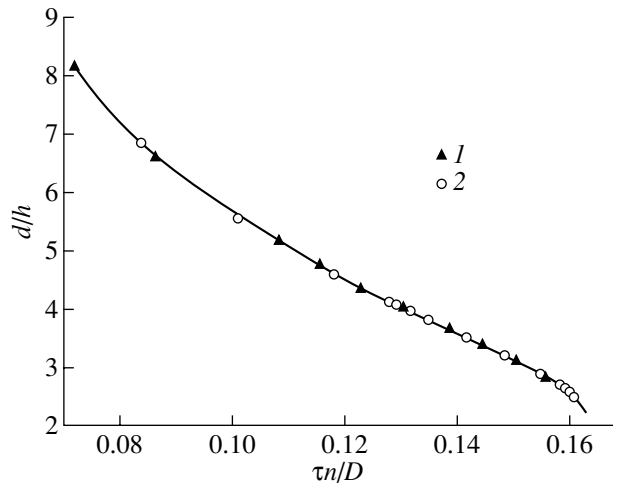

Fig. 3. Dependence of the distance between head dislocations on the applied stress for an AT: (*1*) $n_1 = 10$, $n_2 = 12$; and (*2*) $n_1 = 20$, $n_2 = 30$.

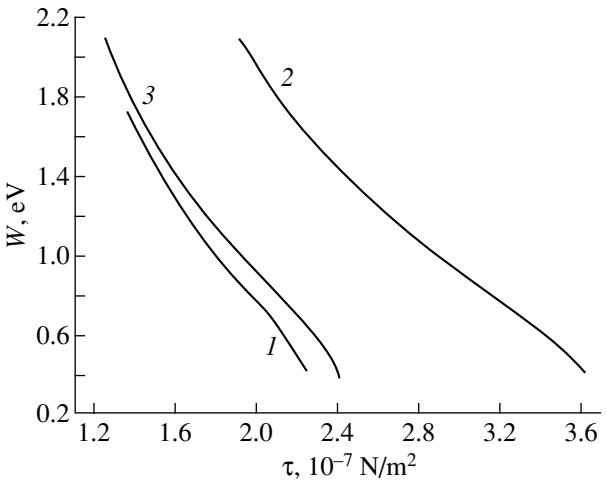

Fig. 4. Dependence of the double-kink energy W on the external stress: (*1*) TB, $n = 50$; (*2*) ST, $n_1 = n_2 = 25$; and (*3*) AT, $n_1 = 20$, $n_2 = 30$.

The calculated activation energy for the crack nucleation is shown in Fig. 4. In comparing these results with the data presented in Fig. 2, we see that the thermally activated nucleation corresponds to lower values of critical stress, but the difference is not large (~25%). The values of double-kink energy amount to ~0.5 eV provided that the force criterion $d = 2.41h$ is satisfied.

REFERENCES

1. V. N. Rybin and Sh. K. Khannanov, Fiz. Tverd. Tela (Leningrad) **11** (4), 1048 (1969) [Sov. Phys. Solid State **11**, 854 (1969)].
2. V. I. Vladimirov and Sh. Kh. Khannanov, Fiz. Met. Metalloved. **31** (4), 838 (1971).
3. V. A. Fedorov and Yu. I. Tyalin, Kristallografiya **26** (4), 775 (1981) [Sov. Phys. Crystallogr. **26**, 439 (1981)].
4. V. A. Fedorov, V. M. Finkel', V. P. Plotnikov, *et al.*, Kristallografiya **33** (5), 1244 (1988) [Sov. Phys. Crystallogr. **33**, 737 (1988)].
5. J. Ortega and W. Rheinboldt, *Iterative Solution of Nonlinear Equations in Several Variables* (McGraw-Hill, New York, 1970; Mir, Moscow, 1975).
6. A. N. Stroh, Adv. Phys. **6** (24), 418 (1957).
7. V. I. Vladimirov, *Physical Nature of Metal Fracture* (Metallurgiya, Moscow, 1984).
8. A. N. Orlov, *Introduction to the Theory of Defects in Crystals* (Vysshaya Shkola, Moscow, 1983).

Translated by N. Wadhwa

Physics of the Solid State, Vol. 44, No. 6, 2002, pp. 1106–1110. Translated from Fizika Tverdogo Tela, Vol. 44, No. 6, 2002, pp. 1060–1063.

MAGNETISM AND FERROELECTRICITY

The Influence of Crystalline Grain Size on the Thermal Stability of the $Er_{0.45}Ho_{0.55}Fe_2$ Compound

Kh. Ya. Mulyukov, I. Z. Sharipov, and G. F. Korznikova

Institute of Metal Superplasticity Problems, Russian Academy of Sciences, ul. Khalturina 39, Ufa, 450001 Bashkortostan, Russia

e-mail: Ilgiz@anrb.ru

Received July 13, 2001

Abstract—The phase composition and the temperature dependence of the magnetization of the $Er_{0.45}Ho_{0.55}Fe_2$ compound in coarse-grained, microcrystalline, and submicrocrystalline states are investigated experimentally. It is found that, upon heating under vacuum, the $Er_{0.45}Ho_{0.55}Fe_2$ microcrystalline powder with a crystalline grain size of ~1 μm undergoes decomposition into pure iron and rare-earth (erbium and holmium) oxides and nitrides at a temperature of 500 K. The changes observed in the phase composition of the microcrystalline powder due to annealing are confirmed by x-ray diffraction analysis. Heating of the $Er_{0.45}Ho_{0.55}Fe_2$ submicrocrystalline sample leads to a partial change in the phase composition. The phase composition of a large crystal (~1 mm in size) remains unchanged upon heating to 1080 K. It is shown that the thermal stability of the $Er_{0.45}Ho_{0.55}Fe_2$ compound depends on the crystalline grain size. © *2002 MAIK "Nauka/Interperiodica".*

1. INTRODUCTION

Earlier investigations into the magnetic properties of Fe–Nd–B submicrocrystalline alloys prepared by crystallization of rapidly quenched amorphous ribbons revealed that pure iron precipitates in the course of annealing [1, 2]. The phase instability of multicomponent compounds has also been observed in other studies. In particular, Vereshchagin *et al.* [3] and Absalyamov and Mulyukov [4] observed transformations of higher metal oxides into lower metal oxides and reduction of metal oxides to pure metal during vacuum annealing of microcrystalline powders. Yermakov [5] described the phase separation upon treatment of alloy powders in a ball mill. In these works, the phase instability is attributed to the influence of severe plastic deformation on the crystal structure. The question now arises as to why a similar phenomenon is observed during annealing of a multicomponent compound with a submicrocrystalline structure formed through crystallization of the amorphous alloy.

With the aim of obtaining additional information on the phase instability of multicomponent compounds, we analyzed the phase composition and the temperature dependence of the magnetization of the $Er_{0.45}Ho_{0.55}Fe_2$ compound in coarse-grained, microcrystalline, and submicrocrystalline states. The choice of the $Er_{0.45}Ho_{0.55}Fe_2$ compound as the object of investigation was made for the following reasons: (i) this compound is a ferrimagnet containing iron, and (ii) the temperature dependence of the magnetization can serve as a highly sensitive indicator of changes in the phase composition of the studied sample.

2. SAMPLE PREPARATION AND EXPERIMENTAL TECHNIQUE

A coarse-grained sample in the form of a parallelepiped with a maximum linear size of 1 mm was cut from an ingot of the $Er_{0.45}Ho_{0.55}Fe_2$ compound. A sample with a microcrystalline structure was prepared by grinding in an agate mortar because of the high brittleness of the chosen material. In order to ensure against oxidation, the powder was ground in ethanol. The microcrystalline powder with a particle size of ~1 μm was separated through sedimentation. The size of powder particles was determined on a JSM-840 scanning electron microscope. Samples with a submicrocrystalline structure were obtained under the conditions of severe plastic deformation with the use of Bridgman anvils under a pressure of 10 GPa at room temperature.

The temperature dependence of the magnetization of the samples under investigation was measured using a vacuum automated magnetic balance [6] in the temperature range from 80 to 1080 K. The phase composition of the samples was analyzed on a DRON-3M automated x-ray diffractometer with computer processing of the results obtained.

The microstructure of the submicrocrystalline samples was examined using a JEM 2000EX transmission electron microscope.

3. EXPERIMENTAL RESULTS

Figure 1 shows the temperature dependence of the magnetization $\sigma(T)$ for a coarse-grained sample. It can be seen from Fig. 1 that, upon heating, the magnetization of the sample decreases drastically and becomes

1063-7834/02/4406-1106$22.00

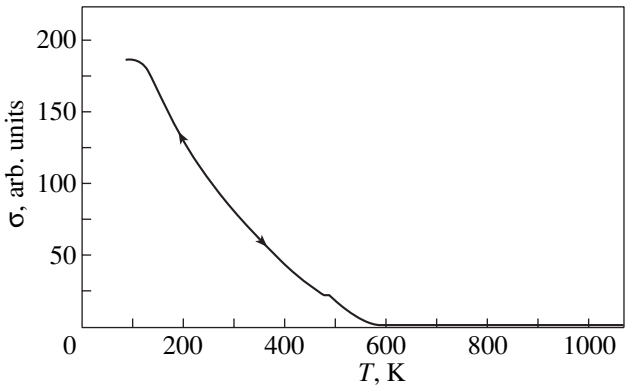

Fig. 1. Temperature dependence of the magnetization of a coarse-grained sample.

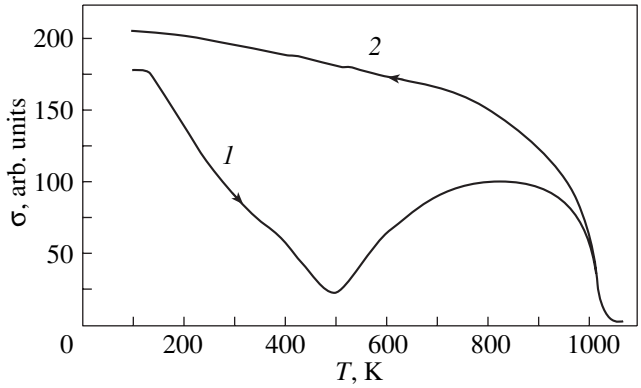

Fig. 2. Temperature dependence of the magnetization of a microcrystalline powder.

equal to zero at 570 K. This dependence is characterized by an abrupt transition from a ferrimagnetic state to a paramagnetic state. The curves $\sigma(T)$ measured during heating and cooling of the sample are virtually identical. This confirms the assumption that the phase composition of the coarse-grained sample remains stable up to 1080 K.

The temperature dependence of the magnetization $\sigma(T)$ for a microcrystalline sample is depicted in Fig. 2. It is seen from this figure that the dependence $\sigma(T)$ obtained upon heating of the microcrystalline sample (Fig. 2, curve *1*) differs substantially from the heating curve of the coarse-grained sample (Fig. 1). As the temperature increases, the magnetization first decreases, as is the case with the coarse-grained sample, but does not reach zero and begins to increase at temperatures above 500 K. With a further increase in the temperature, the magnetization passes through a maximum at 830 K, decreases, and becomes equal to zero at 1033 K. Another feature in the dependence $\sigma(T)$ of the microcrystalline sample is that curve *2*, which was measured during cooling of the sample, differs noticeably from curve *1*, which was recorded during heating. Note that curve *2* is similar to the temperature dependence of the saturation magnetization of pure 3*d* ferromagnets. Moreover, the Curie temperature determined by the extrapolation of the steepest portion in curve *2* to the temperature axis coincides with the reverence Curie point of pure iron.

Figure 3 shows the dependence $\sigma(T)$ for a submicrocrystalline sample upon heating and cooling. In this case also, curve *1*, which was measured during heating of the submicrocrystalline sample to 600 K, coincides with the heating curve for the coarse-grained sample. At higher temperatures, the magnetization of the submicrocrystalline sample increases, passes through a maximum at 950 K, and decreases to zero at 1033 K. It is worth noting that the increase in the magnetization of the submicrocrystalline sample at temperatures above 600 K (Fig. 3, curve *1*) is less pronounced than that of the microcrystalline powder (Fig. 2, curve *1*). Curve *2*, which was measured during cooling of the submicrocrystalline sample (see Fig. 3), does not coincide with the cooling curve of the microcrystalline powder (Fig. 2, curve *2*) and consists of two portions. The low-temperature portion virtually follows the dependence $\sigma(T)$ measured during heating of the sample, whereas the high-temperature portion is similar to the dependence $\sigma(T)$ for pure 3*d* ferromagnets.

The x-ray diffraction pattern of the microcrystalline powder immediately after grinding is displayed in Fig. 4a. All the peaks revealed in the x-ray diffraction pattern correspond to the main phase of the $Er_{0.45}Ho_{0.55}Fe_2$ compound. The x-ray diffraction pattern of the same powder annealed at 1080 K exhibits many additional peaks (Fig. 4b). The new phases formed upon annealing were identified according to the angular positions of additional peaks. It is found that heating of the microcrystalline powder of the studied compound leads to the formation of pure iron and different phases of rare-earth compounds. The additional peaks observed in the x-ray diffraction pattern of the annealed powder (Fig. 4b) correspond to the following phases: Ho_2O_2 and Er_2O_3 (lines *2*, *6*, *15*, *16*, and *19–21*), ErO_2 (lines *3*, *16*, and *21*), Ho_2N_3 (lines *2*, *6*, *15*, *16*, and *19–21*), HoN

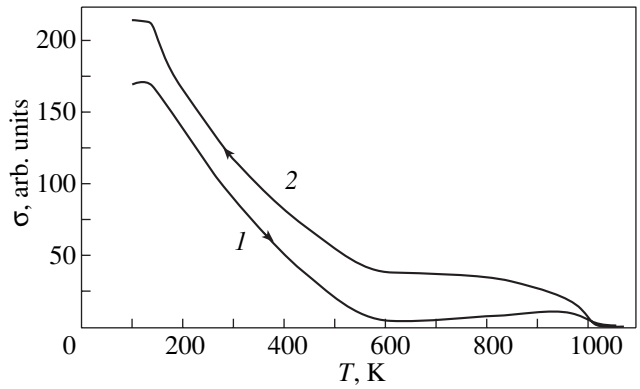

Fig. 3. Temperature dependence of the magnetization of a submicrocrystalline sample.

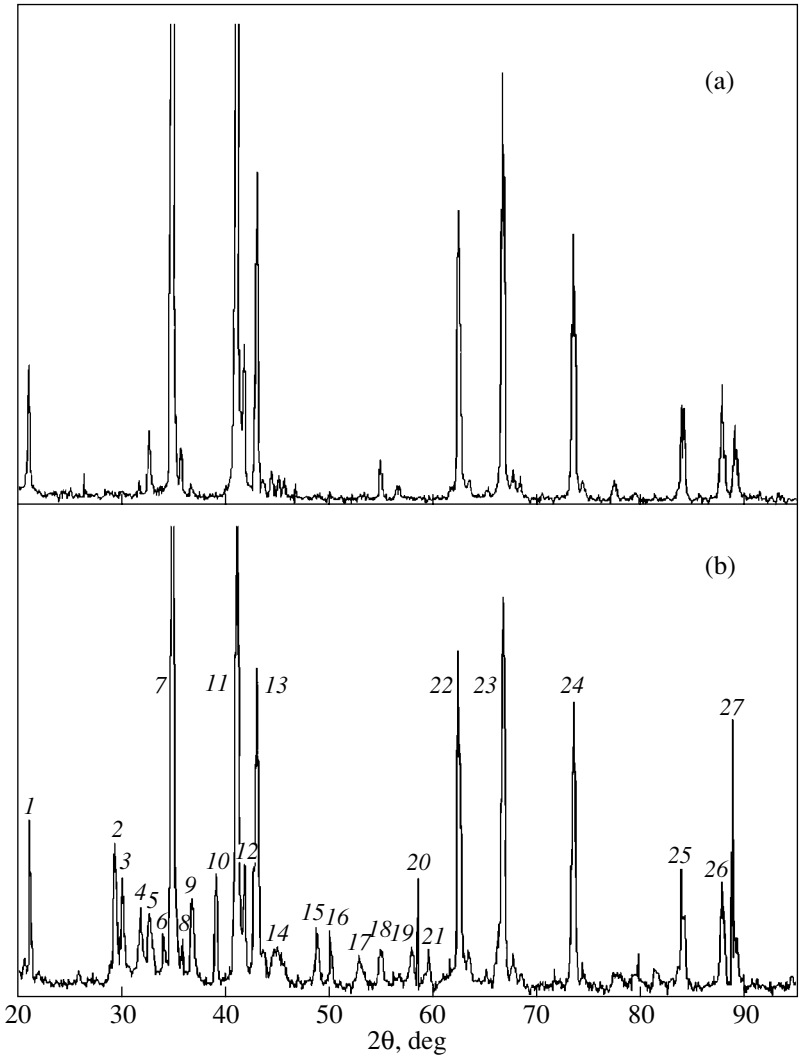

Fig. 4. X-ray powder diffraction pattern of a microcrystalline sample (a) prior to and (b) after heating to 1080 K.

(lines *4* and *9*), Fe_4N (lines *10*, *16*, *19*, and *20*), $HoFe_8$ (line *9*), Er_2Fe_{17} (lines *3*, *9*, *19*, and *20*), and Fe (lines *14* and *16*).

The electron microscopic investigation revealed that the structure of the submicrocrystalline sample consists of crystalline grains with a mean size of less than 100 nm (Fig. 5). As can be seen from the electron microscope image of the submicrocrystalline sample, the crystalline grains have diffuse boundaries and involve cells with a size of the order of 10 nm.

4. DISCUSSION

The experimental results demonstrate that the temperature dependences of the magnetization of samples in different structural states differ significantly. Specifically, upon heating of the microcrystalline and submicrocrystalline samples above 500 K, their magnetization increases and passes through a maximum. This increase in the magnetization can be associated with the precipitation of a new ferromagnetic phase with a high Curie temperature. The curve $\sigma(T)$ measured during cooling of the microcrystalline sample corresponds to the precipitated phase. Judging from this curve, the precipitated phase consists of pure iron, because the temperature at which the magnetization of the sample becomes equal to zero coincides with the Curie point of iron.

In order to confirm the above inference, which was made on the basis of magnetic measurements, the phase composition of the microcrystalline sample was additionally investigated using x-ray powder diffraction. As

was noted above, the diffraction pattern in Fig. 4a corresponds to the main phase of the $Er_{0.45}Ho_{0.55}Fe_2$ alloy. Consequently, the phase composition of the studied compound remains unchanged in the course of grinding.

The x-ray diffraction pattern of the annealed powder exhibits sharp peaks assigned to the new phases (Fig. 4b). It should be noted that this diffraction pattern also contains maxima associated with the main phase; however, no indications of the main phase are revealed in the temperature dependence of the magnetization measured during cooling of the microcrystalline sample below 1080 K. The matter is that x-ray powder diffraction experiments require a sufficiently large amount of the studied compound. For this reason, the sample was prepared from the whole of the ground powder without separation into fractions with different particle sizes. As a consequence, upon heating of the sample intended for x-ray diffraction measurements, the compound undergoes decomposition within small-sized crystalline grains of the powder, whereas the main phase is retained in large-sized crystalline grains. On the other hand, the presence of the maxima associated with the main phase in the x-ray diffraction pattern is convenient for the following reasons: first, these maxima serve as reference points, and, second, they clearly demonstrate that no decomposition of the compound occurs in larger sized particles.

Thus, the magnetic measurements made it possible to reveal only pure iron precipitated upon heating of the microcrystalline sample, whereas x-ray powder diffraction analysis identified both the pure iron phase and other phases formed in the course of decomposition of the studied compound.

This raises the following question: Why does pure iron precipitate during heating of the microcrystalline sample? A close examination of the x-ray diffraction pattern of the annealed microcrystalline sample shows that the diffraction maxima revealed after the annealing are attributed to oxides and nitrides of erbium and holmium in different valent states. Consequently, rare-earth metal ions within a crystalline grain exhibit an increased reactivity and interact with a residual gas (heating was performed under vacuum at a residual pressure of 1.33×10^{-2} Pa). One reason for this reactivity is that the microcrystalline powder possesses a well-developed surface. Hence, rare-earth metals in contact with a residual gas actively interact with oxygen and nitrogen. However, under the same conditions of measurements, similar interactions in the coarse-grained sample are not observed.

For the purpose of elucidating the influence of the crystalline grain size on the reactivity of rare-earth metal ions, we carried out a similar investigation of the sample with a submicrocrystalline structure. Since severe plastic deformation of the material with the use of Bridgman anvils results in the formation of a monolithic sample, the surface area of its contact with a residual gas virtually coincides with that of the coarse-grained sample. However, no indications of oxidation are observed after heating of the coarse-grained sample to 1070 K (the magnetization was measured accurate to within 1%), whereas the heating of the submicrocrystalline sample under the same conditions is accompanied by the decomposition of the studied compound with the precipitation of pure iron in considerable amounts.

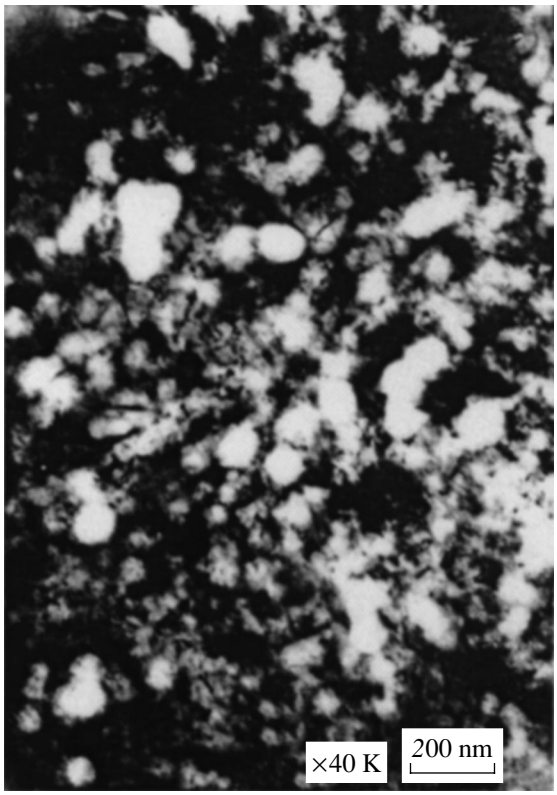

Fig. 5. Electron microscope image of the submicrocrystalline structure of the studied compound.

Analysis of the temperature dependences of the magnetization $\sigma(T)$ (Figs. 2, 3) indicates that, in the submicrocrystalline sample, unlike the microcrystalline sample, the studied compound undergoes partial decomposition. This fact demonstrates the role played by the free surface in the interaction with a residual gas. The partial decomposition of the submicrocrystalline sample can be associated with the specific features of the submicrocrystalline structure, because this structure is characterized by a substantial volume fraction of crystalline grain boundaries and a high density of defects (Fig. 5). It is known that the coefficient of grain boundary diffusion in nanocrystalline materials is several orders of magnitude larger than that in coarse-grained materials [7]. Most likely, it is this circumstance that encourages diffusion of oxygen and nitrogen atoms into the submicrocrystalline sample and

results in the formation of iron and rare-earth metal compounds with oxygen and nitrogen.

5. CONCLUSION

Thus, our investigation has demonstrated that the thermal stability of the $Er_{0.45}Ho_{0.55}Fe_2$ compound depends on the crystalline grain size.

ACKNOWLEDGMENTS

This work was supported by the Russian Foundation for Basic Research (project no. 00-02-17723) and the State Program of Support for Leading Scientific Schools of the Russian Federation (project no. 00-15-99093).

REFERENCES

1. T. Miyazaki, H. Takada, and M. Takahashi, Phys. Status Solidi A **99**, 611 (1987).
2. Kh. Ya. Mulyukov, R. Z. Valiev, G. F. Korznikova, and V. V. Stoljarov, Phys. Status Solidi A **112**, 137 (1989).
3. L. F. Vereshchagin, E. V. Zubova, K. P. Budrina, and G. L. Aparnikov, Dokl. Akad. Nauk SSSR **196** (4), 817 (1971).
4. S. S. Absalyamov and Kh. Ya. Mulyukov, Dokl. Akad. Nauk **375** (4), 469 (2000) [Dokl. Phys. **45**, 657 (2000)].
5. A. Ye. Yermakov, Mater. Sci. Forum **179–181**, 455 (1995).
6. Kh. Ya. Mulyukov, I. Z. Sharipov, and S. S. Absalyamov, Prib. Tekh. Éksp., No. 3, 149 (1998).
7. H. Gleiter, Nanostruct. Mater. **1**, 1 (1992).

Translated by O. Borovik-Romanova

Physics of the Solid State, Vol. 44, No. 6, 2002, pp. 1111–1116. Translated from Fizika Tverdogo Tela, Vol. 44, No. 6, 2002, pp. 1064–1069.

MAGNETISM AND FERROELECTRICITY

Magnetostatic Energy and Stripe Domain Structure in a Ferromagnetic Plate of Finite Width with In-Plane Anisotropy

Yu. V. Gulyaev*, P. E. Zil'berman*, R. J. Elliott, and É. M. Épshteĭn***

** Institute of Radio Engineering and Electronics, Russian Academy of Sciences, pl. Vvedenskogo 1, Fryazino, Moscow oblast, 141120 Russia*

*** University of Oxford, Department of Physics, 1 Keble Road, Oxford, OX1 3NP United Kingdom*

Received July 30, 2001

Abstract—The magnetostatic energy and domain structure (DS) in a long ferromagnetic plate of a finite width with in-plane anisotropy are calculated for the case of the domain magnetization vectors lying in the plane of the plate. The situation where the DS period is much shorter than the width but is considerably larger than the thickness of the plate is analyzed in detail. The equilibrium DS period and the width ratio of two adjacent domains are determined as functions of an external magnetic field parallel to the plane of the plate by minimizing the energy. The DS period is found to be proportional to the plate width and the domain wall energy and inversely proportional to the squared saturation magnetization. While the width of the favorable domains (with the magnetization parallel to the field) grows with increasing field, the unfavorable domains, rather than disappearing completely, form relatively narrow transition regions between the favorable domains, i.e., 360° domain walls. *© 2002 MAIK "Nauka/Interperiodica".*

1. INTRODUCTION

Calculations of the magnetostatic energy of a domain structure (DS) in ferromagnets have a long history dating back to the works of Landau and Lifshitz [1] and Kittel [2]. The most widely used model considered in many monographs and textbooks (see, e.g., [3–5]) is a ferromagnetic plate (film) of finite thickness with the easy axis perpendicular to the large plate face. In this model, the DS is represented by an array of alternating antiparallel magnetized stripes of equal width whose magnetization is perpendicular to the large face. Following [6], we shall call these formations Faraday domains. The width of a Faraday domain is proportional to the square root of the plate thickness. Application of an external magnetic field along the easy axis increases both the domain structure period and the relative width of the favorable domains with the magnetization parallel to the field. By contrast, the width of the unfavorable domains tends to zero. In a sufficiently strong magnetic field, the unfavorable domains disappear and the favorable ones merge to form a single-domain structure. The theory of Faraday domains is presently a subject of renewed interest, which was apparently stimulated by the application of bubble domains in information storage systems.

The recent development of an area of research called spintronics [7] has initiated an intense study of thin metal ferromagnetic films with high magnetization and in-plane anisotropy (with the easy axis lying in the film plane). The magnetization vector of such plates and films should also lie in the film plane, such that the DS, if it forms, depends to a large extent on the magnetic charges on the small-area end faces. The DS does form in such films, which was confirmed experimentally by various methods, for instance, by observing the Faraday effect in visualization media applied to a film [8] and by transmission electron microscopy [9–11]. The most copious information was obtained in studies [9–11], which reported on the observation of a DS with nearly parallel stripes having curved walls. The stripe width was on the order of a few microns and tens of microns, with the magnetization lying in the film plane.

The theory of such Cotton domains (using the terminology of [6]) has not been well elaborated, which impedes experimental interpretation. The experimentally established properties of Cotton domains contrast with those of Faraday domains. At the same time, while the existing theories (see, e.g., [6, 12]) provide a general basis for analysis, they are not sufficient to interpret these differences directly. Their interpretation requires further progress in theory; this work is an attempt along these lines.

We will show that the dependence of domain width on the geometric parameters of the plate, magnetization, and external magnetic field changes its character in comparison to the behavior described in [2–5]. In particular, unfavorable domains, rather than disappearing with increasing field, form transition layers between the favorable domains, which may be treated as 360° domain walls. The formation of such walls was reported in experimental studies [9, 11].

1063-7834/02/4406-1111$22.00

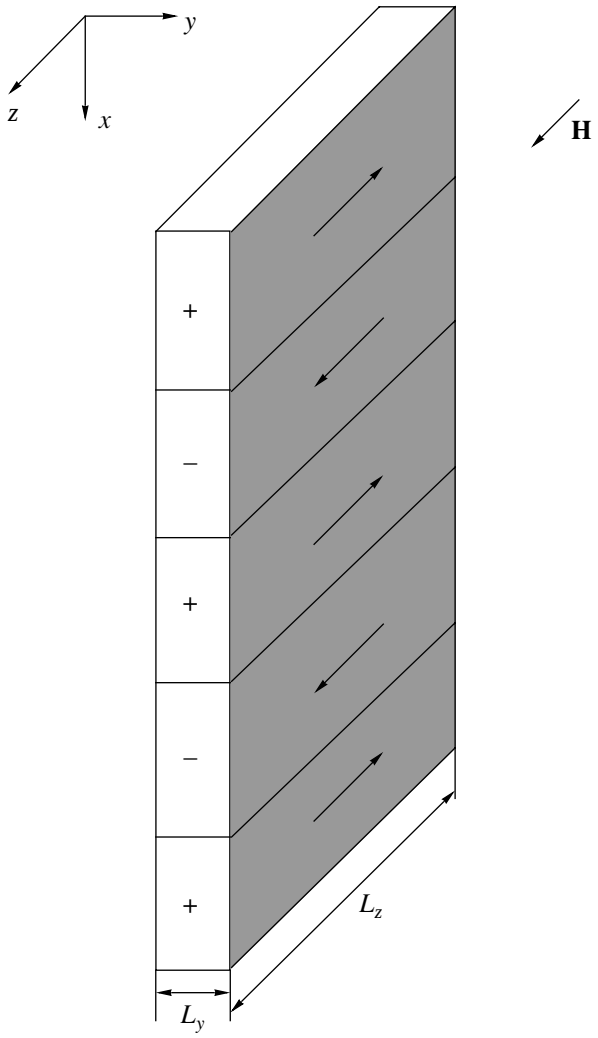

Fig. 1. Ferromagnetic plate with a domain structure. The arrows specify the direction of the magnetization vectors in domains and the external magnetic field **H**. On the end face, the signs of the surface magnetic charges are specified. Also shown are the coordinate axes and the plate width L_y and thickness L_z.

In this work, we make some simplifying assumptions. In particular, while the plate is of finite thickness, the plate length is assumed to be infinite in this stage of consideration. We also assume that the plate's easy axis lies in the large face and is perpendicular to the end faces. We neglect the magnetic flux closing in the plate, i.e., the effect of closure domains [1, 12]. This neglect rests on the following grounds. First, as will be shown later, the DS period can be substantially shorter than the plate width, such that the contribution due to the closure domains to the magnetostatic energy will not be overly large. Second, an external magnetic field destroys closure domains. In this situation, a periodic DS forms in the plate. The geometry of the plate and of the DS is shown in Fig. 1.

2. MAGNETOSTATIC ENERGY

We assume the plate to occupy the region $-\infty < x < \infty$, $-\frac{L_y}{2} \le y \le \frac{L_y}{2}$, $-\frac{L_z}{2} \le z \le \frac{L_z}{2}$ in space (Fig. 1). The DS is periodic along the x axis, and the magnetization in the domains is parallel or antiparallel to the z axis.

The magnetostatic potential $\varphi(x, y, z)$ is described by the Poisson equation

$$\frac{\partial^2\varphi}{\partial x^2} + \frac{\partial^2\varphi}{\partial y^2} + \frac{\partial^2\varphi}{\partial z^2} = -4\pi\rho(x, y, z), \tag{1}$$

where

$$\rho(x, y, z) = \sigma(x) f(y)\left[\delta\left(z - \frac{L_z}{2}\right) - \delta\left(z + \frac{L_z}{2}\right)\right], \tag{2}$$

$$f(y) = \begin{cases} 1, & |y| \le \dfrac{L_y}{2} \\ 0, & |y| > \dfrac{L_y}{2}, \end{cases} \tag{3}$$

and $\sigma(x)$ is the surface density of magnetic charges on the $z = L_z/2$ plane, which is a periodic function of period W (we do not specify its explicit form in this stage). It is these charges that generate the magnetostatic field φ and increase the magnetostatic energy. The DS formation is a consequence of the energy minimization requirement. To calculate the energy and the DS, one has to solve Eq. (1). In doing this, we do not impose any constraints on L_y and L_z.

A solution to Eq. (1) has the form

$$\begin{aligned}\varphi(x, y, z) &= \int_{-\infty}^{\infty} dx' \int_{-\infty}^{\infty} dy' \int_{-\infty}^{\infty} dz' \frac{\rho(x', y', z')}{\sqrt{(x-x')^2 + (y-y')^2 + (z-z')^2}} \\ &= \int_{-\infty}^{\infty} dx' \int_{-\frac{L_y}{2}}^{\frac{L_y}{2}} dy' \sigma(x') \left[\frac{1}{\sqrt{(x-x')^2 + (y-y')^2 + \left(z - \frac{L_z}{2}\right)^2}}\right. \\ &\quad \left. - \frac{1}{\sqrt{(x-x')^2 + (y-y')^2 + \left(z + \frac{L_z}{2}\right)^2}}\right].\end{aligned} \tag{4}$$

Expanding $\sigma(x)$ in a Fourier series

$$\sigma(x) = \sum_{n=-\infty}^{\infty} \sigma_n e^{inkx}, \quad k = \frac{2\pi}{W}, \tag{5}$$

substituting Eq. (5) into Eq. (4), and integrating over x', we obtain, after some manipulations,

$$\varphi(x, y, z) = \int_{-\frac{L_y}{2}}^{\frac{L_y}{2}} dy' \left\{ \sigma_0 \ln \frac{(y-y')^2 + \left(z + \frac{L_z}{2}\right)^2}{(y-y')^2 + \left(z - \frac{L_z}{2}\right)^2} + 2\sum_{n=1}^{\infty} (\sigma_n e^{inkx} + \sigma_{-n} e^{-inkx}) \times \left[K_0\left(nk\sqrt{(y-y')^2 + \left(z - \frac{L_z}{2}\right)^2}\right) - K_0\left(nk\sqrt{(y-y')^2 + \left(z + \frac{L_z}{2}\right)^2}\right)\right] \right\}, \quad (6)$$

where K_0 is the McDonald function (modified Bessel function of the second kind).

Knowing the potential φ and the surface magnetic-charge density σ, we can calculate the magnetostatic energy. By definition, this energy per unit volume of the plate can be written as

$$E_m = \frac{1}{2WL_yL_z}\int_0^W dx\sigma(x) \times \int_{-\frac{L_y}{2}}^{\frac{L_y}{2}} dy\left[\varphi\left(x, y, \frac{L_z}{2}\right) - \varphi\left(x, y, -\frac{L_z}{2}\right)\right]. \quad (7)$$

Substituting Eqs. (5) and (6) into Eq. (7), we obtain for σ and φ

$$E_M = \frac{2}{WL_yL_z}\int_0^W dx\sigma(x)\int_0^{L_y} d\eta(L_y - \eta) \times \left\{ \sigma_0 \ln\frac{\eta^2 + L_z^2}{\eta^2} + 2\sum_{n=1}^{\infty}(\sigma_n e^{inkx} + \sigma_{-n}e^{-inlx}) \times [K_0(nk\eta) - K_0(nk\sqrt{\eta^2 + L_z^2})] \right\}. \quad (8)$$

Using the relations

$$\frac{1}{W}\int_0^W \sigma(x)e^{-inkx}dx = \sigma_n, \quad \sigma_{-n} = \sigma_n^*,$$

we perform integration over x in Eq. (8) and finally obtain

$$E_M = \frac{2}{L_yL_z}\int_0^{L_y} d\eta(L_y - \eta)\left\{ |\sigma_0|^2 \ln\frac{\eta^2 + L_z^2}{\eta^2} + 4\sum_{n=1}^{\infty}|\sigma_n|^2[K_0(nk\eta) - K_0(nk\sqrt{\eta^2 + L_z^2})] \right\}. \quad (9)$$

This is the equation for the average magnetostatic energy density we have been looking for; this expression is valid for arbitrary ratios of the lengths L_y, L_z, and W ($W = 2\pi/k$).

First, we consider how this relation behaves in the known limiting cases. The limit of $L_y \longrightarrow \infty$, i.e., $L_y \gg L_z$ and $L_y \gg W$, is considered. We also assume that $L_z \gg W$. It is these assumptions that were made in [13] in the calculation of the energy E_M. This limiting case corresponds essentially to a plate in which the domain magnetization vectors are perpendicular to the large face, i.e., to a plate containing Faraday domains. In this case, the second of the McDonald functions in Eq. (9) is exponentially small. We obtain

$$E_M = \frac{2}{L_yL_z}\left\{ |\sigma_0|^2 \left[\frac{1}{2}L_y^2 \ln\left(1 + \frac{L_z^2}{L_y^2}\right) - \frac{1}{2}L_z^2 \ln\left(\frac{L_y^2}{L_z^2} + 1\right) + 2L_yL_z \arctan\frac{L_y}{L_z}\right] + 4\sum_{n=1}^{\infty}|\sigma_n|^2 \int_0^{L_y}(L_y - \eta)K_0(nk\eta)d\eta \right\}$$
$$\approx 2\pi|\sigma_0|^2 + \frac{8}{L_yL_z}\sum_{n=1}^{\infty}|\sigma_n|^2\left[\frac{L_y}{nk}\int_0^{\infty}K_0(x)dx - \frac{1}{n^2k^2}\int_0^{\infty}xK_0(x)dx\right] \approx 2\pi|\sigma_0|^2 + \frac{2W}{L_z}\sum_{n=1}^{\infty}\frac{1}{n}|\sigma_n|^2, \quad (10)$$

which coincides with [13], Eq. (17).

Now we consider another limiting case, namely, that of a long thin rod ($L_y \ll W$, $L_z \ll W$). In this case,

$$K_0(nk\eta) - K_0(nk\sqrt{\eta^2 + L^2}) \approx \frac{1}{2}\ln\frac{\eta^2 + L_z^2}{\eta^2},$$

such that

$$E_M = \frac{2}{L_y L_z}\left(|\sigma_0|^2 + 2\sum_{n=1}^{\infty}|\sigma_n|^2\right) \times \int_0^{L_y} d\eta (L_y - \eta)\ln\frac{\eta^2 + L_z^2}{\eta^2}. \quad (11)$$

According to Parseval's theorem,

$$|\sigma_0|^2 + 2\sum_{n=1}^{\infty}|\sigma_n|^2 = \frac{1}{W}\int_0^W [\sigma(x)]^2 dx.$$

If the plate contains a stripe DS, $\sigma(x)$ takes on only two values, $+M_0$ and $-M_0$, where M_0 is the absolute value of magnetization in a domain. Therefore, $[\sigma(x)]^2 = M_0^2$. Thus, the presence or absence of a DS does not affect the magnetostatic energy in any way. The latter statement implies that a DS does not originate at all, because its formation would not bring about a decrease in energy.

We turn now to the case of most interest to us (Fig. 1), namely, $L_z \gg W \gg L_y$. This relation corresponds to a thin ferromagnetic plate in which the domain magnetization vectors are parallel to the large face. In this case, Eq. (9) assumes the form

$$E_M = \frac{2L_y}{L_z}\left\{|\sigma_0|^2\left(\ln\frac{L_z}{L_y} + \frac{3}{2}\right) - 2\sum_{n=1}^{\infty}|\sigma_n|^2\left[\ln(nkL_y) - \ln 2 - \frac{3}{2} + C\right]\right\}, \quad (12)$$

where $C = 0.5772\ldots$ is Euler's constant.

3. DOMAIN STRUCTURE

We consider the periodic stripe DS with a period W shown in Fig. 1; the domain width is w_+ and w_- for the domains with the magnetization oriented parallel and antiparallel to the z axis, respectively. The relation between the widths of these domains can be conveniently characterized by the parameter $\xi \equiv w_+/W$ with $W = w_+ + w_-$.

For the stripe DS of interest, we can write

$$|\sigma_0|^2 = M_0^2(2\xi - 1)^2, \quad (13)$$

$$|\sigma_n|^2 = 2\left(\frac{M_0}{\pi n}\right)^2(1 - \cos 2\pi n\xi). \quad (14)$$

Substituting these relations into Eq. (12) for the magnetostatic energy yields

$$E_M = \frac{2L_y}{L_z}M_0^2\left\{(2\xi - 1)^2\left(\ln\frac{\pi L_z}{W} + C\right) - \ln\frac{\pi L_y}{W} - C + \frac{3}{2} - \frac{4}{\pi^2}\sum_{n=1}^{\infty}\frac{\ln n}{n^2}(1 - \cos 2\pi n\xi)\right\}. \quad (15)$$

The value $\xi = 1/2$ corresponds to the minimum of the $E_M(\xi, W)$ function for any W, as should be expected from physical considerations.

We turn now to calculating the equilibrium DS period W_0. To find this period, we have to add to E_M the domain wall energy

$$E_D = \frac{2\gamma}{W}, \quad (16)$$

where γ is the energy per unit domain wall area (the factor 2 appears, because there are two domain walls per period W). As for the anisotropy energy, it should be noted that the magnetization vectors in domains of both types and the easy axis (z axis) are collinear (Fig. 1). Therefore, the anisotropy energy does not change in a DS rearrangement and does not affect the domain parameters; therefore, we disregard this energy in the further calculation. The equilibrium period W_0 is found from the condition

$$\frac{\partial(E_M + E_D)}{\partial W} = 0, \quad (17)$$

where one should substitute the equilibrium value $\xi = 1/2$. We obtain

$$W_0 = \frac{\gamma L_z}{M_0^2 L_y}. \quad (18)$$

4. EFFECT OF AN EXTERNAL MAGNETIC FIELD

In the presence of an external magnetic field **H** parallel to the easy axis, the contributions of Eqs. (15) and (16) to the magnetic energy should be complemented by the Zeeman energy

$$E_H = -HM_0(2\xi - 1). \quad (19)$$

The DS is determined now by minimizing the sum $E_M + E_D + E_H$ with respect to variations in ξ and W. One should bear in mind that E_D does not depend on ξ and E_H is independent of W. The equilibrium value of the ξ parameter should no longer be equal to 1/2, because the favorable domains expand and the unfavorable ones shrink. While Eq. (17) is valid for the calculation of the equilibrium DS period in the presence of an external magnetic field, the ξ parameter in it can now assume

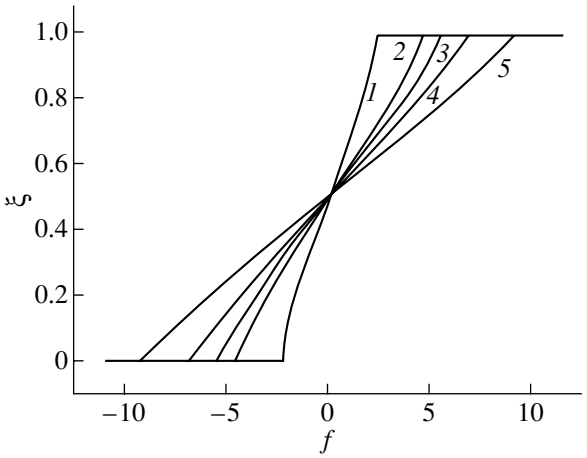

Fig. 2. Relative domain width $\xi = w_+/W$ plotted vs. dimensionless magnetic field $f = (L_z/4L_y)(H/M_0)$ for different values of the ratio $R = 2L_z/W_0$: (*1*) 10, (*2*) 100, (*3*) 250, (*4*) 1000, and (*5*) 10000.

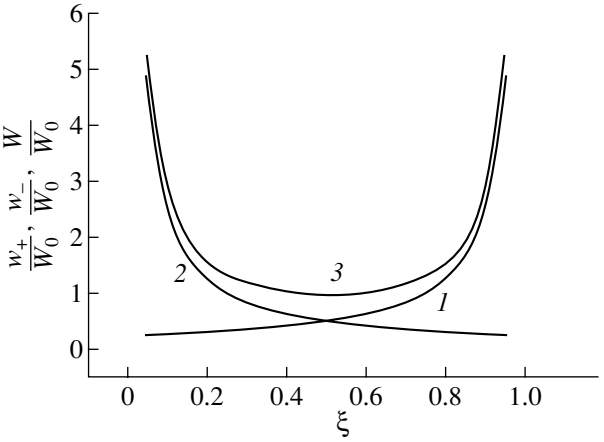

Fig. 3. Domain widths w_+ and w_- and domain structure period $W = (w_+ + w_-)$ plotted vs. parameter ξ: (*1*) w_+/W_0, (*2*) w_-/W_0, and (*3*) W/W_0.

any value in the interval $0 < \xi < 1$. Solving this equation for the DS period as a function of the parameter ξ yields

$$W(\xi) = \frac{W_0}{4\xi(1-\xi)}, \tag{20}$$

where W_0 is given by Eq. (18). The period grows without limit as $\xi \longrightarrow 0$ and $\xi \longrightarrow 1$; however, the condition $W \ll L_z$ we have imposed forces us to restrict the analysis to a region of values not very close to the above boundaries in which the condition $\xi(1-\xi) \gg W_0/4L_z$ is met.

After the substitution of Eq. (20) and summation over n [14], the derivative $\frac{\partial E_M}{\partial \xi}$ becomes

$$\frac{\partial E_M}{\partial \xi} = \frac{8L_y}{L_z} M_0^2 f(\xi),$$

$$f(\xi) = (2\xi - 1)\ln\left(\frac{2L_z}{W_0}\xi(1-\xi)\right) \tag{21}$$

$$- \ln\left(\frac{1}{\pi}\sin\pi\xi\right) - 2\pi\Gamma(\xi).$$

Equation $\frac{\partial(E_M + E_H)}{\partial \xi} = 0$ yields a relation for determination of the equilibrium value of ξ,

$$f(\xi) = \frac{L_z H}{4L_y M_0}. \tag{22}$$

Figure 2 plots the reciprocal function describing the dependence of ξ on H for various values of the ratio of the plate width to the equilibrium DS period in the absence of a magnetic field, $R = 2L_z/W_0$. We readily see that, as the field increases, one comes to a state which can be treated as saturation, because this state does not change as the field is further increased in absolute magnitude. This saturated state corresponds to the values $\xi = 0$ and 1 and is reached for the field

$$|H| = H_s = \frac{4L_y M_0}{L_z}\ln\frac{2M_0^2 L_y}{\gamma}, \tag{23}$$

whence one obtains the effective demagnetization factor

$$N = \frac{4L_y}{L_z}\ln\frac{2M_0^2 L_y}{\gamma}. \tag{24}$$

As follows from Eq. (20), domains of both types persist as one approaches the saturation state ($\xi = 1$). Indeed, for zero relative width of the domains with magnetization antiparallel to the applied magnetic field, their absolute width $w_- = (1-\xi)W$ for $\xi \longrightarrow 1$ tends not to zero but rather to a finite value $w_- = W_0/4$, which is only one half the value for zero external magnetic field. The same holds for $\xi \longrightarrow 0$. The dependence of the widths of domains with parallel and antiparallel magnetization, as well as of their sum (the DS period W), on ξ is shown graphically in Fig. 3.

5. DISCUSSION OF RESULTS

According to Eq. (20), the Cotton DS under study differs substantially from the Faraday DS. Indeed, many authors, starting with Kittel [2], estimated the period of the Faraday structure as $W_0' \sim \sqrt{2\gamma L_z/M_0^2}$ (in the notation used here). A comparison of this estimate with Eq. (20) shows that in our case, the DS period is proportional to the first power (rather than to the square root) of L_z and to the first power (rather than the square root) of domain wall energy γ and is inversely proportional to the square (and not to the first power) of the magnetization M_0.

Because the DS period W_0 depends on the geometric parameters of the plate, one has to establish the cases in which the condition $L_y \ll W_0 \ll L_z$ imposed by us in deriving the simplified expression (12) for magnetostatic energy holds. For this purpose, we use the estimate $\gamma \sim M_0^2\delta$, where δ stands for the domain wall thickness, and substitute this estimate into Eq. (20) for W_0. Then, this condition will take on the form

$$\delta \ll L_y \ll \sqrt{L_y\delta}. \tag{25}$$

According to [1], we have $\delta \sim \sqrt{\alpha/\beta}$, where α is the nonuniform exchange constant, which we estimate here as $\alpha \sim 10^{-12}$ cm^2, and β is a dimensionless anisotropy parameter which determines the anisotropy field $H_a \sim \beta M_0$. As an illustration, we consider a film of cobalt for which $\beta \sim 4.2$ [12]. Putting the geometrical parameters $L_y = 50$ nm and $L_z = 60$ μm, as in [15], we see that condition (25) holds. One can readily verify that condition (25) is also satisfied for the same geometrical parameters for films of iron ($\beta \sim 1.7$ [12]) and nickel ($\beta \sim 0.29$ [1]).

Next, we use inequality (25) to compare the DS periods W_0 and W_0'. Because $W_0 \sim \gamma L_z/M_0^2 L_y \sim \delta L_z/L_y$ and $W_0' \sim \sqrt{2\gamma L_z/M_0^2} \sim \sqrt{\delta L_z}$, Eq. (25) suggests that $W_0 \gg W_0'$; therefore, in plates with the same geometrical parameters, the period of the Cotton domains is substantially larger than that of the Faraday domain. A numerical estimation of the DS period W_0 and of the saturation field H_s given by Eq. (23) for a Co film with parameters $M_0 \sim 1400$ G, $L_y = 50$ nm, and $L_z = 60$ μm yields $W_0 \sim 6$ μm and $H_s \sim 14$ G. These estimates agree in order of magnitude with experimental data (see, e.g., [9–11]).

Another substantial, distinctive feature of the structure under study is the above persistence of the unfavorable domains for $\xi \longrightarrow 1$ and $\xi \longrightarrow 0$ (for zero relative width, their absolute magnitude tends to a finite limit), which implies the persistence of domain walls in a fairly strong magnetic field (in absolute magnitude), $|H| > H_s$ [see Eq. (23)]. As already mentioned, this result correlates with the observation of 360° domain walls in experiments with films containing Cotton domains [9, 11].

We note in conclusion that 360° domain walls separating favorable domains were obtained by us using an approximate expression for the energy E_M, Eq. (15), which is valid for $W \ll L_z$ or, which is the same, for $\xi(1-\xi) \gg W_0/4L_z \sim \delta/4L_y$ [see Eq. (18) and the discussion after Eq. (20)]. Because $\delta/L_y \ll 1$, according to Eq. (25), we can approach the saturation limits, i.e., the points $\xi = 0, 1$, fairly closely. However, these points should be excluded from consideration.

Even if we base our analysis on a more general expression for energy given by Eq. (9), whose validity is not constrained by the condition $W \ll L_z$, we would not, nevertheless, come, within our model, to definite conclusions on the behavior of function $w_-(\xi)$ for $\xi \longrightarrow 0, 1$. The point is that we approximated the domain wall energy with the expression $E_D = 2\gamma/W$, which does not take into account the internal structure of the wall. Indeed, the question of whether domain walls brought closer to one another with increasing field H would annihilate or not should depend on such structural characteristics of the wall as, for instance, the chirality, a point which has been corroborated by direct experimental observations [11]. Theoretical analysis of this important problem requires dedicated consideration.

ACKNOWLEDGMENTS

The authors are indebted to V.G. Shavrov for valuable remarks.

This study was supported by the Russian Foundation for Basic Research (project no. 00-02-16384) and ISTC (grant no. 1522).

REFERENCES

1. L. D. Landau and E. M. Lifshitz, Phys. Z. Sowjetunion **8**, 153 (1935); L. D. Landau, *Collection of Works* (Nauka, Moscow, 1969), Vol. 1, p. 129.
2. C. Kittel, Phys. Rev. **70**, 965 (1946).
3. S. Chikasumi, *The Physics of Ferromagnetism. Magnetic Characteristics and Engineering Applications* (Syokabo, Tokyo, 1984; Mir, Moscow, 1987).
4. G. S. Krinchik, *Physics of Magnetic Phenomena* (Mosk. Gos. Univ., Moscow, 1985).
5. M. I. Kaganov and V. M. Tsukernik, *Nature of Magnetism* (Nauka, Moscow, 1982).
6. V. D. Buchel'nikov, V. A. Gurevich, and V. G. Shavrov, Fiz. Met. Metalloved. **52** (2), 298 (1981).
7. L. Mei, Prog. Nat. Sci. **10** (4), 259 (2000).
8. V. S. Gornakov, V. I. Nikitenko, L. H. Bennett, *et al.*, J. Appl. Phys. **81** (8), 5215 (1997).
9. X. Portier and A. K. Petford-Long, J. Phys. D **32** (1), 1 (1999).
10. A. K. Petford-Long, X. Portier, E. Yu. Tsymbal, *et al.*, IEEE Trans. Magn. **35** (2), 788 (1999).
11. X. Portier and A. K. Petford-Long, Appl. Phys. Lett. **76** (6), 754 (2000).
12. I. A. Privorotskiĭ, Usp. Fiz. Nauk **108** (1), 43 (1972) [Sov. Phys. Usp. **15**, 555 (1972)].
13. Yu. V. Gulyaev, P. E. Zil'berman, and É. M. Épshteĭn, Radiotekh. Élektron. (Moscow) **46** (7), 862 (2001).
14. A. P. Prudnikov, Yu. A. Brychkov, and O. I. Marichev, *Integrals and Series* (Nauka, Moscow, 1981; Gordon and Breach, New York, 1986).
15. A. M. Baranov, A. I. Chmil, R. J. Elliott, *et al.*, Europhys. Lett. **53** (5), 625 (2001).

Translated by G. Skrebtsov

Physics of the Solid State, Vol. 44, No. 6, 2002, pp. 1117–1121. Translated from Fizika Tverdogo Tela, Vol. 44, No. 6, 2002, pp. 1070–1074.

MAGNETISM AND FERROELECTRICITY

Formation of Tetrahedrally Close-Packed Structures in Tb–Fe and Co–Pd Nanocrystalline Films

L. I. Kveglis, S. M. Jarkov, G. V. Bondarenko, V. Yu. Yakovchuk, and E. P. Popel

Kirensky Institute of Physics, Siberian Division, Russian Academy of Sciences, Akademgorodok, Krasnoyarsk, 660036 Russia

e-mail: jarkov@iph.krasnoyarsk.su

Received August 10, 2001

Abstract—The crystal structure of $Tb_{30}Fe_{70}$ and $Co_{50}Pd_{50}$ nanocrystalline films with strong magnetic anisotropy perpendicular to the film plane ($K_\perp \sim 10^6$ erg/cm$_3$) is investigated using electron diffraction and transmission electron microscopy. All the studied films in the initial nanocrystalline phase undergo an explosive crystallization with the formation of dendrite structures. It is demonstrated that, after crystallization, the Tb–Fe and Co–Pd films exhibit a tetrahedrally close-packed atomic structure that has no analogs among these materials in the equilibrium state. The internal stresses in the films under investigation are estimated from an analysis of the bend extinction contours in the electron microscope images. The inference is made that strong perpendicular magnetic anisotropy can be associated with magnetostriction anisotropy due to the specific features of the film structure. © *2002 MAIK "Nauka/Interperiodica".*

1. INTRODUCTION

A unique combination of magnetic properties renders nanocrystalline materials very attractive for practical applications, in particular, for the design of storage media used in magnetic and thermomagnetic data recording devices. The recording density is the most important parameter of storage media. Nanocrystalline materials with magnetic anisotropy perpendicular to the film plane are materials of the future. The recording density provided by nanocrystalline materials with perpendicular magnetic anisotropy considerably exceeds the density achieved in materials with magnetic anisotropy in the film plane. The recording density in materials with perpendicular magnetic anisotropy can be as high as 10^{12} bit/cm^2.

At present, materials with a large perpendicular-magnetic-anisotropy energy constant have been studied extensively. As a rule, these materials are produced from rare-earth metal–transition metal (Dy–Co, Tb–Fe, etc.) and 3*d* metal–3*d* metal (Co–Pd, Co–Cr, etc.) alloys [1–6]. However, despite extensive investigations into the properties of storage media used in magnetic and thermomagnetic recording devices, the question as to the origin of perpendicular magnetic anisotropy remains open. This can be explained by the fact that the perpendicular magnetic anisotropy by itself and the perpendicular-magnetic-anisotropy energy depend on many factors. The basic models thus far applied to the explanation of the origin of perpendicular magnetic anisotropy in films are associated with the following factors [7]: (1) pair atomic interaction, (2) anisotropy of the columnar structure, (3) crystallographic anisotropy, (4) surface anisotropy, (5) exchange anisotropy between multilayers, and (6) magnetostriction anisotropy. Leamy and Dirks [8] proposed one more model, namely, the model of a fractal structure formed perpendicular to the film plane. The role played by each factor in the formation of perpendicular magnetic anisotropy depends on the particular material and technique used for the preparation of the samples.

Earlier [9], we studied Dy–Co films with strong perpendicular magnetic anisotropy ($K_\perp \sim 10^5$ erg/cm^3). It was shown that, in the initial state, these films consist of 10- to 15-Å clusters whose structure is similar to a tetrahedrally close-packed structure of the $CaCu_5$ type [9]. The $SmCo_5$ alloy with the same structure possesses the largest crystallographic magnetic anisotropy constant $K_1 \sim 10^8$ erg/cm^3 [10].

It is common knowledge that rare-earth metal–transition metal alloys belong to materials with the strongest magnetostriction occurring in nature [10]. However, available data on the contribution of magnetostriction anisotropy to perpendicular magnetic anisotropy in nanocrystalline films of transition metal alloys are very scarce. This is associated with the difficulties encountered in evaluating the magnitude of the magnetostriction and its contribution to perpendicular magnetic anisotropy on the basis of experimental data. As is known, there exist two sources of stresses generated in films: (1) stresses induced by a substrate or multilayers and (2) internal stresses due to specific features of the atomic structure. Draaisma *et al.* [2] examined Co–Pd multilayer films and considered different mechanisms responsible for the formation of perpendicular magnetic anisotropy. These authors made the inference that magnetostriction anisotropy due to lattice mismatch between cobalt and palladium plays a decisive role in the formation of perpendicular magnetic anisotropy. Kobayashi *et al.* [11] assumed that strong perpendicular magnetic

1063-7834/02/4406-1117$22.00

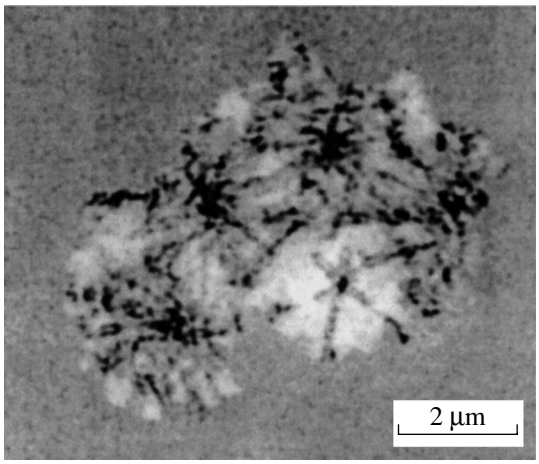

Fig. 1. Electron microscope image illustrating the onset of dendritic crystallization in the Tb–Fe film.

anisotropy in Tb–Fe films ($K_\perp = 2 \times 10^7$ erg/cm^3) is associated with the magnetostriction anisotropy arising from the difference between the thermal expansion coefficients of the film and the substrate.

In our recent works [12, 13], we investigated Co–Pd films with a large perpendicular magnetic anisotropy constant ($K_\perp \sim 10^6$ erg/cm^3). Such a strong perpendicular magnetic anisotropy was explained by the self-organization of crystalline modules through the coalescence of assemblies of these modules according to the general rules. In this case, the three-dimensional space is filled in an imperfect manner. The misorientation angle between the faces of the adjacent module assemblies containing tetrahedra and octahedra can be as large as several degrees. As a consequence, considerable stresses arising in the material can be partly relieved through displacements and rotations of module assemblies and the formation of fractures and cracks in the material. Making allowance for a giant magnetostriction of Co–Pd alloys, it was assumed that the magnetostriction anisotropy makes a substantial contribution to the large perpendicular magnetic anisotropy constant. However, our attempts to describe the structure of Co–Pd films adequately were unsuccessful. The purpose of the present work was to elucidate the structure of Tb–Fe and Co–Pd films with strong perpendicular magnetic anisotropy and to evaluate the contribution of the magnetostriction anisotropy to the perpendicular magnetic anisotropy.

2. SAMPLE PREPARATION AND EXPERIMENTAL TECHNIQUE

In this work, we investigated the structure and magnetic properties of Tb–Fe (30 at. % Tb and 70 at. % Fe) and Co–Pd (50 at. % Co and 50 at. % Pd) nanocrystalline films with strong perpendicular magnetic anisotropy [12, 13]. The films were examined in the initial state and after annealing under vacuum. The film samples were prepared through thermal explosive evaporation under vacuum at a residual pressure of 10^{-5} Torr and magnetron sputtering under vacuum at a residual pressure of 10^{-6} Torr onto different substrates (glass, crystalline and amorphous silicon, fused silica, NaCl, MgO, and LiF). The microstructure and phase composition of the films were analyzed using PRÉM-200 and JEM-100 C transmission electron microscopes. The chemical composition of the films was checked by x-ray fluorescence analysis. The perpendicular magnetic anisotropy constant $K_\perp$ was determined by the torque method at room temperature in magnetic fields with strengths up to 17 kOe.

3. RESULTS

In the initial state, the Tb–Fe and Co–Pd films possess perpendicular magnetic anisotropy ($K_\perp \sim 10^5$ erg/cm^3). The electron diffraction patterns of these films exhibit a diffuse halo. The electron microscopic investigation revealed that the Tb–Fe and Co–Pd films consist of 20- to 30-Å clusters. It is found that dendritic crystallization occurs in the films under the action of an electron beam in the transmission electron microscope or during annealing under vacuum at a residual pressure of 10^{-5} Torr and an annealing temperature T_{ann} = 260–300°C. In the course of crystallization, the perpendicular magnetic anisotropy constant increases to $\approx 5 \times 10^6$ erg/cm^3. The velocity of the crystallization front was estimated visually during electron microscopic observations and reached 1 cm/s. After the completion of dendritic crystallization, particles forming the film did not increase in size as compared to the initial state. Similar effects were observed earlier for Co–Pd films [12].

Figure 1 displays the electron microscope image illustrating the onset of the dendritic crystallization in the Tb–Fe film. It can be seen from Fig. 1 that bend extinction contours clearly manifest themselves in the crystallized region. After further annealing, a continuous network of intersecting bend extinction contours is observed throughout the electron microscope image of the Tb–Fe film (see [13] for Co–Pd films). The electron diffraction pattern of the crystallized region of the Tb–Fe film (Fig. 2a) is identified as the $TbFe_2$ structure ($Fd3m$) with the lattice parameter a = 7.10 Å and the $[0\bar{1}1]$ orientation. The electron diffraction pattern of the crystallized region of the Co–Pd film (Fig. 2b) contains sets of point reflections which disagree with all known structures of Co–Pd alloys. The diffraction reflections observed in the electron diffraction pattern correspond to interplanar distances typical of the (111) and (620) atomic planes in a face-centered cubic structure with the lattice parameter a = 3.75 Å. A similar set of reflections can be observed in the electron diffraction pattern of the face-centered cubic lattice oriented along the [134] zone axis. However, the electron diffraction pattern of the Co–Pd film (Fig. 2b) exhibit superstructure reflections with respect to the CoPd face-centered cubic

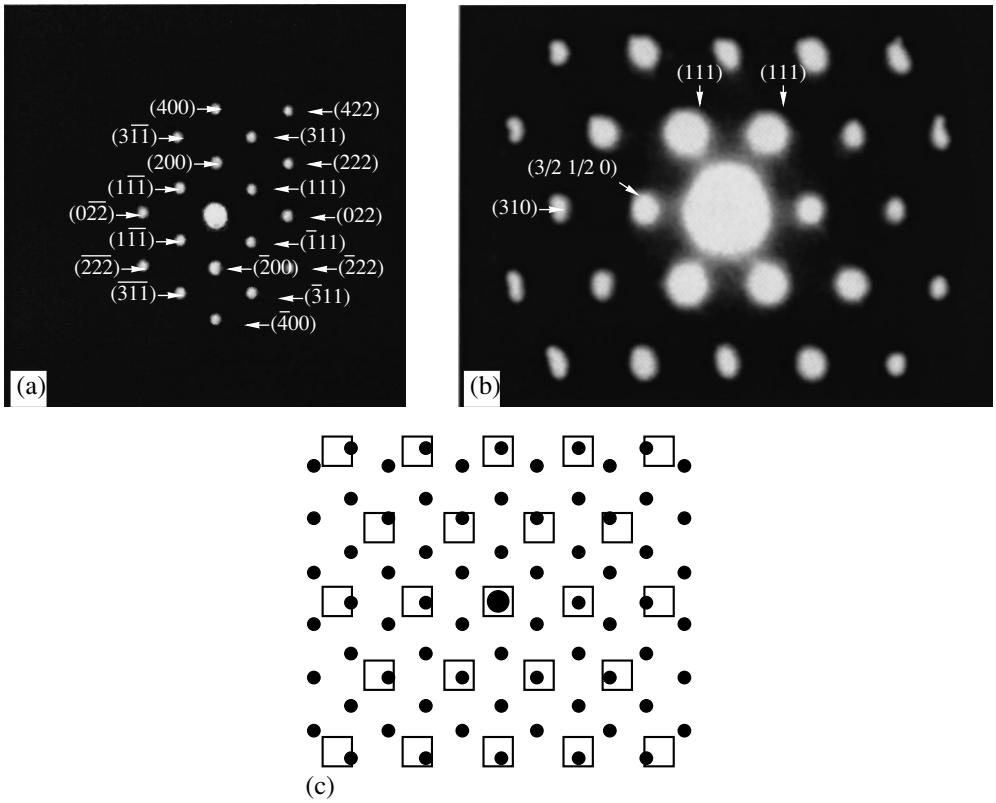

Fig. 2. Electron diffraction patterns of (a) Tb–Fe and (b) Co–Pd films after dendritic crystallization. (c) Schematic representation of a superposition of the diffraction patterns of Tb–Fe and Co–Pd films. Closed circles represent the reflections of $TbFe_2$, and open squares indicate the reflections of CoPd.

lattice, namely, the (3/21/20), (310), and (9/23/20) superstructure reflections. The intensities of the aforementioned superstructure reflections are substantially higher than the intensity of the (620) structure reflection. It is worth nothing that the angle between vectors of the [111] type in the electron diffraction pattern displayed in Fig. 2b is equal to ≈54°, whereas this angle for a cubic lattice should be equal to 70.5°. Attempts to identify the electron diffraction pattern under consideration as a hexagonal close-packed structure showed that this structure should be described by the ratio $c/a \approx 2.18$, which is not characteristic of hexagonal close-packed structures of metallic compounds [13].

A comparison of the electron diffraction patterns of Tb–Fe and Co–Pd films (Figs. 2a, 2b) demonstrates that the directions of the reciprocal lattice vectors in these patterns almost coincide with each other. A schematic representation of a superposition of the electron diffraction patterns is depicted in Fig. 2c. It can be seen that the (111)-type reflections of CoPd are superposed on the (311)-type reflections of $TbFe_2$ and that the (3/21/20)-type superstructure reflections with respect to the CoPd face-centered cubic structure are superposed on the (220)-type reflections of $TbFe_2$.

Annealing at $T_{ann} > 300$°C brings about disturbance of the dendrite structure in Tb–Fe and Co–Pd films. The electron diffraction patterns of the disturbed dendrite structures in Tb–Fe and Co–Pd films are shown in Figs. 3a and 3b, respectively. These diffraction patterns are also not typical and exhibit sets of reflections which, according to the interplanar distances, correspond to the (111) and (200) atomic planes in the $TbFe_2$ structure ($Fd3m$) with the lattice parameter $a = 7.10$ Å (Fig. 3a) and in the CoPd face-centered cubic structure with the lattice parameter $a = 3.75$ Å (Fig. 3b). However, the [111] and [200] vectors in both structures are nearly parallel to each other. This situation is, in principle, impossible for single crystals with a cubic lattice.

After annealing at $T_{ann} \geq 400$–450°C, the structure of the films under investigation relaxes to the equilibrium state. The films have a fine-grained structure which manifests itself in diffuse fringes in the electron diffraction patterns. The electron diffraction pattern of the Tb–Fe film corresponds to the $TbFe_2$ structure ($Fd3m$) with the lattice parameter $a = 7.10$ Å. The electron diffraction pattern of the Co–Pd film is identified as a face-centered cubic structure with the lattice parameter $a = 3.75$ Å. The perpendicular magnetic anisotropy constants of these films are equal to ~10^4–10^5 erg/cm^3.

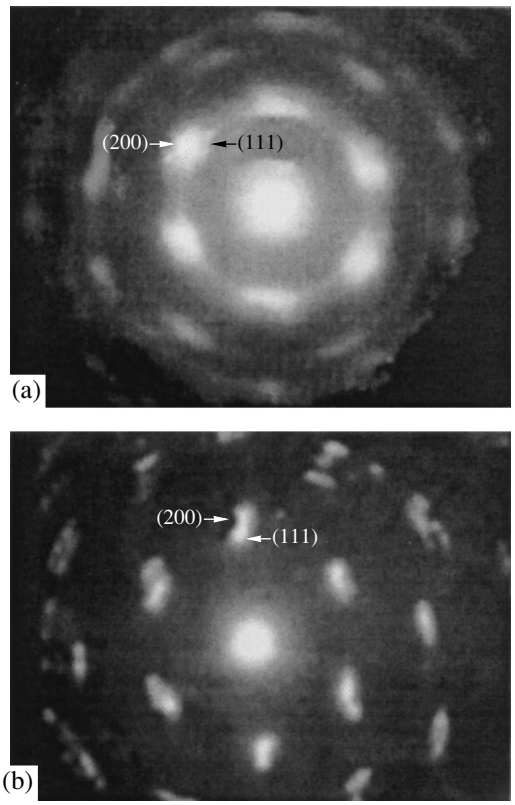

Fig. 3. Electron diffraction patterns of (a) Tb–Fe and (b) Co–Pb films after annealing under vacuum at $T_{ann} > 300°C$.

4. DISCUSSION

The investigation into the magnetic properties and analysis of the electron diffraction patterns of Tb–Fe films revealed that, in the initial nanocrystalline state, these films are characterized by the perpendicular magnetic anisotropy constant $K_\perp \approx 2 \times 10^5$ erg/cm^3. After the dendritic crystallization from the initial nanocrystalline state, the films possess the largest perpendicular magnetic anisotropy constant ($K_\perp \approx 5 \times 10^6$ erg/cm^3) and have a $TbFe_2$-type structure which corresponds to a Laves phase (the $MgCu_2$ type) [10]. Different polytypes of the Laves phase family belong to the group of Frank–Casper tetrahedrally close-packed structures [14]. In the case of a $TbFe_2$-type structure, the tetrahedra involved in the structure form mutually penetrating Frank–Casper polyhedra with coordination numbers of 12 and 16. In turn, the mutually penetrating Frank–Casper polyhedra consist of close-packed tetrahedra. As is known, crystalline materials described by Frank–Casper polyhedra exhibit a tendency for the unit cell parameters to decrease to 30% [14].

In the case of Co–Pd films, we can assume that, after the completion of dendritic crystallization (Fig. 2b), the film structure is described by close-packed tetrahedra, as is the case with a $TbFe_2$-type structure. Apparently, the structure formed in the Co–Pd film is similar to the structure of the Laves phase; however, unlike the latter structure, the former structure is atomically disordered and imperfect. Note that, within the same film, the packing of tetrahedra can undergo changes according to the basic rule of packing; i.e., tetrahedra are packed in such a face-to-face manner as to provide the highest local density [15]. It is believed that film materials with a similar structure can experience strong internal stresses.

The electron diffraction pattern of the Tb–Fe film annealed at $T_{ann} > 300°C$ (Fig. 3a) is similar to the diffraction pattern of the Co–Pd film annealed at $T_{ann} = 320°C$ (Fig. 3b). These diffraction patterns have defied interpretation both with the use of a superposition of the electron diffraction patterns obtained for differently oriented crystalline grains and from the viewpoint of a particular single crystal. In our recent work [13], we proposed a scheme for identifying similar electron diffraction patterns with the use of crystalline-module assemblies. These assemblies are composed of tetrahedra joined together in the same fashion as a Boerdijk spiral. The three-dimensional space is filled with these module assemblies in a percolation manner to form a structure with strong internal stresses. This is indicated by the bend extinction contours observed in the electron microscope images (see Fig. 1 for the Tb–Fe film and [13] for the Co–Pd film).

Analysis of the bend extinction contours was performed according to the procedure described in [16]. For the studied films, the elastic stress is estimated at $\sim 10^{11}$ N/m^2. In the case when the stress in the film does not exceed the elastic limit, the perpendicular magnetic anisotropy constant is approximately equal to $\sim 10^6$ erg/cm^3. However, dark-field electron microscopic examinations of these films revealed a plastic flow. This manifests itself as rotational effects, i.e., rotations of film regions ~1 μm in size. Consequently, stresses arising during the formation of the dendrite structure substantially exceed the elastic limit and can make a considerable contribution to the perpendicular magnetic anisotropy due to magnetostriction effects.

5. CONCLUSION

Thus, the above investigation demonstrated that Tb–Fe and Co–Pd films with large perpendicular magnetic anisotropy constants have a tetrahedrally close-packed structure. The dendritic crystallization of the initial nanocrystalline phase leads to the formation of a film structure similar to the structure of the Laves phase. After the dendrite structure is destroyed, the film structure is built up in the same manner as a Boerdijk spiral. The specific features of the dendritic growth in the films give rise to strong internal stresses. These stresses are responsible for a dominant contribution of the magnetostriction anisotropy to the perpendicular magnetic anisotropy. It should be emphasized that strong internal stresses are associated with the specific features in the film structure and do not depend on substrates.

ACKNOWLEDGMENTS

We would like to thank V.N. Matveev for supplying the samples prepared by magnetron sputtering for our investigations.

This work was supported by the Russian Foundation for Basic Research (project no. 00-02-17358), the International Association of Assistance for the promotion of cooperation with scientists from the New Independent States of the former Soviet Union (project no. 00-100), the 6th Competition of Research Projects of Young Scientists of the Russian Academy of Sciences (1999) (project no. 56), and the Krasnoyarsk Regional Scientific Foundation.

REFERENCES

1. Y. Ochiai, S. Hashimoto, and K. Aso, IEEE Trans. Magn. **25** (5), 3755 (1989).
2. H. J. G. Draaisma, W. J. M. de Jonge, and F. J. A. den Broeder, J. Magn. Magn. Mater. **66** (3), 351 (1987).
3. P. F. Carcia, J. Appl. Phys. **63** (10), 5066 (1988).
4. V. H. Harris, K. D. Aylesworth, B. N. Das, *et al.*, Phys. Rev. Lett. **69** (13), 1939 (1992).
5. T. Miyazaki, K. Hayashi, S. Yamaguchi, *et al.*, J. Magn. Magn. Mater. **75** (3), 243 (1988).
6. T. Tarahashi, A. Yoshihara, and T. Shimamori, J. Magn. Magn. Mater. **75** (3), 252 (1988).
7. W. H. Meiklejohn, Proc. IEEE **74** (11), 1570 (1986).
8. H. J. Leamy and A. G. Dirks, J. Appl. Phys. **50** (4), 2871 (1979).
9. A. S. Avilov, L. I. Vershinina-Kveglis, S. V. Orekhov, *et al.*, Izv. Akad. Nauk SSSR, Ser. Fiz. **55** (8), 1609 (1991).
10. K. N. R. Taylor, Adv. Phys. **20**, 551 (1971).
11. H. Kobayashi, T. Ono, A. Tsushima, and T. Suzuki, Appl. Phys. Lett. **43** (4), 389 (1983).
12. L. I. Vershinina-Kveglis, V. S. Zhigalov, and I. V. Staroverova, Fiz. Tverd. Tela (Leningrad) **33** (5), 1409 (1991) [Sov. Phys. Solid State **33**, 793 (1991)].
13. L. I. Kveglis, S. M. Jarkov, and I. V. Staroverova, Fiz. Tverd. Tela (St. Petersburg) **43** (8), 1482 (2001) [Phys. Solid State **43**, 1543 (2001)].
14. W. B. Pearson, *The Crystal Chemistry and Physics of Metals and Alloys* (Wiley, New York, 1972; Mir, Moscow, 1977).
15. N. A. Bulienkov and D. L. Tytik, Izv. Akad. Nauk, Ser. Khim., No. 1, 1 (2001).
16. I. E. Bolotov and V. Yu. Kolosov, Phys. Status Solidi A **69**, 85 (1982).

Translated by O. Borovik-Romanova

Physics of the Solid State, Vol. 44, No. 6, 2002, pp. 1122–1129. Translated from Fizika Tverdogo Tela, Vol. 44, No. 6, 2002, pp. 1075–1081.

MAGNETISM AND FERROELECTRICITY

Two-Dimensional Heisenberg Model with Spin $s = 1/2$ and Antiferromagnetic Exchange Treated as a Spin Liquid

E. V. Kuz'min

Kirensky Institute of Physics, Siberian Division, Russian Academy of Sciences, Akademgorodok, Krasnoyarsk, 660036 Russia

e-mail: evk@iph.krasn.ru

Received October 1, 2001

Abstract—The spin system of the Heisenberg model ($s = 1/2$) on a square lattice with antiferromagnetic (AFM) exchange between nearest neighbors (in which there is no long-range magnetic order at any $T \neq 0$) is treated as a spatially homogeneous isotropic spin liquid. The double-time temperature Green's function method is used in the framework of a second-step decoupling scheme. It is shown that, as $T \longrightarrow 0$, the spin liquid goes over (without any change in symmetry) to a singlet state with energy (per bond) $\varepsilon_0 = -0.352$ and the correlation length diverges as $\xi \propto T^{-1}\exp(T_0/T)$. The spatial spin correlators oscillate in sign with distance, as in the AFM state. The theory allows one to calculate the main characteristics of the system in all temperature ranges. © *2002 MAIK "Nauka/Interperiodica".*

1. INTRODUCTION

The objective of this paper is to discuss the problem of the ground state and the main thermodynamic properties of the $s = 1/2$ spin system described by the isotropic Heisenberg model on a square lattice with antiferromagnetic (AFM) exchange interaction between nearest neighbors ($J > 0$). The Hamiltonian H and the total spin $\mathbf{S}$ are

$$H = \frac{1}{2}J\sum_{\mathbf{fa}}\mathbf{s_f}\mathbf{s_{f+a}}, \quad \mathbf{S} = \sum_{\mathbf{f}}\mathbf{s_f}. \qquad (1)$$

We will consider the general case of the Hamiltonian (1) on an alternant lattice[1] of N sites with periodic boundary conditions. In Eq. (1), $\mathbf{f}$ specifies the lattice sites, D is the lattice dimensionality, z is the number of nearest neighbors, and $\mathbf{a}$ are the vectors connecting nearest neighbors. The ground state and the thermodynamic properties of the system essentially depend on its dimensionality D.

The problem of the ground state (at $T = 0$) for the two-dimensional model ($D = 2$, $z = 4$) still remains unsolved. Marshall [1, 2] argued that the ground state of the Hamiltonian (1) on alternant lattices is a nondegenerate singlet with total spin $S = 0$ (this statement has been rigorously proved only for a one-dimensional chain). On the other hand, on alternant lattices of $D = 2$ and 3, the spin distribution can have a chessboard pattern described by the Néel wave function of an antiferromagnet with two equivalent sublattices which are mirror images of each other. It is generally agreed that at $T = 0$, the two-sublattice AFM state with long-range order is the closest approximation to the ground state of the system [3]. However, Anderson [4] assumed that the ground state of the Hamiltonian (1) on a square lattice can be disordered and described by a wave function with resonant valence bonds (RVBs). Later [5], the energy of the disordered (singlet) state was calculated numerically with RVB wave functions on 128×128 and 256×256 lattices and was found to be –0.3344 per bond, which is equal, within 0.1%, to the best result for the energy of the ordered AFM state. However, in [6], using exact diagonalization for a small (4×4) cluster, the energy of the singlet state was calculated to be –0.3509. Different methods for solving this problem are reviewed in [3].

The thermodynamic properties are also of fundamental importance. According to the Mermin–Wagner theorem [7], long-range magnetic order can exist at $T \neq 0$ only on three-dimensional (or quasi-two-dimensional) lattices ($D = 3$) up to the critical temperature T_c. Therefore, the AFM state on a square ($D = 2$) lattice is represented by the "pricked-out" temperature point and the problem arises of describing the system at $T \neq 0$. In a sense, the case of dimensionality $D = 2$ is critical or intermediate between a one-dimensional system (in which the long-range magnetic order can never occur) and three-dimensional systems with a long-range magnetic order at temperatures below the critical point.

The theory of the thermodynamic properties of this system was developed in [8–11], where the long-range AFM order of the Néel type was postulated to occur at $T = 0$.

[1] A lattice is termed alternant if it is made up of two interpenetrating equivalent sublattices A and B, such that the nearest neighbors of a site of sublattice A are sites of sublattice B alone and *vice versa*.

In this paper, the two-dimensional system is assumed to be in a nonmagnetic state with a well-developed short-range AFM order. This state is referred to as the spin liquid (SL). In describing the thermodynamic properties of the SL, we make some assumptions and follow the method used in [8–11]. As $T \longrightarrow 0$, the SL goes over, without any change in symmetry, to a singlet state with an energy per bond ε_0. However, it is not known in advance whether or not this state is the ground state, because the AFM state with energy ε_{AF} can also arise. Only a comparison between ε_0 and ε_{AF} will allow one to draw a conclusion as to the type of the ground state.

2. SPIN LIQUID: CORRELATION FUNCTIONS AND GREEN'S FUNCTIONS

We define the spin liquid as a spatially homogeneous state (with the short-range order symmetry unbroken) in which (i) the spin correlation functions are isotropic, i.e.,

$$\frac{1}{N}\sum_{\mathbf{f}}\langle s_{\mathbf{f}}^x s_{\mathbf{f}+\mathbf{r}}^x\rangle = \frac{1}{N}\sum_{\mathbf{f}}\langle s_{\mathbf{f}}^y s_{\mathbf{f}+\mathbf{r}}^y\rangle = \frac{1}{N}\sum_{\mathbf{f}}\langle s_{\mathbf{f}}^z s_{\mathbf{f}+\mathbf{r}}^z\rangle \equiv \frac{1}{4}K_r, \tag{2}$$

and depend only on the magnitude $r = |\mathbf{r}|$ of the space vector, with $K_0 = 1$ and, hence, $\langle s_{\mathbf{f}}^2\rangle = 3/4$ (here and henceforth, $\langle\ldots\rangle$ is a thermodynamic average at $T \neq 0$ or the expectation value in the singlet state $|\Psi_0\rangle$ at $T = 0$), and (ii) the following averages are zero:

$$\langle s_{\mathbf{f}}^a\rangle = 0, \quad \langle S^\alpha\rangle = 0, \tag{3a}$$

$$\langle s_{\mathbf{f}}^\alpha s_{\mathbf{m}}^\beta s_{\mathbf{n}}^\gamma\rangle = 0, \quad \mathbf{f} \neq \mathbf{m} \neq \mathbf{n}; \tag{3b}$$

the averages of any other odd products of the operators at different sites are also zero ($\alpha = x, y, z$ or $+, -, z$).

The properties of the SL state are mainly determined by the temperature dependence of the spin correlation functions. The SL state energy per bond (in units of J) is

$$\varepsilon = \frac{\langle H\rangle}{(1/2)zNJ} = -\frac{3}{4}K_1, \tag{4}$$

where $K_a = -K_1$ ($K_1 > 0$) is the correlation function for nearest neighbors (a is the lattice parameter). At $T = 0$, Eq. (4) gives the energy of the singlet state ε_0.

To describe the SL state, we go over to the Fourier transforms of the spin operators and introduce the Fourier transform of the correlation function

$$K(\mathbf{q}) = \sum_{\mathbf{r}} e^{-i\mathbf{qr}}K_r = 4\langle s^z(\mathbf{q})s^z(-\mathbf{q})\rangle = 2\langle s^+(\mathbf{q})s^-(-\mathbf{q})\rangle, \tag{5}$$

$$K_r = \frac{1}{N}\sum_q e^{i\mathbf{qr}}K(\mathbf{q})$$

with evident properties $K(\mathbf{q}) = K(-\mathbf{q})$ and $K_r = K_{-r}$. Given the Fourier transform $K(\mathbf{q})$, one can calculate any space correlators K_r. We follow the method applied in [8–11] and calculate $K(\mathbf{q})$ using the double-time retarded temperature Green's functions [12]. Below, we calculate the function $\langle\langle s^z(\mathbf{q})|s^z(-\mathbf{q})\rangle\rangle_\omega \equiv G(\mathbf{q}, \omega)$. Since the spin correlators are isotropic, we have $\langle\langle s^+(\mathbf{q})|s^-(-\mathbf{q})\rangle\rangle_\omega = 2G(\mathbf{q}, \omega)$.

3. EQUATIONS OF MOTION

It is convenient to go over to the dimensionless Hamiltonian $h = H/zJ$; all energetic parameters will also be measured in units of zJ. The equations of motion have the form ($\hbar = 1$)

$$i\dot{s}_{\mathbf{f}}^+ = \frac{1}{z}\sum_{\mathbf{a}}(s_{\mathbf{f}}^z s_{\mathbf{f}+\mathbf{a}}^+ - s_{\mathbf{f}+\mathbf{a}}^z s_{\mathbf{f}}^+),$$

$$i\dot{s}_{\mathbf{f}}^z = \frac{1}{2z}\sum_{\mathbf{a}}(s_{\mathbf{f}}^+ s_{\mathbf{f}+\mathbf{a}}^- - s_{\mathbf{f}+\mathbf{a}}^+ s_{\mathbf{f}}^-), \tag{6}$$

$$-\frac{\partial^2 s_{\mathbf{f}}^z}{\partial t^2} = \frac{1}{2z^2}\sum_{\mathbf{a}}(s_{\mathbf{f}}^z - s_{\mathbf{f}+\mathbf{a}}^z) + R_{\mathbf{f}}, \tag{7}$$

where

$$R_{\mathbf{f}} = \frac{1}{z^2}\sum_{\mathbf{a}\neq\mathbf{a}'}\Big[s_{\mathbf{f}}^z s_{\mathbf{f}+\mathbf{a}}^+ s_{\mathbf{f}+\mathbf{a}'}^- + s_{\mathbf{f}+\mathbf{a}-\mathbf{a}'}^z\frac{1}{2}(s_{\mathbf{f}}^+ s_{\mathbf{f}+\mathbf{a}}^- + s_{\mathbf{f}+\mathbf{a}}^+ s_{\mathbf{f}}^-) - s_{\mathbf{f}+\mathbf{a}}^z\frac{1}{2}(s_{\mathbf{f}}^+ s_{\mathbf{f}+\mathbf{a}-\mathbf{a}'}^- + s_{\mathbf{f}+\mathbf{a}-\mathbf{a}'}^+ s_{\mathbf{f}}^-) - s_{\mathbf{f}+\mathbf{a}'}^z\frac{1}{2}(s_{\mathbf{f}}^+ s_{\mathbf{f}+\mathbf{a}}^- + s_{\mathbf{f}+\mathbf{a}}^+ s_{\mathbf{f}}^-)\Big]. \tag{8}$$

In the second-order differential equation, the kinematic properties of spin operators at one site are exactly taken into account, which is of fundamental importance.

The chain of equations is cut off at the second step by linearizing the operator $R_{\mathbf{f}}$ ($\mathbf{a} \neq \mathbf{a}'$) according to the scheme [8–11]

$$s_{\mathbf{f}}^z s_{\mathbf{f}+\mathbf{a}}^+ s_{\mathbf{f}+\mathbf{a}'}^- \approx \alpha_2\langle s_{\mathbf{f}+\mathbf{a}}^+ s_{\mathbf{f}+\mathbf{a}'}^-\rangle s_{\mathbf{f}}^z = \frac{1}{2}\alpha_2 K_{\mathbf{a}-\mathbf{a}'}s_{\mathbf{f}}^z,$$

$$s_{\mathbf{f}+\mathbf{a}'}^z s_{\mathbf{f}}^+ s_{\mathbf{f}+\mathbf{a}}^- \approx \alpha_1\langle s_{\mathbf{f}}^+ s_{\mathbf{f}+\mathbf{a}}^-\rangle s_{\mathbf{f}+\mathbf{a}'}^z = \frac{1}{2}\alpha_1 K_{\mathbf{a}}s_{\mathbf{f}+\mathbf{a}'}^z, \tag{9}$$

where α_1 is a factor which corrects the decoupling approximation for nearest neighbors ($K_a = -K_1$) and

α_2 is an analogous factor for the correlators at distances $r = d = \sqrt{2}\,a$ (along a diagonal) and $r = 2a$ (in what follows, we put $a = 1$). Thus, we have

$$(R_{\mathbf{f}})_{\text{lin}} = \frac{1}{2}\frac{1}{z^2}\sum_{a \neq a'}[\alpha_2 K_{\mathbf{a}-\mathbf{a}'}(s^z_{\mathbf{f}} - s^z_{\mathbf{f}+\mathbf{a}}) + \alpha_1 K_1(s^z_{\mathbf{f}+\mathbf{a}'} - s_{\mathbf{f}+\mathbf{a}'-\mathbf{a}})], \quad (10)$$

$$K_2 = \frac{1}{z^2}\sum_{\mathbf{a},\,\mathbf{a}'} K_{\mathbf{a}-\mathbf{a}'} = \frac{1}{z}[1 + (z-2)K_d + K_{2a}]. \quad (11)$$

Using Eqs. (6) and linearized equation (7), the Fourier transform of the Green's function in the second-step decoupling scheme is routinely found to be

$$G(\mathbf{q}, \omega) = \frac{A(\mathbf{q})}{\omega^2 - \Omega_{\mathbf{q}}^2}, \quad A(\mathbf{q}) = \frac{K_1}{2}(1 - \gamma_{\mathbf{q}}) \quad (12)$$

with the excitation spectrum

$$\Omega_{\mathbf{q}} = \lambda E_{\mathbf{q}}(\Delta), \quad E_{\mathbf{q}}(\Delta) = \sqrt{(1-\gamma_{\mathbf{q}})(1+\gamma_{\mathbf{q}}+\Delta)}, \quad \gamma_{\mathbf{q}} = \frac{1}{D}\sum_j \cos q_j, \quad (13)$$

where λ is the hardness parameter of the excitation spectrum,

$$\lambda^2 = \alpha_1 K_1/2, \quad (14)$$

and the pseudogap Δ at $\mathbf{q} = \mathbf{Q} = (\pi, \pi)$ (where $\gamma_{\mathbf{Q}} = -1$) is given by

$$1 + \Delta = \frac{1}{2\lambda^2}\left[\frac{1 + 2\lambda^2}{z} + \alpha_2\left(K_2 - \frac{1}{z}\right)\right]. \quad (15)$$

The spectrum $\Omega_{\mathbf{q}} \geq 0$ describes collective triplet excitations from the singlet state. All parameters of the spectrum are temperature-dependent and should be calculated self-consistently.

4. SELF-CONSISTENCY EQUATIONS

The imaginary part of the Green's function (12) is equal to

$$-\frac{1}{\pi}\text{Im}G(\mathbf{q}, \omega + i0) = \frac{A(\mathbf{q})}{2\Omega_{\mathbf{q}}}[\delta(\omega - \Omega_{\mathbf{q}}) - \delta(\omega + \Omega_{\mathbf{q}})] \equiv n(\mathbf{q}, \omega); \quad (16)$$

therefore, the spectral density for the z components is

$$J(\mathbf{q}, \omega; \tau) = \frac{e^{\omega/\tau}}{e^{\omega/\tau} - 1}n(\mathbf{q}, \omega), \quad (17)$$

where $\tau = T/zJ$ is the dimensionless temperature. Using a spectral theorem [12], the equal-time correlation function can be written as

$$\langle s^z(\mathbf{q})s^z(-\mathbf{q})\rangle \equiv \frac{1}{4}K(\mathbf{q}) = \frac{A(\mathbf{q})}{2\Omega_{\mathbf{q}}}\coth\left(\frac{\Omega_{\mathbf{q}}}{2\tau}\right) \quad (18)$$

or

$$K(\mathbf{q}) = \frac{K_1}{\lambda}\frac{1 - \gamma_{\mathbf{q}}}{E_{\mathbf{q}}(\Delta)}\coth\left(\frac{\lambda E_{\mathbf{q}}(\Delta)}{2\tau}\right). \quad (19)$$

Using the definition of the space correlators K_r of Eq. (5), one can derive the relations

$$K_n = \frac{1}{N}\sum_{\mathbf{q}}(-\gamma_{\mathbf{q}})^n K(\mathbf{q}) = \frac{K_1}{\lambda}I_n(\Delta, \tau), \quad K_0 = 1, \quad (20)$$

where

$$I_n(\Delta, \tau) = \frac{1}{N}\sum_{\mathbf{q}}\frac{(1-\gamma_{\mathbf{q}})(-\gamma_{\mathbf{q}})^n}{E_{\mathbf{q}}(\Delta)}\coth\left(\frac{\lambda E_{\mathbf{q}}(\Delta)}{2\tau}\right), \quad n = 0, 1, 2. \quad (21)$$

These equations should be solved self-consistently in combination with Eq. (15) for the pseudogap and Eq. (14).

As in [8–11], there are five parameters (K_1, K_2, α_1, α_2, Δ) to be found from three equations (20) ($n = 0$, 1, 2) and Eq. (15). The needed fifth equation can be chosen arbitrarily to some extent. Shimahara and Takada [8] put $r_\alpha = (\alpha_1 - 1)/(\alpha_2 - 1) = \text{const}$ and found this parameter from the condition that the AFM state with sublattice magnetization $m = 0.3$ exist at $T = 0$; that is, the ground state is postulated to be antiferromagnetic. We will refer to this as the Shimahara–Takada (ST) condition.

In this paper, the needed fifth equation for closing the set of equations is chosen on the basis of Eq. (3b). Using the rules for calculating the products of spin operators at one site and Eq. (3b), one can exactly calculate the average:

$$\langle R_{\mathbf{f}}s^z_{\mathbf{f}}\rangle = \frac{1}{4z^2}\sum_{\mathbf{a}\neq\mathbf{a}'}\langle s^+_{\mathbf{f}+\mathbf{a}}s^-_{\mathbf{f}+\mathbf{a}'}\rangle = \frac{1}{8}\tilde{K}_2, \quad \tilde{K}_2 = K_2 - 1/z, \quad (22)$$

which allows one to find

$$\left\langle\left(-\frac{\partial^2 s^z_{\mathbf{f}}}{\partial t^2}\right)s^z_{\mathbf{f}}\right\rangle = \frac{1}{8}\left(K_2 + \frac{1}{z}K_1\right). \quad (23)$$

In the framework of the linear theory used here, we have

$$\left\langle \left(-\frac{\partial^2 s_{\mathbf{f}}^z}{\partial t^2} \right)_{\text{lin}} s_{\mathbf{f}}^z \right\rangle = \frac{1}{8}\left(\frac{1+K_1}{z} + [\alpha_2(1+K_1) - \alpha_1 K_1]\tilde{K}_2 - \frac{z-1}{z}\alpha_1 K_1^2 \right). \tag{24}$$

From the condition that exact equation (23) and approximate equation (24) be the same, we obtain the fifth equation needed to close the set of equations.

Equation (24) is conveniently represented in an equivalent form by expressing it in terms of the second moment. Using the spectral theorem, the single-site average can be written as

$$\langle s_{\mathbf{f}}^z(t) s_{\mathbf{f}}^z(0)\rangle = \int_{-\infty}^{\infty} e^{-i\omega t} J_0(\omega) d\omega,$$
$$J_0(\omega) = \frac{1}{N}\sum_{\mathbf{q}} J(\mathbf{q}, \omega; \tau), \tag{25}$$

where $J_0(\omega)$ is the spectral density of the single-site Green's function $G_{\mathbf{ff}}(\omega) \equiv G_0(\omega)$.

The zeroth moment is defined as the average in Eq. (25) at $t = 0$:

$$M_0 = \langle s_{\mathbf{f}}^z(0) s_{\mathbf{f}}^z(0)\rangle = \langle s_{\mathbf{f}}^z s_{\mathbf{f}}^z\rangle = \frac{1}{4} = \int_{-\infty}^{\infty} J_0(\omega) d\omega = \frac{1}{N}\sum_{\mathbf{q}} \frac{A(\mathbf{q})}{2\Omega_{\mathbf{q}}} \coth\left(\frac{\Omega_{\mathbf{q}}}{2\tau}\right). \tag{26}$$

This relation is a sum rule and reproduces the expression for the correlator K_0. Differentiating Eq. (25) with respect to time and putting $t = 0$, we obtain the first moment

$$M_1 = \left\langle \left(i\frac{\partial s_{\mathbf{f}}^z(t)}{\partial t} \right) s_{\mathbf{f}}^z(0) \right\rangle_{t=0} = \int_{-\infty}^{\infty} \omega J_0(\omega) d\omega. \tag{27}$$

The left-hand side of Eq. (27) can be exactly calculated using Eq. (6), which gives $K_1/4$. The same is obtained by calculating the right-hand side; that is, we have an identity. The second moment is defined as

$$M_2 = \left\langle \left(-\frac{\partial^2 s_{\mathbf{f}}^z(t)}{\partial t^2} \right) s_{\mathbf{f}}^z(0) \right\rangle_{t=0} = \int_{-\infty}^{\infty} \omega^2 J_0(\omega) d\omega. \tag{28}$$

The left-hand side of Eq. (28) is given by exact expression (23). Calculating the right-hand side, we represent Eq. (28) in the form

$$\frac{1}{8}(K_2 + K_1/z) = \frac{1}{4}\lambda K_1 P(\Delta, \tau),$$
$$P(\Delta, \tau) = \frac{1}{N}\sum_{\mathbf{q}} (1 - \gamma_{\mathbf{q}}) E_{\mathbf{q}}(\Delta) \coth\left(\frac{\Omega_{\mathbf{q}}}{2\tau}\right). \tag{29}$$

Equation (29) is equivalent to the requirement that $\langle R_{\mathbf{f}} s_{\mathbf{f}}^z\rangle = \langle (R_{\mathbf{f}})_{\text{lin}} s_{\mathbf{f}}^z\rangle$ and, therefore, that Eq. (23) be identical to Eq. (24). Thus, instead of the ST condition used in [8], we derived a new self-consistency condition in the form of Eq. (29). Therefore, the self-consistent second-step decoupling scheme can be based on the requirement that the first three moments (M_0, M_1, M_2) be calculated exactly.

5. SELF-CONSISTENT SOLUTION OF THE EQUATIONS

In what follows, the set of equations (20), (15), and (29) with $\Omega_{\mathbf{q}} = \lambda E_{\mathbf{q}}(\Delta)$ and $\lambda^2 = \alpha_1 K_1/2$ will be solved analytically and numerically. For this purpose, we represent Eq. (21) in the form

$$I_n(\Delta, \tau) = I_n(\Delta) + B_n(\Delta, \tau),$$
$$I_n(\Delta) = \frac{1}{N}\sum_{\mathbf{q}} \frac{(1-\gamma_{\mathbf{q}})(-\gamma_{\mathbf{q}})^n}{E_{\mathbf{q}}(\Delta)}, \tag{30}$$

$$B_n(\Delta, \tau) = \frac{1}{N}\sum_{\mathbf{q}} \frac{(1-\gamma_{\mathbf{q}})(-\gamma_{\mathbf{q}})^n}{E_{\mathbf{q}}(\Delta)} \times \frac{2}{\exp(\lambda E_{\mathbf{q}}(\Delta)/\tau) - 1}. \tag{31}$$

The integrals $I_n(\Delta)$ correspond to zero temperature ($\tau = 0$); therefore, we put $\Delta = \Delta(0)$ in them. The energy of the system given by Eq. (4) is minimal when K_1 reaches its maximum and, as can be easily shown, when $\Delta(0) = 0$. In this case, the integrals take the form

$$I_n(0) \equiv I_n = \frac{1}{N}\sum_{\mathbf{q}} \sqrt{\frac{1-\gamma_{\mathbf{q}}}{1+\gamma_{\mathbf{q}}}} (-\gamma_{\mathbf{q}})^n = \int_{-1}^{1} D(\gamma) \sqrt{\frac{1-\gamma}{1+\gamma}} (-\gamma)^n d\gamma. \tag{32}$$

Here, $D(\gamma)$ is the density of states (on the square lattice) for the dispersion law $\gamma_{\mathbf{q}} = 0.5(\cos q_x + \cos q_y)$; this den-

sity of states is expressed through the complete elliptic integral of the first kind $\mathbf{K}(x)$ as

$$D(\gamma) = \frac{2}{\pi^2}\mathbf{K}(\sqrt{1-\gamma^2}) \approx \frac{1}{\pi} - \left(\frac{1}{2} - \frac{1}{\pi}\right)\ln|\gamma|, \qquad \int_{-1}^{1} D(\gamma)d\gamma = 1. \tag{33}$$

A calculation gives the following values: $I_0 = 1.396$ and $I_1 = I_2 = 0.555$. The integrals $B_n(\Delta, \tau)$ can also be expressed through the density of states.

5.1. Low-Temperature Regime

In the case of $\tau \longrightarrow 0$, we calculate the integrals B_n following the procedure employed in [8, 13]. When $\tau \longrightarrow 0$, the vicinity of the point $\mathbf{q} = \mathbf{Q}$ is the most important, because this region can lead not only to power-law terms but also to anomalous terms that do not vanish as $\tau \longrightarrow 0$. Calculations give

$$B_0(t) = C(t) + \frac{D(1)}{2}t^3, \qquad B_1(t) = B_2(t) = C(t) - \frac{3}{2}D(1)t^3 \tag{34}$$

to within terms $O(t^5)$. Here, $D(1) = 1/\pi$ and

$$C(t) = \frac{2}{\pi}\ln\left(\frac{t^2}{2\Delta}\right), \quad t = \tau/\lambda(0). \tag{35}$$

We represent the low-temperature dependence of the energy gap parameter in the most general form,

$$\Delta(t) = \Delta_0 t^{2\beta}\exp\left(-\frac{2t_0}{t}\right), \tag{36}$$

which allows us to consider two scenarios: we will have power-law behavior ($\beta > 0$) if $t_0 = 0$ and exponential behavior if $t_0 \neq 0$. As in [8–11], we will say that condensation occurs in the vicinity of the point $\mathbf{q} = \mathbf{Q} = (\pi, \pi)$ (where $\gamma_{\mathbf{Q}} = -1$) if the function given by Eq. (35) tends to a nonzero value as $\tau \longrightarrow 0$:

$$C(0) = \lim_{t\to 0} C(t) = \frac{4t_0}{\pi} \equiv C, \tag{37}$$

which is independent of the preexponential factor in Eq. (36).

5.2. The Ground State of the System on a Square Lattice

The set of equations (20), (15), and (22), which allows the parameters of the system to be determined self-consistently, possesses the following solution for $\tau = 0$, $\Delta = 0$, and $P(0, 0) = 0.84$:

$$\lambda = 0.744, \quad K_1 = 0.469, \qquad \alpha_1 = 2.236, \quad \alpha_2 = 2.65, \quad C = 0.189. \tag{38}$$

The energy of the system per bond (in units of J) is

$$\varepsilon_0 = -(3/4)K_1 = -0.352, \tag{39}$$

which is lower than the energy of the AFM state $\varepsilon_{AF} = -0.335$ (the best result of the spin-wave theory [3]). An energy very close to this numerical value was found in [8] ($\varepsilon_{AF} = -0.3508$) for the sublattice magnetization $m = 0.3$ and in [9, 10] ($\varepsilon_{AF} = -0.345$). We will show that the solution found is a singlet. A singlet state at $\tau = 0$ must satisfy the condition $\langle \mathbf{S}^2 \rangle = 0$. Let us consider the function

$$S^2(\tau) \equiv \frac{1}{N}\langle \mathbf{S}^2 \rangle = \frac{1}{N}\sum_{\mathbf{fm}} \langle \mathbf{s_f s_m} \rangle = \frac{1}{N}\sum_{\mathbf{fr}} \langle \mathbf{s_f s_{f+r}} \rangle = \frac{3}{4}\sum_{\mathbf{r}} K_r = \frac{3}{4}K(0). \tag{40}$$

From Eq. (19), it follows that

$$K(0) = \lim_{\mathbf{q}\to 0} K(\mathbf{q}) = \frac{K_1}{\lambda}\lim_{\mathbf{q}\to 0}\frac{1-\gamma_{\mathbf{q}}}{E_{\mathbf{q}}(\Delta)}\coth\left(\frac{\Omega_{\mathbf{q}}}{2\tau}\right) = \frac{4\tau}{\alpha_1(2+\Delta)}, \tag{41}$$

which gives $K(0) = 0$ and $\langle \mathbf{S}^2 \rangle = 0$ at $\tau = 0$. Thus, according to the approximate analytical theories developed to date, the ground state of the spin system on a square lattice is a singlet. This conclusion is supported by the result $\varepsilon_0 = -0.3509$ [6] obtained by the exact-diagonalization method for a cluster.

5.3. The Equation for Δ

The solution with $C \neq 0$ obtained above implies an exponential $\Delta(\tau)$ dependence, according to Eq. (36), and allows one to find the parameter $\tau_0 = \lambda t_0 = (\pi\lambda/4)C = 0.11$. In the case of a pure power-law $\Delta(\tau)$ dependence (for which $C = 0$), the set of equations has no self-consistent solution. It should be noted that in the three-dimensional case, the condensate does not occur ($C = 0$) because of the square-root dependence of the density of states near the limits of the spectrum.

In the low-temperature range, Eq. (15) for the energy gap Δ has a solution

$$2\Delta(\tau) \approx \left(\frac{\tau}{\lambda}\right)^2 \exp(-2\tau_0/\tau). \tag{42}$$

It follows from Eq. (42) that in this temperature range, the parameters λ, α_1, and α_2 show a pure power-law dependence (as was found in [8]) with the main contribution $\propto\tau^3$:

$$\lambda(\tau) = \lambda - \frac{3}{2\pi}(\tau/\lambda)^3, \qquad \alpha_1(\tau) = \alpha_1 - A_1\tau^3, \quad \alpha_2(\tau) = \alpha_2 - A_2\tau^3. \tag{43}$$

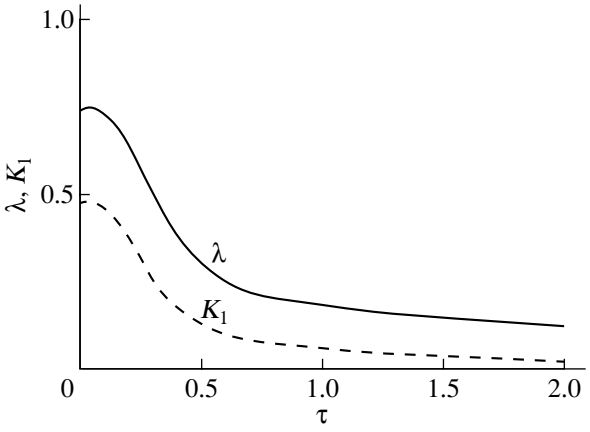

Fig. 1. Dependence of the hardness parameter of the excitation spectrum $\lambda(\tau)$ (solid curve) and the modulus of the correlator for nearest neighbors $K_1(\tau)$ (dashed curve) on dimensionless temperature $\tau = T/zJ$ for a square lattice ($z = 4$).

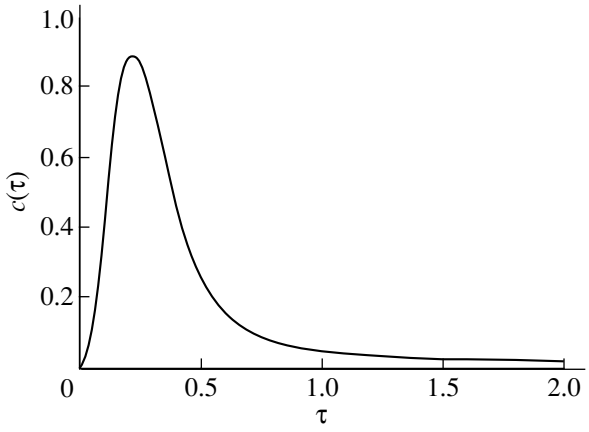

Fig. 2. Specific heat $c(\tau)$ (in dimensionless units) of the spin liquid on a square lattice.

Since $K_1(\tau) = K_1 - \kappa\tau^3$ in this temperature range, the energy of the system behaves as

$$\varepsilon(\tau) = -(3/4)K_1(\tau) = \varepsilon_0 + (3/4)\kappa\tau^3 \qquad (44)$$

and the specific heat $c(\tau) \propto \tau^2$.

5.4. Thermodynamic Properties of the Spin Liquid

The replacement of the ST condition by Eq. (29) does not affect the character of the temperature dependence of the model parameters; however, the numerical values of the coefficients are changed insignificantly. For this reason, we will only discuss the main results and will not present details concerning self-consistent calculations of the thermodynamic SL characteristics.

Self-consistent calculations of the hardness parameter $\lambda(\tau)$ of the excitation spectrum and the modulus of the correlation function for nearest neighbors $K_1(\tau)$ are represented in Fig. 1. Their asymptotic temperature dependence (for $\tau > 2$) is described by a power law: $\lambda(\tau) \approx 0.18/\tau^{1/2}$ and $K_1(\tau) \approx 0.06/\tau$.

The specific heat (in dimensionless units) is $c(\tau) = \partial\varepsilon(\tau)/\partial\tau$; its temperature dependence is shown in Fig. 2. For $\tau \longrightarrow 0$, we have $c(\tau) \propto \tau^2$ in accordance with Eq. (44); the maximum is reached at the temperature $\tau^* \approx 0.2 \approx 2\tau_0$, and the asymptotic high-temperature dependence is $c(\tau) \propto 1/\tau^2$, because $K_1(\tau) \propto 1/\tau$.

The dynamic susceptibility of the spin system (in dimensionless units) is given by [12]

$$\chi^{\alpha\beta}(\mathbf{q}, \omega) = -\langle\langle s^\alpha(\mathbf{q}) | s^\beta(-\mathbf{q})\rangle\rangle_\omega. \qquad (45)$$

In the SL state, the correlation functions are isotropic and, therefore, $\chi^{+-}(\mathbf{q}, \omega) = 2\chi^{zz}(\mathbf{q}, \omega)$. The static susceptibility (at $\omega = 0$), in accordance with Eq. (12), has the form

$$\chi^{zz}(\mathbf{q}, 0) = \frac{K_1}{2}\frac{(1-\gamma_\mathbf{q})}{\Omega_\mathbf{q}^2} = \frac{K_1}{2\lambda^2}\frac{1}{1+\gamma_\mathbf{q}+\Delta} = \frac{1}{\alpha_1}\frac{1}{1+\gamma_\mathbf{q}+\Delta}. \qquad (46)$$

From Eq. (46), it follows that

$$\chi^{zz}(\mathbf{q} = 0, 0) = 1/2\alpha_1 = 0.212, \quad \tau \longrightarrow 0,$$
$$\chi^{zz}(\mathbf{q} = \mathbf{Q}, 0) = \frac{1}{\alpha_1\Delta} = \frac{2\lambda^2}{\alpha_1}\frac{\exp(2\tau_0/\tau)}{\tau^2}, \qquad (47)$$

with the latter expression diverging as $\tau \longrightarrow 0$ (as in the AFM state).

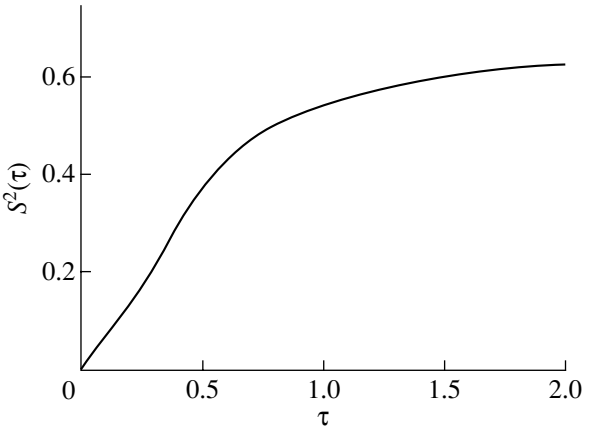

Fig. 3. Temperature dependence of the mean square of the total spin of the system (per lattice site) $S^2(\tau) = N^{-1}\langle\mathbf{S}^2\rangle$.

The thermodynamic longitudinal susceptibility, by definition, is [12]

$$\chi^{zz} = \frac{1}{T}[\langle (S^z(0))^2\rangle - \langle S^z(0)\rangle^2] \equiv \frac{1}{T}\tilde{\chi}_0,$$
$$\tilde{\chi}_0 = \frac{1}{N}\langle (S^z)^2\rangle = \frac{1}{3}S^2(\tau) = \frac{1}{4}K(0) \quad (48)$$

and equals the dynamic susceptibility for $\omega \longrightarrow 0$, $\mathbf{q} \longrightarrow 0$. At low temperatures, we have $\tilde{\chi}^{zz}(\tau) = \tilde{\chi}^{zz}(0) + a_1\tau^3$, in accordance with the temperature dependence of $\alpha_1(\tau)$; the numerical value of $\tilde{\chi}^{zz}(0) = 1/2\alpha_1 = 0.212$ agrees with the result obtained in [8] if the normalization to $z = 4$ is taken into account ($T/J = z\tau$, 0.212/4 = 0.053, as in [8]). The susceptibility $\tilde{\chi}^{zz}(\tau)$ reaches a maximum at $\tau \approx 0.1 \approx \tau_0$ and then decreases, with the asymptotic high-temperature dependence being $1/4\tau$. The temperature dependence of the mean square of the total spin of the system $S^2(\tau)$ is shown in Fig. 3.

The coefficients characterizing the asymptotic temperature dependence of the functions considered above (in the case of $\tau \longrightarrow \infty$, where there are no correlations) can be found analytically under the following assumptions: (i) the excitation spectrum is limited, $\Omega_\mathbf{q} \longrightarrow \lambda\sqrt{\Delta(1-\gamma_\mathbf{q})}$, i.e., $\lambda\sqrt{\Delta} \longrightarrow \text{const} \equiv \bar{c}$; (ii) $S^2(\tau) \longrightarrow 3/4$; and (iii) the decoupling parameters $\alpha_1(\tau) \longrightarrow 1$ and $\alpha_2(\tau) \longrightarrow 1$ and $K_2 \longrightarrow 1/4$. Condition (ii) is equivalent to $K(0) \longrightarrow 1$. Using the strong inequality $\Delta \gg 2$, we find that $\Delta(\tau) \longrightarrow 4\tau$ and condition (i) reduces to $\lambda(\tau) = \bar{c}/2\sqrt{\tau}$. Asymptotically, $I_0 \longrightarrow 2\tau/\lambda\Delta$, $I_2 \longrightarrow (1/z)2\tau/\lambda\Delta$, and Eq. (15) for the energy gap takes the form $\Delta = 1/8\lambda^2$, from which it follows that $\bar{c}^2 = 1/2z = 1/8$ and $c = 0.354$. Thus, we have the following asymptotic ($\tau \longrightarrow \infty$) temperature dependence of the parameters of the system:

$$\Delta(\tau) = 4\tau, \quad \lambda(\tau) = \frac{0.177}{\sqrt{\tau}}, \quad K_1(\tau) = \frac{0.063}{\tau},$$
$$\bar{c} = \lambda(\tau)\sqrt{\Delta(\tau)} = 0.354, \quad \tilde{\chi}^{zz}(\tau) = \frac{1}{4\tau}. \quad (49)$$

These expressions are identical to the numerical calculations to within less than one percent.

6. SPACE CORRELATIONS

Let $\mathbf{r} = (x, y)$ be the vector connecting two arbitrary sites of a square lattice ($a = 1$). According to Eqs. (5) and (19), the space correlators have the form

$$K_r = \frac{1}{N}\sum_\mathbf{q} e^{i\mathbf{qr}}K(\mathbf{q})$$
$$= \frac{K_1}{\lambda}\frac{1}{N}\sum_\mathbf{q} e^{i\mathbf{qr}}\frac{1-\gamma_\mathbf{q}}{E_\mathbf{q}(\Delta)}\coth\left(\frac{\lambda E_\mathbf{q}(\Delta)}{2\tau}\right), \quad (50)$$

$$e^{i\mathbf{Qr}} = (-1)^{x+y}$$

and oscillate in sign with distance, as in the AFM state.

By definition, $K(\mathbf{q}) = \sum_\mathbf{r} \exp(-i\mathbf{qr})K_r$; therefore, at $\mathbf{q} = 0$ and $\mathbf{q} = \mathbf{Q}$, we have

$$K(0) = \sum_\mathbf{r} K_r, \quad K(\mathbf{Q}) = \sum_\mathbf{r} |K_r|. \quad (51)$$

We note that $\langle \mathbf{S}^2\rangle = N(3/4)K(0)$, i.e., $\langle \mathbf{S}^2\rangle = 0$ at $\tau = 0$ (the ground state is a singlet); therefore, as can be seen from the expressions for $K(0)$, the correlations of alternating sign cancel out at $\tau = 0$. It follows from the general expression for $K(\mathbf{q})$ at $\mathbf{q} = \mathbf{Q}$ that

$$K(\mathbf{Q}) = \frac{K_1}{\lambda}\frac{2}{\sqrt{2\Delta}}\coth\left(\frac{\lambda\sqrt{2\Delta}}{2\tau}\right). \quad (52)$$

Substituting the solution for Δ at low temperatures given by Eq. (42), we obtain

$$K(\mathbf{Q}) = 2K_1\tau^{-1}\exp(2\tau_0/\tau), \quad (53)$$

which diverges as $\tau \longrightarrow 0$.

Now, we discuss the behavior of the correlation functions at large distances r of the order of the linear dimensions of the system $\sqrt{N}$ ($D = 2$). At $\tau \equiv 0$, $\Delta = 0$, we obtain from Eq. (50)

$$K_r = \frac{K_1}{\lambda}\frac{1}{(2\pi)^2}\int e^{i\mathbf{qr}}\sqrt{\frac{1-\gamma_\mathbf{q}}{1+\gamma_\mathbf{q}}}d^2\mathbf{q}. \quad (54)$$

In this integral, the main contribution comes from the region (of radius $k_0 \ll \pi$) of the point $\mathbf{q} = \mathbf{Q}$ of the Brillouin zone. Substituting $\mathbf{q} = \mathbf{Q} - \mathbf{k}$, we obtain

$$K_r \approx e^{iQr}\frac{K_1}{\lambda}\frac{\sqrt{2}}{\pi}\int_0^{k_0 r} J_0(x)dx\frac{1}{r},$$
$$|K_r| \approx \frac{0.284}{r}, \quad r \longrightarrow \infty, \quad (55)$$

which is indicative of the absence of long-range order in the ground state. Integrating Eq. (55) over the two-dimensional lattice volume, we find $K(\mathbf{Q}) \propto \sqrt{N}$; that is, we have a divergence in the thermodynamic limit

($N \longrightarrow \infty$). The staggered magnetization m is defined as [3]

$$m^2 = \left\langle \left(\frac{1}{N} \sum_{\mathbf{f}} (-1)^{x+y} \mathbf{s}_{\mathbf{f}} \right)^2 \right\rangle = \frac{1}{N} \frac{3}{4} \sum_{\mathbf{r}} |K_r| = \frac{1}{N} \frac{3}{4} K(\mathbf{Q}). \quad (56)$$

In this definition, the factor $1/N$ is of importance; since $K(\mathbf{Q}) \propto \sqrt{N}$ at $\tau = 0$, we have $m^2 \propto 1/\sqrt{N} \longrightarrow 0$ in the thermodynamic limit.

At low temperatures, the dominant contribution in Eq. (50) also comes from the vicinity of the point $\mathbf{q} = \mathbf{Q}$; this equation can be written as

$$K_r(\tau) \approx e^{i\mathbf{Q}\mathbf{r}} \frac{4\tau}{\alpha_1} \frac{1}{\pi^2} \int \frac{e^{i\mathbf{k}\mathbf{r}}}{k^2 + 4\Delta} d^2\mathbf{k}. \quad (57)$$

The correlation length ξ is commonly defined by the equation $4\Delta(\tau) = \kappa^2 = \xi^{-2}$. For large values of r, we find

$$|K_r(\tau)| = \frac{4\tau}{\alpha_1} \frac{1}{2\pi} \int_0^{k_0 r} \frac{x J_0(x)}{x^2 + \kappa^2 r^2} dx = \frac{4\tau}{\alpha_1} \sqrt{\frac{2}{\pi}} \frac{\exp(-\kappa r)}{\sqrt{\kappa r}} \left(1 - \frac{1}{8\kappa r} + \ldots\right). \quad (58)$$

It follows from Eq. (42) that $\xi/a \propto \tau^{-1}\exp(\tau_0/\tau)$, as in [8, 13, 14]. Despite the fact that there are regions of large values of r, such that $\kappa r = r/\xi \sim 1$, the correlation function possesses the property $|K_r| \longrightarrow 0$ as $\tau \longrightarrow 0$ (there is no long-range order).

It was shown in [14] that the behavior of the two-dimensional Heisenberg model with AFM exchange in the long-wavelength and low-temperature regions can be described in terms of the quantal nonlinear σ model using the renormalization group method. The results obtained above correspond to the classical renormalization regime; however, in a higher order approximation, we have $\xi/a = C_\xi \exp(2\pi\rho_s/T)$, where $C_\xi \approx 1$; that is, the preexponential factor is temperature-independent [3, 14]. Thus, the low-temperature dependence of ξ can be different, but there is always an exponential divergence as $T \longrightarrow 0$ in both AFM and SL singlet states.

7. CONCLUSION

Thus, we have described the Heisenberg model with Hamiltonian (1) on a square lattice as a thermodynamically stable homogeneous isotropic nonmagnetic spin liquid at any temperature T. In the limit as $T \longrightarrow 0$, its state is a singlet (with the total spin $S = 0$) with an energy per bond $\varepsilon_0 = -0.352$. At $T = 0$, the AFM state with energy ε_{AF} can compete with the singlet state. For the best result obtained analytically within the spin-wave theory, we have $\varepsilon_0 \le \varepsilon_{AF}$; that is, the ground state is a singlet. It should be noted that the results of numerical calculations at $T = 0$ are contradictory, because the difference in energy of these states is very small. In the SL state, there is a well-defined short-range AFM order with spin correlators oscillating in sign according to distance. At high temperatures ($T \gg J$), the system asymptotically goes over to the paramagnetic state ($K_1 \longrightarrow 0$, $N^{-1}\langle \mathbf{S}^2 \rangle \longrightarrow 3/4$) with susceptibility $\chi \propto 1/T$.

ACKNOWLEDGMENTS

The author is grateful to participants of the Kourovka-2000 School S.V. Maleev, N.M. Plakida, and Yu.G. Rudoĭ, as well as to V.V. Val'kov, V.I. Zinenko, and A.L. Pantikyurov, for helpful discussions and critical comments.

This study was supported by the Russian Foundation for Basic Research, project no. 00-02-16110.

REFERENCES

1. W. Marshall, Proc. R. Soc. London, Ser. A **232**, 48 (1955).
2. D. C. Mattis, *The Theory of Magnetism* (Harper and Row, New York, 1965; Mir, Moscow, 1967).
3. E. Manousakis, Rev. Mod. Phys. **63** (1), 1 (1991).
4. P. W. Anderson, Mater. Res. Bull. **8**, 153 (1973).
5. S. Liang, B. Doucot, and P. W. Anderson, Phys. Rev. Lett. **61** (10), 365 (1988).
6. K. Fabricius, U. Low, and K.-H. Mutter, Phys. Rev. B **44** (18), 9981 (1991).
7. N. Mermin and G. Wagner, Phys. Rev. Lett. **17** (22), 1136 (1966).
8. H. Shimahara and S. Takada, J. Phys. Soc. Jpn. **60**, 2394 (1991).
9. A. F. Barabanov and V. M. Berezovskiĭ, Zh. Éksp. Teor. Fiz. **106**, 1156 (1994) [JETP **79**, 627 (1994)].
10. A. F. Barabanov and V. M. Beresovsky, Phys. Lett. A **186**, 175 (1994).
11. A. F. Barabanov, V. M. Beresovsky, and E. Zasinas, Phys. Rev. B **52** (14), 10177 (1995).
12. S. V. Tyablikov, *Methods in the Quantum Theory of Magnetism* (Nauka, Moscow, 1975, 2nd ed.; Plenum, New York, 1967).
13. M. Takahashi, Phys. Rev. B **40** (4), 2494 (1989).
14. S. Chakravarty, B. I. Halperin, and D. R. Nelson, Phys. Rev. B **39** (4), 2344 (1989).

Translated by Yu. Epifanov

Physics of the Solid State, Vol. 44, No. 6, 2002, pp. 1130–1134. Translated from Fizika Tverdogo Tela, Vol. 44, No. 6, 2002, pp. 1082–1086.

MAGNETISM AND FERROELECTRICITY

Explanation of the Friedel Rule Violations in Electron Diffraction Patterns of Some Metallic Alloys. A Metallic Ferroelectric?

É. V. Bursian and A. I. Zaĭtsev

Russian State Pedagogical University, St. Petersburg, 191186 Russia

e-mail: bursian@AB3841.spb.edu

Received July 12, 2001; in final form, September 17, 2001

Abstract—An assumption of the possible existence of a kind of condensed state possessing metallic conduction while at the same time being made up of electrically polar unit cells is drawn from an analysis of the specific features of electron diffraction in some metal alloys. Examples of alloys in which such a state may be realized are presented. © *2002 MAIK "Nauka/Interperiodica".*

1. INTRODUCTION

The diffraction of electrons about 100 keV in energy observed in transmission from thin layers of some AuCu-type and other binary alloys exhibits an asymmetry in the reflection intensities that is sometimes very strong [1–3]. The *mnk* and $\bar{m}\bar{n}\bar{k}$ reflections may differ in brightness so strongly as not to be seen on one side of the (000) central reflection at all. This effect could be due to the crystal being inclined with respect to the beam; however, for $\lambda \sim 0.04$ Å and a lattice constant ~4 Å, the Ewald sphere becomes virtually plane, thus complicating this trivial interpretation. In addition, changing the object position does not remove the electron diffraction asymmetry. In diffraction theory, this is called violation of the Friedel rule [4]. This violation is known to be observed in ferromagnetic materials [5, 6], where it is due to the deflecting action of the inherent magnetic field of the magnetized parts of the sample. When the microscope is adjusted to an image in the conjugate plane and the bright-field geometry is used, this, in accordance with the theory of Abbe, does not affect the image at all. However, in the case of vignetting (asymmetric restriction of inclined beams, dark-field geometry), the effect permits the observation of ferromagnetic domains, because the image is produced only by the electrons deflected to one side.

Some authors have assigned the electron diffraction asymmetry in nonmagnetic crystals to absorption [7, 8].

A strong violation of the Friedel rule was also observed in ferroelectrics with spontaneous electric polarization [9]. An asymmetry in charge density in a unit cell possessing a dipole moment results in an echelle-type effect in optics, where for $\lambda < a$ (a is the lattice constant) each lattice unit cell acts simultaneously as a small prism by deflecting the rays predominantly to one side of the central maximum (phase-profiled diffraction grating).

In this communication, we show that the diffraction pattern asymmetry observed in some intermetallic nonmagnetic compounds is likewise associated with the asymmetry of the electric potential within each lattice unit cell.

2. SPECIFIC FEATURES OF ELECTRON DIFFRACTION FROM AN ASYMMETRIC CELL POTENTIAL

It appears natural to describe the propagation, through a solid, of fast electrons with a de Broglie wavelength $\lambda \ll a$, whose kinetic energy is considerably higher than the potential interaction with the crystal lattice, with a wave function in the eikonal approximation [10], which offers a particularly revealing pattern of the wave phase variation inside the medium. We follow the reasoning outlined in [9]. The wave function ψ of electrons striking a layer of a solid of thickness d at normal incidence is changed after the layer transit by a factor $\varphi(x)$ (see Fig. 1, with only one coordinate displayed for the sake of brevity):

$$\varphi(x) = \exp\left[-\frac{i}{\hbar v_z}\int_0^d dz\,U(x,z)\right] \equiv e^{-iW(x)}, \qquad (1)$$

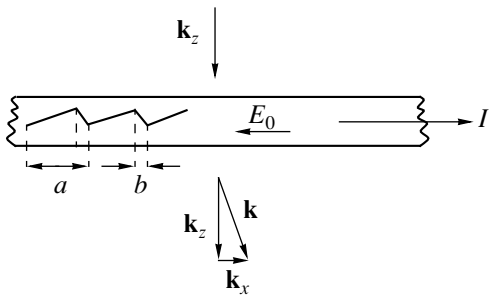

Fig. 1. Wave propagation through an asymmetric potential.

1063-7834/02/4406-1130$22.00

where v_z is the velocity of an electron moving across the film, $v_z = \hbar k_z/m$. Since the potential energy $U(x)$ is a periodic function, $W(x)$ and $\varphi(x)$ are also periodic [$W(x + a) = W(x)$, $\varphi(x + a) = \varphi(x)$].

In the absence of $U(x)$, we obviously have $\varphi(x) = 1$, such that the difference $\varphi(x) - 1$ describes the electron interaction with the solid. Because the interaction is periodic, the electrons will undergo scattering and acquire wave vectors from the set $k_{xn} = 2\pi n/a$, $n = \pm 1, \pm 2, \ldots$, with the scattering amplitude being

$$f_n = \int_{-a/2}^{a/2} \exp(-ik_{xn}x)[\varphi(x) - 1]dx. \quad (2)$$

The intensity of the nth reflection is defined as $I_n \sim |f_n|^2$. Here and subsequently, we drop some factors for the sake of clarity.

We assume the net interaction of the electron with the film to be small ($W \ll 1$), a situation where the electron suffers one or only a few scattering events. Then, $\varphi(x) - 1 \approx iW(x)$, such that, as follows from Eq. (2), $f_n = -f^*_{-n}$ and the intensities of the opposite reflections are equal irrespective of the actual form of W: $I_n = I_{-n}$.

The Friedel rule can be violated only in the dynamic approximation, i.e., only in multiple scattering in not very thin films. Under multiple scattering [$W(x) > 1$], the term with unity in Eq. (2) for $n \neq 0$ virtually does not contribute.

For a potential symmetric with respect to some point [$U(-x) = U(x)$ and $W(-x) = W(x)$, where the origin on the x axis is at the center of symmetry], we have $f_n = -f^*_{-n}$ and the intensities of opposite reflections are equal irrespective of the actual form of W ($I_n = I_{-n}$). Thus, in the case of symmetric potentials, the Friedel rule also holds in multiple scattering.

This equality does not hold, however, in the general case if the following conditions are simultaneously satisfied:

(1) the value of W, which has the meaning of the phase change, is of order unity or larger, and

(2) the potential within the unit cell is asymmetric, i.e.,

$$U(x) \neq U(-x); \quad \varphi(x) \neq \varphi(-x)$$

for any choice of the origin in x.

To estimate the effect of the asymmetry, we use a comb-type approximation for the potential (Fig. 1) and steepen, for simplicity, one side of the comb tooth. Then, we have

$$f_n \approx \frac{\sin(W_0/2)}{W_0 - 2\pi n}. \quad (3)$$

We have taken into account that the phase incursion is

$$W = -W_0\frac{x}{a}, \quad W_0 = \frac{eU_0 d}{\hbar v}. \quad (4)$$

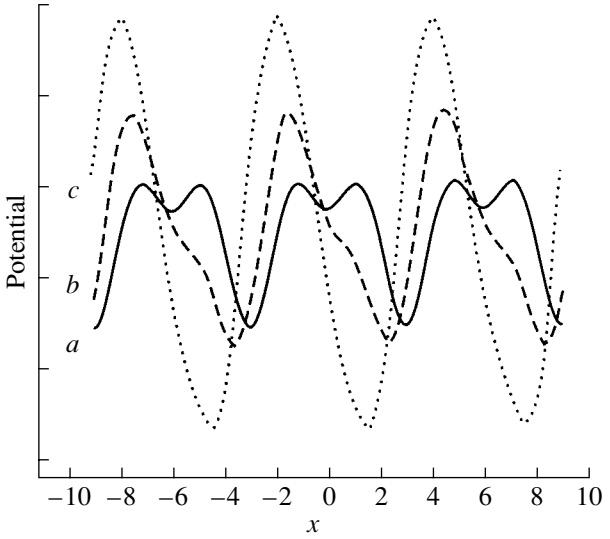

Fig. 2. Potential $U(x)$ for (*a*) a symmetric and (*b*, *c*) asymmetric ion positions.

One can conveniently express W_0 through the mutually related λ and the accelerating voltage V:

$$W_0 = \pi\frac{U_0 d}{V\lambda} \equiv \frac{\pi E_0 a}{V}\frac{d}{\lambda}. \quad (5)$$

As is evident from Eq. (3), for $W_0 \ll \pi$, the intensities are symmetric, but as W_0 grows, an asymmetry appears. For $W_0 = 2\pi$, all reflections except that with $n = 1$ vanish. Similarly, for $W_0 = 2\pi N$, the only reflection retained is that with number $n = N$. Polarization reversal, i.e., the replacement $W_0 \longrightarrow -W_0$, will also bring about the replacement $I_n \longrightarrow I_{-n}$.

Thus, an essential point in explaining a violation of the Friedel rule is the possibility of realization of an asymmetric potential of the electron interaction with the lattice.

3. ENERGY RELATIONS

Such an asymmetry can be obtained if one of the ions in a unit cell is displaced. Consider, for simplicity, a one-dimensional problem. Let us assume that the Cu^+ ion in an AuCu-type alloy does not occupy, for some reason, the central position between the Au^+ ions but is displaced from it by Δx (for instance, $\Delta x = 10^{-2}a$). This is energetically unfavorable. Denote the corresponding loss in energy compared with the original symmetric arrangement of the ions by $\Delta\varepsilon_+$. If, however, the charges of these ions are not equal because of a large difference in electronegativities, the resultant distribution of the potential (the pseudopotential, which is usually employed in the theory of metals) in such a diatomic lattice will naturally be asymmetric (curve *b* in Fig. 2). In this case, the increase in the ion energy can be compensated by a decrease of the electronic band in energy

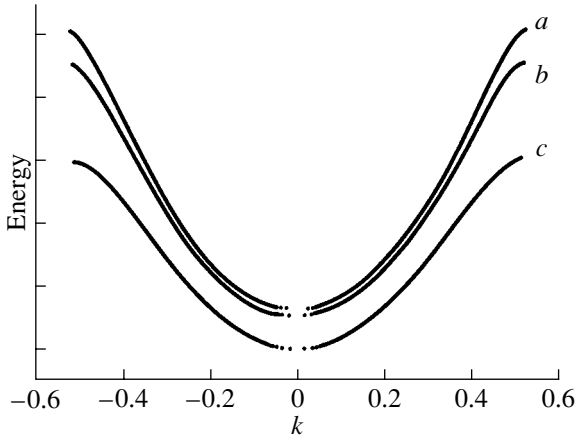

Fig. 3. $E(k)$ calculated numerically for nondisplaced and displaced ion positions (curves *a*–*c* correspond to Fig. 2).

($\Delta\varepsilon_-$). Let us estimate the possibility of such a compensation.

The energy $\Delta\varepsilon_+$ can be estimated from the relation $\Delta\varepsilon_+ \sim m\omega_{LO}^2 x^2$, where ω_{LO} is the frequency of longitudinal optical vibrations. For $x \sim 10^{-2}a$, the cost in energy is of the order of 10^{-2} eV.

Now, we estimate $\Delta\varepsilon_-$. The interaction potential of a free electron with the ion core can be obtained as a sum of effective interaction potentials with the ions $U(x) = \sum_{i,\alpha} U_\alpha(|x - x_{i\alpha}|)$, where $x_{i\alpha}$ is the position of the ion of species α in the ith unit cell and $U_\alpha(x)$ is the effective electron interaction potential with an ion of species α.

We shall choose a sufficiently "shallow" effective pseudopotential of the electron interaction with an ion such that it will accommodate one atomic level only. This is needed to ensure filling of the valence band states with a sufficiently large group velocity (i.e., with a good conductivity).

The electron wave functions $\psi_k(x)$ in the periodic potential are solutions to the Schrödinger equation

$$\psi_k'' + 0.26(E(k) - U(x))\psi_k = 0 \qquad (6)$$

which satisfy, according to Bloch's theorem, the requirement

$$\psi_k(x + a) = \lambda(k)\psi_k(x), \qquad (7)$$

where

$$\lambda(k) = \exp(ikx) \qquad (8)$$

(x is measured in Å; E and U, in eV).

The wave function $\psi_k(x)$ for a given energy E was looked for within a unit cell $-a/2 \le x \le a/2$ as a linear combination of the fundamental solutions $\varphi_1(x)$ and $\varphi_2(x)$ of Eq. (6):

$$\psi_k(x) = C_1(E)\varphi_1(x) + C_2(E)\varphi_2(x). \qquad (9)$$

Here, $\varphi_1(x)$ and $\varphi_2(x)$ are solutions to Eq. (6) for $-a/2 \le x \le a/2$ that satisfy the boundary conditions

$$\begin{aligned} \varphi_1(E, -a/2) &= 1, \quad \varphi_1'(E, -a/2) = 0, \\ \varphi_2(E, -a/2) &= 0, \quad \varphi_2'(E, -a/2) = 1. \end{aligned} \qquad (10)$$

The requirement of Bloch's theorem for the linear combination in Eq. (9)

$$\begin{aligned} \psi_k(a/2) &= \lambda(k)\psi_k(-a/2), \\ \psi_k'(a/2) &= \lambda(k)\psi_k'(-a/2) \end{aligned} \qquad (11)$$

yields a characteristic equation

$$\lambda^2 + (\varphi_1(E, -a/2) + \varphi_2'(E, -a/2))\lambda + w(a/2) = 0 \qquad (12)$$

with real coefficients. The Wronskian of the equation $W = \varphi_1(E, x)\varphi_2'(E, x) - \varphi_2(E, x)\varphi_1'(E, x)$ is a constant [$W(x) = W(0)$] equal, according to Eq. (10), to unity.

By solving this equation, one can find λ as a function of energy and, thus, determine $E(k)$. For this energy to belong to an allowed band (for k to be real), the condition

$$\left|\varphi_1(E, a/2) + \varphi_2'(E, a/2)\right| \le 2 \qquad (13)$$

has to be met.

Figure 3 presents the energies of the lower band $E(k)$ obtained by numerical calculation of the lower-band energy $E(k)$ for several ion displacements. The lower valence band is seen to lower to yield a gain in electron energy $\Delta\varepsilon_-$. Considered from the physical standpoint, this means that ion asymmetry makes one of the potential boxes slightly wider. This conclusion depends only weakly on the actual form of the effective potential.

For displacements of the order of $10^{-2}a$, the values of $\Delta\varepsilon_-$ are also about a few hundredths of an electronvolt, such that, on the whole, the gain in energy for some displacements may, in principle, be real in some cases, thus making a state with displaced core ions energetically favorable.

4. ELECTRON DENSITY DISTRIBUTION AND DIPOLE MOMENT OF THE UNIT CELL

The electronic state thus produced is of particular interest. The electron density distribution (the probability density of an electron being at point x) can be written as

$$\rho(x) = \left\langle \left|\psi_k(x)^2\right| \right\rangle_k,$$

where $\langle f(k)\rangle = \int f(k(E))g(E)dE$. Here, $g(E)$ is the density of states in the band and integration is performed over the band energies. The dipole moment is calculated

as $-\int ex\rho dx = -\int P(x)dx$. The corresponding curves are displayed in Fig. 4. The electron density is naturally the highest at the atom with a deeper potential well.

The total dipole moment of the unit cell is the sum of the ion and electron contributions. We note that the total charge of the unit cell is zero and the ion dipole moment of the cell should not depend on the method used in the calculations. As follows from the calculations, adding these contributions in the case of displaced ions gives a state possessing a nonzero total dipole moment of the unit cell.

5. DISCUSSION

Thus, the asymmetry in reflections reveals an asymmetry in the internal electric field, i.e., the cell polarization, and theoretical estimates support the possibility of realization of this state. Any total dipole moment in a metal crystal becomes naturally screened completely in a time less than 10^{-16} s, and macroscopic polarization is always exactly zero. This does not imply, however, that a unit cell cannot have a dipole moment.

As for matching these moments in direction in adjacent cells, such a coherence between charge displacements is not caused by the dipole–dipole interaction, as is the case with ferroelectrics. Thus, extrapolation of the dielectric approach used when considering conducting ferroelectrics would be invalid. In this case, the long-range interaction is due to a purely quantum effect, namely, the need of joining the electron wave functions (with Bloch's theorem not violated).

Because the potential distribution within a unit cell and within one domain of macroscopic size differ little from the situation in poorly conducting pyroelectrics and ferroelectrics (although for another reason), there are grounds to use, in this case, the term metallic ferroelectric. To be more rigorous, this is one more kind of condensed state.

Revealing this state in a macroscopic experiment (pyroelectric or piezoelectric effect, etc.) appears difficult if at all possible because almost instantaneous screening sets in. It may turn out that electron scattering for $\lambda \ll a$ is the only method by which one can detect spontaneous electrical polarization in strongly conducting crystals, naturally provided that one does not reveal effects where such polarization noticeably affects the macroscopic properties (see, e.g., [11]).

In accordance with the Neumann principle, in order to learn whether a metallic compound can be classed among pyroelectrics, one has to prove that the point group of the crystal does not contain certain symmetry elements. One has to establish that this point group is a subgroup of the limiting group ∞mm, i.e., that it belongs to one of the following classes: 1, 2, 3, 4, 6, *m*, *mm*2, 3*m*, 4*mm*, and 6*mm*. However, metallographic literature and reference books present, as a rule, only the type of Bravais lattice inferred from x-ray and neutron diffraction measurements. We have not succeeded in finding published data on the refinement of point groups of metallic alloys in this context.

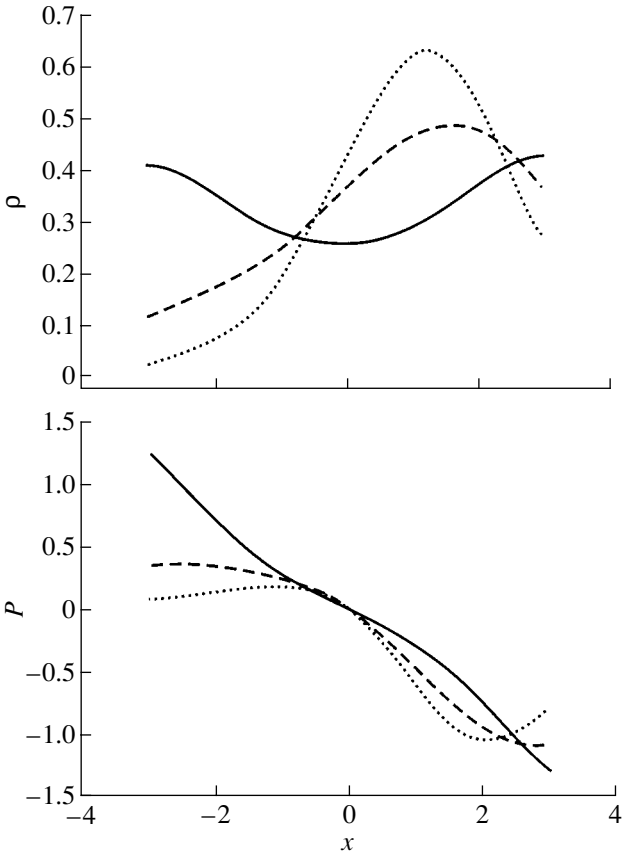

Fig. 4. Distribution of band-averaged electron density ρ and dipole moment P (in arbitrary units) over the unit cell. One of the atoms (with a shallower potential well) is at the center ($x = 0$), and the other is displaced from the unit-cell edge ($x = +d/2 = +3$) to the center by 2/15 (dashed curve) and by 3/15 (dotted line).

A study of the literature on intermetallic alloys [12, 13] shows that, in addition to the ordering phase transi-

Phase transition temperatures in some binary metal alloys

Alloy	Melting temperature, °C	Other phase transitions, °C
AuMn	1260	600, 232, 124
$AuZn_3$	600	515, 225
Au_3Zn	700	425, 230
AuCu	910	410, 385
CuZn	1100	450, 200, –100
Cu_3Zn	1000	500, 210
NiTi	1310	800, 100

Note: The temperatures of the ordering phase transitions are underlined.

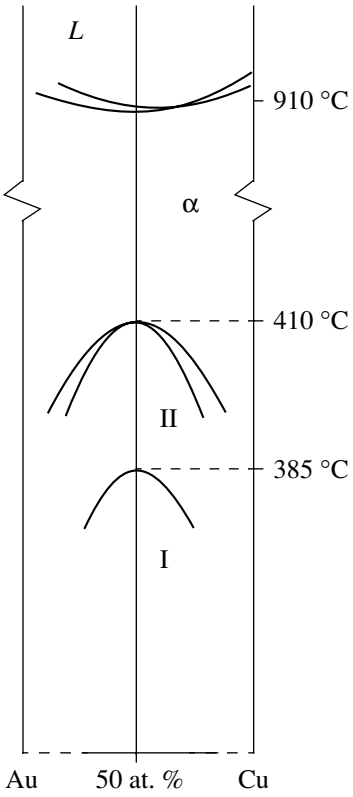

Fig. 5. Part of the phase diagram of AuCu. *L* is liquid, α is the disordered phase, II is the orthorhombic phase with superstructure ($a \sim 3.96$, $b \sim 43$–44, $c \sim 3.85$ Å), and I is the face-centered tetragonal phase ($a \sim 3.95$, $c \sim 3.68$ Å).

tions investigated comprehensively in metallography, one or more structural transitions are observed in many cases at lower temperatures; those transitions involve a change in lattice symmetry and superficially resemble the transitions that occur in ferroelectrics. They are exemplified in the table.

The largest difference between the electronegativities is found in the AuCu alloy, which has been well studied in metallography and can serve as a model compound. Figure 5 shows a part of its phase diagram. Phases existing below 410°C are suggestive of having ordered electrical unit-cell polarization (the onset of quantum phase coherence).

It can be added that there are numerous accounts even of extrareflections, superstructure, and the observation of a fine but distinct domain pattern in AuCu [14]. These domains were called antiphase [6], and they were given another interpretation. The possibility of the unit cells making up a domain having ordered polarity was not considered. At the same time, the presence of such domains suggests the existence of a nontrivial mechanism of long-range interaction and possibly bears on the considerations outlined here.

ACKNOWLEDGMENTS

The authors are indebted to the Chair of Theoretical Physics, RSPU, for fruitful discussions.

This study was supported by the Russian Foundation for Basic Research (project no. 00-02-16735).

REFERENCES

1. J. B. Coreia, H. A. Davies, and C. M. Cellars, Acta Mater. **45** (1), 177 (1997).
2. M. J. Whiting and P. Tsakiropoulos, Acta Mater. **45** (5), 2037 (1997).
3. N. D. Zemtsova, Fiz. Met. Metalloved. **89** (3), 75 (2000).
4. J. M. Cowley, *Diffraction Physics* (American Elsevier, New York, 1975; Mir, Moscow, 1979).
5. R. Heidenreich, *Fundamentals of Transmission Electron Microscopy* (Interscience, New York, 1964; Mir, Moscow, 1966).
6. P. B. Hirsch, A. Howie, R.B. Nicholson, D.W. Pashley, and M.J. Whelan, *Electron Microscopy of Thin Crystals* (Butterworths, London, 1965; Mir, Moscow, 1968).
7. S. Miyake and R. Uyeda, Acta Crystallogr. **8**, 335 (1955).
8. G. Kästner, Acta Crystallogr. **43** (5), 683 (1987).
9. É. V. Bursian, A. B. Vall, and N. N. Trunov, Izv. Akad. Nauk, Ser. Fiz. **58** (5), 219 (1994).
10. L. D. Landau and E. M. Lifshitz, *Course of Theoretical Physics*, Vol. 3: *Quantum Mechanics: Non-Relativistic Theory* (Nauka, Moscow, 1974; Pergamon, New York, 1977).
11. É. V. Bursian and Ya. G. Girshberg, *Coherent Effects in Ferroelectrics* (Prometeĭ, Moscow, 1989).
12. M. Hansen and K. Anderko, *Constitution of Binary Alloys* (McGraw-Hill, New York, 1958; Metallurgizdat, Moscow, 1962).
13. A. E. Vol, *Structure and Properties of Binary Metallic Systems* (Nauka, Moscow, 1960), Vol. 3.
14. D. W. Pashley and A. E. B. Presland, J. Inst. Met. **87**, 419 (1959).

Translated by G. Skrebtsov

Physics of the Solid State, Vol. 44, No. 6, 2002, pp. 1135–1144. Translated from Fizika Tverdogo Tela, Vol. 44, No. 6, 2002, pp. 1087–1095.

MAGNETISM AND FERROELECTRICITY

On the Nature of Ferroelectricity in $Sr_{1-x}A_xTiO_3$ and $KTa_{1-x}Nb_xO_3$ Solid Solutions

O. E. Kvyatkovskiĭ

Ioffe Physicotechnical Institute, Russian Academy of Sciences, ul. Politekhnicheskaya 26, St. Petersburg, 194021 Russia

e-mail: kvyatkovskii@pop.ioffe.rssi.ru

Received October 10, 2001

Abstract—Cluster calculations of the local adiabatic potential for an impurity atom in position *A* in $Sr_{1-x}A_xTiO_3$ (*A* = Mg, Ca, Ba, Pb, Cd, Zn), as well as for the Nb and O atoms in the Ta–O–Nb chain in $KTa_{1-x}Nb_xO_3$, were carried out in the nonempirical Hartree–Fock–Roothaan MO-LCAO formalism. For comparison, similar calculations of the local adiabatic potential were performed for a sublattice-*A* atom in the $ATiO_3$ cubic perovskites (*A* = Ca, Sr, Ba, Pb), for K and Ta atoms in $KTaO_3$, and for Li in $K_{1-x}Li_xTaO_3$. The calculations revealed that in all the cases considered, except the Zn, Mg, and Li impurities, the impurity atoms move in single-well potentials and that the corresponding solid solutions are displacive ferroelectrics. Zn in $Sr_{1-x}Zn_xTiO_3$ and Mg in $Sr_{1-x}Mg_xTiO_3$ were found to occupy off-center positions, as does the Li atom in $K_{1-x}Li_xTaO_3$; i.e., they move in a multiwell local potential. An explanation is proposed for the first-order Raman scattering observed in the paraelectric phase of the above solid solutions with central impurities. The critical concentration x_c for the displacive $KTa_{1-x}Nb_xO_3$ and $Sr_{1-x}A_xTiO_3$ solid solutions was calculated in the virtual-crystal approximation within the soft ferroelectric mode theory. The values of x_c thus obtained agree with the available experimental data. © *2002 MAIK "Nauka/Interperiodica".*

1. INTRODUCTION

The $SrTiO_3$ (STO) and $KTaO_3$ (KTO) quantum paraelectrics [1–4] and the related solid solutions [1–6] have recently attracted considerable interest. Under normal conditions, STO and KTO are incipient ferroelectrics. Having anomalous dielectric properties at low temperatures, these materials remain paraelectrics down to 0 K [7, 8] because of the quantum effects [9–11]; in STO, this is likewise due to the cubic structure becoming distorted below the point of the structural phase transformation (105 K) [12]. STO and KTO are similar in dielectric properties to the paraelectric phase of real perovskite ferroelectrics ($BaTiO_3$, $PbTiO_3$, $KNbO_3$); in fact, there is a soft IR-active transverse optical (TO) mode whose frequency ω_f tends to zero with decreasing temperature [12, 13] and the dielectric permittivity ε grows anomalously for $T \longrightarrow 0$ K [7, 8]. However, the growth of $\varepsilon(T)$ and the decrease in $\omega_f^2(T)$ saturate below 40 K for STO and 30 K in KTO. As a result, the soft mode remains stable down to 0 K and $\varepsilon(T)$ reaches the values $\varepsilon_a = 41900$ and $\varepsilon_c = 9380$ in STO [14] and $\varepsilon = 3800$ in KTO [15], while varying only weakly in the immediate vicinity of 0 K [7, 8].

Because STO and KTO are close to the ferroelectric state, even a weak doping by isoelectronic impurities drives them to a low-temperature ferroelectric state or a glass-type polar phase [1–6, 16–19]. There is a critical concentration x_c above which a maximum in the temperature dependence of the dielectric permittivity appears at a temperature T_m identified with the phase-transition temperature T_C. In accordance with the theoretical predictions made for displacive low-temperature ferroelectrics [10, 11, 18, 28–30], in $KTa_{1-x}Nb_xO_3$ (KTN) [20], $Sr_{1-x}A_xTiO_3$ (*A* = Ca, Ba, Pb, Cd) [5, 6, 21–27], and SrTi $(^{16}O_{1-x}{}^{18}O_x)_3$ [17], the transition temperature near x_c scales with concentration as $T_C(x) = A(x - x_c)^{1/2}$.

For isotopic impurities, both the nature of the ordered state in $SrTi(^{16}O_{1-x}{}^{18}O_x)_3$ [16, 17] and the phase-transition mechanism [18, 19] are presently understood quite well. However, the mechanism of the induced phase transition and the nature of the ordered polar state in quantum paraelectrics doped by nonisotopic impurities still remain unclear. Some authors identify the phase transition as displacive ferroelectric [20, 21, 31], while others [32, 33] believe the low-temperature phase in KTN to have a glasslike character. Ordering in KTN was shown in [34] to exhibit long-range order. The phase transformation in weakly doped $Sr_{1-x}Ca_xTiO_3$ is interpreted in [35–37] as a diffuse, percolation-type ferroelectric transition which is associated with the presence of ferroelectric microregions (FMR) induced by Ca impurities in a strongly polarizable host [38]. The ordered state in $Sr_{1-x}Ba_xTiO_3$ was found [23, 26] to be glasslike for $x_g = 0.0027 < x < x_c = 0.035$ and ferroelectric (with long-range order) for $x > x_c = 0.035$. A similar situation is observed to exist in $Sr_{1-x}Cd_xTiO_3$ [27].

To explain the nature of the FMRs, the specific features in the dielectric properties [32], light scattering experiments [39], and the fine structure in the x-ray absorption spectra (XAFS) [40], the model of an off-center impurity ion moving in a multiwell potential is frequently used. Interaction between the impurity-ion dipole moments via the soft polar TO mode was shown in [41, 42] to play an important role in the low-temperature state of the system in doped incipient ferroelectrics with off-center impurities. This interaction can initiate either a dipole-glass phase or the transition to a long-range order ferroelectric state, depending on the actual impurity concentration [2, 42]. The latter will be an order–disorder phase transition occurring in the system of impurity ions in a strongly polarizable medium. The existence, in the local impurity potential, of several equivalent minima that are displaced from lattice sites and separated by energy barriers suggests an obvious relaxation mechanism capable of accounting for the glasslike behavior that has been observed in many cases [23, 27, 32, 33, 43]. Finally, the existence of off-center impurities may obviously explain the FMR formation.

If an impurity ion occupies, on average, the central position at a lattice site and moves in a single-well potential, the transformation will more likely be a displacive phase transition in a random field of impurity centers. Thus, the shape of the local potential acting on an impurity atom is a problem of crucial importance in understanding the nature of the phenomena observed in doped quantum paraelectrics.

The existence itself of off-center impurities in the compounds under consideration is believed in [43] to have been established reliably. However, the only thing proven to date is the off-center position of the Li^+ ion in $K_{1-x}Li_xTaO_3$ (KTL) [1, 2, 44]. The off-center position of Li^+ in KTL can be assumed based on the considerable difference in size between Li^+ and K^+ [45]. In all other cases, the off-center position of an impurity may be questioned [46]. For instance, the Ba^{2+} and Pb^{2+} ions substituting for the Sr^{2+} ion in STO are larger than Sr^{2+} and they move, most likely, in a single-well potential [45]. The Ca^{2+}, Mg^{2+}, Cd^{2+}, and Zn^{2+} ions are smaller than Sr^{2+} [45]. It would be difficult, however, to make a sound judgement of the shape of the local potential for an impurity ion drawing only from empirical estimates of the ion size. As for KTN, the Nb^{5+} and Ta^{5+} ions have equal ionic radii within the accuracy with which these empirical quantities were determined [45]. The interpretation of experimental data obtained on this compound was based in many studies, starting with the work of Yacoby [39], on the assumption of Nb being off-center. However, the conclusion that Nb atoms occupy off-center positions is based on indirect data, in the sense that one can put forward another explanation of the observed phenomenon. A direct study of the local potential for the Nb atom in KTN based on ^{93}Nb NMR measurements [47] shows Nb to move in a single-well local potential [47], whereas an analysis of ^7Li NMR data suggests that Li in KTL is an off-center ion and moves in a multiwell potential [48].

The above subject of controversy is connected intimately with the problem of the existence of structural disorder in pure perovskites. To explain their experimental results, some authors [49–53] suggest that the Ti and Nb atoms in the cubic phase of $BaTiO_3$ (BTO), $PbTiO_3$ (PTO), and $KNbO_3$ (KNO) are off-center and move in a multiwell local potential. Although the experimentally observed anomalous diffuse x-ray scattering in perovskites [49] can be attributed to specific features in the perovskite phonon spectrum [54–57], one should not disregard the results of other experiments, for instance, of those on inelastic light scattering [51] and XAFS [53], which defy, at present, all attempts to make interpretations in terms of delocalized collective excitations (phonons).

We present here a solution to the problem of the local structure of doped and pure perovskites based on direct nonempirical calculations of the local potential for impurity ions in STO : *X* (*X* = Ca, Ba, Pb, Cd, Mg, Zn) and in KTO : *X* (*X* = Li, Nb), as well as for atoms at the *A* and *B* sites in the pure perovskites BTO, STO, $CaTiO_3$ (CTO), PTO, KNO, and KTO. We discuss the origin of first-order Raman scattering in the paraelectric phase of STO : Ca and KTN. In Section 3, we also consider an approach to describing the static properties of the $Sr_{1-x}A_xTiO_3$ and $KTa_{1-x}Nb_xO_3$ solid solutions with central impurities which is made in the virtual-crystal approximation in terms of the theory of the soft ferroelectric mode.

2. LOCAL POTENTIALS FOR ATOMS IN PEROVSKITES

As already pointed out, adequate description of some properties of perovskite compounds and of the related solid solutions requires knowledge of the shape of the local adiabatic potential for the host and impurity atoms. Cluster *ab initio* calculations for *B*-type and oxygen atoms in pure perovskites were reported in [58, 59]. *Ab initio* local-potential calculations for the impurity atom Li (Li^+ ion) in $KTaO_3$: Li (KTL) were made in [44]. We report here on cluster *ab initio* calculations of the local adiabatic potential for the K, Ta, and oxygen atoms in KTO and for *A*-type atoms in CTO, STO, BTO, and KNO, as well as for the impurity atoms Ba, Ca, Mg, Cd, and Zn in STO, Li in KTL, and Nb in KTN.

2.1. Cluster Model and Method of Calculation of the Total Energy

To find the local adiabatic potential for an atom sitting at a lattice site, one has to calculate the total crystal energy as a function of atomic displacement from the equilibrium position at the site, $\Delta E(\eta)$, assuming the remaining atoms to occupy their equilibrium positions in the perovskite cubic lattice. The supercell [44, 60,

61] and quasimolecular cluster [58, 59] methods are the most suitable approaches to nonempirical calculation of the properties of point defects in crystals.[1] We use here the approach described in [58, 59]; this method is based essentially on isolating the fragment of the crystal of interest, which ensures correct description of the chemical bonding and point symmetry. Thereafter, this fragment is simulated by a quasimolecular cluster with the geometry of the crystal fragment.

The smallest cluster that can reproduce the chemical bonding and the local properties (determined by this bonding) for an atom at site B is the octahedral cluster $(BO_6)^{n-}$ (cluster I). The cluster second in complexity that is appropriate in symmetry to a B atom consists of seven octahedra, more specifically, of a central $(B'O_6)$ and six neighboring (BO_6) octahedra each sharing a common oxygen atom with the central octahedron. This cluster also contains eight A-type atoms occupying the corners of the cubic primitive cell. To reduce the cluster charge, hydrogen atoms are attached to the broken O–B bonds at a distance of 1 Å. All this adds up to $[B'O_6A_8B_6(OH)_{30}]^{n+}$ positively charged clusters, where $n = 2$ for BTO, STO, CTO, and PTO and $n = 1$ for KNO and KTO (cluster VII).

The smallest possible cluster for an A atom is formally $((AO_{12})^{n-})$. However, this cluster cannot provide an adequate description of the local potential for the A atom. Therefore, we shall consider as the minimum cluster for atom A the cluster which is next in complexity and contains seven A atoms (A' at the cluster center and six A atoms at the fourfold axes) and eight octahedra (BO_6) with B-type atoms lying on the threefold axes at the corners of the cubic cell. To reduce the cluster charge, hydrogen atoms were added to the broken O–B bonds at a distance of 1 Å. This results in negatively charged $[A'O_{12}A_6B_8(OH)_{24}]^{n-}$ clusters, where $n = 2$ for BTO, STO, CTO, and PTO and $n = 1$ for KNO and KTO (cluster VIII). In the case of a perovskite solid solution $AB_{1-x}B'_xO_3$, the smallest cluster for the oxygen atom consists of two octahedra, (BO_6) and $(B'O_6)$, sharing a common oxygen atom. This cluster also contains four A atoms (Ca, Sr, Ba, Pb, K) at the corners of the cubic-cell face perpendicular to the B–O–B' chain; in order to reduce the cluster charge, hydrogen atoms were added to the broken O–B outer bonds at a distance of 1 Å from the oxygen atom. This yields a positively charged cluster $[OBB'A_4(OH)_{10}]^{n+}$, where $n = 2$ for KNO and KTO (cluster II).

We shall describe now the way in which the clusters were constructed. The main fragments are the primitive cubic cells for the ABO_3 perovskite structure that are centered on the corresponding atom, namely, on a B atom for cluster VII (Fig. 1a), an A atom for cluster VIII (Fig. 1b), and on an oxygen atom for cluster II (Fig. 1c).

[1] There also exists a method of quantum clusters embedded in a crystal lattice [62]. Strictly speaking, however, this method is semiempirical.

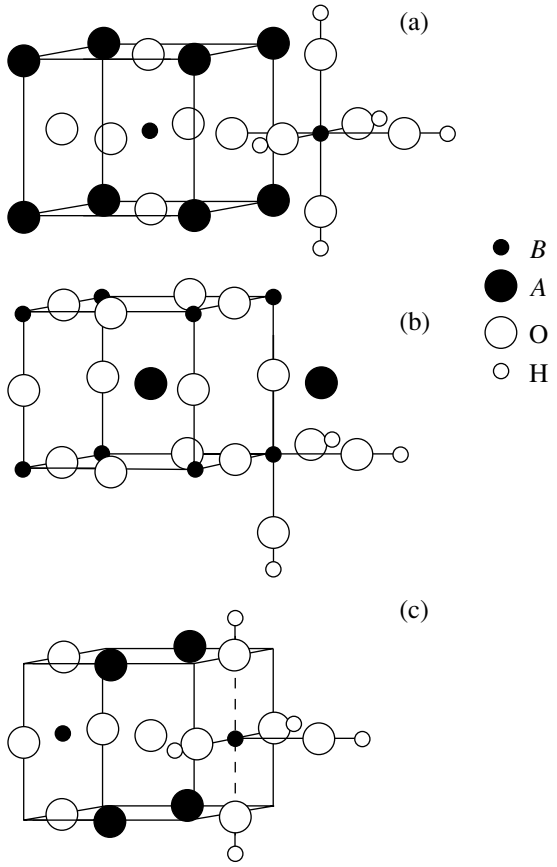

Fig. 1. Main and additional fragments of clusters (a) VII, (b) VIII, and (c) II.

Each cluster also contains additional fragments; one of them is shown in Fig. 1 for each cluster. The total number of additional fragments is determined by the cluster symmetry: six $Ti(OH)_5$ groups in cluster VII, eight $(OH)_3$ groups and six A atoms in cluster VII, and two H_4OH groups in cluster II.

By definition, the local potential is the difference between the total energies of the crystal in the distorted and undistorted configurations:

$$\Delta E(\eta) = E(\eta) - E_0, \quad (1)$$

where η is the displacement of the central atom from the lattice site. The calculations were made using the approximation $\Delta E(\eta) \approx \Delta E^{cl}(\eta)$, where $E^{cl}(\eta)$ is the total energy of the corresponding cluster. The total energies and the one-electron cluster properties were calculated by the Hartree–Fock–Roothaan nonempirical MO LCAO SCF formalism [63] using the PC GAMESS version [64] of the GAMESS (US) QC package [65]. The correlation effects were taken into account (for simple octahedral clusters) within the Möller–Plescet perturbation theory (MP2) [65]. The calculations were made using the following sets of atomic basis functions: for the oxygen atoms, the basis sets were TZV (10*s*6*p*)/[5*s*3*p*] [65, 66] with *d*-type

Table 1. Local force constants k^{loc} (determined by short-range interaction) for atoms at the *A* and *B* sites in ABO_3 perovskite compounds obtained by cluster *ab initio* calculations

Compound	Atom	Cluster	k^{loc}, eV/Å^2	a_0, Å
$CaTiO_3$	Ca	VIII	7.6	3.8367
	Ti	I	32.2 (29.4)	
		VII	32.0	
$SrTiO_3$	Sr	VIII	13.5	3.905
	Ti	I	28.6 (26.0)	
		VII	28.5	
$BaTiO_3$	Ba	VIII	15.9	3.996
	Ti	I	24.5 (22.2)	
		VII	23.9	
$PbTiO_3$	Pb	VIII	6.8	3.970
	Ti	I	25.6 (23.2)	
		VII	20.1	
$KTaO_3$	K	VIII	7.0	3.9845
	Ta	I	43.7 (43.4)	
		VII	39.0	
$KNbO_3$	K	VIII	6.4	4.0214
	Nb	I	35.7 (35.7)	
		VII	30.6	

Note: The values shown in parentheses include the correlation corrections to k^{loc}. The values of $k^{loc}(B)$ for STO, BTO, PTO, and KNO were taken from [59]. The values of the lattice constant a_0 were taken from [73] (for KTO, from [15]).

Table 2. Force constants k^{loc} for *A*' atoms in the ABO_3 : *A*' perovskite compounds and for Nb atoms in $KTaO_3$: Nb obtained from nonempirical cluster calculations

Compound	Cluster	k^{loc}, eV/Å^2
STO : Ca	VIII	6.4
STO : Ba	VIII	19.4
STO : Pb	VIII	8.6
STO : Cd	VIII	3.6
STO : Mg	VIII	≤ 0
STO : Zn	VIII	≤ 0
KTO : Li	VIII	≤ 0
KTO : Nb	VII	35.3

polarization functions [67]; for the hydrogen atoms, the DZV of Dunning and Hay [65]; and for Ti and Nb, (13*s*7*p*5*d*) and (14*s*8*p*7*d*), respectively, taken from [68]. The basis sets used for the Li, K, Mg, Ca, Sr, Ba, Pb, Cd, and Zn at the center of cluster VIII, as well as for the Ta atom at the center of clusters I and VII, were WTBS [69]. For the Li, Mg, Ca, and Zn atoms in the *A*' position, we also used the Roos ADZ ANO sets [70]. For the remaining K, Ca, Sr, Ba, and Pb atoms in clusters VIII, as well as for Ta in clusters VII, we used the effective core potential with the corresponding basis sets for valence orbitals [71]. The WTBS and Roos ADZ ANO basis sets and the relevant information were obtained from [72].

2.2. Pure Perovskites

We consider a crystal with only one atom belonging, for example, to sublattice *s* and displaced from the central equilibrium position (at the lattice site). We define local force constants $k^{loc}(s)$ as coefficients of the quadratic terms in the expansion of the total crystal energy in powers of displacements $\eta_i(s)$ of this atom:

$$\Delta E(\eta) = E(\eta) - E(0) = \frac{1}{2}k^{loc}(s)\eta_i\eta_j + \mathbb{O}(\eta^4), \quad (2)$$

where the second term on the right-hand side includes the anharmonic terms of expansion ΔE.[2] According to Eq. (2), $k^{loc} = 2\Delta E(\eta)/\eta^2|_{\eta \to 0}$ [for symmetry considerations, Eq. (2) does not contain linear terms].

Table 1 presents the results of cluster *ab initio* calculations of the local force constants $k^{loc}(s)$ performed for the *A*- and *B*-type atoms in the cubic perovskites CTO, STO, BTO, PTO, KNO, and KTO. We readily see that all the k^{loc} constants are large compared to the atomic force constant for the perovskites $k_{at} = e^2/r_0^3 \approx 2$ eV/Å^2, where $r_0 \approx 2$ Å is the *B*–O bond length, as well as in comparison to the k^{loc} for cations in typical ionic crystals [58]. The values of k^{loc} are the largest for the oxides of tantalum, niobium, and titanium, which is indicative of the stabilizing effect the *B*–O bond covalency exerts on the stability of the central position of these atoms in the $(BO_6)^{n-}$ oxygen octahedron [59]. These results suggest that the assumption of the *B* atoms in the paraelectric phase of perovskite ferroelectrics being off-center, which is frequently used in interpreting XAFS [40, 53] and in inelastic light scattering [51] experiments, is apparently erroneous.

2.3. Doped Perovskites

Table 2 presents the results of cluster *ab initio* calculations of the force constants k^{loc} for the impurity atoms Ca, Ba, Pb, and Cd substituting for Sr in STO and

[2] In contrast to the optical force constant $k(s)$, which corresponds to the displacement of sublattice *s* as a whole and whose magnitude in the perovskites is affected noticeably by the long-range dipole–dipole interaction [59], the local force constant $k^{loc}(s)$ contains contributions due to short-range interactions only, i.e., $k^{loc}(s) = k^{sr}(s)$. The contribution of the dipole–dipole interaction to the restoring force in a lattice with one displaced atom falls off with distance *R* as R^{-6}. The contribution due to the Madelung energy to $k^{loc}(s)$ for the *A* and *B* sites in cubic perovskites is zero.

for the Nb impurity atom substituting for Ta in KTO. Let us compare k^{loc} from Table 2 for the atom acting as an impurity with that from Table 1 for the same atom, but in the dissolved component of the solid solution, namely, Ca in STO : Ca and CTO, Ba in STO : Ba and BTO, Pb in STO : Pb and PTO, and Nb in KTN and KNO. We readily see that the corresponding k^{loc} constants have close values and that the differences are caused primarily by the difference in the lattice constants between the host and the dissolved component. According to Table 2, the impurity atoms in these solid solutions move in a single-well potential; i.e., they are central impurities. The situation with the Nb impurity in $KTaO_3$ is particularly interesting. Contrary to the fairly common idea of the Nb impurity in $KTaO_3$ being off-center [39, 40], calculations show (Tables 1, 2) that the $KTaO_3$ lattice is too tight for the Nb impurity atom.[3] Thus, STO : Ca, STO : Ba, STO : Pb, STO : Cd, and KTN can be considered to be displacive ferroelectrics (we shall call them, for brevity, displacive solid solutions).

The situation with materials doped by Mg, Zn, and Li is radically different (Tables 2, 3). The harmonic force constants k^{loc} for the Mg, Zn, and Li impurity atoms are small in magnitude ($|k^{loc}| \lesssim 0.5$ eV/Å^2) and negative, as shown by exact calculations making use of large basis sets [70] for impurity atoms.[4] This means that the Mg and Zn impurities in STO and Li in KTO are off-center and move in a multiwell local potential, whose shape in the [001] direction is displayed in Figs. 2 and 3. The displacement from the central position η_{min} and the corresponding gain in energy ΔE_{min} calculated in the Hartree–Fock approximation are 0.32 Å and 7 meV for STO : Mg, 0.41 Å and 24 meV for STO : Zn, and 0.63 Å and 22 meV for KTL, respectively.

These results, demonstrating the off-center position of the Mg and Zn impurities in STO and of Li in KTO, are primarily of a qualitative character. Because of the smallness of $k^{loc} \lesssim 1$ eV/Å^2, the values of the local potential parameters can change markedly toward increasing $|k^{loc}|$ when either the electronic correlations or the structural relaxation of the impurity atom neighborhood are taken into account; we have $\eta_{min} \propto |k^{loc}|^{1/2}$ and $\Delta E_{min} \propto |k^{loc}|^2$. At the same time, for $k^{loc} \gg 1$ eV/Å^2, the effect of the electronic correlations is small (Table 1) and their inclusion, as well as taking into account the structural relaxation of the impurity environment, cannot affect the conclusion that the Ca, Ba, Pb, and Cd impurities in STO and Nb in KTO occupy the central positions.

[3] As follows from calculations, the anharmonic contribution to the local potential is positive and virtually does not affect the shape of the potential down to $\eta \approx 0.2$ Å.

[4] As evident from the data for k^{loc} in STO : Ca (Table 3), the basis corrections to k^{loc} are significant only for $k^{loc} \lesssim 1$ eV/Å^2 and small for $|k^{loc}| \gg 1$ eV/Å^2.

Table 3. Local force constants k^{loc} for A' atoms in $ABO_3 : A'$ compounds derived from nonempirical cluster calculations (cluster VIII) for two basis sets for the A' impurity atom (WTBS [69] and Roos ADZ ANO [70])

Compound	k^{loc}, eV/Å^2	
	WTBS	Roos ADZ ANO
STO : Ca	6.4	5.4
STO : Mg	0.25	−0.31
STO : Zn	−0.16	−0.56
KTO : Li	0.004	−0.24

As already mentioned, the paraelectric phase of STO : Ca and KTN exhibit first-order Raman scattering, which is forbidden in the cubic phase of pure perovskites. To explain this phenomenon, the assumption of the impurity atom (Nb) in the cubic cell being off-center was put forward [39]. As shown above, the Nb atom in KTN and the Ca atom in STO : Ca occupy central positions with symmetry O_h in the paraelectric phase. At the same time, the existence of such central impurity atoms brings about a lowering of symmetry for the neighboring oxygen atoms from D_{4h} to C_{2v} in the CaO_{12} complexes in STO : Ca and down to C_{4v} in the NbO_6 complexes in KTN. In view of the fact that oxygen atoms take part in all optical lattice vibrational modes in perovskites, this lifts the forbiddenness from first-order Raman scattering. This reasoning also holds for other solid solutions with central impurity atoms.

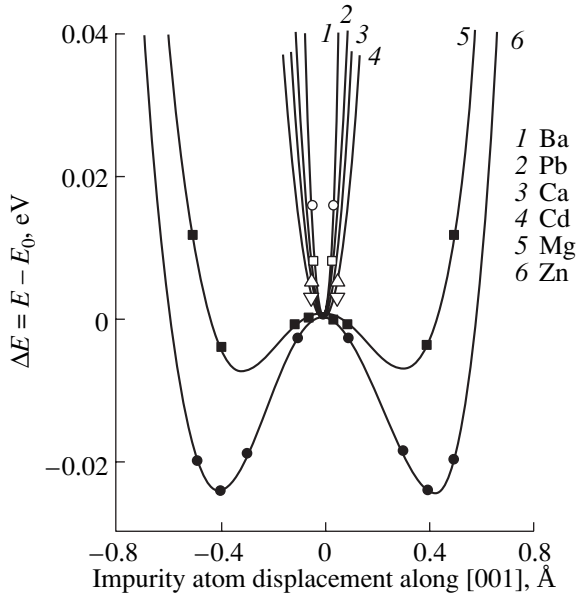

Fig. 2. Local adiabatic potential for the Ca, Ba, Pb, Cd, Mg, and Zn impurity atoms in STO.

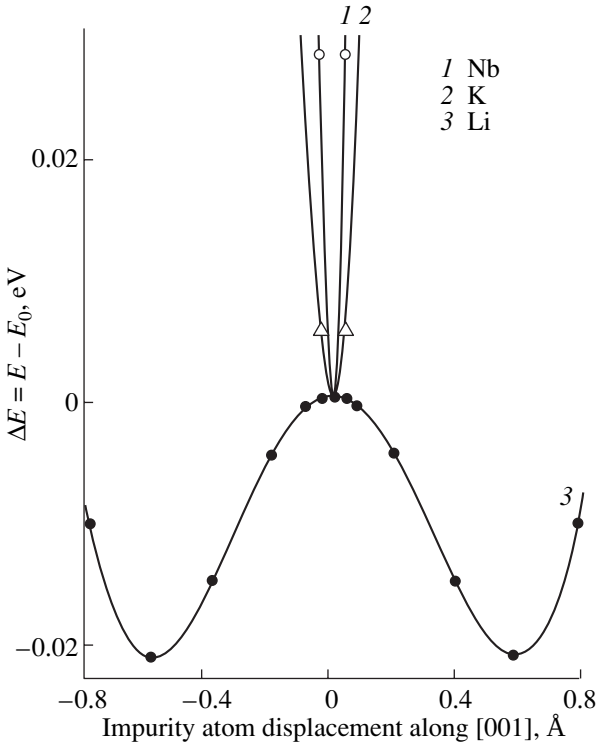

Fig. 3. Local adiabatic potential for the K atom and the Nb and Li impurity atoms in KTO.

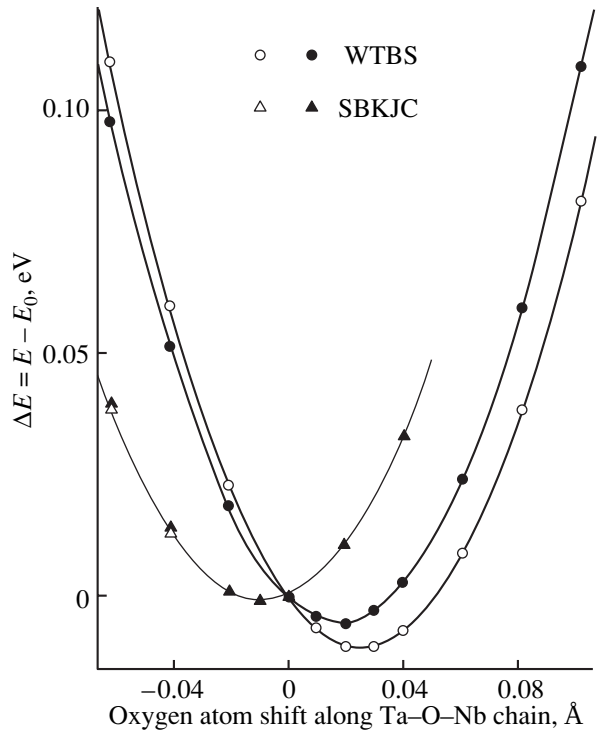

Fig. 4. Local adiabatic potential for the oxygen atom along the Ta–O–Nb chain in KTN calculated in the nonrelativistic approximation (WTBS) and including the relativistic effects in the electronic structure of Nb and Ta (SBKJC). Open symbols refer to calculations made in the Hartree–Fock (HF) approximation, and filled symbols are calculations with due account of the correlation corrections (HF + MP2).

The lowering of symmetry for the oxygen atoms surrounding impurity atoms results in oxygen atom displacements directed either inward or outward, depending on the size of the impurity ion. These considerations are, however, insufficient for determination of the character of the Nb environment relaxation in KTN, because, according to [45], the octahedrally coordinated Nb^{5+} and Ta^{5+} ions have the same radii of 0.6 Å. To establish the character of the relaxation the nearest environment of a Nb atom undergoes in KTN, we carried out a cluster *ab initio* calculation of the local potential for the oxygen atom in the Ta–O–Nb chain in the longitudinal direction which was based on cluster II (Fig. 1c). The results of the calculation are shown graphically in Fig. 4. A calculation made in a nonrelativistic approximation with the WTBS basis set [69] for the Nb and Ta atoms shows that the oxygen atom is displaced from the center of the cubic-cell face toward the Nb atom by 0.018 Å (the attendant energy gain is 10 meV). Taking into account the smallness of this effect, as well as the need of including the influence of the relativistic effects on the electronic structure of Ta, we also performed a calculation using the effective core potentials (ECP) for the Nb and Ta atoms, with the corresponding valence-orbital basis sets (SBKJC), which took into account the relativistic effects in the Dirac–Hartree–Fock equation [65, 71]. In this case, the oxygen atom is displaced from the center of the cubic-cell face toward the Ta atom by 0.01 Å (the gain in energy is 1 meV). Treated in the language of ionic radii, this means that if the relativistic effects are neglected, the tantalum ion is larger, $r_{ion}^{VI}(Ta^{5+}) - r_{ion}^{VI}(Nb^{5+}) = 0.036$ Å. At the same time, if the relativistic effects are included in the calculation of the electronic structure of the Nb and Ta atoms, the niobium ion is larger, $r_{ion}^{VI}(Nb^{5+}) - r_{ion}^{VI}(Ta^{5+}) = 0.02$ Å. The latter result conforms to the lattice constant of the cubic phase of $KNbO_3$ being larger by about 0.04 Å than that of $KTaO_3$ (Table 1).

3. VIRTUAL-CRYSTAL MODEL

As follows from the preceding section, dilute solid solutions STO : Ba, STO : Ca (SCT), STO : Pb, STO : Cd, and KTN belong to the displacive type. This conclusion correlates with the observation of a clearly pronounced soft ferroelectric TO mode in SCT [35, 36] and KTN [31, 74–76] (single-mode behavior in the terminology introduced in [77]). According to [31], the frequency of the soft TO mode decreases at a given temperature with increasing x and no new low-frequency modes associated with Nb are observed. The temperature dependence of the soft TO mode exhibits a minimum at a temperature close to T_m [31, 35, 36, 75, 76]. In KTN, at the minimum $\omega_f \approx 7$ cm^{-1} [31, 75], which is substantially lower than the zero-temperature soft TO mode frequency for pure KTO, $\omega_f(T = 0\ \text{K}) = 20$ cm^{-1} [13]. This suggests the existence, in displacive solid solutions, of a soft ferroelectric mode dressed by

interactions with impurity atoms, i.e., with parameters depending on the impurity concentration.

This suggests that the free energy of the above displacive solid solutions can be expressed in terms of the generalized force constant $k_{f,ss}(T, x)$ corresponding to the soft TO mode of a mixed compound. In considering the soft TO mode amplitude $\mathbf{y}_f$ now to be an order parameter, we can present the free energy F_{ss} of a displacive ferroelectric solid solution, by analogy with a pure displacive ferroelectric [4, 78, 79], in the form of a Landau expansion:

$$F_{ss}(\mathbf{y}_f, T, x) = \frac{1}{2}k_{f,ss}(T)\mathbf{y}_f^2 + F^{ah}(\{\mathbf{y}_f\}) - v_0\mathbf{P}\cdot\mathbf{E}, \quad (3)$$

where F_{ss}^{ah} includes the anharmonic expansion terms.

Treated within this approach, the ferroelectric phase-transition temperature $T_C(x)$, which is a function of the impurity concentration, can be found by solving the equation[5]

$$k_{f,ss}(T_C, x) = 0 \quad (4)$$

and the critical concentration x_c, defined by the condition $T_C(x_c) = 0$, is a solution to the equation

$$k_{f,ss}(T_C = 0, x_c) = 0. \quad (5)$$

To make a quantitative estimation of x_c, we invoke the virtual-crystal (VC) approximation. The compounds under study are solid solutions of two isomorphous compounds. For instance, $Sr_{1-x}A_xTiO_3$ can be represented in the form $(1-x)SrTiO_3 + xATiO_3$, etc. In the VC approximation, a solid solution is treated as a perfect crystal with the average values of the parameters determined by Vegard's rule. The VC approximation provides a simple expression for the critical concentration x_c through the parameters of the matrix (solvent) and solute which automatically takes the effect of quantum fluctuations (zero-point atomic vibrations) on x_c into account. Introducing the notation k_m and k_i for the force constants of the matrix and impurity (dissolved) components, respectively, we write the constant $k_{0,ss} = k_{ss}(T = 0)$ in the form

$$k_{0,ss}(x) = (1-x)k_{0,m} + xk_{0,i}. \quad (6)$$

From Eqs. (5) and (6), we can find x_c:

$$x_c = \frac{k_{0,m}}{k_{0,m} - k_{0,i}}. \quad (7)$$

One can also write an expression for x_c which is similar to Eq. (7) but is written in terms of the frequencies rather than of the force constants:

$$x_c = \frac{\omega_{0,m}^2}{\omega_{0,m}^2 - \omega_{0,i}^2}. \quad (8)$$

[5] The generalized force constant is a static (thermodynamic) quantity which can vanish even if the frequency of the corresponding lattice excitation (in our case, of the soft TO mode) remains finite.

Table 4. Critical concentration x_c for the solid solutions $Sr_{1-x}A_xTiO_3$ (A = Ca, Ba, Pb) and $KTa_{1-x}Nb_xO_3$

Compound	x_c	
	experiment	theory
$Sr_{1-x}Ca_xTiO_3$	0.0018[a]	0.0026–0.0032
$Sr_{1-x}Ba_xTiO_3$	0.035 (0.0027)[b]	0.0013–0.012
$Sr_{1-x}Pb_xTiO_3$	0.0015[c]	0.0029–0.0039
$KTa_{1-x}Nb_xO_3$	0.008[d]	0.01–0.030

[a]—[21], [b]—[22, 23, 26], [c]—[5, 25], [d]—[20]. See text for explanation.

Table 5. Harmonic force constants k_h and frequencies ω_h for the cubic phase of perovskite compounds obtained from *ab initio* calculations

Compound	k_h, eV/Å^2	ω_h, cm^{-1}
$CaTiO_3$	−2.23[a]	153i[c]
		140i[d]
$SrTiO_3$	−0.175[a]	41i[c]
$BaTiO_3$	−3.401[a]	72i[e]
		178i[c]
		219i[f]
$PbTiO_3$	−2.507[a]	125i[g]
		144i[c]
$KTaO_3$	0.48[b]	80i[b]
		61i[h]
$KNbO_3$	−2.993[a]	115i[j]
		143i[c]
		203i[h]
		147i[k]
		197i[l]

[a]—[79], [b]—[80], [c]—[83], [d]—[81], [e]—[82], [f]—[84], [g]—[85], [h]—[86], [j]—[87], [k]—[88], [l]—[89].

Equation (8) is more convenient to use in calculations than Eq. (7), because the frequencies $\omega_{0,m}$, unlike the corresponding force constants, are experimentally measurable quantities. This is essential for $SrTiO_3$ and $KTaO_3$ because of the need to take into account, in these compounds, the zero-point vibration contribution, nonempirical calculations for which (in contrast to the contribution calculated in the harmonic approximation) are still lacking.

In the solid solutions under study, $x_c \ll 1$ (Table 4). This imposes constraints on the parameters of the host matrix and of the impurity component:

$$k_{0,i} < 0, \quad \omega_{0,i}^2 < 0$$

$$\text{and } k_{0,m} \ll |k_{0,i}|, \quad \omega_{0,m}^2 \ll |\omega_{0,i}|^2.$$

For our solid solutions, these conditions are met satisfactorily. Table 4 lists the theoretical values of x_c calculated from Eq. (8). The calculations were made using the experimental values of $\omega_{0,m}$ for STO and KTO available in [12, 13]. To find the frequencies $\omega_{0,i}$ for the impurity component of a solid solution, we assumed the zero-point vibration contributions to ω_f in all perovskites to be of about the same order of magnitude. The ω_{zp} contribution can be estimated using the values quoted in [4] for STO ($\omega_{zp} \approx 35.4$ cm^{-1}) and KTO ($\omega_{zp} \approx 20$ cm^{-1}). Taking into account the values of ω_h given in Table 5 and the equality $\omega_0^2 = \omega_h^2 + \omega_{zp}^2$ [4], we obtain $\omega_0^2 \approx \omega_h^2$ for the cubic phase of CTO, BTO, PTO, and KNO. Thus, one can recast equality (8) for the solid solutions under study in the approximate form

$$x_c \approx \frac{\omega_{0,m}^2}{|\omega_{h,i}|^2} \tag{9}$$

and use the results of the *ab initio* calculations of $\omega_{h,i}$ presented in Table 5. The last column of Table 4 contains the ranges of theoretical estimates of x_c obtained from Eq. (9) with due account of the scatter in the values of ω_h in Table 5.

In view of the fact that the theoretical values of the critical concentration thus found were obtained within such a simple model, they describe fairly well, even though they are slightly high, the available experimental pattern for all the solid solutions except STO : Ba. This overestimation is possibly due to the neglect of the host matrix and impurity lattices undergoing mutual relaxation in the solid solution.

It should be stressed that description of the phenomena accompanying phase transitions in solid solutions is beyond the scope of the present work and, accordingly, outside the limits of applicability of the VC approximation. Such a description would require the invocation of phenomenological theory or a theory based on a model lattice Hamiltonian [90]. The results obtained in this study provide a basis for selecting the appropriate model description.

ACKNOWLEDGMENTS

I am indebted to V.V. Lemanov and P.A. Markovin for numerous discussions of the work and to S.B. Vakhrushev, T.R. Volk, and V.A. Trepakov for valuable comments.

This study was supported by the Russian Foundation for Basic Research (project nos. 00-02-16919, 01-02-17801) and NWO (grant no. 16-04-1999).

REFERENCES

1. U. T. Höchli, K. Knorr, and A. Loidl, Adv. Phys. **39** (5), 405 (1990).
2. B. E. Vugmeister and M. D. Glinchuk, Rev. Mod. Phys. **62** (4), 993 (1990).
3. W. Kleemann, Int. J. Mod. Phys. **7** (13), 2469 (1993).
4. O. E. Kvyatkovskiĭ, Fiz. Tverd. Tela (St. Petersburg) **43** (8), 1345 (2001) [Phys. Solid State **43**, 1401 (2001)].
5. V. V. Lemanov, Ferroelectrics **226**, 133 (1999).
6. V. V. Lemanov, in *Defects and Surface-Induced Effects in Advanced Perovskites*, G. Borstel, A. Krumins, and D. Millers (Kluwer, Dordrecht, 2000), p. 329.
7. K. A. Müller and H. Burkard, Phys. Rev. B **19** (7), 3593 (1979).
8. S. H. Wemple, Phys. Rev. **137** (5A), 1575 (1965).
9. J. H. Barrett, Phys. Rev. **86** (1), 118 (1952).
10. A. B. Rechester, Zh. Éksp. Teor. Fiz. **60** (2), 782 (1971) [Sov. Phys. JETP **33**, 423 (1971)].
11. D. E. Khmel'nitskiĭ and V. L. Shneerson, Fiz. Tverd. Tela (Leningrad) **13** (3), 832 (1971) [Sov. Phys. Solid State **13**, 687 (1971)].
12. A. Yamanaka, M. Kataoka, Y. Inaba, *et al.*, Europhys. Lett. **50** (5), 688 (2000).
13. H. Vogt, Phys. Rev. B **51** (13), 8046 (1995).
14. H. Uwe and T. Sakudo, Phys. Rev. B **13** (1), 271 (1976).
15. G. A. Samara and B. Morosin, Phys. Rev. B **8** (3), 1256 (1973).
16. M. Itoh, R. Wang, Y. Inaguma, *et al.*, Phys. Rev. Lett. **82** (17), 3540 (1999).
17. M. Itoh, R. Wang, and T. Nakamura, Appl. Phys. Lett. **76** (2), 221 (2000).
18. O. E. Kvyatkovskii, Solid State Commun. **117** (8), 455 (2001).
19. A. Bussmann-Holder, H. Büttner, and A. R. Bishop, J. Phys.: Condens. Matter **12**, L115 (2000).
20. U. T. Höchli, H. E. Weibel, and L. A. Boatner, Phys. Rev. Lett. **39** (18), 1158 (1977).
21. J. G. Bednorz and K. A. Müller, Phys. Rev. Lett. **52** (25), 2289 (1984).
22. V. V. Lemanov, E. P. Smirnova, and E. A. Tarakanov, Fiz. Tverd. Tela (St. Petersburg) **37** (8), 2476 (1995) [Phys. Solid State **37**, 1356 (1995)].
23. V. V. Lemanov, E. P. Smirnova, and E. A. Tarakanov, Phys. Rev. B **54** (5), 3151 (1996).
24. P. A. Markovin, V. V. Lemanov, O. Yu. Korshunov, *et al.*, Ferroelectrics **184**, 269 (1996).
25. V. V. Lemanov, E. P. Smirnova, and E. A. Tarakanov, Fiz. Tverd. Tela (St. Petersburg) **39** (4), 714 (1997) [Phys. Solid State **39**, 628 (1997)].
26. P. A. Markovin, V. V. Lemanov, M. E. Guzhva, and W. Kleemann, Ferroelectrics **199**, 121 (1997).
27. M. E. Guzhva, V. V. Lemanov, P. A. Markovin, and T. A. Shuplygina, Ferroelectrics **218**, 93 (1998).
28. R. Oppermann and H. Thomas, Z. Phys. B **22** (4), 387 (1975).
29. T. Schneider, H. Beck, and E. Stoll, Phys. Rev. B **13** (3), 1123 (1976).

30. R. Morf, T. Schneider, and E. Stoll, Phys. Rev. B **16** (1), 462 (1977).
31. R. L. Prater, L. L. Chase, and L. A. Boatner, Phys. Rev. B **23** (1), 221 (1981).
32. G. A. Samara, Phys. Rev. Lett. **53** (3), 298 (1984).
33. K. B. Lyons, P. A. Fleury, and D. Rytz, Phys. Rev. Lett. **57** (17), 2207 (1986).
34. W. Kleemann, F. J. Schäfer, and D. Rytz, Phys. Rev. Lett. **54** (18), 2038 (1985).
35. U. Bianchi, W. Kleemann, and J. C. Bednorz, J. Phys.: Condens. Matter **6**, 1229 (1994).
36. W. Kleemann, U. Bianchi, A. Bürgel, *et al.*, Phase Transit. **55**, 57 (1995).
37. R. Kelz, P. Lehnen, and W. Kleemann, J. Korean Phys. Soc. **32**, S456 (1998).
38. H. Uwe, K. B. Lyons, H. L. Carter, and P. A. Fleury, Phys. Rev. B **33** (9), 6436 (1986).
39. Y. Yacoby, Z. Phys. B **31**, 275 (1978).
40. O. Hanske-Petitpierre, Y. Yacoby, J. Mustre de Leon, *et al.*, Phys. Rev. B **44** (13), 6700 (1991).
41. W. Kleemann, A. Albertini, R. V. Chamberlin, and J. G. Bednorz, Europhys. Lett. **37** (2), 145 (1997).
42. V. S. Vikhnin and Yu. A. Borkovskaya, Fiz. Tverd. Tela (Leningrad) **20** (12), 3603 (1978) [Sov. Phys. Solid State **20**, 2082 (1978)].
43. B. E. Vugmeĭster and M. D. Glinchuk, Zh. Éksp. Teor. Fiz. **79** (3), 947 (1980) [Sov. Phys. JETP **52**, 482 (1980)].
44. I. I. Tupitsyn, A. Deineka, V. Trepakov, *et al.*, Ferroelectrics **237**, 9 (2000).
45. R. D. Schannon, Acta Crystallogr. A **32**, 751 (1976).
46. V. S. Vikhnin, P. A. Markovin, V. V. Lemanov, and W. Kleemann, J. Korean Phys. Soc. **32**, S583 (1998).
47. J. J. van der Klink, S. Rod, and A. Châtelain, Phys. Rev. B **33** (3), 2084 (1986).
48. J. J. van der Klink and F. Borsa, Phys. Rev. B **30** (1), 52 (1984).
49. R. Comes, M. Lambert, and A. Guinier, Solid State Commun. **6**, 715 (1968).
50. K. A. Müller, in *Nonlinearity in Condensed Matter*, Ed. by A. K. Bishop *et al.* (Springer, Berlin, 1987), p. 234.
51. T. P. Dougherty, G. P. Wiederrecht, K. A. Nelson, *et al.*, Science **258**, 770 (1992).
52. G. H. Kwei, S. J. L. Billinge, S.-W. Cheong, and J. G. Saxton, Ferroelectrics **164**, 57 (1995).
53. N. Sicron, B. Ravel, Y. Yacoby, *et al.*, Phys. Rev. B **50**, 13168 (1994).
54. A. Hüller, Solid State Commun. **7**, 589 (1969); Z. Phys. **220**, 145 (1969).
55. R. Comés and G. Shirane, Phys. Rev. **5** (5), 1886 (1972).
56. H. Krakauer, R. Yu, C.-Z. Wang, *et al.*, J. Phys.: Condens. Matter **11**, 3779 (1999).
57. M. Holma, N. Takesue, and H. Chen, Ferroelectrics **164**, 237 (1995).
58. O. E. Kvyatkovskii, Ferroelectrics **153** (1–4), 201 (1994).
59. O. E. Kvyatkovskiĭ and B. F. Shchegolev, Izv. Ross. Akad. Nauk, Ser. Fiz. **64** (6), 1060 (2000).
60. C. H. Park and D. J. Chadi, Phys. Rev. B **57** (22), R13961 (1998).
61. R. I. Eglitis, N. E. Christensen, E. A. Kotomin, *et al.*, Phys. Rev. B **56** (14), 8599 (1997).
62. H. Donnerberg and R. H. Bartram, J. Phys.: Condens. Matter **8**, 1687 (1996).
63. C. C. J. Roothaan, Rev. Mod. Phys. **23**, 69 (1951).
64. A. A. Granovsky, http://classic.chem.msu.su/gran/gamess/index.html.
65. M. W. Schmidt, K. K. Baldridge, J. A. Boatz, *et al.*, J. Comput. Chem. **14**, 1347 (1993).
66. T. H. Dunning, J. Chem. Phys. **55**, 716 (1971).
67. T. H. Dunning and P. J. Hay, in *Methods of Electronic Structure Theory*, Ed. by H. F. Schaefer III (Plenum, New York, 1977), Vol. 2.
68. I. Hyla-Kryspin, J. Demuynck, A. Strich, and M. Benard, J. Chem. Phys. **75**, 3954 (1981).
69. S. Huzinaga and B. Miguel, Chem. Phys. Lett. **175**, 289 (1990); S. Huzinaga and M. Klobukowski, Chem. Phys. Lett. **212**, 260 (1993).
70. P. O. Widmark, P. A. Malmqvist, and B. Roos, Theor. Chim. Acta **77**, 291 (1990); P. O. Widmark, B. J. Persson, and B. Roos, Theor. Chim. Acta **79**, 419 (1991); R. Pou-Amerigo, M. Merchan, I. Nebot-Gil, *et al.*, Theor. Chim. Acta **92**, 149 (1995).
71. W. J. Stevens, H. Basch, and M. Krauss, J. Chem. Phys. **81** (12), 6026 (1984); W. J. Stevens, M. Krauss, H. Basch, and P. G. Jasien, Can. J. Chem. **70**, 612 (1992).
72. EMSL basis set Library, http://www.emsl.pnl.gov:2080/form/basisform.html.
73. Landolt-Börnstein, *Numerical Data and Functional Relationships in Science and Technology*, Ed. by K.-H. Hellwege and A. M. Hellwege (Springer, Berlin, 1981), Group III, Vol. 16a.
74. W. B. Yelon, W. Cochran, G. Shirane, and A. Linz, Ferroelectrics **2**, 261 (1971).
75. H. Chou, S. M. Shapiro, K. B. Lyons, *et al.*, Phys. Rev. B **41** (10), 7231 (1990).
76. P. M. Gehring, H. Chou, S. M. Shapiro, *et al.*, Ferroelectrics **150**, 47 (1993).
77. A. S. Barker and A. J. Sievers, Rev. Mod. Phys. **47** (2), S1 (1975).
78. V. G. Vaks, *Introduction to the Microscopic Theory of Ferroelectrics* (Nauka, Moscow, 1973).
79. R. D. King-Smith and D. Vanderbilt, Phys. Rev. B **49** (9), 5828 (1994).
80. D. J. Singh, Phys. Rev. B **53** (1), 176 (1996).
81. E. Cockayne and B. P. Burton, Phys. Rev. B **62** (6), 3735 (2000).

82. R. E. Cohen and H. Krakauer, Phys. Rev. B **42** (10), 6416 (1990).
83. W. Zhong, R. D. King-Smith, and D. Vanderbilt, Phys. Rev. Lett. **72** (22), 3618 (1994).
84. P. H. Ghosez, X. Gonze, and J.-P. Michenaud, Ferroelectrics **206**, 205 (1998).
85. R. E. Cohen and H. Krakauer, Ferroelectrics **136**, 65 (1992).
86. A. V. Postnikov, T. Newmann, and G. Borstel, Phys. Rev. B **50** (2), 758 (1994).
87. D. J. Singh and L. L. Boyer, Ferroelectrics **136**, 95 (1992).
88. R. Yu and H. Krakauer, Phys. Rev. Lett. **74** (20), 4067 (1995).
89. C.-Z. Wang, R. Yu, and H. Krakauer, Phys. Rev. B **54** (16), 11161 (1996).
90. A.P. Levanyuk and A. S. Sigov, *Defects and Structural Phase Transitions* (Gordon & Breach, New York, 1988).

Translated by G. Skrebtsov

Physics of the Solid State, Vol. 44, No. 6, 2002, pp. 1145–1151. Translated from Fizika Tverdogo Tela, Vol. 44, No. 6, 2002, pp. 1096–1101.

MAGNETISM AND FERROELECTRICITY

Selective Averaging of EPR Transitions of a High-Spin Center in the Vicinity of Their Accidental Coincidence

V. A. Vazhenin, V. B. Guseva, and M. Yu. Artemov

Research Institute of Physics and Applied Mathematics, Ural State University, Yekaterinburg, 620083 Russia

e-mail: vladimir.vazhenin@usu.ru

Received June 26, 2001

Abstract—The averaging of a part of spin packets for two transitions of the Gd^{3+} trigonal center in ferroelectric lead germanite in the vicinity of coincidence of their positions leading to the emergence of an additional EPR signal is investigated. A computer simulation of the experimental spectrum gives the temperature dependence of the spin–lattice relaxation time connecting the doublets in which resonance transitions occur and leading to selective averaging of the packets. An increase in the relaxation rate for intra- and interdoublet transitions is observed in the vicinity of the structural ferroelectric transition. *© 2002 MAIK "Nauka/Interperiodica".*

Electron paramagnetic resonance is successfully used to detect structural phase transitions, to determine the magnitude and temperature variation of the local order parameter, and to analyze relaxation characteristics of paramagnetic defects that reflect the critical dynamics of the lattice [1, 2]. In the case of high-temperature structural transformations, because of the high rates of energy transfer from the spin system to the lattice, only the relaxation parameters obtained from an analysis of the line shape are used. This analysis is extremely complicated due to the existence of alternative temperature-dependent mechanisms of broadening [1, 3]. The effects analyzed in the present work may facilitate the analysis of spin relaxation in the vicinity of structural transformations (at least, in some materials).

1. In gadolinium-doped lead germanate (LG) $Pb_5Ge_3O_{11}$ (ferroelectric transition $P3(C_3^1) \longleftrightarrow P\bar{6}(C_{3h}^1)$ at $T_c = 450$ K [4]), an EPR spectrum of the Gd^{3+} trigonal center is observed for which the strong magnetic field approximation is satisfied to a high degree of accuracy (Fig. 1). For an arbitrary orientation of the magnetic field, the degeneracy of the EPR spectrum for Gd^{3+} ions located in the opposite domains is removed. In our previous works [5–7], we observed an additional signal whose intensity increased upon a decrease in the distance between the initial signals $3 \longleftrightarrow 4$ and $5 \longleftrightarrow 6$ of the same type of domains in the vicinity of coincidence of their resonance positions (for the polar angle of magnetic field $\theta_0 \approx 41°$, $z \parallel C_3$) (Fig. 2). It was proved that this signal cannot be due to a multiquantum transition, although two-quantum transitions can be clearly observed in the vicinity of the intersection of the angular dependences corresponding to transitions $4 \longleftrightarrow 5$ and $3 \longleftrightarrow 4$, as well as $4 \longleftrightarrow 5$ and $5 \longleftrightarrow 6$, $3 \longleftrightarrow 4$ and $2 \longleftrightarrow 3$, and $5 \longleftrightarrow 6$ and $6 \longleftrightarrow 7$.

In order to explain the emergence of an additional signal, we assumed [5–7] the existence of rapid relaxation transitions between the $3 \longleftrightarrow 4$ and $5 \longleftrightarrow 6$ doublets, which led to averaging of a part of the spin packets belonging to the above EPR transitions and corresponding to the same local crystal field (isofield transitions).

The necessary condition of averaging of these packets is the inequality $W > \Delta\nu$, where W is the probability of relaxation transitions between doublets and $\Delta\nu$ is the

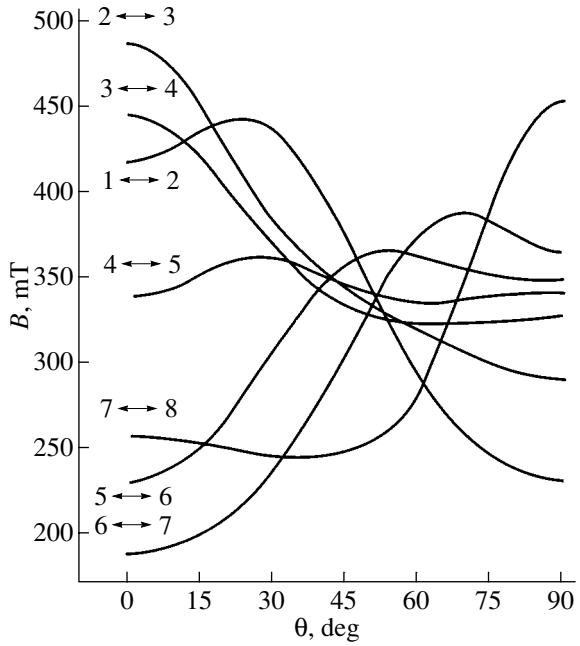

Fig. 1. Polar angular dependence of the positions of transitions in the Gd^{3+} trigonal center in the *zy* plane. Energy levels are labelled in ascending order.

1063-7834/02/4406-1145$22.00 © 2002 MAIK "Nauka/Interperiodica"

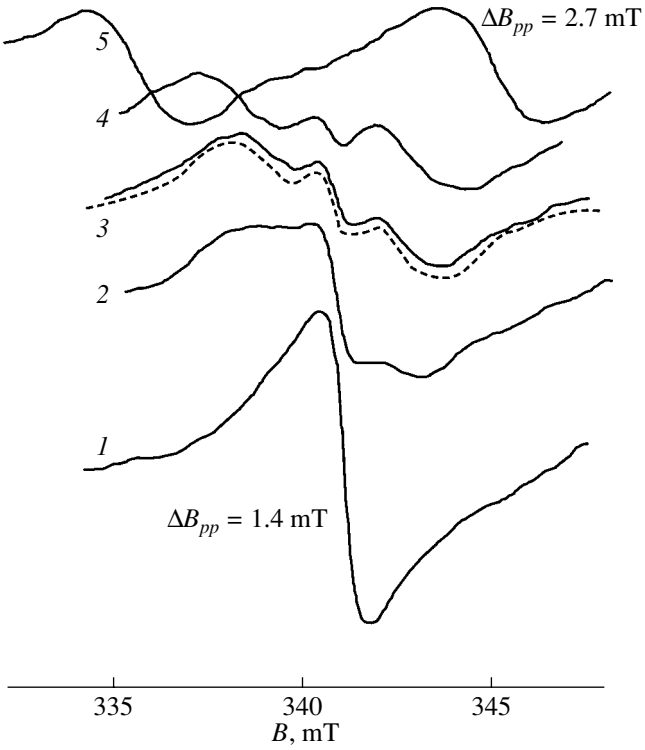

Fig. 2. EPR spectrum in the region of coincidence of positions of the $3 \longleftrightarrow 4$ and $5 \longleftrightarrow 6$ transitions at 458 K (0.05% Gd_2O_3) for (*1*) $\Delta\theta = 0°$, (*2*) 0.5°, (*3*) 0.63°, (*4*) 0.75°, and (*5*) 1.75°. The dashed curve is described by Eq. (4); ΔB_{pp} is the spacing between the extremum points of the absorption signal derivative.

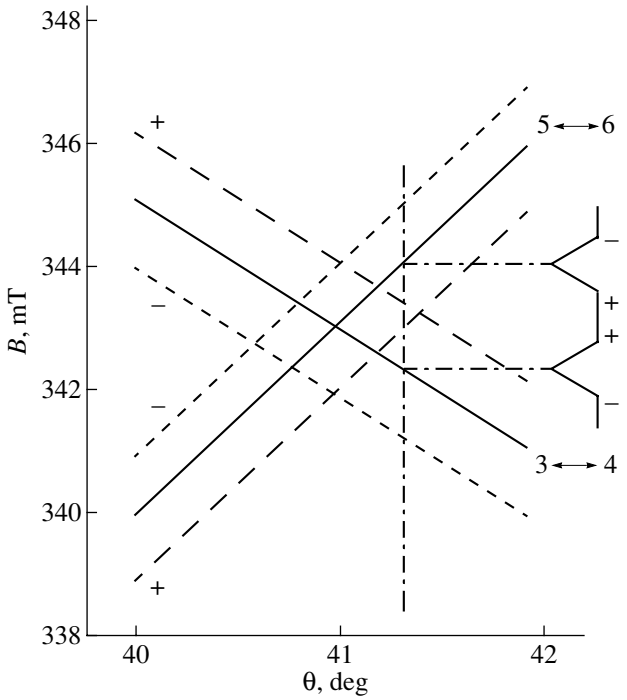

Fig. 3. Fragment of the polar angular dependence of transitions $3 \longleftrightarrow 4$ and $5 \longleftrightarrow 6$ (Fig. 1) illustrating the formation of the quasi-symmetric distribution of spin packets. Solid lines correspond to $b_{21} = 0$; dashed lines, to b_{21} = +100 MHz; and dotted lines, to b_{21} = –100 MHz. Plus and minus signs on the right of the absorption lines indicate the positions of "isofield" packets corresponding to the maximum and minimum values of b_{21}.

distance (in frequency units) between packets in the spectrum. The key point in the proposed model is the quasi-symmetric arrangement (see below and Fig. 3) of isofield spin packets in a pair of initial EPR signals. In the case of antisymmetric arrangement of isofield packets, the value of $\Delta\nu$ is approximately the same for all pairs and no selective averaging takes place. It was assumed in [5–7] that this form of inhomogeneous broadening is due to the spread in the value of spontaneous polarization and, hence, in the value of the spin Hamiltonian parameter b_{43} proportional to it. This enabled us [5–7] to qualitatively describe the main features of the behavior of the additional EPR signal. We considered cross-relaxation and spin–lattice interaction as the mechanisms triggering transitions between initial doublets. Thus, the specific feature of the EPR spectrum observed for LG is analogous to the effects emerging when relaxation without spin flop between Kramers doublets originating from a vibronic doublet split as a result of the interaction with random deformations is taken into account [8, 9]; this phenomenon is also close in nature to cross-singular effects in the NMR of polycrystals [10].

It was shown in [11] that (at least in the ~±50 K neighborhood of the ferroelectric transition) the main mechanism of inhomogeneous broadening of the spectrum of Gd^{3+} trigonal centers in LG for an arbitrary orientation ($\theta \neq 0°, 90°$) of the polarizing magnetic field is static modulation of the spin Hamiltonian parameter b_{21} (c_{21}), which increases as we approach the structural-transition temperature. The spread in the values of b_{43} makes a noticeable but not dominating contribution for azimuthal angles φ close to zero.

According to our calculations, the arrangement of spin packets for the transitions $3 \longleftrightarrow 4$ and $5 \longleftrightarrow 6$ due to the fluctuations in b_{21} (Fig. 3) is similar to the packet distribution as a result of modulation of b_{43}; consequently, the approach developed in [5–7] to explain the emergence of the additional signal remains valid.

The strong dependence of the magnitude of the effect on the extent of inhomogeneous broadening of the initial lines is indicated by the change in the form of the EPR spectrum in the region of coincidence of the resonance positions upon the application of an external electric field (Fig. 4). The observed decrease in the additional-signal intensity is due to a decrease in the inhomogeneous width of the initial signals in the electric field, which was discovered in [11] and is apparently associated with the saturation of polarizability.

The present work aims to quantitatively describe the spectrum with an extra signal in the region of coincidence of the resonance positions of EPR transitions and

to determine the temperature variation of the rates of intra- and interdoublet relaxation in the vicinity of the ferroelectric phase transition point.

2. Measurements were made with the help of a 3-cm EPR spectrometer on LG single crystals grown using the Czochralski method in air or nitrogen from a melt having stoichiometric composition and containing 0.0075 and 0.05 mol % Gd_2O_3 impurity. The specimens were transferred to the single-domain state prior to each cycle of temperature measurement in order to avoid overlapping of the transitions under investigation with the signals from the centers in oppositely magnetized domains.

At each temperature, the EPR spectrum was recorded in the following cases: at the point of coincidence of resonant positions of the initial transitions ($\Delta\theta = \theta - \theta_0 = 0$); for "strong" disorientation ($\Delta\theta$ = 1.5°–2°), where there is no extra signal and the distortion of the initial signals due to the interdoublet relaxation is small; and for "weak" disorientation ($\Delta\theta$ = 0.3°–0.6°), when the averaging of spin packets is most noticeable (Fig. 2). At the first stage of measurements (the magnetic field lies in the *zx* plane corresponding to the maximum splitting between the same transitions in the Gd^{3+} centers in oppositely magnetized domains), it was found that, in the vicinity of T_c the sample is transformed into a multidomain state leading to uncontrollable distortion of the form of the signals being detected, which is especially undesirable for $\Delta\theta$ = 0.3°–0.6°. For this reason, the subsequent measurements were made in the *zy* plane, in which the signals from the centers in different domains coincide.

3. In order to determine the probability of interdoublet transitions, a computer simulation of the EPR spectrum with an extra signal was carried out using an expression [12] derived to describe the spectrum of a spin system with several close frequencies characterized by infinitely narrow lines and performing transitions (motion) between the energy levels corresponding to these frequencies:

$$I(\omega) = \mathrm{Re}\{\mathbf{W}\cdot\mathbf{A}(\omega)^{-1}\cdot\mathbf{1}\}, \qquad (1)$$

where **W** is a vector with components equal to the initial-transition probabilities and **1** is a unit vector; in the case of two close frequencies, the matrix **A** is given by

$$\mathbf{A}(\omega) = \begin{vmatrix} i(-\omega+\delta)-\Omega & \Omega \\ \Omega & -i(\omega+\delta)-\Omega \end{vmatrix}; \qquad (2)$$

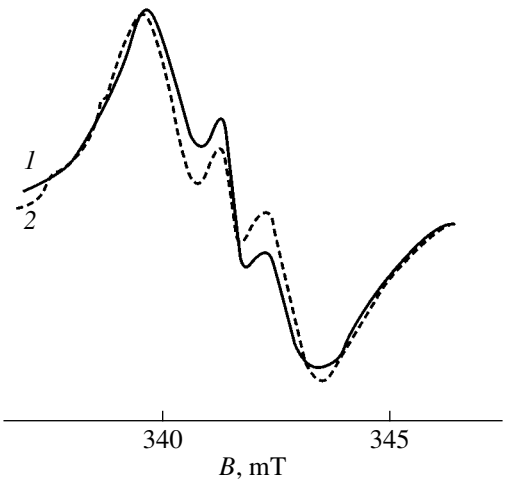

Fig. 4. EPR spectra in the region of coincidence of positions of the 3 ⟷ 4 and 5 ⟷ 6 transitions at 454 K for $\Delta\theta$ = 0.5° for a weakly doped sample (*1*) in zero field and (*2*) for E = 7 kV/cm.

Ω is the transition probability from one frequency to another; and $\pm\delta$ are the initial frequencies.

We assumed that the initial lines consist, in contrast to Eq. (1), of Lorentzian packets with intensities having a Gaussian distribution

$$I(B) = \sum_{n=-m}^{m} \frac{I_0 \exp(-n/\sigma)^2}{1+[\alpha T_{\mathrm{eff}}(B-B_0-n)]^2}, \qquad (3)$$

where B is the magnetic induction, B_0 is the resonance position, $2m + 1$ is the number of spin packets, $\alpha = 2\pi g_{\mathrm{eff}}\beta/h$, T_{eff} is the effective relaxation time associated with the homogeneous line broadening, and σ is the parameter characterizing inhomogeneous broadening.

In this case, the expression describing the shape of the EPR spectrum in the region of accidental coincidence of transitions has the following form (taking into account the above-mentioned quasi-symmetric distribution of the packets):

$$I(B) = -\sum_{n=-m}^{m} \mathrm{Re}(\mathbf{W}\cdot\mathbf{A}(B)^{-1}\cdot\mathbf{1})\exp(-n/\sigma)^2, \qquad (4)$$

$$\mathbf{A}(B) = \begin{vmatrix} i\alpha(a+n-B)-\frac{1}{T_{\mathrm{eff}}}-\frac{1}{2\tau} & \frac{1}{2\tau} \\ \frac{1}{2\tau} & i\alpha(b-nd-B)-\frac{1}{T_{\mathrm{eff}}}-\frac{1}{2\tau} \end{vmatrix}, \qquad (5)$$

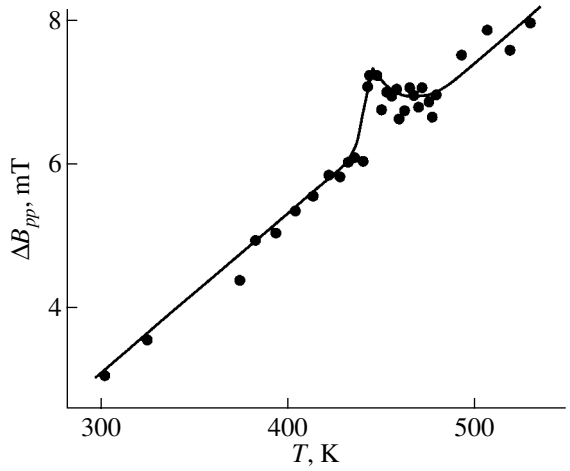

Fig. 5. Temperature dependence of the line width (the distance between the extrema of the first derivative of the absorption signal) of the $4 \longleftrightarrow 5$ transition for $\mathbf{B} \parallel C_3$.

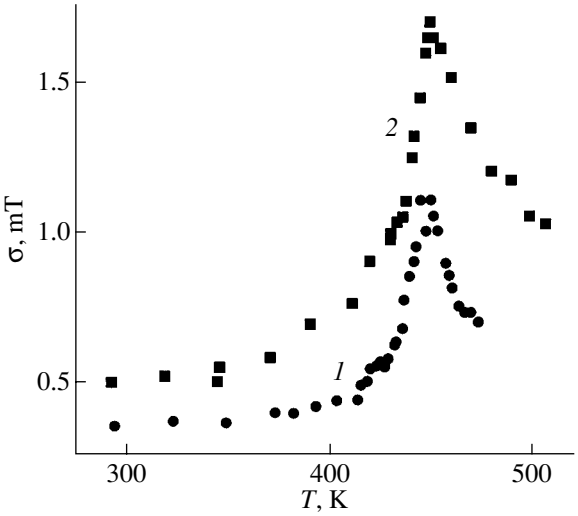

Fig. 6. Temperature dependence of σ for (*1*) 0.0075% Gd_2O_3 and (*2*) 0.05% Gd_2O_3.

where a and b are the resonance positions of the initial signals, $1/2\tau$ is the interdoublet transition probability, and $d = \sigma_b/\sigma = \sigma_b/\sigma_a$ is the ratio of the inhomogeneous-broadening parameters of the initial lines.

The EPR spectrum can also be simulated using the formulas derived in [13] as a result of simultaneous solution of the Bloch equations for two low-spin systems coupled by exchange interaction. However, the lower flexibility of these systems (e.g., the impossibility of correctly taking into account the difference in the probabilities of the initial transitions) noticeably worsens the description of the experimental spectrum.

In order to avoid ambiguity in determining the parameters of the EPR spectrum being constructed, we must accurately determine their initial values. The resonance positions measured for $\Delta\theta = 0$ and 1.5°–2° were used to determine the positions of the initial transitions (a, b) in the absence of the effects of spin packet averaging. The relaxation time T_{eff} was estimated from the temperature dependence of the width of the $4 \longleftrightarrow 5$ transition for $\mathbf{B} \parallel C_3$ (Fig. 5), which has an extremely small width at low temperatures and does not experience broadening due to the spread in the fine-structure parameters. In other words, we assumed that the dependence of the relaxation time on the type of transition and the orientation of the polarizing field is extremely weak. This assumption was made in connection with the complexity of separating the relaxation contribution to the line widths of the transitions $3 \longleftrightarrow 4$ and $5 \longleftrightarrow 6$ due to the strong temperature dependence of inhomogeneous broadening [11] (see also Fig. 6). The values of σ_b, σ_a, and the ratio of the initial-transition probabilities were estimated from the synthesis of the shape of the initial lines for a strong disorientation $\Delta\theta$ with the help of Eq. (3) (for a given value of T_{eff}). The ratios of intensities and inhomogeneous broadening parameters for the initial signals $3 \longleftrightarrow 4$ and $5 \longleftrightarrow 6$ in the region of coincidence were close to unity.

In the case of a weak disorientation $\Delta\theta$, the initial parameters could be varied in the course of simulation only to within the error in their magnitudes. After differentiation, the obtained spectrum was compared with the experimental spectrum which presents the first derivative of the absorption spectrum. Figure 2 shows an example of the description of the observed spectrum on the basis of the proposed model (curve *3*). It can be seen that the stronger discrepancy is observed for the wings of the three-component EPR signal, which fall off at a slower rate than those of the calculated curve. In our opinion, this is due to the existence of a quasi-continuous spectrum of triclinic centers (leading to signals in the wings of the trigonal spectrum and arising as a result of local compensation of the excess charge of Gd^{3+} [14]) and due to the disregard of signals from odd isotopes ^{155}Gd and ^{157}Gd (the natural abundance of each of these isotopes is ≈15%). The inclusion of the signal from the odd isotopes in the computational model is hampered in view of the complex hyperfine structure for $\theta \neq 0°$, 90° (the splitting for $\theta \approx 41°$ amounts to tens of megahertz) associated with the strong quadrupole interaction [15].

The temperature dependences of the inhomogeneous and homogeneous broadening parameters and of the interdoublet relaxation time for two paramagnetic-impurity concentrations, which are obtained as a result of computer simulation of the EPR spectrum, are presented in Figs. 6–8. The $\sigma(T)$ dependences (Fig. 6) are in qualitative agreement with the results [11] on the behavior of inhomogeneous line broadening for Gd^{3+} in the vicinity of the ferroelectric phase transition.

The strong temperature dependence and the weak concentration dependence of T_{eff} (Fig. 7) indicate that the homogeneous broadening of signals is controlled

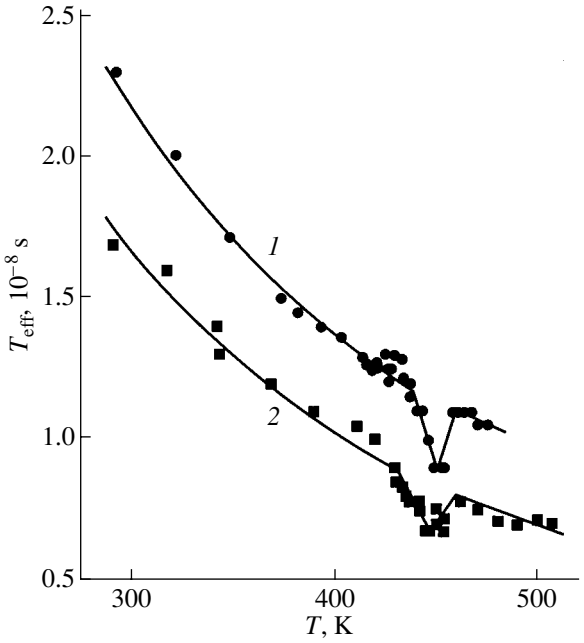

Fig. 7. Temperature dependence of T_{eff} for (*1*) 0.0075% Gd_2O_3 and (*2*) 0.05% Gd_2O_3.

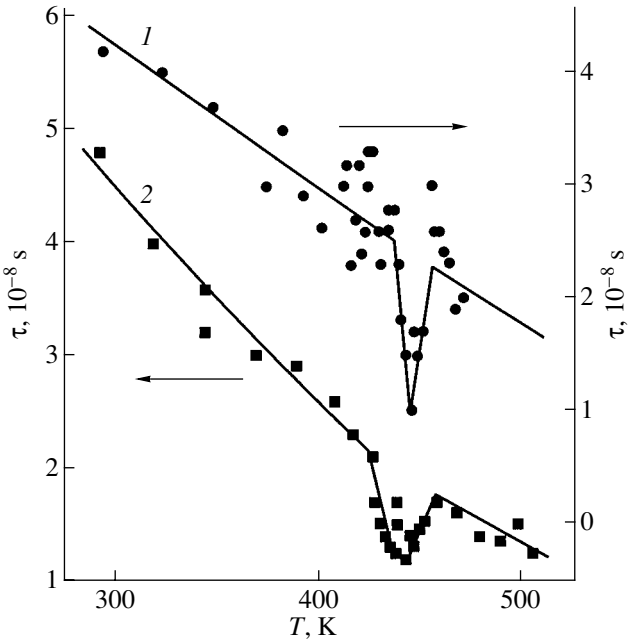

Fig. 8. Temperature dependence of τ for (*1*) 0.0075% Gd_2O_3 and (*2*) 0.05% Gd_2O_3.

by the spin–lattice relaxation. A slight deviation from the monotonic temperature dependence of the $4 \longleftrightarrow 5$ transition line width for $\mathbf{B} \parallel C_3$ in the vicinity of the structural phase transformation (Fig. 5) might be attributed to the measurement error; however, the simulation of a spectrum with an extra signal which would be adequate for the experimental spectrum proved to be impossible under the assumption of a monotonic $T_{eff}(T)$ dependence.

The temperature and concentration dependences of the time τ (Fig. 8) are similar, on the whole, to the respective dependences of T_{eff} (the dependence for a sample with a low Gd concentration is represented by a straight line as a result of the considerable errors encountered in determining τ). This fact confirms the conclusion [7] that interdoublet relaxation is due to spin–lattice interaction. Like $T_{eff}(T)$, the $\tau(T)$ curve has a narrow minimum in the region of the ferroelectric transition. Such a feature in the behavior of the spin–lattice relaxation time determined from the measurements of the EPR line width in the vicinity of T_c was observed in $BaTiO_3 : Mn^{2+}$ [16] and was attributed to the anomalous interaction of the spin system with transverse optical phonons [17–19]. An increase in the spin–lattice relaxation rate in the region of the structural phase transformation was also observed in NMR of $NaNbO_3$ at ^{23}Na nuclei [20] and, probably, at Fe^{3+} impurity ions in $PbTiO_3$ [21]. On the contrary, an increase in the spin–lattice relaxation time was observed in [2] at the Mn^{2+} centers in the vicinity of the phase transition in calcium tris-sarcosine chloride.

4. The observation and investigation of relaxation averaging at other accidental coincidences of resonance positions of EPR transitions (Fig. 1) are undoubtedly of considerable interest.

The effects under investigation cannot take place in the vicinity of intersection of the angular dependences of transitions having a common energy level, while two-quantum transitions can be observed clearly (see Section 1). In the regions of coincidence of the resonance positions of transitions occurring in the doublets separated by a single energy interval (like the transitions $3 \longleftrightarrow 4$ and $5 \longleftrightarrow 6$), a quasi-symmetric arrangement of isofield spin packets is realized only for the transitions $2 \longleftrightarrow 3$ and $4 \longleftrightarrow 5$. An analysis of Eqs. (4) and (5) in the case of antisymmetric distribution of the spin packets revealed that the effect of motion (relaxation transitions) on the line shape and width is minimal in this case.

A detailed analysis of the spectrum in the region of coincidence of the transitions $2 \longleftrightarrow 3$ and $4 \longleftrightarrow 5$ ($\theta_0 \approx 42°$) did not reveal any traces of an extra signal, whose observation is complicated by the strong difference in the intensities and widths of the initial lines, this difference increasing as the temperature approaches T_c.

It was proved in [7], however, that the EPR spectrum is perturbed by the averaging effects even in the case of exact coincidence of the resonance positions ($\Delta\theta = 0$) of the initial transitions. Indeed, it can be clearly seen from Fig. 2 that the width of the resultant line for $\Delta\theta = 0$ (curve *1*) is noticeably smaller than the width of the initial signals (curve *5*). The spectrum of the transitions $2 \longleftrightarrow 3$ and $4 \longleftrightarrow 5$ for $\Delta\theta = 0$ presented in Fig. 9 also

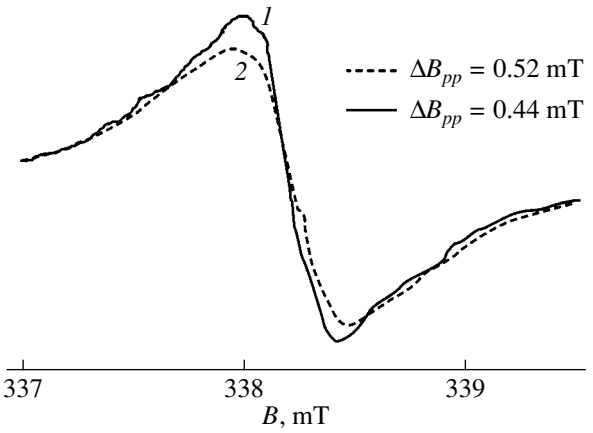

Fig. 9. EPR spectrum in the case of exact coincidence of positions of the 2 ⟷ 3 and 4 ⟷ 5 transitions at room temperature: (*1*) experiment and (*2*) the sum of the initial signals in the absence of interdoublet relaxation.

demonstrates a slight narrowing of the resultant line relative to the sum of the initial lines, indicating the averaging of spin packets in this case also. Unfortunately, the error in determining the relaxation time for exactly coinciding positions of the initial packets is very high.

In the region of the coincidence of resonance positions of transitions occurring in doublets separated by two energy intervals, the spin packets associated with modulation of b_{21} are arranged quasi-symmetrically for the transitions 3 ⟷ 4 and 6 ⟷ 7, 2 ⟷ 3 and 5 ⟷ 6, and 4 ⟷ 5 and 7 ⟷ 8. However, the region of intersection of the angular dependences for the transitions 2 ⟷ 3 and 5 ⟷ 6 is covered by the intense signal of the 4 ⟷ 5 transition, while the intensities of the transitions 4 ⟷ 5 and 7 ⟷ 8 are absolutely incomparable. An analysis of the spectrum in the region of coincidence of the 3 ⟷ 4 and 6 ⟷ 7 signals, which also have noticeably different peak intensities ($I_{34}/I_{67} \approx 3$ for $\Delta B_{pp67}/\Delta B_{pp34} \approx 1.5$), did not reveal any interaction of the spin packets.

No averaging effects were also detected in the region of intersection of the angular dependences for transitions separated by three energy intervals. In this group, the intersection of the dependences for the transitions 2 ⟷ 3 and 6 ⟷ 7 occurring between two high-intensity EPR signals are the most promising for the observation of an extra signal as regards the ratio of intensities ($I_{23}/I_{67} \approx 2.5$).

Computer simulation of the three-component spectrum by Eqs. (4) and (5) proved that increasing the ratio of the intensities of the initial signals up to four or increasing the ratio σ_b/σ_a up to two for conserved values of relaxation parameters leads to a spectrum without any noticeable evidence of an extra signal. In our opinion, this fact completely explains the absence of an additional signal for intersections (other than those for the 3 ⟷ 4 and 5 ⟷ 6 transitions) of the angular dependences of positions of signals with quasi-symmetric arrangement of the spin packets. In addition, a three-component spectrum can be observed only when definite relations are observed between T_{eff}, τ, and σ. It follows from the results presented in Figs. 6–8 that an extra signal is observed for close values of the quantities $g_{\text{eff}}\beta\sigma$, $1/2\pi T_{\text{eff}}$, and $1/2\pi\tau$. The changes in the spectrum associated with interdoublet relaxation become more pronounced upon an increase in the relaxation rate; however, the interdoublet relaxation rate in our model cannot exceed the relaxation rate within a doublet and, hence, the optimal relation connecting τ with T_{eff} has the form $\tau \approx T_{\text{eff}}$. Since an extra signal cannot emerge in the absence of inhomogeneous broadening, another condition for the observation of a three-component spectrum has the form $1/2\pi T_{\text{eff}} \leq g_{\text{eff}}\beta\sigma$.

The shape of the EPR spectrum of a large number of high-spin paramagnetic centers with axial symmetry is mainly determined by the axial parameter of the spin Hamiltonian b_{20}, which fluctuates due to the defect nature of the crystal [22]. If there exists a spread in the values of b_{20} (at least, when the strong magnetic field approximation holds), the polar angular dependence of the positions of transitions contains the points of coincidence of signals with quasi-symmetric distribution of the isofield spin packets. However, the probability of detecting the selective averaging of the EPR spectrum is low in view of the requirement that the above relations between T_{eff}, τ, and σ must be satisfied, as well as of the requirements imposed on the intensity and width of the initial signals.

ACKNOWLEDGMENTS

The authors express their sincere gratitude to A.N. Legkikh for his assistance in measuring and processing spectra and to N.A. Legkikh for valuable discussions of the results.

This research was partly supported by the American Foundation for Civilian Research and Development for CIS countries, grant no. REC-005.

REFERENCES

1. G. F. Reiter, W. Brelinger, K. A. Müller, and P. Heller, Phys. Rev. B **21** (1), 1 (1980).
2. W. Windsch and G. Volkel, Ferroelectrics **24**, 195 (1980).
3. B. E. Vugmeĭster, M. D. Glinchuk, A. A. Karmazin, and I. V. Kondakova, Fiz. Tverd. Tela (Leningrad) **23** (5), 1380 (1981) [Sov. Phys. Solid State **23**, 806 (1981)].
4. Y. Iwata, J. Phys. Jpn. **43**, 961 (1977).
5. V. A. Vazhenin and K. M. Starichenko, Pis'ma Zh. Éksp. Teor. Fiz. **51** (8), 406 (1990) [JETP Lett. **51**, 461 (1990)].
6. V. A. Vazhenin and K. M. Starichenko, Fiz. Tverd. Tela (St. Petersburg) **34** (1), 172 (1992) [Sov. Phys. Solid State **34**, 90 (1992)].

7. V. A. Vazhenin, K. M. Starichenko, and A. D. Gorlov, Fiz. Tverd. Tela (St. Petersburg) **35** (9), 2449 (1993) [Phys. Solid State **35**, 1214 (1993)].
8. J. R. Herrington, T. L. Estle, and L. A. Boatner, Phys. Rev. B **3** (9), 2933 (1971).
9. I. B. Bersuker and V. Z. Polinger, *Vibronic Interactions in Molecules and Crystals* (Nauka, Moscow, 1983; Springer, New York, 1989).
10. É. P. Zeer, V. E. Zobov, and O. V. Falaleev, *Novel Effects in NMR of Polycrystals* (Nauka, Novosibirsk, 1991).
11. V. A. Vazhenin, E. L. Rumyantsev, M. Yu. Artemov, and K. M. Starichenko, Fiz. Tverd. Tela (St. Petersburg) **40** (2), 321 (1998) [Phys. Solid State **40**, 293 (1998)].
12. A. Abragam, *The Principles of Nuclear Magnetism* (Clarendon, Oxford, 1961; Inostrannaya Literatura, Moscow, 1963).
13. H. S. Gutowsky and S. H. Holm, J. Chem. Phys. **25** (6), 1228 (1956).
14. V. A. Vazhenin, K. M. Starichenko, and A. V. Gur'ev, Fiz. Tverd. Tela (Leningrad) **30** (5), 1443 (1988) [Sov. Phys. Solid State **30**, 832 (1988)].
15. A. D. Gorlov, A. P. Potapov, and Yu. A. Sherstkov, Fiz. Tverd. Tela (Leningrad) **27** (3), 625 (1985) [Sov. Phys. Solid State **27**, 388 (1985)].
16. V. V. Shapkin, B. A. Gromov, G. T. Petrov, *et al.*, Fiz. Tverd. Tela (Leningrad) **15** (5), 1401 (1973) [Sov. Phys. Solid State **15**, 947 (1973)].
17. B. I. Kochelaev, Zh. Éksp. Teor. Fiz. **37**, 242 (1959) [Sov. Phys. JETP **10**, 171 (1960)].
18. N. Kumar and K. P. Sinha, Physica (Amsterdam) **34**, 387 (1967).
19. C. Y. Huang, Phys. Rev. **161** (2), 272 (1967).
20. G. Bonera, F. Borsa, and A. Rigamonti, J. Phys. (Paris) **33** (C2), 195 (1972).
21. S. T. Kirillov and Yu. G. Plakhotnikov, Pis'ma Zh. Éksp. Teor. Fiz. **34** (11), 572 (1981) [JETP Lett. **34**, 548 (1981)].
22. N. V. Karlov and A. A. Manenkov, *Quantum Amplifiers* (VINITI, Moscow, 1966).

Translated by N. Wadhwa

Physics of the Solid State, Vol. 44, No. 6, 2002, pp. 1152–1155. Translated from Fizika Tverdogo Tela, Vol. 44, No. 6, 2002, pp. 1102–1105.

LATTICE DYNAMICS AND PHASE TRANSITIONS

Specific Features of Low-Temperature Phonon Scattering in Materials with Tilted Disclination Loops

S. E. Krasavin and V. A. Osipov

Joint Institute for Nuclear Research, Dubna, Moscow oblast, 141980 Russia

e-mail: krasavin@thsun1.jinr.ru

Received August 7, 2001

Abstract—Phonon scattering by static stress fields of circular wedge disclination loops is investigated in the framework of the deformation potential approach. Numerical calculations of the mean free path l and thermal conductivity κ demonstrate that the temperature dependence of κ exhibits a minimum at a certain temperature T^* in the low-temperature range. The thermal conductivity κ sharply increases as T^{-3} with a decrease in temperature ($T < T^*$) and exhibits a dislocation behavior ($\kappa \sim T^2$) with an increase in temperature ($T > T^*$). The results obtained for the wedge disclination loop are compared with the available data for uniaxial disclination dipoles. It is shown that the properties of uniaxial disclination dipoles serving as sources of phonon scattering are similar to those of wedge disclination loops. © *2002 MAIK "Nauka/Interperiodica".*

1. INTRODUCTION

It is well known that dislocations, together with other structural defects and chemical impurities, are the main sources of phonon scattering at temperatures substantially below the Debye temperature Θ_D [1, 2]. In the case of phonon scattering by immobile dislocations, the dependence of the thermal conductivity κ on the temperature T is described by a quadratic relationship. However, the role played by linear rotational defects (disclinations) in phonon scattering is as yet poorly understood despite the fact that these defects are of great importance in nanocrystalline materials [3], composites [4], and topologically disordered systems [5]. The problem of heat transfer in a wide variety of materials with rotational plastic strains remains unsolved. In our recent works [6, 7], we investigated the temperature behavior of the thermal conduction associated with the contribution of static disclination dipoles of the tilted type (wedge disclination dipoles) to heat transfer. Moreover, we examined all types of wedge disclination dipoles, namely, uniaxial dipoles, biaxial dipoles with out-of-place axes of rotation, and biaxial dipoles with in-place axes of rotation. Exact expressions were obtained for the mean free path of phonons due to static stress fields for each type of dipoles in the Born approximation.

It has been found that the wedge disclination dipoles serving as effective centers of phonon scattering are characterized by a specific linear parameter, namely, the dipole arm L, and that the mode of phonon scattering depends on the ratio between the wavelength λ of the incident phonon and the dipole arm L. In particular, we revealed that the scattering mode changes under the condition $\lambda \sim L$, which, in the approximation of thermal phonons, leads to the following estimate of the transition temperature: $T^* \approx \hbar v_s/2Lk_B$ (see, for example, [6]). It was also demonstrated that the uniaxial and biaxial wedge disclination dipoles with in-place axes of rotation, which are the two limiting cases of an arbitrary wedge disclination dipole, are distinctly different objects from the point of view of phonon scattering. The uniaxial wedge disclination dipole is a highly screened system in contrast with the biaxial wedge disclination dipole [6]. This manifests itself in a strong dependence of the mean free path l on the wave vector $\mathbf{k}$ in the long-wavelength limit [$l(k) \sim k^{-5}$ at $\lambda \ll L$]. For a uniaxial wedge disclination dipole in the short-wavelength limit, the phonon scattering exhibits a dislocation nature: $l(k) \sim k^{-1}$. At the same time, the biaxial wedge disclination dipole with in-place axes of rotation obeys the relationships $l(k) \sim k^{-1}$ at $\lambda \ll L$ and $l(k) \longrightarrow$ const in the opposite limit. This behavior sets the biaxial wedge disclination dipole apart from other similar defects.

In the present work, we examined another stable disclination object, namely, a circular wedge disclination loop [8, 9]. Considerable interest expressed in the problem of phonon scattering by static strain fields of circular wedge disclination loops stems from the fact that disclination loops seem to be the most commonly encountered elements of the three-dimensional disclination structure in the majority of real media. The results obtained for the circular wedge disclination loop are compared with the available data for another disclination defect, namely, a uniaxial wedge disclination dipole.

1063-7834/02/4406-1152$22.00

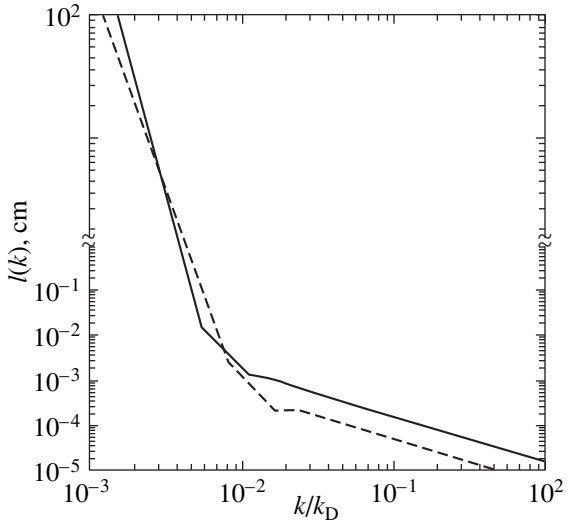

Fig. 1. Dependence of the phonon mean free path [calculated from formula (6)] on the reduced wave vector k/k_D ($k_D = \omega_D/v_s$) at the following parameters: $R = L = 2 \times 10^{-6}$ cm, $\nu = 0.1$, $v_s = 4 \times 10^5$ cm/s, $B = 0.01$, and $n_d = 10^{15}$ cm^{-3}. The dashed line represents the dependence $l(k/k_D)$ for a uniaxial wedge disclination dipole at the same parameters, except for $n_d = 6 \times 10^9$ cm^{-3}.

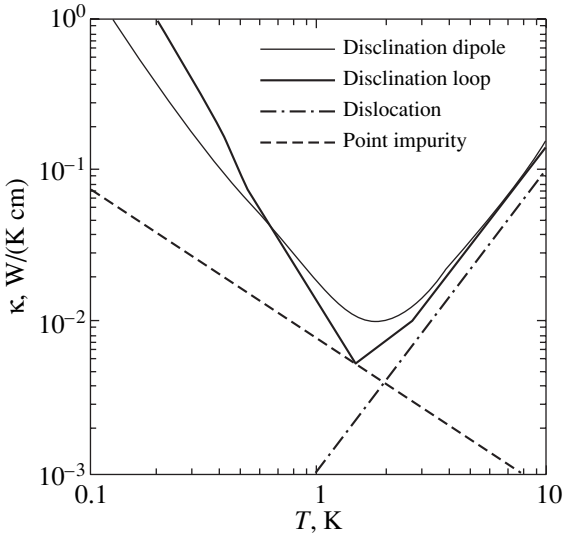

Fig. 2. Temperature dependence of the thermal conductivity calculated from formula (7) for the phonon mean free path determined from formula (6) (for the wedge disclination dipole, the mean free path is taken from [6]). The parameters used in the calculation are the same as those in Fig. 1 ($\Theta_D = 300$ K). The curves calculated for a dislocation and a point impurity are depicted for comparison.

2. THEORETICAL BACKGROUND

Let us consider the problem of elastic phonon scattering by static stress fields of a wedge disclination loop in the framework of the deformation potential approach [1, 10]. Within this approach, the energy of phonon perturbation is associated with the relative change in the volume due to strains induced by a circular wedge disclination loop placed in the medium. In this case, the deformation potential has the following form [1]:

$$U(\mathbf{r}) = \hbar\omega\gamma \mathrm{Sp}E_{ij}, \tag{1}$$

where $\hbar\omega$ is the energy of a phonon with the wave vector $\mathbf{k}$, $\omega = kv_s$, v_s is the mean velocity of sound in the medium, γ is the Grüneisen constant, and $\mathrm{Sp}E_{ij}$ is the trace of the deformation tensor due to the circular wedge disclination loop.

It is assumed that a loop of radius R is located in the plane $z = 0$ of the cylindrical coordinate system (r, φ, z) with the rotation axis passing through the origin of the coordinates and the Frank vector specified by the coordinates $(0, \Omega, 0)$ with respect to the chosen basis (the in-place circular wedge disclination loop). By using the explicit expression for the deformation tensor of the circular wedge disclination loop with the in-place axis of rotation E_{ij} (see [9, 11]), we obtain the following relationship for the perturbation energy represented by expression (1):

$$U(\mathbf{r}) = A\cos\varphi J(2, 1; 1). \tag{2}$$

Here, $A = \hbar k v_s \pi\gamma\nu(1 - 2\sigma)/(\sigma - 1)$, $\nu = \Omega/2\pi$ is the Frank index, σ is the Poisson ratio, $J(2, 1; 1) = \int_0^\infty J_2(K)J_1(Kr/R)\exp(-K|z|/R)KdK$ is the Lifshitz–Hankel integral, and $J_m(x)$ is the Bessel function of the first kind.

In the Born approximation, the matrix element describing the transition of a phonon from the state $\mathbf{k}$ to the state $\mathbf{k}'$ has the form

$$\langle \mathbf{k}|U(r)|\mathbf{k}'\rangle = \frac{1}{V}\int d^3 r U(\mathbf{r})\exp(i\mathbf{qr}), \tag{3}$$

where $\mathbf{q} = \mathbf{k} - \mathbf{k}''$. Taking into account the axial symmetry of the defect under consideration, it is expedient to introduce the cylindrical coordinate system into relationship (3). In this case, the matrix element with due regard for relationship (2) has the following form:

$$\langle \mathbf{k}|U(r)|\mathbf{k}'\rangle = 4\pi i R^2 \cos\alpha \frac{A}{V}\frac{q_\perp}{q_\perp^2 + q_z^2} J_2(q_\perp R), \tag{4}$$

where α is the angle between $\mathbf{q}_\perp = (q_x, q_y)$ and the x axis. In order to simplify the subsequent calculations, we consider an incident phonon whose momentum is directed along the k_x axis and choose the cylindrical coordinate system $(k_\perp, \phi, k_z)$ in the k space. In this case, we obtain the following expression for the mean free path:

$$l^{-1}(k) = \frac{VNk}{(2\pi\hbar v_s)^2} \times \int_0^{2\pi} d\phi \int_0^k dk_z' \overline{|\langle \mathbf{k}|U(r)|\mathbf{k}'\rangle|^2}(1 - \cos\theta), \tag{5}$$

where N is the number of defects and θ is the angle of scattering (for elastic scattering, $q = |\mathbf{q}| = |\mathbf{k} - \mathbf{k}'| = 2k\sin(\theta/2)$). The bar above the square of the matrix element signifies averaging over the angle α. The angle θ can be expressed through ϕ as follows: $1 - \cos\theta = 1 - \sqrt{1 - (k_z'/k)^2}\cos\phi$. From relationships (4) and (5), we obtain the final expression for the mean free path

$$l^{-1}(k) = n_d R^4 k^2 B \int_0^{2\pi} d\phi \int_0^1 dz \frac{1 - \sqrt{1 - z^2}\cos\phi - z^2/2}{1 - \sqrt{1 - z^2}\cos\phi} \times J^2\left(Rk\sqrt{2 - z^2 - 2\sqrt{1 - z^2}\cos\phi}\right), \quad (6)$$

where $z = k_z'/k$, $n_d = N/V$ is the concentration of defects, and $B = (\pi\gamma\nu(1 - 2\sigma)/(1 - \sigma))^2$.

3. RESULTS AND DISCUSSION

3.1. Figure 1 shows the dependences $l(k)$ calculated numerically for a circular wedge disclination loop according to formula (6) and for a uniaxial wedge disclination dipole (the data are taken from [6]) at $R = L$ (L is the arm of the dipole) under the assumption that the capacities of defects specified by the Frank index ν are equal to each other. It is seen from Fig. 1 that both defects are characterized by two different scattering modes at $kR \lesssim 1$ and $kR \gtrsim 1$ ($k^* \sim 1/R$ is the point on the curve which corresponds to the change in the scattering mode). In the long-wavelength limit $kR \lesssim 1$, the mean free path $l(k)$ sharply increases in phonon scattering by a stress field of the circular wedge disclination loop with a decrease in k (Fig. 1). This increase is even more pronounced than in the case of the uniaxial wedge disclination dipole for which $l(k) \sim k^{-5}$ [6]. From relationship (6) at $k \longrightarrow 0$, we obtain the estimate $l(k) \sim k^{-6}$. Such a strong k-dependence for $l(k)$ is specific to defects of finite size and can be explained by the lack of interference in scattering from different segments of the defect in the long-wavelength limit (the wavelength exceeds the size of the defect) [12]. Therefore, the circular wedge disclination loop is all the more a self-screened system compared to the uniaxial disclination dipole. It should be noted that, in both cases, the dependence $l(k)$ in the long-wavelength limit is stronger than in the case of a point impurity for which $l(k) \sim k^4$ (Rayleigh scattering) [2]. In the opposite limit of short waves ($kR \gtrsim 1$), the dependence $l(k)$ for the circular wedge disclination loop exhibits a dislocation behavior similar to that of the uniaxial wedge disclination dipole: $l(k) \sim 1/k$ (see [6, 7]).

The contribution to the thermal conductivity from phonon scattering by circular wedge disclination loops can be estimated by the standard kinetic formula written in the dimensionless form:

$$\kappa = \frac{k_B^4 T^3}{2\pi^2 \hbar^3 v_s^2} \int_0^{\Theta_D/T} \frac{x^4 e^x}{(e^x - 1)^2} l(x)\,dx, \quad (7)$$

where $x = \hbar k v_s/k_B T = \hbar\omega/k_B T$, $\Theta_D = \hbar\omega_D/k_B$, and $l(x)$ is determined by relationship (6).

The results of numerical calculations of the temperature dependence of the thermal conductivity κ due to phonon scattering by static stress fields of a circular wedge disclination loop are represented in Fig. 2. This figure also depicts the dependences $\kappa(T)$ for a uniaxial wedge disclination dipole, a dislocation, and a point impurity. The behavior of $\kappa(T)$ for the circular wedge disclination loop is explained in terms of the dependence $l(k)$ (see above). It is clearly seen from Fig. 2 that, for the chosen model parameters in relationships (6) and (7), the dependence $\kappa(T)$ exhibits a minimum at $T^* \approx 2$ K for both the circular wedge disclination loop and the uniaxial wedge disclination dipole. The thermal conductivity κ increases drastically in the temperature range below T^*. This increase corresponds to the increase in the mean free path $l(x)$ [see relationship (7)] at $T \longrightarrow 0$ in accordance with the law $l(k) \sim k^{-6}$ for the circular wedge disclination loop and $l(k) \sim k^{-5}$ for the wedge disclination dipole in the long-wavelength limit. As a result, when $T < T^*$, the contribution to the thermal conductivity due to phonon scattering by static stress fields of the circular wedge disclination loop is proportional to T^{-3} (T^{-2} in the case of the wedge disclination dipole). Note that, below T^*, the thermal conductivity κ of both the circular wedge disclination loop and the uniaxial wedge disclination dipole increases more rapidly than that of a point impurity for which $\kappa \sim T^{-1}$ (dashed line in Fig. 2). Near T^*, phonons whose wavelength is comparable to the characteristic size of the defect ($kR \sim 1$) are predominantly excited, in contrast with the case $kR \lesssim 1$, where the defect is a weak scatterer of thermal phonons. For $kR \sim 1$, strong scattering arises at the boundary of the defect. In turn, this brings about the suppression of heat transfer. Above T^*, the thermal conductivity for both the circular wedge disclination loop and the wedge disclination dipole has a dislocation behavior: $\kappa \sim T^2$ [$l(k) \sim 1/k$] (Fig. 2). An increase in the thermal conductivity κ above the minimum point can be explained by the increase in the number of short-wave excitations for which the local heat transfer from one phonon to another proceeds more rapidly than the phonon scattering by circular wedge disclination loops (wedge disclination dipoles), which exhibits a dislocation nature and leads to the suppression of the thermal conduction.

3.2. In this work, we analyzed the contribution to the thermal conductivity due to phonon scattering by static stress fields of the circular wedge disclination loop in the low-temperature range ($T < \Theta_D$). It was demonstrated that the properties of the circular wedge discli-

nation loops serving as sources of phonon scattering are similar to those of disclination dipoles with a common axis of rotation (uniaxial wedge disclination dipoles). Phonon scattering by these defects at different temperatures is characterized by a nontrivial dependence $\kappa(T)$. In a certain range of temperatures near T^*, the thermal conductivity κ is strongly suppressed and increases above and below the temperature T^* (Fig. 2) as T^{-3} (T^{-2} for the wedge disclination dipole) with a decrease in the temperature when $T < T^*$ and as T^2 with an increase in the temperature when $T > T^*$. Thus, the circular wedge disclination loop and the uniaxial wedge disclination dipole are specific defects from the point of view of phonon scattering and exhibit quite a different behavior depending on the phonon wavelength. In the long-wavelength range, the properties of these defects are similar to those of the point impurity (strong screening of stress fields). In the short-wavelength limit, the phonon scattering has a dislocation nature.

It is evident that, for real materials containing these defects, the situation can be somewhat different due to the existence of other scattering sources. For example, in the low-temperature range, phonon scattering should arise at the crystal grain boundaries inside the sample (the sample boundaries correspond to the limiting case), thus limiting an infinite increase in κ below the minimum conductivity. Our calculations demonstrate that the inclusion of this channel of scattering gives rise to an additional maximum in the range of very low temperatures. In the materials under investigation, defects of another type can also exist and contribute to the total thermal conductivity κ. It should be emphasized that the minimum thermal conductivity κ obtained in the numerical calculations is observed in the temperature range $0.1 < T^* < 10$ K, in which other main mechanisms of scattering (for example, umklapp processes) do not contribute appreciably to scattering. For this reason, the effects associated with the suppression of the thermal conduction in the low-temperature range can be revealed experimentally. Moreover, the observed behavior of the thermal conductivity κ is unique and can serve as indirect evidence of the existence of circular wedge disclination loops and wedge disclination dipoles in the studied material.

The calculation of the temperature dependence of the thermal conductivity κ with due regard for other sources of scattering, apart from scattering by wedge disclination loops and uniaxial dipoles, will be performed in the immediate future. The results obtained will be reported in a separate paper.

REFERENCES

1. J. M. Ziman, *Electrons and Phonons* (Clarendon, Oxford, 1960; Inostrannaya Literatura, Moscow, 1962).
2. P. Carruthers, Rev. Mod. Phys. **33** (1), 92 (1961).
3. S. G. Zaĭchenko and A. M. Glezer, Fiz. Tverd. Tela (St. Petersburg) **39** (11), 2023 (1997) [Phys. Solid State **39**, 1810 (1997)].
4. I. A. Ovid'ko, Fiz. Tverd. Tela (St. Petersburg) **41** (9), 1637 (1999) [Phys. Solid State **41**, 1500 (1999)].
5. A. Richter, A. E. Romanov, W. Pompe, and V. I. Vladimirov, Phys. Status Solidi B **122** (1), 35 (1984).
6. V. A. Osipov and S. E. Krasavin, J. Phys.: Condens. Matter **10**, L639 (1998).
7. S. E. Krasavin and V. A. Osipov, J. Phys.: Condens. Matter **13**, 1023 (2001).
8. H. H. Kuo and T. Mura, J. Appl. Phys. **43** (4), 1454 (1972).
9. V. A. Likhachev and R. Yu. Khaĭrov, *Introduction to the Theory of Disclinations* (Leningr. Gos. Univ., Leningrad, 1975).
10. V. F. Gantmakher and Y. B. Levinson, *Carrier Scattering in Metals and Semiconductors* (Nauka, Moscow, 1984; North-Holland, New York, 1987).
11. V. I. Vladimirov and A. E. Romanov, *Disclinations in Crystals* (Nauka, Leningrad, 1986).
12. P. Clemence, in *Low Temperatures Physics* (Springer-Verlag, Berlin, 1956; Inostrannaya Literatura, Moscow, 1959).

Translated by O. Moskalev

Physics of the Solid State, Vol. 44, No. 6, 2002, pp. 1156–1165. Translated from Fizika Tverdogo Tela, Vol. 44, No. 6, 2002, pp. 1106–1115.

LATTICE DYNAMICS AND PHASE TRANSITIONS

Low-Frequency Elastic Properties, Domain Dynamics, and Spontaneous Twisting of $SrTiO_3$ near the Ferroelastic Phase Transition

V. V. Lemanov*, S. A. Gridnev, and E. V. Ukhin****

** Ioffe Physicotechnical Institute, Russian Academy of Sciences, ul. Politekhnicheskaya 26, St. Petersburg, 194021 Russia*
e-mail: lemanov@pop.ioffe.rssi.ru

*** Voronezh State Technical University, Moskovskiĭ pr. 14, Voronezh, 394026 Russia*

Received November 26, 2001

Abstract—The low-frequency elastic properties of strontium titanate near the ferroelastic phase transition were studied by the torsional-vibration technique. Domain wall motion was shown to contribute noticeably to the anomalies in the shear modulus and internal friction. It was established that the wall motion under varying elastic stresses is an unactivated process corresponding to viscous flow with a relaxation time inversely proportional to temperature. Spontaneous twisting of samples at the phase transition was revealed, and a model is proposed to account for the sample chirality and the spontaneous twisting effect. © *2002 MAIK "Nauka/Interperiodica".*

1. INTRODUCTION

Strontium titanate $SrTiO_3$ is an incipient ferroelectric and a quantum paraelectric [1, 2] in which quantum fluctuations suppress the ferroelectric phase transition. It has been recently shown [3] that the improper ferroelastic phase transition in $SrTiO_3$, which occurs at $T_a \approx 110$ K with the symmetry changing from cubic, $Pm3m - O_h^1$ (for $T > T_a$), to tetragonal, $14/mcm - D_{4h}^{18}$, plays a dominant role in inhibiting the ferroelectric phase transition (if the strontium titanate remains cubic, the ferroelectric phase transition can take place, despite the quantum corrections [2]). While the anomalies observed in the elastic properties of $SrTiO_3$ at the improper ferroelastic phase transition have been studied already for more than a quarter of a century, the experiments were performed, as a rule, at frequencies $\Omega \geq 10^8$ s^{-1} (see monograph [4], review [5], and the references therein). Fossheim and Berre [6] were the first to consider the contribution due to ferroelastic domains, which form at the transition temperature $T_a \approx 110$ K, to the anomalies of elastic properties of $SrTiO_3$. This contribution turns out to be particularly large at low frequencies, $\Omega \approx 10^1$–10^2 s^{-1} [7].

It has appeared of interest to study the anomalies in the elastic properties and the domain contribution to these anomalies using the low-frequency technique of torsional vibrations. It is the results of these studies that are dealt with in this paper. Just as we were coming to the end of our experiments, a paper appeared [8] which reported on a study of $SrTiO_3$ by a similar technique. In discussing our results, we shall compare them with literature data, including those from [7, 8].

2. MEASUREMENT TECHNIQUE AND EXPERIMENTAL RESULTS

The measurements were carried out on a setup (Fig. 1) representing an inverse torsion pendulum described in detail in [9]. A long twisting rod (*1*) with a rigidly fixed cross and inertia weights is connected through a grip to sample *2*, whose lower end is clamped in a fixed grip. The sample is twisted through the rod by means of a differential electromagnetic system consisting of two current-carrying coils *3* arranged diametrically relative to the pendulum axis and interacting with two permanent magnets provided by soft-iron pole pieces. Photoelectric sensors *5* with lamps *6* served to measure small torsional strains (10^{-5}–10^{-3}). Large strains were measured with capacitance sensors *7*. When a periodically varying current of low frequency Ω is passed through coils *3*, the sample is twisted periodically to angles from $+\varphi_0$ to $-\varphi_0$ under the action of a torque $M = M_0 \sin \Omega t$ which varies from $+M_0$ to $-M_0$ and produces shear strains varying from $+\sigma_0$ to $-\sigma_0$. The measurements were performed at the natural resonance frequency of composite oscillator *1–2* (twisting rod with the inertial system and the sample), which in our case was 25 Hz. The internal friction Q^{-1} (inverse Q factor) was derived from the decrement of freely decaying vibrations, for which purpose the sample was twisted to a given amplitude by the electromagnetic system and the number of vibrations between two preset vibrational strain amplitudes was counted. The shear modulus G was inferred from the period (frequency) of the resonance vibrations.

The maximum shear stresses in the sample were about 10 MPa. Such stresses corresponded to shear strains on the order of 10^{-4} and to sample twist angles

(the angle of turn of the upper sample cross section relative to the lower, rigidly fixed cross section) $\varphi \approx 0.1° = 1.7 \times 10^{-3}$ rad. We note that the shear modulus G and internal friction Q^{-1} were measured at strain amplitudes substantially below their maximum values.

The experiments were carried out on single-crystal samples of nominally pure strontium titanate. The samples measured typically $2 \times 2 \times 10$ mm. Samples of two orientations were used (Fig. 2). In the [100] samples, the long axis coincided with the [100] direction and the side faces coincided with the (010) and (001) planes. In the [110] samples, the long axis was aligned with [110] and the $(1\bar{1}0)$ and (001) planes were parallel to the side faces.

The temperature dependences of the shear modulus G and internal friction Q^{-1} are shown in Figs. 3 and 4. When the [100] sample undergoes a phase transition from the cubic to tetragonal phase, the shear modulus G decreases abruptly by about 3%, with no anomalies in Q^{-1} seen to occur at the phase transition. In the [110] sample, the modulus G decreases by about 40%, while the internal friction Q^{-1} grows strongly upon the transition. This anisotropy can be assigned to the ferroelastic domains contributing to the elastic properties. As will be shown in the next section, the elastic stresses generated in a twisted sample do not initiate domain wall motion in the [100] sample but activate it in the [110] sample. This implies that the static shear stresses created under static sample twisting should not affect the domain structure in the [100] sample but should make the [110] sample single-domain. The experiment confirmed this expectation. The results presented in Fig. 5 indicate that the change in the shear modulus G and the internal friction Q^{-1} occurring at the phase transition in the [110] sample depend strongly on the static shear stress σ_{00} and decrease as it increases, i.e., as the sample becomes increasingly single-domain. The dependence of the shear modulus G and of the internal friction Q^{-1} on static stress σ_{00} measured in the low-symmetry phase at 80 K is displayed in Fig. 6. The relative changes in the shear modulus G and internal friction Q^{-1} decrease with increasing absolute magnitude of the static shear stress σ_{00} as a result of the sample becoming single-domain. Such processes should, in principle, give rise to a hysteresis dependence of the shear modulus G and internal friction Q^{-1} on the shear stress σ_{00} (the butterfly pattern). While hysteresis was indeed seen in the experiment (not shown in Fig. 6), it was very weak and occurred in an irregular manner. A similar result was obtained in [8], where hysteresis loops were successfully observed in $\varphi(\sigma)$ only after etching off a surface layer about 5 μm thick from the sample.

In addition to measurements of G and Q^{-1} in samples twisted by external forces, we also observed spontaneous twisting of the [110] sample to an angle φ_s in the absence of external forces (Fig. 7). The angle φ_s, which is zero in the symmetric phase, becomes nonzero at $T = T_a$, to grow subsequently as $(T_a - T)^{3/4}$ as the temperature is further lowered.

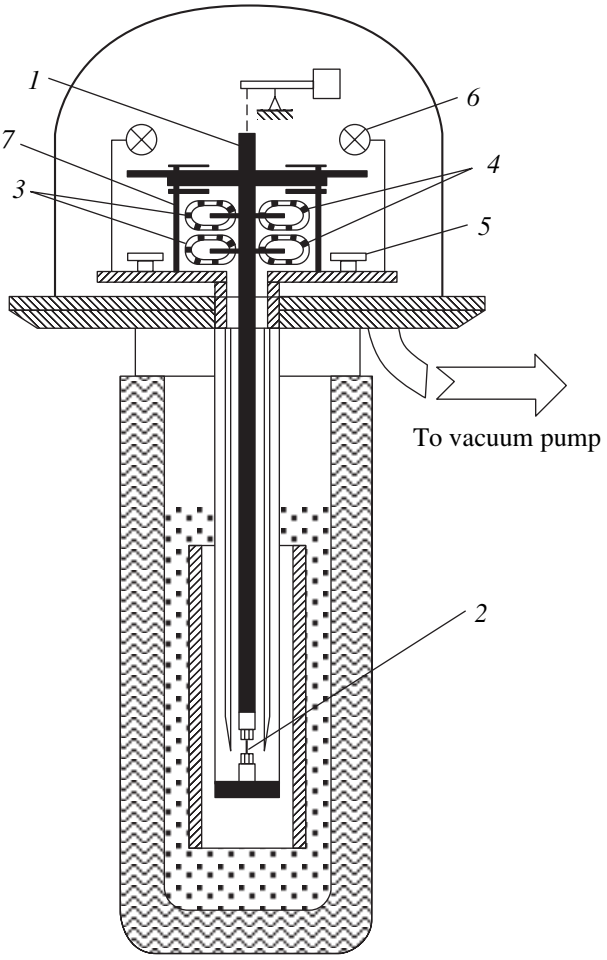

Fig. 1. Experimental setup. (*1*) Twisting rod with cross, (*2*) sample in clamps, (*3*) electromagnetic coils producing torque, (*4*) permanent magnets with annular soft-iron pole pieces, (*5*) photoelectric sensors for small strains, (*6*) electric lamps, and (*7*) capacitance sensors for large strains.

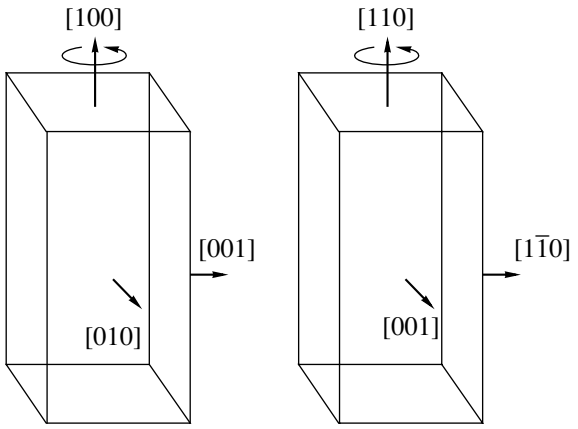

Fig. 2. Sample orientation.

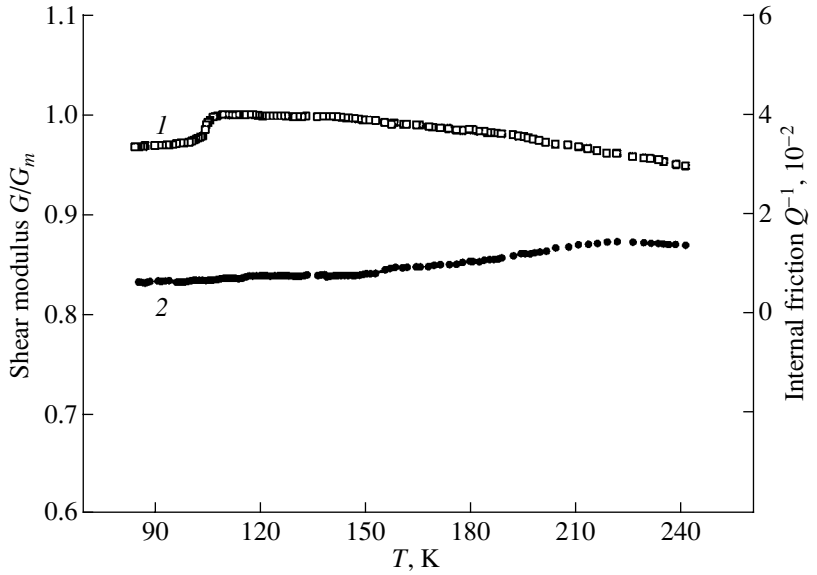

Fig. 3. Temperature dependences of (*1*) shear modulus G/G_m and (*2*) internal friction Q^{-1} in the [100] sample.

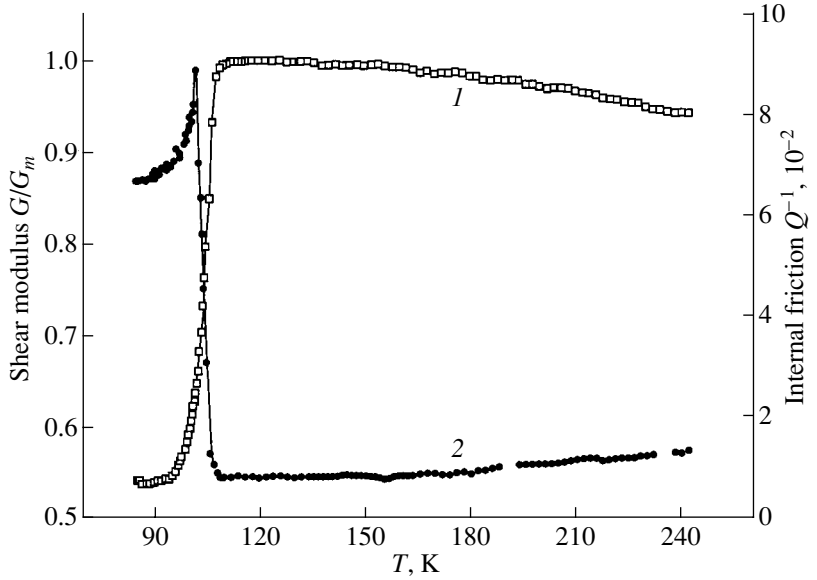

Fig. 4. Temperature dependences of (*1*) shear modulus G/G_m and (*2*) internal friction Q^{-1} in the [110] sample.

3. DISCUSSION OF RESULTS

The results presented in Figs. 3–6 indicate that the ferroelastic domains forming in strontium titanate in the improper ferroelastic phase transition at $T_a \approx 110$ K contribute appreciably to the temperature dependences of the shear modulus G and internal friction Q^{-1}. Domains can obviously affect the shear modulus and internal friction in two ways, namely, through variation of the crystallographic orientation from one domain to another and through domain wall motion under elastic stresses. To establish the mechanism of this effect, one should find, first of all, the relation between the torque applied to the sample (Fig. 1) and the elastic strains created in it.

The problem of thin-rod twisting has been considered in the theory of elasticity [10, 11]. Rather than dealing with exact solutions to this problem, we shall consider only its principal qualitative aspects.

Twisting a thin straight rod with the axis z along the rod axis produces pure shear strains u_{xz} and u_{yz}. The twist angle γ (the angle of turn per unit rod length) is $\gamma = M/C$, where M is the torque and C is the so-called torsional stiffness of the rod.

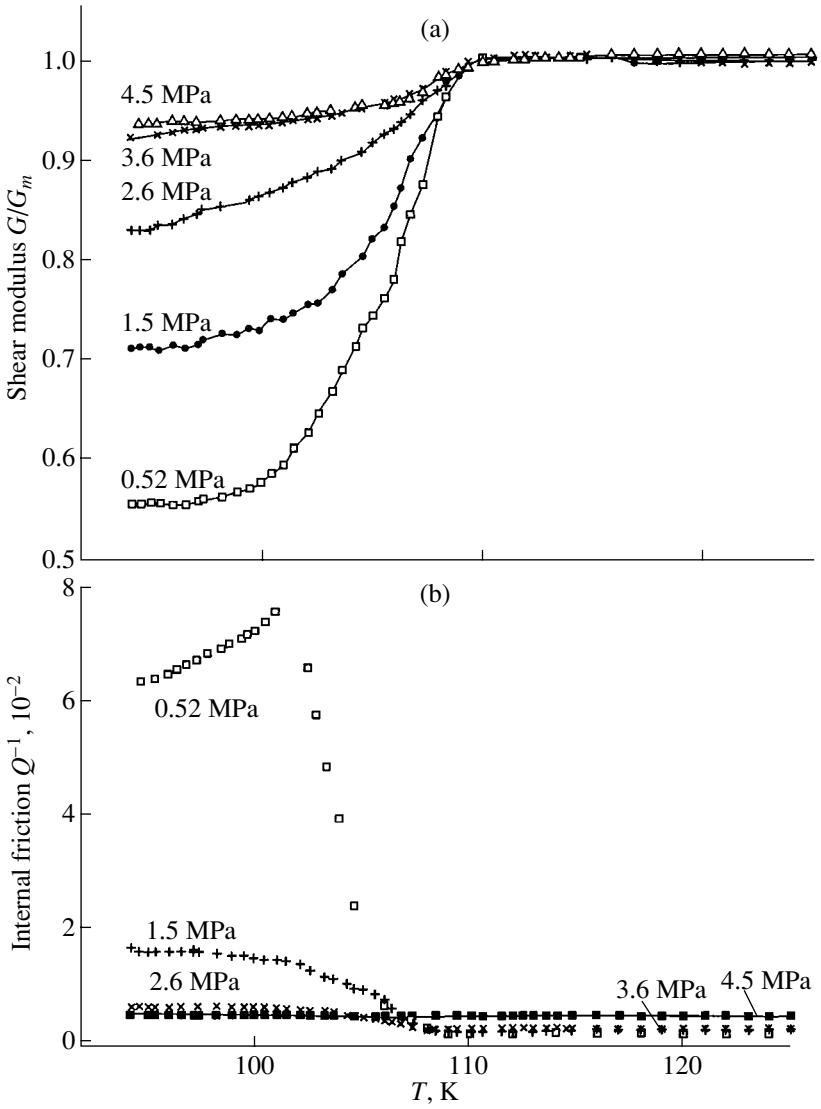

Fig. 5. Temperature dependences of (*1*) shear modulus G/G_m and (*2*) internal friction Q^{-1} in the [110] sample for various static shear stresses σ_{00}.

Approximating our sample with a rod of circular cross section with a radius $R = 10^{-3}$ m, we have $C = (\pi R^4/2)G$, where G is the shear modulus; i.e., the rod's torsional stiffness is $C \approx 2 \times 10^{-12}$ $G \approx 0.2$ J m. This yields the value of the twist angle γ (rad/m) = 5 M (J), and for the stresses and strains, we obtain zero at the center and maximum values at the sample surface: σ_{xz}(Pa) = $-G\gamma R = -10^{-3}G\gamma$; $u_{xz} = -0.5\gamma R = -5 \times 10^{-4}\gamma$; σ_{yz}(Pa) = $+G\gamma R = +10^{-3}G\gamma$; and $u_{yz} = +0.5\gamma R = +5 \times 10^{-4}\gamma$.

Thus, shear strains in the sample turn out to be essentially nonuniform along the rod radius. To obtain an exact quantitative solution to the problem, one has to take into account the sample's shape and the crystallographic anisotropy by invoking the concept of the shear modulus of an anisotropic material for twisting [11]. Significantly, twisting will also bend the rod, which possibly should also be taken into account when analyzing finer effects.

We consider now the domain structure of samples with the long axis aligned with the [100] and [110] directions (Fig. 2).

The canonical form of the thermodynamic potential for strontium titanate is well known [12]:

$$\begin{aligned} F &= b_1(q_1^2 + q_2^2 + q_3^2) + b_{11}(q_1^4 + q_2^4 + q_3^4) \\ &+ b_{12}(q_1^2q_2^2 + q_1^2q_3^2 + q_2^2q_3^2) + 1/2c_{11}(u_1^2 + u_2^2 + u_3^2) \\ &+ c_{12}(u_1u_2 + u_1u_3 + u_2u_3) + 1/2c_{44}(u_4^2 + u_5^2 + u_6^2) \\ &- g_{11}(u_1q_1^2 + u_2q_2^2 + u_3q_3^2) - g_{12}\{u_1(q_2^2 + q_3^2) \\ &+ u_2(q_1^2 + q_3^2) + u_3(q_1^2 + q_2^2)\} \\ &- g_{44}(u_4q_2q_3 + u_5q_1q_3 + u_6q_1q_2). \end{aligned} \quad (1)$$

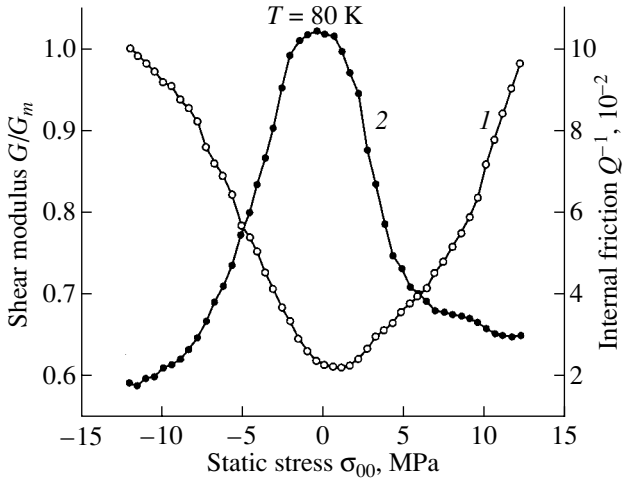

Fig. 6. (*1*) Shear modulus G/G_m and (*2*) internal friction Q^{-1} in the [110] sample plotted vs. static shear stress σ_{00}.

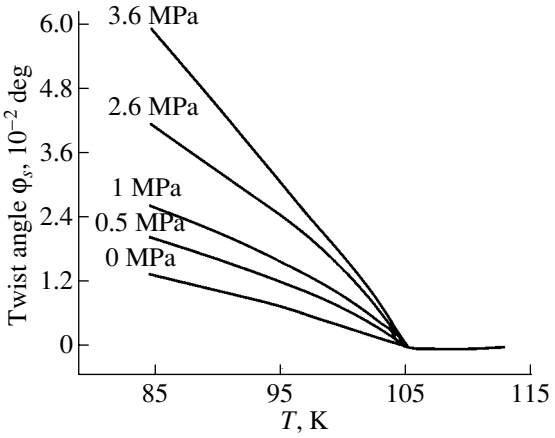

Fig. 7. Temperature dependences of the spontaneous twist angle in the [110] sample plotted for various static shear stresses σ_{00}.

The elastic moduli, quoted in various papers, are c_{11} = 3.30, c_{12} = 1.05, and c_{44} = 1.27 (in units of 10^{11} J/cm^3).

Of all the terms in the thermodynamic potential (1), we are primarily interested in the coupling coefficients g_{ik} of the order parameter with elastic strain. It should be borne in mind that the numerical values of the coefficients in Eq. (1) depend on the quantity used as the order parameter. The order parameter may have the meaning of the angle of turn of the oxygen octahedra θ (in radians) or oxygen displacements $q(m)$. In this case, the coefficients in Eq. (1) will have naturally different dimensionality and different magnitude and their relation will be determined by $\tan\theta \approx \theta = (2/a_0)q$, where a_0 = 3.905 Å is the lattice parameter. Then, $\theta = 5.1 \times 10^9 q$ and the coupling coefficients g_{ik} will have the dimensions J/m^3 and J/m^5, respectively, and will be related through the coefficient 2.62×10^{19} m^{-2}.

The numerical values of the coupling coefficients g_{ik} quoted in different publications [6, 7, 12–14] differ strongly both in magnitude (by a factor of six to eight) and in sign. These differences are particularly large in [7]. We note that the scatter of literature data for the coefficient g_{44} is substantially smaller than that for g_{11} and g_{12}. We believe the values presented in [6, 14] to be the most reasonable. We present these values for both order parameters.

In the case where the order parameter is the angle of turn of the oxygen octahedra θ (in radians), the coupling coefficients (in units of 10^{11} J/m^3) are

$$\begin{aligned} &g_{11} = 0.69, \quad g_{12} = -0.42, \quad g_{44} = 0.88 \ [6], \\ &g_{11} = 0.5, \quad g_{12} = -0.95, \quad g_{44} = 0.88 \ [14]. \end{aligned} \tag{2}$$

If the order parameter is the oxygen ion displacement q (in meters), the coupling coefficients (in units of 10^{30} J/m^5) are

$$\begin{aligned} &g_{11} = 1.8, \quad g_{12} = -1.1, \quad g_{44} = 2.3 \ [6], \\ &g_{11} = 1.3, \quad g_{12} = -2.5, \quad g_{44} = 2.3 \ [14]. \end{aligned} \tag{3}$$

We note that the condition $g_{11} = -2g_{12}$ accepted in [12] is in sharp contrast with the real situation, because this condition implies that the phase-transition temperature T_a is independent of hydrostatic pressure, which disagrees with experiment [6, 15]. We also note that the coupling coefficients g_{ik} are equal, in order of magnitude, to the elastic moduli c_{ik}, as should be.

Let us now consider the elastic strains generated in domains when a [100]- or [110]-oriented sample is twisted. It is known that strontium titanate has three types of tetragonal domains, with the tetragonal axis c (z) along [100] (domain *1*), along [010] (domain *2*), and along [001] (domain *3*).

3.1. Sample [100]

We introduce the reference frame with the axes coinciding with the coordinate axes of domain *1*; i.e., the x, y, and z axes point along [010], [001], and [100], respectively, with the z axis ([100]) aligned with the long axis of the sample. Then, twisting the sample creates the following shear strain components in the domains:

$$\begin{aligned} &\pm u_{zy} \text{ and } \mp u_{zx} \ (\text{domain } 1), \\ &\pm u_{yz} \text{ and } \mp u_{yx} \ (\text{domain } 2), \\ &\pm u_{xz} \text{ and } \mp u_{xy} \ (\text{domain } 3). \end{aligned} \tag{4}$$

Using Eq. (1) for the energy and taking into account that in each domain $q_1 = q_2 = 0$, $q_3 \neq 0$, we obtain for the domain energy $F_1 = F_2 = F_3 = 0$.

Thus, all domains are energetically equivalent under twisting and twisting should not entail domain wall dis-

placement; hence, domains contribute neither to the shear modulus G nor to the internal friction Q^{-1}, which is exactly what is observed in the experiment (Fig. 3). As for the change in the shear modulus at the phase transition, Eq. (1) shows [12] that the phase transition should produce jumps in all the shear moduli except c_{66} ($\Delta c_{66} = 0$). Whence it follows that the magnitude of the experimentally observed jump in a shear modulus depends on the relative numbers of differently oriented domains in the sample.

3.2. Sample [110]

The sample axes (Fig. 2) coincide with the tetragonal axes of domain *3*; namely, the *X*, *Y*, and *Z* axes are along the $[1\bar{1}0]$, [110], and [001] directions, respectively, with the *Y* axis ([110]) aligned with the long axis of the sample. Twisting creates strains $\pm u_{YZ}$ and $\mp u_{YX}$ along these axes.

The strains in the domains can be decomposed into the following components (along the cube axes, with $Z \parallel z$ in domain *3*):

$$\begin{gathered} u_{xx} = -u_{zz} = -a/2, \quad u_{yy} = 0, \\ u_{yz} = u_{xy} = \sqrt{2}a, \quad u_{xz} = -a/2 \ \text{(domain 1)}, \\ u_{xx} = 0, \quad u_{yy} = -u_{zz} = a/2, \\ u_{yz} = -a/2, \quad u_{xz} = u_{xy} = \sqrt{2}a \ \text{(domain 2)}, \\ u_{xx} = -u_{yy} = a/2, \quad u_{zz} = 0, \\ u_{yz} = u_{xz} = \sqrt{2}a, \quad u_{xy} = -a/2 \ \text{(domain 3)}, \end{gathered} \tag{5}$$

where $a = |u_{YZ}| = |u_{YX}|$.

In this case, the domain energies are

$$\begin{aligned} F_1 &= -(g_{11} - g_{12})q_3^2 u_{YX}, \\ F_2 &= (g_{11} - g_{12})q_3^2 u_{YX}, \\ F_3 &= 0. \end{aligned} \tag{6}$$

Taking the values of coefficients g_{11} and g_{12} given in Eqs. (2) and (3), we obtain $(g_{11} - g_{12}) > 0$. This means that for $u_{YX} > 0$, domain *1* is energetically preferable and domain *2* is the least favorable. The situation reverses for $u_{YX} < 0$.

Thus, varying the shear stress and, accordingly, varying the strain u_{YX} gives rise to domain wall motion (vibrations). As a result, domain contributions to the shear modulus G and internal friction Q^{-1} form in the [110] sample (Fig. 4). When a constant torque is applied to the sample together with a variable torque, the sample becomes single-domain gradually because of the increasing fraction of energetically favorable domains. This transition to the single-domain pattern is very specific. The strains on the opposite sample faces have opposite signs; therefore, if domain *1*, according to Eq. (6), is energetically preferable on a sample face, then domain *2* is energetically favorable on the opposite face. Furthermore, because the strain in the sample is nonuniform, the single-domain state does not set in at the sample center at all and the central part of the sample retains its polydomain pattern, while on the surface, the single-domain state is most pronounced.

At the same time, if considered from the viewpoint of the properties studied (the shear modulus G and the internal friction Q^{-1}), the sample becomes fully single-domain (for a large enough torque and, accordingly, a large enough shear stress) in the sense that it is the domains contributing to G and Q^{-1} that disappear. Therefore, as seen from Fig. 5, the anomalies in the shear modulus and internal friction decrease with increasing static shear stress σ_{00}.

We note that, as for the [100] sample, the effective shear modulus and effective coupling coefficient are determined, for the given domain structure and fixed domain walls, by the domain orientation relative to the sample axes and by the fractions of oppositely oriented domains.

In view of the shear modulus G and internal friction Q^{-1} being dependent on static shear stress σ_{00} at a constant temperature (Fig. 6), we note that, in experiments of this kind, one should observe butterfly-type patterns, because G and Q^{-1} cannot reverse sign as σ_{00} reverses sign, and the domain structure rearrangement with variation of σ_{00} should be accompanied by hysteresis. As already mentioned, the hysteresis in the dependence of G and Q^{-1} on σ_{00} observed in our experiments was extremely weak and irregular and the butterfly pattern was effectively absent. The absence of this relation could be assigned only to the fact that the ferroelastic hysteresis loop in the dependence of strain u on stress σ is very narrow, i.e., that the coercive stress σ_c is small and, hence, the domain wall mobility is high. As already mentioned, ferroelastic hysteresis in $\varphi(\sigma)$ [or $u(\sigma)$] only after a surface layer 5 μm thick had been etched off the sample was successfully observed in [8]. This result comes somewhat as a surprise; indeed, the domain wall mobility turns out to be higher in the damaged surface layer than in the damage-free layer. This problem requires further comprehensive investigation.

Regrettably, our experiments do not permit us to determine the coercive stress σ_c and thus it can only be estimated. As follows from Fig. 6, σ_c is considerably less than 10 MPa and, judging from the resolution of the setup, does not apparently exceed 1 MPa. Using the concept of a strong stress ($\sigma > \sigma_h$), at which the strain induced by it exceeds the spontaneous strain [16], we obtain the estimate $\sigma_h = Gu_s \approx 50$ MPa. It may apparently be accepted that the thermodynamic (or intrinsic) coercive stress should be smaller by about an order of magnitude than σ_h [16], i.e., that $\sigma_c \approx 5$ MPa. This means that the experimentally obtained coercive stress $\sigma_c \leq 1$ MPa is substantially smaller than the thermody-

namic coercive stress, exactly as is the case with the coercive fields in ferroelectrics [16].

Now, we consider the information on domain dynamics that can be extracted from the data in Fig. 4.

The large domain contribution to the shear modulus and internal friction at frequencies near 10 Hz, which was observed earlier in [7] and in this work, combined with the considerably smaller high-frequency contribution, suggests that elastic vibrations interact with domain walls through a relaxation mechanism with sufficiently long relaxation times τ_d. Therefore, at high frequencies Ω, such that $\Omega\tau_d \gg 1$, the domain contribution becomes suppressed, as follows from the expressions for $\Delta G/G$ and $\Delta\alpha$ for the relaxation mechanism of damping:

$$\Delta G/G = K_d/(1+\Omega^2\tau_d^2),$$
$$\Delta\alpha = (K_d/2)\Omega^2\tau_d/(1+\Omega^2\tau_d^2), \quad (7)$$

where K_d is the effective coupling coefficient for elastic vibrations with domain walls proportional to the squared coupling coefficient g in Eq. (1).

Turning now from damping to the internal friction ($Q^{-1} = 2\alpha/\Omega$), we obtain

$$\Delta Q^{-1} = K_d\Omega\tau_d/(1+\Omega^2\tau_d^2); \quad (8)$$

whence it follows that

$$\Delta Q^{-1}/\Delta Q_m^{-1} = 2\Omega\tau_d/(1+\Omega^2\tau_d^2), \quad (9)$$

where ΔQ_m^{-1} is the maximum internal friction for $\Omega\tau_d = 1$,

$$\Delta Q_m^{-1} = K_d/2. \quad (10)$$

Equation (9) and the data in Fig. 4 now permit us to estimate the domain-wall relaxation times and their temperature dependence.

Equation (9) yields two values of the domain-wall relaxation time τ_d. One solution yields a value of τ_d that decreases with decreasing temperature, while for the other, τ_d increases with decreasing temperature. In the first case, the relaxation time scales with temperature as $\tau_d \approx 0.1/(T_a - T)$ (s) (within at least the 95–105 K interval), and in the second case, the relaxation time follows the relation $\tau_d = \tau_0\exp(U/kT)$, but with a physically meaningless value $\tau_0 \approx 10^{-22}$ s and with an activation energy for domain wall motion $U = 0.4$ eV, which is obviously too high. We come thus to $\tau_d \approx 0.1/(T_a - T)$ (s) as the choice for the temperature dependence for τ_d.

Thus, in our experiments, domain motion under the action of elastic stresses is activation-free and corresponds to viscous flow with a relaxation time inversely proportional to temperature. For such relaxation times, the change in the shear modulus G at the phase transition is suppressed at high frequencies, as follows from Eq. (7). Strong variations in G will be observed only under the condition $\Omega\tau_d \leq 1$. For example, at the temperature $T = (T_a - 1)$ K, this condition is met for frequencies $\Omega \leq 10$ s^{-1}, which agrees in order-of-magnitude with our experiment. It is at low measuring frequencies that large variations in the shear modulus were observed to occur near the phase transition (Fig. 4) We note that our data on the temperature dependence of the shear modulus G at 25 Hz correlate with the data of [7], where the measurements were performed at 10 Hz using another technique.

It is of interest to compare our results with the available data.

Peaks of 30–300 MHz ultrasound wave damping were observed earlier [6] at temperatures of 105.5–103 K slightly below the phase-transition point. The damping maximum shifted toward lower temperatures with increasing frequency. The observed damping anomalies were attributed to a relaxation mechanism of elastic wave interaction with domain walls, with the relaxation time $\tau_d = 1.6 \times 10^{-9}/(T_a - T)$ (s). Another temperature dependence of the relaxation time was established when using 25–85 MHz ultrasonic waves, with the relaxation-enhanced damping peaks lying in the temperature region of 65–85 K [17]. As the frequency increased, the damping peaks shifted toward higher temperatures, with the relaxation time varying as $\tau_d = \tau_0\exp(U/kT)$ for $\tau_0 = 1.5\times10^{-11}$ s and $U = 0.04$ eV = 464 K.

In contrast to [6], the measurements in [17] were performed on thin plates of strontium titanate $1.5 \times 10 \times 30$ mm in size with the edges aligned with the ⟨110⟩, ⟨100⟩, and ⟨110⟩ directions, respectively, and the ultrasonic waves propagating perpendicular to the plate plane, i.e., along the ⟨110⟩ 1.5-mm edge. While this sample differs strongly in size from the single-domain plate used in [18] ($0.3 \times 3 \times 7$ mm along ⟨110⟩, ⟨110⟩, and ⟨100⟩, respectively), it apparently supports a sufficiently simple domain structure compared to that obtained in samples with dimensions typically employed in ultrasound measurements [6].

Thus, at a temperature, for example, of 100 K, the domain-wall relaxation times τ_d turn out to be 3×10^{-10} [6], 1.5×10^{-9} [17], and 10^{-2} s (this work). It follows that the domain-wall relaxation times in strontium titanate can vary over a broad range extending at least from 10^{-2} to 10^{-10} s. The mechanism of domain wall motion driven by elastic strains can be both thermally activated [17] (with the domain walls breaking away from the pinning centers) and, as follows from [6] and this work, activation-free, i.e., associated with the viscous flow of domain walls.

Damping peaks associated with domains were also reported in other studies [8, 19] (which did not deal with the temperature dependence of the relaxation time τ_d).

Compare the maximum value of internal friction near the phase transition ΔQ_m^{-1} (or of the attenuation $\Delta\alpha_m$) from literature data [6, 8, 17, 19] with our present results. It was found that over a broad frequency range,

extending from 3.5 kHz [19] to 300 MHz [6], internal friction ΔQ_m^{-1} is almost independent (to within a factor two) of frequency and is approximately 2×10^{-3} (a remarkable result, considering that the above studies used different techniques and different samples). Thus, attenuation $\Delta\alpha_m$ turns out to vary in proportion to the frequency. It is such a behavior of the internal friction and attenuation that should be observed, according to Eq. (10), provided that the coupling coefficient of elastic vibrations with domain walls is the same, irrespective of whether the domain wall motion is thermally activated or viscous.

The value of ΔQ_m^{-1} obtained in this work at the frequency 25 Hz is 9×10^{-2}, which is about two orders of magnitude larger than is reported in the literature. This means that at such low frequencies, the coupling coefficient for elastic waves interacting with domain walls is substantially larger than that in the kilohertz or megahertz ranges. It also appears essential that the elastic vibrations interact with domain walls primarily in a surface layer.

Interestingly, the background attenuation α, as reported in the same publications [6, 8, 17, 19] and measured over as broad a frequency range, from 35 kHz [19] to 300 MHz [6], scales approximately as $\alpha \propto \Omega^{1.5}$ and again the attenuation measured by us exceeds by two orders of magnitude the attenuation that should be observed at this frequency if it behaves as $\alpha \propto \Omega^{1.5}$. It is known that, at frequencies above approximately 100 MHz, the attenuation of elastic waves is described by the Akhiezer mechanism with the scaling $\alpha \propto \Omega^2$ and that the attenuation of transverse waves in cubic dielectrics, measured at 1000 MHz and temperatures of 100–300 K, is more or less typically 1–10 dB/μs [20]. It is also known that as the frequency is lowered and, accordingly, the attenuation decreases strongly, the latter becomes dominated by other, zero-phonon (non-Akhiezer) processes, with the frequency dependence of the attenuation becoming progressively weaker and finally disappearing. Such zero-phonon attenuation mechanisms can be associated with the crystallite structure, dislocations, macrodefects, sample surface, etc. It is the sample surface that may play the most substantial role in our technique.

Turning now back to the anomalies in elastic properties near the phase transition, we note the absence of the internal friction (attenuation) peak (Fig. 3) governed by the relation of the elastic vibrations with the order parameter (the Landau–Khalatnikov mechanism). The Landau–Khalatnikov attenuation is also described by the relaxation equation (7), where the relaxation time has the meaning of the order-parameter relaxation time τ_q. This relaxation time depends on temperature as

$$\tau_q = C_q/(T_a - T)\ (\mathrm{s}). \qquad (11)$$

The coefficient C_q is found to be very small, $C_q \approx 10^{-11}$ s K [6] or even $C_q \approx 10^{-13}$ s K [5]. For our frequencies $\Omega \approx 10^2$ s^{-1} and for $(T_a - T) = 1$ K, we have $\Omega\tau_q = 10^{-9}$–10^{-11}. Because the coupling constant of elastic vibrations with the order parameter $K_q < 1$, the change in the internal friction through the Landau–Khalatnikov mechanism at the phase transition should constitute $\Delta Q^{-1} = K_q\Omega\tau_q \leq 10^{-9}$–$10^{-11}$, which is too small a value to be measurable.

Now, let us discuss the results presented graphically in Fig. 7. The sample to which no external torque was applied undergoes spontaneous twisting below the phase-transition point, with the twist angle φ_s increasing with decreasing temperature. If now a static shear stress σ_{00} is applied to the sample, the spontaneous twist angle increases substantially (Fig. 7). We note that for $\sigma_{00} \neq 0$, the contributions to the $\varphi(\sigma)$ dependence come not only from spontaneous twisting but also from the twisting associated with the variation of $G(T)$ and an increase in σ_{00}, which is proportional to $\sigma_{00}/G(T)$. The first contribution is, however, dominant.

Spontaneous twisting upon phase transition was observed earlier to occur in crystals of $KH_3(SeO_3)_2$, K_2ZnCl_4, KH_2PO_4, etc. (see [21] and references therein), as well as in Hg_2Cl_2 crystals [22]. The nature of this spontaneous twisting phenomenon has not been clarified.

We consider possible reasons for the spontaneous twisting. This twisting appears only in the [110] sample (Fig. 2). Retaining the sample frame introduced earlier, namely, with the *X*, *Y*, and *Z* axes lying along $[1\bar{1}0]$, [110], and [001], respectively, we come to the conclusion that such a sample will undergo spontaneous twisting if spontaneous pure shear strains u_{YZ} and u_{YX} are created in it at $T < T_a$.

Furthermore, for the sample to know the sense in which it should twist, it must possess a definite chirality. Then, the "right-handed" sample will twist to the right; the "left-handed" one, to the left. There is no such chirality in the sample symmetry groups either above or below the phase transition. This chirality may appear, in principle, in a unipolar sample with different numbers of different domains.

The spontaneous strains forming in strontium titanate along the cubic axes at the phase transition are $u^s_{xx} = u^s_{yy} = u_{1s}$ and $u^s_{zz} = u_{3s}$. Going over to the sample axes, we find spontaneous shear strains $u^s_{YX} = (1/2)(u_{3s} - u_{1s})$ and $u^s_{YX} = -(1/2)(u_{3s} - u_{1s})$ to occur in domains *1* and *2*, respectively. It would seem that such strains forming even in a unipolar sample should not bring about sample twisting because there are no u^s_{YZ} strains. Let us consider this point in more detail.

As follows from Fig. 7, the spontaneous twist angle φ_s is particularly large in the single-domain sample at

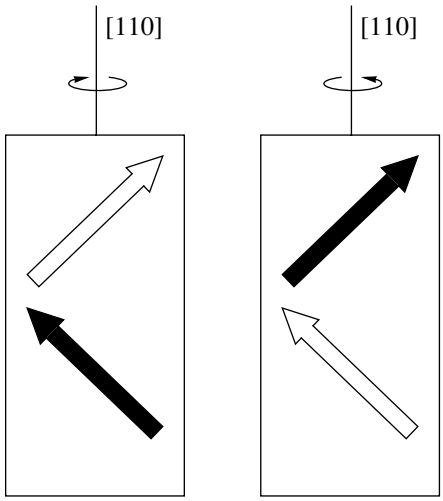

Fig. 8. Left- and right-handed samples of strontium titanate. The filled and open arrows specify the direction of the tetragonal axis *c* on the front and rear faces, respectively.

σ_{00} = 3.6 MPa (the sample is treated as single-domain in the sense specified above). In the single-domain sample, the only domain left on the front face is the favorable domain *1* with its tetragonal axis *c* making an angle of 45° with the [110] sample axis and directed to the left of this axis; the domain left on the rear face is the favorable domain *2* with its *c* axis at 45° to the right of the sample axis. A sample with such a domain structure is chiral; namely, reflection of the sample in the mirror plane reverses the sign of chirality, such that, for example, the left-handed sample becomes right-handed (Fig. 8). Can such a sample twist spontaneously? It has been shown that a spontaneous shear strain $u^s_{YX} = (1/2)(u_{3s} - u_{1s})$ forms at the front face and that the strain at the rear face has the opposite sign, $u^s_{YX} = -(1/2)(u_{3s} - u_{1s})$. As a result, the side faces tilt, as it were, in opposite directions. It is this system of spontaneous strains that apparently brings about spontaneous twisting of the sample.

For $\sigma_{00} = 0$, the sample is in a multidomain state and, for equal numbers of different domains, is no longer chiral and stops twisting. To explain the spontaneous twisting of such a sample, one has to assume that the sample is unipolar (more specifically, that the surface layers on the front and rear faces are unipolar). Such a unipolarity may be induced by internal stresses, whose field makes favorable domains dominant over unfavorable ones. If, for instance, domain *1* is dominant on the front face and domain *2* is dominant on the rear face, the situation will not differ from that in a single-domain sample, but the twist angle in the multidomain sample will be smaller (Fig. 7). In our case, the sample always twisted in the same direction and even when warmed to room temperature it did not forget the sense of the twist. This means that, in order to remove the internal stresses determining the sign of chirality and, hence, the sign of the twisting, the sample has to be annealed substantially above room temperature. We note that when the sign of the static torque M_{00} is reversed, thus reversing the sign of the static shear stress σ_{00}, the sample starts to twist in the opposite sense, which argues for the twist model proposed.

The twist angle φ_s as a function of temperature should be proportional to the spontaneous strain $u_s(T)$. Then, for the second-order phase transition, we obtain $\varphi_s \propto q_s^2 \propto (T_a - T)$. In the case of the tricritical point, $\varphi_s \propto q_s^2 \propto (T_a - T)^{1/2}$. The experimental relation plotted in Fig. 7 for $\sigma_{00} = 0$ is the best fit to the $(T_a - T)^{3/4}$ relation. Although a more accurate determination of the critical index would require a more comprehensive study, it is already possible to conclude that the improper ferroelastic phase transition in strontium titanate is a second-order transformation close to the tricritical point.

We note in conclusion that spontaneous twisting of samples at a phase transition should also occur in other proper and improper ferroelastic and ferroelectric phase transitions. For instance, in the case of the *m*3*m*–4*mm* ferroelectric phase transition ($BaTiO_3$, $PbTiO_3$), the inclusion of the electrostriction coupling gP^2u in the thermodynamic potential results obviously in the same situation as in strontium titanate. Thus, $BaTiO_3$ and $PbTiO_3$ samples cut along the ⟨110⟩ direction should twist spontaneously at the phase transition and the spontaneous twist angle in $BaTiO_3$ and $PbTiO_3$ should be considerably larger than that in $SrTiO_3$ because of the larger spontaneous strain.

ACKNOWLEDGMENTS

One of the authors (V.V.L.) is indebted to O.E. Kvyatkovskiĭ for valuable discussions.

This study was partially supported by NWO, grant no. 16-04-1999.

REFERENCES

1. K. A. Müller and H. Burkard, Phys. Rev. B **19**, 3593 (1979).
2. O. E. Kvyatkovskiĭ, Fiz. Tverd. Tela (St. Petersburg) **43** (8), 1345 (2001) [Phys. Solid State **43**, 1401 (2001)].
3. A. Yamanaka, M. Kataoka, Y. Inaba, *et al.*, Europhys. Lett. **50**, 688 (2000).
4. M. E. Lines and A. M. Glass, *Principles and Applications of Ferroelectrics and Related Materials* (Clarendon, Oxford, 1977; Mir, Moscow, 1981).
5. V. V. Lemanov, Ferroelectrics **265**, 1 (2001).
6. K. Fossheim and B. Berre, Phys. Rev. B **5**, 3292 (1972).
7. A. V. Kityk, W. Schranz, P. Sondergeld, *et al.*, Phys. Rev. B **61**, 946 (2000).
8. A. Binder and K. Knorr, Phys. Rev. B **63**, 094106 (2001).
9. S. A. Gridnev, V. I. Kudryash, and L. A. Shuvalov, Izv. Akad. Nauk SSSR, Ser. Fiz. **43** (8), 1718 (1979).

10. L. D. Landau and E. M. Lifshitz, *Course of Theoretical Physics*, Vol. 7: *Theory of Elasticity* (Nauka, Moscow, 1987; Pergamon, New York, 1986).
11. Yu. I. Sirotin and M. P. Shaskolskaya, *Fundamentals of Crystal Physics* (Nauka, Moscow, 1975; Mir, Moscow, 1982).
12. J. C. Slonczewski and H. Thomas, Phys. Rev. B **1**, 3599 (1970).
13. W. Rehwald, Solid State Commun. **8**, 1483 (1970).
14. H. Uwe and T. Sakudo, Phys. Rev. B **13**, 271 (1976).
15. G. Sorge and E. Hegenbarth, Phys. Status Solidi **33**, K79 (1969); G. Sorge, E. Hegenbarth, and G. Schmidt, Phys. Status Solidi **37**, 599 (1970).
16. L. D. Landau and E. M. Lifshitz, *Course of Theoretical Physics*, Vol. 8: *Electrodynamics of Continuous Media* (Nauka, Moscow, 1982; Pergamon, New York, 1984).
17. E. V. Balashova, V. V. Lemanov, R. Kunze, *et al.*, Ferroelectrics **183**, 75 (1996).
18. K. A. Müller, W. Berlinger, M. Capizzi, and H. Granicher, Solid State Commun. **8**, 549 (1970).
19. O. M. Nes, K. A. Müller, T. Suzuki, and F. Fossheim, Europhys. Lett. **19**, 397 (1992).
20. V. Ya. Avdonin, V. V. Lemanov, I. A. Smirnov, and V. V. Tikhonov, Fiz. Tverd. Tela (Leningrad) **14** (3), 877 (1972) [Sov. Phys. Solid State **14**, 747 (1972)].
21. S. A. Gridnev, O. N. Ivanov, L. P. Mikhaĭlova, and T. N. Davydova, Fiz. Tverd. Tela (St. Petersburg) **43** (4), 693 (2001) [Phys. Solid State **43**, 722 (2001)].
22. A. Binder, K. Knorr, and Yu. F. Markov, Phys. Rev. B **61**, 190 (2000).

Translated by G. Skrebtsov

Physics of the Solid State, Vol. 44, No. 6, 2002, pp. 1166–1170. Translated from Fizika Tverdogo Tela, Vol. 44, No. 6, 2002, pp. 1116–1120.

LOW-DIMENSIONAL SYSTEMS AND SURFACE PHYSICS

Light Magnetoabsorption in Systems with Quantum Confinement in the Field of Resonant Laser Radiation

É. P. Sinyavskiĭ and E. I. Brusenskaya

Institute of Applied Physics, Academy of Sciences of Moldova, Chisinau, MD-2028 Moldova

Received April 12, 2001; in final form, October 9, 2001

Abstract—Near-gap light magnetoabsorption is investigated in systems with quantum confinement in the presence of IR laser radiation. It is shown that if the frequency of laser radiation is equal to the cyclotron frequency, the magnetoabsorption line shape can be fully determined by the IR radiation intensity. The frequency dependence of interband absorption of a weak electromagnetic wave can be changed significantly in the case where the laser radiation frequency is equal to the quantum-confinement frequency in parabolic quantum wells and the polarization vector is parallel to the confinement axis. © *2002 MAIK "Nauka/Interperiodica".*

1. Let us consider a quantum-confined system in a quantizing magnetic field H parallel to the quantum confinement axis z. In this system, the energy of an electron (hole) in the quantum well (QW) is fully quantized. The frequency dependence of the light absorption associated with transitions between hole and electron states (in the absence of a magnetic field, this is interband absorption) is characterized by the number of peaks with half-widths determined by the interaction of carriers with lattice vibrations [1]. At the present time, perfect quantum-confined structures can be fabricated with a small quantity of lattice defects and impurities. It is this factor that determines the presence of high-mobility ($\geq 10^5$ cm^2/V s) carriers at low temperatures [2, 3] and narrow luminescence peaks (~3 meV [4]). We will consider the case of strong magnetic fields where the Coulomb electron–hole interaction is small in comparison with the distance between Landau quantization levels and exciton effects in the light absorption are negligible. A detailed discussion and the criteria of the validity of such an approximation can be found in [5]. When an electron–hole pair is excited by light, the quasi-momentum of the created exciton is equal to the momentum of the absorbed photon and, hence, is very small [6]; therefore, we can neglect the exciton bands appearing in two-dimensional systems in a strong magnetic field [7].

Significant influence of IR laser radiation of frequency ω upon low-power light absorption occurs when ω is equal to the cyclotron frequency ω_c (IR magnetic resonance). In this case, the resonant laser radiation causes the electron states to be nonstationary and, hence, can control the shape of electromagnetic-wave absorption peaks.

We will consider the resonance case of $\omega \sim \omega_c = eH/m_c c$ (where $m_{c(v)}$ is the effective electron (hole) mass); therefore, for the sake of simplicity, the interaction of the laser radiation with holes can be neglected ($\omega \neq \omega_v = eH/m_v c$). The laser radiation intensity is assumed to be low; therefore, we can neglect multiphoton transitions between fully quantized hole states and discrete electron states.

2. Under the assumption made above, the Hamiltonian of the system understudy has the form

$$H = H_0 + W,$$
$$H_0 = \sum_\alpha E_\alpha^c a_\alpha^+ a_\alpha + \sum_\alpha E_\alpha^v \tilde{a}_\alpha^+ \tilde{a}_\alpha + \hbar\omega b^+ b, \qquad (1)$$
$$W = \sum_\alpha V_{\alpha\beta} a_\alpha^+ a_\beta (b^+ + b).$$

Here, $a_\alpha^+(a_\alpha)$, $\tilde{a}_\alpha^+(\tilde{a}_\alpha)$, and $b^+(b)$ are the creation (annihilation) operators of electrons, holes, and photons, respectively; $\alpha(N, n, k_x)$ is a set of quantum numbers characterizing the state of a confined carrier in a quantizing magnetic field; N is the Landau level index; n is the quantum-well level index; and k_x is the projection of the electron quasi-momentum.

For a square QW of width a, we have

$$E_\alpha^c = \hbar\omega_c\left(N + \frac{1}{2}\right) + \varepsilon_c n^2, \quad \varepsilon_c = \frac{\hbar^2\pi^2}{2m_c a^2},$$
$$E_\alpha^v = \hbar\omega_v\left(N + \frac{1}{2}\right) + \varepsilon_v n^2, \quad \varepsilon_v = \frac{\hbar^2\pi^2}{2m_v a^2}. \qquad (2)$$

The matrix element $V_{\alpha\beta}$ of the electron–photon interaction operator between electron wave functions in the QW in a longitudinal magnetic field is

$$V_{\alpha\beta} = id\delta_{k_x, k_x'}\delta_{n, n'}(\sqrt{N}\delta_{N, N_1+1} - \sqrt{N+1}\delta_{N, N_1-1}),$$
$$d = e\hbar\left[\frac{\pi\omega_c}{V\varepsilon_0 m_c \omega}\right]^{1/2}, \qquad (3)$$

where ε_0 is the permittivity and V is the volume of the system under study.

In Eq. (3), it is assumed that the electric field of the linearly polarized laser radiation is directed along the y axis; i.e., the laser beam falls normal to the surface of the system under study.

The weak-light absorption factor $K(\Omega)$ can be expressed through the dipole-moment correlation function [8]. Within the approximations made, we can write

$$K(\Omega) = \frac{2\pi e^2 |\mathbf{P}_{cv}\mathbf{e}_0|^2}{Vm_0^2 c\sqrt{\varepsilon_0}\hbar\Omega} \times \sum_{\alpha}\int_{-\infty}^{\infty} dt \exp\{it[\Omega - (E_\alpha^v + \varepsilon_g)/\hbar]\}\langle a_\alpha(t)a_\alpha^+\rangle. \quad (4)$$

Here, $\mathbf{P}_{cv}$ is the momentum matrix element between the Bloch states, ε_g is the band width, m_0 is the mass of a free electron, $\mathbf{e}_0$ is the polarization vector of the weak electromagnetic wave, and c is the speed of light.

$$a_\alpha(t) = \exp\left\{\frac{it}{\hbar}H\right\}a_\alpha \exp\left\{-\frac{it}{\hbar}H\right\}. \quad (5)$$

Averaging in Eq. (4) is performed using the density matrix of the electron–photon system. According to Eq. (5), the operator

$$\xi_\alpha(t) = \exp\left\{\frac{it}{\hbar}E_\alpha^c\right\}a_\alpha(t) \quad (6)$$

satisfies the equation of motion

$$\dot{\xi}_{Nnk_x}(t) = \frac{d}{\hbar}\sum_{N_1}[\sqrt{N}\delta_{N,N_1+1} - \sqrt{N+1}\delta_{N,N_1-1}] \times (b\exp\{-i\omega t\} + b^+\exp\{i\omega t\}) \times \exp\{it\omega_c(N-N_1)\}\xi_{N_1nk_x}(t). \quad (7)$$

In deriving Eq. (7), we neglected the influence of carriers on the photon spectrum; i.e., we put

$$\exp\left\{\frac{it}{\hbar}H\right\}(b+b^+)\exp\left\{-\frac{it}{\hbar}H\right\} \approx b\exp\{-i\omega t\} + b^+\exp\{i\omega t\}.$$

This approximation is quite natural since all corrections to the photon spectrum are small (on the order of the inverse volume of the system under study).

For further calculations, it is convenient to introduce the operators

$$a_N = \sqrt{N+1}\,l_1^{(N)}, \quad a_N^+ = \sqrt{N}\,l_{-1}^{(N)}, \quad (8)$$

where operators $l_m^{(N)}$ are defined as

$$l_m^{(N)} f(N) = f(N+m), \quad (9)$$

with $f(N)$ being an arbitrary function of the Landau level index N.

Naturally, we have

$$l_m^{(N)} l_{-m}^{(N)} = \hat{I}, \quad (10)$$

where $\hat{I}$ is the unit operator. From Eqs. (8) and (10), it follows that $\left|a_{N_1}a_{N_2}^+\right| = \delta_{N_1N_2}$ and that the operators a_N^+ and a_N can be considered boson operators.

We will solve Eq. (7) in the resonance approximation $|\omega - \omega_c| = |\varepsilon| \ll \omega_c$. In neglecting nonresonant terms (substantiation of this approximation and the corresponding criteria can be found in [9]), Eq. (7) takes the form

$$\dot{\xi}_\alpha(t) = \frac{d}{\hbar}(a_N^+ b\exp(-i\varepsilon t) - a_N b^+\exp(i\varepsilon t))\xi_\alpha(t), \quad (11)$$

where $\varepsilon = \omega - \omega_c$ and $|\varepsilon| \ll \omega_c$.

A solution to Eq. (11) with the initial condition $\xi_\alpha(0) = a_\alpha(0)$ has the form

$$\xi_\alpha(t) = \exp\{-it\varepsilon a_N^+ a_N\} \times \exp\left\{it\left[\varepsilon a_N^+ a_N + \frac{id}{\hbar}(a_N b^+ - a_N^+ b)\right]\right\}\xi_\alpha(0). \quad (12)$$

We substitute Eq. (12) into Eq. (6) and find $a_\alpha(t)$. Thereafter, Eq. (4) for the light absorption factor is represented in the form (for nondegenerated semiconductor systems, $\langle a_\alpha a_\alpha^+\rangle = 1 - n_\alpha \approx 1$)

$$K(\Omega) = K_0\sum_{N,n}\int_{-\infty}^{\infty} dt\int_0^{2\pi} d\varphi\int_0^{\infty} rdrP(r) \times \exp\{it[\Omega - (E_\alpha^* + \varepsilon_g)/\hbar]\}\exp\{-i\varepsilon a_N^+ a_N t\} \times \exp\left\{it\left[\varepsilon a_N^+ a_N + \frac{id}{\hbar}r\{a_N e^{i\varphi} - a_N^+ e^{-i\varphi}\}\right]\right\}. \quad (13)$$

Here, the following notation is introduced:

$$K_0 = \frac{2\pi e^2 |\mathbf{P}_{cv}\mathbf{e}_0|^2}{am_0^2 c\sqrt{\varepsilon_0}\hbar\Omega R^2},$$

$$E_\alpha^* = \hbar\omega_c^*\left(N + \frac{1}{2}\right) + \frac{\pi^2\hbar^2 n^2}{2\mu a^2}, \quad \hbar\omega_c^* = \frac{\hbar eH}{\mu c},$$

$$\mu^{-1} = m_c^{-1} + m_m^{-1}, \quad R^2 = \frac{c\hbar}{eH}.$$

The averaging over the free-photon system was fulfilled in the usual way [10, 11]; in the averaged operator expression, the operator b is replaced with $z = re^{-i\varphi}$, the operator b^+ is replaced with $z^* = re^{i\varphi}$, and integration is performed with respect to d^2z over the complex plane with a weight function $P(r)$.

Using the algebra of boson operators for a_N^+ and a_N [12], we find

$$\exp\{-i\varepsilon a_N^+ a_N t\}$$

$$\times \exp\left\{it\left[\varepsilon a_N^+ a_N + \frac{id}{\hbar} r(a_N e^{i\varphi} - a_N^+ e^{-i\varphi})\right]\right\}$$

$$= \exp\{C(t)a_N^+\}\exp\{-C^*(t)a_N\}\exp\{A(t)\}; \quad (14)$$

$$C(t) = -\frac{ird}{\hbar\varepsilon}e^{-i\varphi}[\exp(it\varepsilon) - 1],$$

$$A(t) = \frac{ir^2d^2}{\hbar^2\varepsilon}\left\{t + \frac{\exp(-i\varepsilon t) - 1}{i\varepsilon}\right\}.$$

Using the definition and properties of the operators a_N^+ and a_N in Eqs. (8) and (9), one can easily show that

$$\exp(C(t)a_N^+)\exp(-C^*(t)a_N)$$

$$= \sum_{m=0}^{N}\sum_{m_1}^{\infty}\frac{(C(t))^m(-C^*(t))^{m_1}}{m!m_1!(N-m)!} \quad (15)$$

$$\times [N!(N+m-m_1)!]^{1/2} l_{m_1-m}^{(N)}.$$

For stationary laser radiation, we have

$$P(r) = \frac{1}{2\pi N_0}\delta(r - \sqrt{N_0}),$$

where N_0 is the average number of photons in the radiating mode.

Using Eq. (15), we represent Eq. (13) for the light absorption factor in the final form

$$K(\Omega) = K_0\sum_{N,n}\int_{-\infty}^{\infty} dt \exp\left\{\frac{it}{\hbar}[\hbar\Omega - (E_\alpha^* + \varepsilon_g)]\right\}$$

$$\times \exp\{i\zeta[t\varepsilon + i(1 - \exp(-i\varepsilon t))]\} \quad (16)$$

$$\times L_N\left[4\zeta\sin^2\left(\frac{\varepsilon t}{2}\right)\right],$$

$$\zeta = \frac{e^2E^2\omega_c}{8\hbar m_c\omega^2\varepsilon^2},$$

where $L_N(z)$ are Laguerre polynomials.

We note that, for a parabolic QW, the absorption factor for a weak electromagnetic wave is similar to Eq. (16), but $E_\alpha^* = \hbar\omega_c^*\left(N + \frac{1}{2}\right) + \hbar\omega_0^*\left(n + \frac{1}{2}\right)$ and, under the summation sign over n, we should introduce the factor $|V_n|^2$:

$$V_n = \frac{(\lambda_c\lambda_v)^{1/4}}{2^n n!\sqrt{\pi}}\int_{-\infty}^{\infty} dz \exp\left\{-\frac{1}{2}(\lambda_c + \lambda_v)z^2\right\}$$

$$\times H_n(\sqrt{\lambda_c}z)H_n(\sqrt{\lambda_v}z),$$

where $\lambda_i = m_i\omega_0^{(i)}/\hbar$ ($i = c, v$), $\hbar\omega_0^{(i)}$ is the spacing between QW levels of electrons (c) and holes (v), $\omega_0^* = \omega_0^{(c)} + \omega_0^{(v)}$, and $H_n(z)$ are Hermite polynomials.

In the case of exact resonance ($\varepsilon = 0$), Eq. (16) takes the form

$$K(\Omega) = K_0\sum_{N,n}\int_{-\infty}^{\infty} dt \exp\left\{\frac{it}{\hbar}[\hbar\Omega - (E_\alpha^* + \varepsilon_g)]\right\}$$

$$\times \exp\left\{-\frac{\gamma t^2}{2}L_N[\gamma t^2]\right\}, \quad \gamma = \frac{e^2E^2}{8m_c\hbar\omega}. \quad (17)$$

From Eq. (17), it immediately follows that in the field of resonant laser radiation ($\omega_c = \omega$), damping of the Gaussian type $\left[\text{proportional to the factor } \exp\left(-\frac{\gamma t^2}{2}\right)\right]$ takes place; i.e., the laser radiation produces nonstationary electron states.

By integrating over t in Eq. (17), one gets

$$K(\Omega) = K_0\sqrt{\frac{2\pi}{\gamma}}\sum_{N,n}\frac{1}{2^n n!}H_n^2\left[\frac{q_{nN}}{\sqrt{2\gamma}}\right]\exp\left\{-\frac{q_{nN}^2}{2\gamma}\right\}, \quad (18)$$

$$q_{nN} = \frac{\hbar\Omega - \varepsilon_g - E_\alpha^*}{\hbar}.$$

Therefore, the frequency dependence of the light absorption due to electron transitions from the lowest hole state ($N = 0$, $n = 0$) to the electron state ($N = 0$, $n = 0$) has a Gaussian profile with half-width $\Delta = 2\hbar\sqrt{2\gamma\ln 2}$. When the intensity of the resonance laser radiation increases, the heights of absorption peaks decrease and their half-widths increase (Fig. 1). If the transition occurs from the hole state ($N = 1$, $n = 0$), the magnetoabsorption peak splits into two (Fig. 2), with the amount of splitting δ being $2\hbar\sqrt{2\gamma}$. For a transition from the hole state N to the Nth Landau level of electrons, the absorption peak splits into $N + 1$ peaks. This splitting corresponds to different quantum numbers for the angular momentum of electron states in the magnetic field.

The absorption line shape of quantum-confined systems in a longitudinal magnetic field is determined by multiphonon processes [1]. The half-width of the magnetoabsorption line Δ_0 associated with the interaction of carriers with acoustic lattice vibration modes is

$$\Delta_0 = 2\sqrt{k_0 T a_0 \ln 2}, \quad a_0 = \frac{3(E_c^2 + E_v^2) m_c \omega_c}{\hbar \pi \rho v^2 a},$$

where $E_c(E_v)$ is the deformation potential constant for an electron (hole), ρ is the density of QWs of width a, v is the velocity of sound in the crystal, and T is the temperature.

The resonance laser radiation electric field E_{cr} for which the absorption line half-width determined by IR radiation is equal to the line half-width due to the interaction of carriers with long-wavelength acoustic phonons ($\Delta = \Delta_0$) can be found to be

$$E_{cr}^2 = \frac{4 m_c \omega a_0 k_0 T}{\hbar e^2}.$$

For typical parameters of a GaAs–AlGaAs square QW ($E_c = 9$ eV, $E_v = 7$ eV, $\rho = 5.4$ g/cm^3, $v = 2 \times 10^5$ cm/s, $m_c = 0.06 m_0$) and $\hbar\omega_c = 10^{-2}$ eV, $T = 10$ K, and $a = 50$ Å, we have $E_{cr} = 10^3$ V/cm. For a parabolic QW with the above parameters and $a = 1000$ Å, we have $E_{cr} = 4 \times 10^2$ V/cm.

3. Let us consider a parabolic QW and let the electric field of the laser radiation be directed along the confinement axis. For this configuration, the matrix element of the electron–photon interaction operator is

$$V_{\alpha\beta} = i d_0 \delta_{k_x, k_{x_1}} \delta_{k_y, k_{y_1}} (\sqrt{n}\,\delta_{n, n_1 + 1} - \sqrt{n+1}\,\delta_{n, n_1 - 1}),$$

where

$$d_0 = e\hbar \left[\frac{\pi \omega_1}{V \varepsilon_0 m_c \omega}\right] 1/2,$$

$\alpha(n, k_x, k_y)$ are quantum numbers of an electron in a parabolic QW, n is the QW level index, k_x and k_y are the electron wave vector projections, and $\hbar\omega_1$ is the spacing between the QW levels.

A calculation of the light absorption induced by transitions from the valence band to the conduction band is made in the same way as above. As a result, in the case of exact resonance ($\omega = \omega_1$), one gets

$$K(\Omega) = \frac{2\mu e^2 |\mathbf{P}_{cv} \mathbf{e}_0|^2}{a m_0^2 c \sqrt{\varepsilon_0} \hbar^2 \Omega} \sum_n |V_n|^2 F(\delta_n, b),$$

$$F(\delta_n, b) = \frac{\pi}{2} + \int_0^\infty dt \frac{\sin(\delta_n t)}{t} \exp\left\{-t - \frac{bt^2}{2}\right\} L_n(bt^2), \tag{19}$$

$$\delta_n = \frac{\hbar\Omega - \tilde{E}_g - n\hbar\omega_0}{\hbar\gamma_0}, \quad b = \frac{\gamma}{\gamma_0^2},$$

$$\hbar\omega_0 = \hbar\omega_1 + \hbar\omega_2, \quad \tilde{E}_g = \varepsilon_g + \frac{\hbar\omega_0}{2},$$

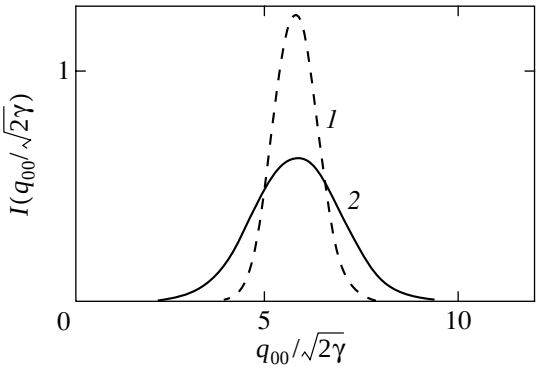

Fig. 1. Frequency dependence of the first magnetoabsorption peak (in relative units). Curves *1* and *2* are drawn for $E = 1500$ and 3000 V/cm, respectively.

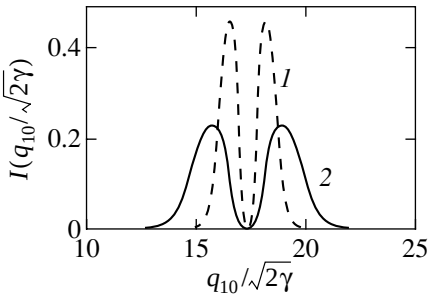

Fig. 2. Frequency dependence of the second magnetoabsorption peak (in relative units). Curves *1* and *2* are drawn for $E = 1500$ and 3000 V/cm, respectively.

where γ_0 is the electron-phonon scattering probability per unit time in the conduction band and $\hbar\omega_2$ is the spacing of the QW levels in the valence band.

In the case of scattering on acoustic phonons in the elastic-scattering approximation, it is easy to show that

$$\hbar\gamma_0 = \frac{k_0 T E_1^2 m_c}{\hbar^2 \rho v^2} \left[\frac{\lambda_c}{2\pi}\right]^{1/2} \quad \left(\lambda_c = \frac{m_c \omega_1}{\hbar}\right). \tag{20}$$

We note that for the typical parabolic-QW parameters at $T = 10$ K and $\hbar\omega = \hbar\omega_1 = 0.01$ eV, we have $b = 1$ if the laser radiation electric field is $E_{cr} = 3.7 \times 10$ V/cm. Therefore, if the laser radiation electric field is such that $E \gg E_{cr}$ ($b \gg 1$), the frequency dependence of the interband light absorption is fully determined by IR laser radiation:

$$F(\delta_n, b) = \frac{\pi}{2} + \int_0^\infty dx \frac{\sin(q_n x)}{x} \exp\left\{-\frac{x^2}{2}\right\} L_n(x^2)$$

$$(b \gg 1), \tag{21}$$

$$q_n = \frac{\Lambda_n}{\hbar\sqrt{2\gamma}}, \quad \Delta_n = \hbar\Omega - \tilde{E}_g - n\hbar\omega_0.$$

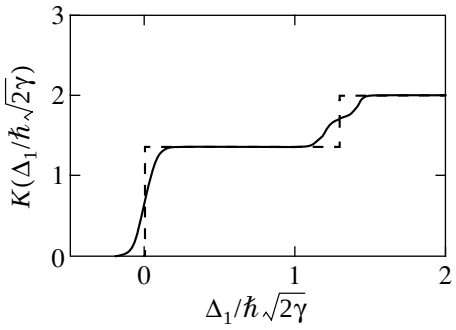

Fig. 3. Frequency dependence of the interband light absorption factor (in relative units) for a parabolic QW under resonant IR laser radiation. The dashed line corresponds to the case where there is no laser radiation.

At a given n, the integral over x in Eq. (21) can be exactly calculated to give

$$F(\delta_0, b) = \frac{\pi}{2}\left[1 + \Phi\left(\frac{\Delta_0}{\hbar\sqrt{2\gamma}}\right)\right], \quad n = 0,$$

$$F(\delta_1, b) = \frac{\pi}{2}\left[1 + \Phi\left(\frac{\Delta_1}{\hbar\sqrt{2\gamma}}\right)\right] \qquad (22)$$

$$- q_1\sqrt{\frac{\pi}{2}}\exp\left\{-\frac{q_1^2}{2}\right\}, \quad n = 1,$$

where $\Phi(z)$ is the probability function.

Figure 3 shows the frequency dependence of $K(\Omega)$ (in relative units) calculated from Eqs. (19) and (22). The dashed line represents the frequency dependence of interband light absorption in the absence of resonant laser radiation; this dependence has a typical stepwise shape [13, 14].

In conclusion, we note that for a chaotic laser radiation for which

$$P(r) = \frac{1}{\pi N_0}\exp\left\{-\frac{r^2}{N_0}\right\},$$

the features of the interband absorption of a weak electromagnetic wave specified above remain the same. For instance, according to Eq. (13), $K(\Omega)$ for chaotic laser radiation takes the form

$$K(\Omega) = K_0\sum_{N,n} 2\sqrt{\frac{2}{\gamma}}\int_0^\infty d\tau \frac{\cos\left(q_{Nn}\sqrt{\frac{2}{\gamma}}\tau\right)(1-\tau^2)^N}{(1+\tau^2)^{N+1}}. \quad (23)$$

At $N = 0$ (transitions to the zero Landau level), we have

$$K(\Omega) = K_0\pi\sqrt{\frac{2}{\gamma}}\sum_n \exp\left\{-|q_{0n}|\sqrt{\frac{2}{\gamma}}\right\}; \qquad (24)$$

at N =1,

$$K(\Omega) = K_0\pi\frac{2}{\gamma}\sum_n |q_{1n}|\exp\left\{-|q_{1n}|\sqrt{\frac{2}{\gamma}}\right\}. \qquad (25)$$

As immediately follows from Eqs. (24) and (25), the half-width of the first magnetoabsorption peak is $\Delta = \hbar\sqrt{2\gamma\ln 2}$ and the second peak splits into two peaks, with the distance between them being $\delta = \hbar\sqrt{2\gamma}$. We note that in this case, Δ and δ are two times smaller than in the case of stationary laser radiation.

REFERENCES

1. É. P. Sinyavskiĭ and E. I. Grebenshchikova, Zh. Éksp. Teor. Fiz. **116** (6), 2069 (1999) [JETP **89**, 1120 (1999)].
2. M. Shayegan, T. Sajoto, M. Santos, and C. Silvestre, Appl. Phys. Lett. **53** (9), 791 (1988).
3. T. Sajoto, M. Santos, and M. Shayegan, Appl. Phys. Lett. **55** (14), 1430 (1989).
4. H. Buhmann, W. Joss, K. V. Klitzing, *et al.*, Phys. Rev. Lett. **66** (7), 926 (1991).
5. W. Edelstem, H. N. Spector, and R. Marasas, Phys. Rev. B **39** (11), 7697 (1989).
6. R. J. Elliot and R. London, Phys. Chem. Solids **15** (1), 196 (1960).
7. I. V. Lerner and Yu. E. Lozovik, Zh. Éksp. Teor. Fiz. **78** (3), 1167 (1980) [Sov. Phys. JETP **51**, 588 (1980)].
8. R. Kubo, J. Phys. Soc. Jpn. **12** (6), 570 (1957).
9. E. Yu. Perlin and V. A. Kovarskiĭ, Fiz. Tverd. Tela (Leningrad) **12** (11), 3105 (1970) [Sov. Phys. Solid State **12**, 2512 (1970)].
10. R. J. Glauber, in *Quantum Optics and Electronics (Les Houches Summer School Lectures)* (Gordon and Breach, New York, 1965; Mir, Moscow, 1967).
11. J. R. Klauder and E. C. G. Sudarshan, *Fundamentals of Quantum Optics* (Benjamin, New York, 1968; Mir, Moscow, 1970).
12. W. H. Louisell, *Radiation and Noise in Quantum Electronics* (McGraw-Hill, New York. 1964; Nauka, Moscow, 1972).
13. D. A. Miller, D. S. Chemla, and S. Schmitt-Rink, Phys. Rev. B **33** (10), 6976 (1986).
14. D. A. Miller, J. S. Weiner, and D. S. Chemla, IEEE J. Quantum Electron. **22** (9), 1815 (1986).

Translated by D. Bayuk

Physics of the Solid State, Vol. 44, No. 6, 2002, pp. 1171–1175. Translated from Fizika Tverdogo Tela, Vol. 44, No. 6, 2002, pp. 1121–1125.

LOW-DIMENSIONAL SYSTEMS AND SURFACE PHYSICS

The Temperature Dependence of Eu Atom Yield Resonances in Electron-Stimulated Desorption from Oxidized Tungsten

V. N. Ageev and Yu. A. Kuznetsov

Ioffe Physicotechnical Institute, Russian Academy of Sciences, ul. Politekhnicheskaya 26, St. Petersburg, 194021 Russia
e-mail: kuznets@ms.ioffe.rssi.ru

Received August 22, 2001

Abstract—This paper reports on the first measurement of the intensity of the resonances in the yield of europium neutrals as a function of temperature observed in electron-stimulated desorption from tungsten surfaces oxidized to different degrees and having different europium coverages. The measurements were carried out by the time-of-flight method with a surface ionization detector. The temperature dependences obtained for resonances due to europium and tungsten core level ionization differ qualitatively. The relation is reversible for temperatures below the onset of europium thermal desorption. *© 2002 MAIK "Nauka/Interperiodica".*

1. INTRODUCTION

Electron-stimulated desorption (ESD) is widely employed in the analysis and modification of adsorbed layers. However, reliable measurements of the fluxes of neutrals produced in ESD are lacking, and this hampers the development of elaborated models of the process involved [1].

We measured the yield and energy distributions of alkali metal atoms emitted in ESD from layers of these metals adsorbed on the surface of oxidized tungsten [2] and molybdenum [3], as well as the yield and energy distribution of barium [4] and the yield of europium [5] atoms observed in the ESD from layers adsorbed on oxidized tungsten. It was found that the mechanism of neutral ESD depends substantially on the structure of the atomic valence shells; in particular, the dependence of the Eu ESD yield from europium layers adsorbed on oxidized tungsten on the incident electron energy has a resonance character, with the electron energies corresponding to the resonance peaks that correlate with the europium 5*p* and 5*s* and tungsten $5p_{3/2}$, $5p_{1/2}$, and 5*s* core-level excitation energies [6].

This paper reports on a study of the temperature dependence of the resonances in the Eu ESD yield from oxidized tungsten.

2. EXPERIMENTAL TECHNIQUE

The instrumentation used and the technique employed in sample preparation for measurements were described in detail in [7]. The measurements were performed in a high-vacuum chamber at a base pressure of less than 5×10^{-10} Torr. The targets were textured tungsten ribbons with preferential (100) orientation measuring $70 \times 2 \times 0.01$ mm. The ribbons were cleaned of carbon by heating in an oxygen environment at a pressure of 1×10^{-6} Torr and a temperature $T = 1800$ K for 3 h. The ribbon cleanness was checked by Auger electron spectroscopy. The oxygen monolayer was prepared by exposing a ribbon heated to $T = 1600$ K to oxygen at a pressure of 1×10^{-6} Torr for 300 s. The tungsten oxide film was grown on a ribbon heated to $T = 1100$ K at an oxygen pressure of 1×10^{-6} Torr for 600 s [8].

The europium was deposited on a ribbon at $T = 300$ K from a direct-heated evaporator made of a tantalum tube into which metallic europium was placed. The tube was equipped with several holes for uniform europium deposition along the ribbon. The concentration of deposited europium was determined by thermodesorption spectroscopy and monitored by the surface ionization current from the heated ribbon. The monolayer europium coverage was identified with the maximum ESD yield of Eu atoms after the tungsten 5*p* and 5*s* core-level excitation [6]. One europium monolayer (ML) on a tungsten surface coated by an oxygen monolayer corresponds to a europium concentration of 7.5×10^{14} atoms/cm^2, and one europium monolayer on a tungsten oxide surface corresponds to a europium concentration of 1×10^{15} atoms/cm^2.

The temperature of the ribbon was lowered by passing gaseous nitrogen, which was precooled in a coiled copper tube immersed in liquid nitrogen, through its hollow fixtures. The ribbon temperature could be varied from 160 to 300 K by properly controlling the nitrogen flow. The temperature was derived from the temperature dependence of the ribbon electrical resistance, which was found by placing the ribbon into a cooler maintained at a known temperature.

The ribbon was heated by passing an electric current though it. In this case, its temperature was also inferred from the temperature dependence of the electrical resistance, which was calculated by linear extrapolation of

1063-7834/02/4406-1171$22.00

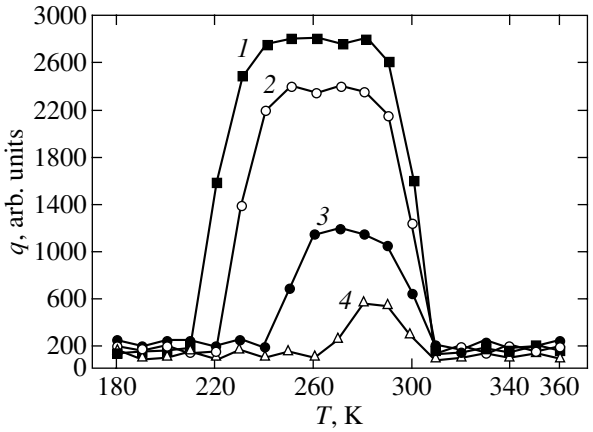

Fig. 1. Eu ESD yield q vs. substrate temperature plots measured at an incident electron energy E_e = 32 eV for different europium coverages Θ of tungsten coated by an oxygen monolayer. Θ: (*1*) 0.05, (*2*) 0.07, (*3*) 0.18, and (*4*) 0.25.

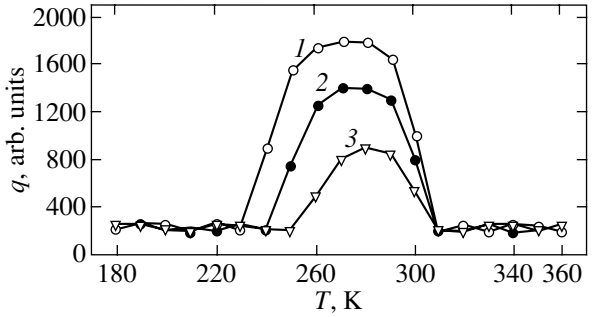

Fig. 2. Eu ESD yield q vs. substrate temperature plots measured at an incident electron energy E_e = 32 eV for different europium coverages Θ of tungsten coated by an oxide film. Θ: (*1*) 0.05, (*2*) 0.15, and (*3*) 0.25.

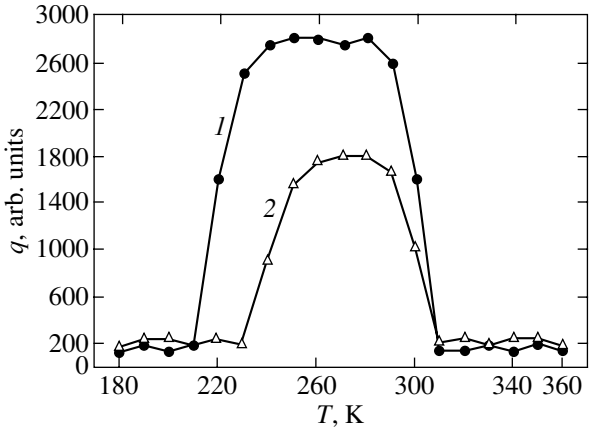

Fig. 3. Eu ESD yield q vs. substrate temperature plots measured at an incident electron energy E_e = 32 eV for a europium coverage Θ = 0.05 of tungsten coated by (*1*) an oxygen monolayer and (*2*) an oxide film.

the relation from the pyrometric region to room temperature.

The ribbon was irradiated by electrons of energies E_e = 0–300 eV in stationary conditions at an electron current density of 5×10^{-6} A/cm^2; this a regime did not produce noticeable ribbon overheating. The desorbing Eu atoms were ionized in a surface ionization detector in which a tungsten ribbon heated to T = 2000 K served as the ion emitter. The ion current was measured in the particle counting mode.

3. RESULTS

The temperature dependences of the Eu ESD yield from an oxidized tungsten surface coated by an adsorbed europium film are governed by the energy E_e of the electrons striking the surface, the surface coverage by europium Θ, and the degree of tungsten surface oxidation.

Figure 1 displays the ESD yield q of Eu atoms from a tungsten surface coated by an oxygen monolayer plotted vs. the substrate temperature for four values of the europium coverage and an incident electron energy E_e = 32 eV. As the substrate temperature is increased, the yield q is seen to pass through a broad maximum which decreases with increasing europium coverage and shifts toward higher temperatures. The europium appearance threshold temperature increases with Θ, while the temperature at which the Eu ESD stops is virtually independent of the europium coverage.

Figure 2 shows similar plots obtained for the ESD of Eu neutrals from a tungsten oxide surface coated by europium to various coverages. These curves resemble the temperature dependence of the Eu yield from the tungsten surface coated by an oxygen monolayer. However, at low europium coverages, Eu atoms start to desorb at substantially higher temperatures. This effect is illustrated by the curves in Fig. 3, which were obtained at Θ = 0.05 and an incident electron energy E_e = 32 eV for a tungsten surface coated by an oxygen monolayer (curve *1*) and by a tungsten oxide film (curve *2*). These graphs provide supportive evidence for the Eu ESD disappearance temperature being independent of the extent of tungsten oxidation at E_e = 32 eV.

Figure 4 presents, in graphical form, the EuO molecule ESD yield vs. substrate temperature plot for a europium layer adsorbed on a tungsten surface coated by an oxygen monolayer and obtained at Θ = 0.70 and E_e = 50 and 80 eV. The EuO yield grows slowly with temperature within the temperature interval T = 180–460 K, after which it drops to zero at T = 500 K, with the ESD disappearance temperature being independent of the incident electron energy.

Figure 5 displays similar curves for the ESD of EuO molecules from an adsorbed europium layer on a tungsten surface coated by an oxygen monolayer obtained with electrons of energy E_e = 50 eV for several values of the europium coverage. The curves are similar in

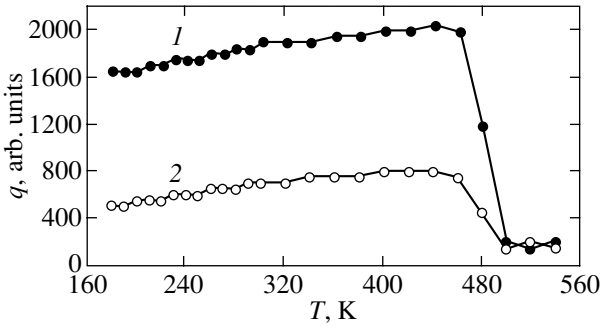

Fig. 4. EuO ESD yield q vs. substrate temperature plots measured at incident electron energies E_e of (*1*) 50 and (*2*) 80 eV for a europium coverage $\Theta = 0.70$ of tungsten coated by an oxygen monolayer.

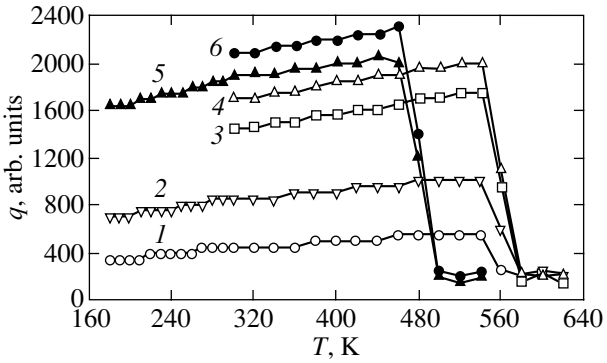

Fig. 5. EuO ESD yield q vs. substrate temperature plots measured at an incident electron energy $E_e = 50$ eV for different europium coverages Θ of tungsten coated by an oxygen monolayer. Θ: (*1*) 0.18, (*2*) 0.35, (*3*) 0.53, (*4*) 0.63, (*5*) 0.70, and (*6*) 0.85.

shape to the relations presented in Fig. 4. However, the temperature at which the EuO yield begins to decrease changes abruptly with increasing europium coverage Θ. For $\Theta > 0.60$, the EuO ESD disappearance temperature is 500 K, while for $\Theta < 0.60$, it increases to 580 K. We note that, at temperatures below the point at which the EuO yield starts to decrease, the yield grows almost in proportion to the europium coverage, which agrees with the relations plotted in Fig. 3 in [9]. For electron energies $E_e = 80$ eV, the EuO disappearance temperature also drops in a jump from 570 to 500 K within the europium coverage interval of 0.60 to 0.70 (Fig. 6). The ESD disappearance temperature of EuO molecules increases from 500 to 560 K as one crosses over from tungsten coated by an oxygen monolayer to a tungsten oxide film for a europium coverage $\Theta = 0.70$ and an electron energy $E_e = 50$ eV (Fig. 7). Moreover, the EuO ESD disappearance temperature for a tungsten oxide film decreases smoothly with the europium coverage increasing to one monolayer.

It should be pointed out that all the relations describing the ESD yield of Eu atoms and EuO molecules are reversible within the temperature variation region where these particles are detected; in other words, europium thermodesorption in this region can be neglected.

Figure 8 plots the Eu ESD yield q for $E_e = 32$ eV vs. europium coverage of a tungsten ribbon with an oxygen monolayer (curve *1*), with an oxygen monolayer overlaid by a 0.05 barium monolayer (curve *2*), and with an oxide film (curve *3*) for $T = 300$ K. We readily see that the yield q of Eu neutrals from an oxygen monolayer-coated ribbon becomes noticeable only after the deposition of 0.03 ML europium and reaches a maximum at 0.05 ML europium, after which it decreases with increasing europium coverage, to disappear altogether for $\Theta > 0.35$. In the case of the ribbon coated by an oxide film or an oxygen monolayer with 0.05 ML barium, no appearance threshold was observed in the dependence of q on the deposited europium concentration and the yield reached a maximum for $\Theta = 0.03$. The Eu yield from the ribbon coated by an oxygen monolayer with 0.05 ML barium decreases with increasing Θ almost in the same way as for a ribbon coated by an oxygen monolayer, while for the oxide-coated ribbon, the yield q falls off more slowly with increasing Θ, to disappear for $\Theta = 0.40$.

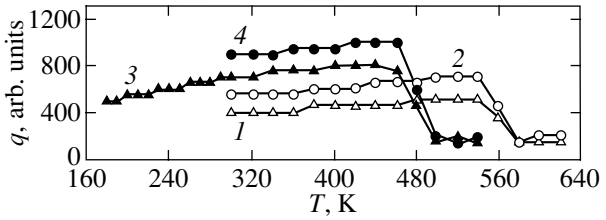

Fig. 6. EuO ESD yield q vs. substrate temperature plots measured at an incident electron energy $E_e = 80$ eV for different europium coverages Θ of tungsten coated by an oxygen monolayer. Θ: (*1*) 0.53, (*2*) 0.63, (*3*) 0.70, and (*4*) 0.85.

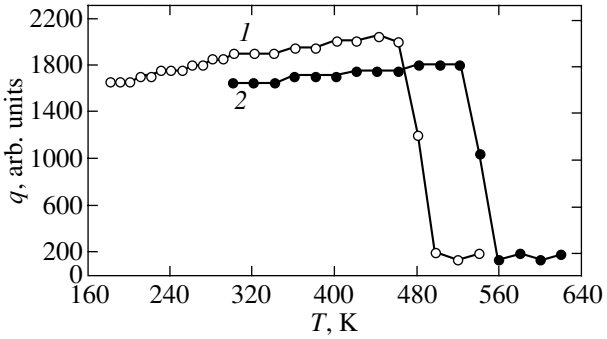

Fig. 7. EuO ESD yield q vs. substrate temperature plots measured at an incident electron energy $E_e = 50$ eV for a europium coverage $\Theta = 0.70$ of tungsten coated by (*1*) an oxygen monolayer and (*2*) an oxide film.

4. DISCUSSION OF RESULTS

Europium adsorbed on oxidized tungsten lowers the work function of the surface and, hence, resides partially in ionic form [10]. As established by Auger electron spectroscopy and thermodesorption measurements, europium is distributed uniformly over the surface of oxidized tungsten even at below monolayer coverages, while at above monolayer coverages, it forms three-dimensional islands even at $T = 300$ K [11]. The temperature dependence of the Eu yield from a europium layer adsorbed on oxidized tungsten can apparently be interpreted in terms of the model proposed by us earlier [5, 9]. According to this model, excitation of the europium 5*p* and 5*s* core levels is accompanied by the formation of core excitons, which decay partially with the formation of Eu^{2+} ions. These ions start to move toward the surface as a result of the increasing image potential and of the decreasing repulsion forces which appear when the electronic shells of the europium and oxygen ions touch [12]. The Eu^{2+} ions become neutralized by the conduction band electrons if the energy of the core holes of the ions moving toward the surface drops below the substrate Fermi level [13]. The electron density in the conduction band increases with temperature as the electrons leave the donor levels formed in europium adsorption, and, accordingly, the probability of europium ion neutralization also increases. Estimation of the activation energy of this process yields ~0.8 eV, a figure substantially less than the band gap width of the WO_3 oxide, which is about 3.0 eV [14]. The probability of Eu^{2+} neutralization decreases as one goes over from a substrate coated by an oxygen monolayer to that with an oxide film, which may be associated with the increase in the potential barrier for electrons tunneling from the substrate to the Eu^{2+} ions. This conclusion is supported by the increase in the temperature of Eu ESD appearance from a substrate coated by an oxide film compared to that for a substrate with an oxygen monolayer for the same europium coverages.

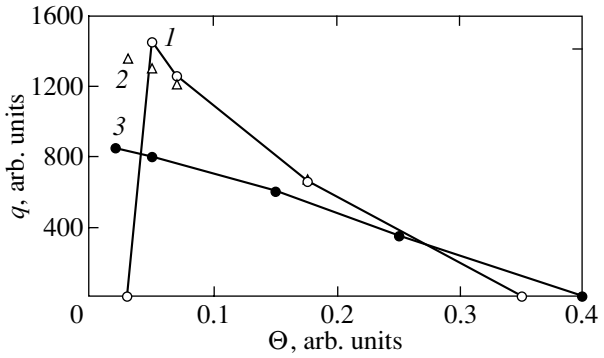

Fig. 8. Eu ESD yield q vs. Eu coverage Θ plots measured at an incident electron energy $E_e = 32$ eV at temperature $T = 300$ K for (*1*) tungsten coated by an oxygen monolayer, (*2*) tungsten coated by an oxygen monolayer and a 0.05-ML Ba^+ film deposited after europium adsorption, and (*3*) tungsten coated by an oxide film.

The increase in the substrate temperature entails an increase in the exciton hole and electron recombination rate [15], which brings about a decrease in the Eu^{2+} ion flux to the surface and, accordingly, in the flux of Eu neutrals reflected from the surface. We note that the yield disappearance temperature of the Eu atoms associated with excitation of the europium core levels does not depend on the concentration of deposited europium and the substrate oxidation. It is apparently determined by the properties of the europium core exciton only.

The Eu atoms passing through the film of adsorbed europium ions undergo resonance charge exchange, whose probability grows with decreasing distance between the Eu atoms and the adsorbed Eu^{2+} ions. Accordingly, the yield of Eu atoms decreases with increasing europium coverage.

The emergence of neutrals at electron energies corresponding to the tungsten core-level excitation can be interpreted as desorption of EuO molecules. At least, the surface ionization method does not discriminate the desorption of the latter from that of Eu atoms [9]. Moreover, it is hard to conceive how excitation could be transferred from a tungsten core level through oxygen to initiate desorption of Eu atoms. The formation of the localized tungsten core exciton breaks the bond between the tungsten and oxygen and favors EuO desorption. The yield of EuO molecules grows sublinearly with the substrate temperature increasing to $T \sim 460$ K; this is apparently caused by the increase with temperature in the amplitude of tungsten ion vibrations, which produce additional repulsion of the EuO molecules [16]. For $T > 470$ K, the tungsten core exciton begins to break up, thus giving rise to a sharp decrease in the Eu yield. The exciton breakup temperature depends on the nature of both the exciton and the surrounding host matrix [15]; therefore, there is nothing strange in that the yield of Eu atoms and the yield of EuO molecules start to decrease at different temperatures (Figs. 1, 4).

The abrupt decrease in the ESD yield disappearance temperature of EuO molecules from an oxygen monolayer with the europium coverage increasing from 0.60 to 0.70 and the smooth falloff of this temperature with increasing europium coverage on the tungsten oxide film are accounted for by the different patterns of lateral interaction between the europium particles adsorbed on these surfaces. This conclusion is supported by the fact that one europium monolayer on these surfaces corresponds to different europium concentrations.

The existence of a concentration threshold of Eu ESD appearance from a tungsten surface coated by an oxygen monolayer (Fig. 8) suggests that this surface has a limited number of sites on which europium can adsorb to $\Theta < 0.03$ and from which the Eu ESD yield is negligible. Ba^+ ions adsorb by substituting for europium at these sites, and the concentration threshold of Eu ESD appearance vanishes. The oxide-coated

tungsten surface does not have sites with low Eu yield. These sites are probably associated with direct contact between the Eu and tungsten atoms, where the electronic excitations of Eu^{2+} ions relax before the latter reach the surface.

Thus, we have presented the first measurement of the temperature dependence of the ESD yield from a europium adatom layer on the surface of oxidized tungsten. This dependence is reversible in temperature. The yield of Eu atoms and EuO molecules passes through a maximum as the temperature increases and drops to zero at 310 and 500 K, respectively, which is associated with different thermal stability of the europium and tungsten core excitons.

ACKNOWLEDGMENTS

This study was partially supported by the Russian Foundation for Basic Research (project no. 99-02-17972) and the State Program of the RF "Surface Atomic Structures" (grant no. 4.5.99).

REFERENCES

1. V. N. Ageev, Prog. Surf. Sci. **47** (1–2), 55 (1994).
2. V. N. Ageev, Yu. A. Kuznetsov, and N. D. Potekhina, Fiz. Tverd. Tela (St. Petersburg) **38** (2), 609 (1996) [Phys. Solid State **38**, 335 (1996)].
3. V. N. Ageev and Yu. A. Kuznetsov, Phys. Low-Dimens. Struct. **1/2**, 113 (1999).
4. V. N. Ageev, Yu. A. Kuznetsov, and N. D. Potekhina, Surf. Sci. **367**, 113 (1996).
5. V. N. Ageev and Yu. A. Kuznetsov, Pis'ma Zh. Tekh. Fiz. **26** (13), 86 (2000) [Tech. Phys. Lett. **26**, 579 (2000)].
6. V. N. Ageev, Yu. A. Kuznetsov, and T. E. Madey, J. Vac. Sci. Technol. A **19** (4), 1481 (2001).
7. V. N. Ageev, O. P. Burmistrova, and Yu. A. Kuznetsov, Fiz. Tverd. Tela (Leningrad) **29** (6), 1740 (1987) [Sov. Phys. Solid State **29**, 1000 (1987)].
8. V. N. Ageev and N. I. Ionov, Fiz. Tverd. Tela (Leningrad) **11**, 3200 (1969) [Sov. Phys. Solid State **11**, 2593 (1970)].
9. V. N. Ageev, Yu. A. Kuznetsov, and N. D. Potekhina, Fiz. Tverd. Tela (St. Petersburg) **43** (10), 1894 (2001) [Phys. Solid State **43**, 1972 (2001)].
10. S. Yu. Davydov, Pis'ma Zh. Tekh. Fiz. **27** (7), 68 (2001) [Tech. Phys. Lett. **27**, 295 (2001)].
11. V. N. Ageev and A. Yu. Afanas'eva, Fiz. Tverd. Tela (St. Petersburg) **43** (4), 739 (2001) [Phys. Solid State **43**, 772 (2001)].
12. P. R. Antoniewicz, Phys. Rev. B **21** (9), 3811 (1980).
13. A. G. Borisov and J. P. Ganyacq, Surf. Sci. **445**, 430 (2000).
14. C. G. Granqvist, *Handbook of Inorganic Electrochromic Materials* (Elsevier, Amsterdam, 1995).
15. Ch. B. Lushchik and A. Ch. Lushchik, *Decay of Electron Excitations with Defect Formation in Solids* (Nauka, Moscow, 1989), p. 183.
16. V. F. Kuleshov, Yu. A. Kukharenko, S. A. Fridrikhov, V. I. Zaporzhchenko, V. I. Rakhovskiĭ, A. G. Naumovets, and A. E. Gorodetskiĭ, *Spectroscopy and Diffraction of Electrons when Used to Study Solid Surfaces* (Nauka, Moscow, 1985), p. 211.

Translated by G. Skrebtsov

Physics of the Solid State, Vol. 44, No. 6, 2002, pp. 1176–1180. Translated from Fizika Tverdogo Tela, Vol. 44, No. 6, 2002, pp. 1126–1130.

LOW-DIMENSIONAL SYSTEMS AND SURFACE PHYSICS

Reactive Epitaxy of Cobalt Disilicide on Si(100)

M. V. Gomoyunova, I. I. Pronin, D. A. Valdaĭtsev, and N. S. Faradzhev

Ioffe Physicotechnical Institute, Russian Academy of Sciences, ul. Politekhnicheskaya 26, St. Petersburg, 194021 Russia

Received September 13, 2001

Abstract—The growth of cobalt disilicide on the Si(100) surface by reactive epitaxy at $T = 350$°C was studied within the 10–40 ML cobalt coverage range. A new method of mapping the atomic structure of the surface layer by inelastically scattered medium-energy electrons was employed. The films thus formed were shown to consist of $CoSi_2$(221) grains of four azimuthal orientations turned by 90° with respect to one another. This domain structure originates from substrate surface faceting by (111) planes, a process occurring during silicide formation. *B*-oriented $CoSi_2$(111) layers grow epitaxially on (111) facets. © *2002 MAIK "Nauka/Interperiodica"*.

1. INTRODUCTION

Thin cobalt disilicide films grown on the surface of silicon single crystals enjoy broad application in solid-state microelectronics for the production of atomically sharp metal/semiconductor interfaces and are particularly promising for use in ultralarge-scale integration purposes. The formation of $CoSi_2$/Si contacts is presently best studied for the Si(111) surface. At the same time, of prime interest for silicon technology is the Si(100) face. However, the formation of a phase boundary in this system is a substantially more complex problem and recent publications have even reported on self-organization of the cobalt disilicide clusters, thus opening the possibility of using not only planar $CoSi_2$/Si(100) contacts but also $CoSi_2$ quantum dot systems [1, 2].

Numerous studies have demonstrated that the properties of cobalt disilicide films grown on Si(100) are very sensitive both to the initial state of the substrate and to the silicide formation regime [1–9]. In the conditions favoring growth of epitaxial $CoSi_2$(111) layers on Si(111), one observes the growth on this surface of cobalt disilicide grains oriented differently relative to the substrate [3, 9–13]. To overcome the difficulties associated with the problem of nucleation, the techniques based on the use of the so-called templates, representing preformed ultrathin $CoSi_2$(100) layers, were developed [9, 10, 14, 15]. The growth of silicide films on the templates reduces to upgrowing these perfect layers. The best results are obtained under codeposition of Co and Si, a process which removes the problem of mass transport of components in the system [9, 16, 17].

In real practice, however, molecular beam epitaxy is not always appropriate [18]. This makes investigation of the growth of $CoSi_2$ layers on Si(100) by reactive and solid-state epitaxy a topical problem. In this work, we used for this purpose a new method which permits one to visualize the atomic structure of a nanometer-scale surface layer [19–21]. The method is based on analyzing spatial distributions of inelastically scattered medium-energy electrons. It has been already used to advantage in studying the epitaxial growth of ultrathin $CoSi_2$ films on Si(111) [22, 23].

2. EXPERIMENTAL TECHNIQUE

The instrument used in this study is described in considerable detail elsewhere [24]. We note here only its most important features. The sample is irradiated by a 2-keV electron beam striking the surface under a grazing incidence (~10°). The beam current is $\sim 10^{-7}$ A, and its cross-sectional area does not exceed 0.1 mm. We study the spatial distributions of electrons that are scattered in the surface layer of the sample and lose no more than 10% of their initial energy in reflection. The electrons are detected by a small retarding-field energy analyzer with two spherical grids. The electron flux passing through the analyzer grids is amplified by a microchannel plate and forms (on the luminescent screen) a diffraction pattern, which is recorded through the optical window of the vacuum chamber by a computer-interfaced videocamera. The pattern is observed within a cone of half-angle 57°.

The measurements were performed in ultrahigh vacuum ($\sim 10^{-8}$ Pa). The single-crystal silicon substrates on which the cobalt disilicide layers were to be formed were cut of KÉF-1 plates and measured $22 \times 14 \times 0.25$ mm. The crystal surface was aligned with the (100) face to no worse than 20′. The samples were pretreated by the method of Shiraki [25] and subsequently cleaned by heating in vacuum [22], the two procedures culminating in the obtainment of an atomically clean silicon surface with a (2×1)-type reconstruction.

The cobalt was deposited from a source in which a wire of 99.99%-pure material was heated by electron bombardment. The cobalt deposition rate was about 2 ML/min. We accepted one Co monolayer to be equal to 6.78×10^{14} atoms/cm^2, which corresponds to the surface concentration of Si atoms on the (100) face. The elemental composition of the sample surface was mon-

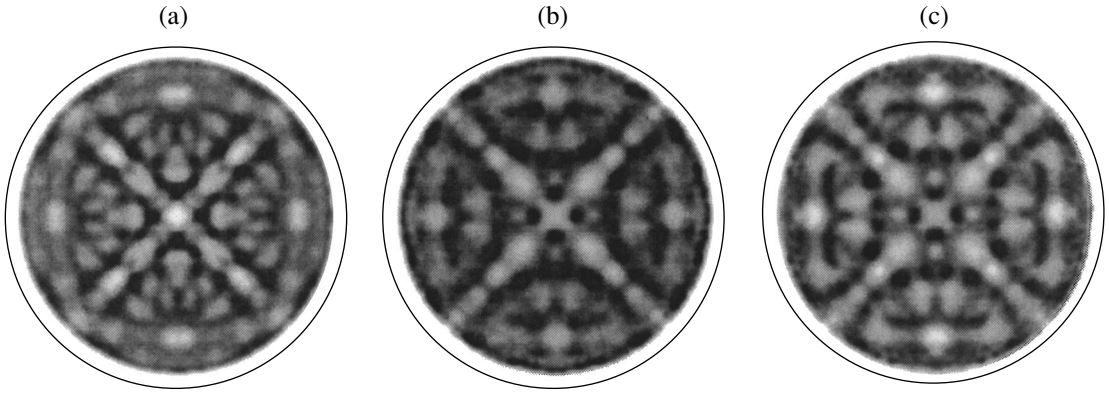

Fig. 1. Diffraction patterns observed in the deposition of cobalt on a single-crystal silicon surface heated to 350°C. (a) Initial pattern from the Si(100) facet, (b) after deposition of 10 ML Co and heating of the sample to 600°C, and (c) after repeated deposition of 10 ML Co and heating of the sample to 600°C.

itored by Auger electron spectroscopy. All the measurements were carried out at room temperature after the samples had cooled down.

3. RESULTS OF MEASUREMENTS AND DISCUSSION

Because the data relating to the earliest stages in silicide formation are controversial, it appeared reasonable to start the work with a study of $CoSi_2$ films of thickness in excess of the depth probed by the method to be employed, i.e., in the conditions where the substrate does not contribute directly to the formation of the diffraction patterns observed. Therefore, the measurements were conducted on films prepared by deposition of ten or more cobalt monolayers on Si(100). The substrate temperature chosen was 350°C, i.e., where, according to [14], the silicide formation already takes place.

Figure 1a shows the starting diffraction pattern of Si(100). The data are presented in the form of two-dimensional maps of electron reflection intensity in the polar and azimuthal emergence angles which are constructed in stereographic projection in the linear gray-scale contrast code. The bright regions relate in this case to maxima in the angular distributions; the dark ones, conversely, to the minima. The center of the pattern corresponds to electrons emerging along the surface normal; the outer circle, to electrons leaving the sample at a polar angle of 60°.

Deposition of cobalt changes the observed pattern dramatically. As the adsorbate dose increases in the 1–10 ML range, the diffraction maxima associated with the substrate smear out gradually and new features appear. The strengthening of their development brings about a new diffraction pattern, shown in Fig. 1b, which shows the structure of the grown cobalt disilicide layers. While this pattern retains the symmetry of the substrate, its general appearance changes appreciably. As for the elemental composition of the grown layer, the ratio between the Co($M_{2,3}VV$) and Si(LVV) low-energy Auger electron peaks of 53 and 92 eV, respectively, is approximately 0.1, which is characteristic of a Si-rich $CoSi_2$ surface [14, 26].

Further increase in the deposited dose to ~20 ML results in a gradual weakening of the diffraction pattern and the appearance of a diffuse background. This is accompanied by a substantial decrease in the silicon Auger electron signal and an increase in the Co Auger electron peak, which indicates the growth of a disordered cobalt film with a silicon admixture. Whence it follows that the cobalt disilicide layer produced after the deposition of the first 10 ML Co already forms a noticeable diffusion barrier, which suppresses further $CoSi_2$ growth at 350°C. Annealing the sample to T = 600°C for ≈1 min restores the diffraction pattern (Fig. 1b), as well as the magnitude of the cobalt to silicon Auger signal ratio observed after the deposition of 10 ML Co. Further growth of the silicide film in subsequent depositions of cobalt and sample heatings to 600°C follows the above scenario. This can be inferred, for instance, from the fact that all the features in the diffraction patterns obtained after the first cobalt deposition (Fig. 1b) and on deposition of 20 ML (Fig. 1c) almost coincide. The only difference between the patterns consists in their contrast, which increases with the thickness of the silicide layer.

We consider now the diffraction pattern typical of $CoSi_2$ films grown on Si(100). Because differently oriented $CoSi_2$ layers can form on this substrate, we shall first discuss the diffraction patterns produced by different facets of cobalt disilicide. Such patterns can be obtained by computer processing of the experimental data presented in [22] for $CoSi_2$(111). This procedure is based [27] on the experimental observation that when a crystal is turned, the corresponding diffraction pattern turns as a whole by the same angle. Therefore, if the pattern due to $CoSi_2$(111) is turned so as to bring an $\langle hkl \rangle$ crystallographic direction to the center of the screen (at zero polar angle), the diffraction pattern

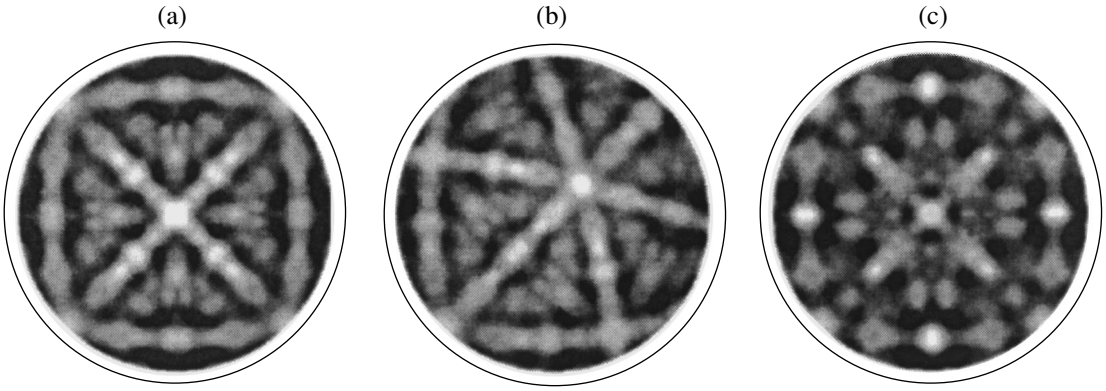

Fig. 2. Diffraction patterns of different $CoSi_2$ facets obtained by computer treatment of experimental data on $CoSi_2$(111) for (a) $CoSi_2$(100) and (b) $CoSi_2$(221). Pattern (c) was obtained by summing the patterns of four (221) domains turned azimuthally relative to one another by 90°.

observed will be that of the (*hkl*) face. The part of the pattern which is absent can be filled using the symmetry elements of the (*hkl*) face by extrapolating the part of the image thus obtained.

The relevant publications primarily discuss three possible orientations of the $CoSi_2$ epitaxial layers which correspond to the (100), (110), and (221) faces. Only the $CoSi_2$(100) face possesses the fourfold mirror-rotational symmetry seen in the pattern of Fig. 1c. Figure 2a displays the diffraction pattern of this face. As is obvious from a comparison of the patterns in Figs. 1c and 2a, this pattern does not agree with the experiment; hence, the film grown has another orientation. We also analyzed the possibility of the (110) orientation. Because this face is characterized by a twofold rotation axis, the fourfold symmetry observed in the experiment can be obtained if we accept the possibility of formation, on the (100) substrate facet, of two types of physically equivalent (110) domains turned by 90° with respect to one another [9] and add their diffraction patterns. The pattern thus obtained was also found to disagree with experiment. This means that no $CoSi_2$(110) grains form in our case.

Now, we consider the third possible orientation of the $CoSi_2$ layers. The diffraction pattern corresponding to the (221) face is shown in Fig. 2b. It has the lowest symmetry and possesses only one mirror-reflection plane. Therefore, the observed fourfold symmetry of this image can arise only if four types of physically equivalent $CoSi_2$(221) domains, turned azimuthally by 90° relative to one another, coexist on the substrate surface. The net pattern obtained by superposition of the contributions due to such domains is presented in Fig. 2c. We readily see that it almost coincides with the experimental results (Fig. 1c). This implies that the $CoSi_2$ film grown by us consists of grains whose (221) planes are oriented parallel to the substrate surface. As for the azimuthal orientation of these grains, a comparison of the patterns shown in Figs. 1a and 2b suggests that the (110) planes of cobalt disilicide are parallel to the silicon (110) planes.

The reason for the growth of $CoSi_2$(221) grains on Si(100) under reactive epitaxy can be readily understood if we take into account the instability of the (100) face in the course of silicide formation and the possibility of its faceting [10, 28]. Facet growth can be initiated by intense mass transport of silicon occurring in the course of cobalt disilicide formation at an elevated temperature, which brings about rearrangement of the crystal surface and faceting by the energetically preferable (111) planes. Further deposition of cobalt onto the Si(111) facets results in epitaxial growth of $CoSi_2$(111) domains, which have a *B*-type azimuthal orientation antiparallel to the substrate under the conditions of reactive epitaxy [22]. The driving force of the process is the formation of the most energetically favorable $CoSi_2$(111)/Si(111) interface. Because the growing $CoSi_2$(111) domains are *B*-oriented, it is the (221) planes that turn out to be parallel to the (100) planes of the original substrate surface; this exactly is observed experimentally. Thus, the observed growth of $CoSi_2$(221) grains is initiated by the surface of the starting silicon crystal becoming faceted by the (111) planes in the course of the silicide formation. We note that the $CoSi_2$/Si interface forming in these conditions is not plane and its roughness governs the relief of the growing film to a considerable extent.

Of particular importance for application purposes of thin silicide films is the establishment of the region within which these films are thermally stable. It is well-known that high-temperature annealing of cobalt disilicide films results first in the formation of pinholes and, thereafter, of $CoSi_2$ islands [14, 29]. We studied the thermal destruction of a $CoSi_2$ layer on silicon using a film obtained by depositing 40 ML of cobalt on the crystal. To do this, the sample was subjected to stepped anneals at increasing temperatures (up to $T = 1200$°C), with diffraction patterns measured in between. These patterns revealed noticeable changes. Figure 3 presents

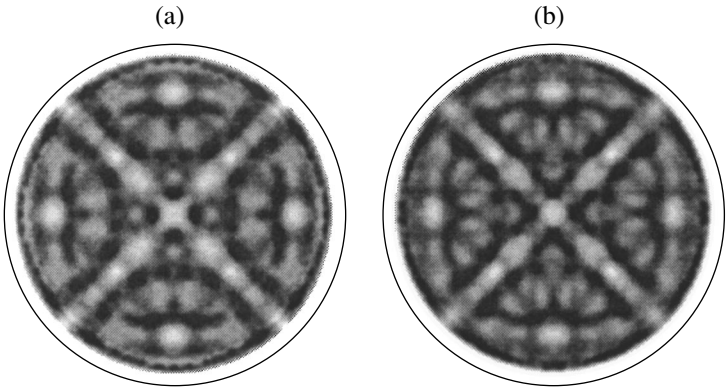

Fig. 3. Diffraction patterns of a cobalt disilicide film on silicon annealed to temperatures of (a) 1000 and (b) 1200°C.

patterns obtained after two such anneals. Computer simulation was used to assist in interpreting the experimental data. The measured patterns were compared with calculations obtained by summing up the patterns due to $CoSi_2$(221) islands and Si(100) pinholes under variation of the statistical weights of the two contributions. The experimental data presented in Figs. 1a and 1c, respectively, were used as reference patterns of the phases. The calculations were compared with experiment values using reliability factors, as was done in our study of silicide formation on Si(111) [22].

As follows from our analysis, an increase in the annealing temperature is indeed accompanied by a change in the film morphology, with the substrate becoming increasingly bare. In particular, after the sample was annealed to 1000, 1120, and 1200°C, the regions of the substrate free of the silicide were found to occupy 8, 34, and 50% of its area, respectively. Bare substrate regions were also observed in the case of the films forming in the initial stages of reactive epitaxy. For instance, after deposition of 10 ML of cobalt (Fig. 1b), bare regions occupied about 10% of the surface area, and after 10 ML more were deposited and the sample was annealed to 600°C, their fraction decreased to 4%.

Thus, application of the new structural method to the investigation of cobalt disilicide formation on the Si(100)–(2×1) surface revealed that a film consisting of $CoSi_2$(221) grains turned azimuthally by 90° with respect to one another grows on it under reactive epitaxy performed at $T = 350$°C. This domain structure is produced by the substrate surface being faceted by (111) planes in the course of the silicide formation. The $CoSi_2$(111) epitaxial layers growing on the (111) facets are *B*-oriented, and this accounts for the (221) planes of cobalt disilicide becoming parallel to the substrate plane. In the initial stage of the process, the film is not continuous, leaving about 10% of the surface area bare. Preparation of continuous $CoSi_2$ films with a better structure requires that after the cobalt deposition, the sample be annealed additionally to higher temperatures.

ACKNOWLEDGMENTS

This study was supported by the Russian Foundation for Basic Research (project no. 01-02-17288) and the Ministry of Science, Industry, and Technology of the RF ("Surface Atomic Structures" Program, project no. 5.10.99).

REFERENCES

1. I. Goldfarb and G. A. D. Briggs, Phys. Rev. B **60** (7), 4800 (1999).
2. H. L. Meyerheim, U. Dobler, and A. Puschmann, Phys. Rev. B **44** (11), 5738 (1991).
3. D. D. Chambliss, T. N. Phodin, and J. E. Rowe, Phys. Rev. B **45** (3), 1193 (1992).
4. P. A. Bennett, S. A. Parikh, and D. G. Cahill, J. Vac. Sci. Technol. A **11**, 1680 (1993).
5. M. Sosnowski, S. Ramae, W. L. Broun, and Y. O. Kim, Appl. Phys. Lett. **65**, 2943 (1994).
6. G. Rangelov, P. Augustin, J. Stober, and Th. Fauster, Phys. Rev. B **49** (11), 7535 (1994).
7. O. P. Karpenko and S. M. Yalisove, J. Appl. Phys. **80** (11), 6211 (1996).
8. H. Ikegami, H. Ikeda, S. Zaima, and Y. Yasuda, Appl. Surf. Sci. **117/118**, 275 (1997).
9. S. M. Yalisove, R. T. Tung, and D. Lorentto, J. Vac. Sci. Technol. A **7** (3), 1472 (1989).
10. J. R. Jiménez, L. J. Schowalter, L. M. Hsiung, *et al.*, J. Vac. Technol. A **8** (3), 3014 (1990).
11. L. J. Schowalter, J. R. Jiménez, L. M. Hsiung, *et al.*, J. Cryst. Growth **111**, 948 (1991).
12. C. W. T. Bulle-Lieuwma, A. H. van Ommen, J. Hornstra, and C. N. A. M. Aussems, J. Appl. Phys. **71** (5), 2211 (1992).
13. V. Scheuch, B. Voigtlander, and H. P. Bonzel, Surf. Sci. **372**, 71 (1997).
14. J. M. Gallego, R. Miranda, S. Molodsov, *et al.*, Surf. Sci. **239** (3), 203 (1990).
15. V. Buschmann, M. Rodewald, H. Fuess, and G. van Tendeloo, J. Cryst. Growth **191**, 430 (1998).
16. R. Tung, F. Schrey, and S. M. Yalisove, Appl. Phys. Lett. **55** (1), 2005 (1989).

17. R. Stadler, C. Schwarz, H. Sirringhaus, and H. von Kanel, Surf. Sci. **271**, 355 (1992).
18. B. Ilge, G. Palasantzas, J. de Nijis, and L. J. Geerlings, Surf. Sci. **414**, 279 (1998).
19. N. S. Faradzhev, M. V. Gomoyunova, and I. I. Pronin, Phys. Low-Dimens. Struct. **3/4**, 93 (1997).
20. I. I. Pronin and M. V. Gomoyunova, Prog. Surf. Sci. **59** (1–4), 53 (1998).
21. M. V. Gomoyunova and I. I. Pronin, Zavod. Lab. **67** (4), 24 (2001).
22. M. V. Gomoyunova, I. I. Pronin, D. A. Valdaĭtsev, and N. S. Faradzhev, Fiz. Tverd. Tela (St. Petersburg) **43** (3), 549 (2001) [Phys. Solid State **43**, 569 (2001)].
23. I. I. Pronin, D. A. Valdaitsev, N. S. Faradzhev, *et al.*, Appl. Surf. Sci. **175/176**, 83 (2001).
24. I. I. Pronin, D. A. Valdaĭtsev, M. V. Gomoyunova, *et al.*, Zh. Tekh. Fiz. **68** (12), 80 (1998) [Tech. Phys. **43**, 1475 (1998)].
25. A. Ishizaka and Y. Shiraki, J. Electrochem. Soc. **133**, 666 (1986).
26. U. Starke, W. Weiss, K. Heinz, *et al.*, Surf. Sci. **352–354**, 89 (1996).
27. I. I. Pronin, N. S. Faradzhev, and M. V. Gomoyunova, Fiz. Tverd. Tela (St. Petersburg) **40** (7), 1364 (1998) [Phys. Solid State **40**, 1241 (1998)].
28. K. Rajan, L. M. Hsiung, J. R. Jiménez, *et al.*, J. Appl. Phys. **70** (9), 4853 (1991).
29. W. Weiss, U. Starke, K. Heinz, *et al.*, Surf. Sci. **347**, 117 (1996).

Translated by G. Skrebtsov

Physics of the Solid State, Vol. 44, No. 6, 2002, pp. 1181–1187. Translated from Fizika Tverdogo Tela, Vol. 44, No. 6, 2002, pp. 1131–1136.

LOW-DIMENSIONAL SYSTEMS AND SURFACE PHYSICS

Formation of Island Structures in the Course of Deposition of Weakly Supersaturated Aluminum Vapors

V. I. Perekrestov*, A. V. Koropov, and S. N. Kravchenko***

** Sumy State University, Sumy, 40007 Ukraine*

*** Sumy State Agricultural University, Sumy, 40021 Ukraine*

e-mail: kpe@ssu.sumy.ua

Received May 18, 2001; in final form, November 1, 2001

Abstract—The formation of island structures in the course of deposition of weakly supersaturated aluminum vapors is investigated by transmission electron (TEM) and scanning electron (SEM) microscopies and electron microdiffraction. The aluminum layers are prepared by dc magnetron sputtering in a high-purity Ar atmosphere. The conditions of formation of statistically homogeneous nanocrystalline layers depend on the deposition temperature and the partial pressures of Ar and reactive gases. The wetting angle between islands and the substrate is calculated from the derived relationships as a function of the condensation temperature. © *2002 MAIK "Nauka/Interperiodica".*

1. INTRODUCTION

The particular interest expressed by researchers in island structures is associated with their unique electrical properties. Nanocrystalline layers can be produced using different techniques. It is well known that, at the early stage of vapor deposition of metals, the formation of a condensate is accompanied by the formation of island films in the form of a layer consisting of supercritical nuclei [1–3]. Further vapor condensation leads to the Ostwald ripening of islands and to the formation of a channel structure and a continuous film. On this basis, we consider three possible variants of the preparation of island structures. The first variant consists in interrupting the technological process prior to the formation of a channel structure.

The second variant is based on the suppression of the Ostwald ripening and intergrowth of islands during the deposition of metals in an atmosphere of reactive gases (O_2, N_2, CO_2, etc.) [4]. However, this brings about the formation of continuous getter films that are composed of metallic crystals joined through interlayers of oxides, nitrides, and other compounds. These structures are referred to as granular films [2].

Koropov *et al.* [5, 6] theoretically established that the third variant of the formation of impurity-free island structures can be accomplished through deposition of vapors with an extremely weak supersaturation. In this case, the growth of island structures is associated with the resorption of subcritical nuclei due to diffusion processes which encourage the formation of individual, relatively large islands, because they exhibit a higher degree of equilibrium. Therefore, the formation of large-sized island structures upon vapor condensation can be treated as a qualitative criterion for weak supersaturation of vapors.

The purpose of the present work is to investigate the formation of nanocrystalline layers upon deposition of aluminum vapors with a weak supersaturation. The choice of aluminum as a model material for the formation of island structures is motivated by its relatively low melting temperature at which vapor condensation can proceed by the following mechanisms: *vapor* $\longrightarrow$ *liquid phase* $\longrightarrow$ *crystal* [1] and *vapor* $\longrightarrow$ *crystal*. In turn, this extends the range of technological procedures used for producing island structures.

2. EXPERIMENTAL TECHNIQUE

Experimentally, the growth of island structures is impeded by the diffusion of adatoms, because low rates of layer formation favor the interaction between the condensate and reactive residual gases. For this reason, a stationary aluminum vapor flux was produced by dc magnetron sputtering in an atmosphere of argon subjected to deep purification. The partial pressure of reactive residual gases during the growth of island structures did not exceed 8×10^{-8} Pa, as was required.

The structure and phase composition of the condensates were examined by scanning electron (SEM) and transmission electron (TEM) microscopies and electron microdiffraction. The TEM investigation of the structure was performed using layers deposited onto KCl cleavages. Moreover, island structures were prepared on glass-ceramic and glass substrates.

The mechanisms of nucleation and growth are governed primarily by technological parameters, such as the pressure of a working gas (for example, argon) P_{Ar}, the partial pressure of reactive residual gases P_g, the condensation temperature T_c, and the growth rate of a layer R_c. In turn, the parameters T_c and R_c determine the

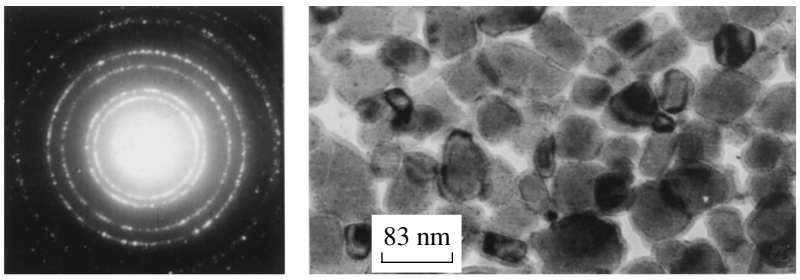

Fig. 1. Structure of an Al layer formed at $T_c \sim 500$°C, $P_g \sim 8 \times 10^{-8}$ Pa, and $P_{Ar} = 9$ Pa.

degree of vapor supersaturation, whereas a decrease in the partial pressure P_{Ar} leads to an increase in the energy of atoms at the instant of deposition [7, 8]. Unlike thermal evaporation, ion sputtering brings about the condensate nucleation at any weak supersaturation of deposited vapors [7]. In other words, ion sputtering provides extremely low rates R_c and, thus, encourages diffusion processes on the deposition surface. According to the classical theory of capillarity [9], the nucleation rate is determined by the following relationship:

$$I = CP\exp[(\Delta G_{des} - \Delta G_{sd} - \Delta G_0)/kT],$$

where ΔG_0 is the free energy of a critical nucleus, ΔG_{sd} is the free activation energy of surface diffusion of adatoms, ΔG_{des} is the free activation energy of desorption, P is the vapor pressure over the deposition surface at temperature T, and $C \approx 10^{22}$ N^{-1} s^{-1}.

Consequently, the concentration of critical nuclei increases with an increase in the adatom–substrate bonding energy, a decrease in the diffusion rate, and lowering of the deposition temperature. Undeniably, in this situation, a continuous film can be formed even at the early growth stage. In order to decrease the adatom–substrate bonding energy upon ion sputtering, it is necessary to decrease the energy of atoms at the instant of condensation. For this reason, the experiments were performed at minimum discharge voltages (~60–35 V) and, if required, at sufficiently high pressures P_{Ar} (~9 Pa). With the aim of maintaining a stationary growth rate R_c in the range 0.03–0.05 nm/s irrespective of the partial pressure P_{Ar}, the power supplied to the sputtering apparatus was made equal to 3 W.

3. RESULTS AND DISCUSSION

The structure of a layer formed at $T_c \sim 500$°C, $P_g \sim 8 \times 10^{-8}$ Pa, and $P_{Ar} = 9$ Pa is shown in Fig. 1. Since the condensation temperature T_c is higher than $(2/3)T_m$ (where T_m is the melting temperature of aluminum), the condensate nucleation proceeds through the following mechanism: *vapor* ⟶ *liquid phase* ⟶ *crystal* [1]. This is confirmed by the presence of bulk crystals and the absence of any orienting effect of the KCl(001) substrate (see the electron diffraction pattern in Fig. 1). This variant of the growth becomes possible in the case of a weak interaction between islands and the substrate; i.e., when the wetting angle θ is considerably larger than π/2.

A change in the condensation mechanism *vapor* ⟶ *liquid phase* ⟶ *crystal* can occur for several reasons. The main reason is a decrease in the condensation temperature T_c to 400–420°C without variations in the aforementioned technological parameters. In this case, the crossover to the nucleation mechanism *vapor* ⟶ *crystal* [1] is characterized by the following features in the formation of the condensate structure.

(1) At the initial stage, islands predominantly grow in the substrate plane so that the growth rate is proportional to the area of the diffusion zone adjacent to the islands. Consequently, prior to their intergrowth, the islands are equally spaced (Fig. 2a), in contrast with the structure shown in Fig. 1.

(2) Upon the crossover to the nucleation mechanism *vapor* ⟶ *crystal*, the wetting angle θ decreases to at least π/2. As a result, the KCl(001) substrate exhibits an orienting effect, which leads to the formation of a structure with preferred orientation, i.e., texture (see the electron diffraction pattern in Fig. 2a).

(3) The growth of islands to the point where they come into contact is accompanied by the formation of a layer that does not break into pieces after separation from the substrate. The time it takes for this layer to be formed is referred to as the overgrowth time t_0 [6]. It is worth noting that a decrease in the condensation temperature T_c from 500 to 400°C and the corresponding change in the mechanism of the layer formation result in an increase in the time t_0 from 20 to 110 min. Moreover, the deposition at $T_c = 400$°C for 4 h does not lead to the formation of a continuous crystalline layer (Fig. 2b). In this case, the SEM data indicate a substantial increase in the island volume (Fig. 2c).

(4) A further decrease in the condensation temperature T_c is attended by a gradual decrease in the overgrowth time t_0 and an enhancement in the tendency toward the formation of a nearly continuous crystalline layer. For example, an increase in the rate of crystal growth in the substrate plane at relatively low temperatures T_c (~120°C) results in the formation of a continuous crystalline layer within 6–8 min after the onset of permanent deposition (Fig. 3). Moreover, the orienting effect of the KCl(001) substrate becomes more pro-

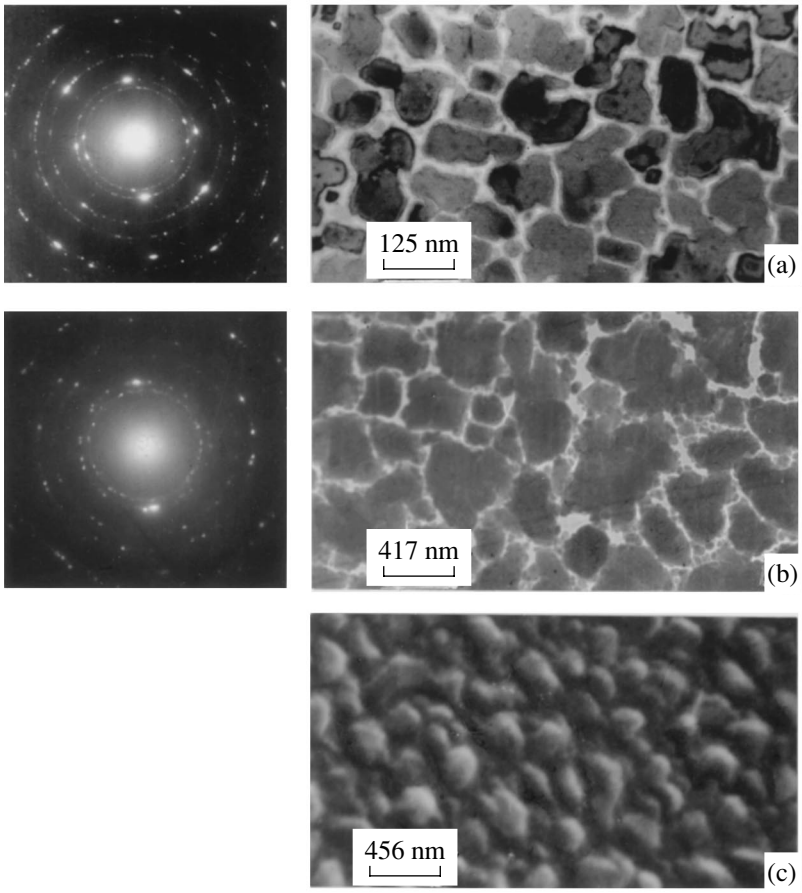

Fig. 2. Structures of Al layers formed upon condensation through the nucleation mechanism *vapor* ⟶ *crystal* at (a) $T_c \sim 400$–420°C, $P_g \sim 8 \times 10^{-8}$ Pa, and $P_{Ar} = 9$ Pa and (b) $T_c = 400$°C, $P_g \sim 8 \times 10^{-8}$ Pa, and $P_{Ar} = 9$ Pa for 4 h. (c) SEM image of the surface of an Al island film.

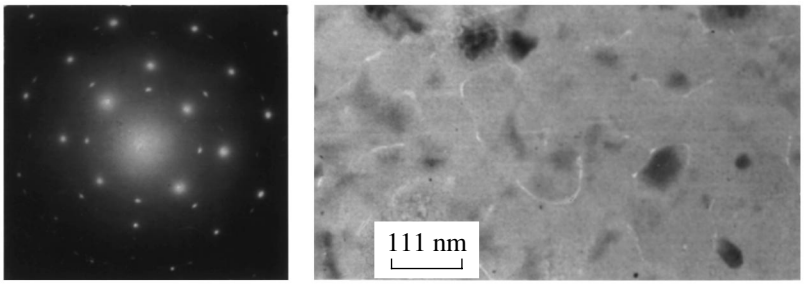

Fig. 3. Structure of an Al film prepared at $T_c \sim 120$°C (the time of continuous deposition is 6–8 min).

nounced and brings about the formation of a texture with the relationship Al(001) || KCl(001); in this case, some islands are rotated in the azimuthal plane through an angle of $\pi/4$ with respect to the principal direction of growth (see the electron diffraction pattern in Fig. 3). We did not reveal a crossover from the Volmer–Weber mechanism of condensation to the Stranski–Krastanov mechanism with a decrease in the condensation temperature T_c.

For the above experiments, the overgrowth time t_0 can be estimated by ignoring the evaporation of adatoms from the substrate (under the condition $\tau_s \longrightarrow \infty$, where τ_s is the lifetime of adatoms prior to evaporation) and atoms from the island surface. For this purpose, we will use the notion of a domain of island influence whose radius is designated as R_0 [5]. If the reevaporation is insignificant ($\tau_s \longrightarrow \infty$), the radius R_0 can be determined from the following condition: all the atoms

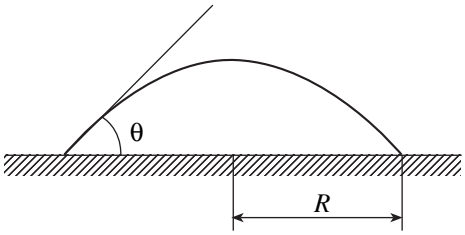

Fig. 4. An island in the form of a spherical segment with a wetting angle $\theta < \pi/2$.

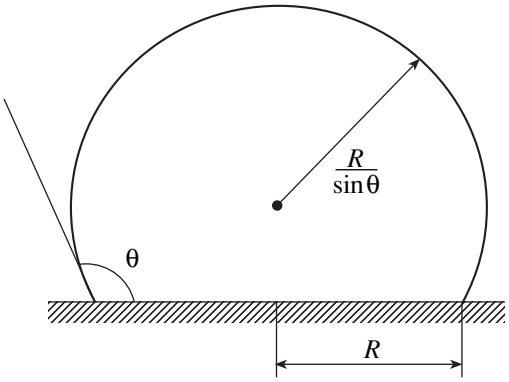

Fig. 5. An island in the form of a spherical segment with a wetting angle $\theta > \pi/2$.

introduced by an external source into the domain of influence of a particular island are adsorbed by it. Hence, the total flux I (s^{-1}) of atoms caught in this island can be calculated from the relationship

$$I = \pi R_0^2 K, \tag{1}$$

where K is the flux of atoms condensed on the substrate ($m^{-2}\ s^{-1}$), $R_0 = R_0(R)$, and R is the radius of the island base.

The rate of change in the island volume V is given by

$$\frac{dV}{dt} = I\omega, \tag{2}$$

where ω is the volume occupied by an atom in the island. For islands in the form of a spherical segment (Figs. 4, 5), we have

$$V = \kappa R^3; \quad \kappa = \frac{\pi}{3}\frac{2 - 3\cos\theta + \cos^3\theta}{\sin^3\theta}.$$

The rate dV/dt is related to the rate of change in the radius R of the island base through the expression

$$\frac{dV}{dt} = 3\kappa R^2\frac{dR}{dt}. \tag{3}$$

From relationships (1)–(3), we obtain the equation

$$3\kappa R^2\frac{dR}{dt} = \pi R_0^2 K\omega,$$

in which the variables R and t can be separated as follows:

$$dt = \frac{3\kappa R^2 dR}{\pi R_0^2 K\omega}. \tag{4}$$

In order to estimate t_0 at $\theta \le \pi/2$, we integrate Eq. (4) with respect to the time t from 0 to t_0 and over the radius R from $\bar{R}$ ($\bar{R}$ is the mean radius of the island base at the instant $t = 0$) to $R_0(\bar{R})$. When integrating, we take into account that the quantity R_0^2 weakly (logarithmically) depends on R and, to a first approximation, can be treated as a constant [5]. Then, we obtain

$$\int_0^{t_0} dt = \frac{3\kappa}{\pi R_0^2 K\omega}\int_{\bar{R}}^{R_0(\bar{R})} R^2 dR, \tag{5}$$

from whence it follows that

$$t_0 = \frac{\kappa}{\pi R_0^2 k\omega}(R_0^3(\bar{R}) - \bar{R}^3).$$

Making allowance for the fact that $R_0(\bar{R}) = \frac{1}{\sqrt{\pi N_i}}$ (where N_i is the island density) [5] and by assuming that $R_0^3(\bar{R}) \gg \bar{R}^3$, we finally derive the relationship

$$t_0 = \frac{\kappa R_0(\bar{R})}{\pi K\omega} = \frac{\kappa}{\pi\sqrt{\pi N_i}K\omega}. \tag{6}$$

At $\theta = \pi/2$, we have

$$t_0 = \frac{2}{3\sqrt{\pi N_i}K\omega}.$$

If $\theta > \pi/2$ (Fig. 5), relationship (5) takes the form

$$\int_0^{t_0} dt = \frac{3\kappa}{\pi R_0^2 K\omega}\int_{\bar{R}}^{R_0(\bar{R})\sin\theta} R^2 dR,$$

because, in this case, the condition of joining islands (the overgrowth of the substrate with islands) is defined by the expression $R(t_0)/\sin\theta = R_0(\bar{R})$. As a result, we have

$$t_0 = \frac{\kappa}{\pi R_0^2 K\omega}(R_0^3(\bar{R})\sin^3\theta - \bar{R}^3).$$

Under the assumption that $R_0^3(\bar{R})\sin^3\theta \gg \bar{R}^3$, we obtain

$$t_0 = \frac{\kappa R_0(\bar{R})\sin^3\theta}{\pi K\omega} = \frac{\kappa\sin^3\theta}{\pi\sqrt{\pi N_i}K\omega}. \quad (7)$$

Here, the multiplier $\kappa\sin^3\theta \equiv \kappa_1$ is determined by the formula

$$\kappa_1 = \frac{\pi}{3}(2 - 3\cos\theta + \cos^3\theta).$$

The flux K can be estimated from the film growth rate: $K \approx 2 \times 10^{18}$ m^{-2} s^{-1}. By using relationships (6) or (7) and the experimental values of t_0 and N_i, the angle θ can be easily determined by a graphical method. Figure 6 depicts the obtained dependence $\theta(T_c)$, which confirms the aforementioned regularities in the formation of island structures.

The crossover of the condensate nucleation mechanism (*vapor* ⟶ *liquid phase* ⟶ *crystal*) can also be caused by a decrease in the partial pressure P_{Ar} to 3–0.8 Pa (at T_c = 500°C and $P_g = 8 \times 10^{-8}$ Pa). This decrease in the pressure P_{Ar} favors the formation of the amorphous phase at the stage of condensate nucleation. The mechanism of nucleation of an amorphous phase was considered in our recent works [8, 10]. It was demonstrated that the nucleation of an amorphous phase is governed primarily by high energies of atoms at the instant of their deposition and depends on the impurities adsorbed on the substrate surface. An increase in the thickness of the continuous amorphous film (approximately to 3–5 nm) leads to an increase in the degree of its nonequilibrium. In turn, this brings about the formation of crystal inclusions on the film surface (Fig. 7a). It should be noted that these crystals grow only in the course of aluminum vapor deposition. The condensation mechanism *vapor* ⟶ *amorphous phase* ⟶ *crystal* substantially affects the shape and size of the islands and the texture of their growth. Indeed, unlike the island structures growing through the mechanism *vapor* ⟶ *liquid phase* ⟶ *crystal*, thin crystals (up to 10 nm thick) grow on the amorphous phase even at T = 500°C. Consequently, the formation of a continuous crystalline layer occurs within 7–10 min after the onset of permanent deposition. Note that, prior to the formation of the continuous crystalline layer, intercrystalline regions are filled with the binding amorphous phase. Analysis of the bright-field (Fig. 7b) and dark-field (Fig. 7c) images indicates that the contrast observed in the intercrystalline regions stems from diffuse electron scattering. This is the reason why the intercrystalline regions in dark-field images are universally darkened. At the same time, examinations of dark-field images and microdiffraction investigations demonstrate that the same texture is formed only in local regions of the layer. This can be associated with a misorienting effect of the amorphous interlayers.

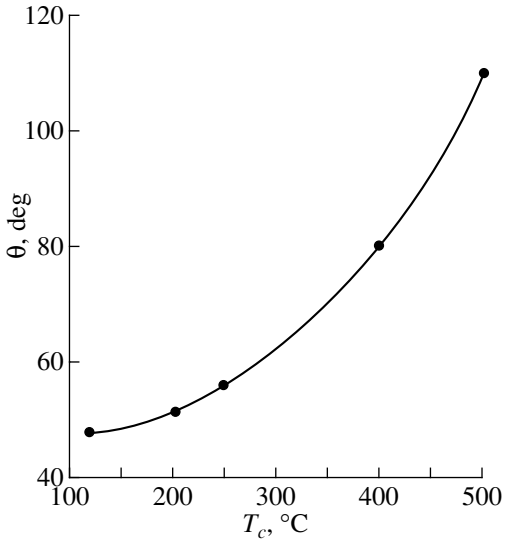

Fig. 6. Dependence $\theta(T_c)$.

An increase in the partial pressure P_g to 10^{-6} Pa (P_{Ar} ~ 7–9 Pa and T_c = 500°C) results in the formation of granular films within 30 min after the onset of permanent deposition (Fig. 8a). In this case, the electron diffraction patterns contain additional diffraction maxima attributed to the impurity phase and the intensity ratios of the diffraction lines change significantly. It can be assumed that the microstructure shown in Fig. 8a contains dark spherical aluminum inclusions surrounded by the binding impurity phase. The inference regarding the formation of granular films is confirmed to some extent by the SEM investigation (Fig. 8b). In actual fact, the contrast observed in the SEM images stems from phase inhomogeneities of the condensate. Brighter regions correspond to the reflection of electrons from denser aluminum inclusions, and the dark background surrounding the inclusions is formed through weaker reflections from the impurity phase.

The mechanisms responsible for the structure formation of island films can be conveniently interpreted in terms of the energies of bonding between an adatom and the substrate surface (E_s), an adatom and the amorphous phase (E_a), and an adatom and the crystal (E_{cr}). It can be assumed that aluminum vapor deposition onto glass, glass-ceramic, and KCl substrates satisfies the following inequality: $E_s < E_a < E_{cr}$. It is reasonable that thermal accommodation of atoms deposited onto the surface proceeds more efficiently at high bonding energies. On the other hand, low energies of bonding between adatoms and the deposition surface encourage their reevaporation and migration. The inequality $E_s < E_a$ also accounts for the crossover from the bulk growth to the surface growth of crystals upon formation of the amorphous phase (Figs. 1, 7b). The diffusion Ostwald ripening and intergrowth of islands are efficiently sup-

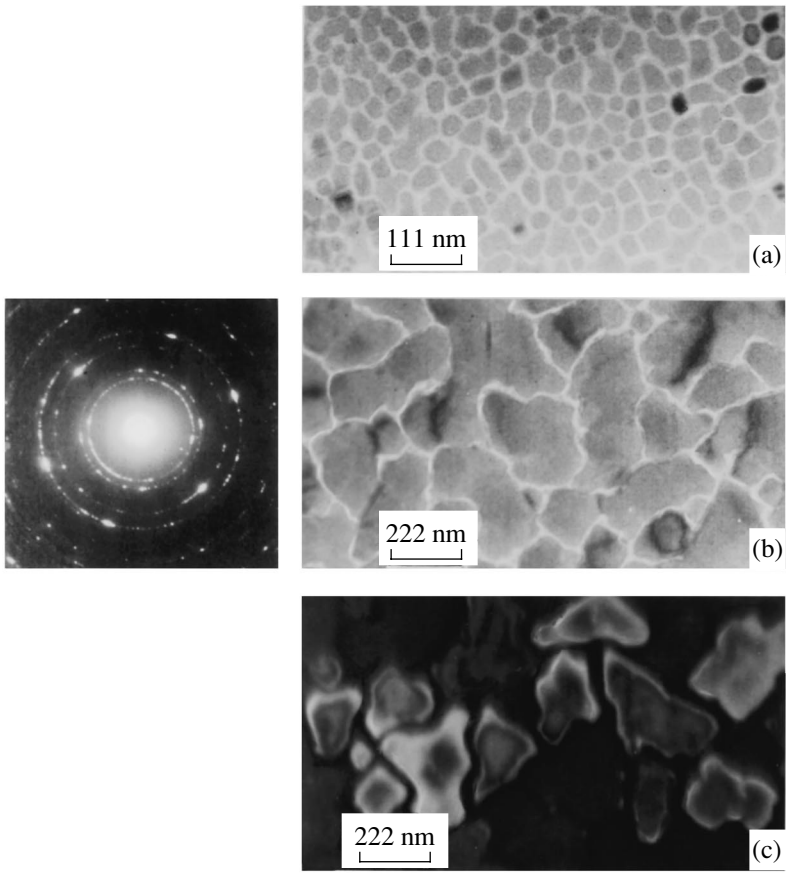

Fig. 7. Structures of Al layers formed at T_c = 500°C, $P_g = 8 \times 10^{-8}$ Pa, and P_{Ar} = 3–0.8 Pa: (a) initial stage of crystal nucleation on the surface of the amorphous phase, (b) bright-field image of the structure, and (c) dark-field image of the structure.

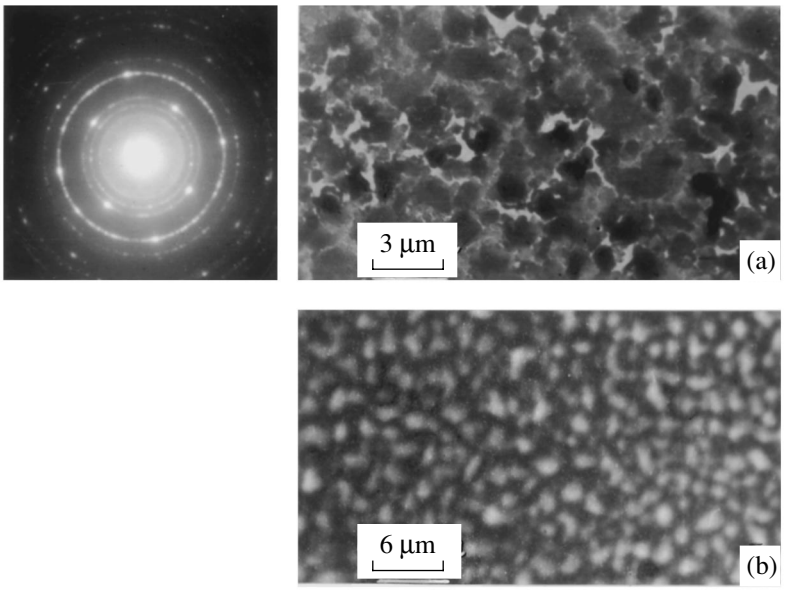

Fig. 8. (a) Microstructure of an Al granular film prepared at T_c = 500°C, $P_g = 10^{-6}$ Pa, and $P_{Ar} \sim$ 7–9 Pa (the deposition time is 30 min) and (b) SEM image of the Al granular film.

pressed in the case when the diffusion flux of adatoms from the intercrystalline region onto the crystal and the flux of atoms reevaporated from the intercrystalline region add up to the flux of atoms deposited onto the same intercrystalline region. However, in this situation, at $T_c < 420$°C, the crystals should grow in the substrate plane, which must necessarily result in the formation of a continuous crystalline layer. The tendency toward the formation of this layer can be considerably depressed in the case when the energy of bonding between the atoms and the lateral face of the crystal is less than the energy of bonding between the atoms and the crystal surface oriented nearly parallel to the front of the deposited flux. This ratio of the bonding energies can actually hold, because, according to experimental data [4], the lateral faces of crystals are usually enriched with impurities. Most likely, this is the reason why the increase in the island volume rather than the formation of a continuous crystalline layer is observed even after aluminum deposition for 4 h (Fig. 2c).

It is known that, in the course of magnetron sputtering, the condensation surface is irradiated by a secondary-electron flux [11], thus increasing the condensation temperature T_c. Therefore, the thermal conductivity of the substrate material also plays an important role in the formation of island structures. Since the thermal conductivity of the glass is less than those of the glass-ceramic and KCl substrates, the growth of statistically homogeneous island structures on the glass substrate is more pronounced. In particular, it is revealed that the growth of island structures on the glass substrate is accompanied by a change in the layer color from blue to pink and then to white. This regularity of the change in color is explained by the corresponding increase in the degree of periodicity of the statistically homogeneous island structure on which the diffraction of light occurs. The change in color to white is observed upon disturbance of this periodicity due to the intergrowth of some islands. Note that the change in color and its brightness upon condensation on the KCl and glass-ceramic substrates are less pronounced.

4. CONCLUSIONS

The results obtained in this work allowed us to make the following inferences.

(1) The deposition of weakly supersaturated aluminum vapors does not result in the classical variant of the formation of a channel structure through island intergrowth followed by a high-rate overgrowth of channels with the formation of bridges [7].

(2) The results of calculations of the wetting angle θ between islands and the substrate on the basis of the theoretical concepts advanced in this work are quite consistent with the physics of processes responsible for the formation of island structures.

(3) The condensation of weakly supersaturated vapors can be used to control technological processes of producing nanocrystalline layers with a specified structure by varying the parameters P_g, P_{Ar}, and T_c.

ACKNOWLEDGMENTS

This work was supported by the Ministry of Education and Science of Ukraine, project no. 84.02.04.00-02.

REFERENCES

1. L. S. Palatnik, M. Ya. Fuks, and V. M. Kosevich, *Mechanism of Formation and the Structure of Condensed Films* (Nauka, Moscow, 1972).
2. Yu. F. Komnik, *Physics of Metal Films: Size and Structural Effects* (Atomizdat, Moscow, 1979).
3. S. A. Kukushkin and A. V. Osipov, Usp. Fiz. Nauk **168** (10), 1083 (1998) [Phys. Usp. **41**, 983 (1998)].
4. V. S. Kogan, A. A. Sokol, and V. M. Shulaev, *Influence of Vacuum Conditions on the Formation of Condensate Structure. Structure of Metal Films Doped with Gases: A Review* (TsNIIatominform, Moscow, 1987), Part 2.
5. A. V. Koropov, P. N. Ostapchuk, and V. V. Slezov, Fiz. Tverd. Tela (Leningrad) **33** (10), 2835 (1991) [Sov. Phys. Solid State **33**, 1602 (1991)].
6. A. V. Koropov and V. V. Sagalovich, Poverkhnost, No. 2, 17 (1990); No. 5, 55 (1989); No. 6, 50 (1987).
7. *Handbook of Thin-Film Technology*, Ed. by L. I. Maissel and R. Glang (McGraw-Hill, New York, 1970; Sov. Radio, Moscow, 1977), Vol. 2.
8. V. I. Perekrestov and S. N. Kravchenko, Vopr. At. Nauki Tekh., No. 4, 80 (2001).
9. J. P. Hirth, S. J. Hruska, and G. M. Pound, in *Single-Crystal Films: Proceedings of the International Conference, Blue Bell, 1963*, Ed. by M. H. Francombe and H. Sato (Pergamon, Oxford, 1964; Mir, Moscow, 1966).
10. V. I. Perekrestov, S. N. Kravchenko, and A. V. Pavlov, Fiz. Met. Metallogr. **88** (5), 72 (1999).
11. B. S. Danilin, *Application of Low-Temperature Plasma for Deposition of Thin Films* (Énergoatomizdat, Moscow, 1989).

Translated by O. Borovik-Romanova

Physics of the Solid State, Vol. 44, No. 6, 2002, pp. 1188–1195. Translated from Fizika Tverdogo Tela, Vol. 44, No. 6, 2002, pp. 1137–1144.

POLYMERS AND LIQUID CRYSTALS

Resonant Raman Spectroscopy of Ethylene–Acetylene Copolymers Doped with Iodine

V. A. Marikhin*, I. I. Novak*, V. B. Kulik*, L. P. Myasnikova*, E. I. Radovanova*, and G. P. Belov**

** Ioffe Physicotechnical Institute, Russian Academy of Sciences, Politekhnicheskaya ul. 26, St. Petersburg, 194021 Russia*

*** Institute of Chemical Physics in Chernogolovka, Russian Academy of Sciences, Chernogolovka, Moscow oblast, 142432 Russia*

e-mail: v.marikhin@pop.ioffe.rssi.ru

e-mail: gbelov@cat.icp.ac.ru

Received August 2, 2001; in final form, September 10, 2001

Abstract—The relative contents of short and long conjugated chains in ethylene–acetylene copolymers (EAC) are determined by varying the lasing wavelength, as was done earlier for pure poly(acetylene). The Raman spectra of the copolymer samples doped with iodine contain the bands attributed to the iodine polyions I_3^- and I_5^-. Unlike poly(acetylene), the ethylene–acetylene copolymer is characterized by the Raman spectra in which the intensities of the bands assigned to the I_5^- polyions are higher than those of the I_3^- polyions even at low degrees of doping. The structural features responsible for this difference are discussed. © *2002 MAIK "Nauka/Interperiodica".*

1. INTRODUCTION

Among the polymers with conjugated chains, poly(acetylene) (PA) possesses the highest conductivity (up to $10^5\ \Omega^{-1}\ cm^{-1}$) comparable to theoretical estimates [1, 2]. However, poly(acetylene) is highly susceptible to oxidative destruction in air and, consequently, has not found practical application. According to Pochan [3], the oxidation is initiated by molecular defects formed in the course of synthesis and (or) *cis–trans* isomerization of the synthesis products upon heat treatment.

Over the last decade, considerable efforts have been made to search for methods of improving synthesis procedures [1, 2]. This has allowed one to decrease substantially the concentration of molecular defects (and, hence, to increase the conductivity). However, the oxidation resistance of the high-conductivity PA samples thus far synthesized remains extremely low.

It has been found that the introduction of sufficiently flexible poly(ethylene) (PE) spacers into PA molecules through the synthesis of ethylene–acetylene block copolymers (EAC) is an effective method of increasing the oxidation resistance of poly(acetylene) [4, 5]. Nascent EAC powders can be kept in air over many years without indications of destruction. Earlier [6], we revealed that doping of copolymers with iodine leads to a substantial increase in dc conductivity. However, the maximum conductivity achieved in EAC is estimated to be $\sigma \le 10^{-2}\ \Omega^{-1}\ cm^{-1}$ [7], which is seven orders of magnitude less than the maximum conductivity of PA [1, 2]. It can be assumed that such an essential difference is associated with appreciable differences in both the length and the length distribution of macromolecular fragments with conjugated bonds in PA and EAC.

However, our investigations with the use of resonant Raman scattering have revealed that the size distribution of conjugated regions in EAC is similar to that observed in PA synthesized by a conventional method [8].

It is known that ethylene–acetylene copolymers contain conjugated chains tens and hundreds of angstroms in length. These chains are separated from one another by extended dielectric PE regions. In this respect, it is of interest to elucidate whether the low conductivity of EAC is associated with an insufficient percolation of conducting regions or the doping of the copolymer occurs through a mechanism differing from that observed in PA.

Resonant Raman scattering investigations have demonstrated that, upon doping of PA with iodine, charge-transfer complexes of the I_3^- and I_5^- types are formed in conjugated fragments. These complexes are responsible for the generation of free charge carriers in the conjugated chains and conduction in PA in electric fields. According to the results obtained in [9–12], the relative content of these complexes depends on the molar concentration of introduced iodine and the degree of orientation of PA samples. Wang *et al.* [12] showed that the concentration of the I_3^- complexes in oriented high-conductivity PA samples is one order of magnitude higher than that of the I_5^- complexes. More-

1063-7834/02/4406-1188$22.00

over, the doping of PA samples leads to a considerable change in the distribution of conjugated regions over the length toward an increase in the percentage of short fragments [13].

To the best of our knowledge, the specific features of the doping mechanism in EAC have never been analyzed. In this respect, the main objective of the present work was to perform this investigation.

2. SAMPLES AND EXPERIMENTAL TECHNIQUE

The experiments were carried out using unoriented copolymer films 100–150 μm thick. The films were prepared by pressing powders at room temperature. The content of double bonds in the copolymer was determined by the ozonization technique and was estimated at 20 mol %. The iodine diffusion was performed at a temperature of 25°C either from a gas phase or from an iodine solution in heptane. After doping, the samples were placed in an evacuated tube in order to remove the iodine which was not incorporated into the charge-transfer complexes. The molar concentration y of iodine in the copolymer samples was calculated from the relative increment of the mass of the studied sample $[(m - m_0)/m_0]$ according to the formula

$$y = \frac{m - m_0}{m_0}\frac{1}{n}\frac{M_{CH}}{M_I}, \quad (1)$$

where M_I is the molecular mass of iodine, M_{CH} is the molecular mass of the acetylene unit (CH), m_0 is the mass of the sample prior to diffusion, m is the mass of the sample after diffusion, and n is the fraction of the acetylene moiety in the mass of the copolymer.

The Raman spectra were recorded on a SPEX Industries spectrometer with holographic gratings at a linear ruling density of 1800 mm^{-1} at room temperature in air. The measurements were performed with radiation at wavelengths λ_L = 632.8 nm (helium–neon laser) and λ_L = 476.5, 488.0, and 514.5 nm (argon laser). The power of a light beam incident on the sample did not exceed 20 mW. The diameter of an illuminated spot on the sample was approximately equal to 100 μm. The backscattered light in a 180° scattering geometry was recorded using an electronic signal-processing circuit based on a PC486DX computer.

3. RESULTS AND DISCUSSION

Figure 1 shows the overall Raman spectra of the undoped and doped copolymer samples.

According to the analysis performed in our recent work [8], all the intense bands observed in the Raman spectrum of the copolymer are assigned to the conjugated PA fragments in a *trans* conformation. The band at 1085 cm^{-1} is associated with a mixing of the stretching vibrations of the single C–C and C–H bonds. The band in the range of 1470 cm^{-1} is attributed to the stretching vibrations of the double C=C bonds in *trans* chains. A broader band centered at about 2170 cm^{-1} corresponds to the overtone of the band at 1085 cm^{-1}, and the band at about 2550 cm^{-1} results from a mixing of vibrations at frequencies of 1085 and 1470 cm^{-1}.

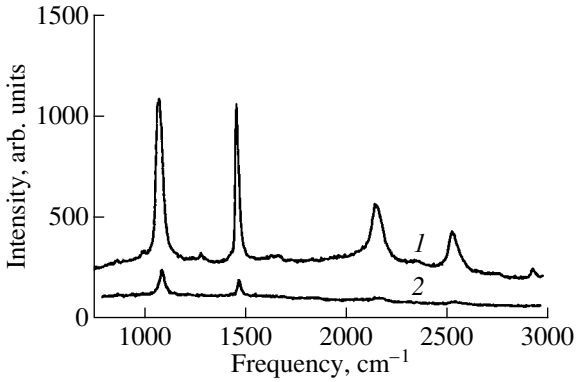

Fig. 1. Raman spectra of (*1*) undoped and (*2*) iodine-doped (y = 0.16) EAC samples at λ_L = 632.8 nm.

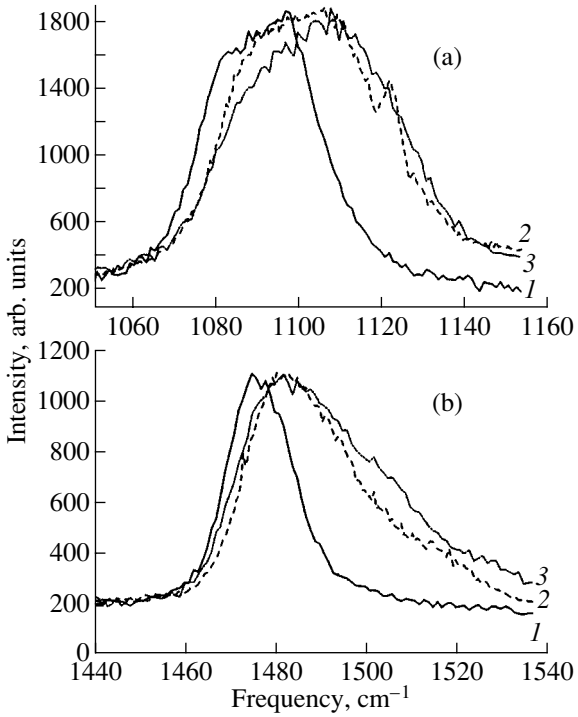

Fig. 2. Profiles of the fundamental bands in the Raman spectra of EAC at different lasing wavelengths λ_L (nm): (*1*) 632.8, (*2*) 514.5, and (*3*) 476.5.

Earlier [13–15], it was demonstrated that the considerable half-width and asymmetry of the bands at about 1100 and 1500 cm^{-1} are due to a superposition of a set of elementary resonant Raman bands whose frequencies are close to one another and depend on the length of conjugated chains.

As is known [13–15], the incident light in the red lasing wavelength range (λ_L > 600 nm), for the most

Sizes of conjugated regions in undoped and doped ethylene–acetylene block copolymer samples

λ_L, nm	Band in the range of 1100 cm^{-1}					Band in the range of 1500 cm^{-1}				
	frequency of elementary components, cm^{-1}	half-width, cm^{-1}	fraction of the elementary component in the overall spectrum, %	size of the conjugated region $N_{C=C}$		frequency of elementary components, cm^{-1}	half-width, cm^{-1}	fraction of the elementary component in the overall spectrum, %	size of the conjugated region $N_{C=C}$	
				according to the method described in [16]	according to the method described in [17]				according to the method described in [16]	according to the method described in [17]
Undoped sample										
632.8	1080.25	15.46	23.25	28	47	1471.0	8.2	22.8	26	40
	1087.0	18.55	20.04	24	34	1474.7	14.7	1.3	25	33
	1096.6	17.04	28.93	21	24	1476.2	7.9	31.3	24	32
	1100.84	24.22	9.21	20	21	1479.4	14.2	10.1	22	26
	1114.62	24.75	0.11	17	15	1482.2	10.8	29.5	21.5	25
	1145.72	7.67	0.52	–	–	1497.5	24.5	4.75	16	15
	1162.76	18.4	0.29	–	–	1514.8	12.1	0.21	15	12
476.5	1080.55	12.5	7.25	27	46	1474.2	11.5	16.9	25	35
	1087.44	12.2	6.12	23	33	1480.7	10.9	18.6	2	26
	1095.4	22.0	26.9	20	25	1487.6	11.7	17.8	19	21
	1105.85	19.9	27.5	19	17	1494.9	13.0	18.3	18	17
	1113.42	15.1	9.5	17	13	1502.9	7.0	4.6	17	15
	1120.1	15.8	14.0	16	10	1507.0	7.6	4.5	16.5	13
	1129.0	18.3	8.65	15	–	1513.1	17.0	10.9	16.0	–
	1170.55	7.6	0.15	–	–	1527.8	20.0	8.44	13	–
488.0	1080.84	13.32	9.7	26	45	1473.3	9.9	9.7	25	36
	1087.23	12.35	10.0	23	32	1478.9	11.7	20.4	23	28
	1095.23	17.72	22.0	20	25	1486.4	13.7	27.4	20	21
	1105.54	18.75	28.0	19	18	1494.4	12.0	10.5	19	17
	1111.21	16.83	11.1	18	15	1500.5	15.0	9.8	18	15
	1119.22	14.71	12.3	16	13	1500.2	18.8	10.5	17	13
	1130.0	16.59	5.9	14.5	10	1521.9	25.8	10.5	15	10
	1170.0	14.45	1.1	–	–	1563.1	28.7	1.1	–	–
Doped sample (y = 0.016)										
488.0	1079.23	16.6	5.8	27	50	1475.4	10.8	9.2	24	32
	1086.5	14.6	4.2	24	35	1481.8	12.8	10.2	22	25
	1994.5	19.2	18.9	21	25	1487.0	9.8	5.4	20	20
	1105.6	17.2	18.0	19	18	1496.0	21.2	33.2	18	16
	1115.0	17.6	17.2	17	15	1504.6	8.0	2.6	17	15
	1122.6	16.8	14.8	16	12	1513.6	21.4	22.8	16	12
	1129.5	16.2	15.6	15	10	1523.5	12.4	2.9	15	10
	1141.0	20.4	5.4	–	–	1531.7	28.4	13.7	14	8

part, resonantly excites long chains, whereas short chains, in this case, are excited nonresonantly; i.e., the intensity of the corresponding bands in the Raman spectrum is underestimated out of proportion. By contrast, the incident light at shorter wavelengths ($\lambda_L \geq 350$ nm) gives rise primarily to resonant excitation of short chains involving only a few double C=C bonds.

The profiles of the fundamental Raman bands at different lasing wavelengths are depicted in Figs. 2a and 2b. As can be seen, the expected effect of the wavelength λ_L most clearly manifests itself in the scattering range corresponding to short conjugated chains. This effect can be determined quantitatively from the data (see table) obtained by computer decomposition of the complex Raman band profiles at frequencies of 1100 and 1500 cm^{-1} with the use of the standard Pick fit program (by analogy with the decomposition performed earlier in [8]).

It is seen from Fig. 1 that the doping leads to a drastic decrease in the intensity of all the observed bands. This is especially pronounced for the bands at 2170 and 2550 cm^{-1}, which become almost indistinguishable even at $y = 0.16$. As regards the fundamental bands, the intensity of the band at about 1470 cm^{-1} decreases more steeply compared to that of the band at 1085 cm^{-1}. In our opinion, this result is quite reasonable because the charge-transfer complexes formed in the vicinity of the double bonds should bring about considerable distortions of local vibrations near these bonds.

The profiles of the fundamental bands (normalized to the same intensity of the band at a maximum) in the Raman spectra of the undoped and doped copolymer samples at the lasing wavelength $\lambda_L = 488.0$ nm are displayed in Figs. 3a and 3b. The actual intensity ratio of these bands is illustrated in Fig. 3c. As can be seen from Fig. 3, the doping results in a significant asymmetrical change in the shape of the bands at about 1100 and 1500 cm^{-1} due to a sharp decrease in the scattering intensity in the wavelength range corresponding to the longest chains. This effect is caused by the separation of long chains into shorter fragments during the formation of charge-transfer complexes upon doping [13–15].

The results of computer spectral decomposition (see table) clearly demonstrate that, upon doping, the fraction of short conjugated fragments considerably increases compared to that of longer fragments.

Thus, analysis of the fundamental Raman bands attributed to the conjugated PA fragments in EAC shows that the regularities observed in changes of these fragments upon doping are similar to those found for PA [13–15].

It should be noted that the type of charge-transfer complexes formed upon iodination of conjugated chains can also be determined by Raman spectroscopy. The formation of different complexes was first observed in methanol solutions of iodine and in a number of compounds (with a known chemical structure) containing iodine polyions of specific types: I_3^-, I_5^-, I_7^-, I_8^{2-}, etc.

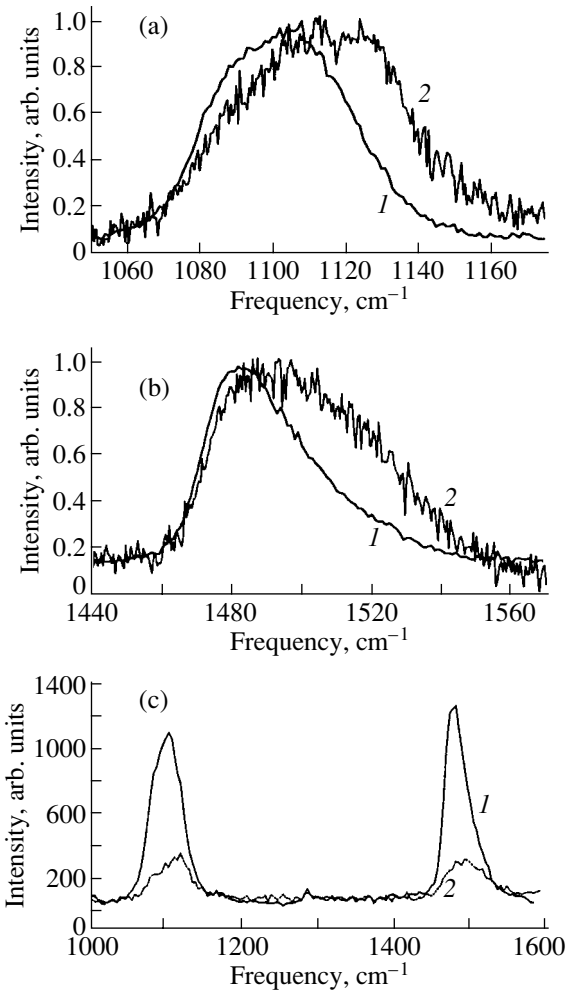

Fig. 3. Profiles of the fundamental bands in the Raman spectra of (*1*) undoped and (*2*) iodine-doped ($y = 0.016$) EAC samples at $\lambda_L = 488.0$ nm. (a, b) The bands of the undoped and doped samples are normalized to the same intensity of the band at a maximum. (c) The bands illustrating the actual intensity ratio for the undoped and doped samples.

[18, 19]. In the simplest case, the structure of these polyions is considered a combination of I^-, I_2^-, and I_3^- ions. For each type of ions, there are particular frequencies in the Raman spectra upon excitation at lasing wavelengths in the visible spectral range. Ions I^- do not manifest themselves in the Raman spectra but can be revealed by ^{129}I Mössbauer spectroscopy [20].

In the Raman spectra of iodine solutions, molecules I_2 can be identified from the broad band which is observed at about 209 cm^{-1} and assigned to the stretching vibrations of iodine molecules [19]. The polyions I_3^- and I_5^- are most frequently formed upon doping of conjugated polymers. As follows from the calculations performed by Marks and Kalina [19], the Raman spectrum of the I_3^- polyion substantially depends on its geometric structure. In the case when the ion has a symmetric lin-

ear shape, the Raman spectrum, according to the selection rules, should exhibit only one active polarized mode at the frequency $\nu_1 = 118$ cm^{-1}, which corresponds to the symmetric stretching vibrations involving the motion of only terminal atoms with respect to the central atom. The in-phase composition of the stretching vibrations of two iodine atoms I–I in the I_3^- ion results in the band at 118 cm^{-1}.

The other two modes at frequencies $\nu_3 = 145$ cm^{-1} (asymmetric vibrations involving the motion of the central atom) and $\nu_2 = 69$ cm^{-1} (bending vibrations) are active only in the IR spectrum. However, if the symmetry of the polyion structure is violated (for example, due to the difference in the distances between terminal atoms and the central atom or the deviation of the ion structure from the linear geometry), the ν_2 and ν_3 modes can manifest themselves in the Raman spectrum due to the violation of the selection rules. This would indicate that the geometry of the I_3^- polyion had changed in response to force fields induced by surrounding atoms or molecules. The high lability of the I_3^- structure can be explained by the fact that the halogen–halogen bonds in the iodine polyion are substantially weakened as the result of an appreciable increase (by 0.2 Å) in the interatomic distances. In this case, the tensile force constants are less than one-half the corresponding constant for the I_2 molecule [21]. Consequently, the location of the central atom can easily change under the action of sufficiently weak forces induced, for example, by neighboring molecules or chemical and conformational defects. This feature permits the polyions to be readily incorporated into paracrystal lattices formed by conjugated macromolecules. In the case when the I_3^- ions are distributed in a nonrandom manner but form a linear regular chain (this situation can occur in well-oriented PA samples [22, 23]), the Raman spectrum contains a very intense (slightly shifted in frequency) band at $\nu_1 = 110$ cm^{-1}. This band is accompanied by a clearly defined progression of overtones up to the ninth overtone. For asymmetric I_3^- ions, an intense band at $\nu_3 = 150$ cm^{-1} can be observed in addition to the intense band at $\nu_1 = 105$ cm^{-1}. The aforementioned frequencies ν_1 for the I_3^- polyions vary significantly (from 118 to 105 cm^{-1}) for different compounds and PA in the works of different authors [18, 19]. This implies that, in the studied compounds, the distances between iodine atoms should differ noticeably. As is known, a decrease in the ν_1 frequency suggests an increase in the halogen–halogen distance. As was noted above, this seems to be quite reasonable because the interatomic distances in the polyions can readily change as the result of an appreciable decrease in the force constants.

In the case of the I_5^- polyion, there exists a large number of geometric structures, including a symmetric linear chain, a chain symmetrically bent with respect to the central atom, and a zigzag chain. It has been shown that the low-frequency Raman spectrum is very sensitive to the configuration of the I_5^- polyion. Note that the I_5 polyion can be treated both as the combination $I_2 + I_3$ and as the combination of the I^- ion with two symmetrically added units I_2. For a symmetric linear chain of the type I–I–I$^-$–I–I, the resonant Raman spectrum exhibits an intense band at $\nu = 160$ cm^{-1}. This band is attributed to the I–I valence transition and is most frequently observed upon doping of conjugated polymers. As regards the I_2–I^-–I_2 chain, the symmetric stretching vibrations can be responsible for the appearance of a weak band at 107 cm^{-1}.

For the other combination ($I_2 + I_3^-$), the changes in the interatomic distances in the I_2 units result in the appearance of the band at $\nu = 185$ cm^{-1} instead of the band at 209 cm^{-1} [19].

For the I_5^- polyions with symmetrically bent and zigzag geometries, the Raman spectra exhibit a more complex structure. These spectra are presented in [19].

It is quite reasonable that linear polyions of the I_3^- and I_5^- types are most stable. These are singly charged ions whose stability and size are important factors.

Upon heating of iodine-doped PA, the charge-transfer complexes I_3^- and I_5^- decompose to form the I_2^- ions. These processes were observed by mass spectrometry in the course of temperature measurements. The formation of the I_2^- ions was judged from the appearance of broad peaks in the mass spectra with variations in the temperature [24]. The intensity and location of these peaks depend on the degree of doping. At $y = 0.07$, only one peak is observed at a temperature of 70°C. For this concentration of iodine in PA, the Raman scattering data indicate the occurrence of only the I_3^- ions, which, most likely, are thermally stable up to 70°C. At $y = 0.22$, the mass spectra exhibit two peaks: the first peak at $T = 50$°C and the second (more intense) peak at $T = 100$°C. By comparing these findings with the Raman scattering data, Saalfeld *et al.* [24] attributed the low-temperature peak to the formation of I_2^- upon decomposition of the I_5^- complexes and assigned the high-temperature peak to the decomposition of the I_3^- complexes. From the foregoing it follows that, upon the formation of chains from the I_3^- and I_5^- anions, the stability of the I_3^- anions increases by 20–30 K. The predominant formation of these polyanions upon doping of partly crystalline conjugated polymers should be expected for the following reasons. In PA crystals, linear segments of macromolecules are separated by channels whose walls are formed by hydrogen atoms of the CH groups. These channels can involve molecules I_2. Coppens [18] proved that the potential of the covalent interaction between hydrogen and iodine atoms has a minimum at $r = 3.36$ Å; hence, the diameter of the channels should be no less than 6–7 Å. It is evident that channels of similar sizes should encourage the predominant formation of linear iodine polyions.

Among the currently known polyanions of iodine, the I_3^- polyion has the largest constant of formation, which is almost two orders of magnitude greater than that for the I_5^- polyion [19]. This accounts for the predominant for-

mation of I_3 polyions upon doping of PA, which has been observed by many authors [9–15, 18–25].

From the aforesaid it is clear that a similar analysis of the low-frequency Raman spectra can provide reliable and valuable information regarding the specific features of the doping of conducting polymers and the real structure of iodine polyanions.

Figure 4 displays the Raman spectra of lightly doped ($y = 0.04$) EAC samples in the range $\Delta\nu < 200$ cm^{-1}, which we obtained upon excitation with red laser light ($\lambda_L = 632.8$ nm). For the iodine-doped sample, the spectrum exhibits two rather broad (with a half-width of approximately 20 cm^{-1}), well-pronounced bands with maxima near 107 and 157 cm^{-1}. According to the aforementioned data available in the literature, we can state that, upon doping of EAC, charge-transfer complexes of two types, namely, I_3^- and I_5^-, are formed in poly(acetylene) fragments, as was observed earlier for pure poly(acetylene). At the same time, the doping kinetics in the copolymer differs in that the concentration of I_5^- anions is three or four times higher than that of I_3^- anions even at initial low degrees of doping ($y < 0.04$, Fig. 4). With a further increase in the degree of doping, the intensity of the band associated with the I_5^- anions becomes progressively higher than that of the band attributed to the I_3^- anions. As a consequence, the latter band completely disappears at $y = 0.2$–0.3. However, the authors of all published works dealing with the doping of PA have argued that, at the early stages of doping, either only the band of the I_3^- anions is observed in the spectrum or the intensity of the band attributed to the I_3^- anions always exceeds the intensity of the band assigned to the I_5^- anions. The intensities of these bands level off at $y = 0.25$, and the band of the I_5^- anions begins to dominate over the band of the I_3^- anions only at higher (limiting) iodine concentrations. In the spectra of high-conductivity oriented poly(ethylene) samples with different degrees of extension, the band of the I_3^- anions invariably dominates over the band of the I_5^- anions even at the highest degrees of doping [12]. Furthermore, at the maximum extension ($L/L_0 = 8$), the spectra contain only the band at $\nu = 107$ cm^{-1}, which corresponds to the I_3^- complex. The highest conductivity observed in these samples was attributed by Wang *et al.* [12] not only to the absence of the I_5^- polyions but also to the formation of a specific linear lattice composed of I_3^- polyanions and aligned along the direction of macromolecule orientation. Similar conclusions were drawn in [26].

The formation of particular complexes with an increase in the degree of doping can be represented in the form of a dynamic equilibrium according to the scheme

$$(CH)_x \xleftrightarrow{I_2} (CH)_x^+ I_3^- \xleftrightarrow{I_2} (CH)_x^+ I_5^-. \qquad (2)$$

It is clear that the larger the amount of iodine I_2 introduced into a polymer, the greater the shift of the equilibrium toward the right. And vice versa, the removal of I_2 leads to the shift of the equilibrium toward the left. We believed that the specific features in the supramolecular structure of polymers should substantially affect the character and the rate of diffusion into PA crystals.

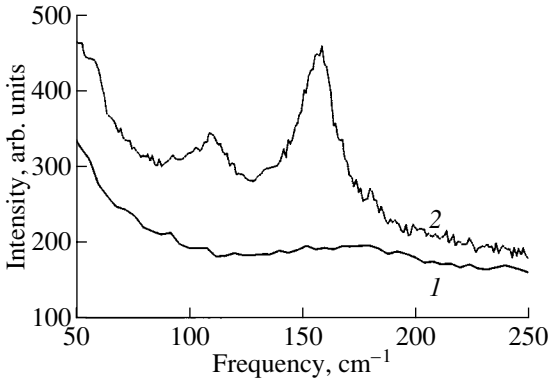

Fig. 4. Raman spectra of (*1*) undoped and (*2*) iodine-doped ($y = 0.04$) EAC samples in the short-wavelength range at $\lambda_L = 632.8$ nm.

As is known [1, 2], high conductivities have been achieved upon doping of specially synthesized low-defect PA samples with an increased content of long conjugated chains. Electron microscopic and diffraction investigations have revealed that these samples contain more perfect and extended PA microfibrils [26, 27]. Furthermore, these samples can be oriented to higher degrees of extension. This results in a very close packing of microfibrils with respect to each other and a considerable decrease in the porosity of the samples. In our opinion, all the aforementioned factors hinder the diffusion of I_2 inside the fibrils into the crystal lattice of PA and bring about the predominant formation of I_3^- anions and, also, column structures composed of these anions. By contrast, if the PA crystals have a more loose structure and are surrounded by a free volume, the amount of penetrating iodine I_2 can be appreciably larger, which results in a shift of reaction (2) toward the right.

This mechanism is confirmed by the x-ray photoelectron spectroscopic data obtained by Ikemoto *et al.* [28], who showed that only the surface layers of PA fibrils are doped at the initial stages ($y < 0.05$) and then dopants are more homogeneously distributed over the bulk of the sample.

Note that, in this case, a substantial amount of iodine in the surface region is in a weakly bound state and can be readily removed by evacuation.

It is significant that the I_5^- / I_3^- ratio for the surface layers in PA (determined from the x-ray spectroscopic data) proves to be considerably larger than the I_5^- / I_3^- ratio averaged over the sample thickness (obtained from the Raman spectroscopic data) [28].

We believe that the specific structure of EAC favors the diffusion of iodine into crystalline regions of PA

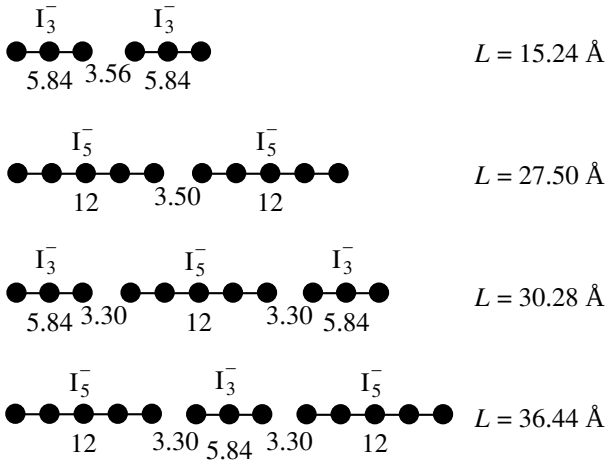

Fig. 5. Linear sizes of the I_3^- and I_5^- polyions and their combinations according to x-ray diffraction data [23].

fragments. In our earlier works [6–8], we made the inference that, in the structure of copolymers, well-ordered (from the standpoint of x-ray diffraction) PA crystalline grains involving extended conjugated regions alternate with crystalline grains consisting of PE *trans* chains. The size of crystalline grains of both types is estimated at 100 Å [6]. Moreover, the copolymers involve rather narrow, strongly defective layers between crystalline grains of both types. These interlayers accumulate conformational, disclination, and chemical defects, including isolated double bonds and short conjugated chains. It can be assumed that a more loose (compared to crystalline grains) structure of these interlayers facilitates access for iodine to end faces of crystalline grains composed of conjugated chains, which is unexpected for PA.

Furthermore, our x-ray structural investigations demonstrated that the crystalline grains of poly(acetylene) in copolymers are less perfect than those in pure poly(acetylene).

Thus, the above arguments and easier diffusion indicate that equilibrium (2) for the copolymer should more readily shift toward the right. As a result, the concentration of I_5^- anions exceeds the concentration of I_3^- anions. This can also mean that the actual local degrees of doping y can be higher than those determined from the increment of the sample mass due to the diffusion.

Analysis of the data available in the literature shows that an increased concentration of I_5^- anions as compared to that of I_3^- anions is an undesirable factor as regards the possibility of achieving high conductivities [9–12, 16–26]. First and foremost, making allowance for the actual geometric sizes obtained by the diffraction methods for these singly charged anions and their combinations (Fig. 5) [23], it becomes evident that different numbers of free carriers are generated in conjugated chains with the same length upon doping. It is easy to determine that the generated charge has the highest density per unit length of the conjugated region (0.131 e/Å) for a one-dimensional lattice of I_3 anions and the lowest density (0.073 e/Å) for a one-dimensional lattice of I_5^- anions. The intermediate densities should be observed for combinations of the $I_3^-I_5^-I_3^-$ (0.099 e/Å) and $I_5^-I_3^-I_5^-$ (0.082 e/Å) types. The former combination is most frequently encountered in PA (according to x-ray diffraction and Raman spectroscopy). Judging from the intensity ratio of the low-frequency bands in the Raman spectrum of the copolymer (Fig. 4), it can be assumed that our samples contain combinations of the $I_5^-I_3^-I_5^-$ type. However, the ultimate answer to this question calls for large-angle x-ray diffraction investigation.

It can be seen from Fig. 5 that, upon formation of the $I_3^-I_5^-I_3^-$ and $I_5^-I_3^-I_5^-$ combinations, the minimum lengths of conducting PA regions should be equal to 30 and 36.5 Å, respectively. This implies that shorter conjugated chains (for the given frequently realized type of doping) do not participate in the generation of free charge carriers, because they cannot combine with the dopant in the given form. As a consequence, the attainable macroscopic conductivities decrease appreciably. Unfortunately, the copolymer samples studied in the present work are characterized not only by an increased content of short conjugated chains (see table) but also by a considerable number of isolated double bonds [6–8]. It seems likely that all these factors are responsible for the sufficiently low electrical conductivities thus far attained in EAC [6–8].

The analysis performed also demonstrates that, in order to improve the electrical properties of poly(acetylene) and its copolymers with ethylene, special attention should be focused on the doping process. In particular, the doping needs to be carried out under the mildest conditions with the aim of forming only the I_3^- anions and the column structures composed of these anions.

It is in this case that the number of generated charge carriers can be increased at the expense of short conjugated chains. Moreover, the high conductivity can be achieved only with a strict order in the arrangement of the I_3^- anions in order to prevent disturbance of the potential distribution along the molecular axis of PA [27]. The incorporation of anions of other types (I_5^-) leads to a decrease in the conductivity along the chain. As is known [29], hopping conductivity—a characteristic property of polymers—is determined not only by the transfer of carriers along the chain but also by hoppings from one conjugated chain to another chain both within a particular crystalline domain and between poly(acetylene) domains. Using poly(acetylene) as an example, Murthy *et al.* [23] showed that the efficiency of the transverse carrier transfer is substantially affected by the type of more complex structures consisting of column conjugated chains formed in the course of doping. These can be layers of alternating PA molecules and incorporated iodine structures in different molar ratios or even continuous layers and iodine anions. For the purpose of elucidating the real structure

of doped copolymer samples, we are, at present, performing large-angle x-ray diffraction investigations.

ACKNOWLEDGMENTS

This work was supported by the Russian Foundation for Basic Research, project no. 98-03-33264.

REFERENCES

1. H. Naarmann, Synth. Met. **17** (1), 223 (1987).
2. J. Tsukamoto, A. Takahashi, and K. Kovasaki, Jpn. J. Appl. Phys. **92** (1), 125 (1990).
3. J.M. Pochan, in *Handbook of Conducting Polymers*, Ed. by T. A. Skotheim (Marcel Dekker, New York, 1986), Vol. 2, p. 1383.
4. L. N. Russiyan, P. E. Matkovskiĭ, V. N. Noskova, *et al.*, Vysokomol. Soedin., Ser. A **33** (2), 280 (1991).
5. L. N. Raspopov, P. E. Matkovskiĭ, G. P. Belov, *et al.*, Vysokomol. Soedin., Ser. A **33** (2), 425 (1991).
6. A. N. Aleshin, E. G. Guk, V. A. Marikhin, *et al.*, Vysokomol. Soedin., Ser. A **37** (7), 1179 (1995).
7. A. N. Aleshin, E. G. Guk, V. A. Marikhin, and L. P. Myasnikova, Macromol. Symp. **102**, 309 (1966).
8. V. A. Marikhin, I. N. Novak, E. G. Guk, *et al.*, Fiz. Tverd. Tela (St. Petersburg) **39** (11), 2106 (1997) [Phys. Solid State **39**, 1885 (1997)].
9. S. Lefrant, L. S. Lichtmann, H. Temkin, *et al.*, Solid State Commun. **29** (3), 191 (1979).
10. K. Kamija and J. Tanaka, Synth. Met. **25** (1), 59 (1988).
11. L. S. Hsu, A. J. Signorelli, G. P. Pez, and R. H. Baughman, J. Chem. Phys. **69** (1), 106 (1978).
12. D. Wang, J. Tsukamoto, A. Takahashi, *et al.*, Synth. Met. **65** (1), 117 (1994).
13. H. Kuzmany, Phys. Status Solidi B **97** (2), 521 (1980).
14. J. Kurty and H. Kuzmany, Phys. Rev. B **44** (2), 597 (1991).
15. G. P. Brivio and E. Mulazzi, Phys. Rev. B **30** (2), 876 (1984).
16. E. Mulazzi, G. P. Brivio, E. Faulqnes, and S. Lefrant, Solid State Commun. **46** (12), 851 (1983).
17. Y. Furakawa, T. Arakawa, H. Takeushi, *et al.*, J. Chem. Phys. **81** (7), 2907 (1984).
18. P. Coppens, in *Extended Linear Chain Compounds*, Ed. by J. S. Miller (Plenum, New York, 1982), Vol. 1, p. 333.
19. T. J. Marks and D. W. Kalina, in *Extended Linear Chain Compounds*, Ed. by J. S. Miller (Plenum, New York, 1982), Vol. 1, p. 197.
20. W. Kiefer and H. J. Bernstein, Appl. Spectrosc. **25** (4), 500 (1971).
21. P. Klaboe, J. Am. Chem. Soc. **89** (15), 3667 (1967).
22. R. H. Baughman, N. S. Murthy, G. G. Miller, and L. W. Shacklette, J. Chem. Phys. **79** (2), 1065 (1983).
23. N. S. Murthy, G. G. Miller, and R. H. Baughman, J. Chem. Phys. **89** (4), 2523 (1988).
24. F. E. Saalfeld, J. J. De Corpo, and J. R. Wyatt, in *Extended Linear Chain Compounds*, Ed. by J. S. Miller (Plenum, New York, 1982), Vol. 1, p. 33.
25. *Handbook of Conducting Polymers*, Ed. by T. A. Skotheim (Marcel Dekker, New York, 1986), Vol. 1, Chap. 2.
26. A. Montaner, M. Rolland, J. L. Souvajol, *et al.*, Polymer **29** (6), 1101 (1988).
27. K. Shimamura, Y. Yamashita, H. Kasahara, and K. Monobe, Synth. Met. **17** (1), 485 (1987).
28. I. Ikemoto, M. Sakairi, T. Tsutsumi, *et al.*, Chem. Lett. 1189 (1979).
29. S. Curran, A. Stark-Hauser, and S. Roth, in *Handbook of Organic Conductive Molecules and Polymers*, Ed. by H. S. Nalwa (Wiley, Chichester, 1997), Vol. 2.

Translated by O. Borovik-Romanova

Physics of the Solid State, Vol. 44, No. 6, 2002, pp. 1196–1202. From Fizika Tverdogo Tela, Vol. 44, No. 6, 2002, pp. 1145–1150.

POLYMERS AND LIQUID CRYSTALS

Orientation of Discotic and Ferroelectric Liquid Crystals in a Macroporous Silicon Matrix[1]

T. S. Perova*, E. V. Astrova, S. E. Tsvetkov*, A. G. Tkachenko**, J. K. Vij*, and S. Kumar*****

** Department of Electronic & Electrical Engineering, Trinity College, Dublin, 2 Ireland*

*** Ioffe Physicotechnical Institute, Russian Academy of Sciences, St. Petersburg, 194021 Russia*

**** Institute for Liquid Crystal Research, Bangalor, India*

e-mail: perovat@tcd.ie

Received April 10, 2001; in final form, October 18, 2001

Abstract—Macroporous silicon with deep regular channels 3–4.5 μm in diameter was infiltrated with discotic and ferroelectric liquid crystals (LCs) at the temperature of the isotropic phase, and then, the system was slowly cooled to room temperature, with the liquid crystalline mesophase formed. The orientation of the LC molecules in the porous matrix was studied by FTIR spectroscopy. The alignment of LCs was ascertained by comparing the behavior of various vibrational bands of a liquid crystal introduced into the porous matrix with that for LC inside the bulk cells of planar and homeotropic alignment. The molecules of the discotic LC show a planar orientation of their column's axis with respect to the surface of the macroporous silicon wafer; i.e., they are perpendicular to the channel axis. The long molecular axis of the ferroelectric LC is aligned with the pore walls, having homeotropic orientation with respect to the wafer surface. In a macroporous silicon matrix, both kinds of LCs show unexpected enhancement of the low-frequency vibrational bands. *© 2002 MAIK "Nauka/Interperiodica".*

Over the last decade, considerable scientific effort has been focused on studying liquid crystals within a confined geometry. Liquid crystals are a crucially important enabling technology for the manufacture of displays. The understanding of the layer structure, phase transitions, order parameter fluctuations, liquid-solid interface, and dynamics of collective modes and molecular motions will be significantly advanced if results on samples restricted to confined geometries are compared with those in the bulk [1–4].

Porous systems are suitable hosts for liquid crystal molecules. These systems are characterized by a high surface-to-volume ratio and, therefore, are very sensitive to any interactions between the infiltrated molecules and the surrounding walls. A possible interaction of this kind is the aligning power of the walls [5], which can give rise to such subphases as a quasi-nematic layer [6].

Polarized infrared spectroscopy with normal and oblique incidence of light is one of the most powerful techniques that can be used to investigate the orientation of liquid crystal (LC) molecules with respect to a substrate [7, 8]. The application of this technique to confined LCs is frequently restricted by the nature of the host material (e.g., Vocor glass), which is usually opaque to light in the IR region. However, this problem can be overcome by using porous silicon for LC infiltration. In this case, the size and depth of pores and the porosity can be varied widely.

Regular porous structures, such as microporous superlattices and macroporous silicon, have attracted considerable scientific interest because of their having a photonic band gap [9–11]. Infiltration of porous systems of this kind with liquid crystals gives control over the position of their photonic band gap, if one relies on the fact that the refractive index of LC changes with temperature [12] or external electric field [13]. It is important to find out how different kinds of liquid crystal molecules will behave in a macroporous silicon (*ma*-PS) matrix. In this study, Fourier Transform Infrared Spectroscopy (FTIR) was used to investigate the alignment of liquid crystals, both discotic and ferroelectric, infiltrated into *ma*-PS.

1. EXPERIMENTAL

Two different types of liquid crystal materials were used in this study: (i) a commercial ferroelectric liquid crystal (FLC) mixture SCE8 (ii) and a triphenylene-based discotic liquid crystal (DLC) H5T–NO_2 [14]. These LCs were chosen for experimental convenience, as they both have a mesophase at room temperature. The structural formulae and phase sequences of these compounds are shown in Fig. 1a. These liquid crystals were infiltrated into macroporous silicon (shown in Fig. 1b) by means of the capillary effect at temperatures approximately 10°C above the temperature of transition to the isotropic phase.

The macroporous silicon used in this study (Fig. 1b) has a system of regular cylindrical pores of micrometer

[1] This article was submitted by the authors in English.

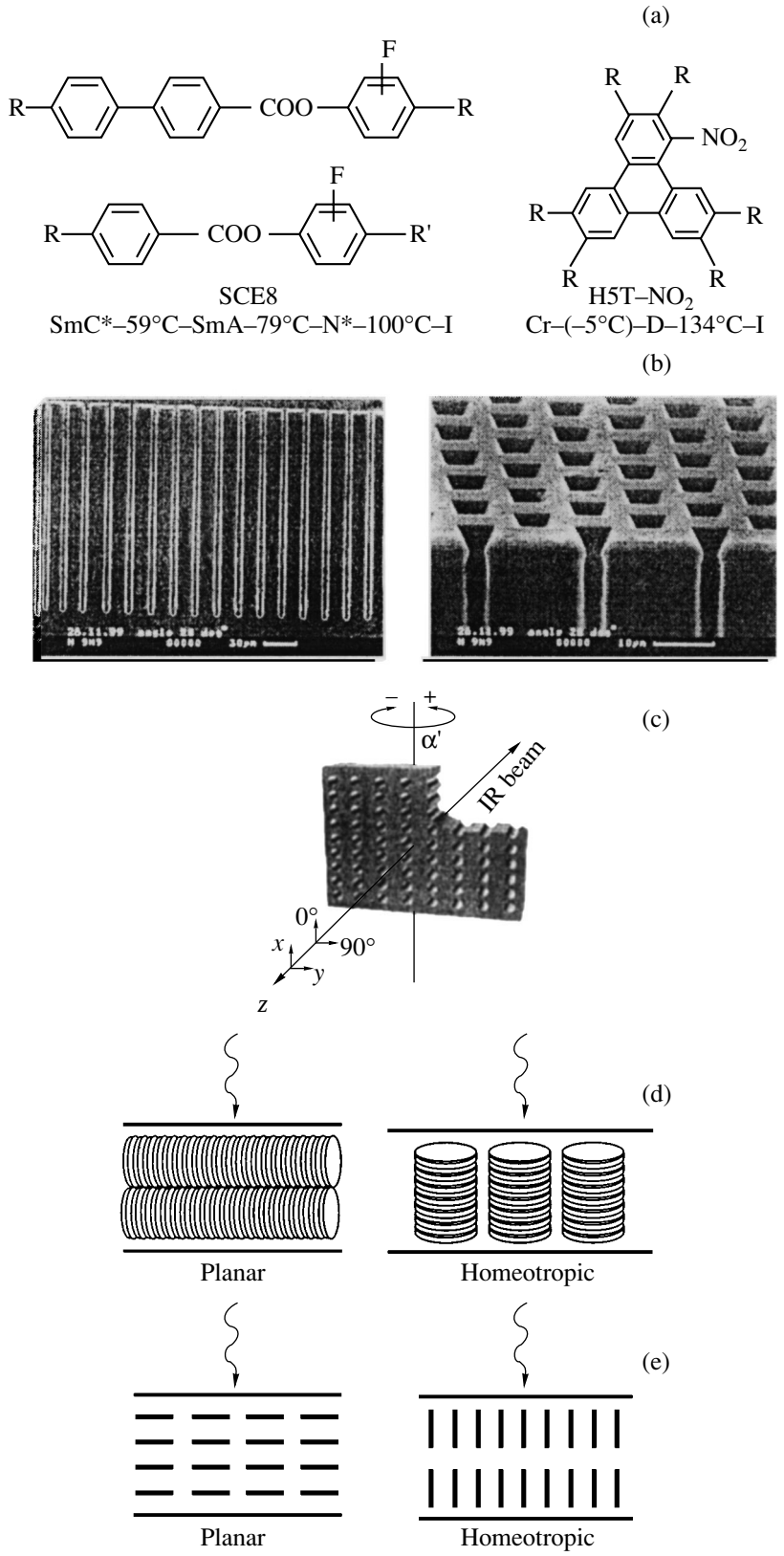

Fig. 1. Material properties and experimental setup: (a) structural formulas and phase sequences of ferroelectric liquid crystalline mixture SCE8 and tryphenylene-based discotic liquid crystal H5T–NO_2 ($R = OC_5H_{11}$); (b) SEM image of the macroporous silicon matrix (cross section side and top view) used to infiltrate with the liquid crystals; (c) the schematic view of the FTIR experiment shows the sample rotation angle α' and macroporous Si sample coordinate frame; (d) planar and homeotropic alignment of the discotic liquid crystal in a ZnSe cell; (e) planar and homeotropic alignment of the ferroelectric liquid crystal in a ZnSe cell.

diameter and high aspect ratio. The starting material was single-crystal (100)-oriented Czochralski-grown *n*-type silicon with resistivity $\rho = 15\ \Omega$ cm. A standard photolithographic process was employed to form pits spaced 12 μm apart on the polished surface of the silicon wafer. Deep pores were etched electrochemically in a 2.5% aqueous-ethanol solution of HF for 300 to 450 min under backside illumination [15] at a voltage of 5 V and a constant current density $j = 3$ mA/cm^2. The pore depth and diameter d were, respectively, 200–250 μm and $d = 3$–4.5 μm, with these parameters corresponding to a porosity of 5.7–12.8% for our triangular lattice.

FTIR measurements were performed using a Biorad FTS60A spectrometer fitted with a liquid-nitrogen-cooled MCT detector. A schematic of the FTIR experiment is shown in Fig. 1c. Scans were performed between 450–4000 cm^{-1} with a resolution ranging from 2 to 8 cm^{-1}. A total of 64 scans were coadded to improve the signal-to-noise ratio. IR spectra were initially recorded for an empty macroporous silicon wafer and then for a matrix infiltrated with the liquid crystal. The difference between these two spectra was taken to be the spectrum of a liquid crystal infiltrated into the porous matrix. The alignment of the LCs within the porous silicon matrix was deduced from a comparison of the relative intensities and positions of the different vibrational bands in the obtained spectra with those of the bulk liquid crystal. For this purpose, a number of liquid-crystal cells with different types of alignment (homeotropic and planar, Figs. 1d, 1e) were prepared as follows.

A planar cell with H5T–NO_2 was fabricated with ZnSe windows (with a spacer of thickness ~12 μm). A homeotropic cell was obtained when two ZnSe windows were coated with nylon 6/6 (see [7] for more details). A planarly aligned cell with SCE8 was obtained using two ZnSe windows coated with commercial (Nissan Chemical Industries, Ltd.) orientant RN-1266 (a 0.4% solution in a mixture of 10% butyl cellosolve and 90% N-methyl pyrrolidone) and rubbed with velvet in one direction. The thickness of this cell, found from infrared fringes, was ~9 μm. A homeotropically aligned SCE8 cell, of approximate thickness 9 μm, was prepared using ZnSe windows coated with a carboxylato chromium complex (chromolane) (see [16] for more details). All these cells were filled by means of the capillary effect at a temperature of ~10°C above the transition to the isotropic phase.

2. RESULTS AND DISCUSSION

Complete information on the structure and orientation of LC molecules can be obtained by studying a combination of polarized and oblique infrared transmissions [7, 8]. However, our investigations show that additional interference effects appear in the frequency range 700–1500 cm^{-1} for tilted macroporous silicon samples. This makes the analysis of the IR spectra of the liquid crystal itself impossible for oblique incidence of the light. Therefore, the alignment of LCs was determined by comparing the behavior of various vibrational bands in the spectra obtained at normal incidence of the infrared beam on liquid crystals contained in a porous matrix with that in spectra of planar and homeotropic bulk LC cells.

The alignment of liquid crystals is usually considered with respect to the orientation of the long molecular axis (in the case of rodlike molecules) and with respect to the column axis **n** (which is, in general, perpendicular to the core plane) for discotic liquid crystals. The alignment will be planar if the long molecular axis (column axis) is oriented parallel to the substrate plane and is homeotropic in the case of perpendicular orientation. Therefore, conclusions about the alignment can be drawn from the behavior of bands associated with vibrations exhibiting the transition dipole moment parallel (||) and perpendicular (⊥) to the rigid part or core of the molecules. These bands are listed in the table for both kinds of liquid crystals under study. It should be noted that the spectral position of the majority of the vibrational bands of liquid crystals in a porous matrix is the same as that in the bulk LC cells.

2.1. Discotic Liquid Crystal

There are two methods for determining the type and extent of alignment for discotic liquid crystals: (i) from the ratio of the peak intensities for a particular vibrational band in the isotropic and in the discotic phase ($R_{DI} = A_{iD}/A_{iI}$) and (ii) from the ratio of the peak intensities for the same band in the discotic phase at normal and oblique incidence of light ($R = A_{i\parallel}/A_{i\perp}$), which allows the intensity of the vibrational band to be determined for vibrations with transition dipole moments parallel ($A_\parallel$) and perpendicular ($A_\perp$) to the substrate plane (see [7] for more details). Neither of these techniques is suitable for our purposes for the technical reasons described above.

We introduce here a third method for determining the type of alignment by measuring the ratio intensities of two different vibrational bands, i and j, observed in the mesophase (a type of dichroic ratio):

$$R_{ij} = A_i/A_j, \tag{1}$$

where A_i is the intensity of the band associated with vibrations parallel to the LC molecule core and A_j is that associated with vibrations perpendicular to the core. Particular care should be taken in choosing the appropriate set of bands for calculating the dichroic ratio by means of Eq. (1). These bands should correspond to vibrations with transition dipole moments at a right angle (~90°) with respect to each other. Our previous investigation [7] performed for a number of triphenylene derivatives (H5T, H7T, and H7T–NO_2 discotic liquid crystals) demonstrated that the aromatic C–C

stretching vibrations at ~1510 and ~1610 cm^{-1} are parallel to the core (*i*-band) while the C–H aromatic out-of-plane deformation at ~830 cm^{-1} is purely perpendicular to the core (*j*-band). These vibrational bands are shown in Figs. 2a and 2b for the H5T–NO_2 discotic liquid crystal in the porous matrix and for both homeotropic and planar alignment of the molecules in a liquid-crystal cell.

Qualitative information on the type of alignment in the porous matrix can be obtained by comparing the spectra of different samples in the region 800–890 cm^{-1}. Although the vibrational band in this region is rather complicated, it can be clearly seen that the main maximum of this band is shifted to ~830 cm^{-1} for the cell with planar alignment and for the porous matrix, whereas for the cell with homeotropic alignment, the peak lies at ~820 cm^{-1}.

In order to obtain more precise information on the alignment of H5T–NO_2 molecules in a porous silicon matrix, we estimated the dichroic ratio for three samples using Eq. (1). For this purpose, we fitted the composite band in the region 800–890 cm^{-1} with four (for the bulk planar cell) or five (for the bulk homeotropic cell) Voight functions in order to determine the intensity of the band at ~830 cm^{-1}. The results of this fit are shown in Figs. 3a, 3b. It can be seen that the C–H aromatic out-of-plane deformation occurs at 831 cm^{-1} for both liquid crystal cells and for the porous matrix. The dichroic ratio R_{ij} is 31 for the cell with homeotropic alignment, 7 for the cell with planar alignment, and is only 0.4 for H5T–NO_2 infiltrated into the porous matrix. At first glance, it seems that the alignment in the porous matrix is even better than that for the bulk cell with planar alignment, but a more detailed analysis of both types of alignment for a number of triphenylene derivatives shows that this is not the case. The best planar alignment is observed for hexapentyltryphenylene (H5T) [7]. R_{ij} was found to be in the range from 3 to 5 for H5T.

We conclude that the obtained small value of the dichroic ratio is due either to the enhancement of the intensity of the low-frequency vibrational bands or to the dampening of the intensity of the high-frequency vibrational bands. In order to obtain more precise data on this issue, we compared the results obtained with all three samples in terms of absorption per unit volume. This was particularly important for the porous matrix in which the liquid crystal occupied only a part (V_{LC}) of the volume probed by the IR beam. This fraction was evaluated by multiplying the total volume (V) by the porosity (p = 9.5%). This comparison enabled us to conclude that strong intensity enhancement is observed for the low-frequency vibrational bands. This conclusion is further supported by a comparison of the intensities of the vibrational bands for the alkyl chain in the region 2800–3200 cm^{-1}. It is accepted that the alkyl chain is rather disordered for discotic liquid crystals and its absorption intensity in this range for different cells depends only on thickness, being independent of the alignment.

Assignment of infrared vibrational bands

Band assignment and orientation of the transition dipole moment with respect to the core		H5T–NO_2 cm^{-1}	SCE8 cm^{-1}
CH_2 symmetric stretching	⊥	2861	2856
asymmetric stretching		2934	2926
CH_3 symmetric stretching	⊥	2873	2873
asymmetric stretching		2957	2955
N=O asymmetric stretching	⊥	1530	–
C–C aromatic stretching	∥	1507	1513
		1521	
		1616	1606
NO bending	⊥	845	–
C–H aromatic out-of-plane	⊥	890	846
deformation		831	829
		818	
		791	
C–C aromatic out-of-plane deformation	⊥		765
NO_2 wagging	∥	750	–
C–H rocking	⊥	733	722

Therefore, we compared the spectra of different samples by reducing their intensity in the range 2600 cm^{-1} to the same value. This normalization procedure allowed us to conclude that there is a strong intensity enhancement (~15 times) for the low-frequency vibrational bands.

Finally, it is obvious from our results that the alignment of H5T–NO_2 in *ma*-PS is planar with respect to the wafer surface. However, as seen from Fig. 4b, the alignment of discotic LCs is homeotropic with respect to the pore walls. This is in agreement with the results of a previously published work [7], where a high stability of homeotropic alignment was found for discotic liquid crystals deposited on untreated substrates.

2.2. Ferroelectric Liquid Crystals

It should be noted that for this type of molecular shape, we have to take into account the polarization of light when measuring the spectrum of the cell with planar alignment. We use the following notation: $P = 0°$ for the electric vector of the incident light coinciding with the long molecular axis, and $P = 90°$ otherwise. The IR spectra of SCE8 introduced into a porous silicon matrix show that the relative intensities of (*i*) "parallel" and (*j*) "perpendicular" bands are, in this case, close to that observed for the bulk LC cell with homeotropic alignment (Fig. 5). In particular, as seen from Figs. 5a and 5b, the intensity of the C–C aromatic stretching vibration

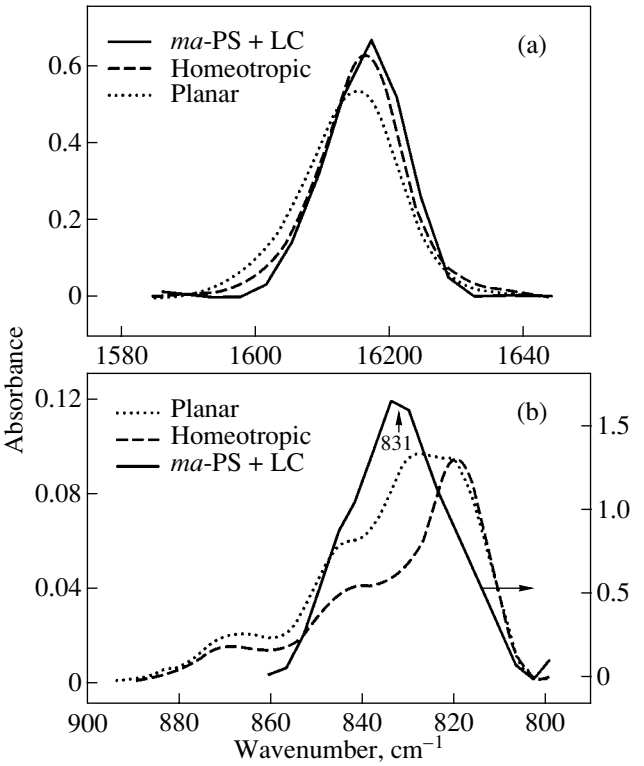

Fig. 2. FTIR spectra of the H5T–NO_2 discotic liquid crystal infiltrated into porous silicon (solid line) and embedded in ZnSe cells with planar (dotted line) and homeotropic (dashed line) alignments. (a) C–C stretching band, parallel to the core; (b) C–H aromatic out-of-plane deformation band, perpendicular to the core. (Note the different scales for the heavy line in (b) and the fact that the absorption of all the samples is reduced in accordance with the intensity of the alkyl chain vibrations in the region 2800–3200 cm^{-1}.)

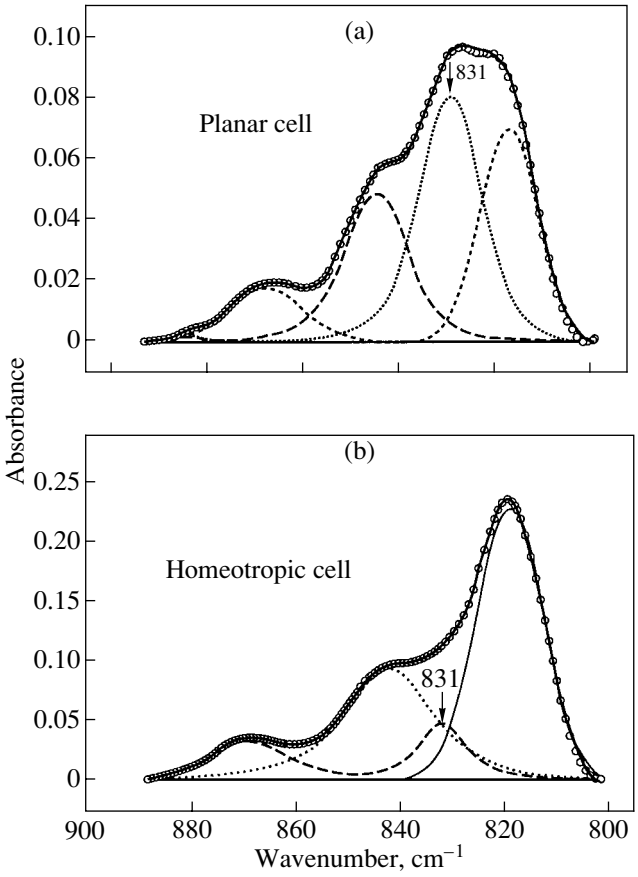

Fig. 3. Example of the fitting procedure for the low-frequency band for H5T–NO_2 contained in (a) planar and (b) homeotropic cells. Note that the thickness of the homeotropic cell is 2.45 times that of the planar cell.

(*i*-band at ~1513 cm^{-1}) in the case of the planar cell is much higher with a polarizer angle of 0° (II polarization) when the electric vector of the incident light coincides with the orientation of the transition dipole moment for this molecular unit. At the same time, the intensity of the *j*-bands perpendicular to the core vibrations (e.g., C–H out-of-plane deformation at ~828, C–C aromatic out-of-plane deformation at ~765, and CH_2 rocking vibrations at ~722 cm^{-1}) is smaller. The intensity ratio found for these bands in the case of a planar cell at a polarizer angle of 0° is $R_{ij} = A_{1513}/A_{765} = 4.3$. For the homeotropic LC cell, the intensity of the perpendicular bands increases, at least, in comparison with the intensity of the parallel bands, owing to the difference in oscillator strength. In this case, the intensity ratio $R_{ij} = A_{1513}/A_{765} = 1.1$. For the SCE8 infiltrated into the porous matrix, this ratio of $R_{ij} = A_{1513}/A_{765} = 0.4$ is even smaller than that obtained for the homeotropic LC cell and indicates that the alignment of a ferroelectric liquid crystal in a confined porous silicon matrix is definitely homeotropic with respect to the substrate's plane (Fig. 4a). This result coincides with the alignment obtained for nematic LCs deposited on untreated surfaces of Anapore membranes [17] and infiltrated into both microporous [18] and macroporous [12] silicon. Such an orientation is expected if one considers the alignment of rodlike molecules with respect to the surface of the pore, in which case the alignment is planar. The planar alignment is typically observed for rodlike molecules on various untreated surfaces, including crystalline silicon [19]. Only a special surface treatment or coating of the substrate surface by a surfactant

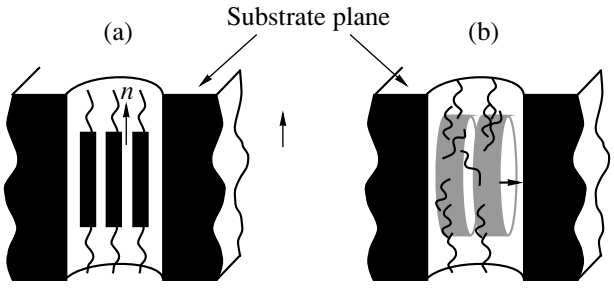

Fig. 4. Side view of the orientation of (a) ferroelectric and (b) discotic liquid crystals in the macroporous silicon matrix.

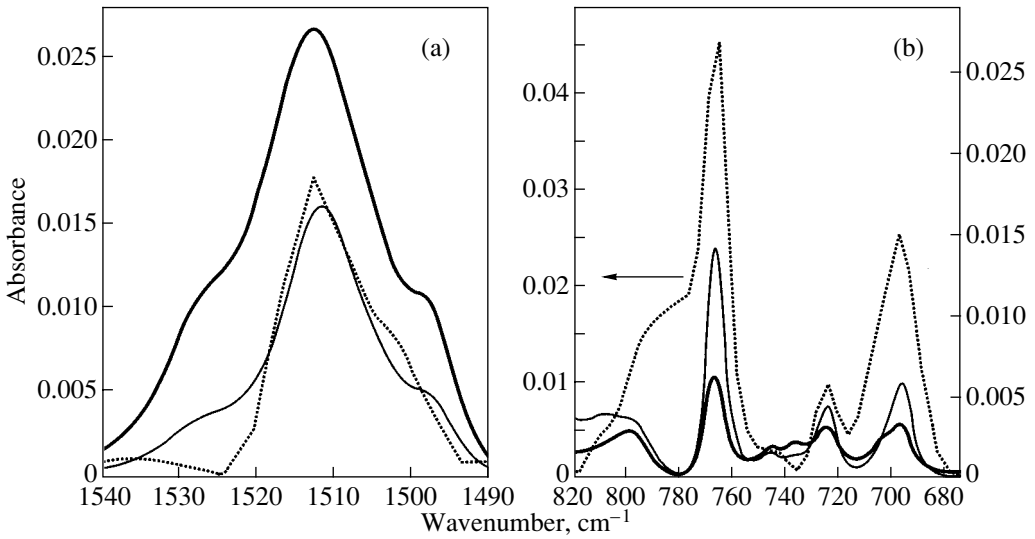

Fig. 5. FTIR spectra of the SCE8 ferroelectric liquid crystal infiltrated into porous silicon (short dotted line) and contained in ZnSe cells with planar (heavy solid line) and homeotropic (thin solid line) alignments. (Note the different scales for the heavy line in (b) and the fact that the absorption of the FLC cells decreases by a factor of 20 for both cells.)

may give a homeotropic alignment of LCs formed from rodlike molecules.

In the course of these investigations, we found strong intensity enhancement of the low-frequency vibrational bands in the region 600–900 cm^{-1} for both types of liquid crystals in *ma*-PS. This enhancement becomes noticeable when comparing the intensity ratios for the parallel and perpendicular bands. As already mentioned, this intensity ratio is much smaller than that obtained for both LC cells with homeotropic alignment. Moreover, this enhancement is observed for both parallel and perpendicular vibrational bands shown in the low-frequency region. A similar effect has been observed by Alieva *et al.* [20] for the species in the microcavity of a 1*D* photonic structure. It is worth noting that the enhancement takes place as soon as the light wavelength becomes close to the period of the artificial lattice (12 μm). Although the frequency range is, in our case, outside the main photonic band gap, which is expected in the lower frequency range, this observation seems to be related to the properties of holey wave guides [21].

Thus, we conclude that traditional IR methods cannot establish the alignment of liquid crystals infiltrated into a macroporous silicon matrix. We propose a new technique for determining the alignment which is based on FTIR investigation of LCs in the mesophase and implies a comparison of the intensity of different vibrational bands, namely, those with the transition dipole moment parallel and perpendicular to the core. This method is of particular interest for discotic liquid crystals, since it allows the alignment to be determined without heating a sample to the temperature of the isotropic phase or using oblique transmission IR spectroscopy.

With this method, the alignments of two kinds of liquid crystals infiltrated into a macroporous silicon matrix have been determined. The channel walls of macroporous silicon affect the orientation of LC molecules such that the column axis of the discotic LC is perpendicular to the walls. The long molecular axis of the rodlike molecules of the ferroelectric LC is aligned along the channel walls. A strong intensity enhancement of the low-frequency vibrational bands was detected for both kinds of LCs infiltrated into the porous silicon matrix

ACKNOWLEDGMENTS

The financial support of Enterprise Ireland through the International Collaboration Program IC/2001/042, the Russian State Program “Nanostructures in Physics,” and the St. Petersburg Science Center Program “Low Dimensional Structures” are gratefully acknowledged.

REFERENCES

1. T. Bellini, N. A. Clark, C. D. Muzny, *et al.*, Phys. Rev. Lett. **69** (5), 788 (1992).
2. N. A. Clark, T. Bellini, R. M. Malzbender, *et al.*, Phys. Rev. Lett. **71** (21), 3505 (1993).
3. G. S. Iannacchione, G. P. Crawford, S. Zumer, *et al.*, Phys. Rev. Lett. **71** (16), 2595 (1993).
4. H. Xu, J. K. Vij, A. Rappaport, and N. Clark, Phys. Rev. Lett. **79** (2), 249 (1997).
5. P. Ziherl, A. Sarlah, and S. Žumer, Phys. Rev. E **58** (1), 602 (1998).
6. P. Ziherl and S. Žumer, Phys. Rev. Lett. **78** (4), 682 (1997).
7. T. S. Perova, J. K. Vij, and A. Kocot, Adv. Chem. Phys. **113**, 341 (2000).

8. A. Kocot, J. K. Vij, and T. S. Perova, Adv. Chem. Phys. **113**, 203 (2000).
9. O. Bisi, S. Ossicino, and L. Pavesi, Surf. Sci. Rep. **38** (1–3), 1 (2000).
10. U. Gruning and V. Lehmann, Appl. Phys. Lett. **68** (6), 747 (1996).
11. A. Chelnokov, K. Wang, S. Rowson, *et al.*, Appl. Phys. Lett. **77** (19), 2943 (2000).
12. S. W. Leonard, J. P. Mondia, H. M. van Driel, *et al.*, Phys. Rev. B **61** (4), R2389 (2000).
13. M. Thonissen, M. Marso, R. Arens-Fisher, *et al.*, J. Porous Mater. **7** (1/3), 205 (2000).
14. S. Kumar, M. Manickam, V. S. K. Balagurusamy, and H. Schonherr, Liq. Cryst. **26** (10), 1455 (1999).
15. V. Lehmann and H. Foll, J. Electrochem. Soc. **137** (2), 653 (1990).
16. N. M. Shtykov, J. K. Vij, M. I. Barnik, and H. T. Nguyen, Kristallografiya **45** (4), 745 (2000) [Crystallogr. Rep. **45**, 682 (2000)].
17. H. Binder, H. Schmiedel, G. Lantzsch, *et al.*, Liq. Cryst. **21** (3), 415 (1996).
18. M. V. Wolkin, S. Chan, and P. M. Fauchet, Phys. Status Solidi A **182** (1), 573 (2000).
19. A. Sonin, *The Surface Physics of Liquid Crystals* (Gordon & Breach, Amsterdam, 1995).
20. E. V. Alieva, L. A. Kuzik, G. Mattei, *et al.*, Phys. Status Solidi A **175** (1), 115 (1999).
21. A. M. Zheltikov, Usp. Fiz. Nauk **170** (11), 1203 (2000).